sensors

Special Issue Reprint

EEG Signal Processing Techniques and Applications

2nd Edition

Edited by
Yifan Zhao, Fei He, Yuzhu Guo and Hua-Liang Wei

mdpi.com/journal/sensors

MDPI

EEG Signal Processing Techniques and Applications—2nd Edition

EEG Signal Processing Techniques and Applications—2nd Edition

Guest Editors

Yifan Zhao
Fei He
Yuzhu Guo
Hua-Liang Wei

MDPI

Basel • Beijing • Wuhan • Barcelona • Belgrade • Novi Sad • Cluj • Manchester

Guest Editors
Yifan Zhao
Faculty of Engineering and Applied Sciences
Cranfield University
Cranfield
UK

Fei He
Centre for Computational Science and Mathematical Modelling
Coventry University
Coventry
UK

Yuzhu Guo
School of Automation Science and Electrical Engineering
Beihang University
Beijing
China

Hua-Liang Wei
School of Electrical and Electronic Engineering
The University of Sheffield
Sheffield
UK

Editorial Office
MDPI AG
Grosspeteranlage 5
4052 Basel, Switzerland

This is a reprint of the Special Issue, published open access by the journal *Sensors* (ISSN 1424-8220), freely accessible at: https://www.mdpi.com/journal/sensors/special_issues/864QWXBQH7.

For citation purposes, cite each article independently as indicated on the article page online and as indicated below:

Lastname, A.A.; Lastname, B.B. Article Title. *Journal Name* **Year**, *Volume Number*, Page Range.

ISBN 978-3-7258-3607-9 (Hbk)
ISBN 978-3-7258-3608-6 (PDF)
https://doi.org/10.3390/books978-3-7258-3608-6

Contents

About the Editors . . . . **vii**

Hua-Liang Wei, Yuzhu Guo, Fei He and Yifan Zhao
EEG Signal Processing Techniques and Applications—2nd Edition
Reprinted from: *Sensors* **2025**, *25*, 805, https://doi.org/10.3390/s25030805 . . . . **1**

Tat'y Mwata-Velu, Edson Niyonsaba-Sebigunda, Juan Gabriel Avina-Cervantes, Jose Ruiz-Pinales, Narcisse Velu-A-Gulenga and Adán Antonio Alonso-Ramiréz
Motor Imagery Multi-Tasks Classification for BCIs Using the NVIDIA Jetson TX2 Board and the EEGNet Network
Reprinted from: *Sensors* **2023**, *23*, 4164, https://doi.org/10.3390/s23084164 . . . . **9**

Vedran Jurdana, Miroslav Vrankic, Nikola Lopac and Guruprasad Madhale Jadav
Method for Automatic Estimation of Instantaneous Frequency and Group Delay in Time–Frequency Distributions with Application in EEG Seizure Signals Analysis
Reprinted from: *Sensors* **2023**, *23*, 4680, https://doi.org/10.3390/s23104680 . . . . **29**

Rodrigo Vitório, Ellen Lirani-Silva, Diego Orcioli-Silva, Victor Spiandor Beretta, Anderson Souza Oliveira and Lilian Teresa Bucken Gobbi
Electrocortical Dynamics of Usual Walking and the Planning to Step over Obstacles in Parkinson's Disease
Reprinted from: *Sensors* **2023**, *23*, 4866, https://doi.org/10.3390/s23104866 . . . . **58**

Qi Wang, Daniel Smythe, Jun Cao, Zhilin Hu, Karl J. Proctor, Andrew P. Owens and Yifan Zhao
Characterisation of Cognitive Load Using Machine Learning Classifiers of Electroencephalogram Data
Reprinted from: *Sensors* **2023**, *23*, 8528, https://doi.org/10.3390/s23208528 . . . . **71**

Yanting Xu, Hongyang Zhong, Shangyan Ying, Wei Liu, Guibin Chen, Xiaodong Luo and Gang Li
Depressive Disorder Recognition Based on Frontal EEG Signals and Deep Learning
Reprinted from: *Sensors* **2023**, *23*, 8639, https://doi.org/10.3390/s23208639 . . . . **87**

Ilaria Siviero, Davide Bonfanti, Gloria Menegaz, Silvia Savazzi, Chiara Mazzi and Silvia Francesca Storti
Graph Analysis of TMS–EEG Connectivity Reveals Hemispheric Differences following Occipital Stimulation
Reprinted from: *Sensors* **2023**, *23*, 8833, https://doi.org/10.3390/s23218833 . . . . **105**

Andrea Farabbi and Luca Mainardi
Domain-Specific Processing Stage for Estimating Single-Trail Evoked Potential Improves CNN Performance in Detecting Error Potential
Reprinted from: *Sensors* **2023**, *23*, 9049, https://doi.org/10.3390/s23229049 . . . . **126**

Ibrahim Alreshidi, Desmond Bisandu and Irene Moulitsas
Illuminating the Neural Landscape of Pilot Mental States: A Convolutional Neural Network Approach with Shapley Additive Explanations Interpretability
Reprinted from: *Sensors* **2023**, *23*, 9052, https://doi.org/10.3390/s23229052 . . . . **142**

Jusciaane Chacon Vieira, Luiz Affonso Guedes, Mailson Ribeiro Santos and Ignacio Sanchez-Gendriz
Using Explainable Artificial Intelligence to Obtain Efficient Seizure-Detection Models Based on Electroencephalography Signals
Reprinted from: *Sensors* **2023**, *23*, 9871, https://doi.org/10.3390/s23249871 . . . . **162**

Tustanah Phukhachee, Suthathip Maneewongvatana, Chayapol Chaiyanan, Keiji Iramina and Boonserm Kaewkamnerdpong
Identifying the Effect of Cognitive Motivation with the Method Based on Temporal Association Rule Mining Concept
Reprinted from: *Sensors* **2024**, *24*, 2857, https://doi.org/10.3390/s24092857 . . . . **183**

Joharah Khabti, Saad AlAhmadi and Adel Soudani
Optimal Channel Selection of Multiclass Motor Imagery Classification Based on Fusion Convolutional Neural Network with Attention Blocks
Reprinted from: *Sensors* **2024**, *24*, 3168, https://doi.org/10.3390/s24103168 . . . . **203**

Baiyang Wang, Yidong Xu, Siyu Peng, Hongjun Wang and Fang Li
Detection Method of Epileptic Seizures Using a Neural Network Model Based on Multimodal Dual-Stream Networks
Reprinted from: *Sensors* **2024**, *24*, 3360, https://doi.org/10.3390/s24113360 . . . . **232**

Colince Meli Segning, Rubens A. da Silva and Suzy Ngomo
An Innovative EEG-Based Pain Identification and Quantification: A Pilot Study
Reprinted from: *Sensors* **2024**, *24*, 3873, https://doi.org/10.3390/s24123873 . . . . **249**

Sun Zhou, Pengyi Zhang and Huazhen Chen
Latent Prototype-Based Clustering: A Novel Exploratory Electroencephalography Analysis Approach
Reprinted from: *Sensors* **2024**, *24*, 4920, https://doi.org/10.3390/s24154920 . . . . **268**

Li Ji, Leiye Yi, Haiwei Li, Wenjie Han and Ningning Zhang
Detection of Pilots' Psychological Workload during Turning Phases Using EEG Characteristics
Reprinted from: *Sensors* **2024**, *24*, 5176, https://doi.org/10.3390/s24165176 . . . . **290**

Arnau Dillen, Mohsen Omidi, Fakhreddine Ghaffari, Olivier Romain, Bram Vanderborght, Bart Roelands, et al.
User Evaluation of a Shared Robot Control System Combining BCI and Eye Tracking in a Portable Augmented Reality User Interface
Reprinted from: *Sensors* **2024**, *24*, 5253, https://doi.org/10.3390/s24165253 . . . . **309**

Sumair Aziz, Muhammad Umar Khan, Khushbakht Iqtidar and Raul Fernandez-Rojas
Diagnosis of Schizophrenia Using EEG Sensor Data: A Novel Approach with Automated Log Energy-Based Empirical Wavelet Reconstruction and Cepstral Features
Reprinted from: *Sensors* **2024**, *24*, 6508, https://doi.org/10.3390/s24206508 . . . . **326**

Doli Hazarika, K. N. Vishnu, Ramdas Ransing and Cota Navin Gupta
Dynamical Embedding of Single-Channel Electroencephalogram for Artifact Subspace Reconstruction
Reprinted from: *Sensors* **2024**, *24*, 6734, https://doi.org/10.3390/s24206734 . . . . **346**

About the Editors

Yifan Zhao

Yifan Zhao is a full Professor of Data Science in the Faculty of Engineering and Applied Sciences at Cranfield University, UK. He has over 20 years of experience in signal processing, computer vision and artificial intelligence (AI) for degradation assessment and anomaly detection in complex engineering systems. He is dedicated to developing and applying advanced data analysis approaches in order to solve real-world problems in the sectors of construction ('TRAMS', Innovate UK, 10093011, 'Fuel Coach', BEIS, EEF8037; 'The Learning Camera', Innovate UK, 104794; 'One Source of Truth', Innovate UK, 105881), transport ('CogShift', EPSRC, EP/N012089/1), healthcare ('SecureUltrasound', EPSRC, EP/R013950/1) and supply chain ('RECBIT', Lloyd's Register Foundation (GA/100113). He holds the Royal Academy of Engineering Industrial Fellowship (IF2223B-110) for the development of innovative data-centric solutions aimed at reducing greenhouse gas emissions and fuel consumption. He has published more than 200 peer-reviewed journal and conference papers, four books and three patents.

Fei He

Dr Fei He is an Associate Professor at Coventry University, UK. His research interests lie at the interface of control systems engineering, signal processing and neuroscience. Dr He has been developing nonlinear system identification, frequency-domain analysis, and deep learning techniques to study complex interactions in human brain network related to neurological disorders. He is the PI and Co-I of several EPSRC grants. Dr He is a Senior Member of IEEE and serves as an Associate Editor of *IEEE Transactions on Neural Systems and Rehabilitation Engineering*, *Frontiers in Neurology*, and *IET Healthcare Technology Letters*.

Yuzhu Guo

Dr Yuzhu Guo, Ph.D., is an Associate Professor at the School of Automation Science and Electrical Engineering and director of the BAIoT Beihang-Boardware-Barco joint Lab of Brain and Intelligence, Beihang University, Beijing, China. His current research interests include brain mode decomposition theory, neurorehabilitation, neural field dynamics, acceleration cells and brain-inspired navigation, emphasising the application of dynamic system theory and Al technologies in EEG/sEEG decoding and multimodal information integration. He is the PI and co-PI of over 10 scientific projects and has co-authored over 60 journal papers. He has also contributed to customer-grade EEG acquisition devices and new applications of brain–computer interfaces.

Hualiang Wei

Hua-Liang Wei received the Ph.D. degree in the Department of Automatic Control and Systems Engineering (ACSE), the University of Sheffield, UK, in 2004. Dr Wei is currently a Senior Lecturer (Associate Professor) with the School of Electrical and Electronic Engineering (SoEEE) at the University of Sheffield. He is head of the Digital Medicine & Computational Neuroscience (DMCN), head of the laboratory of Dynamic Modelling and head of the laboratory Data Mining and Decision Making (3DM). He has been awarded grants (as PI and Co-I) from a variety of funding bodies including EPSRC, NERC, STFC, EU H2020, the Royal Society and so on. He has published more than 160 peer-reviewed papers. His main research interests are in signal processing, nonlinear system identification, interpretable machine learning and explainable AI, data-driven modelling, knowledge-informed predictive modelling, intelligent fault detection and diagnosis. He has been devoting to these areas for over 20 years, tackling challenging issues at the interface of Data Science, Computer Science and Control & Systems Engineering, to develop new and fundamental methods that can be adapted to solve challenging, complex systems modelling problems in multi- and inter-disciplinary areas including EEG signal processing, medical and bio-medical, weather and climate, space weather, neurophysiology, neuroscience and healthcare.

sensors

MDPI

Editorial

EEG Signal Processing Techniques and Applications—2nd Edition

Hua-Liang Wei [1], Yuzhu Guo [2], Fei He [3] and Yifan Zhao [4,*]

[1] Department of Automatic Control and Systems Engineering, School of Electrical and Electronic Engineering, The University of Sheffield, Sheffield S1 3JD, UK; w.hualiang@sheffield.ac.uk
[2] School of Automation Science and Electrical Engineering, Beihang University, Beijing 100191, China; yuzhuguo@buaa.edu.cn
[3] Centre for Computational Science and Mathematical Modelling, Coventry University, Coventry CV1 2JH, UK; fei.he@coventry.ac.uk
[4] Faculty of Engineering and Applied Sciences, Cranfield University, Cranfield MK43 0AL, UK
* Correspondence: yifan.zhao@cranfield.ac.uk

Received: 7 January 2025
Accepted: 24 January 2025
Published: 29 January 2025

Citation: Wei, H.-L.; Guo, Y.; He, F.; Zhao, Y. EEG Signal Processing Techniques and Applications—2nd Edition. *Sensors* **2025**, *25*, 805. https://doi.org/10.3390/s25030805

1. Introduction

Electroencephalography (EEG), as a well-established, non-invasive tool, has been successfully applied to a wide range of conditions due to its many evident advantages, such as economy, portability, easy operation, easy accessibility, and widespread availability in hospitals. EEG signals, with ultra-high time resolution, are vital in understanding brain functions. Traditionally, considerable attention in EEG signal processing and analysis has been paid to understanding brain activities from various perspectives, such as the detection and identification of abnormal frequencies in specific biological states, spatial–temporal and morphological characteristics of neurological disorder behaviours (e.g., paroxysmal or persistent discharges), the response of the brain nervous/neurological system to external stimuli, and the effects and responses to intermittent photic stimulation [1].

The past few years have seen rapid and significant advancement in signal processing, signal-based analysis, artificial intelligence (AI), machine learning (ML), and many other signal-based and data-driven techniques, propelling EEG signal processing into a new era with exciting progress in many areas, in order to meet growing demands and challenges in various real applications [2]. For example, some important nonlinear features of brain dynamics, which cannot be uncovered using traditional methods, may be revealed through analyzing associated EEG signals using state-of-the-art techniques and therefore facilitate the applications of EEG in various fields [3,4].

Recent years have witnessed an increasing number of EEG signal processing applications, aided by ML, AI, and other signal-based techniques in nearly all fields of science and engineering including neuroscience [5], clinical studies [6], brain–machine interfaces [7], cognitive science and psychology [8], human factors [9], and social interactions [10], to mention but a few. Methods and algorithms have been or are being developed to solve either the existing problems or emerging challenges faced by the world [11].

It is now the right time to delve further and deeper into investigations of EEG signal processing techniques. This Special Issue serves as a platform for the dissemination of the latest research results, findings, and trends in EEG signal processing and their applications, with particular attention to applications of machine learning and deep neural network methods. A total of 18 papers were collated as a part of this Special Issue and they can be roughly classified into six groups as follows:

- Brain–computer interfaces (Papers 1, 7, 11, and 16)
- Brain and neurological disorder detection and diagnosis (Papers 2, 3, 9, 12, 14, and 17)
- Cognitive and psychology studies (Papers 4, 10 and 15)
- Healthcare including mental health, pain identification, and depression diagnosis (Papers 5, 8, and 13)
- Brain functional connectivity (Paper 6)
- EEG artifact reduction and removal (Paper 18)

2. Overview of Contributions

In the following section, a short overview of each of the above six topics is provided, followed by a brief summary of each of the papers in the corresponding topic group.

2.1. EEG-Based Brain–Computer Interface

An EEG-based Brain–Computer Interface (BCI) is a system that uses EEG electrodes to measure brain activity and translate the associated signals into specific commands to drive external devices [12]. Initially, these applications were developed to assist patients, helping them regain normalcy in their lives. However, over time, BICs have also found significant use in non-medical domains, improving efficiency and collaboration among healthy individuals and aiding in personal development [12].

The authors of Paper 1 (Mwata-Velu et al.) proposed an embedded multi-task classifier based on motor imagery using the EEGNet toolbox (which is a compact Convolutional Network platform for EEG-based BCIs) and implemented the designed BCI system into a NVIDIA Jetson TX2 hardware platform. The performance of the proposed EEG-BCI system was tested on a public dataset, with the experimental results showing that the proposed system was suitable for online applications.

The authors of Paper 7 (Farabbi and Mainardi) presented a novel approach to enhancing Error Potential (ErrP) detection during single-trial (ST) stimulation tasks using conventional Convolutional Neural Networks (CNNs). The performance of the proposed approach was tested on an open-access EEG dataset, with the experimental results providing strong evidence that the proposed method was highly effective in improving ST-ErrP accuracy compared with several baseline methods.

The authors of Paper 11 (Khabti et al.) proposed a new Fusion Convolutional Neural Network with Attention blocks (FCNNA) model for optimal channel selection and multiclass Motor Imagery (MI) classification. The experimental results on a benchmark dataset (i.e., the BCI IV 2a dataset) showed that the proposed EEG-MI model outperformed the compared channel selection and classification methods.

The authors of Paper 16 (Dillen et al.) proposed an innovative control approach to assistive robotics by integrating BCI and eye-tracking techniques into a shared control system for a mobile augmented reality user interface. The system was designed to facilitate individuals with physical disabilities, particularly those with impaired motor function. While the research findings indicated that the shared BCI control system is effective for task completion and demonstrated the feasibility of the shared control strategy, the current efficiency of the BCI still requires further improvement for practical real-world applications.

2.2. Brain and Neurological Disorder Detection and Diagnosis

Brain and neurological disorders represent major global healthcare issues. Early detection of any disorder is crucial for curing patients or helping to prevent disease progression. Signal-based and data-driven modelling techniques, such as time–frequency analysis, information theory, machine learning, and artificial intelligence methods, are being increasingly used in brain and neurological disorder detection and diagnosis [13].

The authors of Paper 2 (Jurdana et al.) introduced a novel method for estimating instantaneous frequencies and group delays, which can be used to better detect seizures with both spike and oscillatory characteristics. The main advantage of the proposed method is that it makes use of Localised Rényi Entropies (LREs) to generate time–frequency information that better characterises the relevant signals.

The authors of Paper 3 (Vitório et al.) aimed to understand Parkinson's disease (PD) by analysing the associated scalp EEG (sEEG) signals. The authors delve into investigating whether PD patients present distinct brain electrocortical activity during regular walking and during obstacle avoidance walking in comparison with healthy individuals. Experiments were carried out on 14 healthy older adults and 15 patients with PD. The research findings suggest that the PD patent EEG signals showed a greater proportion of low-frequency neuronal firing in brain areas related to motor commands and sensorimotor integration during walking.

The authors of Paper 9 (Vieira et al.) presented a feature dimensionality reduction method for epileptic seizure detection, aimed at reducing the number of channels required for classification and therefore making better use of the interpretability of machine learning models. The performance of the proposed method was tested on a publicly accessible dataset provided by the University of Beirut Medical Center. The proposed method showed an advantage in solving tasks with a relatively smaller number of channels, enabling the development of effective mobile applications for epileptic seizure detection.

The authors of Paper 12 (Wang et al.) proposed a feature extraction method by designing a multimodal dual-stream neural network model, constructed using convolution and Long Short-Term Memory (LSTM) neural networks. An advantage of the proposed method is that it can make use of several types of features in time and frequency domains, in addition to various signal differential features. According to the experimental results for experiments performed on several benchmark datasets, the proposed method outperformed comparable methods.

The authors of Paper 14 (Zhou et al.) designed a novel and interesting unsupervised approach for exploratory EEG analysis by defining low-dimensional prototypes in latent space, based on which EEG clustering and classification are performed. The proposed method was acquired by using Wavelet transform, a Generative Adversarial Network (GAN), and an extended Stein Latent Optimisation (SLO) scheme for the GAN. The proposed approach, W-SLOGAN, showed promising performance for diagnosing epilepsy subtypes and classifying multiple labelled EEG data.

The authors of Paper 17 (Aziz et al.) introduced an innovative automated approach for detecting Schizophrenia based on EEG signals. The approach was developed by using a fast independent component analysis method to remove artefacts from raw EEG data first and then using a novel Automated Log Energy-based Empirical Wavelet Reconstruction (ALEEWR) method to reconstruct decomposed signals to obtain relevant EEG signatures. The results of experiments performed on a benchmark dataset showed that the proposed approach appeared to achieve exceptionally excellent performance for Schizophrenia detection compared to many existing methods.

2.3. EEG for Cognitive and Psychology Studies

In addition to its application in studying brain and neurological disorders as mentioned above, EEG has been increasingly applied to different areas of cognitive and psychology research, such as cognitive load, attention, memory, and emotional processing [14,15]. One important application is neurofeedback training, where individuals learn to regulate their brain activity, showing promise in treating conditions such as Attention-Deficit/Hyperactivity Disorder (ADHD) and anxiety [16]. EEG is also used in conjunction with other neuroimaging techniques, such as fMRI and MEG, to provide a more comprehensive and better understanding of brain dynamics [17].

The authors of Paper 4 (Wang et al.) presented a feasibility study on investigating drivers' brain activity patterns by performing simulations of various levels of cognitive load based on four designed driving tasks. The authors used deep neural networks and four Support Vector Machines (SVMs) to classify EEG signals measured to differentiate driving conditions. The research results and findings show potential in improving the performance of the human–machine interface of vehicles and thus help to improve safety.

The authors of Paper 10 (Phukhachee et al.) introduced a new method to identify the cognitive motivation effect with a reduced number of EEG electrodes. The authors hypothesised that the temporal relationship of brain activities between attention- and memorisation-related areas could aid in identifying the effect of motivation on remembering the associated stimulus, with the number of electrodes reduced to two (i.e., the FCz and P3 electrodes). They proposed a method based on the temporal association rule mining (TARM) concept to identify the motivation effect from the temporal relationship of brain activities between attention and memorisation areas while the participants are being motivated. The proposed approach was implemented using an SVM, whose hyper-parameters were obtained by using the Artificial Bee Colony (ABC) algorithm. The results of experiments on a benchmark dataset provide valuable support for the original hypothesis.

The authors of Paper 15 (Ji et al.) carried out investigations on understanding and detecting pilots' psychological workload during turning phases using EEG signals collected from pilots during left and right turns in simulated flight scenarios. The analysis includes the changes in EEG signals, variations in EEG power, and the correlations between EEG power and turning maneuvers. The results given by the designed SVM classifier showed that significant changes occurred in the energy ratio of beta waves and Shannon entropy during left and right turns compared to the cruising phase. The research findings are potentially useful for flight training and enhancing flight safety.

2.4. Healthcare—Mental Health, Pain Identification, and Depression Diagnosis

EEG represents a powerful tool in healthcare, particularly for mental health, pain identification, and depression diagnosis. In mental health, EEG is used to diagnose and monitor psychiatric and neuropsychiatric disorders [18,19]. It helps in identifying abnormalities in brain activity that may be associated with conditions such as epilepsy, which often coexists with psychiatric disorders [19]. EEG can also be used to study and modify local cerebral disorders related to abnormal behaviour [18]. In pain identification, EEG-based pain identification involves analyzing brain signals to detect and quantify pain [20,21]. In depression diagnosis, EEG is used in diagnosing depression by detecting specific physiological changes in the brain [22]. Advanced machine learning and deep learning techniques have been applied to EEG data to improve diagnostic accuracy [23]. These methods involve the analysis of neural oscillations and asymmetries in brain activity to identify depression more precisely.

The authors of Paper 5 (Xu et al.) proposed a framework for depressive disorder (DD) recognition based on six frontal-channel EEG data sources. Two deep learning models, a multi-resolution CNN (MRCNN) combined with LSTM and an MRCNN combined with residual squeeze and excitation (RSE), were built to extract features and classify EEG signals. The results of experiments performed on a publicly available dataset with 128 EEG channels showed that the proposed approach effectively diagnosed depressive disorder.

The authors of Paper 8 (Alreshidi et al.) focused on predicting pilot mental states using EEG data. They developed an interpretable model to detect four mental states, namely, channelised attention, diverted attention, startle/surprise, and normal state. The SHapley Additive exPlanations (SHAP) values were used to identify the top 10 most influential features for each mental state. The work represents a significant advancement in the field of EEG-based pilot mental state detection.

The authors of Paper 13 (Segning et al.) presented a pilot study on the detection and evaluation of the magnitude of chronic pain. They introduced a scale-independent measure, referred to as the coefficient of variation of the upper envelope (CVUE), to characterise the associated EEG signals and used the measure to compare the degree of variation from one time-series to another. Experiments were carried out on three groups of volunteers, involving 41 participants with different types and different levels of chronic pain. The experimental results showed that the proposed method can effectively quantify pain in a population living with chronic pain.

2.5. Brain Functional Connectivity

Functional connectivity (FC) is a concept in neuroscience that is concerned with the temporal dependency of neuronal activation patterns in different brain regions, reflecting the statistical dependencies between these areas. Essentially, this concept is concerned with understanding how different parts of the brain communicate with one another over time. The main statistical measures used in FC include correlation, covariance, spectral coherence, and phase locking. Correlation measures the strength and direction of the linear relationship between two variables. Covariance indicates the extent to which two variables change together. Spectral coherence assesses the consistency of the phase relationship between two signals across different frequencies. Phase locking measures phase synchronisation between two signals. These dependencies can be highly time-dependent, fluctuating on multiple time scales from milliseconds to seconds, reflecting the dynamic nature of brain activity. Functional connectivity has important applications in both research and clinical settings. It can be used to understand normal brain function, identify biomarkers for neurological and psychiatric disorders, and even guide interventions and treatments [24].

The authors of Paper 6 (Siviero et al.) applied a Bayesian estimation approach to estimate Transcranial Magnetic Stimulation (TMS)-evoked potentials (TEPs) from EEG data; such an approach has not been investigated in the context of transcranial magnetic stimulation combined with electroencephalography (TMS–EEG). The authors designed a self-tuning optimised Kalman (STOK) filter in conjunction with the information partial directed coherence (iPDC) measure to capture the rapid dynamics of information flow patterns, based on which time-varying connectivity matrices were derived. Graph analysis was then conducted to assess key network properties, offering a better understanding of how visual information is propagated across brain networks.

2.6. EEG Artifact Reduction and Removal

Artifacts are always undesired in EEG modelling and analysis as they distort the measurements of the signals of interest [25]. EEG signals can be compromised to some degree in either the time or frequency domain or both by artifacts stemming from internal or external sources [26]. There are a few major challenges in EEG artifact reduction and removal in many real applications, such as the requirement of calibration and effective evaluation criteria, the lack of EEG artifact benchmarks, and the existence of diversified artifacts.

The authors of Paper 18 (Hazarika et al.) proposed a novel approach that employed the artifact subspace reconstruction (ASR) algorithm to remove artifacts from single-channel EEG data. They introduced an embedded ASR (E-ASR) method to improve the efficiency of artifact removal. The proposed method was tested on a self-created, semi-simulated dataset. The experimental results showed the excellent overall performance of the proposed approach for handling single-channel EEG data.

Author Contributions: Conceptualization, H.-L.W. and Y.Z.; writing—original draft preparation, H.-L.W.; writing—review and editing, Y.G., F.H., Y.Z.; project administration, Y.Z. All authors have read and agreed to the published version of the manuscript.

Conflicts of Interest: The authors declares no conflicts of interest.

List of Contributions

1. Mwata-Velu, T.; Niyonsaba-Sebigunda, E.; Avina-Cervantes, J.G.; Ruiz-Pinales, J.; Velu-A-Gulenga, N.; Alonso-Ramírez, A.A. Motor imagery multi-tasks classification for BCIs using the NVIDIA Jetson TX2 Board and the EEGNet network. *Sensors* **2023**, *23*, 4164. https://doi.org/10.3390/s23084164.
2. Jurdana, V.; Vrankic, M.; Lopac, N.; Jadav, G.M. Method for automatic estimation of instantaneous frequency and group delay in time–frequency distributions with application in EEG seizure signals analysis. *Sensors* **2023**, *23*, 4680. https://doi.org/10.3390/s23104680.
3. Vitório, R.; Lirani-Silva, E.; Orcioli-Silva, D.; Beretta, V.S.; Oliveira, A.S.; Gobbi, L.T.B. Electrocortical dynamics of usual walking and the planning to step over obstacles in Parkinson's Disease. *Sensors* **2023**, *23*, 4866. https://doi.org/10.3390/s23104866.
4. Wang, Q.; Smythe, D.; Cao, J.; Hu, Z.; Proctor, K.J.; Owens, A.P.; Zhao, Y. Characterisation of cognitive load using machine earning classifiers of electroencephalogram data. *Sensors* **2023**, *23*, 8528. https://doi.org/10.3390/s23208528.
5. Xu, Y.; Zhong, H.; Ying, S.; Liu, W.; Chen, G.; Luo, X.; Li, G. Depressive disorder recognition based on frontal EEG signals and deep learning. *Sensors* **2023**, *23*, 8639. https://doi.org/10.3390/s23208639.
6. Siviero, I.; Bonfanti, D.; Menegaz, G.; Savazzi, S.; Mazzi, C.; Storti, S.F. Graph analysis of TMS–EEG connectivity reveals hemispheric differences following occipital stimulation. *Sensors* **2023**, *23*, 8833. https://doi.org/10.3390/s23218833.
7. Farabbi, A.; Mainardi, L. Domain-specific processing stage for estimating single-trail Evoked potential improves CNN performance in detecting error potential. *Sensors* **2023**, *23*, 9049. https://doi.org/10.3390/s23229049.
8. Alreshidi, I.; Bisandu, D.; Moulitsas, I. Illuminating the neural landscape of pilot mental states: a convolutional neural network approach with Shapley additive explanations interpretability. *Sensors* **2023**, *23*, 9052. https://doi.org/10.3390/s23229052.
9. Vieira, J.C.; Guedes, L.A.; Santos, M.R.; Sanchez-Gendriz, I. Using explainable artificial intelligence to obtain efficient seizure-detection models based on electroencephalography signals. *Sensors* **2023**, *23*, 9871. https://doi.org/10.3390/s23249871.
10. Phukhachee, T.; Maneewongvatana, S.; Chaiyanan, C.; Iramina, K.; Kaewkamnerdpong, B. Identifying the effect of cognitive motivation with the method based on temporal association rule mining concept. *Sensors* **2024**, *24*, 2857. https://doi.org/10.3390/s24092857.
11. Khabti, J.; AlAhmadi, S.; Soudani, A. Optimal channel selection of multiclass motor imagery classification based on fusion convolutional neural network with attention blocks. *Sensors* **2024**, *24*, 3168. https://doi.org/10.3390/s24103168.
12. Wang, B; Xu, Y.; Peng, S.; Wang, H.; Li, F. Detection method of epileptic seizures using a neural network model based on multimodal dual-stream networks. *Sensors* **2024**, *24*, 3360. https://doi.org/10.3390/s24113360.
13. Segning, C.M.; da Silva, R.A.; Ngomo, S. An innovative EEG-based pain identification and quantification: A pilot study. *Sensors* **2024**, *24*, 3873. https://doi.org/10.3390/s24123873.

14. Zhou, S.; Zhang, P.; Chen, H. Latent prototype-based clustering: a novel exploratory electroencephalography analysis approach. *Sensors* **2024**, *24*, 4920. https://doi.org/10.3390/s24154920.
15. Ji, L.; Yi, L.; Li, H.; Han, W.; Zhang, N. Detection of pilots' psychological workload during turning phases using EEG characteristics. *Sensors* **2024**, *24*, 5176. https://doi.org/10.3390/s24165176.
16. Dillen, A.; Omidi, M.; Ghaffari, F.; Romain, O.; Vanderborght, B.; Roelands, B.; Nowé, A.; De Pauw, K. User evaluation of a shared robot control system combining BCI and eye tracking in a portable augmented reality user interface. *Sensors* **2024**, *24*, 5253. https://doi.org/10.3390/s24165253.
17. Aziz, S.; Khan, M.U.; Iqtidar, K.; Fernandez-Rojas, R. Diagnosis of Schizophrenia using EEG sensor data: a novel approach with automated log energy-based empirical wavelet reconstruction and cepstral features. *Sensors* **2024**, *24*, 6508. https://doi.org/10.3390/s24206508.
18. Hazarika, D.; Vishnu, K.N.; Ransing, R.; Gupta, C.N. Dynamical embedding of single-channel electroencephalogram for artifact subspace reconstruction. *Sensors* **2024**, *24*, 6734. https://doi.org/10.3390/s24206734.

References

1. Sanei, S.; Chambers, J.A. *EEG Signal Processing and Machine Learning*; John Wiley & Sons: Hoboken, NJ, USA, 2021.
2. Hosseini, M.P.; Hosseini, A.; Ahi, K. A Review on machine learning for EEG signal processing in bioengineering. *IEEE Rev. Biomed. Eng.* **2020**, *14*, 204–218. [CrossRef]
3. Gu, Y.; Yang, Y.; Dewald, J.P.A.; van der Helm, F.C.T.; Schouten, A.C.; Wei, H.-L. Nonlinear modeling of cortical responses to mechanical wrist perturbations using the NARMAX method. *IEEE Trans. Biomed. Eng.* **2021**, *68*, 948–958. [CrossRef]
4. Cao, J.; Zhao, Y.; Shan, X.; Wei, H.; Guo, Y.; Chen, L.; Erkoyuncu, J.A.; Sarrigiannis, P.G. Brain functional and effective connectivity based on electroencephalography recordings: A review. *Hum. Brain Mapp.* **2022**, *43*, 860–879. [CrossRef] [PubMed]
5. Ienca, M.; Ignatiadis, K. Artificial Intelligence in Clinical Neuroscience: Methodological and Ethical Challenges. *Neuroscience* **2020**, *11*, 77–87. [CrossRef]
6. Tveit, J.; Aurlien, H.; Plis, S.; Calhoun, V.D.; Tatum, W.O.; Schomer, D.L.; Arntsen, V.; Cox, F.; Fahoum, F.; Gallentine, W.B.; et al. Automated Interpretation of Clinical Electroencephalograms Using Artificial Intelligence. *JAMA Neurol.* **2023**, *80*, 805–812. [CrossRef] [PubMed]
7. Wang, X.; Hersche, M.; Magno, M.; Benini, L. Mi-bminet: An efficient convolutional neural network for motor imagery brain–machine interfaces with eeg channel selection. *IEEE Sens. J.* **2024**, *24*, 8835–8847. [CrossRef]
8. Gong, X.; Li, X. Human–robot interactive communication and cognitive psychology intelligent decision system based on artificial intelligence—Case study. *Int. J. Humanoid Robot.* **2023**, *20*, 2240005. [CrossRef]
9. Chignell, M.; Wang, L.; Zare, A.; Li, J. The evolution of HCI and human factors: Integrating human and artificial intelligence. *ACM Trans. Comput.-Hum. Interact.* **2023**, *30*, 1–30. [CrossRef]
10. Bolotta, S.; Dumas, G. Social neuro AI: Social interaction as the "dark matter" of AI. *Front. Comput. Sci.* **2022**, *4*, 846440. [CrossRef]
11. Ein Shoka, A.A.; Dessouky, M.M.; El-Sayed, A.; Hemdan, E.E.D. EEG seizure detection: Concepts, techniques, challenges, and future trends. *Multimed. Tools Appl.* **2023**, *82*, 42021–42051. [CrossRef]
12. Lotte, F.; Bougrain, L.; Cichocki, A.; Clerc, M.; Congedo, M.; Rakotomamonjy, A.; Yger, F. A review of classification algorithms for EEG-based brain–computer interfaces: A 10 year update. *J. Neural Eng.* **2018**, *15*, 031005. [CrossRef]
13. Acharya, U.R.; Oh, S.L.; Hagiwara, Y.; Tan, J.H.; Adeli, H. Deep convolutional neural network for the automated detection and diagnosis of seizure using EEG signals. *Comput. Biol. Med.* **2018**, *100*, 270–278. [CrossRef]
14. Allen, J.J.B.; Keune, P.M.; Schönenberg, M.; Nusslock, R. Frontal EEG alpha asymmetry and emotion: From neural underpinnings and methodological considerations to psychopathology and social cognition. *Psychophysiology* **2018**, *55*, e13028. [CrossRef] [PubMed]
15. Babayan, A.; Erbey, M.; Kumral, D.; Reinelt, J.D.; Reiter, A.M.; Röbbig, J.; Schaare, H.L.; Uhlig, M.; Anwander, A.; Bazin, P.L.; et al. A mind-brain-body dataset of MRI, EEG, cognition, emotion, and peripheral physiology in young and old adults. *Sci. Data* **2019**, *6*, 180308. [CrossRef] [PubMed]
16. Markovska-Simoska, S.; Pop-Jordanova, N. Quantitative EEG in Children and Adults with Attention Deficit Hyperactivity Disorder: Comparison of Absolute and Relative Power Spectra and Theta/Beta Ratio. *Clin. EEG Neurosci.* **2017**, *48*, 20–32. [CrossRef] [PubMed]
17. Garcés, P.; Pereda, E.; Hernández-Tamames, J.A.; Del-Pozo, F.; Maestú, F.; Pineda-Pardo, J. Ángel Multimodal description of whole brain connectivity: A comparison of resting state MEG, fMRI, and DWI. *Hum. Brain Mapp.* **2015**, *37*, 20–34. [CrossRef]

18. Badrakalimuthu, V.R.; Swamiraju, R.; de Waa, H. Is EEG a useful test in adult psychiatry? *Adv. Psychiatr. Treat.* **2011**, *17*, 114–121. [CrossRef]
19. Sand, T.; Bjørk, M.H.; Vaaler, A.E. Is EEG a useful test in adult psychiatry? *Tidsskr. Nor. Legeforen.* **2013**, *133*, 1200–1204. [CrossRef]
20. Prichep, L.S.; Shah, J.; Merkin, H.; Hiesiger, E.M. Exploration of the pathophysiology of chronic pain using quantitative EEG source localization. *Clin. EEG Neurosci.* **2018**, *49*, 103–113. [CrossRef] [PubMed]
21. Sun, G.; Wen, Z.; Ok, D.; Doan, L.; Wang, J.; Chen, Z. Detecting acute pain signals from human EEG. *J. Neurosci. Methods* **2021**, *347*, 108964. [CrossRef] [PubMed]
22. Steiger, A.; Kimura, M. Wake and sleep EEG provide biomarkers in depression. *J. Psychiatry Res.* **2010**, *44*, 242–252. [CrossRef]
23. Khosla, A.; Khandnor, P.; Chand, T. Automated diagnosis of depression from EEG signals using traditional and deep-learning approaches: A comparative analysis. *Biocybern. Biomed. Eng.* **2022**, *42*, 108–142. [CrossRef]
24. Lang, E.W.; Tomé, A.M.; Keck, I.R.; Górriz-Sáez, J.M.; Puntonet, C.G. Brain connectivity analysis: A short survey. *Comput. Intell. Neurosci.* **2012**, *2012*, 12512. [CrossRef] [PubMed]
25. Urigüen, J.A.; Garciazapirain, B. EEG artifact removal—State-of-the-art and guidelines. *J. Neural Eng.* **2015**, *12*, 031001. [CrossRef] [PubMed]
26. Islam, M.K.; Rastegarnia, A.; Yang, Z. Methods for Artifact Detection and Removal from Scalp EEG: A Review. *Clin. Neurophysiol.* **2016**, *46*, 287–385. [CrossRef] [PubMed]

sensors

MDPI

Article

Motor Imagery Multi-Tasks Classification for BCIs Using the NVIDIA Jetson TX2 Board and the EEGNet Network

Tat'y Mwata-Velu [1,2,3,*], Edson Niyonsaba-Sebigunda [2], Juan Gabriel Avina-Cervantes [3], Jose Ruiz-Pinales [2], Narcisse Velu-A-Gulenga [4] and Adán Antonio Alonso-Ramírez [5]

1 Centro de Investigación en Computación, Instituto Politécnico Nacional (CIC-IPN), Avenida Juan de Dios Bátiz Esquina Miguel Othón de Mendizábal Colonia Nueva Industrial Vallejo, Alcaldía Gustavo A. Madero, Ciudad de Mexico C.P. 07738, Mexico
2 Institut Supérieur Pédagogique Technique de Kinshasa (I.S.P.T.-KIN), Av. de la Science 5, Gombe, Kinshasa 3287, Democratic Republic of the Congo; eniyonsaba@isptkin.ac.cd (E.N.-S.); pinales@ugto.mx (J.R.-P.)
3 Telematics and Digital Signal Processing Research Groups (CAs), Department of Electronics Engineering, Universidad de Guanajuato, Salamanca 36885, Mexico; avina@ugto.mx
4 Institut Supérieur Pédagogique de Kikwit (I.S.P. KIKWIT), Av Nzundu 2, Com. Lukolela, Kikwit 8211, Democratic Republic of the Congo
5 Instituto Tecnológico Nacional de México en Celaya (TecNM-Celaya), Av. Antonio García Cubas Pte 600, Celaya C.P. 38010, Guanajuato, Mexico; d2203002@itcelaya.edu.mx
* Correspondence: tmwata@cic.ipn.mx; Tel.: +52-4641818932

Abstract: Nowadays, Brain–Computer Interfaces (BCIs) still captivate large interest because of multiple advantages offered in numerous domains, explicitly assisting people with motor disabilities in communicating with the surrounding environment. However, challenges of portability, instantaneous processing time, and accurate data processing remain for numerous BCI system setups. This work implements an embedded multi-tasks classifier based on motor imagery using the EEGNet network integrated into the NVIDIA Jetson TX2 card. Therefore, two strategies are developed to select the most discriminant channels. The former uses the accuracy based-classifier criterion, while the latter evaluates electrode mutual information to form discriminant channel subsets. Next, the EEGNet network is implemented to classify discriminant channel signals. Additionally, a cyclic learning algorithm is implemented at the software level to accelerate the model learning convergence and fully profit from the NJT2 hardware resources. Finally, motor imagery Electroencephalogram (EEG) signals provided by HaLT's public benchmark were used, in addition to the k-fold cross-validation method. Average accuracies of 83.7% and 81.3% were achieved by classifying EEG signals per subject and motor imagery task, respectively. Each task was processed with an average latency of 48.7 ms. This framework offers an alternative for online EEG-BCI systems' requirements, dealing with short processing times and reliable classification accuracy.

Keywords: electroencephalogram; motor imagery; EEGNet; NVIDIA Jetson TX2; brain–computer interface; HaLT dataset

Citation: Mwata-Velu, T.; Niyonsaba-Sebigunda, E.; Avina-Cervantes, J.G.; Ruiz-Pinales, J.; Velu-A-Gulenga, N.; Alonso-Ramirez, A.A. Motor Imagery Multi-Tasks Classification for BCIs Using the NVIDIA Jetson TX2 Board and the EEGNet Network. *Sensors* **2023**, *23*, 4164. https://doi.org/10.3390/s23084164

Academic Editors: Yifan Zhao, Hua-Liang Wei, Yuzhu Guo and Fei He

Received: 13 March 2023
Revised: 15 April 2023
Accepted: 17 April 2023
Published: 21 April 2023

1. Introduction

Applications based on Brain–Computer Interfaces (BCI) are numerous in the recent literature due to their benefits in various domains [1]. Typically, BCI systems use brain signals to allow effective communication between a given user and local surroundings. BCI-based electroencephalographic signals (EEG) are the most implemented because of recent advances in brain electrical functioning studies and reliable technologies [2,3]. Such EEG signals were used by Fraiwan et al. [4] to evaluate the subjects' enjoyment and visual interest in experiencing museum expositions. For instance, BCI-based EEG signals are used in biomedical applications for mental and cognitive disease diagnoses and rehabilitation [5,6]. Lastly, Hekmatmanesh et al. [7] proposed a systematic review of terrestrial and aerial Brain–Controlled Vehicles (BCVs) based on EEG, Electrooculographic

(EOG), and Electromyographic (EMG) signals. Commonly, for BCI-based control systems, EEG signal patterns such as Steady-State Evoked Potentials (SSVEP) [8] and their variants are converted into commands to control wheelchairs, drones, prostheses, and arm robots, to cite a few.

Motor Imagery EEG signals (MI–EEG) are more interesting for EEG–BCI systems because the subject under test voluntarily generates such signals; thus, it can be used to control external applications [9,10] or for medical research [11,12]. Recent advances in developing BCIs based on MI signals focus on improving classification accuracy while reducing processing time and processing-unit computational resources [13,14]. This prevailing tendency is mainly motivated by online application requirements in robotics and specialized medicine to complete accurate and brief tasks satisfactorily [15]. In this sense, Huang et al. [16] controlled an integrated wheelchair robotic arm implementing a hybrid BCI based on EEG and EOG signals. Therefore, the robotic arm and wheelchair applications needed both high-accuracy classifications of left- and right-hand MI tasks and system portability to complete reliable actions. In another study, Al-Nuaimi et al. [17] implemented a controlled drone-based P300 BCI for military use, dealing with high accuracy, brief processing time, and BCI portability.

Concretely, numerous methods are used in the literature to conjointly address short processing time, reliable accuracy, and portability challenges. In this sense, channel selection -based strategies aim to process signals from a few discriminant electrodes instead of using all electrodes, reducing data size and processing algorithms' complexity and, consequently, the processing time. For example, Moctezuma et al. [18] proposed the Non-dominated Sorting Genetic Algorithm II in the emotion recognition BCI with wearable EEG systems, selecting a set of 8–10 EEG channels instead of the 32 available. In parallel, various techniques based on deep learning offer satisfactory results without EEG signal preprocessing or implementing complex learning acceleration algorithms. Such an approach reduces the processing time significantly depending on the implemented neural architectures [19,20]. Other strategies typically work on hardware-based levels using traditionally powerful processing units despite the robustness of reliable data and algorithms [21,22].

Fortunately, advances in hardware re-configurable design technology have enabled the development of embedded electronic boards with powerful computing resources [23]. Those embedded boards are microcomputers generally supporting complex data processing, ensuring portability and reduced signal processing time because of dedicated core resources. Meanwhile, Majoros and Oniga [24] implemented a MI–EEG classifier based on a deep learning architecture for BCI applications on a Field-Programmable Gate Arrays (FPGA) card. Their work achieved an accuracy of 97.7%, classifying imagined tasks of opening and closing fists or feet into three classes; the neutral task was included. Further, Dabas et al. [25] used the Arduino Uno board to classify hand-gripping MI trials from channels C3 and C4 using the Support Vector Machines (SVM) classifier.

On the other hand, deep learning architectures have proven to have high performance as EEG signal classifiers in recent works, especially the compact convolutional neural network for EEG-based BCI (EEGNet) and its variants proposed by Lawhern et al. [26]. In this sense, Zhu et al. [27] developed an ensemble learning coupled to the EEGNet network to improve the ear-EEG signals' classification for SSVEP-based BCI, achieving an accuracy of 81.74%. Lastly, Feng et al. [28] implemented a real-time EEGNet classifier on an FPGA board, using only 2.54% of the board's resources and consuming 3.66% of the maximum power available. Similarly, Tsukahara et al. [29] achieved an accuracy of 88.75%, implementing the EEGNet architecture on a Virtex-7 FPGA platform to classify EEG data from the MNE dataset.

This work develops an embedded MI tasks classifier for BCI systems based on the EEGNet network by using the NJT2 board. The framework develops a subject-dependent classification approach, where data from each subject are processed separately. Therefore, the MI movements to be classified are the tongue, passive, left and right hands, and left and right legs. In the first step, the Accuracy Rating-based Classifier method (ARbC) and Channels Mutual Information-based Approach (CMIbA) are developed to make up discriminant channel subsets. Next, MI signals from discriminant channels are processed to be classified into the six aforementioned classes using the EEGNet network.

The main contributions of this paper are summarized as follows,

1. Results comparison of channel selection between the ARbC method and CMIbA.
2. Reliable accuracy results of the tongue, passive, left and right hands, and left and right legs MI tasks classification.
3. Processing time reduction using the NJT2 platform resources.
4. Convergence acceleration of the learning process implementing the Cyclic Learning Rate (CLR) algorithm.

In sum, this work deals with processing time reduction and reliable classification accuracy for embedded EEG BCI-based applications.

2. Related Works

In the recent literature on embedded BCIs (EBCI) based on MI–EEG signals, numerous works dealing with brief processing time and high classification accuracy have been proposed [30,31]. Embedded platform-based BCI designs aim to build low-cost and low-power consumption systems, meeting user adaptability and dedicating available resources to application-specific functions. Belwafi et al. [23] proposed a review of EBCI systems focusing on pathological disorders, functional substitution, and most implemented architectures. Despite recent advances in embedding computational architectures design, they reported a few of the EBCI systems presented in the related literature.

Generally, the central processing unit of the EBCI is ported by a microprocessor or microcontroller integrated into FPGA cards, Arduino boards, Nvidia's developer cards, or specifically dedicated platforms. In this sense, Ma et al. [32] implemented a classifier-based convolutional neural network into a Xilinx FPGA platform to classify MI–EEG signals. Comparatively, implementing the same model on a portable computer equipped with the NVIDIA GeForce GTX1070 i7-7700 resources, the configured FPGA was revealed to be eight times faster than the PC, achieving an average classification accuracy of over 80%. Lately, EBCI systems-based EEG classifiers have been implemented into the NJT2 board, taking advantage of the NVIDIA® Jetson™ board deployment [33]. In fact, Khatwani et al. [34] implemented a convolutional neural network model into Artix-7 FPGA and NJT2 platforms to detect artifacts carried in EEG signals of multiple channels. Based on the basic ICA algorithm, their method achieved an average accuracy of 74 %, detecting seven different artifact types using 64 EEG channels. In another recent framework [35], convolutional stacked auto-encoder and convolutional long short-term memory models were proposed to classify MI–EEG signals for drone control using the NJT2 board. A latency time of 10 ms was reported for generating drone navigation commands based on left-hand and right-hand imagined movement. Similarly, Ascari et al. [36] implemented a networked nodes modular architecture hosted on the NJT2 platform for outdoor portability. The average accuracy of 50% was achieved based on the subject-specific classification processing EEG signals from Cz, Pz, and {Cz, Pz} channels with an average offset between streams of 0 ± 0 ms.

On the other hand, the EEGNet has been implemented more frequently on FPGA boards than on other platforms for EBCI-based EEG signals in the recent literature [37]. Moreover, Hernandez-Ruiz et al. [38] implemented an EEGNet-based architecture into an FPGA board to classify MI–EEG signals, achieving accuracies of 83.15%, 75.74%, and 65.75% for the defined tasks. Lately, Enériz et al. [39] utilized the Xilinx Zynq FPGA to set up a real-time EEGNet-based BCI. Table 1 summarizes the recent state-of-the-art focused on related works.

Table 1. The state-of-the-art summary of related works. Ch means the number of channels.

Works	Platform	Dataset	Ch	Latency per Task
Khatwani et al. [34]	NJT2	Own	64	$\leq$84.1 ms
Maiti et al. [35]	NJT2	BCI competition IV	3	9–10 ms
Ascari et al. [36]	NJT2	Own	2	0 $\pm$ 0 ms

Finally, regarding the recent literature based on HaLT's dataset [40], Yan et al. [41] used the referred public dataset to improve classification accuracy by designing an attention mechanism and global features aggregation based on deep learning. They reported an average accuracy of 76.7% for classifying EEG signals of twelve subjects with the EEGNet network. In another work, Keerthi Krishnan and Soman [42] proposed a variational mode-decomposed EEG-spectrum image model for MI classification using the dataset provided by [40]. Their work achieved an average accuracy of 90.2 $\pm$ 4.34% with the EEGNet network converting EEG signals from C3, Cz, and C4 channels into spectrum images by using the variational mode decomposition (VMD) and the short-time Fourier transform (STFT). Likewise, a generative adversarial network (GAN) was proposed by An et al. [43] to denoise MI-EEG signals using the same dataset. Lately, the EEGNet network has been implemented to classify MI–EEG signal-based BCI utilizing HaLT's benchmark [44]. An average classification accuracy of 80.9 $\pm$ 8.6% was achieved by classifying EEG signals from eight channels. In sum, taking advantage of more than five BCI interaction paradigms, Kaya's dataset offers a wide range of BCI implementation possibilities to the related literature. Table 2 presents Kaya's experiment's data organization related to six mental imagery tasks. The referred BCI interaction paradigm contemplates 6 MI tasks executed by 12 subjects, each with a determined number of sessions.

Table 2. Summary of BCI interaction paradigm data related to six mental imagery tasks, as presented in [40].

No.	Subject	Classes	Sessions	Samples
1	A	6	3	2877
2	B	6	3	2869
3	C	6	2	1916
4	E	6	3	2855
5	F	6	3	2879
6	G	6	3	2867
7	H	6	2	1912
8	I	6	2	1836
9	J	6	1	946
10	K	6	2	1914
11	L	6	2	1904
12	M	6	3	2866
13	All	6	29	27,641

3. Materials and Methods

The method developed in this work addresses the practical challenge of multi-class classification and expedited processing of EEG signals on dedicated platforms using the NJT2 development board and the artificial neural network EEGNet. All developed processing algorithms are integrated directly into the NJT2 embedded platform to exploit hardware resources.

3.1. Overall Flowchart

Figure 1 presents the high-level general diagram of the proposed method. Two main steps are developed to process MI–EEG signals. The first one aims to select discriminant channels employing two approaches (ARbC and CMIbA), while the second implements the EEGNet network to classify discriminant channel features. The ARbC approach also utilizes the EEGNet architecture but with parameters adapted to single-channel signals.

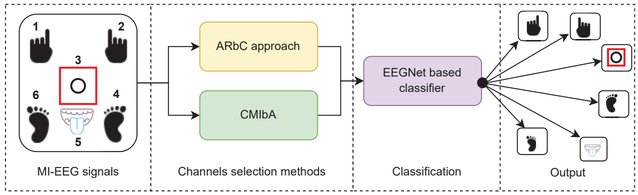

Figure 1. The proposed method overall flowchart. EEG signals of six MI tasks are provided by [40]. The red rectangle centered on the circle refers to "Passive" and moves according to the subject's MI task. The first step consists of selecting discriminant channels from the 19 provided. Next, two comparative methods are used: the ARbC method and the CMIbA. Therefore, the EEGNet network classifies the feature signals into six classes to give the output.

3.2. Referred Public Dataset

The dataset published in [40] was used to implement the proposed method. Explicitly, this work used EEG data provided by the BCI interaction paradigm related to six mental imagery states. On a Graphical User Interface (eGUI), a fixation point considered the neutral starting point for tasks was presented to experiment participants. Each trial began with an action signal to imagine movements of the right and left hands, closing and opening the respective fist once, movements of the right and left leg briefly, and movements of the tongue or a circle as a passive response for 1.0 s. For example, the tongue MI task was interpreted as the imaginative pronunciation of a distinct letter as "el". At the same time, participants did not engage in any voluntary mental imagery until the subsequent trial began for the passive state. These visual stimuli were presented on the eGUI once to the participants in each trial and in sequential order, as presented in Table 3.

Table 3. The BCI interaction segment for imagining limbs motion, following the eGUI's visual stimuli.

Relaxation	**1** ⟶	**2** ⟶	**3** ⟶	**4** ⟶	**5** ⟶	**6** ⟶
	Left hand	Right hand	Passive	Left leg	Tongue	Right leg

A total of 29 recording sessions were performed by seven males and five females aged between 20 and 35 who were declared healthy for the experiment. Each session contains a sequence of BCI interaction segments recorded with a break of 2.0 min, and each trial requires an average of 3.0 s. Accordingly, this BCI interaction contains 87 interaction segments for all 29 sessions in the referred dataset.

MI–EEG signals were recorded using the EEG-1200 JE-921A standard medical equipment. A total of 19 EEG channels placed according to the standard 10–20 electrodes placement system (see Figure 2) provided the benchmark EEG signals.

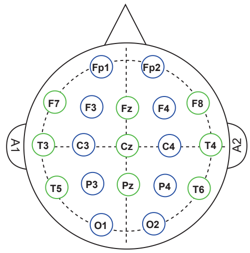

Figure 2. Channels' spatial location on the skull in making the referred dataset. According to the 10–20 system, uppercase letters define the brain cortex where an electrode is placed. F for Frontal, T for temporal, P for parietal, and O for occipital cortex. The lowercase "z" is utilized to locate electrodes on the skull's longitudinal axis. A1 and A2 mean left and right reference voltage electrodes, respectively.

The Neurofax software was used to record data at 200 Hz, and hardware pass-band filters of 0.53–70 Hz were applied to all recorded EEG signals. It is worth mentioning that the EEG-1200 equipment integrates a hardware notch filter at 50 or 60 Hz to isolate EEG signals from electrical grid interference. Figure 3 presents the experimental paradigm's data acquisition and processing overview.

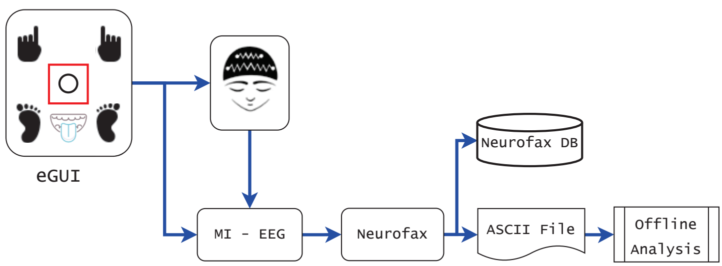

Figure 3. Overview of the EEG acquisition and processing in the experimental paradigm. The red rectangle on the eGUI moves over the specific limb icon as a visual stimulus to engage the respective mental task of imagined movement. MI–EEG signals from six mental states were recorded by EEG-1200 equipment and processed using Neurofax recording software [40]. In addition, ASCII data were converted into Matlab files for further processing.

3.3. NVIDIA Jetson TX2 Embedded Board

The NJT2 is a power-efficient embedded computing device mainly designed for artificial intelligence applications. Building around an NVIDIA Pascal$^{\text{TM}}$-family GPU with 8 GB and 59.7 GB/s of memory and bandwidth, respectively, this supercomputer on a module integrates a wide range of standard hardware interfaces. It is also considered a fast and power-efficient platform for robust data applications; the NJT2 card has been used successfully in recent research [34–36].

The NVIDIA SDK manager based on Ubuntu is the operating system used on the NJT2 card, accessible from [45]. After installing the operating system, a host computer must load the modules into a Micro-SD card following the steps provided in [46]. Once the Jetson software with the SDK Manager is installed, the NJT2 card is ready to be used as an embedded computer. Additionally, the specific libraries are installed according to the application requirements. Table 4 summarizes the main characteristics of the NJT2 card used to implement the present project, according to the serial number provided.

Table 4. NVIDIA Jetson TX2 main characteristics and resources.

Label	Characteristics
NJT2 board	Serial 0320218091017, model 699-82597-0000-501 C
GPU	256-core NVIDIA Pascal™ GPU architecture with 256 NVIDIA CUDA cores
CPU	Dual-Core NVIDIA Denver 2 64-Bit CPU Quad-Core ARM® Cortex®-A57 MPCore
Memory	8 GB 128-bit LPDDR4 Memory 1866 MHx—59.7 GB/s
Storage	32 GB eMMC 5.1
Computing capacity	1.33 TFLOPs
Power consumption	7.5 W/15 W
Mechanical	69.6 mm × 45 mm, 260-pin edge Connector
Networking	10/100/1000 BASE-T, 802.11ac WLAN, Bluetooth

3.4. The EEGNet Network Architecture

EEGNet is a compact convolutional network proposed by Vernon et al. [26]. It demonstrated its effectiveness in processing EEG signals for BCI-based systems, considering the numerous related works [47–49]. Three convolutional layers are configured in the EEGNet. EEG raw data are first convolved in the temporal layer (Part a) using frequency filters, as shown in Figure 4.

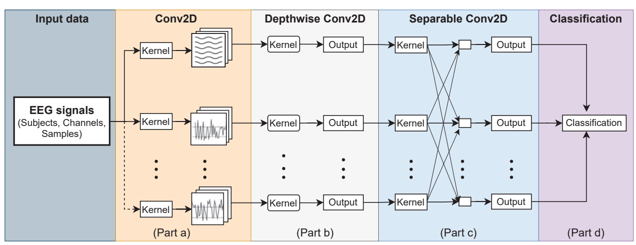

Figure 4. The encapsulated EEGNet structure. EEG signals were organized by subject, channel, and sample length. This data matrix was expanded to four dimensions fulfilling the EEGNet input matrix dimension. In Part (a), temporal features are extracted by Conv2D, and in Part (b), spatial filters are applied to enhance feature maps. Then, feature maps are combined in Separable Conv2D (Part (c)), providing the output class probability (Part (d)).

Next, EEG feature maps extracted from the temporal convolutional layer (Part (a)) serve as input for the depthwise convolutional layer (Part (b)), where frequency-specific spatial filters are applied to each feature map. Finally, the separable convolution layer (Part (c)) combines the depthwise and pointwise convolutions of feature maps, both individually and together, to provide an optimal classification (Part (d)). The depthwise and separable convolution layers are activated by the Exponential Linear Unit (ELU) function, defined by

$$f(\vec{x}_i) = \begin{cases} x_i & \text{for } x \geq 0, \\ e^{x_i} - 1 & \text{otherwise,} \end{cases} \tag{1}$$

while the output dense layer uses the Softmax activation function,

$$\sigma(\vec{x}_i) = \frac{e^{x_i}}{\sum_{j=1}^{N} e^{x_j}}, \quad \forall\, \vec{x} = [x_1, x_2, \ldots, x_N]^\intercal, \tag{2}$$

to predict the output probability of sequence $\vec{x}_i$ to be classified in class N. Therefore, Equation (2) is considered a normalized probability distribution of output feature sequences. Consequently, an important key for implementing EEGNet is the number of filters for each layer and the kernels' length. Table 5 shows the EEGNet's input parameters.

Table 5. Configurable input parameters of the EEGNet network, modified from [26].

Parameters	Descriptions
nb_classes	Number of classes to classify
Chans	Number of channels
Samples	Number of EEG data time points
DropourRate	Dropout fraction
kerneLength	Length of temporal convolution in the first layer (Conv2D).
F1, F2	Numbers of temporal filters (F1) and pointwise filters (F2) to learn.
D	Number of spatial filters to learn within each kerneLength
dropoutType	Either SpatialDropout2D or Dropout

3.5. Data Processing

Subjects and channels provide EEG data from the referred benchmark. The number of samples was set to 170, corresponding to the duration of 0.85 s per task, remembering that dataset signals were recorded at 200 Hz. This allowed the removal of artifacts at the beginning and the end of each task signal. Therefore, the first signal processing step consists of channel discrimination to constitute contributing channel subsets. Two strategies were implemented to select the discriminant channels among the 19 provided. The ARbC approach uses the EEGNet network to classify signals of each channel, aiming to constitute the subset of six and eight channels with higher classification accuracy. In contrast, CMIbA utilizes the channels' mutual information to evaluate how different the cross-entropy measurement value is. The channel selection by the above-mentioned methods was made on the mixed signals of all 12 subjects, i.e., considering signals of the whole dataset. In fact, the constituted discriminant channel subsets can be more suitable for any subject considered separately and be served for the subjects' performance comparison purposes.

Thus, the ARbC method aims to increase the amount of useful training data allowing the neural network to learn more discriminating features. In fact, the proposed software-level approach uses a group-utility metric-based channel selection strategy to improve classification accuracy [50,51]. Hence, the EEGNet network was configured by setting temporal filters (F1), pointwise filters (F2), and spatial filters (D) to four. This EEGNet filter value choice was made according to preliminary training tests to find the classifier's optimal configuration according to data features. The model was compiled with the categorical cross-entropy loss function, and the Nadam optimizer was set to 0.001. The network was trained with 2000 epochs, with a batch size of 330, using 10-fold cross-validation. Consequently, two subsets of six and eight discriminant channels were formed.

According to information theory, the mutual information between two random variables σ and ρ is given by

$$I(\sigma,\rho) = K(\sigma) + K(\rho) - K(\sigma,\rho), \tag{3}$$

where K represents the complexity of information carried by each variable. In the case of probabilistic variables, (3) can be written as

$$I(\mathbb{X},\mathbb{Y}) = H(\mathbb{X}) + H(\mathbb{Y}) - H(\mathbb{X},\mathbb{Y}), \tag{4}$$

where H is the self-information entropy. Based on the assumption that independent random variables should not share mutual information, Kullback–Leibler Divergence (KLD) was used to assess how far a joint distribution of channel signals is from the distribution of their products.

Let P and Q be two probability distributions on the finite channel set $S = [1, i, \cdots, j, \cdots, 19]$, clustering channels signals of the nth subject. KLD, or the relative entropy between P and Q, is given by

$$\mathrm{KLD}(P \mid\mid Q) = \sum_{a \,\in\, S} P(a) \log \frac{P(a)}{Q(a)}, \tag{5}$$

where P(a) is the occurrence probability of the *a*th datum. Therefore, mutual information is found evaluating the KLD as,

$$\mathrm{I}(S_i\,;\,S_j) = \mathrm{KLD}(P(S_i\,,\,S_j)\;||\;P(S_i)P(S_j)), \tag{6}$$

where $P(S_i)$ and $P(S_j)$ represent signal distributions of channels i and j, respectively, and $P(S_i\,,\,S_j)$ is a joint distribution. Equation (6) was computed by considering a given channel and its neighbors, two by two, then by pair grouping, based on channel individual distribution to obtain the discriminating channels subset.

- If S_i and S_j are independents,

$$P(a\,,\,b) = P(a)P(b). \tag{7}$$

Therefore,

$$\mathrm{KLD}(P(a)\cdot P(b)||(P(a)\cdot P(b)) = 0. \tag{8}$$

- If $S_i = S_j$,

$$\begin{aligned} I(S_i\,;\,S_i) &= \sum_{a\,\in\,S} S_i(a)\log\frac{S_i(a)}{S_i(a)^2} \\ &= \sum_{a\,\in\,S} S_i(a)\log\frac{1}{S_i(a)} = H(S_i), \end{aligned} \tag{9}$$

where H is the self-entropy distribution. Entropy values of two-by-two channel combinations are calculated, that is, the entropy of 171 combinations considering 19 channels. Next, channel combinations with entropy values different from zero are combined with the remaining channels to constitute discriminating channel groups. This process is repeated until a group of n channels with the same self-entropy distribution is constituted. Finally, the Discriminant Channel Subset (DCS) is constituted as follows,

$$\mathrm{DCS} = [1,\cdots,n], \quad \forall\, n \leq 19 \;\;\&\;\; \mathrm{DCS} \subset S, \tag{10}$$

where n is the nth discriminant channel for all subjects' signals.

In the next stage, signals of discriminant channel subsets were processed by configuring the EEGNet with new parameters in Keras and TensorFlow, as shown in Table 6. New parameter configuration changes took into account the number of channels, the optimization of hyperparameters, and the learning acceleration at the software level.

EEG data were arranged as a four-dimension tensor to meet the EEGNet's input dimension [26], receiving the number of samples, the number of channels, the length of the sample, and the unitary position by the input layer. Parameter k in Table 6 refers to the number of channels, taking a value of six or eight depending on the channel discriminant set. The proposed architecture was configured with four temporal filters (F1) in the Conv2D convolutional layer, using 16 parameters for k set to six or eight. After the batch normalization, the Depthwise Conv2D layer activated by the ELU function uses 96 or 128 parameters depending on the discriminating set to learn spatial filters in the temporal convolution, setting the number of spatial filters (D) to 4. For its part, the separable Conv2D layer was configured with 16 pointwise filters (F2), and 512 parameters were used to learn within each kernel length. Both EEGNet configurations for the channel selection and processing steps were compiled and trained into the NJT2 board using a batch size of 330, a categorical cross-entropy loss function, and the Nadam optimizer set to 0.0001. The CLR algorithm with a triangular window was also set between 10^{-6} and 5×10^{-2} to accelerate the learning process by training the EEGNet model with a low number of epochs. Thus, the EEGNet model in the classification stage was trained with 1500 instead of 2000 epochs, using 10 repetitions to validate the results.

Table 6. EEGNet parameters for processing k discriminant channel signals. This study used $k = 6$ and $k = 8$ discriminant channels.

Layer (Type)	Output Shape	Parameters
Input Layer	(None, k, 170, 1)	0
Conv2D	(None, k, 170, 4)	16
Batch_normalization_1	(None, k, 170, 4)	16
Depthwise_conv2D	(None, 1, 170, 16)	96/128
Batch_normalization_2	(None, 1, 170, 16)	64
Activation_1	(None, 1, 170, 16)	0
Average_pooling2D_1	(None, 1, 42, 16)	0
Dropout_1	(None, 1, 42, 16)	0
Separable_conv2D	(None, 1, 42, 16)	512
Batch_normalization_3	(None, 1, 42, 64)	64
Activation_2	(None, 1, 42, 16)	0
Average_pooling2D_2	(None, 1, 5, 16)	0
Dropout_2	(None, 1, 5, 16)	0
Flatten	(None, 80)	0
Dense	(None, 6)	486
Softmax	(None, 6)	0

4. Numerical Results

The k-fold cross-validation method was used both in the channel selection and processing steps to validate the achieved results. Therefore, numerical results were obtained by setting k to 10, meaning that the dataset was repeatedly partitioned into ten subsets, where nine were used for training and one for testing each kth iteration. This validation method allows for checking that the model is efficient for different randomized inputs or for some data streams, nothing else. In the channel selection steps, for the ARbC method and CMIbA, training and test sets were formed from signals of all subjects, using nine for training and one for testing. Once the sets of discriminating channels have been constituted, the classification process is performed by exploiting the signals of each subject, taken individually. The proposed model was evaluated using the classification metric given by

$$Accuracy = \frac{TP + TN}{TP + TN + FP + FN}, \tag{11}$$

where TP corresponds to true positive when k features are correctly assigned to class K, TN means true negative when m features of other classes than K are unassigned to class K, and FP as false positive are all features erroneously classified into class K. Additionally, the confusion matrix metric was used to evaluate the implemented classifier performance discriminating MI tasks.

4.1. Channel Selection Results

Processing EEG signals of all subjects by channel, higher classification accuracies were obtained in the order reported in Table 7. Hence, discriminant channel subsets for all the subjects were formed by combining signals of the channel, providing higher accuracy than those of the seven remaining channels, delivering the best accuracies. In the case of P4 and O2 channel selection giving the same classification accuracy (36.7%), tests revealed reliable accuracies in adding the P4 channel to the seven discriminant channels already constituted instead of the O2 channel.

Table 7. Achieved classification accuracies by implementing the ARbC approach to constitute discriminating channel sets. The highest accuracy is highlighted in blue, while the seven highest accuracies are shown in boldface.

Ref.	Channel	Brain Area	Accuracy (%)
1	Fp1	Frontal (attention)	39.5
2	Fp2	Frontal (Judgment restrains impulses)	**39.1**
3	F7	Frontal (Verbal expression)	**38.4**
4	F3	Frontal (Motor planning of left-upper extremity)	36.4
5	Fz	Frontal central (Motor planning (midline))	36.4
6	F4	Frontal (Motor planning of left-upper extremity)	35.1
7	F8	Frontal (Emotional expression)	**39.2**
8	T3	Temporal (Verbal memory)	34.7
9	C3	Central (sensorimotor integration (right))	36.5
10	Cz	Central (sensorimotor integration (midline))	**37.0**
11	C4	Central (sensorimotor integration (left))	35.9
12	T4	Temporal (Emotional memory)	35.9
13	T5	Temporal (Verbal understanding)	36.3
14	P3	Parietal (cognitive processing special temporal)	**37.4**
15	Pz	Parietal (cognitive processing)	35.7
16	P4	Parietal ("Math word problems", "Non-verbal reasoning")	**36.7**
17	T6	Temporal (Emotional understanding and motivation)	36.4
18	O1	Occipital (visual processing)	**37.0**
19	O2	Occipital (visual processing)	36.7

Meanwhile, the channel mutual information approach allowed the formation of six and eight discriminant channel subsets, as presented in Table 8. The number of discriminant channels was determined according to the algorithm proposed in [47], where 6 discriminant electrodes were chosen among the 19 available. In addition, the same subjects participated in the paradigm explored in [47] that was presented in this work, where EEG signals were recorded with the same equipment. Concisely, channel combination tests revealed reliable classification accuracy for subsets of six and eight discriminant channels.

The EEG data point distribution was explored using a t-distributed Stochastic Neighborhood Embedding approach (t-SNE) [52] to visualize data clusters according to the class labels. In the case of multi-class EEG data, t-SNE distributions help to visualize high dimensional data considering the nonlinear relationship between features and targeted classes. Therefore, Figure 5 shows the EEG data clusters after selecting six and eight discriminant channels using the ARbC method and CMIbA.

Therefore, only MI–EEG signals from discriminant channel subsets were processed to evaluate the proposed method's performance.

4.2. Results Processing Discriminant Channel Signals

From a general point of view, the results obtained by developing the ARbC method and CMIbA revealed differences considering achieved accuracies and the taxonomy of discriminant channels. The channel selection methods developed refer to whole dataset signals. Table 7 presents average accuracies using the ARbC to classify all dataset signals by channel. According to the ARbC selection algorithm, the eight high-accuracy values were obtained with Fp1, F8, Fp2, F7, P3, Cz, O1, and P4 channel signals, in this order, respectively. For its part, CMIbA allowed the forming of a discriminant channel subset by selecting P4, T6, T3, P3, F4, O2, Fp2, and Fz channels. Therefore, {Fp1,F8,Fp2,F7,P3,Cz,O1,P4} and {P4,T6,T3,P3,F4,O2,Fp2,Fz} discriminant channel subsets were constituted from the 19 provided, proceeding by the ARbC method and CMIbA. Both approaches have the Fp2, P3, and P4 channels in common, considering the subset of eight discriminant channels, while five of those are different. The difference in the taxonomy of channel subsets is explained by the particularity of metrics used by the ARbC method and CMIbA, and also by the signal spread of each channel when mixed with data from other channels.

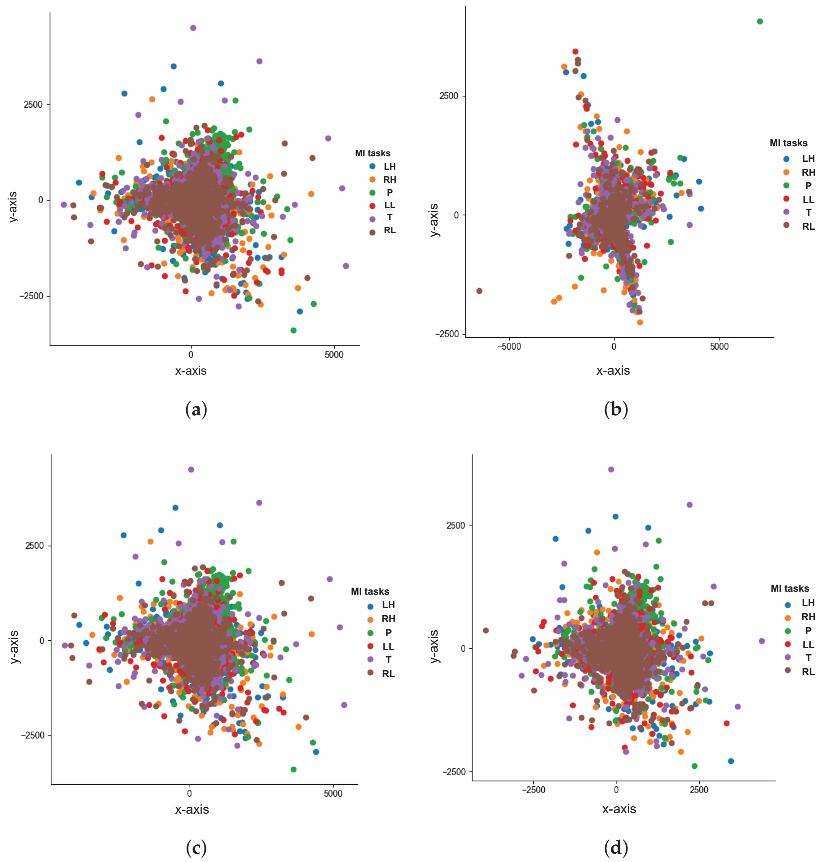

Figure 5. t-SNE distribution illustrations of selected channels' signals for all subjects using the ARbC method and CMIbA before the main processing step. All figures were plotted in 2-D embedded space using the Euclidean metric, setting the nearest neighbors' number at 10, the number of iterations for the optimization at 1000, and the gradient norm at 0.0001. (**a**) ARbC: six-channel combination: distribution of {Fp1,F8,Fp2,F7,P3,Cz} channel signals, (**b**) CMIbA: six-channel combination: distribution of {P4,T6,T3,P3,F4,O2} channel signals, (**c**) ARbC: eight-channel combination: distribution of {Fp1,F8,Fp2,F7,P3,Cz,O1,P4} channel signals, (**d**) CMIbA: eight-channel combination: distribution of {P4,T6,T3,P3,F4,O2,Fp2,Fz} channel signals.

The results of processing MI–EEG signals from the discriminant channel subset are shown in Table 8. Next, the signals of the selected channels per subject are processed; subject A performed EEG data classification, achieving 86.8% and 89.0% accuracy with the ARbC method and CMIbA, respectively. For its part, subject B achieved an accuracy of 68.0% using the ARbC method using data from eight discriminant channels, compared to 76.3% with CMIbA. For all subjects, increasing the number of discriminant channels revealed improvements in classification accuracy, except for subject K using the ARbC method. According to Table 7, adding two more discriminant channels to subject H using the ARbC method decreased the classification accuracy compared to other subjects. The same observation is made for subject J. The best accuracy was achieved by subject J combining eight discriminating channels with CMIbA (99.7%), while the lower accuracy of 53.7% was obtained using subject I, processing six channel signals.

Table 8. Results achieved with the implemented channel selection approaches.

Subject	Channel	Average Accuracies (%) Depending on the Number of Channels			
	Selection	6	Accuracy	8	Accuracy
A	ARbC	{Fp1,F8,Fp2,F7,P3,Cz}	80.6	{Fp1,F8,Fp2,F7,P3,Cz,O1,P4}	86.8
	CMIbA	{P4,T6,T3,P3,F4,O2}	86.5	{P4,T6,T3,P3,F4,O2,Fp2,Fz}	89.0
B	ARbC	{Fp1,F8,Fp2,F7,P3,Cz}	63.9	{Fp1,F8,Fp2,F7,P3,Cz,O1,P4}	68.0
	CMIbA	{P4,T6,T3,P3,F4,O2}	68.7	{P4,T6,T3,P3,F4,O2,Fp2,Fz}	76.3
C	ARbC	{Fp1,F8,Fp2,F7,P3,Cz}	89.1	{Fp1,F8,Fp2,F7,P3,Cz,O1,P4}	90.9
	CMIbA	{P4,T6,T3,P3,F4,O2}	83.0	{P4,T6,T3,P3,F4,O2,Fp2,Fz}	92.2
E	ARbC	{Fp1,F8,Fp2,F7,P3,Cz}	76.6	{Fp1,F8,Fp2,F7,P3,Cz,O1,P4}	78.3
	CMIbA	{P4,T6,T3,P3,F4,O2}	70.8	{P4,T6,T3,P3,F4,O2,Fp2,Fz}	82.5
F	ARbC	{Fp1,F8,Fp2,F7,P3,Cz}	71.6	{Fp1,F8,Fp2,F7,P3,Cz,O1,P4}	79.2
	CMIbA	{P4,T6,T3,P3,F4,O2}	72.4	{P4,T6,T3,P3,F4,O2,Fp2,Fz}	80.4
G	ARbC	{Fp1,F8,Fp2,F7,P3,Cz}	84.0	{Fp1,F8,Fp2,F7,P3,Cz,O1,P4}	86.0
	CMIbA	{P4,T6,T3,P3,F4,O2}	81.9	{P4,T6,T3,P3,F4,O2,Fp2,Fz}	87.3
H	ARbC	{Fp1,F8,Fp2,F7,P3,Cz}	57.0	{Fp1,F8,Fp2,F7,P3,Cz,O1,P4}	57.8
	CMIbA	{P4,T6,T3,P3,F4,O2}	56.2	{P4,T6,T3,P3,F4,O2,Fp2,Fz}	65.5
I	ARbC	{Fp1,F8,Fp2,F7,P3,Cz}	56.4	{Fp1,F8,Fp2,F7,P3,Cz,O1,P4}	57.6
	CMIbA	{P4,T6,T3,P3,F4,O2}	53.7	{P4,T6,T3,P3,F4,O2,Fp2,Fz}	67.9
J	ARbC	{Fp1,F8,Fp2,F7,P3,Cz}	99.6	{Fp1,F8,Fp2,F7,P3,Cz,O1,P4}	99.5
	CMIbA	{P4,T6,T3,P3,F4,O2}	98.8	{P4,T6,T3,P3,F4,O2,Fp2,Fz}	99.7
K	ARbC	{Fp1,F8,Fp2,F7,P3,Cz}	83.0	{Fp1,F8,Fp2,F7,P3,Cz,O1,P4}	79.4
	CMIbA	{P4,T6,T3,P3,F4,O2}	76.8	{P4,T6,T3,P3,F4,O2,Fp2,Fz}	79.3
L	ARbC	{Fp1,F8,Fp2,F7,P3,Cz}	85.7	{Fp1,F8,Fp2,F7,P3,Cz,O1,P4}	93.9
	CMIbA	{P4,T6,T3,P3,F4,O2}	90.4	{P4,T6,T3,P3,F4,O2,Fp2,Fz}	98.0
M	ARbC	{Fp1,F8,Fp2,F7,P3,Cz}	78.7	{Fp1,F8,Fp2,F7,P3,Cz,O1,P4}	83.7
	CMIbA	{P4,T6,T3,P3,F4,O2}	79.5	{P4,T6,T3,P3,F4,O2,Fp2,Fz}	81.9
{A,B, . . ., M}	ARbC	{Fp1,F8,Fp2,F7,P3,Cz}	55.5	{Fp1,F8,Fp2,F7,P3,Cz,O1,P4}	59.3
	CMIbA	{P4,T6,T3,P3,F4,O2}	52.2	{P4,T6,T3,P3,F4,O2,Fp2,Fz}	55.2

Finally, concerning the classification accuracy per MI task, Table 9 summarizes the confusion matrix average results by classifying each mental imagery task. Confusion matrices diagonal results reported in the aforementioned table represent the coincidence percentage between the predicted and the true labels for a given output data sequence.

For illustration purposes, Figure 6 presents EEG data related to the described imagined movements for subject J's Fp1 channel signals. It can be observed that signals corresponding to the passive task are relatively close to magnitude zero before classifying.

Table 9. Summary of confusion matrices' diagonal results classifying MI tasks separately. The average accuracies per MI task do not include "{A,B, . . ., M}" subjects. The CMIbA was used for that purpose.

Subject	Average Accuracies (%) per MI Task					
	Left Hand	**Right Hand**	**Passive**	**Left Leg**	**Tongue**	**Right Leg**
A	80	80	80	80	80	80
B	75	75	75	75	75	75
C	90	90	90	90	90	90
E	75	75	75	75	75	75
F	77	77	77	77	77	77
G	85	85	85	85	85	85
H	67	67	67	67	67	67
I	67	67	67	67	67	67
J	100	100	100	100	100	100
K	80	80	80	80	80	80
L	100	100	100	100	100	100
M	80	80	80	80	80	80
Average	81.3	81.3	81.3	81.3	81.3	81.3
{A, B, . . ., M}	57	57	57	57	57	57

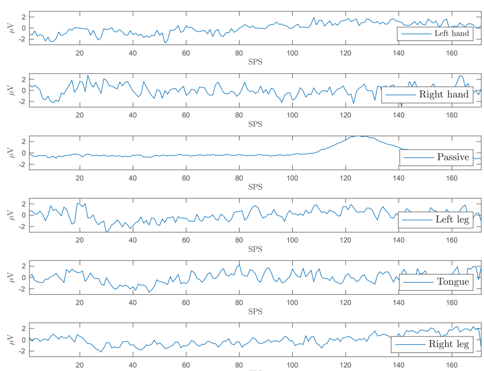

(**a**)

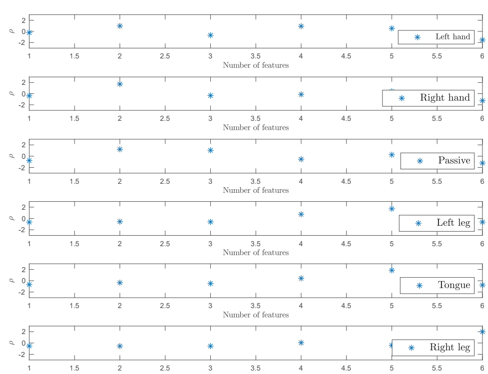

(**b**)

Figure 6. Illustration of MI–EEG features before and after the classification using the EEGNet network. In this example, subject J's data are provided by the Fp1 channel. The window was set to 170 samples, corresponding to task duration. The normalized magnitude is given in μV, while SPS and ρ mean the number of samples per second and feature magnitude, respectively. (**a**) MI–EEG signals before classification. (**b**) MI–EEG features after classification.

5. Discussions

Two EEG channel-selection methods are evaluated on how each affects the classification accuracy by increasing the number of channels, considering the same test subject and network architecture. Regarding the cerebral cortices' spatial activation and for all database signals, almost all brain areas are activated during the experience paradigm. This behavior does not mean that a particular subject would not have had a more activated cortex than others, only that channels were selected based on all subjects' signals. Further, classifying the set of signals as indicated in Table 8 was carried out illustratively to provide information on the classifier's average performance (59.3% and 55.2%). However, practically, a BCI system can exclusively be used by one subject at a time; what matters more is each subject's performance. The results demonstrate that one selection approach can be more effective than the other, depending on the EEG data provided by each subject and on the number of channels.

For subjects K and M, the ARbC method is efficient. In contrast, the CMIbA is suitable for subjects A, B, C, E, F, G, H, I, J, and L. For subjects, C, E, G, H, I, J, and M, either the ARbC method or CMIbA may be recommended depending on the number of discriminating channels. For six discriminant channels, the ARbC method is suitable, while for eight discriminant channels, the CMIbA is desirable.

Regarding classification accuracies, results achieved in this work are compared to those published in the recent related works, as presented in Table 10. In [42], a VMD mode approach to extract EEG features was implemented before using the EEGNet in the classification step. Their work also implemented a subject-dependent classification approach using the referred dataset. Comparing their results with those achieved in this work, subjects A, C, J, and L performed data classification, while the remaining subjects obtained the best results with the approach developed in [42]. This difference in the accuracy evaluation is essentially due to the implemented strategies in the preprocessing before classifying EEG signals. Lately, Yan et al. [41] proposed a similar work based on Kaya's benchmark. They reported an average accuracy of 76.79% in classifying MI-EEG signals from 19 channels. This work achieved an average accuracy of 83.7% using eight channel features.

Table 10. Comparison with other state-of-the-art methods related to the Halt dataset. Sel.Ch. means selected channels, and μ is the average classification accuracy.

Subject	Works					
	Keerthi et al. [42] **VMD + STFT + EEGNet**		**Yan et al.** [41] **EEGNet**		**Proposed Method CbA/CbMI + EEGNet**	
	Sel.Ch.	**Acc.(%)**	**Sel.Ch.**	**Acc.(%)**	**Sel.Ch.**	**Acc.(%)**
A	3	86.74	19	87.40	8	89.0
B	3	97.42	19	67.22	8	76.3
C	3	82.93	19	82.36	8	92.2
E	3	91.84	19	76.94	8	82.5
F	3	94.27	19	70.32	8	80.4
G	3	89.02	19	89.33	8	87.3
H	3	87.25	19	43.46	8	65.5
I	3	90.18	19	44.25	8	67.9
J	3	88.55	19	98.84	8	99.7
K	3	85.76	19	81.03	6	83.0
L	3	92.49	19	95.35	8	98.0
M	3	96.01	19	84.93	8	83.7
μ	–	90.20	–	76.79	–	83.7

Focusing on the processing unit and the latency, another aspect targeted in this work, Table 11 presents the latency per MI task per subject. The lower average latency of 36.7 ms was obtained by subject J while classifying MI tasks; because of the low number of subject J's sessions.

Table 11. Summary of average latency per subject for classifying each MI task.

Subject	Average Latency (ms) per MI Task					
	Left Hand	**Right Hand**	**Passive**	**Left Leg**	**Tongue**	**Right Leg**
A	56.1	56.1	56.1	56.1	56.1	56.1
B	55.7	55.7	55.7	55.7	55.7	55.7
C	42.7	42.7	42.7	42.7	42.7	42.7
E	55.2	55.2	55.2	55.2	55.2	55.2
F	57.2	57.2	57.2	57.2	57.2	57.2
G	55.8	55.8	55.8	55.8	55.8	55.8
H	42.3	42.3	42.3	42.3	42.3	42.3
I	43.8	43.8	43.8	43.8	43.8	43.8
J	36.7	36.7	36.7	36.7	36.7	36.7
K	42.1	42.1	42.1	42.1	42.1	42.1
L	41.8	41.8	41.8	41.8	41.8	41.8
M	56.0	56.0	56.0	56.0	56.0	56.0
Average	48.7	48.7	48.7	48.7	48.7	48.7
{A,B, . . ., M}	135	135	135	135	135	135

Therefore, Table 12 compares this framework with similar works in the recent literature. The purpose is to compare EEGNet network successful implementations on the NJT2 board with the proposed method. Khatwani et al. [34] achieved a latency inferior to 84.1 ms using 64 EEG channels to detect an artifact type. The maxima latency was evaluated at 84.1 ms classifying EEG artifacts. In this work, the average latency per task and per subject was evaluated at 48.7 ms. For their parts, Maiti et al. [35] controlled a drone generating commands with a maximum latency of 10 ms. From a particular point of view, this latency improvement is essentially due to the few channels, compared to the number of channels used in this work. In another work, Ascari et al. [36] processed EEG signals with an average latency of 0 ± 0 ms using two channels. Despite the size of the datasets used in the above-mentioned works, the number of channels used is a determinant factor in evaluating the latency per MI task.

Table 12. Comparison with related works using neural network architectures on the NJT2 board.

Methods	Platform	Dataset	Number of Channels	Latency per Task
Khatwani et al. [34]	NJT2	Own	64	$\leq$84.1 ms
Maiti et al. [35]	NJT2	BCI competition IV	3	9–10 ms
Ascari et al. [36]	NJT2	Own	2	0 ± 0 ms
Proposed method	NJT2	HaLT [40]	6, 8	48.7 ms

Therefore, this framework uses robust EEG data provided by twelve subjects in comparison to the mentioned works. Each MI task needed 48.7 ms to be classified, processing signals from eight discriminant channels. Only 7.6% of the proposed method's NJT2 resources were used.

6. Conclusions

This work developed a multi-class classification of MI–EEG signals for BCI systems, implementing EEGNet on the NJT2 platform. Prior to processing signals, two channel -selection approaches were used to determine the discriminant channel subsets, the ARbC approach, and CMIbA. Since discriminant channel subsets were made up, the EEGNet classified MI–EEG signals into six classes. The results obtained prove the classification accuracy improvement using the two proposed channel selection approaches. Increasing the number of channels allowed one approach to achieve more reliable accuracies than the other approach, depending on the subject data. Processing acceleration strategies implemented by utilizing the NJT2 platform resources and the CLR algorithm allowed for dealing with the processing time challenge. The highest classification accuracy of 99.7% was achieved with subject J's signals, processing data with a latency of 36.7 ms per task. The successful carrying out of the classifier presented in this work is offered as an alternative for the embedded BCI system's development. However, based on the approaches developed in this work, increasing the number of discriminating channels beyond eight tends to decrease the classification accuracy. In future work, we expect to control an electric car using the results achieved in this work. Moving forward, backward, turning right and left, neutral, and accelerating are the expected tasks to be performed. The framework's source codes are available from 1 January 2023, on GitHub https://github.com/Tatyvelu/Motor-Imagery-Multi-Tasks-Classification-for-BCIs-Using-the-Jetson-TX2-board-and-a-Modified-EEGNet-A.

Author Contributions: Conceptualization, T.M.-V.; data curation, T.M.-V., A.A.A.-R. and E.N.-S.; formal analysis, N.V.-A.-G. and J.G.A.-C.; funding acquisition, J.G.A.-C. and T.M.-V.; investigation, T.M.-V., J.R.-P., E.N.-S., N.V.-A.-G. and A.A.A.-R.; methodology, T.M.-V. and N.V.-A.-G.; software, T.M.-V. and A.A.A.-R.; validation, J.R.-P. and J.G.A.-C.; writing—original draft, T.M.-V.; writing—review and editing, T.M.-V., N.V.-A.-G. and J.R.-P. All authors have read and agreed to the published version of the manuscript.

Funding: This work was supported by the Centro de Investigación en Computación—Instituto Politécnico Nacional through the Dirección de Investigación (Folio SIP/1988/DI/DAI/2022) and the Mexican Council of Science and Technology CONACyT under the postdoctoral grant 2022–2024 CVU No. 763527. Additionally, this study was partly supported by the University of Guanajuato CIIC (Convocatoria Institucional de Investigación Científica, UG) Project 094/2023 and Grant NUA 145790.

Institutional Review Board Statement: Ethical review and approval are waived for this study.

Informed Consent Statement: No formal written consent was required for this study.

Data Availability Statement: Data are available under a formal demand.

Acknowledgments: The authors would like to thank Institut Supérieur Pédagogique Technique de Kinshasa and Institut Supérieur Pédagogique de Kikwit for their valuable contributions to this research.

Conflicts of Interest: The authors declare no conflict of interest. The funders had no role in the design of this study; in the collection, analyses, or data interpretation; in the manuscript writing, or in the decision to publish the results.

Abbreviations

BCI	Brain–Computer Interface
EEG	Electroencephalogram
BCV	Brain–Controlled Vehicle
EOG	Electrooculogram
EMG	Electromyogram
SSVEP	Steady-State Evoked Potentials
MI	Motor Imagery
MI–EEG	Motor Imagery EEG
FPGA	Field-Programmable Gate Arrays
SVM	Support Vector Machines
EEGNet	Compact convolutional neural network for EEG-based BCI
NJT2	NVIDIA Jetson TX2

STFT	Short-Time Fourier Transform
VMD	Variational Mode Decomposition
GAN	Generative Adversarial Network
ARbC	Accuracy Rating-based Classifier
CMIbA	Channels Mutual Information-based Approach
CLR	Cyclic Learning Rate
EBCI	Embedded Brain–Computer Interface
ICA	Independent Component Analysis
PC	Portable Computer
CNN	Convolutional Neural Network
eGUI	Graphical User Interface
ASCII	American Standard Code for Information Interchange
CPU	Central Processing Unit
GPU	Graphics Processor Unit
SDK	Software Development Kit
LPDDR4	Low Power Double Data Rate
eMMC	Embedded Multi-Media Card
TFLOPS	Trillion Floating-Point Operations Per Second
WLAN	Wireless Local Area Network
ELU	Exponential Linear Unit
KLD	Kullback–Leibler Divergence
DCS	Discriminant Channel Subset
t-SNE	t-distributed Stochastic Neighborhood Embedding
LUT	Look-Up-Table
SPS	Samples Per Second
CLR	Cyclical Learning Rate
MFLOPS	Million Floating-Point Operations Per Second

References

1. He, B.; Yuan, H.; Meng, J.; Gao, S. Brain–computer interfaces. In *Neural Engineering*; Springer: Berlin/Heidelberg, Germany, 2020; pp. 131–183.
2. Herbet, G.; Duffau, H. Revisiting the functional anatomy of the human brain: Toward a meta-networking theory of cerebral functions. *Physiol. Rev.* **2020**, *100*, 1181–1228. [CrossRef]
3. Gao, X.; Wang, Y.; Chen, X.; Gao, S. Interface, interaction, and intelligence in generalized brain-computer interfaces. *Trends Cogn. Sci.* **2021**, *25*, 671–684. [CrossRef]
4. Fraiwan, M.; Alafeef, M.; Almomani, F. Gauging human visual interest using multiscale entropy analysis of EEG signals. *J. Ambient. Intell. Humaniz. Comput.* **2021**, *12*, 2435–2447. [CrossRef]
5. Alafeef, M.; Fraiwan, M. On the diagnosis of idiopathic Parkinson's disease using continuous wavelet transform complex plot. *J. Ambient. Intell. Humaniz. Comput.* **2019**, *10*, 2805–2815. [CrossRef]
6. Papanastasiou, G.; Drigas, A.; Skianis, C.; Lytras, M. Brain computer interface based applications for training and rehabilitation of students with neurodevelopmental disorders. A literature review. *Heliyon* **2020**, *6*, e04250. [CrossRef]
7. Hekmatmanesh, A.; Nardelli, P.H.; Handroos, H. Review of the state-of-the-art of brain-controlled vehicles. *IEEE Access* **2021**, *9*, 110173–110193. [CrossRef]
8. Zhang, Y.; Xie, S.Q.; Wang, H.; Zhang, Z. Data analytics in steady-state visual evoked potential-based brain-computer interface: A review. *IEEE Sens. J.* **2020**, *21*, 1124–1138. [CrossRef]
9. Shajil, N.; Mohan, S.; Srinivasan, P.; Arivudaiyanambi, J.; Arasappan Murrugesan, A. Multiclass classification of spatially filtered motor imagery EEG signals using convolutional neural network for BCI based applications. *J. Med. Biol. Eng.* **2020**, *40*, 663–672. [CrossRef]
10. Yu, X.; Aziz, M.Z.; Sadiq, M.T.; Fan, Z.; Xiao, G. A New Framework for Automatic Detection of Motor and Mental Imagery EEG Signals for Robust BCI Systems. *IEEE Trans. Instrum. Meas.* **2021**, *70*, 1006612. [CrossRef]
11. Al-Qazzaz, N.K.; Alyasseri, Z.A.A.; Abdulkareem, K.H.; Ali, N.S.; Al-Mhiqani, M.N.; Guger, C. EEG feature fusion for motor imagery: A new robust framework towards stroke patients rehabilitation. *Comput. Biol. Med.* **2021**, *137*, 104799. [CrossRef]
12. Cuomo, G.; Maglianella, V.; Ghanbari Ghooshchy, S.; Zoccolotti, P.; Martelli, M.; Paolucci, S.; Morone, G.; Iosa, M. Motor imagery and gait control in Parkinson's disease: Techniques and new perspectives in neurorehabilitation. *Expert Rev. Neurother.* **2022**, *22*, 43–51. [CrossRef]
13. Abenna, S.; Nahid, M.; Bouyghf, H.; Ouacha, B. EEG-based BCI: A novel improvement for EEG signals classification based on real-time preprocessing. *Comput. Biol. Med.* **2022**, *148*, 105931. [CrossRef] [PubMed]
14. Jiao, Y.; Zhou, T.; Yao, L.; Zhou, G.; Wang, X.; Zhang, Y. Multi-View Multi-Scale Optimization of Feature Representation for EEG Classification Improvement. *IEEE Trans. Neural Syst. Rehabil. Eng.* **2020**, *28*, 2589–2597. [CrossRef] [PubMed]

15. Khan, M.A.; Das, R.; Iversen, H.K.; Puthusserypady, S. Review on motor imagery based BCI systems for upper limb post-stroke neurorehabilitation: From designing to application. *Comput. Biol. Med.* **2020**, *123*, 103843. [CrossRef]
16. Huang, Q.; Zhang, Z.; He, S.; Li, Y. An EEG-/EOG-Based Hybrid Brain-Computer Interface: Application on Controlling an Integrated Wheelchair Robotic Arm System. *Front. Neurosci.* **2019**, *13*, 1243. [CrossRef] [PubMed]
17. Al-Nuaimi, F.A.; Al-Nuaimi, R.J.; Al-Dhaheri, S.S.; Ouhbi, S.; Belkacem, A.N. Mind Drone Chasing Using EEG-based Brain-Computer Interface. In Proceedings of the 2020 16th International Conference on Intelligent Environments (IE), Madrid, Spain, 20–23 July 2020; pp. 74–79. [CrossRef]
18. Moctezuma, L.; Abe, T.; Molinas, M. Two-dimensional CNN-based distinction of human emotions from EEG channels selected by Multi-Objective evolutionary algorithm. *Sci. Rep.* **2022**, *12*, 3523. [CrossRef] [PubMed]
19. Mwata-Velu, T.; Ruiz-Pinales, J.; Rostro-Gonzalez, H.; Ibarra-Manzano, M.A.; Cruz-Duarte, J.M.; Avina-Cervantes, J.G. Motor Imagery Classification Based on a Recurrent-Convolutional Architecture to Control a Hexapod Robot. *Mathematics* **2021**, *9*, 606. [CrossRef]
20. Smith, L.N. Cyclical Learning Rates for Training Neural Networks. In Proceedings of the 2017 IEEE Winter Conference on Applications of Computer Vision (WACV), Santa Rosa, CA, USA, 24–31 March 2017; IEEE: Piscataway, NJ, USA, 2017; pp. 464–472. [CrossRef]
21. Ramzan, M.; Dawn, S. A survey of brainwaves using electroencephalography EEG to develop robust brain-computer interfaces (BCIs): Processing techniques and algorithms. In Proceedings of the 2019 9th International Conference on Cloud Computing, Data Science & Engineering (Confluence), Noida, India, 10–11 January 2019; IEEE: Piscataway, NJ, USA, 2019; pp. 642–647.
22. Al-Saegh, A.; Dawwd, S.A.; Abdul-Jabbar, J.M. Deep learning for motor imagery EEG-based classification: A review. *Biomed. Signal Process. Control* **2021**, *63*, 102172. [CrossRef]
23. Belwafi, K.; Gannouni, S.; Aboalsamh, H. Embedded Brain Computer Interface: State-of-the-Art in Research. *Sensors* **2021**, *21*, 4293. [CrossRef]
24. Majoros, T.; Oniga, S. Overview of the EEG-Based Classification of Motor Imagery Activities Using Machine Learning Methods and Inference Acceleration with FPGA-Based Cards. *Electronics* **2022**, *11*, 2293. [CrossRef]
25. Dabas, D.; Lakhani, M.; Sharma, B. Classification of EEG signals for hand gripping motor imagery and hardware representation of neural states using Arduino-based LED sensors. In Proceedings of the International Conference on Artificial Intelligence and Applications, Crete, Greece, 17–20 June 2021; Springer: Berlin/Heidelberg, Germany, 2021; pp. 213–224.
26. Lawhern, V.J.; Solon, A.J.; Waytowich, N.R.; Gordon, S.M.; Hung, C.P.; Lance, B.J. EEGNet: A compact convolutional neural network for EEG-based brain–computer interfaces. *J. Neural Eng.* **2018**, *15*, 056013. [CrossRef] [PubMed]
27. Zhu, Y.; Li, Y.; Lu, J.; Li, P. EEGNet with ensemble learning to improve the cross-session classification of SSVEP-based BCI from Ear-EEG. *IEEE Access* **2021**, *9*, 15295–15303. [CrossRef]
28. Feng, L.; Yang, L.; Liu, S.; Han, C.; Zhang, Y.; Zhu, Z. An efficient EEGNet processor design for portable EEG-Based BCIs. *Microelectron. J.* **2022**, *120*, 105356. [CrossRef]
29. Tsukahara, A.; Anzai, Y.; Tanaka, K.; Uchikawa, Y. A design of EEGNet-based inference processor for pattern recognition of EEG using FPGA. *Electron. Commun. Jpn.* **2020**, *104*, 53–64. [CrossRef]
30. Ak, A.; Topuz, V.; Midi, I. Motor imagery EEG signal classification using image processing technique over GoogLeNet deep learning algorithm for controlling the robot manipulator. *Biomed. Signal Process. Control* **2022**, *72*, 103295. [CrossRef]
31. Ingolfsson, T.M.; Hersche, M.; Wang, X.; Kobayashi, N.; Cavigelli, L.; Benini, L. EEG-TCNet: An accurate temporal convolutional network for embedded motor-imagery brain-machine interfaces. In Proceedings of the 2020 IEEE International Conference on Systems, Man, and Cybernetics (SMC), Toronto, ON, Canada, 11–14 October 2020; IEEE: Piscataway, NJ, USA, 2020; pp. 2958–2965.
32. Ma, X.; Zheng, W.; Peng, Z.; Yang, J. Fpga-based rapid electroencephalography signal classification system. In Proceedings of the 2019 IEEE 11th International Conference on Advanced Infocomm Technology (ICAIT), Jinan, China, 18–20 October 2019; IEEE: Piscataway, NJ, USA, 2019; pp. 223–227.
33. Manjunath, N.K.; Paneliya, H.; Hosseini, M.; Hairston, W.D.; Mohsenin, T. A low-power lstm processor for multi-channel brain eeg artifact detection. In Proceedings of the 2020 21st International Symposium on Quality Electronic Design (ISQED), Santa Clara, CA, USA, 25–26 March 2020; IEEE: Piscataway, NJ, USA, 2020; pp. 105–110.
34. Khatwani, M.; Hosseini, M.; Paneliya, H.; Mohsenin, T.; Hairston, W.D.; Waytowich, N. Energy Efficient Convolutional Neural Networks for EEG Artifact Detection. In Proceedings of the 2018 IEEE Biomedical Circuits and Systems Conference (BioCAS), Cleveland, OH, USA, 17–19 October 2018; pp. 1–4. [CrossRef]
35. Maiti, S.; Mandal, A.S.; Chaudhury, S. Classification of Motor Imagery EEG Signal for Navigation of Brain Controlled Drones. In Proceedings of the Intelligent Human Computer Interaction: 11th International Conference, IHCI 2019, Allahabad, India, 12–14 December 2019; Proceedings 11; Tiwary, U.S., Chaudhury, S., Eds.; Springer: Cham, Switzerland, 2020; pp. 3–12.
36. Ascari, L.; Marchenkova, A.; Bellotti, A.; Lai, S.; Moro, L.; Koshmak, K.; Mantoan, A.; Barsotti, M.; Brondi, R.; Avveduto, G.; et al. Validation of a Novel Wearable Multistream Data Acquisition and Analysis System for Ergonomic Studies. *Sensors* **2021**, *21*, 8167. [CrossRef] [PubMed]
37. Lucan Orășan, I.; Seiculescu, C.; Căleanu, C.D. A Brief Review of Deep Neural Network Implementations for ARM Cortex-M Processor. *Electronics* **2022**, *11*, 2545. [CrossRef]
38. Hernandez-Ruiz, A.C.; Enériz, D.; Medrano, N.; Calvo, B. Motor-Imagery EEGNet-Based Processing on a Low-Spec SoC Hardware. In Proceedings of the 2021 IEEE Sensors, Sydney, Australia, 31 October–3 November 2021; IEEE: Piscataway, NJ, USA, 2021; pp. 1–4.

39. Enériz, D.; Medrano, N.; Calvo, B.; Hernández-Ruiz, A.C.; Antolín, D. Real-Time EEG Acquisition System for FPGA-based BCI. In Proceedings of the 2022 37th Conference on Design of Circuits and Integrated Circuits (DCIS), Pamplona, Spain, 16–18 November 2022; IEEE: Piscataway, NJ, USA, 2022; pp. 1–5.
40. Kaya, M.; Binli, M.; Ozbay, E.; Yanar, H.; Mishchenko, Y. A large electroencephalographic motor imagery dataset for electroencephalographic brain-computer interfaces. *Sci. Data* **2018**, *5*, 180211. [CrossRef] [PubMed]
41. Yan, Z.; Yang, X.; Jin, Y. Considerate motion imagination classification method using deep learning. *PLoS ONE* **2022**, *17*, e0276526. [CrossRef] [PubMed]
42. Keerthi Krishnan, K.; Soman, K. CNN-based classification of motor imaginary using variational mode decomposed EEG-spectrum image. *Biomed. Eng. Lett.* **2021**, *11*, 235–247. [CrossRef]
43. An, Y.; Lam, H.K.; Ling, S.H. Auto-Denoising for EEG Signals Using Generative Adversarial Network. *Sensors* **2022**, *22*, 1750. [CrossRef] [PubMed]
44. Pérez-Velasco, S.; Santamaria-Vazquez, E.; Martinez-Cagigal, V.; Marcos-Martinez, D.; Hornero, R. EEGSym: Overcoming Inter-Subject Variability in Motor Imagery Based BCIs With Deep Learning. *IEEE Trans. Neural Syst. Rehabil. Eng.* **2022**, *30*, 1766–1775. [CrossRef] [PubMed]
45. NVIDIA SDK Manager. Available online: https://developer.nvidia.com/nvidia-sdk-manager (accessed on 15 October 2022).
46. JETPACK SDK 4.6.2. Available online: https://developer.nvidia.com/embedded/jetpack-sdk-462 (accessed on 15 October 2022).
47. Mwata-Velu, T.; Avina-Cervantes, J.G.; Ruiz-Pinales, J.; Garcia-Calva, T.A.; González-Barbosa, E.A.; Hurtado-Ramos, J.B.; González-Barbosa, J.J. Improving Motor Imagery EEG Classification Based on Channel Selection Using a Deep Learning Architecture. *Mathematics* **2022**, *10*, 2302. [CrossRef]
48. Shoji, T.; Yoshida, N.; Tanaka, T. Automated detection of abnormalities from an EEG recording of epilepsy patients with a compact convolutional neural network. *Biomed. Signal Process. Control* **2021**, *70*, 103013. [CrossRef]
49. Waytowich, N.; Lawhern, V.J.; Garcia, J.O.; Cummings, J.; Faller, J.; Sajda, P.; Vettel, J.M. Compact convolutional neural networks for classification of asynchronous steady-state visual evoked potentials. *J. Neural Eng.* **2018**, *15*, 066031. [CrossRef]
50. Bertrand, A. Utility Metrics for Assessment and Subset Selection of Input Variables for Linear Estimation [Tips & Tricks]. *IEEE Signal Process. Mag.* **2018**, *35*, 93–99. [CrossRef]
51. Narayanan, A.M.; Bertrand, A. Analysis of miniaturization effects and channel selection strategies for EEG sensor networks with application to auditory attention detection. *IEEE Trans. Biomed. Eng.* **2019**, *67*, 234–244. [CrossRef]
52. Van der Maaten, L.; Hinton, G. Visualizing data using t-SNE. *J. Mach. Learn. Res.* **2008**, *9*, 2579–2605.

sensors

Article

Method for Automatic Estimation of Instantaneous Frequency and Group Delay in Time–Frequency Distributions with Application in EEG Seizure Signals Analysis

Vedran Jurdana [1,*], Miroslav Vrankic [1,*], Nikola Lopac [2,3] and Guruprasad Madhale Jadav [1]

[1] Faculty of Engineering, University of Rijeka, 51000 Rijeka, Croatia; jguruprasad@riteh.hr
[2] Faculty of Maritime Studies, University of Rijeka, 51000 Rijeka, Croatia; nikola.lopac@pfri.uniri.hr
[3] Center for Artificial Intelligence and Cybersecurity, University of Rijeka, 51000 Rijeka, Croatia
* Correspondence: vjurdana@riteh.hr (V.J.); miroslav.vrankic@riteh.hr (M.V.)

Abstract: Instantaneous frequency (IF) is commonly used in the analysis of electroencephalogram (EEG) signals to detect oscillatory-type seizures. However, IF cannot be used to analyze seizures that appear as spikes. In this paper, we present a novel method for the automatic estimation of IF and group delay (GD) in order to detect seizures with both spike and oscillatory characteristics. Unlike previous methods that use IF alone, the proposed method utilizes information obtained from localized Rényi entropies (LREs) to generate a binary map that automatically identifies regions requiring a different estimation strategy. The method combines IF estimation algorithms for multicomponent signals with time and frequency support information to improve signal ridge estimation in the time–frequency distribution (TFD). Our experimental results indicate the superiority of the proposed combined IF and GD estimation approach over the IF estimation alone, without requiring any prior knowledge about the input signal. The LRE-based mean squared error and mean absolute error metrics showed improvements of up to 95.70% and 86.79%, respectively, for synthetic signals and up to 46.45% and 36.61% for real-life EEG seizure signals.

Keywords: time–frequency distributions; Rényi entropy; instantaneous frequency; group delay; EEG

Citation: Jurdana , V.; Vrankic, M.; Lopac, N.; Jadav, G.M. Method for Automatic Estimation of Instantaneous Frequency and Group Delay in Time–Frequency Distributions with Application in EEG Seizure Signals Analysis. *Sensors* **2023**, *23*, 4680. https://doi.org/10.3390/s23104680

Academic Editors: Yifan Zhao, Hua-Liang Wei, Yuzhu Guo and Fei He

Received: 7 April 2023
Revised: 6 May 2023
Accepted: 10 May 2023
Published: 11 May 2023

1. Introduction

Electroencephalogram (EEG) recordings are widely used for assessing brain disorders [1–3]. EEG is a noninvasive approach for detecting and predicting seizures [4–7], which can be difficult to identify in infants. Recurrent seizures are the hallmark of epilepsy, one of the most prevalent neurological disorders in humans. Identifying seizures in EEG recordings typically requires real-time observation by a neurologist, leading to growing interest in automated methods for seizure detection.

EEG signals are nonstationary, and therefore, time–frequency (TF) and time-scale representations are commonly used for their analysis [6,8–21]. A time–frequency distribution (TFD) enables us to describe signal energy simultaneously in time and frequency. However, the most widely used TFDs, the quadratic TFDs (QTFDs), create highly oscillatory artifacts, known as cross-terms, for signals with several components or at least one nonlinear frequency-modulated (non-LFM) component [22–24]. Although the 2D low-pass filters in the ambiguity function (AF) domain are often used to suppress cross-terms, they may also suppress important components known as autoterms, resulting in a trade-off between cross-term reduction and autoterm resolution. To overcome this trade-off, a variety of filtering methods in the TF domain have been developed [22,25] as an alternative to conventional filtering methods utilizing nonstationary signals in the time domain [26–28]. One of these advanced filtering methods that outperforms others is the adaptive directional TFD (ADTFD), which achieves high resolution for multicomponent signals having multiple directions of energy distribution in the TF domain, such as EEG seizure signals [7,29–32].

Instantaneous frequency (IF) provides vital information on the time-varying spectral changes in nonstationary signals. In the TF signal analysis, a number of IF estimation methods have been developed [29,33–44]. However, IF is not as useful to characterize signals composed of spikes, where an infinite amount of frequencies is present [45–47]. Such behavior is present in EEG seizure signals, for which the group delay (GD) has been proven to be a better alternative to IF [46,47]. However, the limitation of the IF estimation method proposed in [48], and hence, the approach in [46,47], is that the number of components is required as input from a user, which limits its usage when no a priori information is available and when the number of components varies over time.

In this paper, we present a novel method for generating a binary map that automatically identifies distinct regions within the signal's TFD, where either the IF or GD measure is particularly suitable for analysis. Our method utilizes information about the local number of signal components obtained from the localized Rényi entropy (LRE) information, namely the short-term Rényi entropy (STRE) [33,34] and the narrow-band Rényi entropy (NBRE) [35,36], to detect components and segment the TFD accordingly. Unlike other methods that require a priori knowledge of the number of components, our approach is applicable to signals with unknown and time-varying numbers of components.

The resulting binary map is used in a joint IF and GD estimation method, which was applied to two commonly used IF estimation algorithms in EEG signal analysis, namely image-based [22,37,38] and blind-source separation (BSS) [15,39,40]. These methods were selected for their suitability in an automatic environment, as they effectively use the component time support information from the STRE. Our approach further incorporates the frequency support information from the NBRE to estimate the GD and reduce the dependency of the IF algorithms on the STRE accuracy, which can be achieved for the considered signal examples.

Furthermore, we demonstrate that the shrinkage operator proposed in [35,36] for sparse TFD reconstruction can be effectively used for IF and GD estimation, with competitive performance compare with the image-based and BSS algorithms. We evaluate the performance of our method using mean squared error (MSE) between the local number of signal components before and after estimation, and we show the superior performance of our combined IF and GD estimation approach over IF estimation alone on both synthetic signals with additive noise and real-life EEG seizure signals.

The rest of this paper is organized as follows. Background theory, the proposed method and the EEG dataset used in this study are described in Section 2. The obtained results are thoroughly presented and discussed in Section 3. Finally, the paper's conclusions are summarized in Section 4.

2. Materials and Methods

2.1. Time–Frequency Signal Analysis

A multicomponent nonstationary signal, denoted as $z(t)$, is defined as the analytic associate of a real signal $s(t)$ as

$$z(t) = \sum_{i=1}^{NC} a_i(t) e^{j\varphi_i(t)}, \tag{1}$$

where NC is the number of components, while $a_i(t)$ and $\varphi_i(t)$ denote the instantaneous amplitude and instantaneous phase of the signals i-th component, respectively. The ideal TFD, $\hat{\rho}(t, f)$, is a unit delta function following the crests of the ridges which represent the IF, $f_{0_i}(t)$, of the i-th component:

$$\hat{\rho}(t, f) = \sum_{i=1}^{NC} a_i^2(t) \delta(f - f_{0_i}(t)), \tag{2}$$

$$f_{0_i}(t) = \frac{1}{2\pi} \frac{d}{dt} \arg z(t) = \frac{1}{2\pi} \frac{d\varphi_i(t)}{dt}, \tag{3}$$

indicating the dominant frequency of the signal's i-th component at a given time. A dual (or inverse) of the IF, namely the GD, $\tau_{d_i}(f)$, indicates the dominant time of the signal's i-th component at a given frequency:

$$\tau_{d_i}(f) = -\frac{1}{2\pi}\frac{d}{df}\arg Z(f), \tag{4}$$

where $Z(f)$ is the Fourier transform of $z(t)$. The definitions of IF and GD are closely related, involving interchanging the time and frequency variables, with an extra minus sign in Equation (4). In practice, the IF is obtained by determining the signal's component ridge across time slices of its TFD, while the GD is determined by determining the signal's component ridge across frequency slices of the TFD. In the vast majority of instances, the ideal TFD is not achievable, because practical TFDs are not precisely localized and may be affected by cross-terms [22].

The Wigner–Ville Distribution (WVD) is widely used as the most fundamental TFD, defined as [22]:

$$W(t,f) = \int_{-\infty}^{\infty} z\left(t+\frac{\tau}{2}\right)z^*\left(t-\frac{\tau}{2}\right)e^{-j2\pi f\tau}d\tau, \tag{5}$$

and it provides an estimate of the IF/GD for a signal with a single LFM component in the TF plane that is almost perfect. Yet, the cross-term vulnerability (when dealing with multicomponent signals) necessitates proper cross-terms suppression. Using the AF, $A(\nu,\tau)$, calculated as

$$A(\nu,\tau) = \int_{-\infty}^{\infty}\int_{-\infty}^{\infty} W_z(t,f)e^{j2\pi(f\tau-\nu t)}dtdf, \tag{6}$$

the highly oscillatory cross-terms can be suppressed with a 2D low-pass filter, defining a QTFD class of TFDs, $\rho(t,f)$:

$$\mathcal{A}(\nu,\tau) = A(\nu,\tau)g(\nu,\tau), \tag{7}$$

$$\rho(t,f) = \int_{-\infty}^{\infty}\int_{-\infty}^{\infty} \mathcal{A}(\nu,\tau)e^{j2\pi(\nu t-f\tau)}d\nu d\tau, \tag{8}$$

where $g(\nu,\tau)$ is the low-pass filter kernel in the AF. The conventional approaches to kernel design typically entail a compromise between the concentration of autoterms and the suppression of cross-terms [22].

2.2. Adaptive Directional TFD

To circumvent the above problem of the conventional TFDs, the adaptive directional TFD (ADTFD) that adjusts the direction of the smoothing kernel at each TF point in the TF plane is introduced [7,29], and it is mathematically expressed as follows:

$$\rho_{(ad)}(t,f) = \rho(t,f) \underset{t}{*}\underset{f}{*} \gamma_\theta(t,f), \tag{9}$$

where $\gamma_\theta(t,f)$ is the smoothing kernel whose direction is controlled by θ, while the double asterisk denotes double convolution in t and f. In this work, we used the Extended Modified B Distribution (EMBD) as an underlying QTFD with its kernel:

$$g(\nu,\tau) = \frac{\int_{-\infty}^{\infty}\cosh^{-2\beta_E}(t)e^{j2\pi\nu t}dt}{\int_{-\infty}^{\infty}\cosh^{-2\beta_E}(t)dt}\cosh^{-2\alpha_E}(\tau), \tag{10}$$

where $\alpha_E = \beta_E = 0.25$ are the time and frequency smoothing parameters [7,29,31,32]. As $\gamma_\theta(t, f)$, we selected the double-derivative directional Gaussian filter (DGF) as in [7,29,31,32]:

$$\gamma_\theta(t, f) = \frac{ab}{2\pi} \frac{\mathrm{d}^2}{\mathrm{d}f_\theta^2} e^{-a^2 t_\theta^2 - b^2 f_\theta^2}, \tag{11}$$

where $t_\theta = t\cos(\theta) + f\sin(\theta)$ and $f_\theta = -t\sin(\theta) + f\cos(\theta)$, while parameters a and b control the extent of smoothing along the time and frequency axes. The DGF has low-pass characteristics along the time axis $(e^{-a^2 t_\theta^2})$, while it performs second-order differentiation along the frequency axis $\frac{ab}{2\pi}(\frac{\mathrm{d}^2}{\mathrm{d}f_\theta^2} e^{-b^2 f_\theta^2})$. The direction angle of $\gamma_\theta(t, f)$ is adapted locally for each point in the TF domain by maximizing the correlation between the $\gamma_\theta(t, f)$ and TF ridges as

$$\theta(t, f) = \arg\max_\theta \left| |\rho(t, f)| \underset{t}{*} \underset{f}{*} \gamma_\theta(t, f) \right|, \tag{12}$$

where $-\pi/2 \leq \theta \leq \pi/2$. The implementation of directional smoothing results in the suppression of cross-terms and the enhancement of autoterms. The optimization of smoothing kernel parameters and shape is necessary for achieving optimal performance, as they are dependent on the signal being analyzed. Previous studies [7,29,31,32] have indicated that assigning a small value to parameter a results in intensive smoothing along the major axis, whereas a larger value for parameter b prevents the merging of close components. To be more precise, $a \in [2, 3]$, while $b \in [5, 30]$. In addition to shape parameters a and b, the window length, WL, of the $\gamma_\theta(t, f)$ affects the performance of the ADTFD. A filter with a small WL value fails to resolve close components and eliminate cross-terms, but it preserves the energy of short-duration components. Conversely, a larger WL value achieves the opposite effect. The computational demand of the exhaustive search involving all possible combinations of (a, b, WL) is significant. Therefore, we used a method for the automatic parameter optimization of ADTFD, namely the locally adaptive-ADTFD (LO-ADTFD) proposed in [31], where the final LO-ADTFD is obtained by choosing TF points with the minimum value from a given set of ADTFDs $\{\rho_{(ad)_1}(t, f), \rho_{(ad)_2}(t, f), \ldots\}$ and their respective parameters $\{(a_1, b_1, WL_1), (a_2, b_2, WL_2), \ldots\}$:

$$\rho_{(lo)}(t, f) = \min_k(\rho_{(ad)_k}(t, f)), \tag{13}$$

where $\rho_{(ad)_k}(t, f)$ is the k-th ADTFD in the defined set. That way, the LO-ADTFD preserves the energy of short-duration signals while achieving high-resolution TFD with resolved close components and suppressed cross-terms. In this work, we selected the parameter (a, b) values from the following set $\{(3, 6), (3, 8), (2, 20), (2, 30)\}$, while WL was optimized for each (a, b) pair using the concentration measure proposed in [41]:

$$M = \frac{1}{N_t N_f} \left(\sum_{t=1}^{N_t} \sum_{f=1}^{N_f} |\rho_{(ad)}(t, f)|^{\frac{1}{2}} \right)^2, \tag{14}$$

where N_t and N_f denote the numbers of time samples and frequency bins, respectively, in range $[N_t/8 : 4 : N_t/4]$ for the pairs $\{(3, 6), (2, 20)\}$ and $[N_t/4 : 4 : 3N_t/8]$ for the pairs $\{(3, 8), (2, 30)\}$, as suggested in [31].

2.3. The Localized Rényi Entropy

The Rényi entropy, denoted by $R(\rho(t, f))$, is a comprehensive metric for signal complexity in the TF plane [42–44], defined as

$$R(\rho(t, f)) = \frac{1}{1 - \alpha_R} \log_2 \int_{-\infty}^{\infty} \int_{-\infty}^{\infty} \left(\frac{\rho(t, f)}{\int_{-\infty}^{\infty} \int_{-\infty}^{\infty} \rho(t, f)\, dtdf} \right)^{\alpha_R} dtdf, \tag{15}$$

where for the odd integer parameter $\alpha_R > 2$ the cross-terms get integrated out from the QTFD, $\rho(t, f)$, which is normalized with respect to its total energy [34,42].

To refine the global approach mentioned earlier, the counting attribute of the Rényi entropy has been utilized to extract the local number of signal components from $\rho(t, f)$ using STRE [34]. To achieve this, the Rényi entropy of the extracted signal's TFD is compared with that of a reference TFD with a known number of component as follows:

$$NC_t^{\rho(t,f)}(t_0) = 2^{R(\Gamma_{t_0}\{\rho(t,f)\}) - R(\Gamma_{t_0}\{\rho_{\mathrm{ref}}(t,f)\})}, \tag{16}$$

where t denotes localization using time slices, and t_0 is the observed time slice, while $\rho(t, f)$ and $\rho_{\mathrm{ref}}(t, f)$ denote the considered and reference TFD, respectively. The time-localization operator Γ_{t_0} sets all TFD samples to zero, except those in the vicinity of t_0:

$$\Gamma_{t_0}\{\rho(t,f)\} = \begin{cases} \rho(t,f), & t \in [t_0 - \Theta_t/2, t_0 + \Theta_t/2], \\ 0, & \text{otherwise}, \end{cases} \tag{17}$$

where Θ_t is the parameter controlling the time-window length. The reference signal is a cosine signal with an amplitude of 1 and a constant normalized frequency of 0.1, providing a reference energy of a single component in each time slice [34].

In [35,36], more research reveals the weaknesses of STRE for specific signal types and introduces NBRE to counteract them. Using NBRE, one may determine the local number of signal components per frequency slice, f_0, by substituting the frequency-localization operator for the time-localization parameter in Equation (16) with the frequency-localization operator:

$$\Gamma_{f_0}\{\rho(t,f)\} = \begin{cases} \rho(t,f), & f \in [f_0 - \Theta_f/2, f_0 + \Theta_f/2], \\ 0, & \text{otherwise}, \end{cases} \tag{18}$$

where Θ_f is the frequency window length. The reference signal is a delta function centered at $t = 15$ [36]. Note that $\rho(t, f)$ and $\rho_{\mathrm{ref}}(t, f)$ have to be obtained with the same TFD with reduced interference in order for the comparison to be valid.

The comparison between local numbers of components obtained from STRE and NBRE are shown in Figure 1 for the synthetic signal $z_{4\mathrm{LFM}}$, with $N_t = 256$ samples composed of four LFM components with different amplitudes embedded in additive Gaussian noise (AWGN) with a signal-to-noise ratio (SNR) SNR $= 3$ dB. Figure 1b,c show the reasoning behind introducing NBRE in [35,36]—an inaccurate increase in the local number of signal components, $NC_t(t)$, is evident for signals whose components are more aligned with the frequency axis (i.e., deviate from the method's reference component), such as the signal $z_{4\mathrm{LFM}}$, whose LO-ADTFD is shown in Figure 1a. On the other hand, when signals have components more aligned with the time axis, STRE presents more accurate estimations of the local number of signal components [35,36].

2.4. Multicomponent Instantaneous Frequency Estimation Algorithms

2.4.1. Image-Based Method

The first method for estimating the IF is an image processing method [37], which is divided into two sequential steps. In the first step, local peaks of the TFD are detected using its first and second derivatives as

$$B^{(\mathrm{IM})}(t,f) = \begin{cases} 1, & \frac{\mathrm{d}}{\mathrm{d}f}\rho(t,f) = 0 \text{ and } \frac{\mathrm{d}^2}{\mathrm{d}f^2}\rho(t,f) < 0, \\ 0, & \text{otherwise}, \end{cases} \tag{19}$$

which generates a binary (t, f) image consisting of ones on all peak locations and zeros on all other points. This step usually provides peaks that do not belong exclusively to the autoterms. Hence, in the second step, the IFs of signal components are extracted by using the m-connectivity criterion derived from image processing. In this work, we used $m = 10$, as in [7,22,37], which defines a 10-neighborhood set for a detected peak at location (x, y) as $\{(x-1, y), (x-1, y-1), (x-1, y+1), (x-1, y+2), (x-1, y-2), (x+1, y), (x+1, y-1), (x+1, y+1), (x+1, y+2), (x+1, y-2)\}$. According to this criterion, the points above and below the IF curves are not included, meaning that there can be only one frequency at any time instant for any given signal component.

Finally, a threshold must be specified for the minimum time duration of a valid signal component so that the final TFD contains only components that meet the threshold. In our example, where no prior knowledge of the input signal is available, the threshold is determined by the least component time support information provided by the STRE. This method demonstrated good computing efficiency and performance for real-world signals without requiring previous knowledge of the components' IF laws and amplitudes [7,22,37,38].

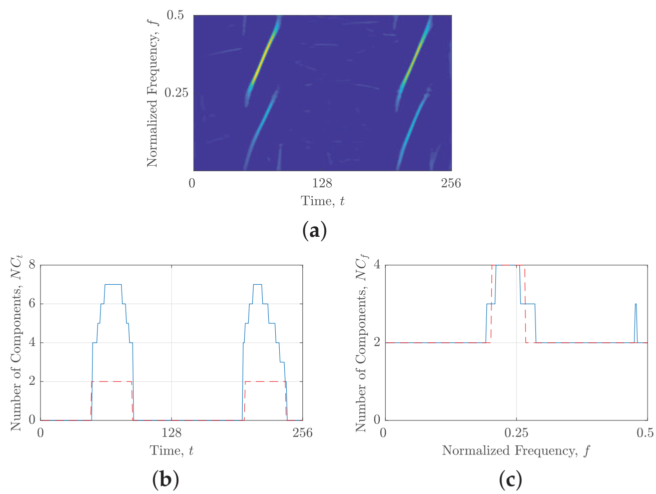

Figure 1. For the considered signal $z_{\mathrm{LFM}}(t)$: (**a**) $\rho_{(lo)}(t, f)$; (**b**) the local number of signal components, $NC_t(t)$, (ideal—dashed red line; obtained—solid blue line) obtained from the STRE; and (**c**) the local number of signal components, $NC_f(f)$, (ideal—dashed red line; obtained—solid blue line) obtained from the NBRE.

2.4.2. Blind-Source Separation Method

The second IF estimation method applied in this study is the blind-source separation (BSS) method, which is an efficient method for the localization and extraction of components from multicomponent signals in the TF domain [39]. The term "blind" refers to the provision of a mixture of statistically independent components without prior knowledge of its structure or number of components. The STRE's information on the time supports of components is included in the version of the approach utilized in this study, namely the BSS-STRE [40], thus removing the need for several thresholds required by the original method [39]. The steps of the BSS component extraction method are summarized below.

First, the TFD of a signal is computed, $\rho(t, f)$, and the corresponding $NC_t(t)$ from the STRE is obtained. The algorithm then locates the largest TFD peak at (t_0, f_0) and calculates the adaptive neighboring component frequency band, $\Delta B = B_L + B_R$, for the time slice $\rho(t_0, f_0 - B_L : f_0 + B_R)$. Next, the component is extracted at time-slice t_0, and $NC_t(t_0)$ is reduced by 1. Following that, the previous steps of the method are repeated in both directions around t_0 as $t_0 \leftarrow t_0 - 1$ and $t_0 \leftarrow t_0 + 1$ until the component edges are detected by the first derivation of $|NC_t(t)|$, $|NC_t'(t)| \neq 0$. If there is at least one component remaining in $\rho(t, f)$, the above steps are repeated for the succeeding component. The full pseudocode of this method may be found in [15,40].

The BSS method results in several TFDs, each containing a single extracted component from which the component IF is estimated in a separate vector. In order to be comparable with the $B^{(\mathrm{IM})}(t,f)$, all estimated IFs will be displayed within a single binary TFD, denoted by $B^{(\mathrm{BSS})}(t,f)$.

Note that the ADTFD, or more precisely, its automatically optimized version LO-ADTFD, is used as the underlying TFD in both estimation methods for this work, as its superior performance has been demonstrated in numerous IF estimation applications studies [38,45,46].

2.4.3. Limitations of the Considered IF Estimation Algorithms Based on STRE

The accuracy of IF estimation methods is highly dependent on the accuracy of STRE. The findings in [35,36] indicate that STRE is unsuitable for signals whose components deviate from the time axis, resulting in artificially increased $NC_t(t)$ and reduced estimation accuracy. Since this issue may occur in real-life signals, the question arises as to which IF estimation approach should be used for such signals. An incorrect $NC_t(t)$ in the image-based IF estimation method can lead to either too low a threshold, resulting in interference being classified as a true signal component, or too high a threshold, causing some true signal components to be rejected. In the case of the BSS method, an incorrect $NC_t(t)$ can result in incomplete extraction of signal components, and higher $NC_t(t)$ values may cause the estimation of interference IFs.

In this paper, we aim to demonstrate the negative consequences of using an inappropriate localization approach in estimating the IFs of signal components. Specifically, we show that such an approach can cause estimated IFs to be discontinuous and shifted away from the true component ridge. Although polynomial functions can approximate discontinuous estimation samples, the approximation error increases as more estimated samples do not belong to the autoterms. This phenomenon is particularly problematic for the image-based method, which requires a larger m-connectivity criterion to connect true signal components. Otherwise, discontinuous signal components are often classified as interference and fail to meet the threshold criteria. Increasing the m-connectivity criterion is not recommended, as it can lead to the linking of interference terms. Our paper aims to address these limitations by proposing the use of the frequency localization approach and the estimation of the GD with information from the NBRE method for certain signals. By doing so, we can minimize the negative effects of an inappropriate localization approach on IF estimation.

2.5. The Proposed Rényi-Entropy-Based Method for Component Alignment Detection towards Time or Frequency Axis

In this section, we present a novel method for the automatic detection of TFD regions that require a time or frequency localization strategy. Such a strategy involves using TFD analysis with time or frequency slices, linked to an estimate of IFs or GDs. To detect such regions, we implemented the STRE and NBRE methods, which are sensitive to estimate errors when dealing with signal components that vary from the methods' respective reference components. In this method, this sensitivity is turned into an advantage, as a considerable increase in the local number of signal components can indicate the need for an alternate localization strategy in a certain TFD region.

Next, the proposed method validates the detected increase in the local number of signal components by comparing the quality of IF and GD estimations in the identified TFD region. We observed that an incorrect localization approach can lead to discontinuous and inaccurate IF or GD estimations.

To estimate the IF and GD trajectories, we employed an approach based on the shrinkage operator proposed in [35,36] for sparse TFD reconstruction. The shrinkage operator, denoted with $\mathrm{shrink}_{t,f}$, operates independently for each time and frequency slice and removes samples that do not belong to the autoterms. The autoterms are locally associated with the $NC_t(t)$ or $NC_f(f)$ largest areas, where an area is calculated as a sum of samples between the minima to the left and right of the detected local maxima. This operator involves parameters δ_t and δ_f, which control the number of samples around local maxima classified as autoterms [35,36]. Hence, by applying the shrinkage operator on desired TFD with parameters $\delta_t = \delta_f = 1$, we may extract only local maxima belonging to signal autoterms, which basically represent the IF and GD estimations of signal components:

$$\rho^t(t,f) = \text{shrink}_t\{\rho(t,f)\}\big|_{\delta_t=1}, \quad \rho^f(t,f) = \text{shrink}_f\{\rho(t,f)\}\big|_{\delta_f=1}, \tag{20}$$

where the t, f notation denotes shrinkage performed over time or frequency slices, while $\rho^t(t,f)$ and $\rho^f(t,f)$ denote the signal's estimated IFs and GDs (or ridges), respectively.

To demonstrate the proposed method's steps, we created a synthetic signal, $z_{\text{mix}}(t)$, with $N_t = 256$ samples, consisting of two constant FM and four non-LFM components with various different directions and time/frequency supports. Figure 2 illustrates the LO-ADTFD of the signal, as well as its estimated IFs, $\rho^t_{(lo)}(t,f)$, and GDs, $\rho^f_{(lo)}(t,f)$. Observe that the estimate quality of signal components is distinct between $\rho^t_{(lo)}(t,f)$ and $\rho^f_{(lo)}(t,f)$. Specifically, Figure 2b displays four discontinuous non-LFM components in $\rho^t_{(lo)}(t,f)$ whose alignment deviates from the time axis. Alternatively, Figure 2c depicts the same occurrence for $\rho^f_{(lo)}(t,f)$ but with inverse results. Now, the identical four non-LFM components exhibit stronger connectivity than two constant FM components that are aligned with the time axis.

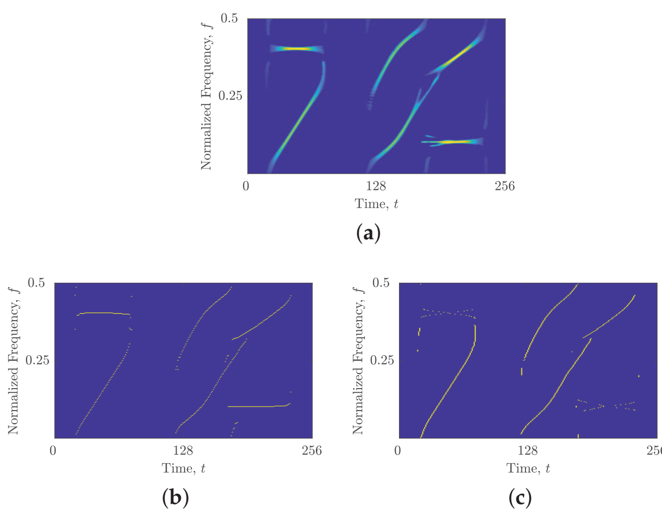

Figure 2. For the considered signal $z_{\text{mix}}(t)$: (**a**) $\rho_{(lo)}(t,f)$; (**b**) estimated IFs, $\rho^t_{(lo)}(t,f)$; and (**c**) estimated GDs, $\rho^f_{(lo)}(t,f)$.

To evaluate the quality of estimated IFs and GDs, we propose a metric based on the number of continuously connected regions of TFD samples denoted by N_r. Specifically, a TFD sample at location (x,y) is considered to be part of a region if it is connected to at least one sample in its 8-neighborhood set: $\{(x-1,y-1),(x-1,y),(x-1,y+1),(x,y-1),(x,y+1),(x+1,y-1),(x+1,y),(x+1,y+1)\}$. The resulting components are then counted to obtain N_r. This way, the proposed metric detects and penalizes discontinuities in the estimated IF or GD trajectories. Higher values of N_r indicate lower consistency among the estimated components (i.e., autoterms), reflecting a lower quality of the estimated IF or GD trajectories. In our proposed method, the result of the N_r metric serves as a decision-making factor in each TFD region under consideration.

The objective of our proposed method is to generate a binary component alignment map, denoted by $BM(t,f)$, that distinguishes TFD regions with components suitable for time or frequency localization using ones and zeros, respectively. We provide a comprehensive description of the proposed method's steps below:

1. The first step in the proposed approach involves calculating the TFD for a given signal in the time domain, followed by estimation of the IFs and GDs using the shrinkage operator, resulting in $\rho^t(t,f)$ and $\rho^f(t,f)$, as shown in Figure 2.
2. Now, the values of $N_r(\rho^t(t,f))$ and $N_r(\rho^f(t,f))$ are computed and compared. If $N_r(\rho^t(t,f)) \leq N_r(\rho^f(t,f))$, the proposed method assumes that signal components are primarily aligned with the time axis and generates $BM(t,f)$ using ones. Additionally, the STRE method is employed to calculate $NC_t(t)$, which is used to investigate local component behavior. Conversely, if $N_r(\rho^t(t,f)) > N_r(\rho^f(t,f))$, the proposed method generates $BM(t,f)$ using zeros and uses the NBRE with $NC_f(f)$ as the initial localization approach.
3. The proposed algorithm examines the input $NC_t(t)$ or $NC_f(f)$ for pronounced local maxima, which may indicate an inadequate local component for the current STRE or NBRE approach. To identify such maxima, we first locate all local maxima within $NC_t(t)$ (or $NC_f(f)$), followed by the calculation of the difference in the local number of signal components, denoted as ΔNC, between the observed maximum and the minima to the left and right. We consider all $\Delta NC \geq 1.50$ as "suspicious" intervals that require further analysis. The chosen threshold value of 1.50 is based on the desire to detect components that deviate from the respective time or frequency axis more than the LFM component, with a starting and stopping normalized frequency at 0 and 0.5, respectively. This component showed marginal accuracy for both approaches, with mean numbers of local components obtained as $\frac{1}{N_t}\sum_{t=1}^{N_t} NC_t(t) \approxeq \frac{1}{N_f}\sum_{f=1}^{N_f} NC_f(f) \approxeq 1.48$. If all ΔNC values are less than 1.50, the algorithm outputs a $BM(t,f)$ consisting of only ones or zeros and terminates. Otherwise, the algorithm proceeds to the next step for further analysis.
4. Next, the algorithm identifies a segment of time (or frequency) slices from $NC_t(t)$ (or $NC_f(f)$), where the edges are defined by local minima satisfying $\Delta NC \geq 1.50$. An example of $NC_f(f)$ for the signal $z_{\text{mix}}(t)$ is shown in Figure 3a, where the first segment is indicated by red dashed lines at frequency bins f_1 and f_2. The same segment is then extracted from a TFD, within which an unsuitable signal component for the current localization approach may be present. Figure 3b illustrates an example of $\rho_{(lo)}(t,f)$ with the segment constrained by the previously detected frequency bins f_1 and f_2, where a constant FM component needs to be further detected in the subsequent algorithm steps as unsuitable for the frequency localization approach.
5. At this point, additional localization is performed within the segmented TFD by computing the LRE in the opposite direction of the previous step. In particular, $NC_f(f)$ is calculated if $N_r(\rho^t(t,f)) \leq N_r(\rho^f(t,f))$, and $NC_t(t)$ is calculated if $N_r(\rho^t(t,f)) > N_r(\rho^f(t,f))$. We follow the same procedure as in the previous two steps, identifying all local maxima and minima with $\Delta NC \geq 1.50$. Then, we detect all segments with borders satisfying $\Delta NC \geq 1.50$, which define a 2D TF region or block within $\rho^t(t,f)$ and $\rho^t(t,f)$ that are evaluated in reference to the N_r value. If N_r is lower for a TFD block within $\rho^t(t,f)$ than in $\rho^f(t,f)$, it implies that a time localization technique is more suited, and $BM(t,f)$ in positions specified with a TFD block is set to 1; otherwise, it is set to 0. All the remaining estimated signal components that are saturated inside minima with $\Delta NC < 1.50$ belong to the current localization approach (which differs from the localization approach in the previous step), and the corresponding TFD block within the final $BM(t,f)$ changes its values from $1 \leftrightarrow 0$. Finally, the N_r value is compared in $\rho^t(t,f)$ and $\rho^f(t,f)$ for time samples or frequency bins where no component was detected (i.e., $NC_f(f) = 0$ or $NC_t(t) = 0$), and the $BM(t,f)$ is set to 0 or 1 based on the lower N_r value.

   Figure 4 illustrates the procedure described in this section. Firstly, an LO-ADTFD segment bounded in the range $[f_1, f_2]$ is extracted and subjected to an opposite LRE approach, such as STRE, to obtain the $NC_t(t)$, as shown in Figure 4a,b. The red dashed lines in Figure 4b denote the segment detected using the $NC_t(t)$, which defines a TFD block $(t_1 : t_2, f_1 : f_2)$ for evaluation in $\rho^t_{(lo)}(t, f)$ and $\rho^f_{(lo)}(t, f)$, shown in Figure 4c,d, respectively. The estimation of GDs within TFD blocks in red dashed lines exhibits superior connectivity than IF estimation, leading to the $BM(t_1 : t_2, f_1 : f_2)$ to remain unchanged from the initial values of zero. Since the constant FM component detected inside the green dashed lines does not produce inaccuracies in the $NC_t(t)$, as shown in Figure 4b, the $BM(t_3 : t_4, f_1 : f_2)$ is changed to one.

6. Steps 4 and 5 are repeated for the remaining detected segments in the $NC_t(t)$ (or $NC_f(f)$) input, i.e., until all $\Delta NC \geq 1.50$ are examined.

Figure 5 illustrates the $BM(t, f)$ obtained for the signal $z_{\text{mix}}(t)$, demonstrating that the proposed method effectively labeled both constant FM components for the time localization approach.

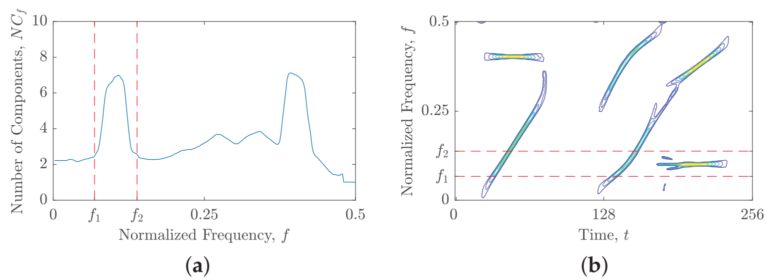

Figure 3. For the considered signal $z_{\text{mix}}(t)$: (**a**) the local number of signal components, $NC_f(f)$, obtained from the NBRE method; (**b**) LO-ADTFD. Red dashed lines mark the first segment $[f_1, f_2]$ chosen from $NC_f(f)$ in which a significant increase in $NC_f(f)$ is detected.

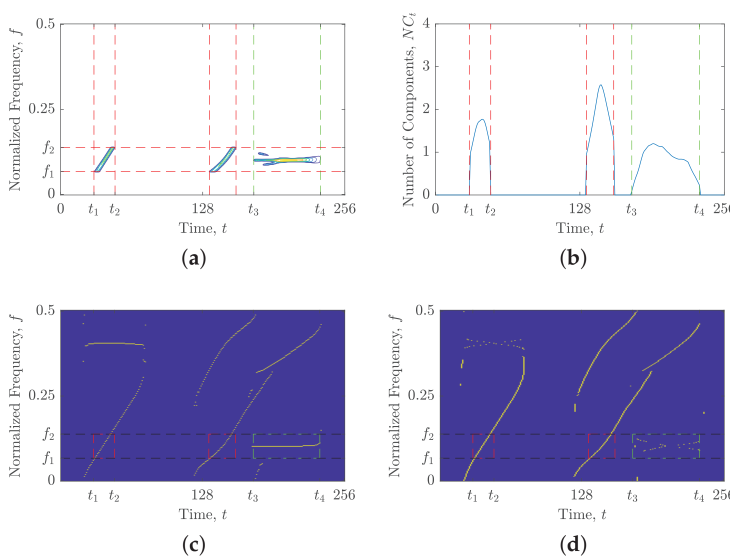

Figure 4. For the considered signal $z_{\text{mix}}(t)$: (**a**) segmented LO-ADTFD; (**b**) the local number of signal components $NC_t(t)$ calculated on segmented LO-ADTFD; and (**c**) $\rho^t_{(lo)}(t, f)$; (**d**) $\rho^f_{(lo)}(t, f)$. Red dashed lines mark detected segments that are evaluated with N_r measure in $\rho^t_{(lo)}(t, f)$ and $\rho^f_{(lo)}(t, f)$. Green dashed lines mark a segment that is considered to have components suitable for the current time localization approach.

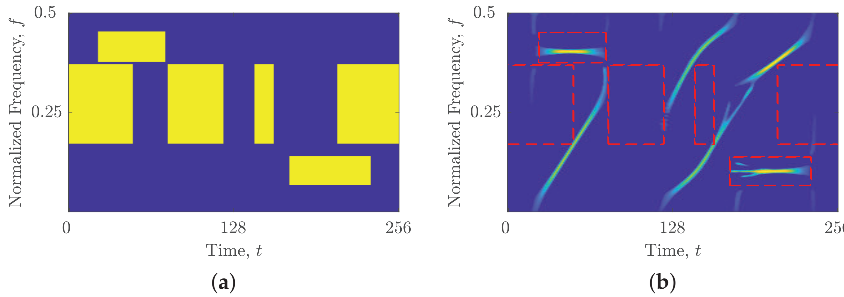

Figure 5. For the considered signal $z_{\mathrm{mix}}(t)$: (**a**) $BM(t,f)$; (**b**) $BM(t,f)$ with LO-ADTFD. Yellow and dashed red rectangles point to the TF regions suitable for analysis using time slices, while the rest of the TFD in blue should be analyzed using frequency slices.

2.6. Component Extraction Using the Component Alignment Map

The $BM(t,f)$ map obtained provides the means to extract signal components in the TFD. Extraction of these components is not achieved individually but through two sets of components: one suitable for localization through time slices and the other suitable for localization through frequency bins. The extraction process is simplified by multiplying the $BM(t,f)$ map with the TFD using the operator $\kappa\{\cdot\}$, which we defined in two ways. To derive the signal components corresponding to the localized approach through time slices, the operator $\kappa_t\{\cdot\}$ is used:

$$\kappa_t\{\rho(t,f)\} = \begin{cases} \rho(t,f), & BM(t,f) = 1, \\ 0, & BM(t,f) = 0, \end{cases} \tag{21}$$

where, by multiplying the $BM(t,f)$ map with TFD, only the regions defined by the units in $BM(t,f)$ are retained in TFD. Likewise, the operator $\kappa_f\{\cdot\}$ is employed to obtain the components corresponding to the localized approach through frequency bins:

$$\kappa_f\{\rho(t,f)\} = \begin{cases} \rho(t,f), & BM(t,f) = 0, \\ 0, & BM(t,f) = 1, \end{cases} \tag{22}$$

by means of which only the TFD regions that are defined by zeros in $BM(t,f)$ are kept in TFD.

Consequently, when $\max\{BM(t,f)\} = 1$ and $\min\{BM(t,f)\} = 0$, the input TFD can be split into two TFDs, $\kappa_t\{\rho(t,f)\}$ and $\kappa_f\{\rho(t,f)\}$, enabling the local number of signal components to be computed using the STRE and NBRE methods, respectively. Since both $\kappa_t\{\rho(t,f)\}$ and $\kappa_f\{\rho(t,f)\}$ are expected to contain components corresponding to the chosen localization approach, more precise estimates of the local number of signal components can be obtained compared with those obtained from the original TFD.

Figure 6 illustrates the results of applying the operators κ_t and κ_f to the signal $z_{\mathrm{mix}}(t)$. The obtained $\kappa_t\{\rho_{(lo)}(t,f)\}$ and $\kappa_f\{\rho_{(lo)}(t,f)\}$, shown in Figure 6a,b, respectively, contain components suitable for the chosen localization approach. This is further corroborated by the $NC_t(t)$ and $NC_f(f)$ estimates in $\kappa_t\{\rho_{(lo)}(t,f)\}$ and $\kappa_f\{\rho_{(lo)}(t,f)\}$, respectively, which lack significant inaccurate local maxima. Notably, the $NC_t(t)$ and $NC_f(f)$ estimates obtained from the split TFDs are considerably more precise than those obtained from the original TFD, as demonstrated in Figure 6c,d. However, it is important to emphasize that the estimates of the local number of signal components should be interpreted in conjunction with $BM(t,f)$, since they do not represent estimates of the entire TFD but rather of the TFD regions specified within $BM(t,f)$.

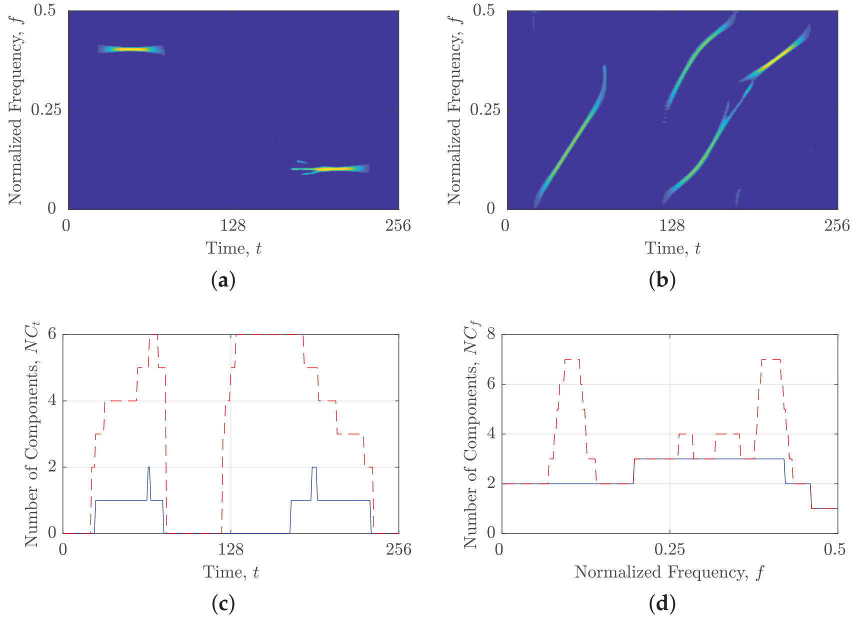

Figure 6. For the considered signal $z_{\text{mix}}(t)$: (**a**) $\kappa_t\{\rho_{(lo)}(t,f)\}$; (**b**) $\kappa_f\{\rho_{(lo)}(t,f)\}$; (**c**) the local number of signal components obtained by the STRE in starting TFD (red dashed line) and $\kappa_t\{\rho_{(lo)}(t,f)\}$ (blue solid line); and (**d**) the local number of signal components obtained by the NBRE in starting TFD (red dashed line) and $\kappa_f\{\rho_{(lo)}(t,f)\}$ (blue solid line).

2.7. Method for an Automatic Estimation of IF and GD

Upon completion of the necessary prerequisites, we propose a new method that can automatically estimate both the IF and GD of signal components in a TFD. This method leverages the use of the binary map $BM(t,f)$ to identify the TFD regions that require IF or GD estimation. Meanwhile, the behavior of the signal components, or autoterms, is defined by the local number of signal components obtained through the STRE and NBRE methods applied on TFDs with extracted components, $\kappa_t\{\rho(t,f)\}$ and $\kappa_f\{\rho(t,f)\}$, respectively.

The proposed method is composed of the following steps:

1. First, the input signal's TFD is processed using the $\kappa_{t,f}\{\cdot\}$ operator to obtain two TFDs: one TFD, $\kappa_t\{\rho(t,f)\}$, containing signal components suitable for IF estimation using a time-slice approach, and another TFD, $\kappa_f\{\rho(t,f)\}$, containing signal components suitable for GD estimation using a frequency-slice approach.
2. Next, the IFs are estimated from $\kappa_t\{\rho(t,f)\}$ using any IF estimation algorithm, the result of which is denoted as $B_t(t,f)$.
3. A matrix transpose is applied to the discrete version of $\kappa_f\{\rho(t,f)\}$, which interchanges the time and frequency axes and enables GD estimation in frequency slices using the same IF estimation algorithm approach, resulting in $B_f(t,f)$.
4. Finally, the IF and GD estimations are combined within a resulting binary TFD, $B(t,f)$, which is an output of the proposed method summing $B_t(t,f)$ and $B_f(t,f)$.

The proposed method's steps are visualized in Figure 7. We implemented the above-proposed method in the considered IF estimation methods, which may be now considered as IF/GD estimation algorithms utilizing both LRE methods, namely the image-based STRE-NBRE and BSS-STRE-NBRE.

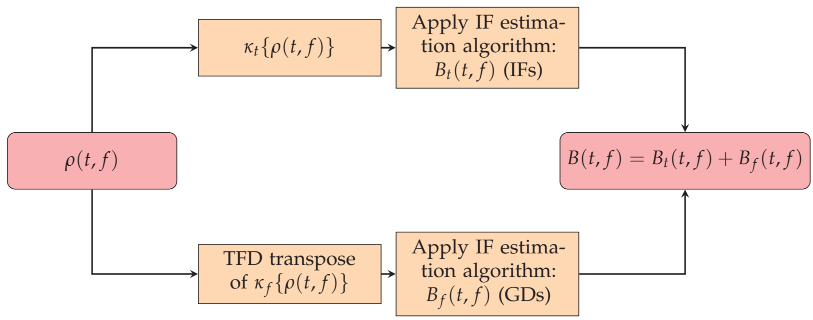

Figure 7. Simplified flowchart for the automatic IF and GD estimation for a given TFD.

It is worth noting that the combined estimates of the IF and GD may be extracted from the estimates generated by the operator $\text{shrink}_{t,f}\{\cdot\}$, previously used in the proposed method for $BM(t,f)$ as

$$B^{(\text{shrink})}(t,f) = \kappa_t\{\rho^t(t,f)\} + \kappa_f\{\rho^f(t,f)\}. \tag{23}$$

In the following section, the performance of the $B^{(\text{shrink})}(t,f)$ estimation is compared with that of the image-based and BSS methods.

2.8. EEG Dataset Description

Seizure signals in EEG recordings are often modeled as multicomponent piecewise FM signals:

$$s(t) = \sum_{i=1}^{NC} a_i(t) e^{j2\pi \int f_{0_i}(\tau)d\tau}. \tag{24}$$

However , this model does not take into consideration the spikes or short-duration transients that are regularly seen in EEG readings. In order to account for these spikes, the updated signal model that we use in this study is mathematically given as follows [7,30]:

$$s(t) = \sum_{i=1}^{NC} a_i(t) e^{j2\pi \int f_{0_i}(\tau)d\tau} + \sum_{i=1}^{NC} \delta(t - T_i), \tag{25}$$

where T_i is a time-varying shift.

Analyzing signals that contain both rhythmic and spike features using traditional TF techniques is challenging, as they have energy distributed along both the time and frequency axes. Smoothing along the frequency axis can eliminate cross-terms created by spikes, but it also reduces the resolution of the sinusoidal signal components. In addition, such signals require the use of a combined IF and GD estimation method, as estimating only the IFs fails to recover spike features [47,48].

We used a database of 200 EEG seizure segments, which were previously uploaded as supplementary material in [38] and have been used in [7,30,32,47], from which an illustrative example was chosen, as used in additional studies [22,31]. The data and relevant code are publicly available at https://github.com/nabeelalikhan1/EEG-Classification-IF-and-GD-features (accessed on 1 October 2022). The EEG recordings were obtained from newborns at the NICU of the Royal Brisbane and Women's Hospital, Brisbane, Australia, using the MEDELEC Profile System. Twelve electrodes were placed according to the international 10–20 standard, which were used to construct a 20-channel bipolar montage. The recordings underwent prefiltering using an analog bandpass filter with a bandwidth of 0.5 to 70 Hz. The signal was then sampled to 256 Hz before being digitally resampled to 32 Hz, as the majority of the signal energy is typically found below 12 Hz. The resulting signal segment is 8 s in duration and acquired at a sampling rate of 32 Hz, resulting in a total of $N_t = 256$ samples [7,30,32,38,47]. Previous studies have shown that a differentiator filter can be used to whiten the EEG background and enhance the signature of spikes in EEG signals [30,47,49,50]. Hence, the proposed IF/GD estimation method's performance was tested on EEG seizure signal without, denoted as $z_{\text{EEG}}(t)$, and with a differentiatior filter, denoted as $z_{\text{EEG}_{\text{filt}}}(t)$.

3. Results and Discussion

We compared the performance of the combined IF and GD estimation approach with that of the IF estimation approach alone for both synthetic signals, $z_{\text{LFM}}(t)$ and $z_{\text{mix}}(t)$, and real-life EEG seizure signals, $z_{\text{EEG}}(t)$ and $z_{\text{EEG}_{\text{filt}}}(t)$. It is important to note that for IF estimation only, algorithms use the STRE method applied to an input LO-ADTFD. However, for IF and GD estimation, the algorithms utilize the proposed method with $BM(t,f)$, along with the STRE and NBRE methods applied to the extracted components from an input LO-ADTFD using the proposed operators κ_t and κ_f. We calculated the STRE and NBRE using the parameter $\alpha_R = 3$, with $\Theta_t = \Theta_f = 11$ for the synthetic signals $z_{\text{LFM}}(t)$ and $z_{\text{mix}}(t)$ and $\Theta_t = \Theta_f = 5$ for the signals $z_{\text{EEG}}(t)$ and $z_{\text{EEG}_{\text{filt}}}(t)$, in order to capture spike features more precisely, which have been shown to be stable in [33,35,36,51].

To supplement the visual inspection of the results, it is important to quantify the impact of missing estimated IFs and GDs on the connectivity of components in the signal. Since the loss of components can occur at any point in the TFD, it is necessary to use a performance indicator that can monitor local components. To achieve this, we utilized an LRE-based indicator that has been shown to be effective in detecting reconstructed TFDs with discontinuous autoterms in prior work [36]. Specifically, we employed two performance indicators that measure the error between the local number of signal components in the original LO-ADTFD with fully preserved auto terms ($\rho_{(lo)}(t,f)$) and the TFD with estimated IFs/GDs ($B(t,f)$), using mean squared error (MSE) given as

$$\text{MSE}_t = \frac{1}{N_t}\sum_{t=1}^{N_t}\left(\frac{NC_t^{\rho_{(lo)}(t,f)}(t) - NC_t^{B(t,f)}(t)}{\max\left(NC_t^{\rho_{(lo)}(t,f)}(t), NC_t^{B(t,f)}(t)\right)}\right)^2, \tag{26}$$

$$\text{MSE}_f = \frac{1}{N_f}\sum_{f=1}^{N_f}\left(\frac{NC_f^{\rho_{(lo)}(t,f)}(f) - NC_f^{B(t,f)}(f)}{\max\left(NC_f^{\rho_{(lo)}(t,f)}(f), NC_f^{B(t,f)}(f)\right)}\right)^2, \tag{27}$$

$$\text{MSE}_{t,f} = \frac{\text{MSE}_t + \text{MSE}_f}{2}, \tag{28}$$

and mean absolute error (MAE) given as

$$\text{MAE}_t = \frac{1}{N_t}\sum_{t=1}^{N_t}\left|\frac{NC_t^{\rho_{(lo)}(t,f)}(t) - NC_t^{B(t,f)}(t)}{\max\left(NC_t^{\rho_{(lo)}(t,f)}(t), NC_t^{B(t,f)}(t)\right)}\right|, \tag{29}$$

$$\text{MAE}_f = \frac{1}{N_f}\sum_{f=1}^{N_f}\left|\frac{NC_f^{\rho_{(lo)}(t,f)}(f) - NC_f^{B(t,f)}(f)}{\max\left(NC_f^{\rho_{(lo)}(t,f)}(f), NC_f^{B(t,f)}(f)\right)}\right|, \tag{30}$$

$$\text{MAE}_{t,f} = \frac{\text{MAE}_t + \text{MAE}_f}{2}. \tag{31}$$

Higher values of $\text{MSE}_{t,f}$ and $\text{MAE}_{t,f}$ indicate a greater amount of missing estimated IFs and/or GDs in $B(t,f)$, suggesting that an inappropriate estimation strategy has been employed. Normalizing the local component count enabled a fair MSE and MAE comparison across signals.

3.1. Results for Synthetic Signals

The efficacy of the proposed $BM(t, f)$ was evaluated on the synthetic signal example $z_{\mathrm{LFM}}(t)$, with the results presented in Figure 8. Since all four LFM components of the signal $z_{\mathrm{LFM}}(t)$ deviate from the time axis, the estimated GDs, shown in Figure 8b, offer a better connection than the estimated IFs, shown in Figure 8a. Consequently, the proposed method generates the $BM(t, f)$ map, correctly highlighting the TFD regions along the signal's components for the frequency localization approach, as shown in Figure 8c,d.

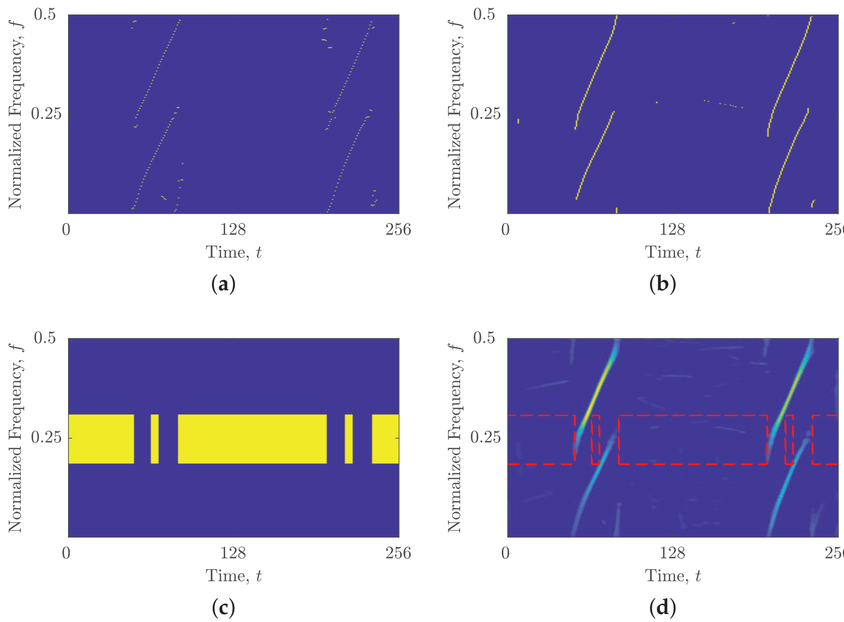

Figure 8. For the considered signal $z_{\mathrm{LFM}}(t)$: (**a**) estimated IFs, $\rho^{t}_{(lo)}(t, f)$; (**b**) estimated GDs, $\rho^{f}_{(lo)}(t, f)$; (**c**) $BM(t, f)$; and (**d**) $BM(t, f)$ with LO-ADTFD. Yellow and dashed red rectangles point to the TF regions suitable for analysis using time slices, while the rest of the TFD in blue should be analyzed using frequency slices.

In the case of the signal $z_{\mathrm{LFM}}(t)$, Figure 9a demonstrates that the image-based STRE method was incapable of linking TF peaks that deviate from the time axis, resulting in the rejection of all four LFM autoterms and the estimation of interference terms that were almost parallel to the time axis. However, when utilizing the proposed combined IF and GD estimation, the autoterms were fully estimated with high connectivity (as shown in Figure 9b). Nevertheless, some interference and noise terms were also estimated due to the obtained spike in $NC_f(f)$ estimation shown in Figure 1c, which provided a frequency support threshold that is too small. While the BSS-STRE method did not experience difficulties with missing components, the estimated IFs were highly discontinuous, and not all of them belonged to the autoterms, as shown in Figure 9c. Conversely, Figure 9d demonstrates that the combined IF and GD estimation resulted in significantly improved component connectivity, with nearly all samples belonging to the autoterms.

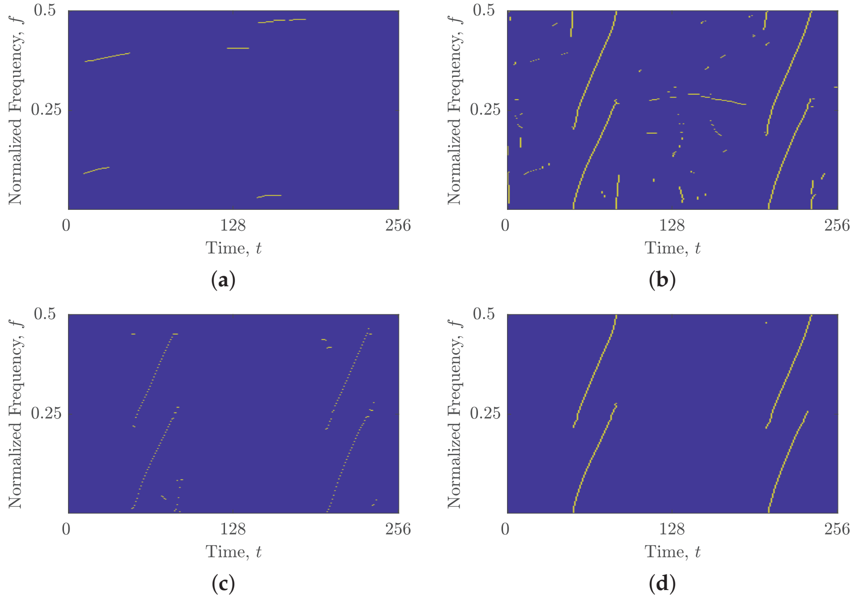

Figure 9. Estimated IFs and GDs for the signal $z_{\mathrm{LFM}}(t)$ in AWGN with SNR = 3 dB using (**a**) the image-based STRE method; (**b**) the image-based STRE-NBRE method; (**c**) the BSS-STRE method; and (**d**) the BSS-STRE-NBRE method.

Similar results were obtained for the signal $z_{\mathrm{mix}}(t)$. The image-based STRE method was unable to connect non-LFM components (or parts of components) that deviated from the time axis, as illustrated in Figure 10a. Meanwhile, the BSS-STRE method produced IF estimates that were discontinuous and dislocated from the true component ridge, as seen in Figure 10c. However, the proposed combined IF and GD estimation significantly improved the performance of both methods, as shown in Figure 10b,d. The performance of the $B^{(\mathrm{shrink})}(t,f)$ obtained by the shrinkage operator is depicted in Figure 11. For both signal examples, the estimated component ridges in the TFD showed superior performance compared with those obtained using the image-based method, while being very similar to the BSS method, demonstrating high component connectivity and belonging to the autoterms of the signal.

The results presented in Table 1 demonstrate a significant reduction in $\mathrm{MSE}_{t,f}$ and $\mathrm{MAE}_{t,f}$ when using the proposed method for combined IF and GD estimation with STRE and NBRE information. For the signals $z_{\mathrm{LFM}}(t)$ and $z_{\mathrm{mix}}(t)$, the image-based method's estimation improved by 71.25% and 81.11% in terms of $\mathrm{MSE}_{t,f}$ and 50.09% and 62.70% in terms of $\mathrm{MAE}_{t,f}$, respectively. The BSS method's estimation also improved by 92.95% and 83.17% in terms of $\mathrm{MSE}_{t,f}$ and 82.37% and 65.07% in terms of $\mathrm{MAE}_{t,f}$, respectively.

Moreover, the results demonstrate that the $B^{(\mathrm{shrink})}(t,f)$ obtained using the shrinkage-operator-based method for IF and GD estimation outperformed the image-based STRE and BSS-STRE methods—$\mathrm{MSE}_{t,f}$ and $\mathrm{MAE}_{t,f}$ values improved by up to 95.62% and 86.52%, respectively, for the signal $z_{\mathrm{LFM}}(t)$ and 90.01% and 72.79%, respectively, for the signal $z_{\mathrm{mix}}(t)$. Moreover, the results show that the obtained $B^{(\mathrm{shrink})}(t,f)$ is competitive with the $B^{(\mathrm{BSS})}(t,f)$ obtained using the BSS-STRE-NBRE algorithm, showing a reduction in $\mathrm{MSE}_{t,f}$ for $z_{\mathrm{LFM}}(t)$ by 3.20%, while the rest of the indicators are slightly in favor of the BSS-STRE-NBRE method (by up to 2.01%).

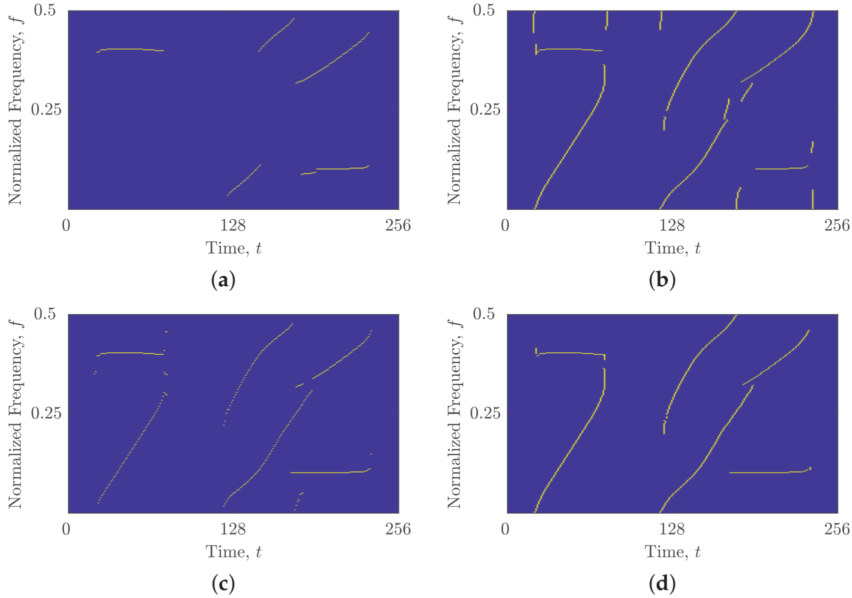

Figure 10. Estimated IFs and GDs for the signal $z_{\mathrm{mix}}(t)$ using (**a**) the image-based STRE method; (**b**) the image-based STRE-NBRE method; (**c**) the BSS-STRE method; and (**d**) the BSS-STRE-NBRE method.

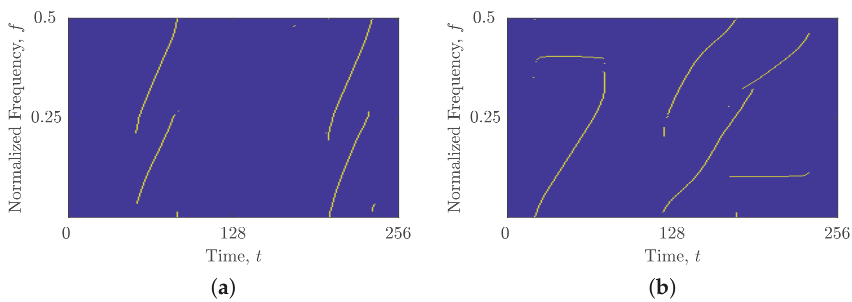

Figure 11. Estimated IFs and GDs obtained in $B^{(\mathrm{shrink})}(t,f)$ using the shrinkage operator for the signals: (**a**) $z_{\mathrm{LFM}}(t)$; (**b**) $z_{\mathrm{mix}}(t)$.

Table 1. Performance comparison between the combined IF and GD estimation versus the IF estimation for the synthetic signals: $z_{\mathrm{LFM}}(t)$ in AWGN with SNR $= 3$ dB and $z_{\mathrm{mix}}(t)$. Values in bold indicate the best-performing algorithm.

Algorithm	**Image-Based**	**Image-Based**	**BSS**	**BSS**	**Shrinkage Operator**
Support Information	**STRE**	**STRE and NBRE**	**STRE**	**STRE and NBRE**	**STRE and NBRE**
Estimation	IF	IF and GD	IF	IF and GD	IF and GD
Signal $z_{\mathrm{LFM}}(t)$ in AWGN with SNR $= 3$ dB					
$\mathrm{MSE}_{t,f}$	0.2487	0.0715	0.1517	**0.0107**	0.0109
$\mathrm{MAE}_{t,f}$	0.4059	0.2026	0.3041	**0.0536**	0.0547

Table 1. *Cont.*

Algorithm	Image-Based	Image-Based	BSS	BSS	Shrinkage Operator
Support Information	STRE	STRE and NBRE	STRE	STRE and NBRE	STRE and NBRE
Signal $z_{\mathrm{mix}}(t)$					
$\mathrm{MSE}_{t,f}$	0.2123	0.0401	0.1301	0.0219	**0.0212**
$\mathrm{MAE}_{t,f}$	0.3925	0.1464	0.3046	**0.1064**	0.1068

Sensitivity to Noise

In this study, the proposed shrinkage-operator-based, BSS-STRE-NBRE and image-based STRE-NBRE methods for estimating IF and GD were evaluated for their robustness to noise. Synthetic signals, including $z_{\mathrm{LFM}}(t)$ and $z_{\mathrm{mix}}(t)$, were embedded in AWGN with an SNR that varied between 0 and 10 dB in 1000 independent simulations. The F1 score metric, which combines precision and recall, was used to evaluate the algorithm's performance, given as

$$\mathrm{Precision} = \frac{\mathrm{TP}}{\mathrm{TP} + \mathrm{FP}}, \tag{32}$$

$$\mathrm{Recall} = \frac{\mathrm{TP}}{\mathrm{TP} + \mathrm{FN}}, \tag{33}$$

$$\mathrm{F1} = 2 \cdot \frac{\mathrm{Precision} \cdot \mathrm{Recall}}{\mathrm{Precision} + \mathrm{Recall}}, \tag{34}$$

where true positives (TP) and true negatives (TN) indicate the number of samples that were correctly estimated as a signal or noise/interference component, respectively, while false positives (FP) and false negatives (FN) refer to the number of noise/interference or signal samples that were incorrectly identified as signal or noise, respectively. Note that F1 values range from 0 to 1, with higher values indicating better performance.

To further validate the F1 score metric, the 2D MSE between the noise-free and noisy TFDs was calculated using the scaled and squared Frobenius norm as follows:

$$\text{F-norm} = \frac{1}{N_t N_f} ||B(t,f) - B^{(\mathrm{noise})}(t,f)||_{\mathrm{F}}^2 = \frac{1}{N_t N_f} \sum_{t=1}^{N_t} \sum_{f=1}^{N_f} |B(t,f) - B^{(\mathrm{noise})}(t,f)|^2. \tag{35}$$

The F-norm value was defined as the squared norm of the difference between the two TFDs, divided by the total number of time–frequency bins, $N_t \times N_f$. A lower F-norm value indicates better performance.

We evaluated the accuracy of the local number of signal component estimates by computing the MSE between $NC_t(t)$ and $NC_f(f)$ for both noise-free and noisy signals using Equation (3). The results, depicted in Figure 12, show that the LRE methods produce stable estimates for SNR values above 1 dB. Moreover, the noise sensitivity of all IF/GD estimation algorithms considered is determined by the sensitivity of LRE methods, as indicated by the F1 and F-norm values shown in Figures 13 and 14. Notably, the image-based STRE-NBRE method is more sensitive to noise than the shrinkage-operator-based and BSS-STRE-NBRE methods, as even minor inaccuracies in the estimated local number of signal components can result in poor threshold values, as seen in Figure 9b.

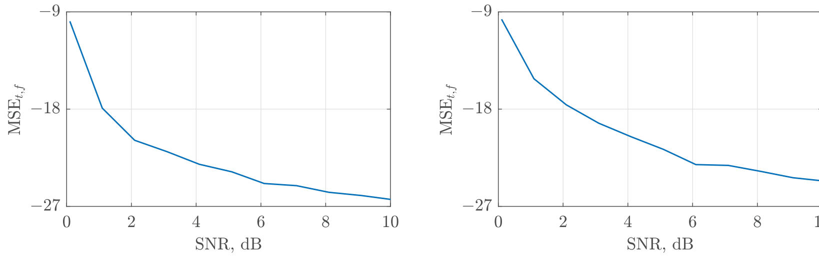

(a) **(b)**

Figure 12. MSE between the local number of signal components estimated from noise-free and noisy LO-ADTFDs in AWGN with SNR $= [0, 10]$ dB for the considered signals: **(a)** $z_{\mathrm{LFM}}(t)$; **(b)** $z_{\mathrm{mix}}(t)$.

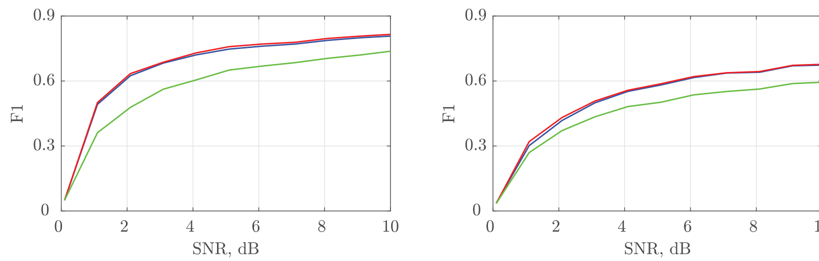

(a) **(b)**

Figure 13. F1 values for evaluating the shrinkage-operator-based (blue line), BSS-STRE-NBRE (red line) and image-based STRE-NBRE (green line) IF/GD estimation algorithms' sensitivity to AWGN in SNR $= [0, 10]$ dB for the considered signals: **(a)** $z_{\mathrm{LFM}}(t)$; **(b)** $z_{\mathrm{mix}}(t)$.

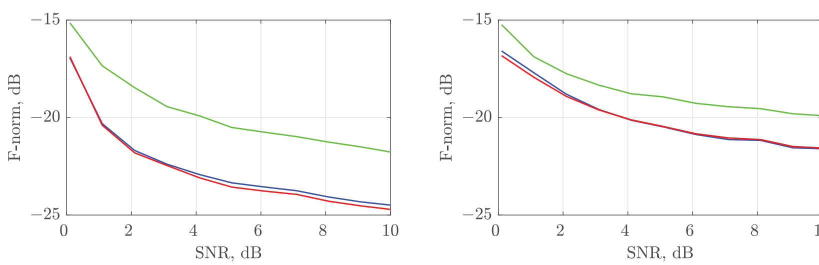

(a) **(b)**

Figure 14. F-norm values for evaluating the shrinkage-operator-based (blue line), BSS-STRE-NBRE (red line) and image-based STRE-NBRE methods' (green line) IF/GD estimation algorithms' sensitivity to AWGN in SNR $= [0, 10]$ dB for the considered signals: **(a)** $z_{\mathrm{LFM}}(t)$; **(b)** $z_{\mathrm{mix}}(t)$.

3.2. Results for Real-Life EEG Seizure Signals

Figure 15a presents the time-domain representation of the signal $z_{\mathrm{EEG}}(t)$, revealing several spikes. These spikes are effectively captured in the TF domain using LO-ADTFD, as demonstrated in Figure 15b,c for the original and filtered signals, $z_{\mathrm{EEG}}(t)$ and $z_{\mathrm{EEGfilt}}(t)$, respectively, which also reveal an additional single sinusoidal component. Notably, the differentiator filter significantly reduced the background noise and enhanced the desired spike components, leading to a cleaner signal, $z_{\mathrm{EEG_{filt}}}(t)$.

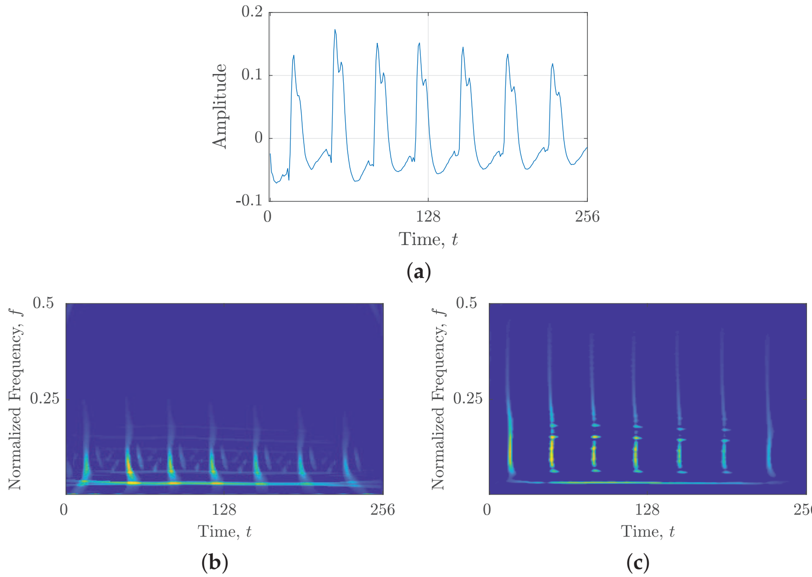

Figure 15. (**a**) EEG seizure signal considered in this study, $z_{\mathrm{EEG}}(t)$, represented in time domain; (**b**) LO-ADTFD of the signal $z_{\mathrm{EEG}}(t)$; and (**c**) LO-ADTFD of the signal $z_{\mathrm{EEG_{filt}}}(t)$.

Figure 16 demonstrates that the proposed $BM(t,f)$ effectively identified and separated the spike and sinusoidal components in both signals, $z_{\mathrm{EEG}}(t)$ and $z_{\mathrm{EEG_{filt}}}(t)$. As a result, Figure 17 displays the extracted sinusoidal and spike components in separate TFDs. The local number of components, $NC_t(t)$ and $NC_f(f)$, estimated from these TFDs, shows a significant reduction in inaccurate local maxima compared with those obtained from the input LO-ADTFD, as illustrated in Figure 18.

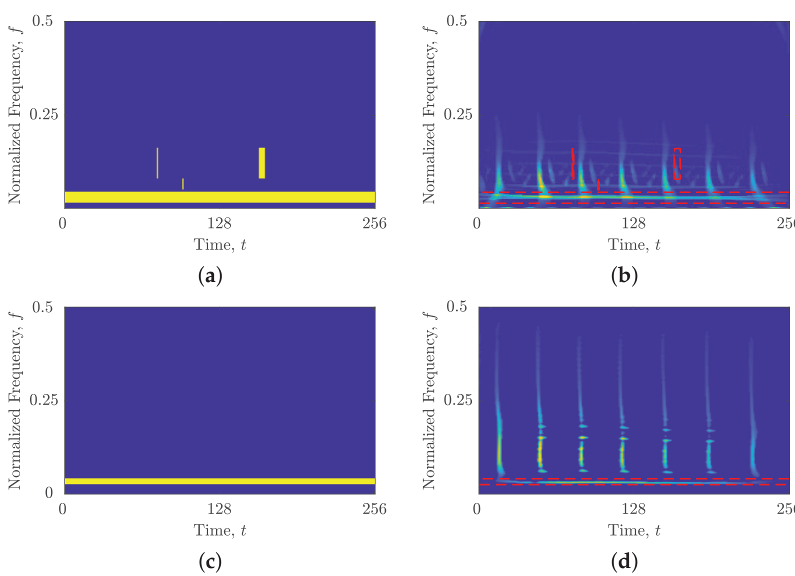

Figure 16. (**a**) $BM(t,f)$ for the signal $z_{\mathrm{EEG}}(t)$; (**b**) $BM(t,f)$ with LO-ADTFD for the signal $z_{\mathrm{EEG}}(t)$; (**c**) $BM(t,f)$ for the signal $z_{\mathrm{EEG_{filt}}}(t)$; and (**d**) $BM(t,f)$ with LO-ADTFD for the signal $z_{\mathrm{EEG_{filt}}}(t)$.

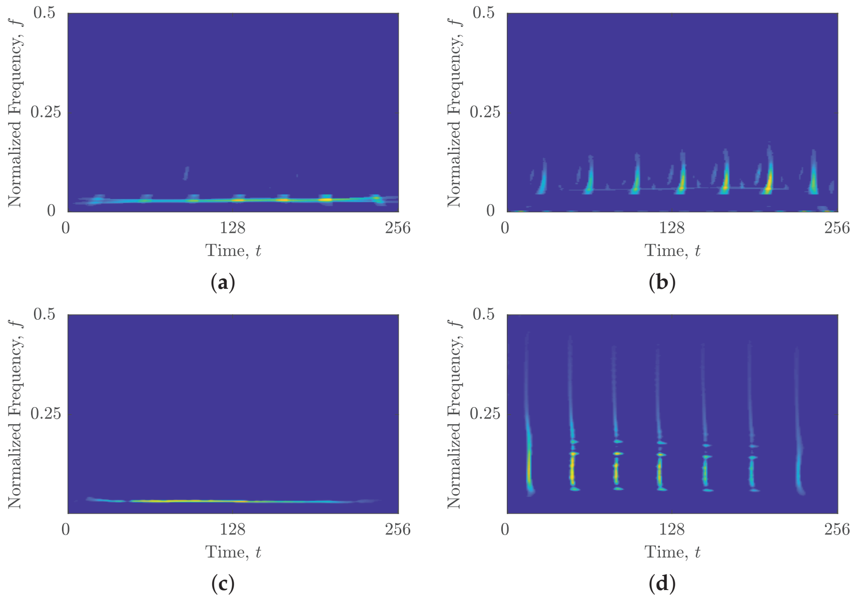

Figure 17. Extracted components with (**a**) $\kappa_t\{\rho_{(lo)}(t, f)\}$ for the signal $z_{\mathrm{EEG}}(t)$; (**b**) $\kappa_f\{\rho_{(lo)}(t, f)\}$ for the signal $z_{\mathrm{EEG}}(t)$; (**c**) $\kappa_t\{\rho_{(lo)}(t, f)\}$ for the signal $z_{\mathrm{EEG_{filt}}}(t)$; and (**d**) $\kappa_f\{\rho_{(lo)}(t, f)\}$ for the signal $z_{\mathrm{EEG_{filt}}}(t)$.

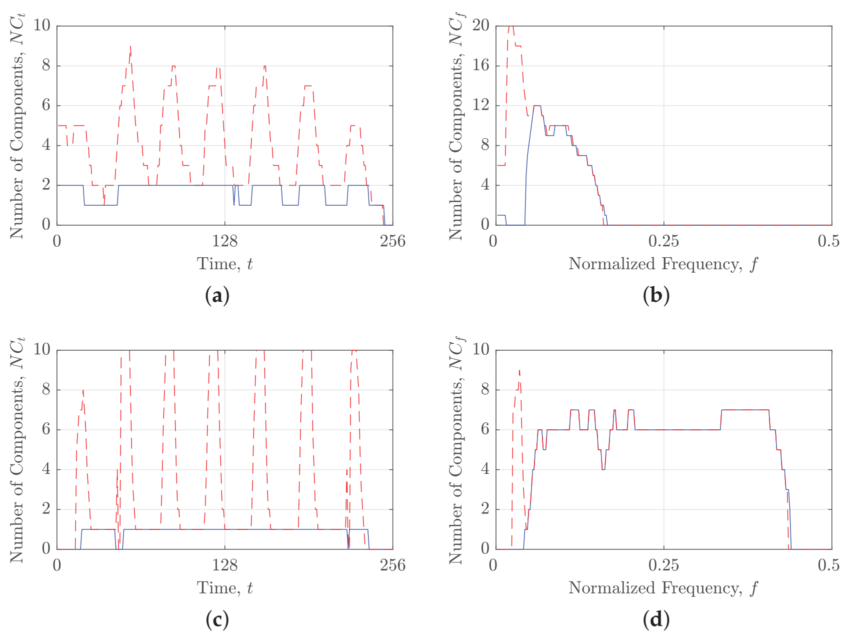

Figure 18. Comparison between the local number of signal components obtained by STRE and NBRE in starting TFD (dashed red line) and from extracted components using the proposed operators κ_t and κ_f (solid blue line) for the signals: (**a**,**b**) $z_{\mathrm{EEG}}(t)$; (**c**,**d**) $z_{\mathrm{EEG_{filt}}}(t)$.

Figure 19 displays the estimated IFs and GDs of the existing approach in [47] for the signals $z_{\mathrm{EEG}}(t)$ and $z_{\mathrm{EEGfilt}}(t)$. The IFs are estimated from the signal in the time domain, while the GDs are obtained from the Fourier transform of a signal using the duality property, which transposes a signal in the TF domain [47]. The results indicate that the approach is effective in estimating the IFs and GDs for the filtered EEG signal $z_{\mathrm{EEGfilt}}(t)$ used in the original study [47]. However, the approach proved unsuitable for estimating the GDs of the unfiltered signal $z_{\mathrm{EEG}}(t)$ due to the presence of background noise and the inconsistent number of components over the TF domain, leading to inaccurate GD estimates, as illustrated in Figure 19d. Furthermore, it is worth noting that the user needs to provide the global number of components to obtain these estimates, which may present a practical limitation when acquiring an unknown signal.

Figures 20 and 21 compare the performance of the IF estimation methods against the proposed mutual IFs and GDs estimations. As the spike and sinusoidal components are perpendicular to each other, their estimated IFs exhibit completely opposite performances. Specifically, all IF estimation methods successfully estimated the IFs of the sinusoidal component, while the IF estimates of the spike components were highly discontinuous and, especially for the unfiltered signal $z_{\mathrm{EEG}}(t)$, indistinguishable from the background samples. However, estimating the GDs for the spike components significantly improved their connectivity and overall preservation, as shown in Figures 20 and 21, using all considered IF and GD estimation methods.

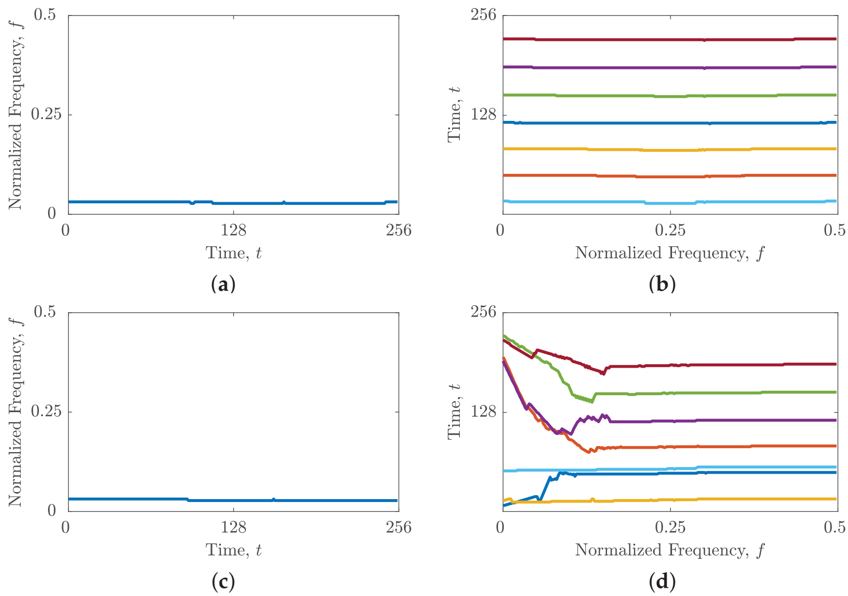

Figure 19. Using the method proposed in [47]: (**a**) estimated IFs of the signal $z_{\mathrm{EEG_{filt}}}(t)$; (**b**) estimated GDs of the signal $z_{\mathrm{EEG_{filt}}}(t)$; (**c**) estimated IFs of the signal $z_{\mathrm{EEG}}(t)$; and (**d**) estimated GDs of the signal $z_{\mathrm{EEG}}(t)$.

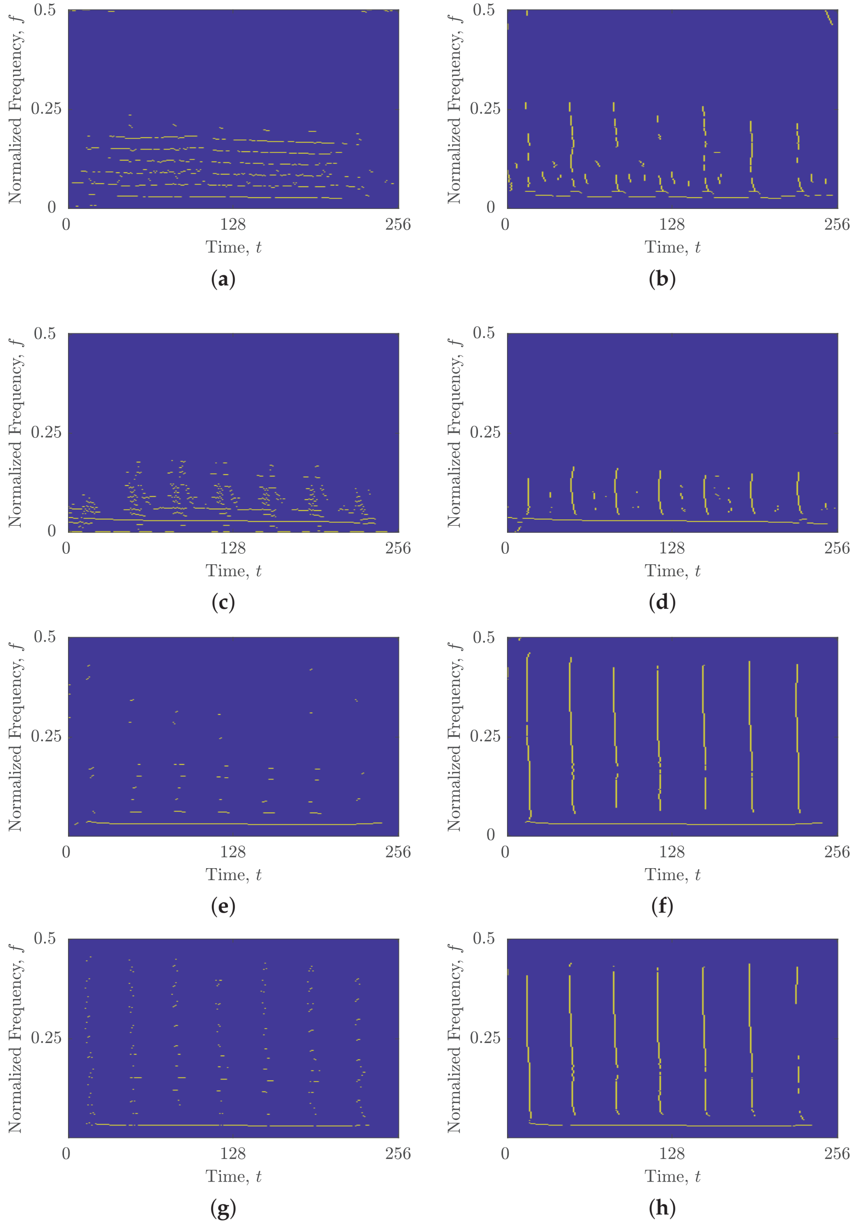

Figure 20. Estimated IFs and GDs using (**a**) the image-based STRE method for the signal $z_{\mathrm{EEG}}(t)$; (**b**) the image-based STRE-NBRE method for the signal $z_{\mathrm{EEG}}(t)$; (**c**) the BSS-STRE method for the signal $z_{\mathrm{EEG}}(t)$; (**d**) the BSS-STRE-NBRE method for the signal $z_{\mathrm{EEG}}(t)$; (**e**) the image-based STRE method for the signal $z_{\mathrm{EEG_{filt}}}(t)$; (**f**) the image-based STRE-NBRE method for the signal $z_{\mathrm{EEG_{filt}}}(t)$; (**g**) the BSS-STRE method for the signal $z_{\mathrm{EEG_{filt}}}(t)$; and (**h**) the BSS-STRE-NBRE method for the signal $z_{\mathrm{EEG_{filt}}}(t)$.

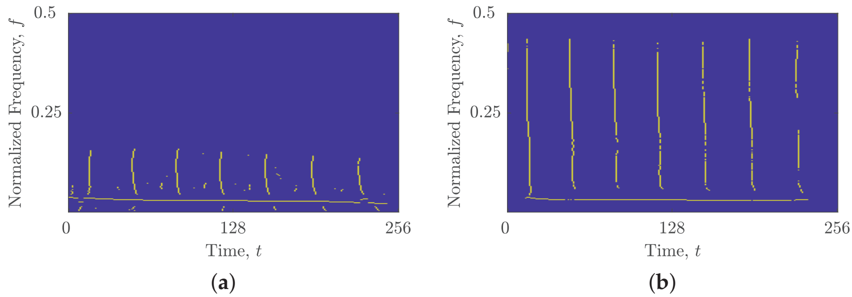

Figure 21. Estimated IFs and GDs obtained in $B^{(\mathrm{shrink})}(t,f)$ using the shrinkage operator for the signals: (**a**) $z_{\mathrm{EEG}}(t)$; (**b**) $z_{\mathrm{EEG_{filt}}}(t)$.

The numerical results of the mutual IF and GD estimations, presented on illustrative $z_{\mathrm{EEG}}(t)$ and averaged on a dataset containing 200 examples, are summarized in Table 2. The results confirm that the combined IF and GD estimation approach outperforms the IF estimation alone. Specifically, for the EEG dataset of unfiltered $z_{\mathrm{EEG}}(t)$ signals, the image-based STRE-NBRE and BSS-STRE-NBRE algorithms improved the $\overline{\mathrm{MSE}}_{t,f}$ and $\overline{\mathrm{MAE}}_{t,f}$ indicators by up to 42.23% and 30.08%, respectively, compared with the image-based STRE and BSS-STRE algorithms. Improvements were obtained for the dataset of filtered EEG signals $z_{\mathrm{EEGfilt}}(t)$ also, where the $\overline{\mathrm{MSE}}_{t,f}$ and $\overline{\mathrm{MAE}}_{t,f}$ indicators were reduced by up to 34.96% and 33.41%, respectively, considering the same algorithms, namely the image-based STRE-NBRE and BSS-STRE-NBRE. Furthermore, the obtained results show the superiority of the shrinkage operator to the image-based STRE and BSS-STRE algorithms, with improvements of up to 46.45% and 36.61% for the dataset of $z_{\mathrm{EEG}}(t)$ signals and up to 31.71% and 30.35% for the dataset of $z_{\mathrm{EEGfilt}}(t)$ signals in terms of $\overline{\mathrm{MSE}}_{t,f}$ and $\overline{\mathrm{MAE}}_{t,f}$, respectively. Again, the shrinkage operator approach was shown to be competitive with the BSS-STRE-NBRE algorithm.

Table 2. Performance comparison between the combined IF and GD estimation versus the IF estimation for EEG seizure signals $z_{\mathrm{EEG}}(t)$ and $z_{\mathrm{EEG_{filt}}}(t)$. Values in bold indicate the best-performing algorithm.

Algorithm	**Image-Based**	**Image-Based**	**BSS**	**BSS**	**Shrinkage Operator**
Support Information	**STRE**	**STRE and NBRE**	**STRE**	**STRE and NBRE**	**STRE and NBRE**
Estimation	IF	IF and GD	IF	IF and GD	IF and GD
			Illustrative example of $z_{\mathrm{EEG}}(t)$		
$\mathrm{MSE}_{t,f}$	0.0488	0.0265	0.0399	0.0215	**0.0196**
$\mathrm{MAE}_{t,f}$	0.1505	0.1081	0.1194	0.0955	**0.0894**
			Illustrative example of $z_{\mathrm{EEG_{filt}}}(t)$		
$\mathrm{MSE}_{t,f}$	0.0642	0.0516	0.0738	**0.0481**	0.0487
$\mathrm{MAE}_{t,f}$	0.2897	0.2012	0.3033	**0.1972**	0.1987
			Dataset containing 200 examples of $z_{\mathrm{EEG}}(t)$		
$\overline{\mathrm{MSE}}_{t,f}$	0.0521	0.0301	0.0481	0.0288	**0.0279**
$\overline{\mathrm{MAE}}_{t,f}$	0.1732	0.1211	0.1411	0.1122	**0.1098**
			Dataset containing 200 examples of $z_{\mathrm{EEG_{filt}}}(t)$		
$\overline{\mathrm{MSE}}_{t,f}$	0.0728	0.0588	0.0801	**0.0521**	0.0547
$\overline{\mathrm{MAE}}_{t,f}$	0.3120	0.2312	0.3325	**0.2214**	0.2316

3.3. Interpretation of Obtained Results

The experimental results show that the proposed method, which generates a binary map $BM(t, f)$, successfully identifies regions in the TFD that contain signal components requiring different time or frequency localization approaches for all considered synthetic and real-life EEG signals. Furthermore, it is shown that estimating the local number of signal components on extracted TFDs significantly reduces local estimation inaccuracies compared with the original estimate on the TFD with all components present.

The results obtained when comparing mutual IF and GD estimation with IF estimation alone show a significant improvement in estimated component connectivity and preservation for all considered synthetic and real-life EEG signals. The image-based STRE-NBRE and BSS-STRE-NBRE methods effectively used frequency support information from NBRE, providing IF and GD estimates without requiring prior knowledge about the signal. The results also show that IF and GD estimates can be obtained using the shrinkage operator derived from sparse reconstruction, which has competitive performance compared with the BSS algorithm, while both outperforming the image-based algorithm. Additionally, the considered algorithms' robustness to noise was connected with the STRE and NBRE methods, where the BSS-STRE-NBRE and shrinkage-operator-based estimations outperformed the image-based STRE-NBRE algorithm for all considered SNRs. The image-based algorithm's dependence on LRE accuracy is the reason behind this, where even the smallest error can cause a threshold that is too small or too large for the method.

The advantage of the BSS algorithm over the shrinkage operator is that it extracts components one by one using the double-directional approach. This implies that the estimated samples follow a line, which is evident when comparing Figures 9d and 11a. However, this can be a disadvantage if interference is falsely chosen as a component due to its higher maxima than the autoterm's, as the BSS algorithm will force the estimation of an interference. In this case, tracking the largest local surfaces instead of only local maxima in the shrinkage operator can avoid some interference samples, as shown in Figures 20d and 21a.

The results show that the proposed method is feasible to be used for estimating IFs and GDs of EEG seizure signals, $z_{\mathrm{EEG}}(t)$ and $z_{\mathrm{EEG}_{\mathrm{filt}}}(t)$. In the case of the filtered signal $z_{\mathrm{EEG}_{\mathrm{filt}}}(t)$, the estimated IFs and GDs using the proposed method are competitive with the approach in [47], with the significant advantage that the proposed method does not require the number of components to be set in advance. However, for the unfiltered signal $z_{\mathrm{EEG}}(t)$, the proposed method outperforms the approach in [47] and shows feasibility for signals whose number of components changes over time.

It should be noted that when extracting intersecting components that require different localization approaches, a small portion of components near the intersection point may be extracted in a different TFD. This phenomenon is evident in Figure 17a,b for the unfiltered EEG signal $z_{\mathrm{EEG}}(t)$, where we observe that small parts of spike components have been extracted alongside the sinusoidal component. This behavior can be attributed to the practical calculation of STRE and NBRE, where the sliding window with size Θ_t or Θ_f within the stable range defined in [33,51] detects a component's time or frequency support as a few samples or bins more than the ideal. Consequently, the TFD region borders in the proposed $BM(t, f)$ are slightly wider than the actual component's time or frequency support to accommodate for this behavior.

4. Conclusions

The analysis of signals that exhibit both rhythmic and spike features, such as EEG seizure signals, presents a significant challenge when utilizing conventional TF methods. In order to extract valuable components that are distributed across both the time and frequency axes, a comprehensive method is necessary. In this paper, we introduced a novel method for automatically estimating the IF and GD of a signal in the TF domain. In order to define TFD regions requiring a different time or frequency localization strategy, we proposed a method for generating a binary map $BM(t, f)$ based on the information from

LRE methods. An increase in the local number of signal components obtained using the LRE methods was indicative of the presence of a component that may require a different localization approach than what was observed, whereas measuring IF and GD estimates with the proposed measure N_r was effective for identifying discontinuous estimates.

Through the implementation of the suggested $BM(t, f)$, we successfully extracted components that necessitate either a time or frequency localization approach, thereby yielding more accurate evaluations of the numbers of local components using the STRE and NBRE methods. The STRE method's reduced accuracy for certain signals prompted modifications to image-based and BSS IF estimation algorithms, enabling them to efficiently incorporate the NBRE method and decrease their dependence on the STRE method. The proposed method yielded a notable enhancement in performance and facilitated the simultaneous estimation of IF and GD.

The results obtained demonstrate that the proposed method's combined IF and GD estimation outperforms the IF estimation alone. This was demonstrated through the analysis of noisy synthetic and real-life EEG seizure signals with characteristic rhythmic and spike features. In contrast to current methodologies, the proposed approach does not necessitate an a priori understanding of an input signal and is applicable to signals whose number of components varies with time or frequency.

The following research efforts will focus on the advancement of characteristics that can distinguish and categorize EEG signals from the surrounding environment, utilizing the IF and GD evaluations derived from this study. Furthermore, a research area of interest involves the creation of a concentration measure for TFDs utilizing the estimated IFs and GDs. The primary objective of this measure will be to impose a penalty for the lack of autoterms that occurs in signal processing using advanced TF techniques.

Author Contributions: Conceptualization, V.J., M.V., N.L. and G.M.J.; methodology, V.J. and M.V.; software, V.J.; validation, V.J.; formal analysis, V.J. and M.V.; investigation, V.J.; resources, V.J.; data curation, V.J. and M.V.; writing—original draft preparation, V.J.; writing—review and editing, V.J., M.V., N.L. and G.M.J.; visualization, V.J.; supervision, M.V.; project administration, M.V. and N.L.; funding acquisition, M.V. and N.L. All authors have read and agreed to the published version of the manuscript.

Funding: This research was funded by the University of Rijeka under the projects "Analysis and Classification of Non-Stationary Signals Using Advanced Deep Learning Methods" (uniri-mladi-tehnic-22-16), "Computer-Aided Digital Analysis And Classification of Signals" (uniri-tehnic-18-17), and the ZIP UNIRI project "Development of computational algorithms based on digital signal processing and artificial intelligence methods with application in modern transport systems".

Institutional Review Board Statement: Not applicable.

Informed Consent Statement: Not applicable.

Data Availability Statement: Not applicable.

Conflicts of Interest: The authors declare no conflict of interest.

Abbreviations

The following abbreviations are used in this manuscript:

ADTFD	Adaptive directional time–frequency distribution
AF	Ambiguity function
AWGN	Additive white Gaussian noise
BSS	Blind-source separation
DGF	Derivative directional Gaussian filter
EEG	Electroencephalogram
EMBD	Extended modified B distribution
GD	Group delay

IF	Instantaneous frequency
LFM	Linear frequency-modulated
LO-ADTFD	Locally optimized adaptive directional time–frequency distribution
LRE	Local Rényi entropy
MAE	Mean absolute error
MSE	Mean squared error
NBRE	Narrow-band Rényi entropy
SNR	Signal-to-noise ratio
STRE	Short-term Rényi entropy
TF	Time–frequency
TFD	Time–frequency distribution
WVD	Wigner–Ville distribution
QTFD	Quadratic time–frequency distribution

References

1. Varsavsky , A.; Mareels, I.; Cook, M. *Epileptic Seizures and the EEG: Measurement, Models, Detection and Prediction*; Taylor & Francis: Abingdon, UK, 2011.
2. del Rincon, J.M.; Santofimia, M.J.; del Toro, X.; Barba, J.; Romero, F.; Navas, P.; Lopez, J.C. Non-linear classifiers applied to EEG analysis for epilepsy seizure detection. *Expert Syst. Appl.* **2017**, *86*, 99–112. [CrossRef]
3. Joshi, V.; Pachori, R.B.; Vijesh, A. Classification of ictal and seizure-free EEG signals using fractional linear prediction. *Biomed. Signal Process. Control.* **2014**, *9*, 1–5. [CrossRef]
4. Pachori, R.B.; Bajaj, V. Analysis of normal and epileptic seizure EEG signals using empirical mode decomposition. *Comput. Methods Programs Biomed.* **2011**, *104*, 373–381. [CrossRef]
5. Kumar, T.S.; Kanhangad, V.; Pachori, R.B. Classification of seizure and seizure-free EEG signals using local binary patterns. *Biomed. Signal Process. Control.* **2015**, *15*, 33–40. [CrossRef]
6. Yuan, Q.; Zhou, W.; Zhang, L.; Zhang, F.; Xu, F.; Leng, Y.; Wei, D.; Chen, M. Epileptic seizure detection based on imbalanced classification and wavelet packet transform. *Seizure* **2017**, *50*, 99–108. [CrossRef]
7. Khan, N.A.; Ali, S. Classification of EEG Signals Using Adaptive Time-Frequency Distributions. *Metrol. Meas. Syst.* **2016**, *23*, 251–260. [CrossRef]
8. Sharma, M.; Pachori, R.B.; Rajendra Acharya, U. A new approach to characterize epileptic seizures using analytic time-frequency flexible wavelet transform and fractal dimension. *Pattern Recognit. Lett.* **2017**, *94*, 172–179. [CrossRef]
9. Bhattacharyya, A.; Pachori, R.B.; Upadhyay, A.; Acharya, U.R. Tunable-Q Wavelet Transform Based Multiscale Entropy Measure for Automated Classification of Epileptic EEG Signals. *Appl. Sci.* **2017**, *7*, 385. [CrossRef]
10. Kalbkhani, H.; Shayesteh, M.G. Stockwell transform for epileptic seizure detection from EEG signals. *Biomed. Signal Process. Control.* **2017**, *38*, 108–118. [CrossRef]
11. Tzallas, A.T.; Tsipouras, M.G.; Fotiadis, D.I. The Use of Time-Frequency Distributions for Epileptic Seizure Detection in EEG Recordings. In Proceedings of the 2007 29th Annual International Conference of the IEEE Engineering in Medicine and Biology Society, Lyon, France, 22–26 August 2007; pp. 3–6. [CrossRef]
12. Tzallas, A.T.; Tsipouras, M.G.; Fotiadis, D.I. Epileptic Seizure Detection in EEGs Using Time–Frequency Analysis. *IEEE Trans. Inf. Technol. Biomed.* **2009**, *13*, 703–710. [CrossRef]
13. Lerga, J.; Saulig, N.; Mozetič, V. Algorithm based on the short-term Rényi entropy and IF estimation for noisy EEG signals analysis. *Comput. Biol. Med.* **2017**, *80*, 1–13. [CrossRef] [PubMed]
14. Tapani, K.T.; Vanhatalo, S.; Stevenson, N.J. Time-Varying EEG Correlations Improve Automated Neonatal Seizure Detection. *Int. J. Neural Syst.* **2019**, *29*, 1850030. [CrossRef] [PubMed]
15. Lerga, J.; Saulig, N.; Stanković, L.; Seršić, D. Rule-Based EEG Classifier Utilizing Local Entropy of Time–Frequency Distributions. *Mathematics* **2021**, *9*, 451. [CrossRef]
16. Madhale Jadav, G.; Lerga, J.; Štajduhar, I. Adaptive filtering and analysis of EEG signals in the time-frequency domain based on the local entropy. *EURASIP J. Adv. Signal Process.* **2020**, *2020*, 7. [CrossRef]
17. Farooq, M.S.; Zulfiqar, A.; Riaz, S. Epileptic Seizure Detection Using Machine Learning: Taxonomy, Opportunities, and Challenges. *Diagnostics* **2023**, *13*, 1058. [CrossRef]
18. Khan, N.A.; Ali, S.; Choi, K. Modified Time-Frequency Marginal Features for Detection of Seizures in Newborns. *Sensors* **2022**, *22*, 3036. [CrossRef]
19. Mir, W.A.; Anjum, M.; Izharuddin.; Shahab, S. Deep-EEG: An Optimized and Robust Framework and Method for EEG-Based Diagnosis of Epileptic Seizure. *Diagnostics* **2023**, *13*, 773. [CrossRef]
20. Deriche, M.; Arafat, S.; Al-Insaif, S.; Siddiqui, M. Eigenspace Time Frequency Based Features for Accurate Seizure Detection from EEG Data. *IRBM* **2019**, *40*, 122–132. [CrossRef]
21. Varlı, M.; Yılmaz, H. Multiple classification of EEG signals and epileptic seizure diagnosis with combined deep learning. *J. Comput. Sci.* **2023**, *67*, 101943. [CrossRef]

22. Boashash, B. *Time-Frequency Signal Analysis and Processing, A Comprehensive Reference*, 2nd ed.; Elsevier: Amsterdam, The Netherlands, 2016.
23. Lopac, N.; Hržić, F.; Vuksanović, I.P.; Lerga, J. Detection of Non-Stationary GW Signals in High Noise From Cohen's Class of Time-Frequency Representations Using Deep Learning. *IEEE Access* **2021**, *10*, 2408–2428. [CrossRef]
24. Lopac, N. Detection of Gravitational-Wave Signals from Time-Frequency Distributions Using Deep Learning. Ph.D. Thesis, University of Rijeka, Faculty of Engineering, Rijeka, Croatia, 2022.
25. Stankovic, L.; Dakovic, M.; Thayaparan, T. *Time-Frequency Signal Analysis with Applications*; Artech House Publishers: Boston, MA, USA, 2013 .
26. Lopac, N.; Lerga, J.; Cuoco, E. Gravitational-Wave Burst Signals Denoising Based on the Adaptive Modification of the Intersection of Confidence Intervals Rule. *Sensors* **2020**, *20*, 6920. [CrossRef] [PubMed]
27. Lopac, N.; Lerga, J.; Saulig, N.; Stanković, L.; Daković, M. On Optimal Parameters for ICI-Based Adaptive Filtering Applied to the GWs in High Noise. In Proceedings of the 2021 6th International Conference on Smart and Sustainable Technologies (SpliTech), Bol and Split, Croatia, 8–11 September 2021; pp. 1–6. [CrossRef]
28. Lopac, N.; Jurdana, I.; Lerga, J.; Wakabayashi, N. Particle-Swarm-Optimization-Enhanced Radial-Basis-Function-Kernel-Based Adaptive Filtering Applied to Maritime Data. *J. Mar. Sci. Eng.* **2021**, *9*, 439. [CrossRef]
29. Khan, N.A.; Boashash, B. Multi-component instantaneous frequency estimation using locally adaptive directional time frequency distributions. *Int. J. Adapt. Control. Signal Process.* **2016**, *30*, 429–442. [CrossRef]
30. Khan, N.A.; Ali, S. A new feature for the classification of non-stationary signals based on the direction of signal energy in the time–frequency domain. *Comput. Biol. Med.* **2018**, *100*, 10–16. [CrossRef]
31. Mohammadi, M.; Pouyan, A.A.; Khan, N.A.; Abolghasemi, V. Locally Optimized Adaptive Directional Time-Frequency Distributions. *Circuits Syst. Signal Process.* **2018**, *37*, 3154–3174. [CrossRef]
32. Mohammadi, M.; Ali Khan, N.; Hassanpour, H.; Hussien Mohammed, A. Spike Detection Based on the Adaptive Time-Frequency Analysis. *Circuits Syst. Signal Process.* **2020**, *39*, 5656–5680. [CrossRef]
33. Sucic, V.; Saulig, N.; Boashash, B. Estimating the number of components of a multicomponent nonstationary signal using the short-term time-frequency Rényi entropy. *EURASIP J. Adv. Signal Process.* **2011**, *2011*, 125. [CrossRef]
34. Sucic, V.; Saulig, N.; Boashash, B. Analysis of Local Time-Frequency Entropy Features for Nonstationary Signal Components Time Supports Detection. *Digit. Signal Process.* **2014**, *34*, 56 – 66. [CrossRef]
35. Jurdana, V.; Volaric, I.; Sucic, V. The Local Rényi Entropy Based Shrinkage Algorithm for Sparse TFD Reconstruction. In Proceedings of the 2020 International Conference on Broadband Communications for Next Generation Networks and Multimedia Applications (CoBCom), Graz, Austria, 7–9 July 2020; pp. 1–8. [CrossRef]
36. Jurdana, V.; Volaric, I.; Sucic, V. Sparse time-frequency distribution reconstruction based on the 2D Rényi entropy shrinkage algorithm. *Digit. Signal Process.* **2021**, *118*, 103225. [CrossRef]
37. Rankine, L.; Mesbah, M.; Boashash, B. IF estimation for multicomponent signals using image processing techniques in the time–frequency domain. *Signal Process.* **2007**, *87*, 1234–1250. [CrossRef]
38. Boashash, B.; Azemi, G.; Ali Khan, N. Principles of time–frequency feature extraction for change detection in non-stationary signals: Applications to newborn EEG abnormality detection. *Pattern Recognit.* **2015**, *48*, 616–627. [CrossRef]
39. Lerga, J.; Sucic (EURASIP Member) , V.; Boashash, B. An Efficient Algorithm for Instantaneous Frequency Estimation of Nonstationary Multicomponent Signals in Low SNR. *EURASIP J. Adv. Signal Process.* **2011**, *2011*, 725189. [CrossRef]
40. Sucic, V.; Lerga, J.; Boashash, B. Multicomponent noisy signal adaptive instantaneous frequency estimation using components time support information. *IET Signal Process.* **2014**, *8*, 277–284. [CrossRef]
41. Stanković, L. A Measure of Some Time–Frequency Distributions Concentration. *Signal Process.* **2001**, *81*, 621 – 631. [CrossRef]
42. Baraniuk, R.G.; Flandrin, P.; Janssen, A.J.E.M.; Michel, O.J.J. Measuring Time-Frequency Information Content Using the Rényi Entropies. *IEEE Trans. Inf. Theory* **2001**, *47*, 1391–1409. [CrossRef]
43. Aviyente, S.; Williams, W.J. Minimum Entropy Time-Frequency Distributions. *IEEE Signal Process. Lett.* **2005**, *12*, 37–40. [CrossRef]
44. Principe, J. *Information Theoretic Learning: Renyi's Entropy and Kernel Perspectives*; Springer: New York, NY, USA, 2010. [CrossRef]
45. Khan, N.A.; Mohammadi, M.; Djurović, I. A Modified Viterbi Algorithm-Based IF Estimation Algorithm for Adaptive Directional Time-Frequency Distributions. *Circuits Syst. Signal Process.* **2019**, *38*, 2227–2244. [CrossRef]
46. Khan, N.A.; Djurović, I. ADTFD-RANSAC For multi-component IF estimation. *Signal Process.* **2022**, *195*, 108494. [CrossRef]
47. Khan, N.A.; Ali, S.; Choi, K. An instantaneous frequency and group delay based feature for classifying EEG signals. *Biomed. Signal Process. Control.* **2021**, *67*, 102562. [CrossRef]
48. Khan, N.A.; Mohammadi, M.; Choi, K. A Rule-Based Classifier to Detect Seizures in EEG Signals. *Circuits Syst. Signal Process.* **2023** . [CrossRef]
49. Majumdar, K. Differential operator in seizure detection. *Comput. Biol. Med.* **2012**, *42*, 70–74. [CrossRef] [PubMed]

50. Stevenson, N.; O'Toole, J.; Rankine, L.; Boylan, G.; Boashash, B. A nonparametric feature for neonatal EEG seizure detection based on a representation of pseudo-periodicity. *Med. Eng. Phys.* **2012**, *34*, 437–446. [CrossRef] [PubMed]
51. Saulig, N.; Lerga, J.; Miličić, S.; Tomasović, Z. Block-Adaptive Rényi Entropy-Based Denoising for Non-Stationary Signals. *Sensors* **2022**, *22*, 8251. [CrossRef] [PubMed]

sensors

MDPI

Article

Electrocortical Dynamics of Usual Walking and the Planning to Step over Obstacles in Parkinson's Disease

Rodrigo Vitório [1,2,3,*], Ellen Lirani-Silva [4], Diego Orcioli-Silva [1,2], Victor Spiandor Beretta [1,2,5], Anderson Souza Oliveira [6] and Lilian Teresa Bucken Gobbi [1,2]

1 Institute of Biosciences, Sao Paulo State University (UNESP), Rio Claro 13506-900, Brazil
2 Graduate Program in Movement Sciences, São Paulo State University (UNESP), Rio Claro 13506-900, Brazil
3 Department of Sport, Exercise and Rehabilitation, Northumbria University, Newcastle upon Tyne NE1 8ST, UK
4 Translational and Clinical Research Institute, Faculty of Medical Sciences, Newcastle University, Newcastle upon Tyne NE2 4HH, UK
5 School of Technology and Sciences, Sao Paulo State University (UNESP), Presidente Prudente 19060-900, Brazil
6 Department of Materials and Production, Aalborg University, 9220 Aalborg, Denmark
* Correspondence: rodrigo.vitorio@northumbria.ac.uk

Abstract: The neural correlates of locomotion impairments observed in people with Parkinson's disease (PD) are not fully understood. We investigated whether people with PD present distinct brain electrocortical activity during usual walking and the approach phase of obstacle avoidance when compared to healthy individuals. Fifteen people with PD and fourteen older adults walked overground in two conditions: usual walking and obstacle crossing. Scalp electroencephalography (EEG) was recorded using a mobile 64-channel EEG system. Independent components were clustered using a k-means clustering algorithm. Outcome measures included absolute power in several frequency bands and alpha/beta ratio. During the usual walk, people with PD presented a greater alpha/beta ratio in the left sensorimotor cortex than healthy individuals. While approaching obstacles, both groups reduced alpha and beta power in the premotor and right sensorimotor cortices (balance demand) and increased gamma power in the primary visual cortex (visual demand). Only people with PD reduced alpha power and alpha/beta ratio in the left sensorimotor cortex when approaching obstacles. These findings suggest that PD affects the cortical control of usual walking, leading to a greater proportion of low-frequency (alpha) neuronal firing in the sensorimotor cortex. Moreover, the planning for obstacle avoidance changes the electrocortical dynamics associated with increased balance and visual demands. People with PD rely on increased sensorimotor integration to modulate locomotion.

Keywords: gait; locomotion; movement disorders; EEG

Citation: Vitório, R.; Lirani-Silva, E.; Orcioli-Silva, D.; Beretta, V.S.; Oliveira, A.S.; Gobbi, L.T.B. Electrocortical Dynamics of Usual Walking and the Planning to Step over Obstacles in Parkinson's Disease. *Sensors* **2023**, *23*, 4866. https://doi.org/10.3390/s23104866

Academic Editors: Yifan Zhao, Hua-Liang Wei, Yuzhu Guo and Fei He

Received: 28 February 2023
Revised: 9 May 2023
Accepted: 17 May 2023
Published: 18 May 2023

1. Introduction

Parkinson's disease (PD) is characterized by the degeneration of dopaminergic neurons of the substantia nigra pars compacta. Consequently, the output nuclei of the basal ganglia become hyperactive and send excessive GABAergic (inhibitory) signaling to the thalamus [1]. It has been shown that PD elicits bursts of activity at the beta band (13–30 Hz) at different regions, which may interfere with the somatosensory control of movements [2]. Moreover, there is a reduction in excitatory signaling from the thalamus to many cortical areas, including the primary motor cortex and primary somatosensory cortex [1]. Then, people with PD show broad cortical dysfunction [3], which includes an overall slowing of cortical activity (e.g., a widespread increase in spectral power in the alpha band as well as a decrease in beta and gamma spectral power) [4]. As previous evidence suggests the involvement of multiple cortical regions in the control of human locomotion [5–8], PD-related cortical dysfunction may play a role in the walking deficits observed in PD [9–11]. Therefore, it is relevant to assess cortical activity during walking tasks in people with PD.

It is well documented that PD impairs walking performance on both level ground (i.e., usual walking) and uneven terrains [12]. Several behavioral studies have reported shortened step length, reduced velocity, increased step-to-step variability, and difficulties in adapting the stepping pattern to accommodate an obstacle in the path during both the approach and crossing phases by people with PD [12–15]. Due to the significant impact of PD on the neural control of locomotion [10,11], gait impairments and tripping over obstacles have been identified as major causes of falls in PD [16,17]. Therefore, it is necessary to underline the distinct influence of PD on the supraspinal control of locomotion when postural control is challenged to avoid tripping over obstacles.

There are different methods to access brain activity during walking, such as functional near-infrared spectroscopy (fNIRS) and scalp electroencephalography (EEG). Studies investigating fNIRS have reported greater prefrontal cortical activation during usual walking in people with PD compared to healthy older adults [18], or during obstacle avoidance compared to unobstructed walking [18–20]. However, fNIRS is not suitable to investigate the rapid changes in brain dynamics required to achieve successful obstacle negotiation during walking. High temporal resolution is possible using scalp EEG. Studies applying mobile EEG have shown that greater balance demands during walking induce reductions in alpha (9–13 Hz) and beta (13–30 Hz) EEG power in sensorimotor cortical areas [7,21,22] in healthy individuals. Further, a recent mobile EEG study demonstrated that healthy young adults present changes in the theta power at the frontal brain region that suggested proactive control when negotiating obstacles [23]. However, only a few studies have applied mobile EEG during locomotor tasks in PD.

PD modifies the electrocortical correlates of control during usual walking and while approaching obstacles. Our recent mobile EEG studies applying single-channel analysis showed an overall slowing of EEG recordings during walking in people with PD [19,20], and condition- (from usual walking to approaching obstacles) and medication-specific modulations. People with PD off medication presented lower gamma power than healthy individuals in the posterior parietal cortex (CPz) while walking and approaching obstacles [20]. This slowing of EEG recordings might represent a physiological marker for the reduction in the excitatory signaling from the thalamus to sensorimotor cortical areas [1], which contributes to gait deficits in PD. Similar findings were obtained by Stuart et al. [24], who observed increased alpha power while walking in people with PD. Levodopa intake increased beta and gamma power (CPz) in both walking conditions [20], suggesting potential effects against the PD-related slowing of EEG recordings. Of particular relevance to the treatment of gait impairments in PD, levodopa-related changes in EEG recordings were associated with levodopa-related changes in gait parameters [20]. In addition, relative to usual walking, people with PD reduced both alpha and beta power in channels corresponding to sensorimotor areas (i.e., FCz, Cz and/or CPz) while approaching obstacles, regardless of their medication state [19,20]. These findings suggest the involvement of alpha and beta reductions to control balance during locomotion. Despite the interesting findings, EEG studies regarding the control of locomotion in PD have been conducted at a single-channel level [9,19,20], limiting the quality of the research outcomes due to difficulties in determining the EEG signal source.

High-density EEG allows the identification of in-brain neural sources of electrocortical dynamics, which present superior quality to describe the supraspinal control of movements [5,25,26]. Extracting power spectral features from neural components related to the electrocortical activity in people with PD during obstacle avoidance is a step forward to better understanding the underlying neural mechanisms of PD-related walking impairments. The power spectral parameters can also be further evaluated by generating specific power ratios, such as the alpha/beta ratio, which has been suggested to indicate aperiodic neural activity, as well as indicate specific neural features in neurological patients [27].

Therefore, the use of power spectrum from in-brain components describing neural sources of electrocortical activity can be a relevant tool for clinical evaluation and may inform the development of enhanced treatment for walking impairments in PD.

The use of high-density EEG can help in unravelling the electrocortical signatures of usual walking and in the planning to avoid an obstacle in PD. Therefore, the aim of this study was to investigate whether people with PD present distinct electrocortical activity in specific brain regions during usual walking and the approach phase of obstacle avoidance when compared to healthy older adults. We first hypothesized that people with PD would present in-brain EEG sources containing greater lower-frequency signals when compared to healthy individuals, corroborating our previous EEG studies applying single-channel-level analysis [19,20]. Second, we hypothesized that adapting the walking pattern to approach an obstacle would reduce alpha and beta EEG power in sensorimotor cortical areas, due to greater demands to modulate balance control [7,21,22]. Moreover, we hypothesized that the obstacle condition would increase beta and/or gamma EEG power in the visual and prefrontal cortices, due to increased visual [28] and cognitive demands [18] of obstacle avoidance relative to usual walking.

2. Materials and Methods

2.1. Participants and Clinical Assessments

Fourteen healthy older adults and fifteen patients with PD participated in this study (see Table 1 for group details). All individuals gave their informed consent for inclusion before they participated in the study. The study procedures were conducted in accordance with the Declaration of Helsinki, and the protocol was approved by the local Ethics Committee (# 39844814.5.0000.5465). Participants were recruited from our lab database. Patients were selected on the criteria of having a confirmed PD diagnosis from at least one neurologist. The participants of both groups were included if they were able to walk unaided and were community-dwelling. Exclusion criteria included the following: diagnosed major depressive disorder; clinical diagnosis of dementia or other severe cognitive impairment (according to recommendations for utilization of the Mini-Mental State Examination—MMSE—in Brazil; cut-off = 20/24 points for illiterates and those who attended formal education, respectively [29]); chronic musculoskeletal or neurological disease (other than PD). An anamnesis was carried out to rule out conditions and impairments that could interfere with the present experimental procedures and to obtain demographic information (e.g., age, height, body mass, etc.). An experienced movement disorder specialist performed a clinical assessment in order to test people with PD on the Unified Parkinson's Disease Rating Scale (UPDRS) and the Hoehn and Yahr Rating Scale (H&Y); they were tested in the ON state of medication (approximately one hour after having taken a dose).

Table 1. Demographic characteristics of both groups.

Variables	Parkinson	Control	Statistics
Sex (male/female)	6/9	5/9	$X^2 = 0.056$, $p = 0.812$
Age (years)	70.8 (10.5)	70.9 (4.9)	$t = -0.02$, $p = 0.984$
Body mass (kg)	69.6 (12.4)	69.4 (12.1)	$t = 0.046$, $p = 0.964$
Height (cm)	162.2 (7.5)	160.8 (8.6)	$t = 0.449$, $p = 0.657$
MMSE (0–30 score)	27.1 (1.5)	28.7 (1.1)	$Z = -2.786$, $p = 0.005$ *
UPDRS I (0–16 score)	3.3 (1.9)	-	-
UPDRS II (0–52 score)	8.8 (4.8)	-	-
UPDRS III (0–108 score)	25.8 (9.3)	-	-
Hoehn and Yahr [1/1.5/2/2.5/3]	1/4/5/4/1	-	-

* significant difference between groups; MMSE, Mini-Mental State Examination; UPDRS, Unified Parkinson's Disease Rating Scale.

2.2. Experimental Design and Gait Assessment

Participants walked, at their preferred pace, for 60 s around a 25.8 m oval circuit (with two 6.5 m parallel straights). Two walking conditions were tested: usual walking and obstacle crossing. For the obstacle condition, participants were instructed to step over four foam obstacles (length $\times$ width $\times$ height: $3 \times 60 \times 10$ cm), evenly spaced along the walking path; this aspect of the protocol was meant to avoid the influence of different inter-obstacle distance on the data as this aspect could add more variability to the study. Four trials for each condition were performed in a random order.

Spatiotemporal gait parameters were recorded by a 5.74 m electronic walkway (200 Hz; GAITRite®, CIR Systems, Inc., Franklin, NJ, USA) placed over one straight segment of the circuit. A customized MATLAB algorithm (Mathworks, Natick, MA, USA) was used to calculate the following gait parameters in both conditions (from the GAITRite output): step length, step duration, step velocity, step width (mean of the recorded steps), and step-to-step variability in the same parameters (standard deviation of the recorded steps). For the obstacle condition, the calculated gait parameters referred to the approach phase (i.e., the last four steps before the obstacle), allowing a fair comparison with the usual walking condition.

2.3. EEG Recordings and Processing

All EEG signals were recorded using a mobile 64-channel system (eegoTM sports, ANT Neuro, Enschede, The Netherlands), sampled at 1024 Hz. All processing and analyses were performed in MATLAB, using scripts and functions based on EEGLAB 13.0.1b (http://www.sccn.ucsd.edu/eeglab). Initially, individual EEG datasets of both usual walking and walking with obstacle conditions were merged into a single dataset for each participant. The instants of the last heel contact prior to the obstacles were registered as events into the EEG data streaming. For each participant, a similar number of events was randomly created for the usual walking condition (relative to the obstacle condition). The full single datasets were down-sampled to 512 Hz and band-pass filtered (2–50 Hz).

The filtered datasets were screened for the removal of channels exhibiting substantial artifacts following procedures described elsewhere [26]. In general, 50 ± 3 EEG channels were retained after applying all rejection methods (range: 44–55). We re-referenced the remaining channels to an average reference. Subsequently, EEG data sectors presenting exacerbated artifacts (originated from cable movements and/or abrupt head movements) were removed from the continuous EEG datasets. No participants were excluded from the analysis due to EEG artifact issues.

2.3.1. Independent Component Analysis (ICA)

To the cleaned datasets, an infomax ICA was applied to transform the EEG channel data into temporally independent component signals. Approximately 1450 independent components were extracted across all participants. The EEGLAB function ADJUST was applied to objectively define independent components carrying artifacts, such as eye blinks, muscle activity artifacts, and movement-related artifacts [30].

2.3.2. EEG Clustering

The DIPFIT function in EEGLAB was used to model each independent component as an equivalent current dipole within a boundary element head model based on the Montreal Neurological Institute standard brain (MNI, Montreal, QC, Canada). Independent components were removed from further analysis if (1) they were marked as artifactual components in the pre-processing analysis; (2) their best-fit equivalent current dipole accounted for <85% of the variance seen at the scalp and (3) presented locations outside the brain. Therefore, the population of independent components used for the clustering was reduced from ~1450 to 198 across all 29 participants from both groups. In this study, the clustering was performed including both PD and controls as a single group. The rationale is that both patients and controls could present independent components at similar cortical regions, but the electrocortical properties of these components may be group-dependent. The clustering was performed using a k-means clustering algorithm available in EEGLAB on vectors jointly coding similarities in dipole location and scalp topography. The clustering algorithm recommended the creation of 8 clusters, which were maintained for analysis. Four of the eight clusters included independent components from more than seven participants from each group (half of the original group study sample) and were located in cortical areas (Table 2). Thus, we performed all further analyses only on these four clusters of interest.

Table 2. Centroid location for all clusters of electrocortical sources containing independent components from ≥7 participants from the Parkinson's disease and control groups.

Functional Area (Centroid Location)	Brodmann Area	No. of Participants (PD/Control)	No. of ICs (PD/Control)
Left sensorimotor cortex	2	9/8	9/8
Right sensorimotor cortex	2	11/9	11/9
Visual cortex	17	11/9	11/9
Central premotor and SMA	6	9/7	9/7

PD, Parkinson's disease; SMA, supplementary motor area; ICs, independent components.

2.3.3. EEG Absolute Power from Independent Components

For the obstacle condition, the EEG signals were epoched from −2.0 s to 0.5 s, from the last step prior to overcoming the obstacle. The 2.5 s epochs allowed for the acquisition of electrocortical activity during the preparation/planning period prior to obstacle crossing [31], including two full gait cycles prior to overcoming the obstacle, and the step avoiding the obstacle. The same window (−2.0 s to 0.5 s) was used as a baseline. For each participant, a matching number of epochs from the usual walking condition was created for comparison with the obstacle condition. The baseline was removed from the epoched datasets and calculated as the average log spectrum across all epochs from both conditions. The absolute power of the power spectrum from each independent component was subsequently averaged in the theta (5–8 Hz), alpha (9–13 Hz), beta (14–30 Hz), and low gamma (31–50 Hz) frequency bands across the epoch time-course. In addition, the EEG alpha/beta ratio was computed using the absolute power from the alpha and beta bands for each independent component.

2.4. Statistical Analysis

For demographic data, unrelated sample Student's t-tests, Mann–Whitney, and chi-square tests were employed for between-group comparisons. For gait and EEG-dependent variables, two-way ANOVAs (group × condition) were carried out, with repeated measures in the condition factor. The interactions were further assessed with post hoc tests using Bonferroni correction for multiple comparisons. Specifically for the EEG data, the analyses were carried out separately for each cluster. All statistical analyses were run on SPSS for Windows 18.0 and the p-value was set to 0.05.

3. Results

The two groups were not significantly different in sex, age, body mass, and height (Table 1). People with PD presented mild to moderate disease severity (Table 1). Moreover, people with PD, despite having preserved global cognitive function, obtained lower scores in MMSE than older adults (Table 1).

3.1. Gait Parameters

The gait parameters for each group and condition are presented in Table 3. A significant interaction between group and condition was observed for step width. Post hoc tests revealed that the two groups had similar step widths during usual walking conditions, but only people with PD increased the step width in the obstacle condition ($p < 0.001$). No other interactions between factors were observed for gait parameters.

Table 3. Gait parameters of people with Parkinson's disease (PD) and healthy older adults in both usual walking and obstacle conditions.

Variables	Parkinson		Control		Group		Condition		Group × Condition		
Step	**USU**	**OBT**	**USU**	**OBT**	**F**	***p***	**F**	***p***	**F**	***p***	**Post Hoc**
Length (cm)	56.0 (6.6)	55.8 (7.3)	63.3 (6.6)	63.7 (8.2)	8.331	**0.008**	0.058	0.811	0.501	0.485	
Duration (s)	0.52 (0.03)	0.56 (0.03)	0.53 (0.05)	0.56 (0.05)	0.137	0.714	176.968	**0.001**	2.622	0.117	
Velocity (cm/s)	108.4 (14.2)	100.5 (15.5)	120.9 (17.4)	114.9 (17.7)	5.083	**0.032**	57.496	**0.001**	1.035	0.318	
Width (cm)	9.2 (2.5)	10.1 (2.7)	8.6 (1.9)	8.6 (2.1)	1.440	0.241	9.737	**0.004**	11.070	**0.003**	PD: USU < OBT
Step variability											
Length (cm)	2.42 (1.01)	6.50 (2.04)	1.93 (0.71)	5.30 (1.49)	4.064	0.054^{t}	132.582	**0.001**	2.623	0.117	
Duration (s)	0.021 (0.011)	0.080 (0.025)	0.016 (0.004)	0.067 (0.017)	2.972	0.096	267.767	**0.001**	1.353	0.255	
Velocity (cm/s)	6.8 (4.0)	11.2 (2.9)	5.3 (1.5)	11.1 (3.1)	0.682	0.416	71.509	**0.001**	1.601	0.217	
Width (cm)	2.05 (0.62)	2.72 (0.86)	2.04 (0.49)	2.55 (0.60)	0.170	0.684	41.485	**0.001**	0.756	0.392	

USU, usual walking; OBT, obstacle; PD, Parkinson's disease; *p*-values marked in bold represent statistically significant results.

A main effect of group was observed for step length and step velocity. Regardless of the experimental condition, people with PD walked slower and with shorter step length than older adults. A trend of group main effect was observed for step length variability, which was greater for people with PD.

A main effect of condition was observed for step duration, step velocity, step length variability, step duration variability, step velocity variability, and step width variability. Both people with PD and older adults showed greater step duration and step-to-step variability and slower step velocity in the obstacle condition than in the usual walking condition.

3.2. *Electroencephalography*

Four clusters presented independent components with neural characteristics and locations in cortical regions: left and right sensorimotor cortex, supplementary motor area, and primary visual cortex. Table 2 contains details regarding the clusters, and topographic scalp maps of these clusters are shown in Figure 1.

3.2.1. Left Sensorimotor Cortex

A significant interaction between group and condition was observed for alpha power [$F = 7.974$; $p = 0.013$] and alpha/beta ratio [$F = 10.501$; $p = 0.005$]. Post hoc tests revealed that people with PD showed lower alpha power in the obstacle condition than in the usual walking condition ($p = 0.002$), whereas older adults did not change alpha power across experimental conditions (Figure 2A). Additionally, people with PD showed a greater alpha/beta ratio than older adults in the usual walking condition ($p = 0.016$), and only people with PD decreased alpha/beta ratio in the obstacle condition ($p = 0.006$; Figure 1). A main effect of condition was observed for gamma power [$F = 8.509$; $p = 0.011$]. Compared to usual walking, both people with PD and older adults increased gamma power in the obstacle condition (Figure 2A).

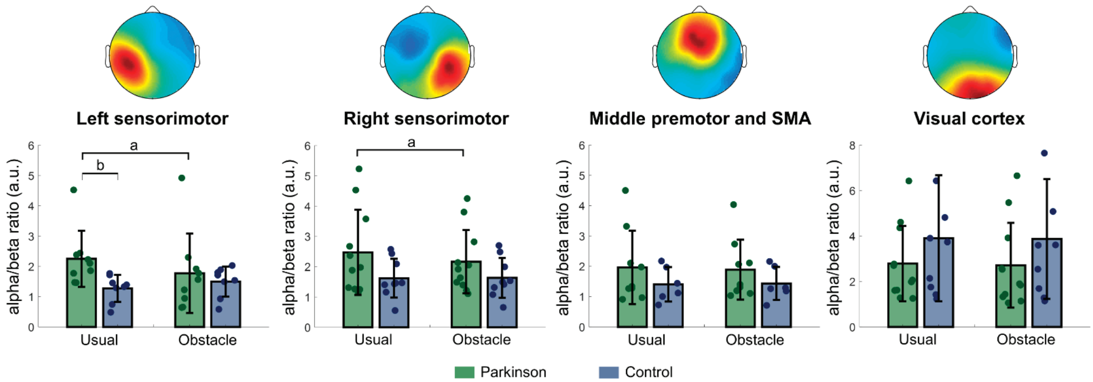

Figure 1. Top: Topographic plots for the four clusters identified. **Bottom**: Bar graphs show alpha/beta ratio for people with PD (green) and healthy older adults (blue) in the usual walking and obstacle condition. Circles represent individual values. a indicates significant differences between usual walking and obstacle condition for people with PD; b indicates significant difference between people with PD and healthy older adults.

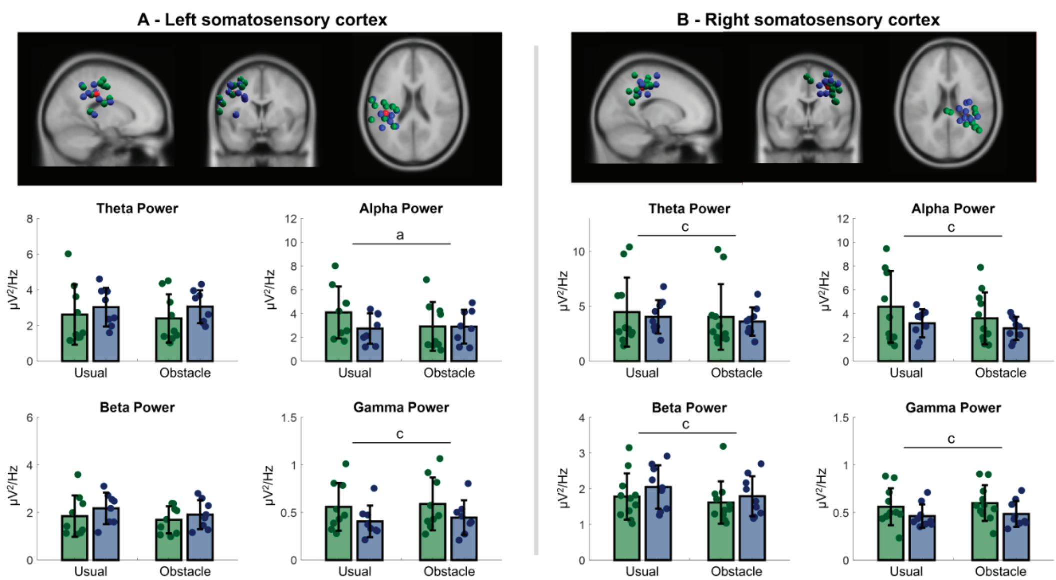

Figure 2. Top: Electrocortical clusters of independent components plotted on the MNI brain. Blue spheres represent independent components of healthy older adults and green spheres represent independent components of people with PD. Red spheres represent the centroid locations for the clusters ((**A**)—left sensorimotor cortex; (**B**)—right sensorimotor cortex). **Bottom:** Bar graphs show absolute power for theta, alpha, beta, and gamma bands in the usual walking and obstacle condition. Circles within the graphs represent individual values. a indicates significant difference between usual walking and obstacle condition for people with PD; c indicates main effect of condition.

3.2.2. Right Sensorimotor Cortex

A significant interaction between group and condition was observed for alpha/beta ratio [F = 4.951; $p = 0.039$]; people with PD presented greater alpha/beta ratio in the usual walking condition than in the obstacle condition ($p = 0.005$; Figure 1), whereas older adults did not change alpha/beta ratio across conditions. A main effect of condition was observed for theta [F = 8.179; *p* = 0.01], alpha [F = 14.910; *p* < 0.001], beta [F = 17.910; *p* < 0.001], and gamma power [F = 6.025; *p* = 0.025]. Compared to usual walking, both people with PD and older adults decreased theta, alpha, and beta power and increased gamma power in the obstacle condition (Figure 2B).

3.2.3. Central Premotor and Supplementary Motor Area

A main effect of condition was observed for beta power [F = 14.623; *p* = 0.002]. Compared to usual walking, both people with PD and older adults decreased beta power in the obstacle condition (Figure 3A).

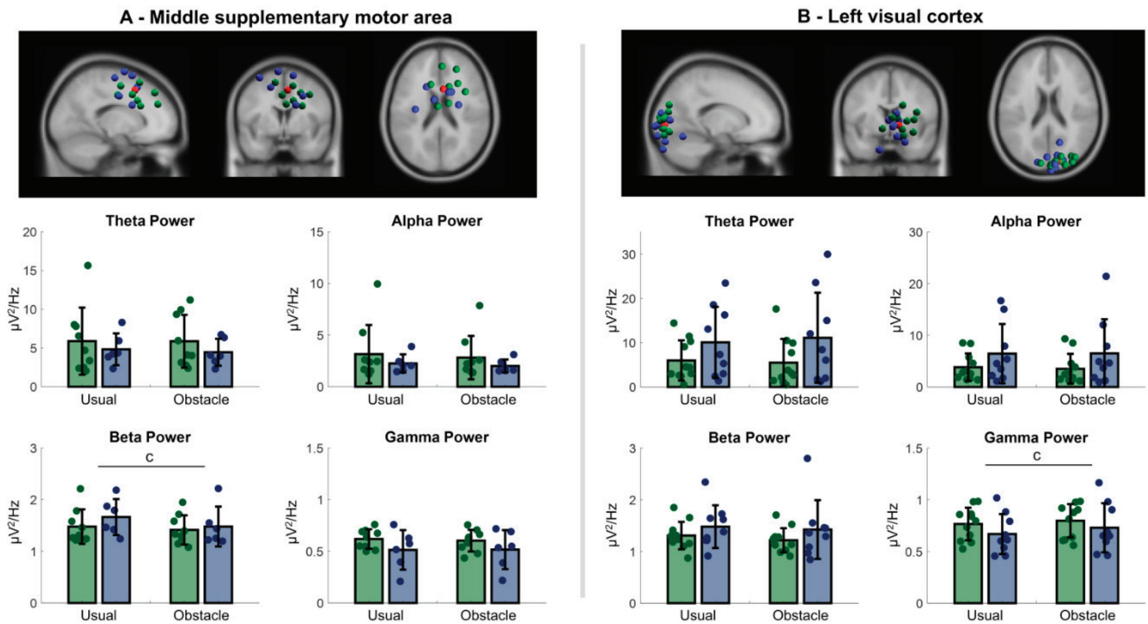

Figure 3. Top: Electrocortical clusters of independent components plotted on the MNI brain. Blue spheres represent independent components of healthy older adults and green spheres represent independent components of people with PD. Red spheres represent the centroid locations for the clusters ((**A**)—middle premotor and supplementary motor area; (**B**)—visual cortex). **Bottom:** Bar graphs show absolute power for theta, alpha, beta, and gamma bands in the usual walking and obstacle condition. Circles within the graphs represent individual values. c indicates main effect of condition.

3.2.4. Primary Visual Cortex

A main effect of condition was observed for gamma power [F = 18.808; *p* < 0.001]. Compared to usual walking, both people with PD and older adults increased gamma power in the obstacle condition (Figure 3B).

4. Discussion

The current study investigated whether people with PD present distinct electrocortical activity in specific brain regions during usual walking and the approach phase of obstacle avoidance when compared to healthy older adults. The following findings reveal PD-related changes in electrocortical activity for the control of locomotion: (i) people with PD showed a greater alpha/beta ratio in the left sensorimotor cortex than older adults during usual walking; (ii) people with PD reduced alpha power on the left sensorimotor cortex and alpha/beta ratio on both left and right sensorimotor cortices when approaching obstacles. Overall, these findings support our primary hypothesis and suggest that PD leads to a greater proportion of low-frequency neuronal firing (i.e., relative slowing of scalp EEG) in the sensorimotor cortex that is responsible for motor commands and sensorimotor integration. In addition, our results may suggest that difficulties in integrating sensorimotor inputs to an ongoing ambulatory modulation in the presence of obstacles might help to explain the tripping-related falls experienced by people with PD [32].

4.1. PD-Related Changes in the Cortical Control of Locomotion

Activity in the sensorimotor cortex during walking is affected by PD [33,34]. The increased alpha/beta ratio observed in the left sensorimotor cortex in people with PD during usual walking may be related to the excessive GABAergic inhibition of the basal ganglia over the thalamus in PD [1,10]. Among other functions, the thalamus redistributes sensory information and sends excitatory projections to several brain structures, including the primary motor cortex and the somatosensory cortex [1,35,36]. As a consequence of the reduced excitatory activity of the thalamus in PD (due to the excessive inhibitory activity of the basal ganglia over the thalamus), patients' sensorimotor cortices function with greater proportion of slower waves (e.g., greater alpha/beta ratio) [4]. This may represent the dysfunction of the so called "automatic locomotor network" [37] and/or deficits in sensorimotor integration in PD [30]. Indeed, reduced gait automaticity and an association between sensory deficits and gait impairments have been observed in PD [32].

PD leads to additional electrocortical changes while approaching an obstacle. In the present study, only people with PD reduced alpha power (left) and alpha/beta ratio (left and right) in the sensorimotor cortex in the obstacle condition. Reductions in the alpha power in the somatosensory and primary motor cortex have been associated with movement execution [38,39]. Therefore, we speculate that the relatively greater motor and cognitive demands to avoid obstacles for people with PD induced the desynchronization of additional cortical regions [13,14]. People with PD may rely on increased sensorimotor integration to modulate locomotion and control balance while approaching an obstacle.

4.2. Gait and Electrocortical Modulations Required for Obstacle Avoidance

Adjustments in spatiotemporal gait parameters in the approach phase are necessary for successful obstacle avoidance. We observed that both people with PD and older adults decreased their walking speed and increased gait variability prior to overcoming obstacles. Similar findings have been previously reported in the literature and can be interpreted as a strategy for obtaining greater postural stability and having more time to plan the crossing phase [14,19,20]. Moreover, only people with PD increased their step width when approaching the obstacles, corroborating previous studies suggesting that PD imposes additional demands on postural control [40]. This PD-specific step width adjustment also aligns with the observed electrocortical modulations associated with increased balance control.

Reductions in alpha and beta power, previously described in young adults [7,21,22], seem to be involved in balance control while walking in people with PD and healthy older adults. Studies using mobile EEG systems have shown the involvement of both sensorimotor and premotor cortical regions in balance control during different locomotor tasks in young adults. Wagner et al. [21] reported decreased alpha and beta power in the sensorimotor cortex during active walking compared to robot-assisted walking, which reduces balance demand, in young adults. Sipp et al. [7] observed a bilateral reduction in the beta power from the sensorimotor cortex in young adults during walking on a balance beam, which increases balance demand, when compared to treadmill walking. Likewise, Bruijn et al. [22] found decreased beta power in the premotor cortex during the less stable single support phase of gait, and increased beta power in this cortical region during externally stabilized treadmill walking. Our results related to the right sensorimotor and premotor cortical regions are in line with these previous studies. Both healthy older adults and people with PD presented reductions in the alpha and beta power from the premotor and sensorimotor cortices when planning how to overcome obstacles. Such a change in electrocortical activity may be linked to a greater involvement of these brain regions in the monitoring of gait stability prior to engaging in obstacle avoidance.

Processing visual information during the approach phase is particularly relevant for successful obstacle crossing. The activity of the primary visual cortex has been associated with the level of visual attention and perception of visual stimuli. Alpha activity characterizes idle arousal of the system, while beta bursts shift the visual system to an attention state that allows for gamma synchronization and perception [41]. For example, Kaminski and colleagues [42] observed that increased alertness, manifested by faster responses to target visual stimuli, is accompanied by increased beta activity in the visual cortex. This higher beta activity in response to visual stimuli was later associated with preserved cognitive function [43]. In the present study, participants from both groups increased gamma power at the primary visual cortex in the obstacle condition, corroborating a previous study from our research group that evaluated EEG at the channel level [19]. Postural and stepping adjustments to avoid obstacles require greater visual and cognitive engagement [28,44], with it being previously shown that increased attentional demands during gait induced greater changes in gamma activation in several cortical regions [45]. Moreover, obstacle avoidance increases the activation of the prefrontal cortex in both healthy older adults and people with PD [18,20], suggesting increased demands for executive function and attention. Precision stepping tasks have also been shown to induce changes in electrocortical activity in the visual cortex to cope with the postural adjustments to perform non-stereotypical gait [46]. Therefore, the increased gamma power in the primary visual cortex in the obstacle condition suggests a greater need for visual information, and, potentially, the integration of inputs from cognitive, motor, and visual brain regions.

4.3. Clinical Implication and Future Directions

Our findings revealed specific PD-related changes in brain dynamics during walking, which may contribute to improving the treatment of walking impairments. Specifically, the greater proportion of low-frequency neuronal firing in the sensorimotor cortex observed in people with PD can be modulated by dopaminergic medication. We have previously shown that levodopa increases beta and gamma power (CPz) during walking [20], suggesting the potential effects of dopaminergic medication against the PD-related slowing of EEG recordings. It is likely that the levodopa-related increases in beta and gamma power (CPz) are due to increased cortical excitability following levodopa intake [47]. Moreover, we have observed that levodopa-related changes in EEG recordings were associated with levodopa-related changes in gait parameters, highlighting specific cortical mechanisms involved in gait improvement [20]. Therefore, high-density EEG outcomes recorded while walking may serve as biomarkers to assess the response to treatment aiming to improve gait in PD [24], but larger studies are needed. Future studies should investigate the effects of other interventions, particularly non-invasive brain stimulation techniques [48–50], on sensorimotor EEG outcomes recorded while walking in people with PD. Finally, future studies should consider the effects of disease progression on EEG recordings during walking in PD.

5. Conclusions

In summary, our results suggest that PD leads to a greater proportion of low-frequency neuronal firing in brain areas related to motor commands and sensorimotor integration during walking. Moreover, planning to avoid an obstacle changes the electrocortical dynamics associated with increased balance and visual demands in both people with PD and healthy older adults. People with PD rely on increased sensorimotor integration to modulate locomotion and avoid obstacles.

Author Contributions: Conceptualization, R.V.; methodology, R.V., E.L.-S., D.O.-S., V.S.B., A.S.O. and L.T.B.G.; data collection, R.V., E.L.-S., D.O.-S. and V.S.B.; formal analysis, R.V., D.O.-S. and A.S.O.; writing—original draft preparation, R.V.; writing—review and editing, R.V., E.L.-S., D.O.-S., V.S.B., A.S.O. and L.T.B.G.; visualization, R.V., E.L.-S., D.O.-S., V.S.B., A.S.O. and L.T.B.G.; supervision,

L.T.B.G.; project administration, R.V.; funding acquisition, R.V. and L.T.B.G. All authors have read and agreed to the published version of the manuscript.

Funding: This research was supported by the Sao Paulo Research Foundation (FAPESP) [2014/22308-0; 2017/19845-1], and the Coordenação de Aperfeiçoamento de Pessoal de Nível Superior—Brasil (CAPES)—Finance Code 001.

Institutional Review Board Statement: The study procedures were conducted in accordance with the Declaration of Helsinki, and the protocol was approved by the Ethics Committee of the Institute of Biosciences from São Paulo State University (# 39844814.5.0000.5465).

Informed Consent Statement: All individuals gave their written informed consent for inclusion before they participated in the study.

Data Availability Statement: All data are available from the corresponding author upon reasonable request.

Acknowledgments: The authors would like to thank the participants.

Conflicts of Interest: The authors declare no conflict of interest.

References

1. Takakusaki, K. Functional Neuroanatomy for Posture and Gait Control. *J. Mov. Disord.* **2017**, *10*, 1–17. [CrossRef] [PubMed]
2. Anidi, C.; O'Day, J.J.; Anderson, R.W.; Afzal, M.F.; Syrkin-Nikolau, J.; Velisar, A.; Bronte-Stewart, H.M. Neuromodulation Targets Pathological Not Physiological Beta Bursts during Gait in Parkinson's Disease. *Neurobiol. Dis.* **2018**, *120*, 107–117. [CrossRef] [PubMed]
3. Han, C.-X.; Wang, J.; Yi, G.-S.; Che, Y.-Q. Investigation of EEG Abnormalities in the Early Stage of Parkinson's Disease. *Cogn. Neurodyn.* **2013**, *7*, 351–359. [CrossRef] [PubMed]
4. Bockova, M.; Rektor, I. Impairment of Brain Functions in Parkinson's Disease Reflected by Alterations in Neural Connectivity in EEG Studies: A Viewpoint. *Clin. Neurophysiol.* **2019**, *130*, 239–247. [CrossRef]
5. Nordin, A.D.; Hairston, W.D.; Ferris, D.P. Human Electrocortical Dynamics While Stepping over Obstacles. *Sci. Rep.* **2019**, *9*, 4693. [CrossRef]
6. Gwin, J.T.; Gramann, K.; Makeig, S.; Ferris, D.P. Electrocortical Activity Is Coupled to Gait Cycle Phase during Treadmill Walking. *Neuroimage* **2011**, *54*, 1289–1296. [CrossRef]
7. Sipp, A.R.; Gwin, J.T.; Makeig, S.; Ferris, D.P. Loss of Balance during Balance Beam Walking Elicits a Multifocal Theta Band Electrocortical Response. *J. Neurophysiol.* **2013**, *110*, 2050–2060. [CrossRef]
8. Hairston, W.D.; König, P.; Ferris, D.P.; Oliveira, A.S.; Schlink, B.R. Restricted Vision Increases Sensorimotor Cortex Involvement in Human Walking. *J. Neurophysiol.* **2017**, *118*, 1943–1951. [CrossRef]
9. Roeder, L.; Boonstra, T.W.; Kerr, G.K. Corticomuscular Control of Walking in Older People and People with Parkinson's Disease. *Sci. Rep.* **2020**, *10*, 2980. [CrossRef]
10. Peterson, D.S.; Horak, F.B. Neural Control of Walking in People with Parkinsonism. *Physiology* **2016**, *31*, 95–107. [CrossRef]
11. Stuart, S.; Vitorio, R.; Morris, R.; Martini, D.N.; Fino, P.C.; Mancini, M. Cortical Activity during Walking and Balance Tasks in Older Adults and in People with Parkinson's Disease: A Structured Review. *Maturitas* **2018**, *113*, 53–72. [CrossRef]
12. Mirelman, A.; Bonato, P.; Camicioli, R.; Ellis, T.D.; Giladi, N.; Hamilton, J.L.; Hass, C.J.; Hausdorff, J.M.; Pelosin, E.; Almeida, Q.J. Gait Impairments in Parkinson's Disease. *Lancet Neurol.* **2019**, *18*, 697–708. [CrossRef]
13. Vitorio, R.; Lirani-Silva, E.; Baptista, A.M.; Barbieri, F.A.; dos Santos, P.C.R.; Teixeira-Arroyo, C.; Gobbi, L.T.B. Disease Severity Affects Obstacle Crossing in People with Parkinson's Disease. *Gait Posture* **2014**, *40*, 266–269. [CrossRef]
14. Vitório, R.; Pieruccini-Faria, F.; Stella, F.; Gobbi, S.; Gobbi, L.T.B. Effects of Obstacle Height on Obstacle Crossing in Mild Parkinson's Disease. *Gait Posture* **2010**, *31*, 143–146. [CrossRef]
15. Orcioli-Silva, D.; Barbieri, F.A.; dos Santos, P.C.R.; Beretta, V.S.; Simieli, L.; Vitorio, R.; Lirani-Silva, E.; Gobbi, L.T.B. Double Obstacles Increase Gait Asymmetry during Obstacle Crossing in People with Parkinson's Disease and Healthy Older Adults: A Pilot Study. *Sci. Rep.* **2020**, *10*, 2272. [CrossRef]
16. Ashburn, A.; Stack, E.; Ballinger, C.; Fazakarley, L.; Fitton, C. The Circumstances of Falls among People with Parkinson's Disease and the Use of Falls Diaries to Facilitate Reporting. *Disabil. Rehabil.* **2008**, *30*, 1205–1212. [CrossRef]
17. Moraca, G.A.G.; Beretta, V.S.; Dos Santos, P.C.R.; Nóbrega-Sousa, P.; Orcioli-Silva, D.; Vitório, R.; Gobbi, L.T.B. Center of Pressure Responses to Unpredictable External Perturbations Indicate Low Accuracy in Predicting Fall Risk in People with Parkinson's Disease. *Eur. J. Neurosci.* **2021**, *53*, 2901–2911. [CrossRef]
18. Maidan, I.; Nieuwhof, F.; Bernad-Elazari, H.; Reelick, M.F.; Bloem, B.R.; Giladi, N.; Deutsch, J.E.; Hausdorff, J.M.; Claassen, J.A.H.; Mirelman, A. The Role of the Frontal Lobe in Complex Walking among Patients with Parkinson's Disease and Healthy Older Adults: An FNIRS Study. *Neurorehabil. Neural Repair* **2016**, *30*, 963–971. [CrossRef]
19. Orcioli-Silva, D.; Vitório, R.; Beretta, V.S.; da Conceição, N.R.; Nóbrega-Sousa, P.; Oliveira, A.S.; Gobbi, L.T.B. Is Cortical Activation During Walking Different between Parkinson's Disease Motor Subtypes? *J. Gerontol. Ser. A* **2021**, *76*, 561–567. [CrossRef]

20. Orcioli-Silva, D.; Vitório, R.; Nóbrega-Sousa, P.; Beretta, V.S.; da Conceição, N.R.; Oliveira, A.S.; Pereira, M.P.; Gobbi, L.T.B. Cortical Activity Underlying Gait Improvements Achieved with Dopaminergic Medication during Usual Walking and Obstacle Avoidance in Parkinson Disease. *Neurorehabil. Neural Repair* **2021**, *35*, 406–418. [CrossRef]
21. Wagner, J.; Solis-Escalante, T.; Grieshofer, P.; Neuper, C.; Müller-Putz, G.; Scherer, R. Level of Participation in Robotic-Assisted Treadmill Walking Modulates Midline Sensorimotor EEG Rhythms in Able-Bodied Subjects. *Neuroimage* **2012**, *63*, 1203–1211. [CrossRef] [PubMed]
22. Bruijn, S.M.; Van Dieën, J.H.; Daffertshofer, A. Beta Activity in the Premotor Cortex Is Increased during Stabilized as Compared to Normal Walking. *Front. Hum. Neurosci.* **2015**, *9*, 593. [CrossRef] [PubMed]
23. Mustile, M.; Kourtis, D.; Ladouce, S.; Learmonth, G.; Edwards, M.G.; Donaldson, D.I.; Ietswaart, M. Mobile EEG Reveals Functionally Dissociable Dynamic Processes Supporting Real-world Ambulatory Obstacle Avoidance: Evidence for Early Proactive Control. *Eur. J. Neurosci.* **2021**, *54*, 8106–8119. [CrossRef] [PubMed]
24. Stuart, S.; Wagner, J.; Makeig, S.; Mancini, M. Brain Activity Response to Visual Cues for Gait Impairment in Parkinson's Disease: An EEG Study. *Neurorehabil. Neural Repair* **2021**, *35*, 996–1009. [CrossRef] [PubMed]
25. Delorme, A.; Palmer, J.; Onton, J.; Oostenveld, R.; Makeig, S. Independent EEG Sources Are Dipolar. *PLoS ONE* **2012**, *7*, e30135. [CrossRef]
26. Oliveira, A.S.; Schlink, B.R.; David Hairston, W.; König, P.; Ferris, D.P. A Channel Rejection Method for Attenuating Motion-Related Artifacts in EEG Recordings during Walking. *Front. Neurosci.* **2017**, *11*, 225. [CrossRef]
27. Donoghue, T.; Dominguez, J.; Voytek, B. Electrophysiological Frequency Band Ratio Measures Conflate Periodic and Aperiodic Neural Activity. *eNeuro* **2020**, *7*, 1–14. [CrossRef]
28. Vitorio, R.; Lirani-Silva, E.; Barbieri, F.A.; Raile, V.; Stella, F.; Gobbi, L.T.B. Influence of Visual Feedback Sampling on Obstacle Crossing Behavior in People with Parkinson's Disease. *Gait Posture* **2013**, *38*, 330–334. [CrossRef]
29. Almeida, O.P. Mini Exame Do Estado Mental e o Diagnóstico de Demência No Brasil. *Arquivos Neuro-Psiquiatria* **1998**, *56*, 605–612. [CrossRef]
30. Chaumon, M.; Bishop, D.V.M.; Busch, N.A. A Practical Guide to the Selection of Independent Components of the Electroencephalogram for Artifact Correction. *J. Neurosci. Methods* **2015**, *250*, 47–63. [CrossRef]
31. Pieruccini-Faria, F.; Jones, J.A.; Almeida, Q.J. Motor Planning in Parkinson's Disease Patients Experiencing Freezing of Gait: The Influence of Cognitive Load When Approaching Obstacles. *Brain Cogn.* **2014**, *87*, 76–85. [CrossRef]
32. Martens, K.A.E.; Almeida, Q.J. Dissociating between Sensory and Perceptual Deficits in PD: More than Simply a Motor Deficit. *Mov. Disord.* **2012**, *27*, 387–392. [CrossRef]
33. Crémers, J.; D'Ostilio, K.; Stamatakis, J.; Delvaux, V.; Garraux, G. Brain Activation Pattern Related to Gait Disturbances in Parkinson's Disease. *Mov. Disord.* **2012**, *27*, 1498–1505. [CrossRef]
34. Hanakawa, T.; Katsumi, Y.; Fukuyama, H.; Honda, M.; Hayashi, T.; Kimura, J.; Shibasaki, H. Mechanisms Underlying Gait Disturbance in Parkinson's Disease. *Brain* **1999**, *122*, 1271–1282. [CrossRef]
35. Viaene, A.N.; Petrof, I.; Sherman, S.M. Properties of the Thalamic Projection from the Posterior Medial Nucleus to Primary and Secondary Somatosensory Cortices in the Mouse. *Proc. Natl. Acad. Sci. USA* **2011**, *108*, 18156–18161. [CrossRef]
36. Mease, R.A.; Metz, M.; Groh, A. Cortical Sensory Responses Are Enhanced by the Higher-Order Thalamus. *Cell Rep.* **2016**, *14*, 208–215. [CrossRef]
37. Hamacher, D.; Herold, F.; Wiegel, P.; Hamacher, D.; Schega, L. Brain Activity during Walking: A Systematic Review. *Neurosci. Biobehav. Rev.* **2015**, *57*, 310–327. [CrossRef]
38. Neuper, C.; Wortz, M.; Pfurtscheller, G. ERD/ERS Patterns Reflecting Sensorimotor Activation and Deactivation. *Prog. Brain Res.* **2006**, *159*, 211–222. [CrossRef]
39. Pfurtscheller, G.; Lopes da Silva, F.H. Event-Related EEG/MEG Synchronization and Desynchronization: Basic Principles. *Clin. Neurophysiol.* **1999**, *110*, 1842–1857. [CrossRef]
40. Galna, B.; Murphy, A.T.; Morris, M.E. Obstacle Crossing in People with Parkinson's Disease: Foot Clearance and Spatiotemporal Deficits. *Hum. Mov. Sci.* **2010**, *29*, 843–852. [CrossRef]
41. Wrobel, A. Beta Activity: A Carrier for Visual Attention. *Acta Neurobiol. Exp.* **2000**, *60*, 247–260.
42. Kaminski, J.; Brzezicka, A.; Gola, M.; Wrobel, A. Beta Band Oscillations Engagement in Human Alertness Process. *Int. J. Psychophysiol.* **2012**, *85*, 125–128. [CrossRef] [PubMed]
43. Guntekin, B.; Emek-Savas, D.D.; Kurt, P.; Yener, G.G.; Basar, E. Beta Oscillatory Responses in Healthy Subjects and Subjects with Mild Cognitive Impairment. *NeuroImage Clin.* **2013**, *3*, 39–46. [CrossRef] [PubMed]
44. Vitorio, R.; Gobbi, L.T.B.; Lirani-Silva, E.; Moraes, R.; Almeida, Q.J. Synchrony of Gaze and Stepping Patterns in People with Parkinson's Disease. *Behav. Brain Res.* **2016**, *307*, 159–164. [CrossRef] [PubMed]
45. Costa, A.; Ianez, E.; Ubeda, A.; Hortal, E.; Del-Ama, A.J.; Gil-Agudo, A.; Azorin, J.M. Decoding the Attentional Demands of Gait through EEG Gamma Band Features. *PLoS ONE* **2016**, *11*, e0154136. [CrossRef] [PubMed]
46. Oliveira, A.S.; Arguissain, F.G.; Andersen, O.K. Cognitive Processing for Step Precision Increases Beta and Gamma Band Modulation During Overground Walking. *Brain Topogr.* **2018**, *31*, 661–671. [CrossRef]
47. Casarotto, S.; Turco, F.; Comanducci, A.; Perretti, A.; Marotta, G.; Pezzoli, G.; Rosanova, M.; Isaias, I.U. Excitability of the Supplementary Motor Area in Parkinson's Disease Depends on Subcortical Damage. *Brain Stimul.* **2019**, *12*, 152–160. [CrossRef]

48. Conceição, N.R.; Gobbi, L.T.B.; Nóbrega-Sousa, P.; Orcioli-Silva, D.; Beretta, V.S.; Lirani-Silva, E.; Okano, A.H.; Vitório, R. Aerobic Exercise Combined with Transcranial Direct Current Stimulation over the Prefrontal Cortex in Parkinson Disease: Effects on Cortical Activity, Gait, and Cognition. *Neurorehabil. Neural Repair* **2021**, *35*, 717–728. [CrossRef]
49. Beretta, V.S.; Santos, P.C.R.; Orcioli-Silva, D.; Zampier, V.C.; Vitório, R.; Gobbi, L.T.B. Transcranial Direct Current Stimulation for Balance Rehabilitation in Neurological Disorders: A Systematic Review and Meta-Analysis. *Ageing Res. Rev.* **2022**, *81*, 101736. [CrossRef]
50. Lee, H.K.; Ahn, S.J.; Shin, Y.M.; Kang, N.; Cauraugh, J.H. Does Transcranial Direct Current Stimulation Improve Functional Locomotion in People with Parkinson's Disease? A Systematic Review and Meta-Analysis. *J. Neuroeng. Rehabil.* **2019**, *16*, 84. [CrossRef]

sensors

Article

Characterisation of Cognitive Load Using Machine Learning Classifiers of Electroencephalogram Data

Qi Wang [1], Daniel Smythe [1], Jun Cao [1], Zhilin Hu [1], Karl J. Proctor [2], Andrew P. Owens [2] and Yifan Zhao [1,*]

[1] School of Aerospace, Transport and Manufacturing, Cranfield University, Cranfield MK43 0AL, UK; qi.wang.090@cranfield.ac.uk (Q.W.); daniel.smythe.685@cranfield.ac.uk (D.S.); jun.cao@cranfield.ac.uk (J.C.); zhilin.hu.729@cranfield.ac.uk (Z.H.)

[2] Jaguar Land Rover Research, Coventry CV4 7AL, UK; kprocto1@jaguarlandrover.com (K.J.P.); aowens5@jaguarlandrover.com (A.P.O.)

* Correspondence: yifan.zhao@cranfield.ac.uk

Abstract: A high cognitive load can overload a person, potentially resulting in catastrophic accidents. It is therefore important to ensure the level of cognitive load associated with safety-critical tasks (such as driving a vehicle) remains manageable for drivers, enabling them to respond appropriately to changes in the driving environment. Although electroencephalography (EEG) has attracted significant interest in cognitive load research, few studies have used EEG to investigate cognitive load in the context of driving. This paper presents a feasibility study on the simulation of various levels of cognitive load through designing and implementing four driving tasks. We employ machine learning-based classification techniques using EEG recordings to differentiate driving conditions. An EEG dataset containing these four driving tasks from a group of 20 participants was collected to investigate whether EEG can be used as an indicator of changes in cognitive load. The collected dataset was used to train four Deep Neural Networks and four Support Vector Machine classification models. The results showed that the best model achieved a classification accuracy of 90.37%, utilising statistical features from multiple frequency bands in 24 EEG channels. Furthermore, the Gamma and Beta bands achieved higher classification accuracy than the Alpha and Theta bands during the analysis. The outcomes of this study have the potential to enhance the Human–Machine Interface of vehicles, contributing to improved safety.

Keywords: electroencephalography; machine learning; Deep Neural Network; Support Vector Machine; cognitive load classification

Citation: Wang, Q.; Smythe, D.; Cao, J.; Hu, Z.; Proctor, K.J.; Owens, A.P.; Zhao, Y. Characterisation of Cognitive Load Using Machine Learning Classifiers of Electroencephalogram Data. *Sensors* **2023**, *23*, 8528. https://doi.org/10.3390/s23208528

Academic Editor: Yvonne Tran

Received: 5 September 2023
Revised: 9 October 2023
Accepted: 16 October 2023
Published: 17 October 2023

1. Introduction

Cognitive load refers to the amount of working memory required to complete a task within a specified time. Driving tasks require drivers to allocate specific amounts of physical and cognitive loads. Cognitive load plays a vital role in daily driving activities. The Department of Transport of the UK government issued a Reported Road Casualties Great Britain Annual Report in 2021 [1], showing that approximately 22% of road accidents caused by distraction were serious or fatal. Numerous distractions, such as performing secondary tasks, roadside distractions, and talking, can add to a driver's cognitive load. Increased driving-related cognitive load can impact the driver's attention and lead to fatigue [2]. Measuring drivers' cognitive loads is important for improving the understanding of driver behaviours and is thus worth investigating to enhance driver–vehicle interactions. Considerable studies on measuring and estimating drivers' cognitive loads have been conducted using various methodologies in recent years. These methods fit into three different categories [3]:

- Subjective Measures are conventionally measured with a questionnaire, asking subjects to rate a task's difficulty. The NASA Task Load Index (TLX) [4–8] and Subjective

Workload Assessment Technique (SWAT) [9] are the two most common subjective measurement methods used in this category. Subjective measurement cannot evaluate time-varying qualities, and this method can also be affected by events towards the end of the experiment at the time of the questionnaire's administration [5,6].

- Performance measures—the performance of a participant is evaluated to gain insight into cognitive load. Driving quality, response latency, and reaction times are frequently used to gauge performance. Such measures are also often employed in detecting distraction and fatigue. Various factors can influence performance measurement, including individual differences, participants' skill levels, and external variables [10–12].
- Psychophysiological measures include brainwave activity, heart rate variability correlated with task demands [13], eye blinking, pupil diameters, and head rotational angles [14].

Electroencephalography (EEG), which records brain electrical activity, is a highly attractive research method in driver-related cognitive load research. Signals from the brain are propagated through the skull and detected on the scalp [15]. Due to the scalp's relatively low conductivity, EEG devices typically detect signals originating from the brain's cortices. EEG devices offer high temporal resolution (>1 kHz) but have limited spatial resolution, typically ranging from 5 to 9 cm [16]. These signals tend to be noisy, with a low signal-to-noise ratio due to susceptibility to physiological phenomena, such as muscle movements, resulting in contaminated EEG data. The most common artefact originates from eye blinks. The features used to classify EEG data in driving-related research vary significantly across the literature. Some studies use frequency bands, such as Delta (0.5–4 Hz), Theta (4–8 Hz), Alpha (8–14 Hz), Beta (14–30 Hz), and Gamma (30–100 Hz), although the specific frequency ranges chosen may differ [17–26]. Other studies use features generated from Power Spectrum Density (PSD) [27,28]. In addition to these frequency-based features, features in the time and spatial domains have been well-studied [28–30]. Furthermore, a wide variety of classification models have been reported to further group these features. The most common methods include Support Vector Machines (SVMs), Long Short-Term Memory (LSTM) [17,31–33], Artificial Neural Networks (ANNs) [19], Stacked Denoising Auto-Encoders (SDAEs) [25,27], and Convolutional Neural Networks (CNNs) [17–19,24,30,33–36].

In recent years, there has been a growing interest in Functional Near-Infrared Spectroscopy (fNIRS) as a research tool. It measures changes in cerebral blood flow (CBF) and related haemoglobin concentrations by utilising near-infrared light sources and detectors placed on the scalp. fNIRS offers portability similar to EEG while avoiding electromyographic and blink artefacts. However, it has fewer channels compared with EEG recordings and can be susceptible to variations in skin perfusion and scalp blood flow [16]. Aghajani et al. [8] achieved an accuracy ranging from 68% to 87% in classifying different cognitive levels during N-Back tasks using an SVM model. Compared with recent fNIRS research [37–39], there has been limited research utilising EEG to classify cognitive load whilst driving. Notably, the study completed by Almogbel et al. [34] was based on the results of a single participant, achieving an accuracy of 87% by using SVM with a Convolutional Neural Network autoencoder (CNN-AE) as a feature extraction method for EEG classification. Cui et al. [11] classified engagement, enjoyment, boredom, and frustration where the cognitive load is not the main focus. It should be noted that in most existing studies, cognitive load levels are simulated using various non-driving tasks, typically N-Back tasks [40], or other visual or auditory tasks, such as the image-responding tasks in research by Takada et al. [41] or the auditory stimuli and calculation task in research by Faure et al. [42]. These tasks often demand high-level attention and can exhibit different workload levels relatively easily, but they lack the context of driving, which requires middle-level attention.

This research proposes a method for classifying different driving environments and traffic densities that demand different cognitive load levels, using various DNN and SVM machine learning-based classifiers. Unlike existing studies that focus on secondary tasks, the novelty of this paper lies in characterising the driver's cognitive load effects during various driving tasks, utilising EEG recordings collected from experimental studies. The main contributions of this study include:

- A simulator-based experiment to generate different levels of cognitive load based on four carefully designed driving tasks.
- Extraction of frequency-based features used to classify driving conditions by employing DNN and SVM machine learning-based classifiers.
- An exploration of the topological patterns of different frequency bands of brain waves under driving tasks demanding varying levels of cognitive load.

2. Methodology

The methodology of this study consists of four main segments: data collection, data pre-processing, feature generation, feature selection, and machine learning, as shown in Figure 1. The data collection stage explains the experimental setup and the data collection goals. The data pre-processing section describes how the obtained data are processed to improve quality and remove artefacts due to eye movements. Feature generation describes how EEG-based features are extracted from the dataset and prepared for machine learning. Feature selection tests different features in frequency and time domains across different EEG channels. Finally, machine learning describes the classification of datasets of features using chosen machine learning models.

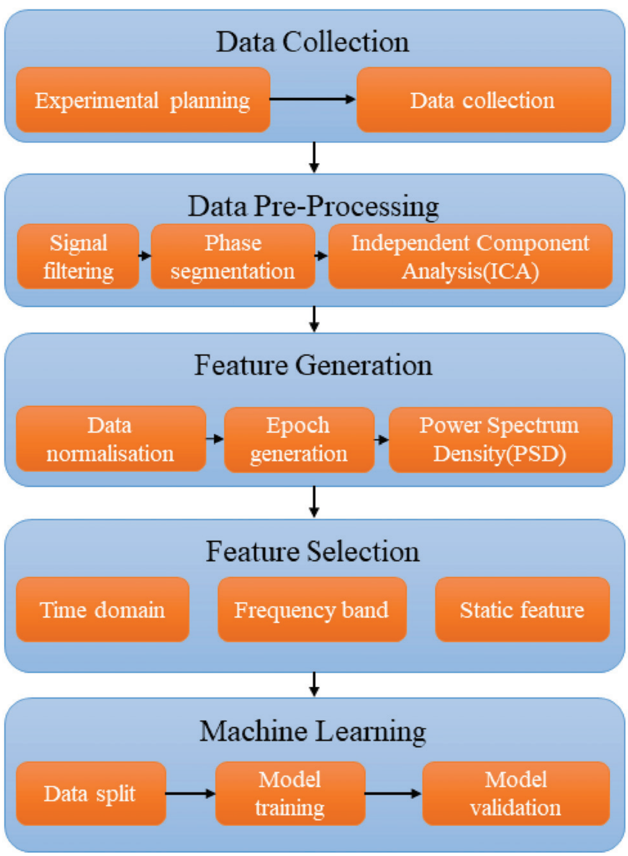

Figure 1. A block diagram displaying the four steps of the overall methodology.

2.1. Data Collection

EEG data were collected for this experiment using a water-based Waveguard Net from Ant Neuro. The device has 24 electrodes and is referenced from the Cz electrode, positioned according to the international 10–20 system [43]. The sample rate was 256 Hz. The device is relatively simple to set up compared with gel-based EEG caps, but it must be bathed in saltwater for at least 10 min before fitting and recording. The complete set of sensors and their locations are shown in Figure 2a. The device is shown in Figure 2c, and one snapshot of the whole experiment setup is shown in Figure 2b. A total of 20 male participants took part in the experiment. Each participant gave informed consent for this research to use and publish the aggregated data. The average age of participants was 27.65 years old (ranging from 22 to 42), and they all owned valid driving licenses. In addition, three participants consumed coffee within 12 h of the experiment. Most of the experiments were conducted in the morning, and participants were encouraged to ensure they had adequate sleep, which was verified through the questionnaire. Experiments were conducted in a quiet office area with stable lighting and air conditioning to minimise external interferences that cause additional eye blinks or head movement. Throughout experiments, participants were not allowed to engage in conversation with others.

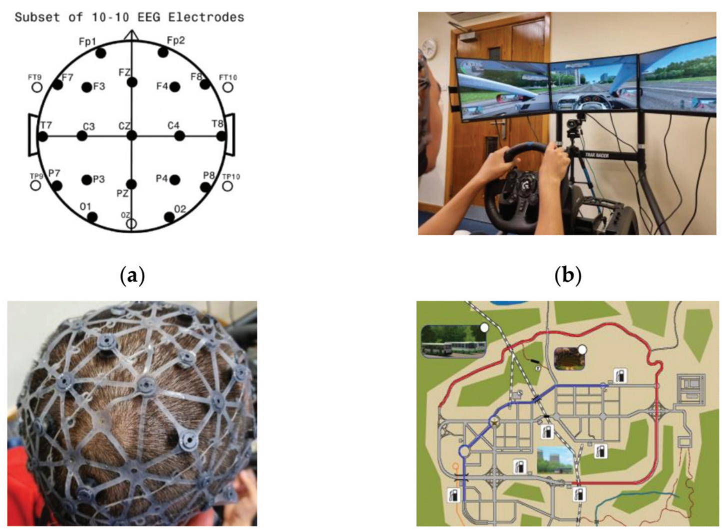

(**a**) (**b**) (**c**) (**d**)

Figure 2. Images displaying the experimental setup and a map showing routes followed by participants. (**a**) Complete sets of sensors and their locations. (**b**) Driver simulator setup. (**c**) Display of the EEG sensor device. (**d**) Route map of the experiment; the red route shows the motorway route, and the blue route shows the urban route.

The City Car Driving software was used for driving simulation. City Car Driving is a PC platform driving simulation software designed for car learners to practice their driving skills. This software can simulate different driving environments with different intensities of cars and pedestrians. All participants were required to drive in automatic gear, partially for simplicity and partly to limit the amount of muscle movement (to reduce the amount of noise in EEG data). There were five sessions in the experiment:

- Practice: Participants were given time to become familiar with the driving simulator and simulation software. After eight minutes, they were prompted and asked whether they wanted to start the experiment. They could become familiar with the system for as long as they wanted.

- Motorway—no cars: Participants were asked to follow a motorway route until being prompted to pull over on the left. In this session, there were no other cars (mean time taken: 6 min and 57 s).
- Motorway—with cars: Participants repeated the same route as above. However, this section included AI-controlled cars on the road (vehicle traffic density of 70%; mean time taken: 8 min and 36 s).
- Urban—no cars: Participants were asked to travel along a route in an urban environment and follow instructions given by a GPS included in the software. In this session, there were no other cars (mean time taken: 6 min and 1 s).
- Urban—with cars: Participants repeated the same route as above. However, this section included AI-controlled cars on the road (vehicle traffic density of 30%; mean time taken: 8 min and 6 s).

Each session took approximately 7–10 min and all participants were given a 5 min break between each section to reduce the effect of build-up fatigue. Figure 2d illustrates the motorway route (shown in red) and the urban route (shown in blue). The motorway section consists of approximately 5 km of a single carriageway and approximately 8 km of a motorway. The speed limit for driving on the motorway section is 110 km/h and 90 km/h on the single carriageway section. The urban route comprises a combination of dual and single street roads, with a total length of approximately 8 km. The urban route includes three traffic light junctions and two roundabout junctions, and all participants are required to follow UK driving regulations at these junctions. In addition, the protocol was counterbalanced so that half of the participants performed two motorway routes first, while the other half completed urban routes first. This arrangement aimed to ensure that any apparent decrease in cognitive load was not due to the participant feeling more familiar with the simulation.

After completing all sessions, participants were required to rate the cognitive load of four driving tasks (the training session was excluded) on a scale ranging from 1 to 10, with 1 indicating the lowest cognitive load level and 10 representing the highest cognitive load level. The outcomes are summarised in Figure 3. As expected, "Motorway—no car" was rated as the task with the lowest load (mean: 1.9); "Urban—with cars" was rated as the task with the highest load (mean: 4.9). Statistical analysis using ANOVA was applied to the questionnaire results. The p-values for driving scenarios with cars and driving scenarios without cars were found to be 0.00112 for the motorway route and 0.00053 for the urban route. This indicates that the cognitive load during driving tasks with other cars is significantly higher than that without other cars. Therefore, this experiment design is promising to potentially simulate scenarios that require high or low cognitive loads.

Additionally, the rated load of the driving tasks with other cars exhibits greater variation than that without other cars. Furthermore, these four tasks potentially represent four different levels of cognitive load. This research hypothesises that the classification of levels of cognitive load can be represented by the classification of EEG data of participants completing these driving tasks.

2.2. Data Pre-Processing

Data from the beginning stage of each session and durations when the driving task was interrupted by accidents or misoperation were excluded. These periods cannot accurately reflect the desired driving workload. In total, 47,000 s of data were collected for all participants, of which 35,000 s were preserved for analysis. This study employed the MNE software package (an open-source Python package for exploring, visualising, and analysing human neurophysiological data) [44] in Python to process the collected EEG data. Firstly, a band-pass filter [0.2 Hz, 40 Hz] was applied to all data. The filter was applied using a Hamming window with a 0.0194 Hz passband ripple and a 53 dB stopband attenuation. Additionally, a low-pass frequency of 40 Hz was chosen to remove noise from the power source. The EEG data from the entire experiment was separated into four segments based on four driving tasks, while the data in the practice phase were neglected. To reduce the interference of muscle activities, such as eye blinks, we applied Independent Component Analysis (ICA). It blindly decomposes a signal into a collection of signals from differing sources using the fastica method in the 'MNE' module with 18 principal components. ICA can determine which parts of EEG signals constitute artefacts due to the movements of ocular muscles. The decomposed signals must be manually labelled, as those are believed to represent the ocular artefacts. Since the ICA cannot perfectly identify the ocular artefacts and there will be some human errors, the artefacts can never be removed entirely but are significantly reduced using this method.

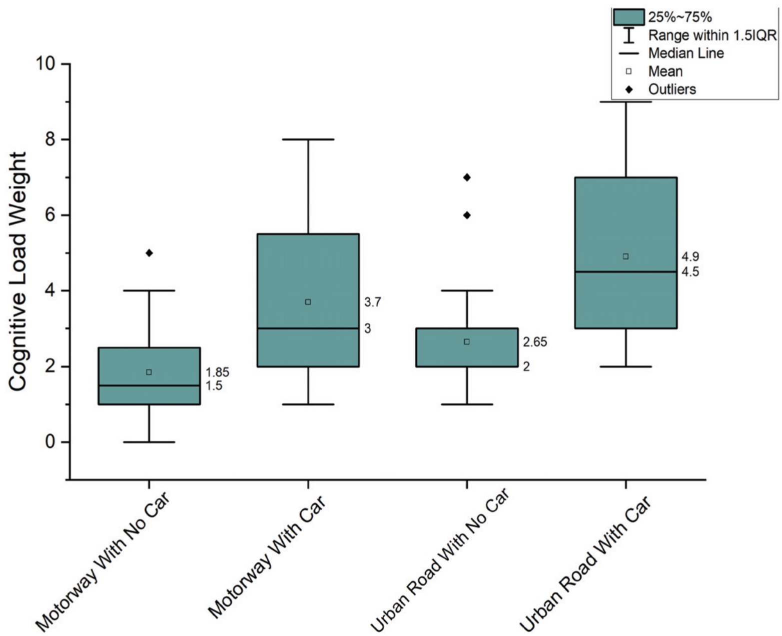

Figure 3. The cognitive load of driving tasks rated by participants.

2.3. Feature Generation and Feature Selection

This step comprises two subsections: feature generation, which primarily focuses on noise reduction and creating features for subsequent selection, and feature selection, which outlines the methodology for choosing various features for building the subsequent model.

2.3.1. Normalisation and Dataset Generation

Before generating the dataset for machine learning-based classification, the EEG data were standardised for each channel to ensure the EEG signals from each participant were normalised with a mean of 0 and a variance of 1. This operation was applied to each segmented data portion before generating a set of features.

Before learning about features, the data were split into discrete time intervals to increase the number of instances. For this purpose, the data were segmented into 1 s time intervals using a sliding window with a 50% overlap. Before training the model, another round of pre-processing was applied for each segment to further reduce the impact of noise. We used a threshold equal to the 95th percentile of the Peak-to-Peak (PTP) values across the data entries individually in each class. It removes any data segment containing a channel with a PTP value above that threshold. PTP is the distance from the minimum to maximum peak representing each data entry's signal range. Any entry with a channel containing a PTP value above the threshold is deemed too noisy and removed from the dataset on which the model was trained and validated. After PTP removal, we were left with 11,559 segments for the session of motorways without cars, 15,211 segments for motorways with cars, 12,131 segments for urban without cars, and 14,760 segments for urban with cars.

2.3.2. Feature Selection

It is evident that the PSD of EEG recordings can effectively measure workload [45], and, therefore, it was used as a single feature in this study. Four frequency bands are defined as Theta (4–8 Hz), Alpha (8–14 Hz), Beta (14–30 Hz), and Gamma (30–40 Hz). First, the PSD using the Welch method [46] was generated for each data entry to produce these features. For each data entry, a PSD was generated using 72 frequency values ranging from 4 to 40 Hz with a resolution of 0.5 Hz.

The selected statistical features for each band include the mean, variance, and absolute maximum amplitude of frequency response. In addition, the band power was generated by integrating the PSD between selected frequency ranges, which was then divided by the total power of the entire frequency range. This step gives a fraction representing the ratio of power this frequency band contains with respect to the full frequency range. Each feature was generated for each EEG channel and each frequency band, giving a set of $4 \times 4 \times 24 = 384$ total features.

2.4. Machine Learning

For this study, the selected features were classified using a Deep Neural Network (DNN) and a Support Vector Machine (SVM). The 'Keras' Module in the Tensorflow Python library was used [47] to implement DNN, and the 'Sklearn' library was used to implement SVM [48].

The first layer of a DNN is the input layer, which contains an array of input values used as the feature inputs to the network. Next are fully connected layers, where the main computation of the model takes place. Each edge in the diagram has an associated weight value. The nodes in the current layer are multiplied by the weight along the edge connected to the node to produce values associated with each node in the next layer. In a fully connected network, each node is connected to each node in the next layer. Once the value is obtained for the node, the next layer of nodes can be computed. An activation function is applied to each layer's output to augment the results. After calculating all the fully connected layers, the output layer can be computed using the same method. An activation function is applied to the output values, and a set of values associated with each class type is obtained. Then, the most probable class is taken as the output class. The training phase consists of learning the values associated with each edge by continuously passing a set of data through the network and updating the edges according to the error in the output. The exact method to update the edge weights depends on the optimiser in 'Keras' [49].

Eight different models were trained, half with a DNN and the other half with an SVM. There are four classification tasks:

- Motorway-High-Low: The condition with other vehicles on the road was labelled as high intensity of cars (indicating high cognitive load scenarios), and the condition without other road users was labelled as intensity of cars (indicating low cognitive load scenarios). Only the motorway data are included in this task.
- Urban-High-Low: The labelling process is the same as Motorway-High-Low, but only the urban data are included.
- Combined-High-Low: The labelling process is the same as Motorway-High-Low, but the urban and motorway data are included.
- Four-Class: In this task, each experiment session is given a separate class, resulting in four classes: urban with no cars, urban with cars, motorway with no cars, and motorway with cars.

Figure 4 shows the architecture of the used DNN model. The DNN architecture includes two layers: one with 200 fully connected neurons and another with 100 fully connected neurons. In three high-low tasks, there are two classes and, therefore, two output layers, while in the four-class task, there are four classes and, therefore, four output layers. All output layers used a sigmoid activation function for all tasks. In addition, a binary-cross-entropy loss function and the Keras' Adam' optimiser [50] were used for both 2-class and 4-class classification tasks. The first layer used a linear activation function, and the second used a Relu activation function. An epoch size of 200 was used to train the model. In addition, three different measurements were used to represent the performance of the produced models. The first is accuracy, which is represented by the following formula:

$$Accuracy = \frac{TP + TN}{TP + FP + FN + TN} \tag{1}$$

where *TP* represents the True Positive, *TN* is the True Negative, *FN* is the False Negative, and *FP* is the False Positive. This value represents the ratio of correct classifications to incorrect classifications. When dealing with multiple classes, this is averaged across all classes. However, additional performance values were measured since there may be a bias in accuracy due to an unbalanced dataset. The following formula represents precision:

$$Precision = \frac{TP}{TP + FP} \tag{2}$$

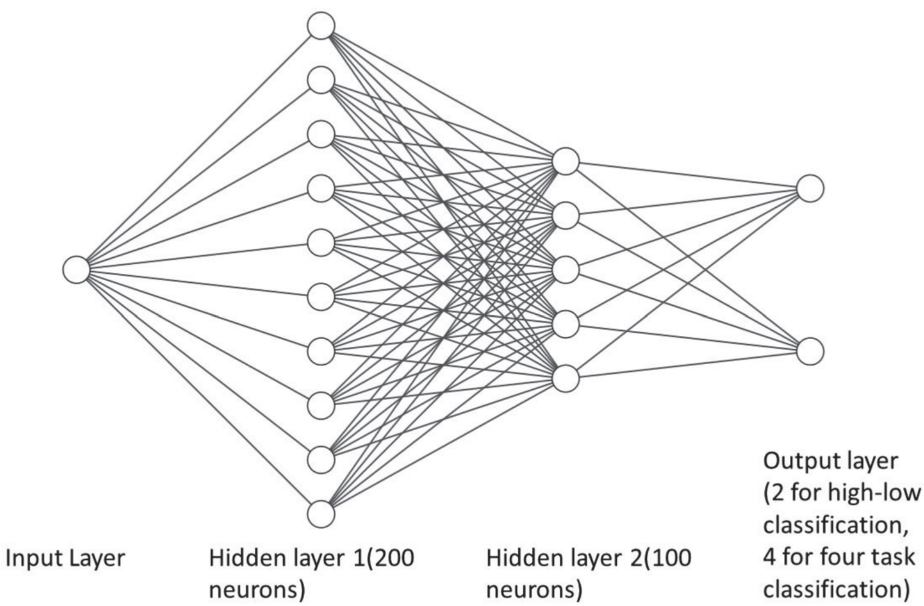

Figure 4. The architecture of the DNN model.

The precision represents the number of correct classifications out of the total number of dataset entries identified as that class by the model. The following formula represents recall:

$$Recall = \frac{TP}{TP + FN} \tag{3}$$

The recall represents the number of correct classifications from the total number of dataset entries in that class. In addition to these classification performance indicators, a confusion matrix is produced for each task to analyse the detailed performance.

For each model, average accuracy, precision, and recall were generated by training the model using 10-fold cross-validation and leave-one-out cross-validation. For the 10-fold cross-validation, the entire dataset was split into ten equally sized sets. Ten different datasets for machine learning were generated, using one of these folds as the testing set and the remainder as the training set. This step was repeated ten times to ensure each folder was used for validation. The drawback of using only one testing set is that the test accuracy can vary greatly depending on which observations were used in the training and testing sets. The resulting accuracy could be much larger or smaller if we used a different set of observations for the training and testing sets. The k-folder cross-validation was employed to address this limitation.

The leave-one-person-out cross-validation applies the same concept, but the data are divided into different folders based on participants. The data from one participant are used as the testing set, and others are used for training. This step is repeated 20 times in this study to ensure each participant is used for validation. This validation approach aims to test the performance of a model that learned from a group of subjects testing on another subject to measure the variation across subjects.

3. Results

Table 1 shows the model performance of two validation approaches for four classification tasks using DNNs and SVMs. Using the selected features from EEG recordings, the DNNs can effectively distinguish high and low intensities of cars with an accuracy of around 85%. Even the four-class classification achieved an accuracy of up to 78%, which indicates the different brain activities during the four driving tasks. Results also suggest that when using the 10-fold cross-validation, the DNNs entirely outperform the SVMs. The urban data show an 18.21% difference between the two models, and the motorway data show a 17.98% difference. It is also observed that the two models behave similarly for the Combined-high-low task and four-class, increasing by 17.41% and 29.90%, respectively. Additionally, the accuracy, precision, and recall values are very close in each model, meaning the models are not heavily biased towards one class in particular. Also, the classification matrices of the DNN presented in Figure 5 show no extreme bias towards one class when using the 10-fold cross-validation.

Table 1. Performance of the DNN and SVM classifiers on four data sets, using 10-fold cross-validation and cross-participant validation.

Method	Classification Task	10-Fold Cross Validation			Cross-Participant Validation		
		Accuracy	Precision	Recall	Accuracy	Precision	Recall
DNN	Urban-High-Low	84.26 ± 0.75%	84.27 ± 0.75%	84.26 ± 0.75%	49.52 ± 9.40%	49.53 ± 9.37%	49.54 ± 9.36%
	Motorway-High-Low	90.37 ± 0.55%	90.37 ± 0.57%	90.37 ± 0.59%	59.52 ± 13.37%	59.54 ± 13.35%	59.52 ± 13.36%
	Combined-High-Low	81.65 ± 0.73%	81.64 ± 0.73%	81.65 ± 0.72%	56.28 ± 6.41%	56.28 ± 6.41%	56.28 ± 6.41%
	Four-Class	78.66 ± 0.56%	77.61 ± 0.73%	76.70 ± 0.94%	31.39 ± 6.76%	31.91 ± 7.24%	28.59 ± 6.50%
SVM	Urban-High-Low	66.05 ± 1.15%	65.87 ± 1.10%	66.00 ± 1.08%	48.96 ± 9.98%	48.42 ± 10.53%	48.65 ± 9.31%
	Motorway-High-Low	72.39 ± 0.74%	72.72 ± 0.77%	73.18 ± 0.73%	58.26 ± 11.91%	58.79 ± 12.94%	57.46 ± 11.95%
	Combined-High-Low	64.24 ± 0.53%	64.65 ± 0.54%	64.83 ± 0.55%	55.54 ± 7.66%	56.63 ± 7.94%	55.40 ± 6.96%
	Four-Class	48.76 ± 0.66%	48.79 ± 0.70%4	49.00 ± 0.75%	30.47 ± 7.08%	30.77 ± 8.12%	30.03 ± 7.02%

However, the same trend is not observed when analysing results from the leave-one-person-out validation. The results from both methods in Table 1 are close to the baseline of 50% for the first three classification tasks and 30% for the last task. It suggests that the features' pattern that can distinguish high and low intensities of cars differs across participants. The model performs more accurately when it sees data from each individual during training. The 10-fold cross-validation mixes each individual's data between the training and validation sets. During the validation process, there is a high chance that the model sees this individual's data previously but in different epochs and learns key features from them. There is, however, a chance that most of these learnt features are individually dependent. The algorithm behaves similarly to a random method for features learnt from certain subjects and tested on other subjects. This observation implies that the learned features are individually specific. However, this can still be useful to determine the load level for individuals where specific machine learning model learns.

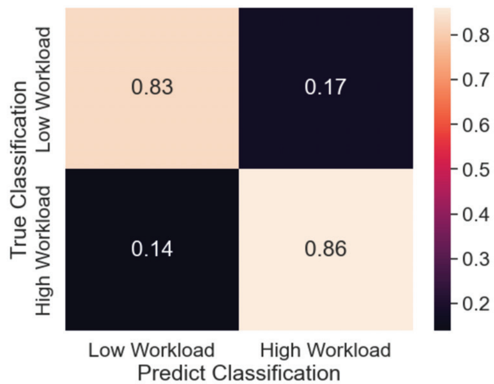

(**a**) Urban-High-Low

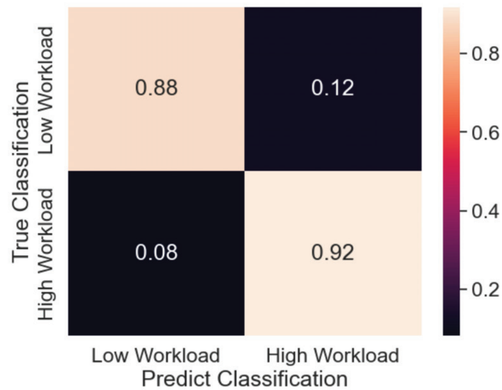

(**b**) Motorway-High-Low

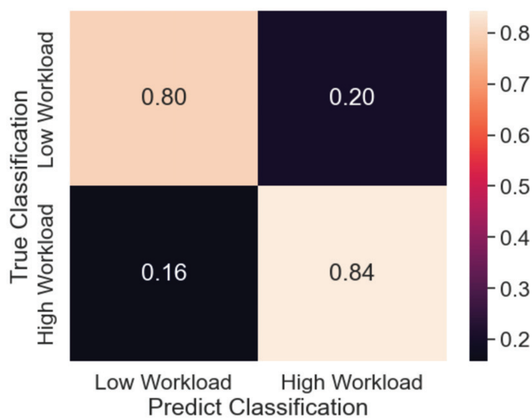

(**c**) Combined-High-Low

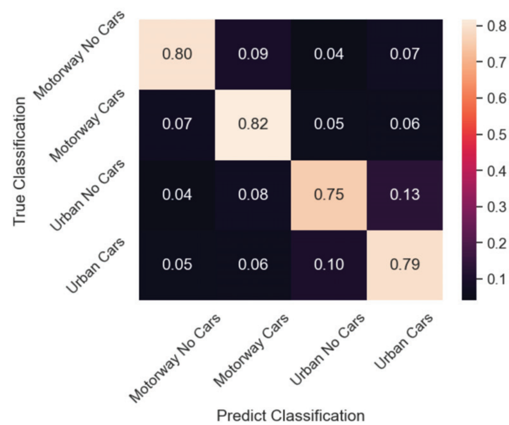

(**d**) Four-class

Figure 5. Classification matrices using DNN for 10-folder cross-validation. (**a**) Classification matrices of High-Low two-class classification in urban environments. (**b**) Classification matrices of High-Low two-class classification in motorway environments. (**c**) Classification matrices of High-Low two-class classification combined. (**d**) Classification matrices of four-class classification.

The results shown here may link back to prior research about how cognitive load is defined in the literature review. As suggested by O'Donnell and Eggemeier [50], the cognitive load is "The portion of an individual's limited mental capacity that is required by task demands". Cognitive load depends on working memory [51], and individuals' perception and cognitive functions to complete a specific task can differ based on their experiences and familiarity. Some individuals may have found each task in this experiment extremely difficult and experienced a much higher load in the same tasks that others found simple.

It was found that the results displayed by using the 10-fold cross-validation are comparable to results shown by other experiments. For example, So et al. [21] reported results ranging from 60.40 to 76.00% using an SVM to classify two levels of cognitive load, while the results in this study display a range of 64.24–72.39% accuracy using an SVM with two classes. However, it should be noted that very limited studies presented the results from a cross-participant validation. Cui et al. [11] used a cross-participant validation and found large variations in some results. The proposed relative power + SVM model had an accuracy ranging from 30.77 to 89.84% between subjects, suggesting the difficulty of finding consistent features to differentiate cognitive load levels for all subjects.

Although the accuracy drops as expected for the four-class model, EEG data can separate these four tasks efficiently with more than 77% accuracy. There may be a variation in the cognitive load resulting in a change in feature values due to the GPS, turns, and roundabouts in the urban route. In other words, the cognitive load level for each task can be different. The model does suffer the same issue as the other three models with cross-participant validation, obtaining an accuracy within 1σ of the random accuracy of 25%.

4. Discussion

This section discusses and analyses the results to uncover significant findings. In the first subsection, various other features, including power ratio, mean, variance, and maximum values, are examined and compared with PSD. The frequency band analysis subsection involves assessing different frequency bands, accompanied by the generation of a topographic map. The limitations of the study are addressed in the last subsection, discussing various constraints encountered.

4.1. Feature Analysis

This subsection explores the contribution to the classification of each feature. A dedicated model was trained for each feature type based on bands and statistical values. There are 32 models for four bands and four statistical values, and they were performed for two-class datasets. The four-class dataset is not investigated here, as this analysis aims to look at each feature's impact on classifying the cognitive load. As analysed previously, the cognitive load distinction is more apparent in two-class datasets. In addition, a DNN with fewer neurons for each feature is available for the four-class dataset. The models were trained using two layers of 10 neurons to reduce the amount of potential overfitting that might occur.

Table 2 displays the results for the four bands and four statistical values. It can be observed that the accuracy is higher when using higher frequency bands. The true reason for this observation is unclear. However, there are studies suggesting that the Beta wave is a carrier of visual attention in humans [51], and Gamma waves are shown to increase when given a visual stimulus [52]. Both factors may cause this observation, as there is an increase in visual stimuli when other cars are included on the road. These frequency bands are further analysed in a later section.

Table 2. Accuracies of the band and statistical features of each dataset.

Feature	Urban-High-Low	Motorway-High-Low	Combined-High-Low
Theta Band	64.22 ± 0.62%	67.66 ± 1.18%	62.99 ± 0.61%
Alpha Band	67.04 ± 0.77%	70.46 ± 0.70%	64.97 ± 0.59%
Beta Band	75.23 ± 0.69%	80.46 ± 0.87%	72.26 ± 0.86%
Gamma Band	81.04 ± 1.46%	87.74 ± 0.75%	79.33 ± 0.71%
Power Ratio	69.26 ± 1.41%	69.10 ± 0.89%	67.01 ± 0.93%
Mean	68.79 ± 0.96%	70.80 ± 1.20%	66.96 ± 0.78%
Variance	72.69 ± 0.91%	79.36 ± 1.06%	70.50 ± 0.45%
Absolute Max	66.63 ± 0.80%	70.02 ± 1.00%	65.25 ± 0.66%

In addition, whilst a high performance is observed in each statistical feature, the variance measure tends to perform most accurately in each dataset. In the Motorway-High-Low dataset, the variance feature achieved an accuracy of 79.36%, which was 8.56%

greater than the following highest result. In the Urban-High-Low dataset, it performed 3.34% better; in the Combined-High-Low dataset, it performed 3.49% better. Among the remaining features, no metric performs significantly worse than the rest. The differences observed are probably due to random chance, as they remain within either 1σ or 2σ of each other.

Figure 6 shows the results of the channel analysis displayed on a topographic map. There is an apparent trend in the accuracy produced for each channel. In this diagram, the red region represents regions of higher accuracy, and the blue region represents regions of lower accuracy. The exact accuracy values are indicated on the colour bar. The greatest-performing regions are consistent throughout each dataset. The most accurate regions occur mainly along the frontal lobe, right temporal lobe, parietal lobe, and occipital lobe. Regions with the most prominent accuracy among channels include 'Fp1', 'Fp2', 'Fz', 'F4', 'F8', 'FT10', 'C3', 'C4', 'T8', 'TP10', 'P3', 'Pz' 'P4', 'P8', and 'O2'. In addition, no channel performed worse than or within 2σ of 50%. Overall, the channel accuracy measurements ranged from 54.96 to 65.38%.

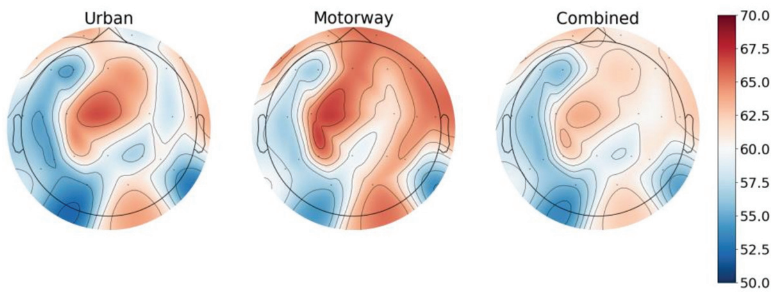

Figure 6. Topographic maps of the accuracy values in each model.

4.2. Frequency Band Analysis

An investigation of frequency bands was performed to observe whether there were any significant trends in the individual frequency bands across the experiments. This was mostly inspired by trends in the previous section, where the accuracy values increased as the frequency values of the bands increased. For this purpose, the mean and variance values of Theta, Alpha, Beta, and Gamma were plotted by taking the median response from each participant in each experimental segment. The purpose of taking the median was to ignore anomalous values where the orders of magnitude were greater than other values.

Figures 7 and 8 display the results of this investigation, where some very noticeable trends are observed. The mean and variance in each diagram's middle parietal and occipital regions consistently exhibited the smallest response values, while the frontal and side regions showed significantly larger responses. Additionally, the contour shapes within each band are highly similar. However, they differ in the intensities displayed within each region, and there are noticeable differences between each classification task.

As should be expected, the intensity of the mean and variance decreased throughout each band due to the natural shape of the PSD expected from the EEG data. Finally, there are noticeable commonalities in shapes displayed by the distributions shown by the two classes with cars and the two classes without cars. Figure 7 shows that although every class peaks within the left and right temporal regions, both classes with cars display a reduced response at the frontal region compared with those without cars in the Beta and Gamma bands. In the Theta and Alpha bands, classes with cars show a stronger frontal response than those without cars. A similar trend is seen in Figure 8. However, such commonalities may be entirely down to random chance, and more work should be put into a detailed investigation of the specifics of the frequency band behaviours in future works.

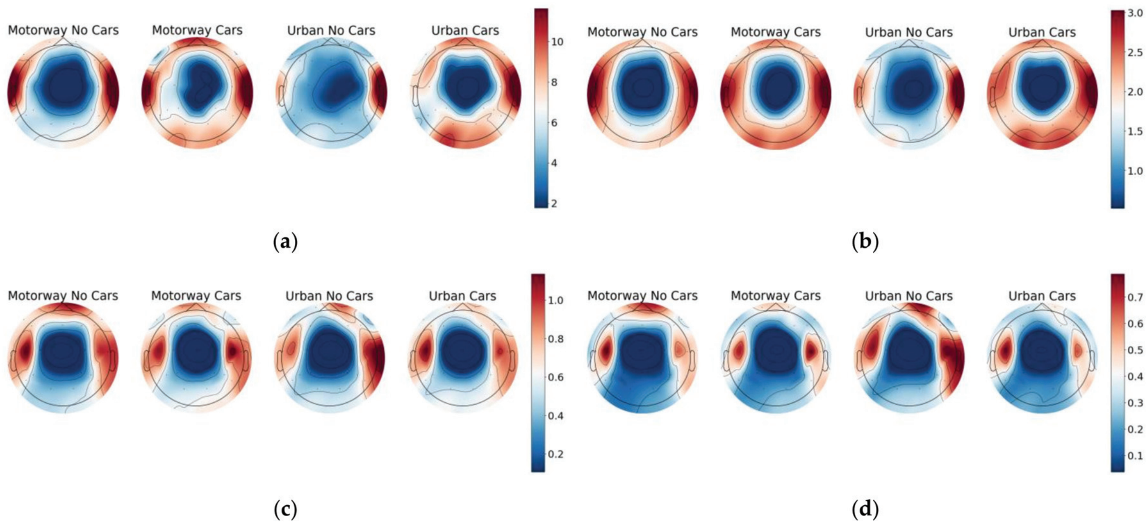

Figure 7. Topographic maps displaying median means of the Theta, Alpha, Beta, and Gamma bands across each section of experiment. (**a**) Theta band. (**b**) Alpha band. (**c**) Beta band. (**d**) Gamma band.

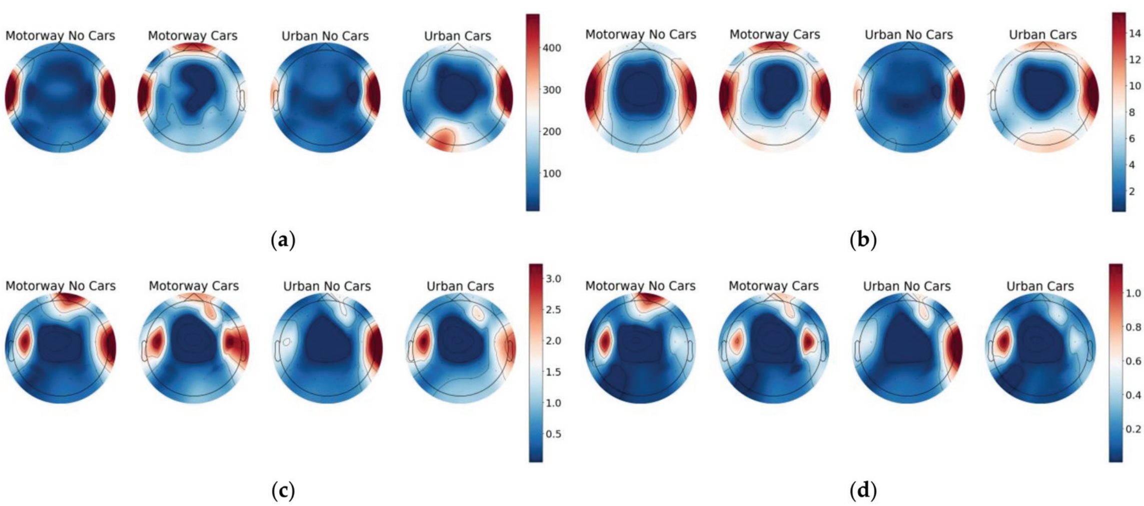

Figure 8. Topographic maps displaying the variance in Theta, Alpha, Beta, and Gamma bands across each experiment section. (**a**) Theta band. (**b**) Alpha band. (**c**) Beta band. (**d**) Gamma band.

4.3. Limitations

Although the goals set for this study were met, there are some limitations which need to be addressed in future studies. Firstly, in this experimental design, a simple self-designed questionnaire was used to rate the cognitive load of each driving task. This could lead to bias in rating the cognitive load with a single parameter. Conducting a NASA-TLX questionnaire after all four sessions is challenging for participants due to memory constraints. Essentially, the cognitive load levels simulated in this study are relative rather than absolute, and we recognise this as a potential limitation. During the experiment, we used an all-male cohort who we did not ask to refrain from neuroactive stimulants, such as caffeine and nicotine. The influence of pulse and lateral eye movement in EEG was considered during the analysis. Moreover, only the PSD was used as the feature for classification. In future studies, we plan to incorporate additional features, such as amplitude-based features, brain functional connectivity, and effective connectivity to improve classification performance further. Although the models perform well with the 10-folder cross-validation, they fail to perform at the same level using the cross-participant validation. It implies the information/pattern the models learned from the dataset is not general enough, and more subjects should be included in a more diverse (e.g., gender, age) and well-described (e.g., quality of previous night's sleep) cohort of participants to enhance these positive initial findings.

5. Conclusions

Through a dedicated experiment, this study investigated drivers' brain activity patterns measured with EEG techniques for four driving tasks that required different levels of cognitive load. Machine learning approaches were employed to classify the features extracted from EEG recordings. This aim can be deemed a success, as the developed models were able to classify the dataset between different tasks when using the 10-cross validation. In addition, the classification accuracy values achieved for high and low cognitive loads were comparable to the results of similar experiments, achieving accuracy values within the ranges of 81.65 to 90.37%% when using a DNN and 64.24 to 72.39% when using an SVM. Furthermore, the models could distinguish between all four classes with a 78.66% accuracy using a DNN and a 48.76% accuracy using an SVM.

A collection of small DNNs trained on small samples of features could be used to estimate each feature's contribution. EEG channels in the scalp's frontal, central, and right regions were found to perform noticeably better. In addition, the Gamma and Beta bands performed significantly better than the Theta and Alpha bands. This observation supports the findings of the existing literature, which implies that Gamma and Beta bands tend to change in response to visual stimuli and tasks [46,47]. Furthermore, it was found that the variance measured outperformed other statistical measures for the PSD regions by between 3.34 and 8.56%, depending on the utilised dataset.

Author Contributions: Conceptualisation, Q.W. and D.S.; methodology, Q.W. and D.S.; software, Q.W. and D.S.; validation, Q.W. and D.S..; formal analysis, Q.W. and D.S.; investigation, Q.W. and D.S.; resources, Q.W. and D.S.; data curation, Q.W.; writing—original draft preparation, Q.W. and D.S.; writing—review and editing, Q.W., J.C., Z.H., K.J.P., A.P.O. and Y.Z.; visualisation, Q.W. and D.S.; supervision, Y.Z.; project administration, Y.Z.; funding acquisition, Y.Z. All authors have read and agreed to the published version of the manuscript.

Funding: This work was supported in part by a Royal Academy of Engineering Industrial Fellowship [#grant IF2223B-110] and a UKRI Future Leaders Fellowship [grant #MR/T021160/1].

Institutional Review Board Statement: This research was approved by the Cranfield University Research Ethics Systems (CURES), Reference: CURES/15656/2022.

Informed Consent Statement: Informed consent was obtained from all subjects involved in the study.

Data Availability Statement: The data presented in this study can be downloaded from: https://doi.org/10.17862/cranfield.rd.23978112 (accessed on 4 September 2023).

Conflicts of Interest: The authors declare no conflict of interest.

References

1. U. G. Department of Transport. *Reported Road Casualties Great Britain: Injury Severity within Injury-Based Reporting Systems Police Forces*; U.K. Department of Transport: London, UK, 2022.
2. Lansdown, T.C.; Brook-Carter, N.; Kersloot, T. Distraction from multiple in-vehicle secondary tasks: Vehicle performance and mental workload implications. *Ergonomics* **2004**, *47*, 91–104. [CrossRef] [PubMed]
3. Galy, E.; Cariou, M.; Mélan, C. What is the relationship between mental workload factors and cognitive load types? *Int. J. Psychophysiol.* **2012**, *83*, 269–275. [CrossRef] [PubMed]
4. NASA. *Nasa Task Load Index (TLX) v. 1.0 Manual*; NASA—Ames Research Center Moffett Field: Mountain View, CA, USA, 1986.
5. Lei, S.; Roetting, M. Influence of Task Combination on EEG Spectrum Modulation for Driver Workload Estimation. *Hum. Factors* **2011**, *53*, 168–179. [CrossRef] [PubMed]

6. Maglione, A.; Borghini, G.; Aricò, P.; Borgia, F.; Graziani, I.; Colosimo, A.; Babiloni, F. Evaluation of the workload and drowsiness during car driving by using high resolution EEG activity and neurophysiologic indices. In Proceedings of the 2014 36th Annual International Conference of the IEEE Engineering in Medicine and Biology Society, EMBC 2014, Chicago, IL, USA, 26–30 August 2014.
7. Helman, S.; Diels, C.; Reed, N.; Chattington, M.; Belyavin, A.; Dickson, B. *Use of Electroencephalography (EEG) and the Tactile Detection Task (TDT) to Improve Mental Workload Estimation in the TRL Car Driving Simulator*; Published Project Report (PPR 500); Transport Research Laboratory (TRL): Wokingham, UK, 2010.
8. Aghajani, H.; Garbey, M.; Omurtag, A. Measuring mental workload with EEG + fNIRS. *Front. Hum. Neurosci.* **2017**, *11*, 359. [CrossRef] [PubMed]
9. Reid, G.B.; Nygren, T.E. The subjective workload assessment technique: A scaling procedure for measuring mental workload. *Adv. Psychol.* **1988**, *52*, 185–218.
10. Wang, H.; Xu, L.; Bezerianos, A.; Chen, C.; Zhang, Z. Linking Attention-Based Multiscale CNN With Dynamical GCN for Driving Fatigue Detection. *IEEE Trans. Instrum. Meas* **2021**, *70*, 2504811. [CrossRef]
11. Cui, J.; Lan, Z.; Sourina, O.; Müller-Wittig, W. EEG-Based Cross-Subject Driver Drowsiness Recognition with an Interpretable Convolutional Neural Network. *IEEE Trans. Neural. Netw. Learn Syst.* **2022**, *34*, 7921–7933. [CrossRef] [PubMed]
12. Lin, C.T.; Chuang, C.H.; Huang, C.S.; Tsai, S.F.; Lu, S.W.; Chen, Y.H.; Ko, L.W. Wireless and Wearable EEG System for Evaluating Driver Vigilance. *IEEE Trans. Biomed. Circuits Syst.* **2014**, *8*, 165–176.
13. Fournier, L.R.; Wilson, G.F.; Swain, C.R. Electrophysiological, behavioral, and subjective indexes of workload when performing multiple tasks: Manipulations of task difficulty and training. *Int. J. Psychophysiol.* **1999**, *31*, 129–145. [CrossRef]
14. Xing, Y.; Lv, C.; Cao, D.; Wang, H.; Zhao, Y. Driver workload estimation using a novel hybrid method of error reduction ratio causality and support vector machine. *Measurement* **2018**, *114*, 390–397. [CrossRef]
15. Hekmatmanesh, A.; Zhidchenko, V.; Kauranen, K.; Siitonen, K.; Handroos, H.; Soutukorva, S.; Kilpeläinen, A. Biosignals in human factors research for heavy equipment operators: A review of available methods and their feasibility in laboratory and ambulatory studies. *IEEE Access* **2021**, *9*, 97466–97482. [CrossRef]
16. Tachtsidis, P.; Hirsch, H.; Aichelburg, G.; Burgess, P.W. The present and future use of functional near-infrared spectroscopy (fNIRS) for cognitive neuroscience. *Ann. N. Y. Acad. Sci. Mar.* **2020**, *1464*, 5–29. [CrossRef]
17. Zuo, X.; Zhang, C.; Cong, F.; Zhao, J.; Hämäläinen, T. Driver Distraction Detection Using Bidirectional Long Short-Term Network Based on Multiscale Entropy of EEG. *IEEE Trans. Intell. Transp. Syst.* **2022**, *23*, 19309–19322. [CrossRef]
18. Lv, C.; Nian, J.; Xu, Y.; Song, B. Compact Vehicle Driver Fatigue Recognition Technology Based on EEG Signal. *IEEE Trans. Intell. Transp. Syst.* **2021**, *23*, 19753–19759. [CrossRef]
19. Baldwin, C.L.; Penaranda, B.N. Adaptive training using an artificial neural network and EEG metrics for within- and cross-task workload classification. *Neuroimage* **2012**, *59*, 48–56. [CrossRef] [PubMed]
20. So, W.K.Y.; Wong, S.W.H.; Mak, J.N.; Chan, R.H.M. An evaluation of mental workload with frontal EEG. *PLoS ONE* **2017**, *12*, e0174949. [CrossRef] [PubMed]
21. Fan, J.; Wade, J.W.; Key, A.P.; Warren, Z.E.; Sarkar, N. EEG-Based Affect and Workload Recognition in a Virtual Driving Environment for ASD Intervention. *IEEE Trans. Biomed. Eng.* **2018**, *65*, 43–51. [CrossRef] [PubMed]
22. Zarjam, P.; Epps, J.; Chen, F.; Lovell, N.H. Estimating cognitive workload using wavelet entropy-based features during an arithmetic task. *Comput. Biol. Med.* **2013**, *43*, 2186–2195. [CrossRef] [PubMed]
23. Wang, S.; Gwizdka, J.; Chaovalitwongse, W.A. Using Wireless EEG Signals to Assess Memory Workload in the *n*-Back Task. *IEEE Trans. Hum. Mach Syst.* **2016**, *46*, 424–435. [CrossRef]
24. Jiao, Z.; Gao, X.; Wang, Y.; Li, J.; Xu, H. Deep Convolutional Neural Networks for mental load classification based on EEG data. *Pattern Recognit* **2018**, *76*, 582–595. [CrossRef]
25. Yin, Z.; Zhang, J. Cross-session classification of mental workload levels using EEG and an adaptive deep learning model. *Biomed. Signal Process Control.* **2017**, *33*, 30–47. [CrossRef]
26. García-Hernández, R.A.; Celaya-Padilla, J.M.; Luna-García, H.; García-Hernández, A.; Galván-Tejada, C.E.; Galván-Tejada, J.I.; Villalba-Condori, K.O. Emotional State Detection Using Electroencephalogram Signals: A Genetic Algorithm Approach. *Appl. Sci.* **2023**, *13*, 6394. [CrossRef]
27. Yin, Z.; Zhang, J. Recognition of Cognitive Task Load levels using single channel EEG and Stacked Denoising Autoencoder. In Proceedings of the 35th Chinese Control Conference (CCC), Chengdu, China, 27–29 July 2016; pp. 3907–3912.
28. Zhang, P.; Wang, X.; Zhang, W.; Chen, J. Learning Spatial–Spectral–Temporal EEG Features with Recurrent 3D Convolutional Neural Networks for Cross-Task Mental Workload Assessment. *IEEE Trans. Neural Syst. Rehabil. Eng.* **2019**, *27*, 31–42. [CrossRef] [PubMed]
29. Hajinoroozi, M.; Mao, Z.; Jung, T.-P.; Lin, C.-T.; Huang, Y. EEG-based prediction of driver's cognitive performance by deep convolutional neural network. *Signal Process Image Commun.* **2016**, *47*, 549–555. [CrossRef]
30. Li, G.; Yan, W.; Li, S.; Qu, X.; Chu, W.; Cao, D. A Temporal-Spatial Deep Learning Approach for Driver Distraction Detection Based on EEG Signals. *IEEE Trans. Autom. Sci. Eng.* **2021**, *19*, 2665–2677. [CrossRef]
31. Gao, Z.; Wang, X.; Yang, Y.; Mu, C.; Cai, Q.; Dang, W.; Zuo, S. EEG-Based Spatio–Temporal Convolutional Neural Network for Driver Fatigue Evaluation. *IEEE Trans. Neural. Netw. Learn Syst.* **2019**, *30*, 2755–2763. [CrossRef] [PubMed]

32. Shang, B.; Duan, F.; Fu, R.; Gao, J.; Sik, H.; Meng, X.; Chang, C. EEG-based investigation of effects of mindfulness meditation training on state and trait by deep learning and traditional machine learning. *Front. Hum. Neurosci.* **2023**, *17*, 1033420. [CrossRef] [PubMed]
33. Fouad, I.A. A robust and efficient EEG-based drowsiness detection system using different machine learning algorithms. *Ain Shams Eng. J.* **2023**, *14*, 101895. [CrossRef]
34. Hajinoroozi, M.; Mao, Z.; Huang, Y. Prediction of driver's drowsy and alert states from EEG signals with deep learning. In Proceedings of the IEEE 6th International Workshop on Computational Advances in Multi-Sensor Adaptive Processing (CAMSAP), Cancun, Mexico, 13–16 December 2015; pp. 493–496.
35. Almogbel, M.A.; Dang, A.H.; Kameyama, W. EEG-signals based cognitive workload detection of vehicle driver using deep learning. In Proceedings of the 2018 20th International Conference on Advanced Communication Technology (ICACT), Chuncheon, Republic of Korea, 11–14 February 2018; pp. 256–259.
36. Hekmatmanesh, A.; HM, A.; Wu, H.; Afsharchi, M.; Li, M.; Handroos, H. Imaginary control of a mobile vehicle using deep learning algorithm: A brain computer interface study. *IEEE Access* **2021**, *10*, 20043–20052. [CrossRef]
37. Foong, R.; Ang, K.K.; Quek, C.; Guan, C.; Wai, A.A.P. An analysis on driver drowsiness based on reaction time and EEG band power. *Annu. Int. Conf. IEEE Eng. Med. Biol. Soc.* **2015**, *2015*, 7982–7985. [CrossRef]
38. Cao, Z.; Chuang, C.-H.; King, J.-K.; Lin, C.-T. Multi-channel EEG recordings during a sustained-attention driving task. *Sci. Data* **2019**, *6*, 19. [CrossRef] [PubMed]
39. Zeng, C.; Mu, Z.; Wang, Q. Classifying Driving Fatigue by Using EEG Signals. *Comput. Intell. Neurosci.* **2022**, *2022*, 1885677. [CrossRef] [PubMed]
40. He, D.; Donmez, B.; Liu, C.C.; Plataniotis, K.N. High cognitive load assessment in drivers through wireless electroencephalography and the validation of a modified N-back task. *IEEE Trans. Hum.-Mach. Syst.* **2019**, *49*, 362–371. [CrossRef]
41. Takada, S.; Ueda, K.; Yamada, N.; Iguchi, Y.; Tao, Y.; Koizumi, K.; Nakao, M. Evaluation of Driver's Cognitive Load when Presented Information on the Windshield using P300 Latency in Eye-fixation Related Potentials. In Proceedings of the 2019 IEEE Intelligent Transportation Systems Conference (ITSC), Auckland, New Zealand, 27–30 October 2019; pp. 4006–4011.
42. Faure, V.; Lobjois, R.; Benguigui, N. The effects of driving environment complexity and dual tasking on drivers' mental workload and eye blink behavior. *Transp. Res. Part F Traffic Psychol. Behav.* **2016**, *40*, 78–90. [CrossRef]
43. Towle, V.L.; Bolaños, J.; Suarez, D.; Tan, K.; Grzeszczuk, R.; Levin, D.N.; Spire, J.P. The spatial location of EEG electrodes: Locating the best-fitting sphere relative to cortical anatomy. *Electroencephalogr. Clin. Neurophysiol.* **1993**, *86*, 1–6. [CrossRef] [PubMed]
44. Gramfort, A.; Luessi, M.; Larson, E.; Engemann, D.A.; Strohmeier, D.; Brodbeck, C.; Hämäläinen, M. MEG and EEG data analysis with MNE-Python. *Front. Neurosci.* **2013**, *7*, 267. [CrossRef] [PubMed]
45. Liu, Y.; Shi, S.; Song, Y.; Gao, Q.; Li, Z.; Song, H.; Pang, S.; Li, D. EEG based Mental Workload Assessment by Power Spectral Density Feature. In Proceedings of the 2022 IEEE International Conference on Mechatronics and Automation (ICMA), Guilin, China, 7–10 August 2022; pp. 450–454.
46. Welch, P.D. The use of Fast Fourier Transform for the estimation of power spectra: A method based on time averaging over short, modified periodograms. *IEEE Trans. Audio Electroacoust.* **1967**, *AU-15*, 70–73. [CrossRef]
47. Abadi, M.; Agarwal, A.; Barham, P.; Brevdo, E.; Chen, Z.; Citro, C.; Corrado, G.S.; Davis, A.; Dean, J.; Devin, M.; et al. Tensorflow: Large-scale machine learning on heterogeneous distributed systems. *arXiv* **2015**, arXiv:1603.04467.
48. Pedregosa, F.; Varoquaux, G.; Gramfort, A.; Michel, V.; Thirion, B.; Grisel, O.; Duchesnay, É. Scikit-learn: Machine Learning in Python. *J. Mach. Learn. Res.* **2011**, *12*, 2825–2830.
49. O'Donnell, R.D.; Eggemeier, F.T. Workload assessment methodology. Handbook of perception and human performance. *Cogn. Process. Perform.* **1986**, *2*, 1–49.
50. Sepp, S.; Howard, S.J.; Tindall-Ford, S.; Agostinho, S.; Paas, F. Cognitive Load Theory and Human Movement: Towards an Integrated Model of Working Memory. *Educ. Psychol. Rev.* **2019**, *31*, 293–317. [CrossRef]
51. Gola, M.; Magnuski, M.; Szumska, I.; Wróbel, A. EEG beta band activity is related to attention and attentional deficits in the visual performance of elderly subjects. *Int. J. Psychophysiol.* **2013**, *89*, 334–341. [CrossRef]
52. Melloni, L.; Molina, C.; Pena, M.; Torres, D.; Singer, W.; Rodriguez, E. Synchronisation of Neural Activity across Cortical Areas Correlates with Conscious Perception. *J. Neurosci.* **2007**, *27*, 2858–2865. [CrossRef]

sensors

Article

Depressive Disorder Recognition Based on Frontal EEG Signals and Deep Learning

Yanting Xu [1,†], Hongyang Zhong [2,†], Shangyan Ying [1], Wei Liu [2], Guibin Chen [2], Xiaodong Luo [3,*] and Gang Li [4,*]

[1] College of Engineering, Zhejiang Normal University, Jinhua 321004, China; xuyanting@zjnu.edu.cn (Y.X.); kalyan2001@zjnu.edu.cn (S.Y.)
[2] College of Computer Science and Technology, Zhejiang Normal University, Jinhua 321004, China; zhonghongyang@zjnu.edu.cn (H.Z.); liuwei@zjnu.edu.cn (W.L.); cgbcvip@zjnu.edu.cn (G.C.)
[3] The Second Hospital of Jinhua, Jinhua 321016, China
[4] College of Mathematical Medicine, Zhejiang Normal University, Jinhua 321004, China
* Correspondence: lxdjhey@sina.com (X.L.); ligang@zjnu.cn (G.L.)
† These authors contributed equally to this work.

Abstract: Depressive disorder (DD) has become one of the most common mental diseases, seriously endangering both the affected person's psychological and physical health. Nowadays, a DD diagnosis mainly relies on the experience of clinical psychiatrists and subjective scales, lacking objective, accurate, practical, and automatic diagnosis technologies. Recently, electroencephalogram (EEG) signals have been widely applied for DD diagnosis, but mainly with high-density EEG, which can severely limit the efficiency of the EEG data acquisition and reduce the practicability of diagnostic techniques. The current study attempts to achieve accurate and practical DD diagnoses based on combining frontal six-channel electroencephalogram (EEG) signals and deep learning models. To this end, 10 min clinical resting-state EEG signals were collected from 41 DD patients and 34 healthy controls (HCs). Two deep learning models, multi-resolution convolutional neural network (MRCNN) combined with long short-term memory (LSTM) (named MRCNN-LSTM) and MRCNN combined with residual squeeze and excitation (RSE) (named MRCNN-RSE), were proposed for DD recognition. The results of this study showed that the higher EEG frequency band obtained the better classification performance for DD diagnosis. The MRCNN-RSE model achieved the highest classification accuracy of 98.48 ± 0.22% with 8–30 Hz EEG signals. These findings indicated that the proposed analytical framework can provide an accurate and practical strategy for DD diagnosis, as well as essential theoretical and technical support for the treatment and efficacy evaluation of DD.

Keywords: depressive disorder (DD); electroencephalogram (EEG); beta rhythm; convolutional neural network (CNN); long short-term memory (LSTM); deep learning

Citation: Xu, Y.; Zhong, H.; Ying, S.; Liu, W.; Chen, G.; Luo, X.; Li, G. Depressive Disorder Recognition Based on Frontal EEG Signals and Deep Learning. *Sensors* **2023**, *23*, 8639. https://doi.org/10.3390/s23208639

Academic Editors: Yifan Zhao, Hua-Liang Wei, Yuzhu Guo and Fei He

Received: 7 September 2023
Revised: 10 October 2023
Accepted: 18 October 2023
Published: 23 October 2023

1. Introduction

Depressive disorder (DD) is characterized by depressed mood, lack of interest, and loss of pleasure, accompanied by corresponding changes in thinking and behavior [1–3]. It is estimated that DD affects more than 300 million people worldwide and covers a wide range of people [4]. According to the World Health Organization, DD is the largest single factor of global disability [5]. As a common mental disease, DD substantially jeopardizes people's regular life, family, and daily work [6–8]. A report in The Lancet claimed that the ratio of DD increased from 9.7% in 2019 to 19.8% in 2020 [9]. The onset of DD is related to a variety of factors, including genetics, environment, individual experience, physiological factors, and gender differences. Previous studies have reported a consistently higher incidence of DD for females than for males [10,11]. Patients with DD lack self-cognition. It is difficult for them to realize that they are suffering from complex psychiatric disorders like DD and may engage in risky behaviors as a result. However, if DD is diagnosed in time and correctly, patients can receive treatment and obtain good curative effects [12]. To sum up, the accurate and practical diagnosis of DD is crucial for patients.

The majority of current diagnostic techniques of DD rely on subjective scale assessments and the clinical expertise of professional psychiatrists according to the diagnostic criteria of DD, such as the Diagnostic and Statistical Manual of Mental Disorders (DSM-5). Psychiatrists can understand the symptoms and manifestations of patients with DD [13,14], including psychological, emotional, and behavioral changes, through these subjective assessment methods. It is well known that different psychiatrists may have different diagnostic results for the same patient with DD, and the diagnostic accuracy varies greatly and is highly subjective [15,16]. To make the diagnosis process of DD more objective and accurate, intelligent diagnostic technology has become a research hotspot [17,18].

Neuroimaging techniques have been widely used to explore the alterations in brain functions in recent years, such as electroencephalogram (EEG) [19], magnetoencephalogram (MEG) [20], functional magnetic resonance imaging (fMRI) [21], etc. These brain imaging techniques have also been applied to understanding the neuromechanisms and realizing the automated intelligent diagnosis of mental disorders [22–24]. Due to the advantages of being non-invasive, economical, and easy to operate, the EEG technique has high research and application values in brain-science-related studies [25,26]. It has been reported that EEG signals have apparent changes in different frequency bands and regions in patients with DD [27–29]. Based on our brain functional mechanism of DD [19], it has been found that the important neuro-electrophysiological characteristics of DD are mainly distributed in the frontal region of the brain. Meanwhile, the response effects of antidepressant drugs are also related to the dynamic change in EEG power in the frontal region [30,31]. To sum up, this study attempted to achieve high DD recognition accuracy using frontal six-channel EEG signals in combination with deep learning algorithms to improve the practicability of DD diagnosis [32].

Deep learning algorithms are evolving rapidly and are widely used in various fields. A deep learning framework can automatically extract features from EEG signals and eliminate the constraints of artificial features. Deep learning can effectively improve the generalization ability of classifiers, which have been widely used in DD diagnosis research [33,34]. Among them, a convolutional neural network (CNN) can learn and extract feature representations that are robust to input data [35], which is the core of the current best architecture for processing data. Acharya et al. [36] used a CNN to detect DD with EEG features and obtained high accuracy. The long short-term memory network (LSTM) is another commonly used deep learning algorithm which has shown excellent performance with many time series data. Combining these two types of networks for EEG signals, Betul et al. developed a deep hybrid model based on CNN-LSTM architecture to classify the EEG signals of left and right hemispheres and obtained accuracies of 99.12% and 97.66%, respectively [37]. In brief, deep learning algorithms have a good application prospect in DD recognition research.

This study attempted to achieve a high-accuracy and practical model for DD diagnosis with frontal six-channel EEG data. Based on prior research, two deep learning models, multi-resolution CNN (MRCNN) combined with LSTM (named MRCNN-LSTM) and MRCNN combined with residual squeeze and excitation (RSE) (named MRCNN-RSE), were proposed for comparison. Both of these models involved MRCNN to extract the time–frequency domain aspects of EEG features, but two different strategies were used for further extraction and the processing of the extracted features. In addition, the classification performance of each rhythm is also discussed in this study to verify the significant change in beta rhythm in DD patients.

2. Materials and Methods

2.1. Subjects

All DD patients, excluding those with depressive episodes due to bipolar disorder, were collected from the designated hospital for psychosis, and the HCs were selected from the local community after a professional screening. We randomly recruited 41 patients with DD (10 males and 31 females, respectively). This is consistent with the existing reports that the prevalence of depression is higher in females than in males. Meanwhile, in order to retain this original imbalance the in control group, we randomly selected 34 HCs (11 males and 23 females, respectively). All participants completed the Hamilton Depression scale (HAMD) before EEG data collection. All the HCs had a HAMD score of less than 7, while DD patients had a HAMD score of more than 17. All included subjects were right-handed and prohibited from drinking alcohol and taking psychotropic drugs for 8 h before EEG recording. The age of patients with DD ranged from 19 to 61 years old, with an average age of 45.22 ± 11.80 years old. The age of the HCs ranged from 21 to 57 years, with a mean age of 40.18 ± 11.67 years. There was no significant difference in age between the DD group and the HC group, and there was a significant difference in HAMD-17 scores, as shown in Figure 1 for basic information. The experiment was approved by the Ethics Committee of Zhejiang Normal University, and all participants signed a written informed consent form before the experiment.

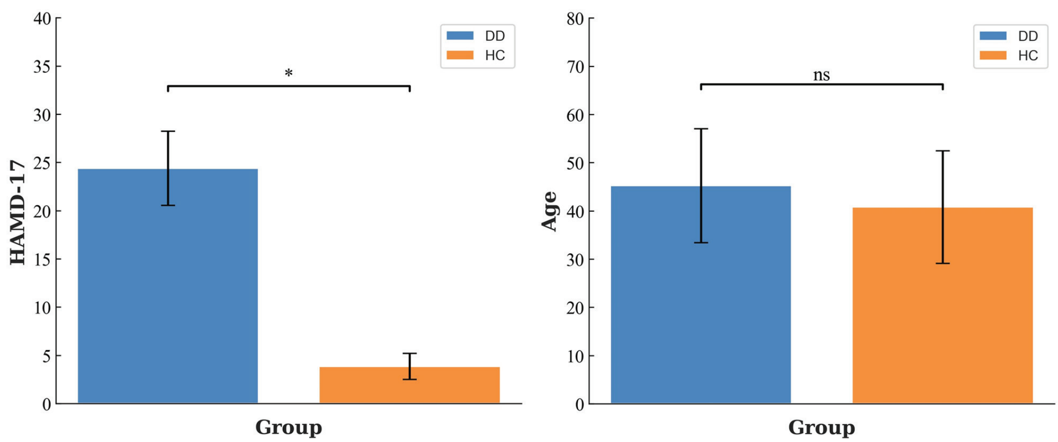

Figure 1. Clinical characteristics of DD and HC. * means $p < 0.05$, and ns means non significant.

2.2. Data Acquisition and Preprocessing

In the study, we collected 10 min of resting-state 16-channel EEG data from each subject. The EEG acquisition device used in this study was an EEG TS215605 from Nicolet Company. The EEG channels' names and positions are shown in Figure 2. The subjects were asked to sit in a chair in a comfortable sitting position with their eyes closed and their attention focused on their breathing. Data acquisition was arranged in the professional EEG lab. The whole EEG collection was implemented in a quiet environment. As is well known, the installation time for EEG recording is highly related to the number of electrodes, especially for non-specialists. An increase in the number of electrodes will naturally lead to high test complexity, high analysis difficulty, and high time and economic costs, which can constrain the practical applications of EEG-related products and systems, particularly to the detriment of large-scale DD early-screening applications in schools and communities. Based on our previous research on DD and the consideration of the accuracy and practicability of the algorithm, this study selected six frontal EEG electrodes (shown in Figure 2) for DD diagnosis.

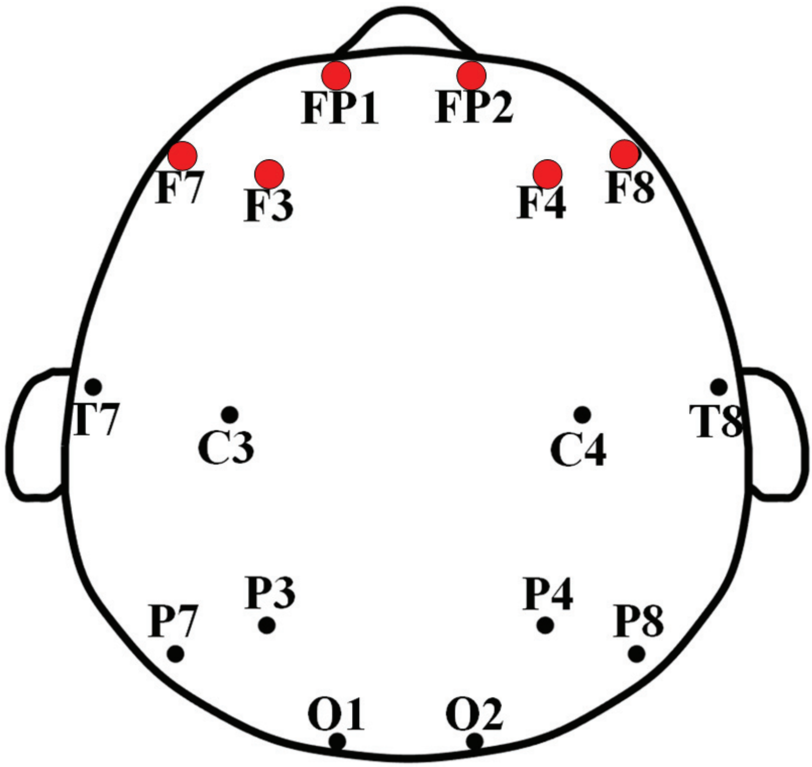

Figure 2. Sixteen EEG channels' names and locations; red dots indicate the frontal six channels selected for this study.

During the acquisition of EEG signals, it is easy to be disturbed by various factors such as the environment, self-physiologies, and body movements. These noises can negatively affect the signal quality. Preprocessing is a very important step in EEG data analysis which can effectively improve the signal-to-noise ratio of the EEG signal and provide a reliable basis for subsequent analysis and interpretation. The specific steps of EEG preprocessing in this study are as follows:

(1) Downsampling

Downsampling refers to a reduction in the high sampling rate to a lower sampling rate for the EEG signal, which mainly aims to reduce the amount of data and improve computational efficiency. In this study, the original EEG signal sampling rate was reduced from 250 Hz to 125 Hz.

(2) Baseline Correction

The main purpose of baseline correction is to eliminate the direct current (DC) offset generated by the recorded signal, which affects the accuracy and comparability of the signals. The baseline correction performed on the EEG signal can remove the DC offset to make the mean of the signal become zero.

(3) Artifact Removal

The purpose of artifact removal is to improve the signal-to-noise ratio and to better reveal the information contained in the EEG signal. The common artifacts in EEG signals include electromyography artifacts, electrocardiograph artifacts, eye movement artifacts, head movement artifacts, etc. In this study, independent component analysis (ICA) was used to remove the artifacts.

(4) Data segmentation

In this study, 4 s continuous EEG data were selected as the sample without data superposition, resulting in 9354 samples for the DD group and 7443 samples for the HC group.

(5) Filtering

Bandpass filtering is used to remove unwanted frequency components from the signal, preserving the signal in a specific frequency range. By setting the cut-off frequency, the bandpass filter filters out the signals below or above the frequency, and only the signals within the range are retained. In this study, a 4-order Butterworth bandpass filter was applied to the EEG data to extract the specific frequency range, such as theta (4–8 Hz), alpha1 (8–10 Hz), alpha2 (10–13 Hz), beta (13–30 Hz), 4–30 Hz, 8–30 Hz, and 10–30 Hz.

After the above five preprocessing procedures, the extracted 4 s continuous EEG data were set as the inputs of the proposed deep learning models to explore the DD diagnosis accuracies of the different frequency ranges. Particularly, among these frequency ranges, the 4–30 HZ EEG signals were called the original data because they included all rhythms in this frequency range.

2.3. Deep Learning Model Framework

In this current study, two deep learning models, MRCNN-LSTM and MRCNN-RSE, were proposed for DD diagnosis. These two models were improved and derived from the reports of previous studies that CNN-LSTM and CNN are the most commonly used basic model frameworks in the DD detection field. In order to make the results more persuasive, we selected four representative deep learning models according to the recent references and applied them to our EEG data. These four models did not change their structures; they only changed their parameters to fit our data. The specific descriptions of these models are as follows.

2.3.1. MRCNN-LSTM Model Framework

The MRCNN-LSTM model structure is shown in Figure 3, and it mainly includes two parts: MRCNN and LSTM. The first part of MRCNN uses three branches with different convolution kernel sizes in parallel to extract EEG features with the CNN model. Each branch uses a convolution kernel with different sizes to extract features with different scales, and uses the ReLU activation function for nonlinear transformation to enhance feature expressiveness. In the second part of LSTM, the features are spliced and input into an LSTM layer to extract the timing information from the EEG features. The LSTM layer remembers the previous state through a long short-term memory unit with a gating mechanism and updates the state according to the new information input to capture the temporal dependence of the data. The output of the LSTM layer is fed into a fully connected layer and a Dropout layer to improve the generalization ability of the model and suppress overfitting. Finally, binary classification is implemented by a softmax classifier to predict the labels of the inputs.

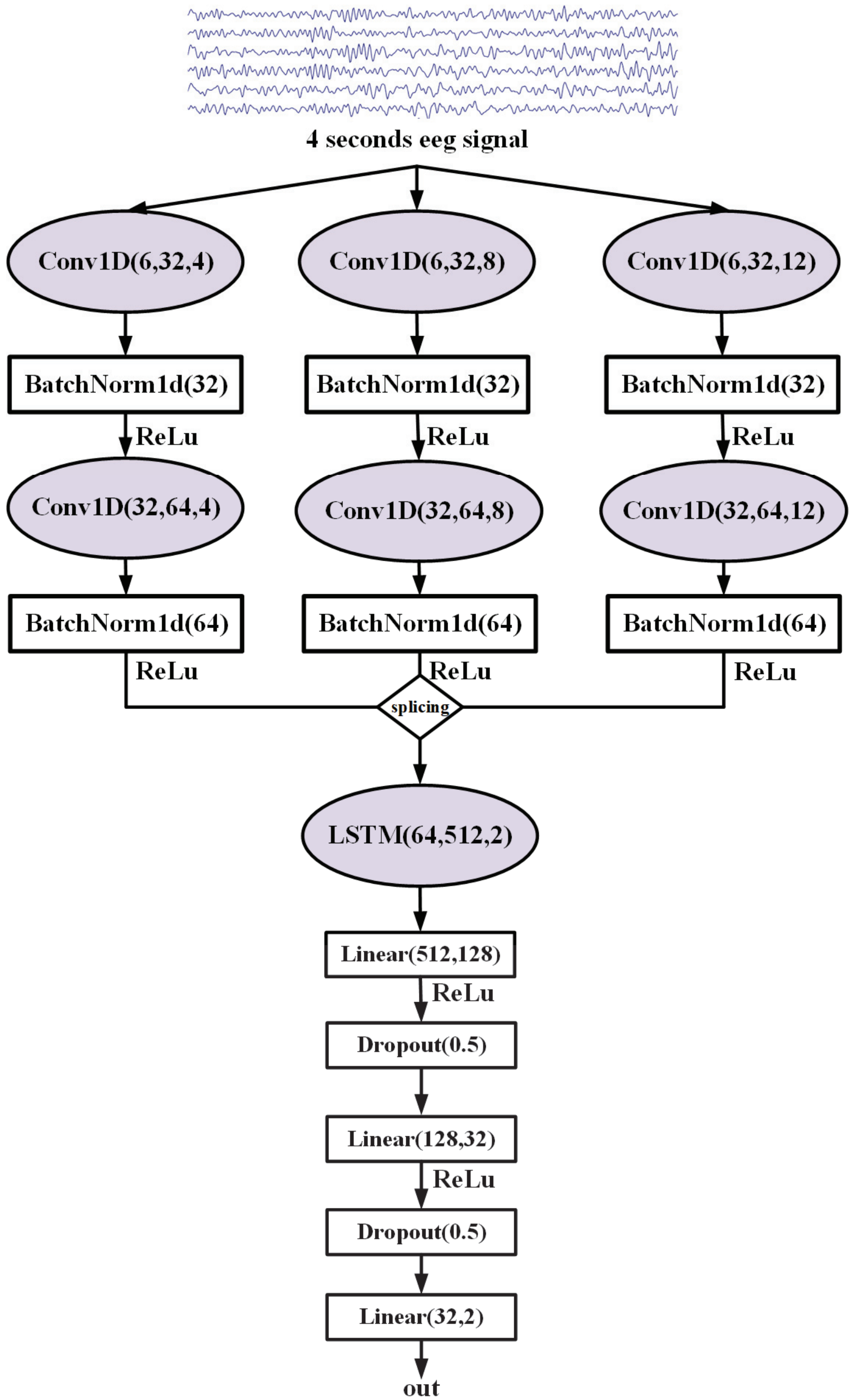

Figure 3. MRCNN-LSTM model architecture.

2.3.2. MRCNN-RSE Model Framework

In accordance with the existing research results, a CNN model with multi-resolution convolution kernels (MRCNN) is proposed in this study. As shown in Figure 4, the MRCNN model contains two branches with two different convolution kernels. Three convolutional layers and two maximum pooling layers are used in each branch. The convolution kernels used in the first branch are set as 4, 3, and 3, respectively. The convolution kernels of the second branch are set as 10, 3, and 3, respectively. In addition, each convolutional layer includes a normalization layer for normalizing the input data, and a Gaussian error linear unit (GELU) is used as the activation function; it is smoother than the traditional ReLU activation function and can better deal with nonlinear features.

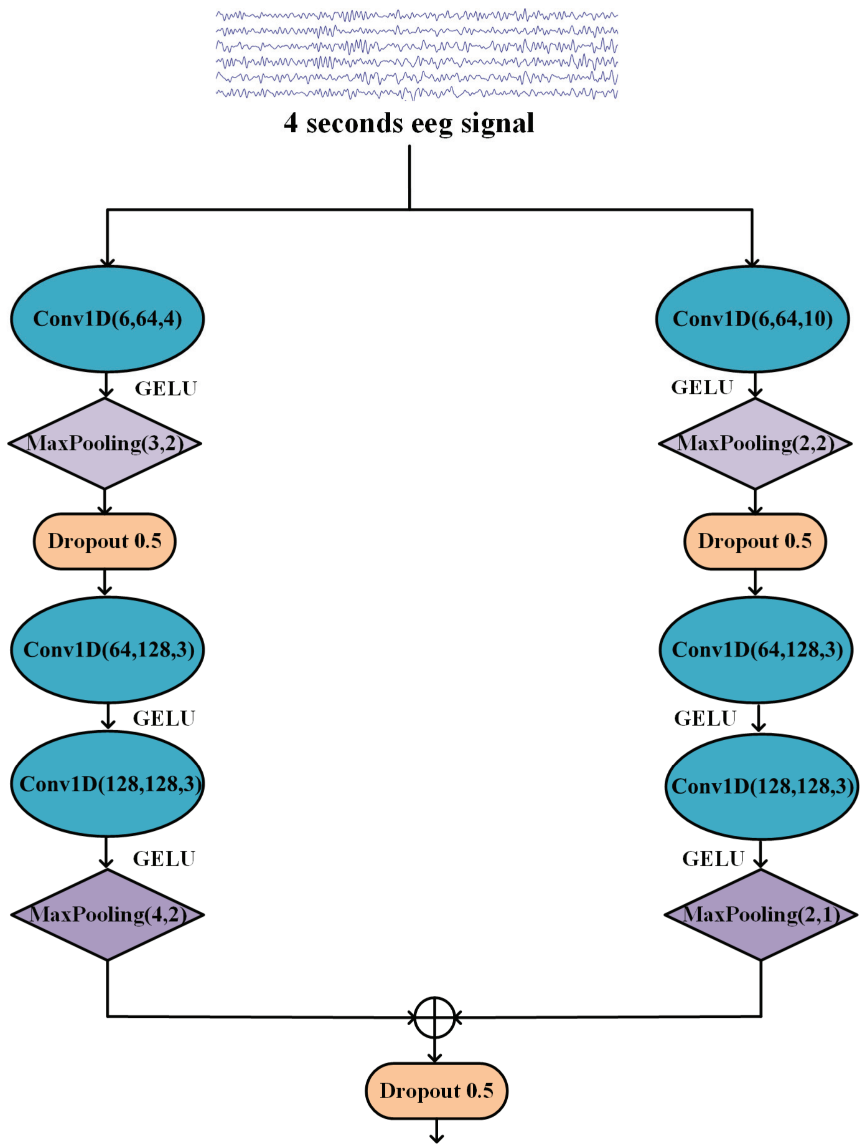

Figure 4. MRCNN architecture.

To improve the learning performance of the MRCNN model, a calibration module was designed for the features extracted by the convolutional layer to model the interdependence between the features. The residual squeeze-and-excitation (RSE) block was used in the MRCNN model, which is named MRCNN-RSE for short, to adaptively select the most discriminative features. Specifically, the RSE block adaptively selects and readjusts features, helping the model to better utilize contextual information in its local sensory field. In the calibration module, two convolutional layers with a kernel and step size of 1 are used to further extract features, the adaptive pooling layer is used to compress the features, and then two fully connected layers are used to aggregate the information. The first layer uses the ReLU activation function to reduce the dimension, and the second layer uses the sigmoid activation function to increase the dimension. The specific structure for the RSE block is shown in Figure 5.

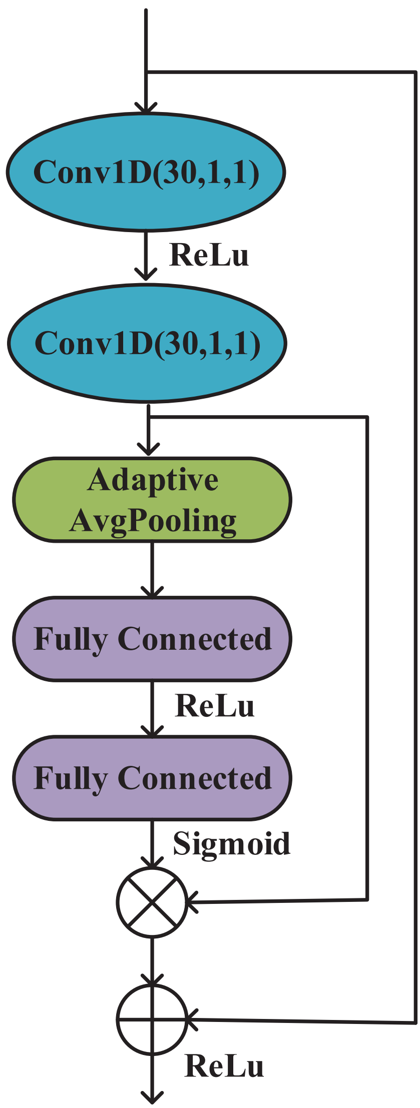

Figure 5. Feature calibration module with RSE block in MRCNN-RSE model.

To extract the interdependence between the extracted features in the MRCNN-RSE model [38], the widely used self-attention mechanism is included in the model, which can adaptively weigh the features of each position for the input data. Specifically, features from each location interact with features from other locations to extract more global context information. In this way, the model can better capture key features for the input data to improve the model performance by assigning higher weights to regions of interest and lower weights to regions of less interest. There are two Add and Normalize layers after the features are weighted by the self-attention mechanism. Finally, the softmax layer is used as the decision function.

2.3.3. Other Model Frameworks

(1) EEGNet

EEGNet is a compact convolutional neural network for EEG analysis. The EEGNet algorithm has better generalization ability and higher performance with limited training data. Liu et al. applied this deep learning framework, EEGNet, to depression diagnosis [39]. The framework consists of four main blocks: convolution, depthwise convolution, separable convolution, and classification. In the convolution block, batch normalization is added. In the depthwise convolutional block and separable convolutional block, batch normalization, activation, average pooling, and Dropout are added. Finally, in the classification block, the two categories, the DD group and the HC group, are identified directly using a fully connected layer.

(2) DeprNet

Ayan Seal et al. proposed a deep learning model based on the convolutional neural network, named DeprNet, for DD detection with EEG signals [40]. The DeprNet model consists of five convolutional layers, five batch normalization layers, five max pooling layers, and three fully connected layers. The softmax activation function is used in the last fully connected layer and the leaky rectified linear unit (LeakyReLU) activation function is used in all other layers, and finally, the classification is conducted using three fully connected layers.

(3) 1DCNN-LSTM

Mumtaz et al. proposed a deep learning model combining one-dimensional CNN (1DCNN) with LSTM (named as 1DCNN-LSTM) to detect depression [34]. The model of 1DCNN-LSTM is a cascaded formation of three 1D convolutional layers and two LSTM layers. Max pooling and Dropout are embedded under each convolutional layer, and finally, classification is performed using a fully connected layer.

(4) 2DCNN-LSTM

Zhang et al. proposed a 2DCNN-LSTM model to analyze the 128-channel EEG signals for DD detection [35]. The model consists of four 2D convolutional layers and one LSTM layer, with an activation function (Tanh) added after each 2D convolutional layer. Max pooling is accessed after the second 2D convolutional layer for dimensionality reduction. Dropout is accessed after the LSTM, and finally, the classification is performed using a fully connected layer. Compared with the 1D convolutional layer, the 2D convolutional layer can extract features in the spatiotemporal dimension, making it more capable for feature extraction.

2.4. Model Evaluation

The confusion matrix is a matrix used to evaluate the performance of a classification model, where each row represents the predicted class and each column represents the actual class, as shown in Table 1. Each cell in the confusion matrix contains the number of samples for the actual and predicted categories that are likely to be classified correctly (true positive, TP; true negative, TN) or incorrectly (false positive, FP; false negative, FN). More precisely, TP represents the number of samples that are positive and correctly predicted to be positive; FP represents the number of samples that are negative but incorrectly predicted to be positive; FN represents the number of samples that are positive but incorrectly predicted to be negative; TN represents the number of samples that are negative and correctly predicted to be negative. Based on the confusion matrix, a series of evaluation indices can be calculated, namely accuracy, precision, recall, and F1_score. As shown in Formulas (1)–(4), accuracy refers to the proportion of correctly classified samples in the total samples; precision refers to the proportion of correctly predicted positive samples in all predicted positive samples; recall refers to the proportion of correctly predicted positive samples in all positive samples; and F1_score is the harmonic average of the accuracy rate and the recall rate.

$$Accuracy = \frac{TP + TN}{TP + TN + FP + FN} \tag{1}$$

$$Precision = \frac{TP}{TP + FP} \tag{2}$$

$$Recall = \frac{TP}{TP + FN} \tag{3}$$

$$F_1 = \frac{2TP}{2TP + FP + FN} \tag{4}$$

Table 1. Confusion matrix.

Predicted Class \ Actual Class	HC	DD
HC	*TP*	*FN*
DD	*FP*	*TN*

In addition, for the training parameters of all deep learning models in this study, batch_size was set as 32 and the maximum number of epochs was set as 200. A warmup learning rate strategy was used, with an initial learning rate strategy of 5e-5, reaching 1e-3 after 20 rounds, and then gradually decaying to 5e-4, and the weight_decay was set as 0.001. Additionally, five cross-validations were used for all models to reduce the risk of model overfitting and improve the generalization ability of the model.

3. Results

3.1. The Results of DD Classification Based on the MRCNN-LSTM Model

The results of DD classification based on the MRCNN-LSTM model are shown in Table 2. The average accuracy rate of five cross-validation results is 95.34 ± 0.41%. Meanwhile, the accuracy of the theta rhythm, alpha1 rhythm, alpha2 rhythm, and beta rhythm are 76.14 ± 0.81%, 76.90 ± 0.41%, 80.28 ± 0.66%, and 92.03 ± 0.37%, respectively. These results indicate that a higher frequency band has a higher accuracy for DD recognition.

Table 2. The results of DD identification among four rhythms and the original data based on the MRCNN-LSTM model.

Data	Accuracy	F1_Score	Precision	Recall
Theta	76.14 ± 0.81%	78.29 ± 1.16%	79.14 ± 1.45%	77.59 ± 3.28%
Alpha1	76.90 ± 0.41%	79.33 ± 0.37%	78.82 ±1.97%	79.98 ± 2.48%
Alpha2	80.28 ± 0.66%	82.56 ± 0.45%	80.98 ± 0.96%	84.21 ± 0.65%
Beta	92.03 ± 0.37%	92.78 ± 0.34%	93.27 ± 1.33%	92.33 ± 1.29%
Original Data	95.34 ± 0.41%	95.79 ± 0.33%	96.03 ± 1.44%	95.57 ± 1.10%

3.2. The Results of DD Classification Based on the MRCNN-RSE Model

As shown in Table 3 and Figure 6, the classification results based on the MRCNN-RSE model have an accuracy of 98.47 ± 0.38% in DD recognition. Compared with the MRCNN-

LSTM model in Table 2, the accuracies of the MRCNN-RSE are significantly improved among all EEG rhythms and original EEG data. In addition, the DD recognition accuracy of the beta rhythm is also higher than those of the other rhythms. As shown in Figure 6, the results based on the MRCNN-RSE model have very smooth classification performances after 100 epochs.

Table 3. DD identification results for the four rhythms and original data based on the MRCNN-RSE model.

Data	Accuracy	F1_Score	Precision	Recall
Theta	80.75 ± 0.78%	82.64 ± 0.62%	83.17 ± 1.63%	82.18 ± 1.82%
Alpha1	79.15 ± 1.07%	81.31 ± 1.19%	81.24 ± 0.67%	81.42 ± 2.45%
Alpha2	83.27 ± 0.53%	84.73 ± 0.59%	85.92 ± 1.38%	83.63 ± 2.12%
Beta	97.13 ± 0.49%	97.36 ± 0.49%	98.30 ± 0.33%	96.44 ± 0.89%
Original Data	98.47 ± 0.38%	98.65 ± 0.36%	98.63 ± 0.46%	98.66 ± 0.51%

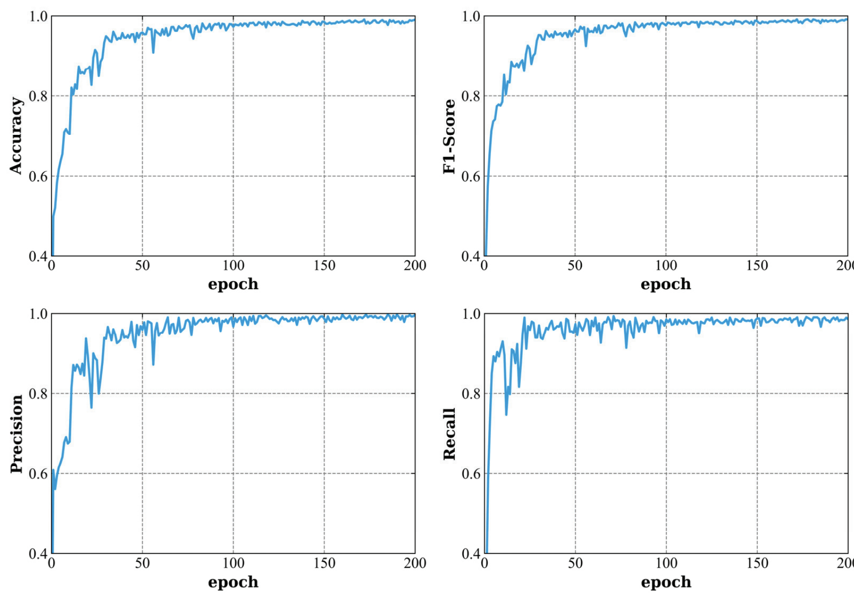

Figure 6. Accuracy, precision, recall, and weighted F1-score using EEG to identify patients with depressive disorder.

3.3. Classification Performances for DD Diagnosis with Different Frequency Bands Based on MRCNN-RSE Model

The results of the classification performances for DD diagnosis with 4–30 Hz, 8–30 Hz, 10–30 Hz, and 13–30 Hz EEG signals are shown in Table 4 and Figure 7. It is shown that 8–30 Hz obtained slightly better classification performances for DD diagnosis compared with 4–30 Hz, with higher Accuracy and a lower standard deviation. In addition, the desired classification performance was also obtained for 10–30 Hz, which was not statistically different from the 4–30 Hz results. However, the 10–30 Hz classification performance was significantly lower. The above results show that we can use higher-frequency bands in the DD automatic diagnostic system, which can effectively improve the efficiency of EEG signal preprocessing.

Table 4. DD identification results with different frequency bands based on MRCNN-RSE model.

Frequency Band	Accuracy	F1_Score	Precision	Recall
13–30 Hz	97.13 ± 0.49%	97.36 ± 0.49%	98.30 ± 0.33%	96.44 ± 0.89%
10–30 Hz	98.07 ± 0.22%	98.15 ± 0.21%	98.43 ± 0.59%	97.87 ± 0.58%
8–30 Hz	98.48 ± 0.22%	98.58 ± 0.17%	99.08 ± 0.33%	98.08 ± 0.34%
4–30 Hz	98.47 ± 0.38%	98.65 ± 0.36%	98.63 ± 0.46%	98.66 ± 0.51%

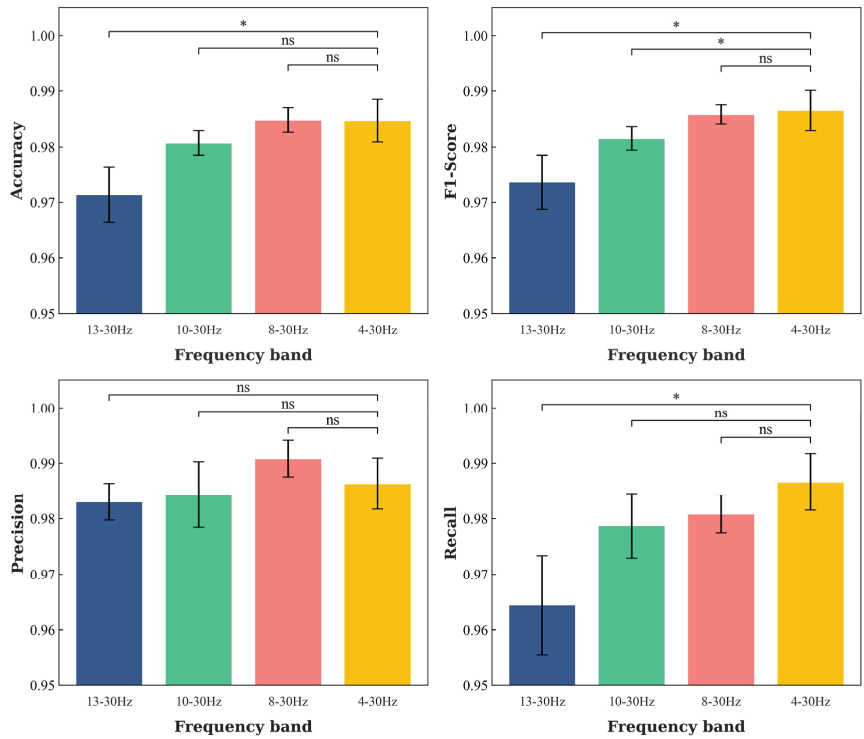

Figure 7. The comparison results of 4–30 Hz, 8–30 Hz, 10–30 Hz, and 13–30 Hz EEG signals for DD diagnosis based on MRCNN-RSE model. * represents $p < 0.05$, and ns represents no statistical difference between the two groups.

3.4. Classification Performances for DD Diagnosis with Different Models Using 8–30 Hz EEG Signals

It has been shown that 8–30 Hz EEG signals obtained the best classification performances based on the MRCNN-RSE model. In this section, the performances of the EEGNet model, the DeprNet model, the 1DCNN-LSTM model, the 2DCNN-LSTM model, and the MRCNN-LSTM model are compared with that of the MRCNN-RSE model on the same 8–30 HZ EEG dataset. These models had the same training settings. The results of the classification performances for DD diagnosis with these models are shown in Table 5. It is shown that the average Accuracy of the EEGNet model, the DeprNet model, the 1DCNN-LSTM model, the 2DCNN-LSTM model, the MRCNN-LSTM model, and the MRCNN-RSE model on the same dataset is 90.07 ± 0.81%, 75.31 ± 0.45%, 87.37 ± 0.65%, 89.75 ± 0.29%, 95.38 ± 0.21%, and 98.47 ± 0.3%, respectively. The MRCNN-RES model still has the best performance among these deep learning models.

Table 5. The results of classification performances for DD diagnosis with different models using 8–30 Hz EEG signals.

Model	Accuracy	F1_Score	Precision	Recall
EEGNet [39]	90.07 ± 0.81%	90.65 ± 0.90%	90.55 ± 1.48%	90.83 ± 2.62%
DeprNet [40]	75.31 ± 0.45%	77.16 ± 1.66%	78.70 ± 2.73%	76.09 ± 5.47%
1DCNN-LSTM [34]	87.37 ± 0.65%	88.54 ± 0.48%	87.59 ± 2.75%	89.72 ± 3.21%
2DCNN-LSTM [35]	89.75 ± 0.29%	90.43 ± 1.53%	90.35 ± 0.80%	90.37 ± 0.41%
MRCNN-LSTM	95.38 ± 0.21%	95.66 ± 0.24%	95.49 ± 0.31%	95.84 ± 0.46%
MRCNN-RSE	98.47 ± 0.38%	98.65 ± 0.36%	98.63 ± 0.46%	98.66 ± 0.51%

4. Discussion

Previous research indicated that individuals with DD have altered functional connectivity in the frontal cortex [19]. Based on the findings of our preceding research, this study proposed to use frontal six-channel EEG signals in conjunction with a deep learning algorithm to diagnose DD, which considerably simplifies data collection efforts and improves the practicability of DD screening. It was discovered that the beta rhythm has a greater accuracy than theta, alpha1, and alpha2 rhythms, which indicated that beta had a significant alteration in patients with DD. Simultaneously, MRCNN-RSE achieved the highest accuracy of 98.48 ± 0.22% with 8–30 Hz EEG signals. A detailed discussion is presented below.

4.1. Frontal Six-Channel EEG Signals Combined with Deep Learning Show an Excellent Performance for DD Diagnosis

DD is highly related to abnormal brain functions and has dramatically altered functional connectivity in the frontal area of the brain [41–44]. The frontal cortex is known to play an important role in emotional cognition and working memory [45]. Bludau et al. reported that patients with DD had a significantly smaller medial frontal pole compared with HCs, which was significantly negatively correlated with the severity and course of DD [43]. Coryell et al. evaluated the volume of the left side of the frontal cortex in 10 DD patients and 10 HCs and concluded that patients with severe depressive disorder were more likely to have an increase in the posterior frontal cortex [46]. There is rising evidence that functional connections in the frontal regions of DD are dramatically altered [19]. Therefore, this study advocated for DD diagnosis using the brain's six frontal EEG channels in conjunction with a current sophisticated deep learning algorithm to attain high accuracy and practicability.

Recently, deep learning has had better predictive performance compared to traditional machine learning for diagnosing depression [33,47]. Qu et al. [48] performed DD identification on a dataset of 2546 veterans using deep learning and five other traditional machine learning algorithms. The results showed that deep learning is more accurate in identifying DD and its risk factors compared to traditional machine learning by ranking the key factors of veterans and capturing the hidden pattern multilayer network structure in the data to obtain better classification performances. Kour et al. [49] combined feature extraction techniques and a hybrid deep learning model of CNN-LSTM for depression classification and compared it with four traditional machine learning models for efficiency comparison, and showed that the recognition accuracy on the benchmark dataset reached 96.78%, which is better than the state-of-the-art traditional machine learning techniques. Deep learning, with its technological advantages, has a stronger predictive ability in DD diagnosis [50]; therefore, this study advocates for the use of deep learning algorithms for the automatic diagnosis of DD.

A previous study has demonstrated that more EEG channels for deep learning can achieve high accuracy and few EEG channels may significantly reduce the accuracy of DD diagnosis. It has been reported that Zhu et al. collected the resting state of 128 EEG channels of 27 DD patients and 28 HCs, and finally achieved an accuracy of 96.50% for DD and HC classification with their proposed CNN model [51]. Yang et al. proposed a gated temporal-separable attention network for EEG-based DD recognition, and the classification accuracy on the EDRA dataset with 62 EEG channels and MODMA dataset with 128 EEG channels was 98.33% and 97.56%, respectively [52]. Wei Liu et al. used a CNN combined with gate-controlled loop units to extract sequence features and obtained an accuracy of 89.63% on the publicly available dataset with 128 EEG channels [53]. In general, more interaction information can be extracted for higher accuracy using high-density EEG. However, high-density EEG (for example, 128 channels) can severely limit the efficiency of data acquisition and reduce the practicability of the model. Some researchers have attempted to detect DD with several EEG channels. For example, Cai et al. employed a three-channel EEG collection system to gather EEG data from the FP1, FP2, and FPz electrodes; nonetheless, the accuracy was only 78.24% [54]. In this study, a deep learning model of MRCNN-RSE that performs well was proposed to identify DD with the frontal six-channel EEG signals, and the accuracy was $98.47 \pm 0.01\%$, which is close to those results of high-density EEG, indicating that the strategy in this study has apparent advantages in classifying DD.

4.2. Beta Rhythm Is Significantly Alerted in DD

EEG signals can be divided into different rhythms according to their frequency and amplitude [55], such as delta, theta, alpha, beta, and gamma, which is an effective approach for psychiatric diseases in EEG-related studies [56]. Studies have shown that EEG signals change significantly with increasing levels of depression [57]. Henriques et al. [58] collected EEG signals from 15 clinically depressed patients and 13 healthy individuals in resting state with eyes closed and found that the activity in the left frontal lobe of depressed patients was significantly lower than that of healthy individuals. Omel et al. found that the activity of the left frontal lobe was significantly lower than that of healthy individuals by examining EEG data [59]. It was found that the regional differences between the anterior and posterior subdivisions of the brain in DD were reduced, and the difference in activity in the left hemisphere relative to the right hemisphere was significant, while the possession attribute of the EEG in depressed patients significantly reduced the relative strength of alpha and beta rhythmic activity. Meanwhile, Knott et al. collected EEG signals from 70 depressed patients and 23 healthy individuals and found that DD patients had relatively reduced overall left hemisphere activity and generally lower delta, theta, alpha, and beta coherence indices. They achieved a classification accuracy of 91.3% for patients and controls [60]. There are significant differences in EEG signals between DD patients and HCs, and brain activity is affected by depression throughout the cerebral cortex.

The results of this study showed that the accuracy obtained in beta rhythm was significantly higher than those in theta rhythm, alpha1 rhythm, and alpha2 rhythm for DD recognition, which revealed that beta rhythm was significantly changed in patients with DD. It is well known that beta rhythms are commonly associated with brain alertness, attentional states, and emotions [19,61]. It has been found that beta EEG power is increased in DD patients compared to HCs and plays an important role in the pathogenesis of DD [62]. Our previous study also found significant changes in the EEG features of power spectral density, fuzzy entropy, and phase lag index of beta rhythms among DD patients, and concluded that the characteristics of beta rhythms play a crucial role in identifying DD [19]. This study further revealed the significant changes in beta rhythms of DD patients through deep learning algorithms, which provided additional important technical support for the diagnosis, treatment, and efficacy assessment of DD.

4.3. Practical High-Frequency EEG Signals for DD Diagnosis: Evidence from Deep Learning

In the current study, we attempted to explore the effect of different EEG frequency bands on the classification performances of DD diagnosis. It was discovered that 8–30 Hz EEG signals obtained superior accuracy in DD diagnosis compared to 4–30 Hz EEG data. High-frequency bands yielded good classification performance in a cognitive impairment diagnostic study [63], with higher accuracy than full-frequency bands. Shalini Mahato et al.

reported that the accuracy of DD diagnosis can be improved by using different frequency combinations [64]. The results of previous studies have showed that frequency has a large impact on DD classification performance [19]. Our results further confirm this conclusion and extended that high- and wide-frequency EEG signals are better for DD classification. More meaningfully, the use of high-frequency-band EEG data can effectively improve the signal-to-noise ratio and reduce the preprocessing time of EEG data. The findings of this study are of great significance for the development of automatic DD diagnosis.

4.4. Limitations

In this study, we achieved exciting DD recognition performance using only a few frontal EEG signals and accelerated practical application of DD automated diagnostics, but this study still has one shortcoming. This research included a limited number of participants, with 41 individuals for the DD group and 34 individuals for the HC group, which may be unable to accurately assess the generalization performance of the MRCNN-RSE model. In future studies, we will continue to gather samples to promote the practical implementation of the classification approach used in this work.

5. Conclusions

In this study, we proposed a technology framework for DD precision recognition based on frontal six-channel EEG data and deep learning models. The MRCNN-RSE model achieved a high accuracy of $98.48 \pm 0.22\%$ with 8–30 Hz EEG signals and was significantly more accurate than other deep learning models, which is consistent with our previous study using 16-channel EEG signals, indicating that this framework based on frontal EEG signals combined with the MRCNN-RSE model for DD diagnosis is accurate and practical. Our findings can provide a basic theory and technological support and greatly promote the practicality and accuracy of DD diagnosis and efficacy evaluation.

Author Contributions: Conceptualization, G.L.; Data curation, X.L.; Formal analysis, Y.X., H.Z., G.C. and G.L.; Funding acquisition, G.L.; Investigation, X.L. and G.L.; Methodology, Y.X., H.Z. and G.L.; Project administration, X.L. and G.L.; Resources, S.Y.; Software, H.Z., W.L. and G.C.; Supervision, X.L. and G.L.; Validation, W.L., X.L. and G.L.; Visualization, G.L.; Writing—original draft, Y.X. and S.Y.; Writing—review and editing, G.L. All authors have read and agreed to the published version of the manuscript.

Funding: This research was funded by the National Natural Science Foundation of China, grant number 82001918, and the Zhejiang Provincial Natural Science Foundation of China, grant number LQ19E050011.

Institutional Review Board Statement: The study was conducted according to the Declaration of Helsinki and approved by the Ethics Committee of Zhejiang Normal University (protocol code ZSRT2022064 and 17 August 2022).

Informed Consent Statement: Informed consent was obtained from all subjects involved in the study.

Data Availability Statement: Not applicable.

Acknowledgments: Thanks are given to Zhongxia Shen and Xinhua Shen for their assistance with the data collection and patients' diagnosis during the study.

Conflicts of Interest: The authors declare no conflict of interest. The funders had no role in the design of the study; in the collection, analyses, or interpretation of data; in the writing of the manuscript, or in the decision to publish the results.

References

1. Kaiser, R.H.; Andrews-Hanna, J.R.; Wager, T.D.; Pizzagalli, D.A. Large-scale network dysfunction in major depressive disorder: A meta-analysis of resting-state functional connectivity. *JAMA Psychiatry* **2015**, *72*, 603–611. [CrossRef] [PubMed]
2. Li, B.J.; Friston, K.; Mody, M.; Wang, H.N.; Lu, H.B.; Hu, D.W. A brain network model for depression: From symptom understanding to disease intervention. *CNS Neurosci. Ther.* **2018**, *24*, 1004–1019. [CrossRef] [PubMed]

3. Cai, H.; Qu, Z.; Li, Z.; Zhang, Y.; Hu, X.; Hu, B. Feature-level fusion approaches based on multimodal EEG data for depression recognition. *Inf. Fusion* **2020**, *59*, 127–138. [CrossRef]
4. Schaakxs, R.; Comijs, H.C.; van der Mast, R.C.; Schoevers, R.A.; Beekman, A.T.; Penninx, B.W. Risk factors for depression: Differential across age? *Am. J. Geriatr. Psychiatry* **2017**, *25*, 966–977. [CrossRef]
5. Stringaris, A. Editorial: What is depression? *J. Child Psychol. Psychiatry* **2017**, *58*, 1287–1289. [CrossRef]
6. Patil, A.U.; Lin, C.; Lee, S.-H.; Huang, H.W.; Wu, S.C.; Madathil, D.; Huang, C.-M. Review of EEG-based neurofeedback as a therapeutic intervention to treat depression. *Psychiatry Res. Neuroimaging* **2023**, *329*, 111591. [CrossRef]
7. Nadeem, A.; Naveed, M.; Satti, M.I.; Afzal, H.; Ahmad, T.; Kim, K.-I. Depression Detection Based on Hybrid Deep Learning SSCL Framework Using Self-Attention Mechanism: An Application to Social Networking Data. *Sensors* **2022**, *22*, 9775. [CrossRef]
8. Ahmadi, A.; Bazregarzadeh, H.; Kazemi, K. Automated detection of driver fatigue from electroencephalography through wavelet-based connectivity. *Biocybern. Biomed. Eng.* **2021**, *41*, 316–332. [CrossRef]
9. Santomauro, D.F.; Herrera, A.M.M.; Shadid, J.; Zheng, P.; Ashbaugh, C.; Pigott, D.M.; Abbafati, C.; Adolph, C.; Amlag, J.O.; Aravkin, A.Y. Global prevalence and burden of depressive and anxiety disorders in 204 countries and territories in 2020 due to the COVID-19 pandemic. *Lancet* **2021**, *398*, 1700–1712. [CrossRef]
10. Kuehner, C. Why is depression more common among women than among men? *Lancet Psychiatry* **2017**, *4*, 146–158. [CrossRef]
11. Salk, R.H.; Hyde, J.S.; Abramson, L.Y. Gender Differences in Depression in Representative National Samples: Meta-Analyses of Diagnoses and Symptoms. *Psychol. Bull.* **2017**, *143*, 783–822. [CrossRef] [PubMed]
12. Sharma, G.; Parashar, A.; Joshi, A.M. DepHNN: A novel hybrid neural network for electroencephalogram (EEG)-based screening of depression. *Biomed. Signal Process. Control* **2021**, *66*, 102393. [CrossRef]
13. Sung, M.; Marci, C.; Pentland, A. *Objective Physiological and Behavioral Measures for Identifying and Tracking Depression State in Clinically Depressed Patients*; Massachusetts Institute of Technology Media Laboratory: Cambridge, MA, USA, 2005; Volume 595.
14. Bhat, S.; Acharya, U.R.; Adeli, H.; Bairy, G.M.; Adeli, A. Autism: Cause factors, early diagnosis and therapies. *Rev. Neurosci.* **2014**, *25*, 841–850. [CrossRef] [PubMed]
15. Pathak, S. Clinical diagnosis of depression in primary care. *Lancet* **2009**, *374*, 1817. [CrossRef]
16. Chen, Y.; Wang, S.; Guo, J. DCTNet: Hybrid deep neural network-based EEG signal for detecting depression. *Multimed. Tools Appl.* **2023**, 1–15. [CrossRef]
17. Yan, W.J.; Ruan, Q.N.; Jiang, K. Challenges for Artificial Intelligence in Recognizing Mental Disorders. *Diagnostics* **2023**, *13*, 2. [CrossRef]
18. Kang, M.; Kwon, H.; Park, J.H.; Kang, S.; Lee, Y. Deep-Asymmetry: Asymmetry Matrix Image for Deep Learning Method in Pre-Screening Depression. *Sensors* **2020**, *20*, 6526. [CrossRef]
19. Li, G.; Zhong, H.; Wang, J.; Yang, Y.; Li, H.; Wang, S.; Sun, Y.; Qi, X. Machine Learning Techniques Reveal Aberrated Multidimensional EEG Characteristics in Patients with Depression. *Brain Sci.* **2023**, *13*, 384. [CrossRef]
20. Wang, H.; Tian, S.; Yan, R.; Tang, H.; Shi, J.; Zhu, R.; Chen, Y.; Han, Y.; Chen, Z.; Zhou, H.; et al. Convergent and divergent cognitive impairment of unipolar and bipolar depression: A magnetoencephalography resting-state study. *J. Affect. Disord.* **2023**, *321*, 8–15. [CrossRef]
21. Li, Y.; Qian, L.; Li, G.; Zhang, Z. Frequency specificity of aberrant triple networks in major depressive disorder: A resting-state effective connectivity study. *Front. Neurosci.* **2023**, *17*, 1200029. [CrossRef]
22. Byeon, H. Exploring factors for predicting anxiety disorders of the elderly living alone in South Korea using interpretable machine learning: A population-based study. *Int. J. Environ. Res. Public Health* **2021**, *18*, 7625. [CrossRef] [PubMed]
23. Liao, S.C.; Wu, C.T.; Huang, H.C.; Cheng, W.T.; Liu, Y.H. Major Depression Detection from EEG Signals Using Kernel Eigen-Filter-Bank Common Spatial Patterns. *Sensors* **2017**, *17*, 1385. [CrossRef] [PubMed]
24. Shen, Z.X.; Li, G.; Fang, J.Q.; Zhong, H.Y.; Wang, J.; Sun, Y.; Shen, X.H. Aberrated Multidimensional EEG Characteristics in Patients with Generalized Anxiety Disorder: A Machine-Learning Based Analysis Framework. *Sensors* **2022**, *22*, 5420. [CrossRef] [PubMed]
25. Khosla, A.; Khandnor, P.; Chand, T. Automated diagnosis of depression from EEG signals using traditional and deep learning approaches: A comparative analysis. *Biocybern. Biomed. Eng.* **2022**, *42*, 108–142. [CrossRef]
26. Hickey, B.A.; Chalmers, T.; Newton, P.; Lin, C.T.; Sibbritt, D.; McLachlan, C.S.; Clifton-Bligh, R.; Morley, J.; Lal, S. Smart Devices and Wearable Technologies to Detect and Monitor Mental Health Conditions and Stress: A Systematic Review. *Sensors* **2021**, *21*, 3461. [CrossRef]
27. Wang, C.; Chen, Y.; Zhang, Y.; Chen, J.; Ding, X.; Ming, D.; Du, J. Quantitative EEG abnormalities in major depressive disorder with basal ganglia stroke with lesions in different hemispheres. *J. Affect. Disord.* **2017**, *215*, 172–178. [CrossRef]
28. Li, Y.; Cao, D.; Wei, L.; Tang, Y.; Wang, J. Abnormal functional connectivity of EEG gamma band in patients with depression during emotional face processing. *Clin. Neurophysiol.* **2015**, *126*, 2078–2089. [CrossRef]
29. Jusseaume, K.; Valova, I. Brain Age Prediction/Classification through Recurrent Deep Learning with Electroencephalogram Recordings of Seizure Subjects. *Sensors* **2022**, *22*, 8112. [CrossRef]
30. Arns, M.; Drinkenburg, W.H.; Fitzgerald, P.B.; Kenemans, J.L. Neurophysiological predictors of non-response to rTMS in depression. *Brain Stimul.* **2012**, *5*, 569–576. [CrossRef]
31. Olbrich, S.; Arns, M. EEG biomarkers in major depressive disorder: Discriminative power and prediction of treatment response. *Int. Rev. Psychiatry* **2013**, *25*, 604–618. [CrossRef]

32. Lin, C.T.; Chuang, C.H.; Cao, Z.; Singh, A.K.; Hung, C.S.; Yu, Y.H.; Nascimben, M.; Liu, Y.T.; King, J.T.; Su, T.P.; et al. Forehead EEG in Support of Future Feasible Personal Healthcare Solutions: Sleep Management, Headache Prevention, and Depression Treatment. *IEEE Access* **2017**, *5*, 10612–10621. [CrossRef]
33. Oh, J.; Yun, K.; Maoz, U.; Kim, T.S.; Chae, J.H. Identifying depression in the National Health and Nutrition Examination Survey data using a deep learning algorithm. *J. Affect. Disord.* **2019**, *257*, 623–631. [CrossRef] [PubMed]
34. Mumtaz, W.; Qayyum, A. A deep learning framework for automatic diagnosis of unipolar depression. *Int. J. Med. Inform.* **2019**, *132*, 103983. [CrossRef] [PubMed]
35. Zhang, J.; Xu, B.; Yin, H. Depression screening using hybrid neural network. *Multimed. Tools Appl.* **2023**, *82*, 26955–26970. [CrossRef] [PubMed]
36. Acharya, U.R.; Oh, S.L.; Hagiwara, Y.; Tan, J.H.; Adeli, H.; Subha, D.P. Automated EEG-based screening of depression using deep convolutional neural network. *Comput. Methods Programs Biomed.* **2018**, *161*, 103–113. [CrossRef] [PubMed]
37. Ay, B.; Yildirim, O.; Talo, M.; Baloglu, U.B.; Aydin, G.; Puthankattil, S.D.; Acharya, U.R. Automated depression detection using deep representation and sequence learning with EEG signals. *J. Med. Syst.* **2019**, *43*, 205. [CrossRef]
38. Eldele, E.; Chen, Z.; Liu, C.; Wu, M.; Guan, C. An Attention-Based Deep Learning Approach for Sleep Stage Classification With Single-Channel EEG. *IEEE Trans. Neural Syst. Rehabil. Eng.* **2021**, *29*, 809–818. [CrossRef]
39. Liu, B.; Chang, H.L.; Peng, K.; Wang, X.N. An End-to-End Depression Recognition Method Based on EEGNet. *Front. Psychiatry* **2022**, *13*, 864393. [CrossRef]
40. Seal, A.; Bajpai, R.; Agnihotri, J.; Yazidi, A.; Herrera-Viedma, E.; Krejcar, O. DeprNet: A Deep Convolution Neural Network Framework for Detecting Depression Using EEG. *IEEE Trans. Instrum. Meas.* **2021**, *70*, 2505413. [CrossRef]
41. Dai, L.; Zhou, H.; Xu, X.; Zuo, Z. Brain structural and functional changes in patients with major depressive disorder: A literature review. *PeerJ* **2019**, *7*, e8170. [CrossRef]
42. Grieve, S.M.; Korgaonkar, M.S.; Koslow, S.H.; Gordon, E.; Williams, L.M. Widespread reductions in gray matter volume in depression. *Neuroimage-Clin.* **2013**, *3*, 332–339. [CrossRef] [PubMed]
43. Bludau, S.; Bzdok, D.; Gruber, O.; Kohn, N.; Riedl, V.; Sorg, C.; Palomero-Gallagher, N.; Mueller, V.I.; Hoffstaedter, F.; Amunts, K.; et al. Medial Prefrontal Aberrations in Major Depressive Disorder Revealed by Cytoarchitectonically Informed Voxel-Based Morphometry. *Am. J. Psychiatry* **2016**, *173*, 291–298. [CrossRef] [PubMed]
44. Diener, C.; Kuehner, C.; Brusniak, W.; Ubl, B.; Wessa, M.; Flor, H. A meta-analysis of neurofunctional imaging studies of emotion and cognition in major depression. *Neuroimage* **2012**, *61*, 677–685. [CrossRef]
45. Bludau, S.; Eickhoff, S.B.; Mohlberg, H.; Caspers, S.; Laird, A.R.; Fox, P.T.; Schleicher, A.; Zilles, K.; Amunts, K. Cytoarchitecture, probability maps and functions of the human frontal pole. *Neuroimage* **2014**, *93*, 260–275. [CrossRef] [PubMed]
46. Coryell, W.; Nopoulos, P.; Drevets, W.; Wilson, T.; Andreasen, N.C. Subgenual prefrontal cortex volumes in major depressive disorder and schizophrenia: Diagnostic specificity and prognostic implications. *Am. J. Psychiatry* **2005**, *162*, 1706–1712. [CrossRef] [PubMed]
47. Iyortsuun, N.K.; Kim, S.H.; Jhon, M.; Yang, H.J.; Pant, S. A Review of Machine Learning and Deep Learning Approaches on Mental Health Diagnosis. *Healthcare* **2023**, *11*, 285. [CrossRef]
48. Qu, Z.; Wang, Y.; Guo, D.; He, G.; Sui, C.; Duan, Y.; Zhang, X.; Lan, L.; Meng, H.; Wang, Y.; et al. Identifying depression in the United States veterans using deep learning algorithms, NHANES 2005–2018. *BMC Psychiatry* **2023**, *23*, 620. [CrossRef]
49. Kour, H.; Gupta, M.K. Predicting the language of depression from multivariate twitter data using a feature-rich hybrid deep learning model. *Concurr. Comput. Pract. Exp.* **2022**, *34*, e7224. [CrossRef]
50. Zogan, H.; Razzak, I.; Wang, X.; Jameel, S.; Xu, G. Explainable depression detection with multi-aspect features using a hybrid deep learning model on social media. *World Wide Web-Internet Web Inf. Syst.* **2022**, *25*, 281–304. [CrossRef]
51. Zhu, J.; Jiang, C.; Chen, J.; Lin, X.; Yu, R.; Li, X.; Hu, B. EEG based depression recognition using improved graph convolutional neural network. *Comput. Biol. Med.* **2022**, *148*, 105815. [CrossRef]
52. Yang, L.; Wang, Y.; Zhu, X.; Yang, X.; Zheng, C. A gated temporal-separable attention network for EEG-based depression recognition. *Comput. Biol. Med.* **2023**, *157*, 106782. [CrossRef] [PubMed]
53. Liu, W.; Jia, K.; Wang, Z.; Ma, Z. A Depression Prediction Algorithm Based on Spatiotemporal Feature of EEG Signal. *Brain Sci.* **2022**, *12*, 630. [CrossRef] [PubMed]
54. Puthankattil, S.D.; Joseph, P.K. Classification of EEG signals in normal and depression conditions by ANN using RWE and signal entropy. *J. Mech. Med. Biol.* **2012**, *12*, 1240019. [CrossRef]
55. Yasin, S.; Othmani, A.; Raza, I.; Hussain, S.A. Machine learning based approaches for clinical and non-clinical depression recognition and depression relapse prediction using audiovisual and EEG modalities: A comprehensive review. *Comput. Biol. Med.* **2023**, *159*, 106741. [CrossRef]
56. Kandilarova, S.S.; Terziyski, K.V.; Draganova, A.I.; Stoyanov, D.S.; Akabaliev, V.H.; Kostianev, S.S. Response to Pharmacological Treatment in Major Depression Predicted by Electroencephalographic Alpha Power—A Pilot Naturalistic Study. *Folia Med.* **2017**, *59*, 318–325. [CrossRef]
57. Berger, C.; Dueck, A.; Perin, F.; Wunsch, K.; Buchmann, J.; Koelch, M.; Reis, O.; Marx, I. Brain Arousal as Measured by EEG-Assessment Differs Between Children and Adolescents With Attention-Deficit/Hyperactivity Disorder (ADHD) and Depression. *Front. Psychiatry* **2021**, *12*, 633880. [CrossRef]
58. Henriques, J.B.; Davidson, R.J. Left frontal hypoactivation in depression. *J. Abnorm. Psychol.* **1991**, *100*, 535–545. [CrossRef]

59. Omel'chenko, V.P.; Zaika, V.G. Changes in the EEG rhythms in endogenous depressive disorders and the effect of pharmacotherapy. *Fiziol. Cheloveka* **2002**, *28*, 30–36.
60. Knott, V.; Mahoney, C.; Kennedy, S.; Evans, K. EEG power, frequency, asymmetry and coherence in male depression. *Psychiatry Res.* **2001**, *106*, 123–140. [CrossRef]
61. Al-Ezzi, A.; Kamel, N.; Faye, I.; Gunaseli, E. Review of EEG, ERP, and Brain Connectivity Estimators as Predictive Biomarkers of Social Anxiety Disorder. *Front. Psychol.* **2020**, *11*, 730. [CrossRef]
62. Grin-Yatsenko, V.A.; Baas, I.; Ponomarev, V.A.; Kropotov, J.D. EEG Power Spectra at Early Stages of Depressive Disorders. *J. Clin. Neurophysiol.* **2009**, *26*, 401–406. [CrossRef] [PubMed]
63. Wen, D.; Zhou, Y.; Li, P.; Zhang, P.; Li, J.; Wang, Y.; Li, X.; Bian, Z.; Yin, S.; Xu, Y. Resting-state EEG signal classification of amnestic mild cognitive impairment with type 2 diabetes mellitus based on multispectral image and convolutional neural network. *J. Neural Eng.* **2020**, *17*, 036005. [CrossRef] [PubMed]
64. Mahato, S.; Paul, S. Classification of Depression Patients and Normal Subjects Based on Electroencephalogram (EEG) Signal Using Alpha Power and Theta Asymmetry. *J. Med. Syst.* **2019**, *44*, 28. [CrossRef] [PubMed]

sensors

MDPI

Article

Graph Analysis of TMS–EEG Connectivity Reveals Hemispheric Differences following Occipital Stimulation

Ilaria Siviero [1], Davide Bonfanti [2], Gloria Menegaz [3], Silvia Savazzi [2], Chiara Mazzi [2] and Silvia Francesca Storti [3,*]

1 Department of Computer Science, University of Verona, Strada Le Grazie 15, 37134 Verona, Italy; ilaria.siviero@univr.it
2 Perception and Awareness (PandA) Lab., Department of Neuroscience, Biomedicine and Movement Science, University of Verona, Piazzale Ludovico Antonio Scuro 10, 37124 Verona, Italy; davide.bonfanti@univr.it (D.B.); silvia.savazzi@univr.it (S.S.); chiara.mazzi@univr.it (C.M.)
3 Department of Engineering for Innovation Medicine, University of Verona, Strada Le Grazie 15, 37134 Verona, Italy; gloria.menegaz@univr.it
* Correspondence: silviafrancesca.storti@univr.it

Citation: Siviero, I.; Bonfanti, D.; Menegaz, G.; Savazzi, S.; Mazzi, C.; Storti, S.F. Graph Analysis of TMS–EEG Connectivity Reveals Hemispheric Differences following Occipital Stimulation. *Sensors* **2023**, *23*, 8833. https://doi.org/10.3390/s23218833

Academic Editors: Yifan Zhao, Hua-Liang Wei, Yuzhu Guo and Fei He

Received: 28 September 2023
Revised: 23 October 2023
Accepted: 28 October 2023
Published: 30 October 2023

Abstract: (1) Background: Transcranial magnetic stimulation combined with electroencephalography (TMS–EEG) provides a unique opportunity to investigate brain connectivity. However, possible hemispheric asymmetries in signal propagation dynamics following occipital TMS have not been investigated. (2) Methods: Eighteen healthy participants underwent occipital single-pulse TMS at two different EEG sites, corresponding to early visual areas. We used a state-of-the-art Bayesian estimation approach to accurately estimate TMS-evoked potentials (TEPs) from EEG data, which has not been previously used in this context. To capture the rapid dynamics of information flow patterns, we implemented a self-tuning optimized Kalman (STOK) filter in conjunction with the information partial directed coherence (iPDC) measure, enabling us to derive time-varying connectivity matrices. Subsequently, graph analysis was conducted to assess key network properties, providing insight into the overall network organization of the brain network. (3) Results: Our findings revealed distinct lateralized effects on effective brain connectivity and graph networks after TMS stimulation, with left stimulation facilitating enhanced communication between contralateral frontal regions and right stimulation promoting increased intra-hemispheric ipsilateral connectivity, as evidenced by statistical test ($p < 0.001$). (4) Conclusions: The identified hemispheric differences in terms of connectivity provide novel insights into brain networks involved in visual information processing, revealing the hemispheric specificity of neural responses to occipital stimulation.

Keywords: TMS–EEG; occipital stimulation; TEP; brain functional connectivity; graph analysis

1. Introduction

Vision is the most frequently used sensory modality in everyday life and understanding what we see around us is conditional upon successful navigation of the external environment. This represents a challenge that our brain is continuously called to face. Within the domain of visual information processing, human brain hemispheres have long been considered functionally comparable. However, a growing body of evidence suggests the existence of a hemispheric specialization, according to which the two hemispheres contribute to visual information processing in a complementary manner, where the left hemisphere is assumed to prevail over the right one in processing local details of visual stimuli, and the right hemisphere is assumed to prevail in handling global information [1]. Characterizing the dynamics of cortical activation over time and disentangling the nature of the contribution of different brain areas to visual perception may provide potential better insight into diagnostic and prognostic markers. In addition, a better knowledge of how the involved brain areas are connected could also be crucial in the search for the recovery mechanisms after brain injuries, thus becoming of great relevance in different clinical applications [2,3], such as assisting brain surgery by minimizing damage to critical brain regions or devising personalized treatments for patients affected by visual field defects.

1.1. Brain Stimulation and Evoked Potentials

The investigation of human brain activity involves various brain stimulation or neuromodulation techniques [4–6], which are typically non-invasive, and limited contraindications and side effects can occur. Among these, transcranial magnetic stimulation is widely adopted for studying cognitive functions for research purposes [4]. The effectiveness of this technology has been validated in clinical applications for treating neurological conditions [7,8], but also in neuropsychiatry [9] and psychology [10]. In principle, TMS stimulates the brain through a brief high-intensity magnetic field applied to the surface of the scalp [11]. TMS is capable of evoking cortical activity without causing significant pain. It offers the flexibility to stimulate different brain areas by adjusting parameters, such as pulse intensity, inter-pulse interval, coil type, coil orientation, and placement. Several stimulation protocols have been developed, including, single-pulse stimulation and paired-pulse TMS [12]. By inducing local neuron depolarization and eliciting action potentials, single-pulse TMS is valuable for causal mapping of neural networks, investigating motor and other non-motor systems, as well as the investigation of cortical excitability, inhibition, and plasticity [13,14].

Extensive research has been conducted on the TMS stimulation of the primary motor cortex (M1) and the dorsolateral prefrontal cortex (DLPFC) resulting in well-understood and reproducible peak responses [15]. On the other hand, the temporo-occipital cortex, occipital, and cerebellar areas have been less investigated [16,17]. In particular, when TMS is applied to the occipital cortex, it can induce visual sensations without light entering the eyes, the so-called 'phosphene' [18,19].

TMS-evoked potentials (TEPs) can be measured when combining TMS with electroencephalography (EEG), a non-invasive technique for monitoring brain activity with high temporal resolution by placing the electrodes on the scalp. Thanks to EEG, complex neural processes can be detected to evaluate the neurophysiological function of the brain at rest or during specific tasks or stimulation paradigms. Indeed, TEPs are complex waveforms with multiple peaks occurring within hundreds of milliseconds after the TMS pulse [15,20]. These waveforms consist of positive (P) and negative (N) deflections that reflect a spatiotemporal superposition of excitatory and inhibitory postsynaptic potentials. A primary response is typically associated with a brain activity underlying the target area and a secondary response is related to the close or distant connected brain regions. Consequently, TEPs provide a means to investigate the excitability and connectivity of the cortex [15].

Despite the great potential of TMS–EEG, the extraction of reliable TEPs is hampered by several instrumental and physiological artifacts, and obtaining a 'true' noise-free response is challenging [21]. The accuracy of the estimated TEPs also depends on the number of trials, which directly impacts the signal-to-noise ratio (SNR). TEPs are embedded in a background of spontaneous EEG activity. Typically, TEPs are determined by conventional averaging (CA) which is performed by averaging the EEG recordings (sweeps or trials) acquired after N stimuli. However, CA assumes that the TEP does not vary with the succession of stimuli and the EEG noise remains stationary during the recordings. However, the EEG signal is not stationary, except in short intervals typically lasting 1–2 s. Additionally, the CA does not leverage any "a priori" knowledge of TEP and EEG, thus it fails to exploit potentially valuable information and it cannot detect any possible TEP changes that may occur during EEG recording. To overcome these limitations, several approaches have been proposed, including weighted averaging techniques, optimal filtering methods, and single-sweep approaches [22]. However, the absence of a "ground truth" against which the acquired signal can be compared poses challenges in determining the most effective approaches to obtain a signal free from artifacts. In the literature, alternative methods have been proposed to improve SNR, especially when the number of trials is limited. These methods perform a single trial analysis based on "a priori" knowledge within Bayesian approaches [23,24], time-frequency techniques [25], and Shannon entropy [26].

1.2. Brain Functional and Effective Connectivity

The co-registration of TMS–EEG represents a necessary step for the quantitative assessment of the cortical excitability and brain connectivity of the human cortex [20,27]. In particular, TMS–EEG offers the possibility of monitoring the temporal dynamics of brain connectivity [28–31]. Over time, the techniques used for analyzing, extracting, and interpreting the brain networks have undergone rapid advancements, from simple assessment of temporal correlation among multiple brain regions to more sophisticated models that incorporate temporal variability and causal non-linear relationships [32]. In this domain, two well-known and established approaches are functional (FC) and effective connectivity (EC).

FC is typically derived from bivariate or multivariate measures and reflects statistical dependencies between different units of the brain. Bivariate synchrony measures capture the level of synchronization between pairs of signals by using either linear measures, such as correlation or coherence, or nonlinear dependencies, such as phase values or mutual information [33]. Conversely, multivariate synchrony approaches aim to assign a singular numerical value that quantifies the degree of synchronization within a group of signals. Some examples are the omega estimator, the S-estimator, and its extension based on the Rényi entropy [34,35]. Thus, FC measures the synchronism between signals allowing the identification of a certain degree of association between different processes. However, it does not give any measure of causality, namely understanding which of the two signals pilots the other.

EC is defined as the influence that one neural system exerts over another through causal or non-causal effects [36]. It focuses on understanding how information flows are integrated within the brain network, delving into specific pathways and mechanisms of neural activity. Specifically, the EC is a directed measure able to distinguish the incoming and outgoing information flows, unlike the FC, which is insensitive to the direction. The estimation of EC has been addressed through several strategies, which can be broadly classified into model-based and model-free techniques. Model-based approaches require the specification of structural parameters, whereas model-free methods, such as Granger causality (GC) or transfer entropy, do not require such specifications. GC is one of the most common methods aiming to statistically determine causality between variables using a linear vector autoregressive (VAR) model. Directed transfer function (DTF) and partial directed coherence (PDC) are two frequency domain representations of the GC [37]. DTF determines the directional influences across the components in a multivariate framework [38]. On the contrary, PDC quantifies the direct pathway from variable j to variable i, excluding the influence of other processes [37]. PDC offers an enhanced estimation of the directional information flow between different regions of the brain compared to DTF. Indeed, it takes into account both the direct and indirect influences among variables, leading to a more comprehensive understanding of the underlying connectivity patterns [39]. The information partial directed coherence (iPDC) is another spectral measure that considers the effects of signal size when evaluating connection strength [40].

Traditionally, brain connectivity studies have focused on static or averaged connectivity patterns, assuming that the brain operates with fixed connectivity. Static connectivity networks are obtained from the above-mentioned methods, thus they do not explain the temporal variability of the brain connections [33]. However, the time course of functional brain connectivity plays an important role in detecting the propagation of neuronal pathways and is a crucial aspect of understanding how the brain works, as it is well known that the brain's functional architecture varies over time [41]. For this reason, other methods have been recently proposed to infer the time-variability of the network [42]. Methods used to study time-varying brain connectivity include dynamic causal modeling (DCM), sliding window approaches [43], and time-frequency analysis such as short-time DTF [39]. Markov model-based frameworks [44] and Kalman filter-based approaches [39,45] are other examples to model the time-varying brain networks. Dynamic functional connectivity (dFC), also known as time-varying connectivity, has been primarily studied in the domain of EEG or epilepsy [46] and functional magnetic resonance imaging (fMRI) [47], but not exclusively. In particular, to obtain a network that is robust from noise, Pascucci et al. proposed a self-tuning optimized Kalman (STOK) filter [48]. Its purpose was to ensure accurate tracking of networks, precise temporal localization, and robustness to noise by incorporating a self-adjusting memory decay and a recursive regularization technique. The STOK filter was tested both in silico and with real data, and its performance was found to be better than the one obtained by employing the traditional Kalman filter.

These methodologies provide insights into the dynamical organization of the brain and its underlying processes in response to cognitive demands, task requirements, or neurological conditions. Connectivity-based analysis has been proposed for many TMS–EEG studies, with applications ranging from pathological conditions, such as Alzheimer's disease [49] to normal brain functioning [50]. Other studies provided tools for consciousness classification (e.g., vegetative state and minimally conscious state). For example, Rosanova et al. proposed a reliable approach to detect the recovery of consciousness by analyzing the differences between hemispheres using EC models [2]. Similar findings were reported by Ragazzoni et al. in an independent TMS–EEG study [51]. Moreover, several studies investigated brain connectivity and the differences in information flow at rest versus the execution of cognitive tasks [52,53]. In the context of occipital TMS, brain connectivity analysis has already been used to examine its network-level effects, but the predominant focus in the literature has mainly been on attention protocols [54] and visual adaptation [55], leaving other potential applications relatively unexplored.

1.3. Brain Graph Networks

Graph theory has emerged as a powerful framework for studying brain connectivity, representing the brain as a network of interconnected nodes (or vertices), which correspond to neurons or brain regions, and links (or edges), which represent the relationships between those regions [56]. Both local (functional segregation) and global (functional integration) properties can be assessed through different measures of graphs. For example, centrality, clustering, modularity, and connectivity patterns can be obtained to understand the importance of specific nodes or regions, the presence of distinct functional modules, and the overall integration of information. Graph theory has found extensive use in neuroscience, particularly in studies using neuroimaging techniques, like fMRI and positron emission tomography (PET). The aim is to establish the human 'connectome', a comprehensive map of connections within the brain. Furthermore, graph networks provide a valuable framework for studying how the activation or manipulation of specific nodes or edges affects cognitive functions, such as perception or attention, and enable the study of network dynamics. For example, Caeyenberghs et al. [57] investigated brain activity during cognitive control tasks in patients with traumatic brain injury. They studied the performance and the topological properties of the functional brain networks using a graph theoretical approach, showing increased connectivity degree and strength, as well as higher values of local efficiency. The effectiveness of the graph theory has been demonstrated in many TMS–EEG studies [53]. Most of them focused on clinical applications with the goal of examining altered networks in various physiological or pathological conditions, since TMS–EEG enables the observation of dynamic responses within the targeted region and other specific connections. However, the dynamics of brain connectivity and relative brain network pose an additional layer of complexity. In terms of analysis, it involves examining the dynamic properties of functional brain networks, such as the aforementioned strength, network efficiency, and modular organization.

1.4. Aim of the Work

The aim of this study is to investigate the hemispheric differences in visual information processing through a dynamic brain connectivity analysis in order to uncover the underlying mechanisms that contribute to the effects of occipital TMS. Specifically, the objective is to analyze EEG data to identify connectivity patterns resulting from single-pulse TMS delivered around the occipital EEG sites, O1 and O2 (in the left and right hemispheres, respectively). To the best of our knowledge, this issue has never been addressed in the literature and, to achieve this, we employed different steps for the processing of EEG signals. Since the aim is to explore the casual interaction among brain areas in a dynamic manner, complex models that consider temporal variability are used. In detail, a Bayesian estimation approach is used to extract the TEPs, which has been demonstrated to be powerful in obtaining a reliable estimate of evoked potentials, especially when the number of trials is limited. Then, the STOK filter is applied to track the fast changes in brain reorganization and estimate the time-varying brain EC using iPDC. Furthermore, to assess the properties and characteristics of the brain network, a graph analysis is performed employing the betweenness centrality and degree measures. Lastly, statistical tests are implemented to uncover the differences in visual processing between left and right TMS.

2. Materials and Methods

In this section, the TMS–EEG experimental protocol and participant recruitment are first described (Sections 2.1–2.3, and Figure 1a). Then, the proposed TMS–EEG signal processing framework is explained as depicted in Figure 1b. In particular, EEG data were filtered as described in Section 2.4. A state-of-the-art Bayesian approach was used to estimate the TEPs from the filtered EEG signals as described in Section 2.5. As described in Section 2.6, the STOK filter was used for tracking the dynamic behavior of the directed brain network, and the iPDC was estimated. Additional mathematical details of the Bayesian approach and the STOK filter are reported in Appendix A and Appendix B, respectively. The edges betweenness centrality and the node degree were calculated for each time-variant directed connectivity matrix as reported in Section 2.7.

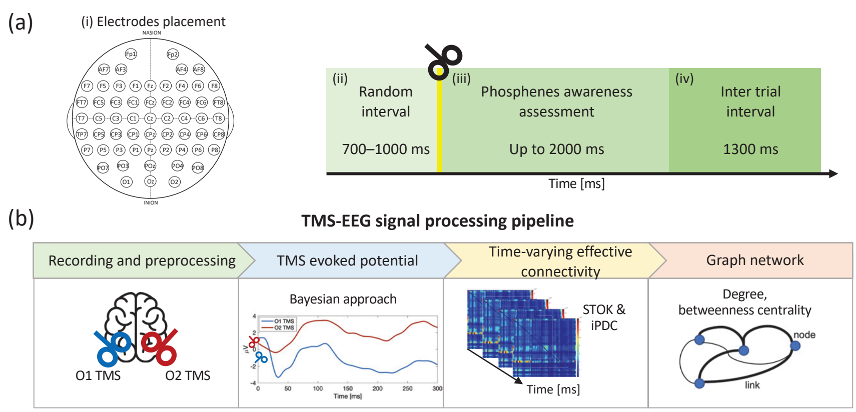

Figure 1. (**a**) Electrode placement and schematic representation of the experimental procedure: (i) random interval (700–1000 ms), (ii) single-pulse TMS stimulation, (iii) phosphene awareness assessment (up to 2000 ms), and (iv) inter-trial interval (1300 ms). (**b**) Signal processing pipeline for assessing the differences between hemispheres after TMS stimulation. The proposed pipeline is divided into preprocessing, TMS-evoked potential estimation, the time-varying effective connectivity calculation, and the graph network.

2.1. Participants

The study recruited eighteen healthy subjects on a voluntary basis (10 females, mean age 23.66 ± 3.54), who were all right-handed and had normal or corrected-to-normal vision. All participants gave their informed consent in accordance with the Declaration of Helsinki. Data were collected according to protocols approved by our local ethics committee. To ensure safety, a questionnaire was used to screen participants for potential TMS hazards, and no contraindications were reported.

2.2. TMS Protocol and Experimental Protocol

Single-pulse TMS was delivered through a 70 mm figure-of-eight coil connected to a Magstim Rapid2 system (maximum output 3.5 T, the Magstim Company Limited, Whitland, UK). To prevent unnecessary neck muscle activation, the coil was positioned tangentially to the scalp surface with the handle pointing upward. Through supra-threshold phosphene induction, stimulation areas were functionally located around electrode positions O1 (left hemisphere) and O2 (right hemisphere) of the 10-10 International System. Electrodes O1 and O2 were used as a starting point around which, in a $\sim$2 cm^2 area, we selected the hotspot eliciting the most consistent and clearest phosphenes while stimulating at supra-threshold intensity. Neuronavigation taking advantage of individual structural MRI images (SofTaxic, E.M.S., Bologna, Italy, and Polaris Vicra, NDI, Waterloo, ON, Canada) was used in the course of the experiment (1) during the hotspot search, to monitor that the stimulation was targeting early visual areas; (2) during the course of the experiment, to check for coil displacements larger than 2 mm accuracy threshold; and (3) to reposition the coil exactly on the hotspot after breaks between sessions. The individual phosphene threshold (PT) was set using the automatic procedure of the 'Method of Constant Stimuli' (MOCS) [58]. After the hotspot for each stimulation site was functionally identified, the PT was evaluated using a computerized MOCS version: seven TMS intensities were used (ranging from 60% to 78% of maximum stimulator output (MSO), with an increasing step of 3%). For each of these intensities, seven pulses were delivered. Pulses from different stimulation intensities were randomly interleaved, resulting in a randomized order of stimulation intensities. After each TMS pulse, participants were asked to report any presence of phosphenes. The resulting data were then fitted with a cumulative Logistic psychometric function via a maximum likelihood criterion using the Matlab 2021b (MathWorks, Natick, MA, USA) Palamedes toolbox (http://www.palamedestoolbox.org, accessed on 1 December 2021). From the obtained function, we derived the PT intensity at which participants perceived phosphenes in 50% of trials, and this intensity was employed during the experiment as stimulation intensity.

2.3. Perception of Phosphenes: Protocol and Testing

Participants sat in a dark room, in front of a monitor, with their heads on a chin rest to keep their eyes aligned with the central fixation point. They were instructed to maintain their gaze on the fixation point throughout the experiment. Before the two experimental sessions, a training session was performed to test participants for the perception of phosphenes. Participants were initially debriefed about the functioning of TMS and phosphenes [58,59]. Afterward, they had to wear a cap on which the positions of electrodes O1 and O2 were labeled.

Experimenters then started administering single-pulse TMS around O1/O2 positions; after each stimulation, participants were asked if they had seen something matching phosphene characteristics in their visual field, and, if so, to give a short description of these percepts. Once participants had sufficiently adapted to darkness and experimenters were confident that they were reporting actual phosphenes, the stimulation conditions (e.g., asking participants to fixate on a different point on the screen or to close their eyes) were changed to test if participant reports still matched the expected characteristics for phosphenes. Once the procedure was completed for one hemisphere, the other one underwent testing. The criteria used to test for real phosphenes are in [59]: they appear in the visual field contralateral to the stimulated hemisphere; they follow the participants' gaze; and they appear independently of the eyes being closed or open. After being assessed for real phosphene perception, participants underwent an MRI scan necessary for neuronavigated TMS. Two consecutive sessions were carried out and single-pulse TMS was administered to the left and right occipital cortex at PT intensity, with the order of the two stimulated sites counterbalanced across participants, while simultaneously recording EEG data. In order to mask the audible TMS click, participants were asked to wear disposable earplugs. First, a random interval with a duration of 700–1000 ms preceded the TMS pulse; the stimulation was then administered and followed by up to 2000 ms, during which participants had to report the presence or absence of a phosphene by pressing one of two keyboard keys (the 'm' key with the right hand for phosphene present, the 'z' key with left hand for phosphene absent). Finally, a 1300 ms inter-trial interval separated each trial (Figure 1a). Moreover, 360 pulses divided into 6 blocks of 60 trials each were administered during each session. Blocks were separated by a few minutes of rest, to prevent excessive fatigue in participants.

2.4. EEG Recording and Preprocessing

A TMS-compatible EEG equipment (BrainAmp, Brain Products GmbH, Munich, Germany) was used to record EEG activity (BrainVision Recorder, version 1.25). The recording setup involved a Fast'n East cap containing a total of 59 scalp channels, with additional electrodes used to monitor horizontal and vertical eye movements, as online reference (RM) and as ground (AFz). All of them were TMS-compatible Ag/AgCl pellet pit electrodes (Easycap GmbH, Herrsching, Germany). The electrode placement followed the extended 10-10 International System (impedance was kept below 5 kΩ).

The EEG signal data analysis was performed offline using Matlab 2021b (MathWorks, Natick, MA, USA) with the EEGLAB toolbox (version 2021.0) and the TMS–EEG signal analyzer (TESA) extension [60]. The continuous raw signal digitized at 5000 Hz was segmented into 1000 ms before and after the TMS pulse. The epochs were demeaned using the entire epoch and the TMS pulse artifact was removed from −2 to 10 ms. It was replaced with cubic interpolation to avoid ringing artifacts. Data were downsampled at 500 Hz. A first independent component analysis (ICA) round, using the 'runica' function, was performed to remove the TMS artifacts followed by a zero-phase fourth-order Butterworth filtering between 0.1 and 100 Hz with a band-stop filter (49–51 Hz). A second ICA was used to remove blinks and muscle activity. To improve component decomposition, the interpolated data from −2 to 10 ms after the TMS pulse were replaced with constant amplitude values before each ICA, and then interpolated again afterward. The REST toolbox was used to re-reference the data to a point at infinity [61]. Then, data were low-pass filtered at 40 Hz, and bad trials were automatically rejected through the TBT toolbox [62]. Further details of the preprocessing pipeline are reported in the study by Rogasch et al. [60].

2.5. TEP Estimation

To estimate the TEPs, we used the Bayesian approach proposed by Sparacino et al., which is based on a sweep-by-sweep filtering strategy [23,24]. This approach incorporates a Bayesian framework by exploiting second-order statistical information on both the unknown EP and the background EEG, which varies from one sweep to another. The pre-stimulus EEG data are fitted with an autoregressive (AR) model and the unknown TEP is treated as a multiple integration of a white noise process. In each single sweep, a filtered response is obtained after the stimulus by applying a smoothing criterion. Then, the TEP is obtained by computing a weighted average of the filtered sweeps. Within the Bayesian framework, each sweep could be weighted according to its reliability, which corresponds to the estimate of the filter error. Thus, the weight assigned from each sweep is inversely proportional to the expected value of the squared norm of the filter error. For a detailed mathematical formulation of this Bayesian smoothing method please refer to Appendix A. Of note that, before computing the TEPs, the mean of pre-stimulus EEG data was subtracted to each single sweep.

In order to compare the TEPs obtained through the CA method with those obtained with Sparacino et al.'s Bayesian approach, the global mean field power (GMFP) was used.

The GMFP is calculated considering the data from all recording electrodes and provides a global measure. The GMFP measure is calculated as follows:

$$\text{GMFP(t)} = \sqrt{\frac{\sum_{i=1}^{K}(V_i(t) - V_{mean}(t))^2}{K}} \tag{1}$$

where t is time, V is the voltage at channel i, V_{mean} is the average of the voltages in all channels, and K is the total number of channels. Finally, a Wilcoxon signed-rank test Bonferroni corrected, $p < 0.05$ was used to compare the two GMFPs for both left and right occipital TMS.

2.6. Time-Varying iPDC Estimated through STOK Filter

In this study, we used the STOK filter, a powerful method for investigating the information flow and causal interactions under unknown noise conditions in the cognitive domain. It embeds a self-tuning memory decay and a recursive regularization to guarantee high accuracy in network tracking, temporal precision, and robustness to noise [48]. The STOK filter is based on the time-varying multivariate autoregressive model (tvMVAR), which provides a valuable framework for describing the dynamic behavior of multiple repeated experiments involving physiological time series, such as the EEG signal. Indeed, the EEG data can be viewed as realizations $\{Y_t, t = t_1, t_2, \ldots t_T\}$ of the same multivariate stochastic process, as follows:

$$Y_t = \begin{bmatrix} y_{1,t}^{(1)} & \cdots & y_{d,t}^{(1)} \\ \vdots & \ddots & \vdots \\ y_{1,t}^{(N)} & \cdots & y_{d,t}^{(N)} \end{bmatrix} \tag{2}$$

where T is the length of each time series, N is the total number of trials, and d is the number of electrodes.

In general, the tvMVAR model can be specified in the form of:

$$Y_t = \sum_{k=1}^{p} A_{k,t} Y_{t-k} + \epsilon_t \tag{3}$$

where $A_{k,t}$ are the AR matrices containing the time-varying model coefficients, ϵ_t is the zero mean white noise with covariance matrix Σ_ϵ, and p is the model order. The STOK filter was used to estimate the AR coefficients and the covariance matrix Σ_ϵ. Then, it was used to calculate the iPDC measure. Please refer to Appendix B for the mathematical formulation of the STOK filter [48].

The iPDC is a multivariate spectral measure that compares only the directed influences between any given pair of signals (i, j). The iPDC stands out among the various approaches for extracting the EC measure by accurately considering the impact of the signal size when evaluating the connection strength [40].

By defining $B(f, t)$ as

$$B(f, t) = I_d - \sum_{k=1}^{p} A_{k,t} e^{-j2\pi fk} \tag{4}$$

where $A_{k,t}$ are the AR matrices estimated by the STOK filter at each time t, I_d is the identity matrix and j is the imaginary unit; the iPDC complex function from the time series j to the time series i is obtained by:

$$\text{iPDC}_{i\leftarrow j}(f, t) = \sigma_{\epsilon_{ii}}^{-1/2} \frac{b_{ij}(f, t)}{\sqrt{b_j^H(f, t)\Sigma_\epsilon^{-1} b_j(f, t)}} \tag{5}$$

where $b_j(f,t)$ and $b_{ij}(f,t)$ are the j-th column and the (j,i)-th element of the matrix $B(f,t)$, respectively, $\sigma_{\epsilon_{ii}}$ is the (i,i)-th element of the innovation covariance matrix Σ_ϵ [63], and the H in $b_j^H(f,t)$ stands for Hermitian transpose. The absolute value of $\text{iPDC}_{i \leftarrow j}(f,t)$ is usually analyzed.

The iPDC has been used in other studies demonstrating good performance. For example, in Rubega et al., the iPDC was adopted to study brain connectivity in the visual EP of face perception and in interictal epileptiform discharges in focal epilepsy [64].

2.7. Graph Networks and Statistical Analysis

By representing the brain as a graph, with nodes as brain regions (in this case EEG electrodes) and edges as connections (in this case iPDC), we can quantify the network properties. Among the network measures available, degree and centrality metrics are particularly interesting in this context [53].

Specifically, the betweenness centrality is a measure of the fraction of all shortest paths in the network that pass through a given node. Degree corresponds to the number of connections of a node, proving an indicator of the node's importance in the network [56]. Nodes with high degrees are considered influential hubs within the brain network. Differently, centrality measures the importance of a node or edge based on its position within the network. Nodes or edges with high centrality are crucial for efficient information transfer within the network. To assess the network centrality, the brain connectivity toolbox (BCT) (https://sites.google.com/site/bctnet/home?authuser=0, accessed on 1 March 2023) was used.

Differences in graph networks between two conditions were tested utilizing a Wilcoxon signed-rank test with a significance level of $p < 0.001$.

3. Results

The following section presents the obtained results aiming at understanding the propagation of the information in the brain network and its organization after the two different TMS brain stimulations. In Section 3.1, we compare the TEPs obtained through the CA and Sparacino et al. Bayesian approaches. Lastly, the statistically significant differences between left and right TMS are presented in terms of iPDC, edges betweenness centrality, and degree in Section 3.2.

3.1. TEPs Estimated through the Sparacino et al.'s Bayesian Approach

Figure 2 compares the GMFP for TEPs obtained using two different methods: the CA and the Bayesian approach. The upper part of the figure represents the GMFP recorded after left TMS stimulation (O1), while the lower part represents the GMFP recorded after right TMS stimulation (O2). Gray-shaded areas indicate statistically significant differences between the CA method and the Bayesian smoothing approach (Wilcoxon signed-rank test Bonferroni corrected, $p < 0.05$). It can be observed that the two time series appear different mainly in the first part of the GMFP after the TMS stimulation. This comparison provides valuable insights into the performance discrepancies between the two. However, it is important to note the lack of a "ground truth", i.e., the true underlying potential in our case, which prevents further validation through TEP simulations. The Bayesian smoothing approach has been successfully validated in silico using other EP data, such as in [23]. This prior validation supports its reliability in estimating TEP characteristics.

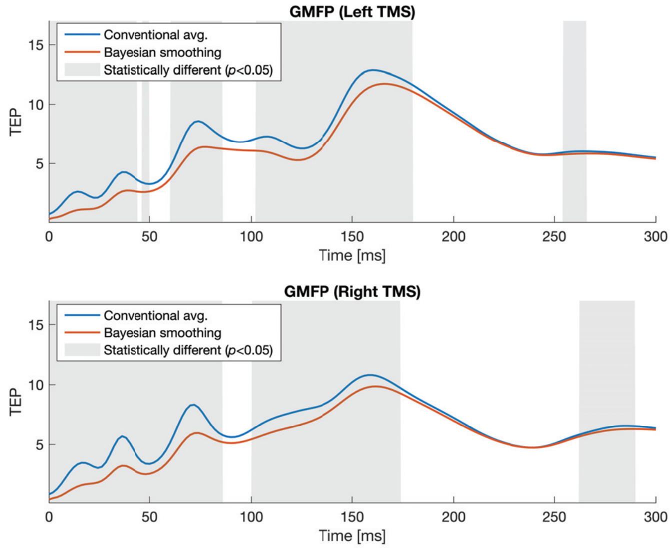

Figure 2. Global mean field power calculated for TEP using the conventional averaging (CA) method (blue) and the Bayesian smoothing approach (red) obtained from 360 sweeps. The upper part referred to the left TMS stimulation and the lower part to the right TMS stimulation. Statistical significance differences between the CA method and the Bayesian smoothing are indicated by gray areas (Wilcoxon signed-rank test Bonferroni corrected, $p < 0.05$). Time is measured in ms and the amplitude is in μV.

3.2. Time-Varying iPDC and Graph Analysis

Brain EC was investigated through time-varying iPDC analysis. Figure 3 illustrates the results of the group analysis for the two stimulation sites. Figure 3a represents the connectivity analysis for the left stimulation at site O1, while Figure 3b depicts the connectivity analysis for the right stimulation at site O2. Each topoplot shows the directed connections between brain channels in five different time windows, which are 12–24 ms, 24–48 ms, 48–92 ms, 92–124 ms, and 124–240 ms. These time windows were selected around the peaks of the GMFP (Figure 2). An empirical threshold, expressed as a fixed percentage (50%) of the max value, was applied to the topographic maps for the O1 and O2 stimulations for visualization purposes, highlighting the strongest connections. To compare the differences between the two hemispheres, the electrodes and their corresponding connectivity for the right TMS stimulation were flipped from right to left (so that the two stimulation sites were overlapped). The arrows in Figure 3c indicate statistically significant differences between the two conditions (Wilcoxon signed-rank test uncorrected $p < 0.001$). These findings provide insights into the dynamic patterns of brain connectivity associated with the different stimulation sites. It is strongly visible that left occipital TMS produces a scalp activation that propagates more along contralateral channels than right occipital TMS (see Figure 3a,b). The statistical analysis reveals a divergence between the two stimulations during the time window spanning from 48 to 92 ms, particularly in the frontal regions of the contralateral hemisphere and between the occipital and frontal electrodes in the same hemisphere. The connections in Figure 3c appear positive when the statistical test detects that the stimulation at O1 is stronger than at O2 (see the blue arrows in Figure 3c). Conversely, the connections are negative when the test detects that the stimulation at O2 is more intense than at O1 (see the red arrows in Figure 3c).

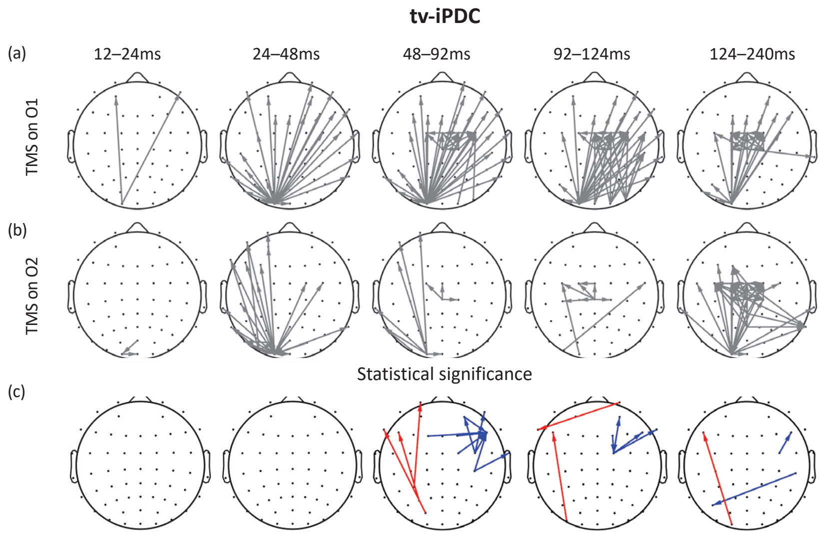

Figure 3. Time-varying brain connectivity analysis for stimulation sites. (**a**) TMS on O1; (**b**) TMS on O2; (**c**) statistical significance differences between conditions are indicated by arrows (Wilcoxon signed-rank test uncorrected $p < 0.001$). Red arrows indicate stronger connections following right stimulation (O2) than left stimulation (O1). By contrast, blue arrows indicate stronger connections following left stimulation (O1) than right stimulation (O2).

Betweenness centrality analysis of time-varying edges was performed to investigate the importance of edges (connectivity links) between stimulation sites. Figure 4 shows the results of this analysis for both left (O1) and right (O2) TMS stimulation. Figure 4a represents the time-varying edges betweenness centrality analysis for left TMS, while Figure 4b corresponds to the analysis for right TMS. The arrows in Figure 4c indicate statistically significant differences between the conditions (Wilcoxon signed-rank test uncorrected, $p < 0.001$). In this case, the significant EC connections are more restricted and occur within the time windows of 48–92 ms and 92–124 ms. However, positive edges (O1 > O2) are observed in the contralateral channels to the stimulation, while negative ones (O2 > O1) are circumscribed to ipsilateral channels. This result suggests that these connections play a central role in information transmission.

Figure 5 shows the degree metric of the graph network for the two stimulation sites. Since the results depicted in Figures 3 and 4 showed stronger connections in the ipsilateral hemisphere and the frontal regions of the contralateral hemisphere over time, here, the brain was divided into four macro areas, i.e., ipsilateral (to the TMS stimulation) occipital, ipsilateral frontal, contralateral occipital, and contralateral frontal. These areas are visually represented as light blue, green, yellow, and orange, respectively. For example, the ipsilateral frontal area (light blue) includes the electrodes Fp1, AF7, AF3, F7, F5, F3, F1, FT7, FC5, FC3, and FC1. All degree values within each specific area were grouped and plotted for every time window by using a boxplot. Statistical differences between the left and right TMS stimulation were depicted by black asterisks above boxplots in each time window. This analysis revealed significant differences in degrees between left and right TMS conditions in the contralateral frontal area from 24 ms to 240 ms, in the ipsilateral occipital area from 124 to 240 ms, and the contralateral occipital area from 92 to 124 ms, as assessed by statistical testing (Wilcoxon signed-rank test uncorrected $p < 0.001$).

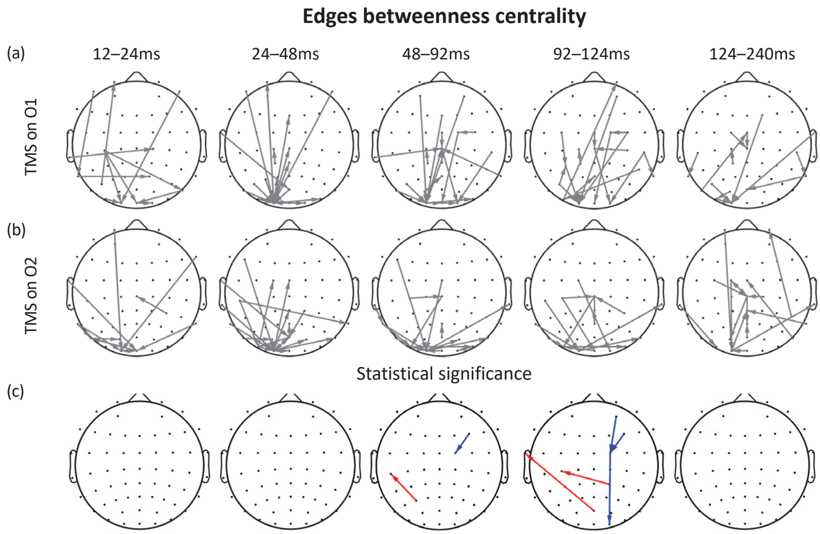

Figure 4. Time-varying edges betweenness centrality for stimulation sites. (**a**) Left (O1) TMS stimulation; (**b**) right (O2) TMS stimulation; (**c**) statistical significance differences between conditions are indicated by arrows (Wilcoxon signed-rank test uncorrected $p < 0.001$). Red arrows indicate stronger values of the edges following right stimulation (O2) than left stimulation (O1). By contrast, blue arrows indicate stronger values of the edge following left stimulation (O1) than right stimulation (O2).

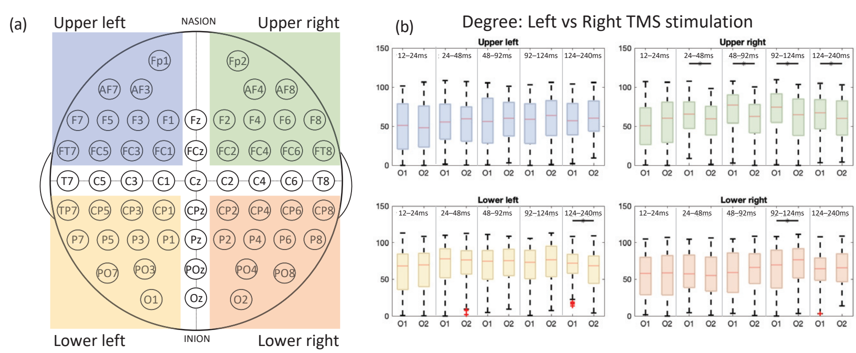

Figure 5. (**a**) Electrode placement using the international 10-10 system covering the ipsilateral frontal channels (highlighted in blue), contralateral frontal channels (highlighted in green), ipsilateral occipital channels (highlighted in yellow), and contralateral occipital channels (highlighted in orange). (**b**) Degree metric of graph networks in response to left vs. right TMS. Statistical significant differences between conditions are indicated by asterisks above boxplots (Wilcoxon signed-rank test uncorrected $p < 0.001$).

4. Discussion

Due to excellent temporal resolution, TMS–EEG has emerged as a powerful technique to characterize TMS-induced connectivity from a functional perspective. Indeed, EEG allows us to trace the trans-synaptic spread of activation to remote but interconnected brain regions as a result of the local activation triggered by the magnetic stimulation of the targeted cortical area. To the best of our knowledge, the study of hemispheric differences within the visual domain has never been addressed by applying TMS to the early visual cortex and concurrently recording EEG signals. For this reason, we aimed at investigating physiological hemispheric differences concerning the spatiotemporal dynamics of signal propagation during occipital stimulation. To do this, a time-varying signal processing pipeline was proposed based on existing techniques in order to understand how the brain areas are involved during the occipital TMS–EEG stimulation.

4.1. Mapping the Asymmetries of Functional Connectivity within Visual Networks after Left and Right Occipital TMS

Our findings show that, by targeting the left early visual cortex (O1), the resulting TMS-induced signal propagation pattern involved more contralateral channels than the right visual cortex stimulation, especially regarding frontal electrodes. Conversely, the stimulation of the right early visual cortex (O2) elicited increased intra-hemispheric connectivity, especially affecting occipital and frontal areas ipsilateral to the (right) stimulated site. These results point towards a complex effect on visual signal propagation, by triggering side-specific spatiotemporal dynamics, providing further support to the hypothesis that a functional left–right hemispheric asymmetry exists for low-level functions as well. Since Broca's work on aphasia paved the way for modern neuropsychology by investigating patients presenting with lateralized focused brain lesions [65,66], the human brain hemispheres have no longer been considered functionally equivalent. Traditionally, however, this lateralization was always thought to selectively concern high-level functions, such as language and attention. The new data presented here prove an asymmetry across the two hemispheres in visual information processing by highlighting that the right hemisphere is the most dominant for visual function, at least under these circumstances. Indeed, when stimulating the right hemisphere, brain connectivity is circumscribed to ipsilateral channels, and no significant involvement of contralateral networks was found. This right-hemispheric specialization for visual function is supported, to date, by many sources of converging evidence, including behavioral and TMS studies [67,68], neuropsychological evidence [69], electrophysiological findings [70], and neuroimaging results [71,72]. Interestingly, evidence from a previous TMS-fMRI study [71] highlights a key role of the right frontal cortex in line with our results, revealing that frontal or parietal TMS administered to the right rather than to the left hemisphere exerts a stronger influence upon the visual cortices via back-projection. Intriguingly, our data show that such an effect can also occur the other way around, namely stimulating the visual cortex and monitoring the signal propagation towards right frontal areas, in a bottom-up fashion. Moreover, our data possibly explain right-hemisphere lesions in frontal or parietal areas that lead to deficits affecting the visual domain. Our results can also corroborate previously cited evidence showing that the left hemisphere prevails in processing local visual details, while the right hemisphere prevails in handling global visual information [67]. Indeed, participants in our study were not asked to actively process any local details of a visual stimulus, and the TMS-induced signal propagation pattern following the left hemisphere stimulation mostly involved contralateral channels, pointing to the need for a right hemisphere involvement. Differences in the brain response between the two hemispheres after single-pulse TMS delivered to the temporo-occipital and dorsolateral prefrontal brain areas were also found by Jarczok et al. [73]. The findings of this study show that TEPs are lateralized towards the stimulated hemisphere.

Finally, in the context of TMS–EEG, a recent study focused on investigating how attention promotes the gating of information from the sending area to the receiving areas, achieved through dynamic changes in EC [54]. To probe the EC and cortical excitability modulated by covertly shifted attention, TMS was used to perturb the right retinotopic visual cortex in relation to attended and unattended locations. Stimulation of the contralateral visual hemisphere resulted in stronger EEG responses and increased connectivity compared to the ipsilateral hemisphere. The time-delayed phase locking value (tdPLV) was used to estimate the effective connectivities between O2 and all other electrodes. However, while this allowed the evaluation of the inter-area phase synchronization, all the other connections were not assessed.

In the long term, understanding whether—and to what extent—visual network connectivity is functionally lateralized in the human brain is of paramount importance for several reasons. Among others, it can have clinical implications [2], thereby helping to predict the outcome of brain surgery when resection involves visually responsive areas. At the same time, being aware of connectivity patterns characterizing the healthy brain can also help to develop and customize rehabilitation interventions for visually impaired patients as a function of the affected hemisphere.

4.2. Exploring Methodological Approaches for Dynamic Connectivity in TMS–EEG

The present study focuses on the methodological aspects that involve the application of existing approaches in a novel context concerning the co-registration of TMS–EEG as a result of early visual area stimulation. We propose a TMS–EEG signal processing pipeline consisting of several phases: EEG preprocessing, TEP estimation, time-varying EC exploration, and graph network analysis. Finally, statistical tests were applied to extract and discern the significant differences between the stimulation sites.

Despite the robust methodology and clear results produced by this study, it is important to address the potential limitations associated with the experimental paradigm and analysis methodologies. Firstly, to estimate the TEPs, we employed a state-of-the-art Bayesian approach proposed by Sparacino et al. [23], which is particularly useful when the number of collected sweeps is limited and high variability is exhibited. In the field of TMS–EEG, the “ground truth” waveform of the TEP following occipital stimulation remains unknown, preventing a direct comparison between the Bayesian approach and the conventional one (i.e. CA) to demonstrate the superior performance of the former. However, the Bayesian approach has been validated on other datasets [24]. In our study, as shown in Figure 2, we observed significant differences between the potentials obtained with the Bayesian framework and the CA method. Secondly, despite the multi-level analysis involved in this study (TEP estimation, connectivity analysis with directionality, and time-varying graph analysis), it is important to note that our methodology does not require any manual parameter adjustment. One of the key strengths lies in the implementation of a Bayesian approach for TEP estimation, where the final prediction error (FPE) is used to determine the optimal order of the AR model. On the other hand, the estimation of the dynamic connectivity is performed using the STOK filter, which does not require any parameter selection, unless the optimal order of the AR model is once again estimated using the Akaike criterion. This automated approach ensures that the methodology is consistent and avoids potential biases that may arise from subjective parameter choices. In addition, the basal activity before each stimulation was subtracted. By applying this normalization, the different effects on brain connectivity after the stimulation can be compared among subjects. Despite this, a larger sample will be considered to enhance reproducibility.

5. Conclusions

To conclude, our study demonstrates the importance of connectivity and graph analysis measures in detecting hemispheric differences resulting from lateralized occipital TMS stimulation protocols. By capturing the time-varying dynamics of brain connectivity, we provided a more comprehensive understanding of how visual information is propagated across brain networks.

Compared with previous studies where the visual system was long considered equivalent across hemispheres, the observed electrophysiological patterns highlight hemispheric-specific effects as a consequence of the TMS stimulation. Knowing that the stimulation of specific brain areas can elicit visual percepts and how this stimulation spreads throughout the brain can provide a theoretical background for many practical and clinical applications. In conclusion, our study paves the way for further investigation in the field of visual area stimulation but other aspects need to be investigated. For example, having a “ground truth" electrophysiological response could help to better analyze the TEPs and related brain networks. Our future work will be focused on the integration of the inverse problem for EEG source localization to study the pattern of communication between the two human brain hemispheres for deep and superficial sources.

Author Contributions: Conceptualization, I.S., D.B., S.S., C.M. and S.F.S.; methodology, I.S. and S.F.S.; software, I.S., D.B. and C.M.; validation, I.S.; formal analysis, I.S.; investigation, I.S., D.B., C.M. and S.F.S.; data curation, D.B. and C.M.; writing—original draft preparation, I.S., D.B., C.M. and S.F.S.; writing—review and editing, I.S., D.B., G.M., S.S., C.M. and S.F.S.; visualization, I.S.; supervision, G.M., S.S., C.M. and S.F.S.; project administration, G.M., S.S., C.M. and S.F.S.; funding acquisition, G.M., S.S. and S.F.S. All authors have read and agreed to the published version of the manuscript.

Funding: Work supported by #NEXTGENERATIONEU (NGEU) and funded by the Ministry of University and Research (MUR), National Recovery and Resilience Plan (NRRP), project MNESYS (PE0000006)—"A Multiscale integrated approach to the study of the nervous system in health and disease" (DN. 1553 11.10.2022); MIUR D.M. 737/2021-AI4Health: empowering neurosciences with eXplainable AI methods; MIUR D.M. 737/2021-Neural correlates of perceptual awareness: from neural architecture to the preservation of conscious vision in brain tumor patients; MIUR PRIN 2017, grant no. 2017TBA4KS_002; Fondazione Cassa di Risparmio di Verona, Vicenza, Belluno e Ancona "Ricerca scientifica d'eccellenza 2018", grant no. 2018.0861; I.S. was supported by REACT EU-PON Ricerca e Innovazione 2014–2020.

Institutional Review Board Statement: The experimental protocol was approved by the Ethics Committee of the University of Verona. The study was conducted in accordance with the Declaration of Helsinki (as revised in 2013).

Informed Consent Statement: Informed consent was obtained from all subjects involved in the study.

Data Availability Statement: The data used in this study can be found at https://gin.g-node.org/DB_123/Phosphenes_occipital.git, accessed on 28 September 2023.

Conflicts of Interest: The authors declare no conflict of interest.

Abbreviations

The following abbreviations are used in this manuscript:

TMS	transcranial magnetic stimulation
EEG	electroencephalography
TEP	TMS-evoked potential
M1	primary motor cortex
DLPFC	dorsolateral prefrontal cortex
MEP	motor-evoked potentials
SNR	signal-to-noise ratio
CA	conventional averaging
FC	functional connectivity
EC	effective connectivity
PLV	phase-lag value
PLI	phase-lag index
GC	Granger causality
VAR	vector autoregressive
DTF	directed transfer function
PDC	partial directed coherence
iPDC	information partial directed coherence
DCM	dynamic causal modeling
dFC	dynamic functional connectivity
fMRI	functional magnetic resonance imaging
PET	positron emission tomography
STOK	self-tuning optimized Kalman
PT	phosphene threshold

MOCS	method of constant stimuli
MSO	maximum stimulator output
ICA	independent component analysis
AR	autoregressive
tvMVAR	time-varying multivariate autoregressive
GMFP	global mean field power
BCT	brain connectivity toolbox
tdPLV	time-delayed phase locking value
FPE	final prediction error
AIC	Akaike's information criterion
SVD	singular value decomposition

Appendix A. Bayesian Framework to Estimate the TEPs

In this section, we present the state-of-the-art Bayesian approach used to obtain the unknown TEPs [23,24]. If n is the number of samples after a certain stimulus, we define the vectors as:

$$\begin{aligned} y &= [y_1, y_2, \ldots, y_n]^T \\ u &= [u_1, u_2, \ldots, u_n]^T \\ v &= [v_1, v_2, \ldots, v_n]^T \end{aligned} \tag{A1}$$

where y is the observable EEG samples, u is the unknown TEP elicited in response to a stimulus, and v is the noise affecting y.

Using the observation model,

$$y = u + v \tag{A2}$$

the aim is to recover u from y in Equation (A2). Assuming that u and v are uncorrelated zero-mean random vectors with "a priori" covariance matrices denominated by Σ_u and Σ_v, we can obtain the linear mean square estimate of u given y as follows:

$$\hat{u} = (\Sigma_v^{-1} + \Sigma_u^{-1})^{-1}\Sigma_v^{-1}y \tag{A3}$$

To solve Equation (A3), "a priori" covariance matrices Σ_v and Σ_u are required. The primary constituent of v is the EEG, which is widely recognized for its non-stationary nature. However, for brief intervals (e.g., 1–2 s), stationary AR models can be used for their description. Thus, Σ_v can be obtained as follows:

$$\Sigma_v = \sigma^2(A^TA)^{-1} \tag{A4}$$

where A is an n-dimensional Toeplitz matrix with its first column $[1, a_1, a_2, \ldots, a_p, 0, \ldots, 0]^T$, $\{a_k\}$ representing the coefficients of the AR model of order p, and σ^2 is the variance of the white noise process that drives the AR model. It is possible to numerically determine $\{a_k\}$, p, and σ^2 before each stimulus using a least-square method, such as the Yule–Walker approach. The optimal AR model order, i.e., p, is selected according to an information criterion, for example, the FPE or Akaike's information criterion (AIC) [74]. Considering the "a priori" known smoothness of the unknown TEP, it is possible to describe it as a realization of a stochastic process derived by the cascade of d integrators driven by a zero-mean white noise process with variance λ^2 [75]. This model can be described as

$$\Sigma_u = \lambda^2(F^TF)^{-1} \tag{A5}$$

where = $F = \Delta^d$, with Δ representing an n-dimensional lower-triangular Toeplitz matrix with its first column $[1, -1, 0, \ldots, 0]^T$.

By substituting Σ_v and Σ_u in Equation (A3), the equation is:

$$\hat{u} = (A^T A + \gamma F^T F)^{-1} A^T A y \tag{A6}$$

where $\gamma = \frac{\sigma^2}{\lambda^2}$ is the unknown "smoothing parameter". The Hall and Titterington criterion can be used to adjust the parameter γ until Equation (A7) is satisfied:

$$WRSS(\gamma) = \sigma^2 EDF(\gamma) \tag{A7}$$

where $WRSS(\gamma) = (y - \hat{u})^T A^T A (y - \hat{u})$ denotes the weighted residuals sum of squares, and $EDF(\gamma) = n - trace[A^T (A^T A + \gamma F^T F)^{-1} A]$ represents the so-called equivalent degree of freedom. Once we have provided $\hat{u}$ and obtained the estimation error as $\widetilde{u} = \hat{u} - u$, we obtained its covariance matrix, as a measure of the reliability of $\hat{u}$:

$$cov(\widetilde{u}) = \sigma^2 (A^T A + \gamma F^T F)^{-1} \tag{A8}$$

If $\hat{u}^i$ is the i-th filtered sweep and $\tilde{u}^i$ is the corresponding estimation error, the estimate of the TEP is defined as follows:

$$\bar{u} = \frac{\sum_{i=1}^{N} w_i \hat{u}^i}{\sum_{i=1}^{N} w_i} \tag{A9}$$

where w_i are the weights given by the inverse of $trace[cov(\tilde{u})^i]$.

Appendix B. Self-Tuning Optimized Kalman (STOK) Filter

A tvMVAR model can be specified in the form of:

$$Y_t = \sum_{k=1}^{p} A_{k,t} Y_{t-k} + \epsilon_t \tag{A10}$$

where $A_{k,t}$ are the AR matrices containing the time-varying model coefficients, ϵ_t is the zero mean white noise with covariance matrix Σ_ϵ, and p is the model order. In general, the state-space model can be used to estimate the unknown variables $A_{k,t}$ and Σ_ϵ, given by:

$$\begin{aligned} x_t &= \Phi_{t-1} x_{t-1} + \omega_{t-1} \\ z_t &= H_t x_t + v_t \end{aligned} \tag{A11}$$

where x_t is the system state, Φ is the transition matrix, ω_{t-1} is a zero-mean white noise of covariance Q, z_t is the observed data, H is the projection measurement matrix, and v_t is a zero-mean white noise (covariance R). The widely employed Kalman filter can effectively estimate the hidden state x and the error covariance at each time $(t = t_1, \ldots, t_T)$ by alternating between the prediction and the update step.

The state and the error covariance can be expressed as:

$$\begin{aligned} \hat{x}_t^{(-)} &= \Phi_{t-1} \hat{x}_{t-1}^{(+)} \\ P_t^{(-)} &= \Phi_{t-1} P_{t-1}^{(+)} \Phi_{t-1}^T + Q_{t-1} \end{aligned} \tag{A12}$$

where $\hat{x}_t^{(-)}$ and $P_t^{(-)}$ are the "a priori" state and error covariance at time t, based on the previous estimated state and covariance $\hat{x}_{t-1}^{(+)}$ and $P_{t-1}^{(+)}$. A posteriori estimates of the state and error are refined in the update step, as:

$$\begin{aligned} K_t &= P_t^{(-)} H_t^T (H_t P_t^{(-)} H_t^T + R_t)^{-1} \\ \hat{x}_t^{(+)} &= \hat{x}_t^{(-)} + K_t (z_t - H_t \hat{x}_t^{(-)}) \\ P_t^{(+)} &= (I - K_t H_t) P_t^{(-)} \end{aligned} \tag{A13}$$

where I is the identity matrix and K_t is the Kalman Gain matrix.

When dealing with neurophysiological time series, the Kalman filter's performance may not be guaranteed due to the absence of a known transition matrix Φ and measurements H. Additionally, the covariance matrices R and Q are unknown.

As a result, the STOK filter was introduced, eliminating the need for explicit assumptions about the covariance matrices R and Q. In Pascucci et al., the $HPH^T \approx cR$ relationship was considered. In particular, the error covariance matrix P, projected onto the measurement space H, is a scaled version of the measurement noise covariance R, with c being a tuning parameter. This assumption allows for a redefinition of the Kalman gain as follows:

$$\begin{aligned} K_t &= P_t^{(-)} H_t^T (H_t P_t^{(-)} H_t^T + R_t)^{-1} \\ &= H_t^+ c R_t (c R_t + R_t)^{-1} \\ &= c H_t^+ (c+1)^{-1} = \frac{c}{1+c} H_t^+ \end{aligned} \tag{A14}$$

where the apex + stands for the Moore–Penrose pseudoinverse. The state update becomes

$$\begin{aligned} \hat{x}_t^{(+)} &= \hat{x}_t^{(-)} + K_t (z_t - H_t \hat{x}_t^{(-)}) \\ &= \hat{x}_t^{(-)} + \frac{c}{1+c} H_t^+ (z_t - H_t \hat{x}_t^{(-)}) \\ &= \frac{\hat{x}_t^{(-)} + c H_t^+ z_t}{1+c} \end{aligned} \tag{A15}$$

where $\hat{x}_t^{(+)}$ is the weighted average of past predictions and the least-squares reconstruction. To prevent overfitting and reduce the model complexity, we use a singular value decomposition (SVD)-based method as described in [48].

References

1. Hellige, J.B.; Laeng, B.; Michimata, C. 13 Processing Asymmetries in the Visual System. In *The Two Halves of the Brain*; The MIT Press: Cambridge, MA, USA, 2010; p. 379.
2. Rosanova, M.; Gosseries, O.; Casarotto, S.; Boly, M.; Casali, A.G.; Bruno, M.A.; Mariotti, M.; Boveroux, P.; Tononi, G.; Laureys, S.; et al. Recovery of cortical effective connectivity and recovery of consciousness in vegetative patients. *Brain* **2012**, *135*, 1308–1320. [CrossRef] [PubMed]
3. Räty, S.; Ruuth, R.; Silvennoinen, K.; Sabel, B.A.; Tatlisumak, T.; Vanni, S. Resting-state Functional connectivity after occipital stroke. *Neurorehabilit. Neural Repair.* **2022**, *36*, 151–163. [CrossRef] [PubMed]
4. Lewis, P.M.; Thomson, R.H.; Rosenfeld, J.V.; Fitzgerald, P.B. Brain neuromodulation techniques: A review. *Neuroscientist* **2016**, *22*, 406–421. [CrossRef] [PubMed]
5. Antal, A.; Luber, B.; Brem, A.K.; Bikson, M.; Brunoni, A.R.; Kadosh, R.C.; Dubljevic, V.; Fecteau, S.; Ferreri, F.; Flöel, A.; et al. Non-invasive brain stimulation and neuroenhancement. *Clin. Neurophysiol. Pract.* **2022**, *7*, 146–165. [CrossRef]
6. Woods, A.J.; Antal, A.; Bikson, M.; Boggio, P.S.; Brunoni, A.R.; Celnik, P.; Cohen, L.G.; Fregni, F.; Herrmann, C.S.; Kappenman, E.S.; et al. A technical guide to tDCS, and related non-invasive brain stimulation tools. *Clin. Neurophysiol.* **2016**, *127*, 1031–1048. [CrossRef]
7. Somaa, F.A.; de Graaf, T.A.; Sack, A.T. Transcranial magnetic stimulation in the treatment of neurological diseases. *Front. Neurol.* **2022**, *13*, 793253. [CrossRef]

8. Lefaucheur, J.P.; Antal, A.; Ayache, S.S.; Benninger, D.H.; Brunelin, J.; Cogiamanian, F.; Cotelli, M.; De Ridder, D.; Ferrucci, R.; Langguth, B.; et al. Evidence-based guidelines on the therapeutic use of transcranial direct current stimulation (tDCS). *Clin. Neurophysiol.* **2017**, *128*, 56–92. [CrossRef]
9. Fregni, F.; El-Hagrassy, M.M.; Pacheco-Barrios, K.; Carvalho, S.; Leite, J.; Simis, M.; Brunelin, J.; Nakamura-Palacios, E.M.; Marangolo, P.; Venkatasubramanian, G.; et al. Evidence-based guidelines and secondary meta-analysis for the use of transcranial direct current stimulation in neurological and psychiatric disorders. *Int. J. Neuropsychopharmacol.* **2021**, *24*, 256–313. [CrossRef]
10. Pitcher, D.; Parkin, B.; Walsh, V. Transcranial magnetic stimulation and the understanding of behavior. *Annu. Rev. Psychol.* **2021**, *72*, 97–121. [CrossRef]
11. Hallett, M. Transcranial magnetic stimulation: A primer. *Neuron* **2007**, *55*, 187–199. [CrossRef]
12. Rossi, S.; Hallett, M.; Rossini, P.M.; Pascual-Leone, A.; Safety of TMS Consensus Group. Safety, ethical considerations, and application guidelines for the use of transcranial magnetic stimulation in clinical practice and research. *Clin. Neurophysiol.* **2009**, *120*, 2008–2039. [CrossRef]
13. Cao, K.X.; Ma, M.L.; Wang, C.Z.; Iqbal, J.; Si, J.J.; Xue, Y.X.; Yang, J.L. TMS-EEG: An emerging tool to study the neurophysiologic biomarkers of psychiatric disorders. *Neuropharmacology* **2021**, *197*, 108574. [CrossRef]
14. Formaggio, E.; Cavinato, M.; Storti, S.F.; Tonin, P.; Piccione, F.; Manganotti, P. Assessment of event-related EEG power after single-pulse TMS in unresponsive wakefulness syndrome and minimally conscious state patients. *Brain Topogr.* **2016**, *29*, 322–333. [CrossRef] [PubMed]
15. Farzan, F.; Bortoletto, M. Identification and verification of a 'true' TMS evoked potential in TMS-EEG. *J. Neurosci. Methods* **2022**, *38*, 109651. [CrossRef]
16. Mattavelli, G.; Rosanova, M.; Casali, A.G.; Papagno, C.; Lauro, L.J.R. Timing of emotion representation in right and left occipital region: Evidence from combined TMS-EEG. *Brain Cogn.* **2016**, *106*, 13–22. [CrossRef] [PubMed]
17. Taylor, P.C.J.; Thut, G. Brain activity underlying visual perception and attention as inferred from TMS–EEG: A review. *Brain Stimul.* **2012**, *5*, 124–129. [CrossRef]
18. Knight, R.; Mazzi, C.; Savazzi, S. Shining new light on dark percepts: Visual sensations induced by TMS. *Exp. Brain Res.* **2015**, *233*, 3125–3132. [CrossRef]
19. Knight, R.; Mazzi, C.; Savazzi, S. Assessing the effects of physical and perceived luminance contrast on RT and TMS-induced percepts. *Exp. Brain Res.* **2015**, *233*, 3527–3534. [CrossRef] [PubMed]
20. Tremblay, S.; Rogasch, N.C.; Premoli, I.; Blumberger, D.M.; Casarotto, S.; Chen, R.; Di Lazzaro, V.; Farzan, F.; Ferrarelli, F.; Fitzgerald, P.B.; et al. Clinical utility and prospective of TMS–EEG. *Clin. Neurophysiol.* **2019**, *130*, 802–844. [CrossRef] [PubMed]
21. Hernandez-Pavon, J.C.; Veniero, D.; Bergmann, T.O.; Belardinelli, P.; Bortoletto, M.; Casarotto, S.; Casula, E.P.; Farzan, F.; Fecchio, M.; Julkunen, P.; et al. TMS combined with EEG: Recommendations and open issues for data collection and analysis. *Brain Stimul.* **2023**, *16*, 567–593. [CrossRef]
22. Davila, C.E.; Mobin, M.S. Weighted averaging of evoked potentials. *IEEE Trans. Biomed. Eng.* **1992**, *39*, 338–345. [CrossRef]
23. Sparacino, G.; Milani, S.; Arslan, E.; Cobelli, C. A Bayesian approach to estimate evoked potentials. *Comput. Methods Programs Biomed.* **2002**, *68*, 233–248. [CrossRef]
24. D'Avanzo, C.; Schiff, S.; Amodio, P.; Sparacino, G. A Bayesian method to estimate single-trial event-related potentials with application to the study of the P300 variability. *J. Neurosci. Methods* **2011**, *198*, 114–124. [CrossRef]
25. Schriever, V.A.; Han, P.; Weise, S.; Hösel, F.; Pellegrino, R.; Hummel, T. Time frequency analysis of olfactory induced EEG-power change. *PLoS ONE* **2017**, *12*, e0185596. [CrossRef]
26. Güdücü, C.; Olcay, B.O.; Schäfer, L.; Aziz, M.; Schriever, V.; Özgören, M.; Hummel, T. Separating normosmic and anosmic patients based on entropy evaluation of olfactory event-related potentials. *Brain Res.* **2019**, *1708*, 78–83. [CrossRef] [PubMed]
27. Rosanova, M.; Casarotto, S.; Pigorini, A.; Canali, P.; Casali, A.G.; Massimini, M. Combining transcranial magnetic stimulation with electroencephalography to study human cortical excitability and effective connectivity. In *Neuronal Network Analysis: Concepts and Experimental Approaches*; Humana Press: Totowa, NJ, USA, 2012; pp. 435–457.
28. Hallett, M.; Di Iorio, R.; Rossini, P.M.; Park, J.E.; Chen, R.; Celnik, P.; Strafella, A.P.; Matsumoto, H.; Ugawa, Y. Contribution of transcranial magnetic stimulation to assessment of brain connectivity and networks. *Clin. Neurophysiol.* **2017**, *128*, 2125–2139. [CrossRef] [PubMed]
29. Ferreri, F.; Rossini, P.M. TMS and TMS-EEG techniques in the study of the excitability, connectivity, and plasticity of the human motor cortex. *Rev. Neurosci.* **2013**, *24*, 431–442. [CrossRef] [PubMed]
30. Manganotti, P.; Formaggio, E.; Storti, S.F.; De Massari, D.; Zamboni, A.; Bertoldo, A.; Fiaschi, A.; Toffolo, G.M. Time-frequency analysis of short-lasting modulation of EEG induced by intracortical and transcallosal paired TMS over motor areas. *J. Neurophysiol.* **2012**, *107*, 2475–2484. [CrossRef] [PubMed]
31. Manganotti, P.; Formaggio, E.; Del Felice, A.; Storti, S.F.; Zamboni, A.; Bertoldo, A.; Fiaschi, A.; Toffolo, G.M. Time-frequency analysis of short-lasting modulation of EEG induced by TMS during wake, sleep deprivation and sleep. *Front. Hum. Neurosci.* **2013**, *7*, 767. [CrossRef]
32. Chiarion, G.; Sparacino, L.; Antonacci, Y.; Faes, L.; Mesin, L. Connectivity Analysis in EEG Data: A Tutorial Review of the State of the Art and Emerging Trends. *Bioengineering* **2023**, *10*, 372. [CrossRef] [PubMed]
33. Luo, C.; Li, F.; Li, P.; Yi, C.; Li, C.; Tao, Q.; Zhang, X.; Si, Y.; Yao, D.; Yin, G.; et al. A survey of brain network analysis by electroencephalographic signals. *Cogn. Neurodyn.* **2022**, *16*, 17–41. [CrossRef]

34. Bakhshayesh, H.; Fitzgibbon, S.P.; Janani, A.S.; Grummett, T.S.; Pope, K.J. Detecting synchrony in EEG: A comparative study of functional connectivity measures. *Comput. Biol. Med.* **2019**, *105*, 1–15. [CrossRef]
35. Yi, C.; Chen, C.; Jiang, L.; Tao, Q.; Li, F.; Si, Y.; Zhang, T.; Yao, D.; Xu, P. Constructing EEG large-scale cortical functional network connectivity based on brain atlas by S estimator. *IEEE Trans. Cogn. Dev. Syst.* **2020**, *13*, 769–778. [CrossRef]
36. Friston, K.J. Functional and effective connectivity: A review. *Brain Connect.* **2011**, *1*, 13–36. [CrossRef]
37. Baccalá, L.A.; Sameshima, K. Partial directed coherence: A new concept in neural structure determination. *Biol. Cybern.* **2001**, *84*, 463–474. [CrossRef]
38. Kaminski, M.; Blinowska, K.J. The influence of volume conduction on DTF estimate and the problem of its mitigation. *Front. Comput. Neurosci.* **2017**, *11*, 36. [CrossRef] [PubMed]
39. Blinowska, K.J. Review of the methods of determination of directed connectivity from multichannel data. *Med. Biol. Eng. Comput.* **2011**, *49*, 521–529. [CrossRef] [PubMed]
40. Sameshima, K.; Baccala, L.A. *Methods in Brain Connectivity Inference through Multivariate Time Series Analysis*; CRC Press: Boca Raton, FL, USA, 2014.
41. Rubega, M.; Storti, S.F.; Pascucci, D. Chasing brain dynamics at their speed: What can time-varying functional connectivity tell us about brain function? *Front. Neurosci.* **2023**, *17*, 1223955. [CrossRef] [PubMed]
42. Chang, C.; Glover, G.H. Time–frequency dynamics of resting-state brain connectivity measured with fMRI. *Neuroimage* **2010**, *50*, 81–98. [CrossRef]
43. Hesse, W.; Möller, E.; Arnold, M.; Schack, B. The use of time-variant EEG Granger causality for inspecting directed interdependencies of neural assemblies. *J. Neurosci. Methods* **2003**, *124*, 27–44. [CrossRef]
44. Williams, N.J.; Daly, I.; Nasuto, S.J. Markov model-based method to analyse time-varying networks in EEG task-related data. *Front. Comput. Neurosci.* **2018**, *12*, 76. [CrossRef]
45. Pagnotta, M.F.; Plomp, G. Time-varying MVAR algorithms for directed connectivity analysis: Critical comparison in simulations and benchmark EEG data. *PLoS ONE* **2018**, *13*, e0198846. [CrossRef] [PubMed]
46. Storti, S.F.; Galazzo, I.B.; Khan, S.; Manganotti, P.; Menegaz, G. Exploring the epileptic brain network using time-variant effective connectivity and graph theory. *IEEE J. Biomed. Health Inform.* **2016**, *21*, 1411–1421. [CrossRef] [PubMed]
47. Sakoğlu, Ü.; Pearlson, G.D.; Kiehl, K.A.; Wang, Y.M.; Michael, A.M.; Calhoun, V.D. A method for evaluating dynamic functional network connectivity and task-modulation: Application to schizophrenia. *Magn. Reson. Mater. Physics. Biol. Med.* **2010**, *23*, 351–366. [CrossRef]
48. Pascucci, D.; Rubega, M.; Plomp, G. Modeling time-varying brain networks with a self-tuning optimized Kalman filter. *PLoS Comput. Biol.* **2020**, *16*, e1007566. [CrossRef] [PubMed]
49. Bagattini, C.; Mutanen, T.P.; Fracassi, C.; Manenti, R.; Cotelli, M.; Ilmoniemi, R.J.; Miniussi, C.; Bortoletto, M. Predicting Alzheimer's disease severity by means of TMS–EEG coregistration. *Neurobiol. Aging* **2019**, *80*, 38–45. [CrossRef]
50. Rogasch, N.C.; Thomson, R.H.; Daskalakis, Z.J.; Fitzgerald, P.B. Short-latency artifacts associated with concurrent TMS–EEG. *Brain Stimul.* **2013**, *6*, 868–876. [CrossRef]
51. Ragazzoni, A.; Pirulli, C.; Veniero, D.; Feurra, M.; Cincotta, M.; Giovannelli, F.; Chiaramonti, R.; Lino, M.; Rossi, S.; Miniussi, C. Vegetative versus minimally conscious states: A study using TMS-EEG, sensory and event-related potentials. *PLoS ONE* **2013**, *8*, e57069. [CrossRef]
52. Esposito, R.; Bortoletto, M.; Miniussi, C. Integrating TMS, EEG, and MRI as an approach for studying brain connectivity. *Neuroscientist* **2020**, *26*, 471–486. [CrossRef]
53. Bortoletto, M.; Veniero, D.; Thut, G.; Miniussi, C. The contribution of TMS–EEG coregistration in the exploration of the human cortical connectome. *Neurosci. Biobehav. Rev.* **2015**, *49*, 114–124. [CrossRef]
54. Okazaki, Y.O.; Mizuno, Y.; Kitajo, K. Probing dynamical cortical gating of attention with concurrent TMS-EEG. *Sci. Rep.* **2020**, *10*, 4959. [CrossRef] [PubMed]
55. López, J.G.; Hernandez-Pavon, J.C.; Lioumis, P.; Mäkelä, J.P.; Silvanto, J. State-dependent TMS effects in the visual cortex after visual adaptation: A combined TMS–EEG study. *Clin. Neurophysiol.* **2022**, *134*, 129–136. [CrossRef] [PubMed]
56. Rubinov, M.; Sporns, O. Complex network measures of brain connectivity: Uses and interpretations. *Neuroimage* **2010**, *52*, 1059–1069. [CrossRef] [PubMed]
57. Caeyenberghs, K.; Leemans, A.; Heitger, M.H.; Leunissen, I.; Dhollander, T.; Sunaert, S.; Dupont, P.; Swinnen, S.P. Graph analysis of functional brain networks for cognitive control of action in traumatic brain injury. *Brain* **2012**, *135*, 1293–1307. [CrossRef]
58. Mazzi, C.; Savazzi, S.; Abrahamyan, A.; Ruzzoli, M. Reliability of TMS phosphene threshold estimation: Toward a standardized protocol. *Brain Stimul.* **2017**, *10*, 609–617. [CrossRef]
59. Kammer, T.; Puls, K.; Erb, M.; Grodd, W. Transcranial magnetic stimulation in the visual system. II. Characterization of induced phosphenes and scotomas. *Exp. Brain Res.* **2005**, *160*, 129–140. [CrossRef]
60. Rogasch, N.C.; Sullivan, C.; Thomson, R.H.; Rose, N.S.; Bailey, N.W.; Fitzgerald, P.B.; Farzan, F.; Hernandez-Pavon, J.C. Analysing concurrent transcranial magnetic stimulation and electroencephalographic data: A review and introduction to the open-source TESA software. *Neuroimage* **2017**, *147*, 934–951. [CrossRef]
61. Dong, L.; Li, F.; Liu, Q.; Wen, X.; Lai, Y.; Xu, P.; Yao, D. MATLAB toolboxes for reference electrode standardization technique (REST) of scalp EEG. *Front. Neurosci.* **2017**, *11*, 601. [CrossRef]
62. Ben-Shachar, M. *TBT: Reject and Interpolate Channels on a Epoch by Epoch Basis (2.6.1)*; Zenodo: Geneva, Switzerland, 2020.

63. Takahashi, D.Y.; Baccalá, L.A.; Sameshima, K. Information theoretic interpretation of frequency domain connectivity measures. *Biol. Cybern.* **2010**, *103*, 463–469. [CrossRef]
64. Rubega, M.; Carboni, M.; Seeber, M.; Pascucci, D.; Tourbier, S.; Toscano, G.; Van Mierlo, P.; Hagmann, P.; Plomp, G.; Vulliemoz, S.; et al. Estimating EEG source dipole orientation based on singular-value decomposition for connectivity analysis. *Brain Topogr.* **2019**, *32*, 704–719. [CrossRef]
65. Broca, P. Nouvelle observation d'aphémie produite par une lésion de la moitié postérieure des deuxième et troisième circonvolutions frontales. *Bull. Soc. Anat. Paris* **1861**, *36*, 398–407.
66. Mazzi, C.; Savazzi, S. The glamor of old-style single-case studies in the neuroimaging era: Insights from a patient with hemianopia. *Front. Psychol.* **2019**, *10*, 965. [CrossRef] [PubMed]
67. Hellige, J.B. Hemispheric asymmetry for visual information processing. *Acta Neurobiol. Exp.* **1996**, *56*, 485–497.
68. Garcia, J.O.; Grossman, E.D.; Srinivasan, R. Evoked potentials in large-scale cortical networks elicited by TMS of the visual cortex. *J. Neurophysiol.* **2011**, *106*, 1734–1746. [CrossRef]
69. Chokron, S.; Perez, C.; Peyrin, C. Behavioral consequences and cortical reorganization in homonymous hemianopia. *Front. Syst. Neurosci.* **2016**, *10*, 57. [CrossRef]
70. Proverbio, A.M.; Zani, A. Hemispheric asymmetry in visual processing: An ERP study on spatial frequency gratings. *Symmetry* **2021**, *13*, 180. [CrossRef]
71. Ruff, C.C.; Blankenburg, F.; Bjoertomt, O.; Bestmann, S.; Weiskopf, N.; Driver, J. Hemispheric differences in frontal and parietal influences on human occipital cortex: Direct confirmation with concurrent TMS–fMRI. *J. Cogn. Neurosci.* **2009**, *21*, 1146–1161. [CrossRef]
72. Fink, G.R.; Halligan, P.W.; Marshall, J.C.; Frith, C.D.; Frackowiak, R.; Dolan, R.J. Neural mechanisms involved in the processing of global and local aspects of hierarchically organized visual stimuli. *Brain A J. Neurol.* **1997**, *120*, 1779–1791. [CrossRef]
73. Jarczok, T.A.; Roebruck, F.; Pokorny, L.; Biermann, L.; Roessner, V.; Klein, C.; Bender, S. Single-pulse TMS to the temporo-occipital and dorsolateral prefrontal cortex evokes lateralized long latency EEG responses at the stimulation site. *Front. Neurosci.* **2021**, *15*, 616667. [CrossRef]
74. Cobelli, C.; Foster, D.; Toffolo, G. *Tracer Kinetics in Biomedical Research: From Data to Model*; Springer Science & Business Media: Berlin/Heidelberg, Germany, 2007.
75. De Nicolao, G.; Sparacino, G.; Cobelli, C. Nonparametric input estimation in physiological systems: Problems, methods, and case studies. *Automatica* **1997**, *33*, 851–870. [CrossRef]

sensors

Article

Domain-Specific Processing Stage for Estimating Single-Trail Evoked Potential Improves CNN Performance in Detecting Error Potential

Andrea Farabbi and Luca Mainardi *

Department of Electronics, Information and Bioengineering, Politecnico di Milano, 20133 Milan, Italy; andrea.farabbi@polimi.it
* Correspondence: luca.mainardi@polimi.it

Abstract: We present a novel architecture designed to enhance the detection of Error Potential (ErrP) signals during ErrP stimulation tasks. In the context of predicting ErrP presence, conventional Convolutional Neural Networks (CNNs) typically accept a raw EEG signal as input, encompassing both the information associated with the evoked potential and the background activity, which can potentially diminish predictive accuracy. Our approach involves advanced Single-Trial (ST) ErrP enhancement techniques for processing raw EEG signals in the initial stage, followed by CNNs for discerning between ErrP and NonErrP segments in the second stage. We tested different combinations of methods and CNNs. As far as ST ErrP estimation is concerned, we examined various methods encompassing subspace regularization techniques, Continuous Wavelet Transform, and ARX models. For the classification stage, we evaluated the performance of EEGNet, CNN, and a Siamese Neural Network. A comparative analysis against the method of directly applying CNNs to raw EEG signals revealed the advantages of our architecture. Leveraging subspace regularization yielded the best improvement in classification metrics, at up to 14% in balanced accuracy and 13.4% in *F1-score*.

Keywords: Brain–Computer Interface; signal processing; electroencephalography; Error Potential; Single-Trial analysis; deep learning; machine learning

Citation: Farabbi, A.; Mainardi, L. Domain-Specific Processing Stage for Estimating Single-Trail Evoked Potential Improves CNN Performance in Detecting Error Potential. *Sensors* **2023**, *23*, 9049. https://doi.org/10.3390/s23229049

Academic Editor: Yifan Zhao

Received: 2 October 2023
Revised: 30 October 2023
Accepted: 3 November 2023
Published: 8 November 2023

1. Introduction

The development of Brain–Computer Interface (BCI) systems holds promise for a wide range of applications, from assisting individuals with disabilities to enhancing human–computer interaction in various domains [1].

In this, Electroencephalography (EEG) has played a pivotal role in BCI research, providing a non-invasive means of capturing neural activity with high temporal resolution [2]. In particular, the Error Potential (ErrP) has gained attention due to its ability to optimize BCI system performance [3]. The ErrP is an Evoked Potential (EP) that represents the neural response associated with the detection and elaboration of mistakes made by the subject itself, by another subject, or by a machine [4]. The activity is located in the medio-frontal areas of the brain, in particular in the anterior cingulate cortex; depending on the task, different ErrPs types can be distinguished. Their realization follows a stereotypical shape characterized by a negative peak occurring at 250 ms after the error, a positive peak at 320 ms, and another negative peak at 450 ms. In the frequency domain, the EEG signal recorded after the erroneous event is particularly localized in the δ (1–3 Hz) and θ (5–8 Hz) brain rhythms [5].

The ErrP holds significant value within BCI systems, serving as a critical resource for rectifying the system's erroneous outputs and enhancing overall performance [6]. Consequently, the extraction of the ErrP waveform from the EEG signal represents a crucial step; however, achieving precise separation of the ErrP from the underlying EEG background remains a non-trivial and complex challenge [7,8].

1.1. ErrP Classification by NN

Recently, the problem of distinguishing between ErrP and Non-ErrP epochs has been approached using Deep Learning algorithms, particularly Convolutional Neural Networks (CNNs).

The study in [9] employed a CNN specifically fine-tuned for ErrP recognition. The architecture of this CNN comprised four convolutional blocks, rendering it a deep CNN (DNN). The network's input consisted of EEG signals epoched in the second following the erroneous stimulus. The signal preprocessing was standard, involving common average re-referencing, band-pass filtering within the desired frequency range, and the exclusion of corrupted electrodes. Furthermore, only the Cz and FCz channels were selected as the input to the CNN, neglecting information from other channels. The results obtained from a publicly available dataset demonstrated test accuracy performance of up to 86.1%.

Lawhern et al. [10] introduced a novel CNN called EEGNet. This CNN is versatile and has been tested across different BCI paradigms (e.g., ErrP, P300, Motor Imagery). The proposed architecture is simple, comprising only two convolutional blocks for frequency and spatial filtering. The low dimension of the architecture facilitates training even with limited data, a significant advantage when working with deep learning algorithms. ErrP prediction results were presented in terms of accuracy following four-fold cross-validation, with the authors claiming performance of up to 83%. In this case, the input signals underwent minimal preprocessing restricted to band-pass filtering within the frequency band of interest (i.e., 1–40 Hz).

In [11], the authors compared the ErrP classification results achieved by using a simple CNN with two different inputs: signals recorded at electrodes Cz and FCz, and signals from all 64 channels. Additionally, they compared the proposed architecture with more traditional machine learning algorithms, i.e., Support Vector Machine, Gaussian classifiers, and Deep Belief Networks. EEG signal preprocessing included frequency filtering, artifact removal using Independent Component Analysis, whitening, and cropping. Their architecture outperformed other baseline methods in terms of validation accuracy, reaching a performance of up to 84.4%. Notably, the best performance was attained when using information from all channels as input to the CNN.

Luo et al. [12] utilized a simple and compact CNN with two convolutional blocks to identify ErrP epochs, which were subsequently used as training data for a reinforcement learning algorithm. The authors applied notch filtering at 50 Hz to reduce interference and applied band-pass filtering within the range of 0.1–30 Hz. The study reported performance in distinguishing ErrP and Non-ErrP epochs in terms of Area Under the Curve (AUC) in the test set, achieving results of up to 88%.

Lastly, we mention the work presented in [13], where the authors proposed a Siamese Neural Network for a four-class problem in predicting Motor Imagery (MI) events. Although this study did not primarily focus on ErrP, the obtained results and adopted architecture hold promise. The authors introduced a neural network scheme in which two identical CNNs were trained in order to determine whether the input of one CNN matched that of the other. The paper did not describe any specific preprocessing steps applied to the data. The results for the multi-class problem were presented as the classifier's performance compared to random labeling of unseen trials, reaching a performance of up to 86.1% on the test set.

All of these studies share the same approach in common, involving a minimal EEG pre-processing step followed by a CNN/DNN classification stage. This methodology entrusts all domain-specific processing to the CNN/DNN stage, making the DNN tasks more difficult and potentially having detrimental impacts on the classification performance.

1.2. Single Trial-Estimation

Different approaches and techniques have been proposed in the literature, ranging from traditional signal averaging to more advanced spatial filtering and time–frequency analysis. The most trivial technique is the Grand Average [14], which consists of averaging the epochs of interest in order to zero out the contribution of the background EEG and emphasize the EP content. However, the main drawback of this method is that the information of the Single Trial (ST) is lost; thus, this approach cannot by applied for real-time detection of the EP of interest [15]. Moreover, the SNR of the signal obtained with this technique is highly dependent on the number of epochs used for averaging. Other methods use more sophisticated filters in order to estimate the ST-ErrP. The first technique presented for ST analysis is ARX modeling [16], a method which estimates the ErrP-ST as a filtered version of the reference ErrP waveform. However, this method finds little application in real-time procedures, as estimating a new ARX model stimulus-by-stimulus can be a computationally demanding and time-consuming procedure.

Denoho et al. [17] proposed a method for estimating ErrP-ST based on the Wavelet Continuous Transform (CWT) and the Mallat algorithm [18]. With these methods, it is possible to decompose the signal at different frequency scales, thereby obtaining detailed and approximated versions of the signal in different frequency bands. At each scale, a set of coefficients is obtained and compared to a threshold by retaining those coefficients related to ErrP and eliminating those related to the background EEG. However, the selection of an appropriate threshold is highly empirical, and the method may not be robust for all applications.

Another interesting method for EP extraction is subspace regularization [19]. Through Bayesian estimation, it is possible to extract the ST from the EEG signal. The computation of the ST epoch is fast, making it suitable for real-time purposes. In the literature, the technique has been found to work well with different types of EPs. However, the main drawback of this method is that a robust estimate of the background is required (i.e., ARX modeling for estimating the background [20]), which can introduce additional computational time.

1.3. Aim of This Study

In this work, we hypothesize that the potential of ST techniques for domain-specific filtering of EEG data can be beneficial in improving the classification of ErrP vs. non-ErrP epochs as performed by CNNs. To validate this hypothesis, we have developed a novel architecture that integrates a domain-specific block used for ErrP-ST estimation into the conventional EEG classification framework consisting of initial EEG preprocessing followed by CNN classification. We demonstrate that the incorporation of this new block can significantly enhance the performance of the CNN classifier.

2. Materials and Methods

This section describes the pre-processing performed on the EEG signal to extract the epochs of interest, the different methods used for ST-ErrP extraction, and the classification performed by different CNNs. These steps are summarized in the pipeline shown in Figure 1 are described in detail in the following sections.

2.1. EEG Dataset

We analyzed EEG data contained in the open access BCI dataset *BNCI Horizon 2020: Monitoring error-related potentials* [21].

This dataset consists of EEG recordings obtained during an ErrP-specific experiment performed on six subjects (mean age 27.83 ± 2.23) in two recording sessions [22].

The experimental paradigm consisted of reaching a target (i.e., a colored square) through a moving cursor. The working area involved twenty possible horizontal positions at which the cursor and the target square could be located. At each time step of 2 s each, the cursor moves a step toward the target. When the target is reached, the cursor remains in place and a new target location appears. Subjects were asked to monitor the position of the cursor without having any control over it, knowing that the objective is to reach the target. In order to elicit the ErrP, there is a 20% probability at each time step of the cursor being moved in the wrong direction.

Each recording session consisted of ten blocks of 3 min each, including approximately fifty cursor movements per block. Subjects performed two recording sessions with a gap of several weeks. For each session, the EEG signal was recorded (512 Hz sampling frequency) with 64 electrodes using a BioSemi ActiveTwo system. Electrodes were placed according to the 10–20 International System.

This data-set is largely unbalanced, being constituted by 6437 epochs, of which only 1322 include the ErrP.

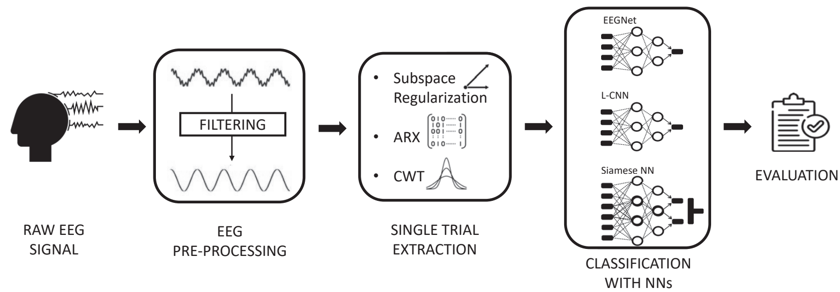

Figure 1. Pipeline of the employed methods. The novelty of our approach consists in the introduction of a Single Trial Extraction block between the EEG preprocessing stage and the NN classification stage.

2.2. Data Preprocessing

A preprocessing pipeline was defined to extract the segments of the signal (epochs) localized just after the presentation of the feedback in which the ErrP may be present. Raw EEG data were spatially filtered with the Common Average Reference (CAR) approach and then band-pass filtered using an FIR filter in the range [1 40] Hz (as suggested in [5]), as the ErrP can be considered a relatively slow cortical potential. Data were then downsampled at 64 Hz and divided into epochs covering the interval $[-1\ \ 1]$s from the instant of cursor movement. This range was chosen in order to include the pre-stimulus window and cover the expected latency/duration of the ErrP signal [5].

In view of the real-time application of the proposed method and in order to ensure an easy and low-computation procedure, no removal of artifacts, eye blinking, or eye movement was employed. While most of the methods for ErrP detection/classification [23] have analyzed data from FCz and Cz channels only, we processed all of the channels in order to include all the information captured by the electrodes.

2.3. Single-Trial Estimation

The epochs were then processed using different ST estimate techniques: the subspace regularization method, ARX modeling, and Continuous Wavelet Transform, which are described in the following subsections.

2.3.1. Subspace Regularization

This method was first introduced in [19] to separate the ErrP waveform from the background ECG noise by incorporating second-order statistical information, specifically, the variances of the evoked potentials. The main concept is to devise a filter that can effectively enhance the signal of interest from among the extraneous brain activity that is unrelated to the mechanisms generating the ErrP. Through this regularization approach, provided that applicable density assumptions for both the signal and noise are satisfied, the obtained solutions can be viewed as Bayesian point estimates. It has been ascertained that the signal under observation (z) is a combination of the signal of relevance (s) and interference (v), which is commonly referred to as spontaneous EEG. The model is

$$z = s + v = H\theta + v, \tag{1}$$

where H is a matrix with columns that are p basis functions ψ_i to be selected according to the specific problem; moreover,

$$H = (\psi_1, ..., \psi_p) \tag{2}$$

where the basis functions are Gaussian-shaped components preselected for their shape and varied in terms of their delays (τ_i), i.e.,

$$\psi_i = e^{-\frac{1}{2d^2}(t-\tau_i^2)}, \tag{3}$$

where $d = 0.1$ is the width parameter and the number of basis functions p is set to 20. The ErrP for the individual tests is determined using the following formula:

$$\hat{s} = (I + \alpha_2^2 D_d^T D_d)^{-1} H (H^T C_v^{-1} H + \alpha^2 H^t (I - K_s K_s^T) H)^{-1} H^T C_v^{-1} z \tag{4}$$

where α and α_2 are regularization terms obtained empirically (set to 0.01 and 10, respectively, in our study), D is the second difference matrix, C_v is the estimate of the covariance matrix of the noise, and K_s is the matrix of the first eight eigenvectors of the correlation matrix of the recorded signal z. To estimate the properties of the background, we modified the original method, which employed an ARX estimate, to simply use the EEG signal recorded in the second before the stimulus. It is reasonable to assume that the properties of the background EEG during the stimulus do not significantly change from the second before the stimulus itself. This choice was motivated by the need to reduce computational burden in the view of the online application of our method.

2.3.2. ARX Modeling

The ARX model for single-sweep estimation is presented in [16]. The recorded EEG signal can be described by the following equation:

$$y_i(t) = \sum_{j=1}^{p} a_j y_i(t-j) + \sum_{k=1}^{q} b_k u(t-k-d) + e_i(t), \tag{5}$$

where the a_js and b_ks are the model coefficients for the AR and exogenous parts, respectively, p and q are the model orders, and d is a delay lag. The model is fed by $e_i(t)$, e.g., a white noise process.

The AR part of Equation (5) is used to model the background EEG activity (not related to error processing), while the exogenous input $u(\cdot)$ is used to model the expected waveform of the ErrP, and is commonly obtained by synchronous averaging of the epochs containing ErrP. The model in Equation (5) can be rewritten in the z-transform domain, as follows:

$$Y_i(z) = \underbrace{\frac{B_i(z)}{A_i(z)} U(z)}_{ErrP} + \underbrace{\frac{1}{A_i(z)} E_i(z)}_{Background\ EEG} \tag{6}$$

where it emerges from the similarity with Equation (1) that the ErrP is obtained as a filtered version of the exogenous input $U(z)$, while the EEG is modeled as a colored version of a Gaussian white noise process. After having estimated $u(\cdot)$ for each patient, the model can be identified by estimating the coefficients a_j and b_k, the polynomial order p and q, and the delay d. To identify the coefficients, a *least square method* approach is performed to minimize the following figure of merit:

$$F_i(t) = \frac{1}{N} \sum_{j=1}^{N} (y_i(t) - \hat{y}_i(t))^2, \tag{7}$$

where N is the number of time samples, $y_i(t)$ is the signal itself, and $\hat{y}_i(t)$ is the model's prediction.

The optimal model orders are selected as those resulting from the minimization of the Akaike Information Criterion (AIC). The model identification is repeated at each i-th epoch and each single evoked response is described through a different model.

2.3.3. Continuous Wavelet Transform

The CWT method was presented by Ahmadi et al. [24] and is based on the Donoho ST estimate technique [17]. The wavelet transform is the inner product of a signal with dilated and translated versions of a wavelet function. For a given signal $x(t)$ and wavelet function $\psi_a, b(t)$, the Continuous Wavelet Transform (CWT) is defined as follows:

$$W_\psi X(a,b) =< x, \psi_{a,b} >, \tag{8}$$

$$\psi_{a,b} = |a|^{-\frac{1}{2}} \psi(\frac{t-b}{a}), \tag{9}$$

where $a, b \in \mathbb{R}$ are the scale and translation parameters, respectively. Through the Mallat algorithm, the details and approximation of the signal can be obtained at different scales with corresponding coefficients. The original work [24] identified a five-scale decomposition and a quadratic B-Spline wavelet as being the most suitable for EP analysis. The CWT is very redundant; without incurring any loss of information, it is more practical to define the wavelet transform only at a discrete set of scales $a_j = 2^j$ and times $b_{j,k} = 2^j k$, thereby obtaining the Dyadic Wavelet Transform (DWT).

The estimation of ErrP is obtained by removing the EEG activity through denoising, which is implemented by selecting DWT coefficients based on scale-dependent thresholding. At each scale j, the threshold is computed as

$$T_j^2 = \sigma_j^2 \sqrt{2 \log_e N}, \tag{10}$$

where σ_j is the estimate of the standard deviation of the noise and N is the number of wavelet coefficients. In order to incorporate information from the neighboring coefficients, the thresholding criterion is as follows:

$$X_{den}(j,k) = \begin{cases} X(j,k) & \text{if } X_{j,k-1}^2 + X_{j,k}^2 + X_{j,k+1}^2 > T_j^2 \\ 0 & \text{if } X_{j,k-1}^2 + X_{j,k}^2 + X_{j,k+1}^2 \leq T_j^2 \end{cases} \tag{11}$$

Moreover, the original authors introduced a dependency between coefficients at coarser scales and those at finer scales such that a coarser coefficient is removed, then its "children" in the finer scales are removed as well. First, the coefficients are selected using the grand average of the epochs of interest as the input signal, then the same coefficients are selected in order to denoise the single epochs and emphasize the ErrP part.

2.4. Classification

Classification of ErrP versus non-ErrP epochs was obtained by three CNN architectures: EEGNet [10], the CNN presented by Luo et al. [12], and a Siamese Neural Network. All of these CNNs have been reported to achieve good performance for BCI purposes, especially for the detection of ErrP epochs. The models obtained with the three architectures were fitted using the *Adam* algorithm defined in [25] and while minimizing the *binary cross-entropy*. They were trained through 300 epochs with a batch size of 16 on an NVIDIA GeForce RTX 2060 GPU. To evaluate the classifier performances, two approaches were followed, namely, population-wise and subject–wise. In the former, all subject data were considered as a unique dataset, while in the latter each subject was considered singularly.

The dataset was shuffled to eliminate any bias related to the sequence of stimulus, then partitioned, with 20% of the data used as a test set and the remaining data subdivided into

80% in the training set and 20% in the validation set. Stratified five-fold cross-validation was performed on the validation set. A majority vote approach was employed to obtain the prediction label for the test set, which was chosen to ensure that it could outperform the best classifier if the classifiers made independent errors [26].

The training set was balanced to obtain an equal amount of epochs for each class. In particular, the ARX balancing technique introduced in [27] was used, as it has previously been found to be robust, especially in ErrP applications.

The three CNNs we used are described in the following subsections.

2.4.1. EEGNet

EEGNet was chosen because of its proven ability to generalize across different EEG-based BCI paradigms, including the ErrP classification, and because it presents a limited number of trainable parameters. The main peculiarity of this network is that it includes both depthwise and separable convolution layers, which are usually adopted in computer vision [28] to find the optimal volume-wise filters while having a reduced number of parameters compared to the classical convolution filter approach.

The architecture can be subdivided into three blocks; the last is a fully connected layer, while the others include dropout and batch normalization layers to prevent overfitting along with pooling layers to reduce the size of the data.

2.4.2. L–CNN

The L-CNN architecture has two convolutional layers, one pooling layer, and one dense layer. The first convolutional layer is employed across the discretized samples to extract temporal features (width = 276) and the second across the electrodes to extract spatial features (width = 276). The temporal convolutional layer has a smaller kernel size (25×1) than the spatial convolutional layer (64×40), allowing for a larger range of transformations in this layer. The following mean pooling layer with a kernel size of 75×1 prevents overfitting. The final dense layer contains a 40×12 size feature map and outputs two predicted labels (correct or incorrect) using a logarithmic activation function.

2.4.3. Siamese Neural Network

Based on the encouraging outcomes demonstrated in [13], we made the decision to explore the influence of the Short-Time (ST) estimate when employing a Siamese Neural Network. The architecture we constructed closely resembles the one outlined in the cited study, with a few customizations for our specific needs. These adaptation were necessary because the original study utilized the covariance matrix of the EEG signal as input for the classifier, whereas we directly used the EEG signal itself.

The Siamese Neural Network that we used consisted of two identical CNNs sharing the same parameters and hyperparameters. Each CNN is structured with two successive convolutional layers followed by two fully connected layers. We computed the Euclidean distance from the features extracted by these two CNNs, then employed this metric to determine whether or not the inputs to the two CNNs belonged to the same class. Training was carried out on all conceivable pairs of observations from the training set. To classify a new observation, we paired it with each observation from the training set. With the knowledge of the labels of the training data, we used a majority voting strategy to predict the class of new observations.

It is noteworthy that we made a deliberate choice not to apply any data augmentation techniques for this particular classifier. This decision was made in order to ensure that the comparison between pairs of observations remained exclusive to the original data, without the introduction of any synthetic data.

2.4.4. Hyperparameter Optimization

To improve classification performance, a hyperparameters optimization process was performed. The pipeline was divided into four cycles, each one optimizing a different set of hyperparameters. Table 1 reports the different cycles and related sets of hyperparameters.

Table 1. Hyperparameter optimization: in each cycle, a different set of hyperparameters is optimized, with each set being composed of related hyperparameters. If convergence or a high number of iterations is reached, the cycle is considered to be optimized.

First Cycle	Second Cycle	Third Cycle	Fourth Cycle
learning rate iterative method batch size	pooling layer dropout layer activation layer	conv layers size (F1, D, F2)	dropout rate momentum learning decay

Each cycle included groups of hyperparameters related to one another; for instance, the hyperparameters involving the number of filters of the layers were included in the same testing cycle. The cycles were numbered to ensure that the first cycle would optimize the most important hyperparameters (i.e., the ones with the greatest affect on performances). The cycle was stopped when convergence was reached for a set of hyperparameters or after a high number of repetitions. Optimization was performed through *grid search* for those hyperparameters with a range known a priori; otherwise, a *random search* was performed. The metric used for optimization purposes was the *F1-score*.

Hyperparamater optimization was performed separately for each subject and for the population as a whole; thus, different sets of parameters were obtained for each analysis.

2.4.5. Performance Metrics

The classification performance was evaluated using three different metrics: balanced accuracy, *F1-score*, and utility gain.

Balanced accuracy and *F1-score* were computed due to the dataset being highly unbalanced, which makes erroneous events much more rare than correct actions. When dealing with an unbalanced dataset, these metrics are preferable to accuracy, which is biased in such cases and does not represent the classifier's real performance.

The utility gain is a metric introduced in [29] that represents the potential gain when introducing an error correction system in a BCI system. It is computed as follows:

$$g(p) = \frac{pr_C + (1-p)r_E + p - 1}{2p - 1}, \tag{12}$$

where p is the performance of the BCI system with no correction, r_C is the recall of correct events, and r_E is the recall of erroneous events, with the latter two respectively computed using the following formulas:

$$r_C = \frac{TN}{TN + FP} \tag{13}$$

$$r_E = \frac{TP}{TP + FN} \tag{14}$$

In particular, a utility gain higher than 1 indicates an improvement in BCI performance through the correction system, while a value lower than 1 indicates that it is counterproductive compared to the original BCI system.

3. Results

3.1. Classification Performance

This section reports the performance of the proposed two-stage procedure for classifying ErrP versus non-ErrP epochs. The results for the EEGNet, L-CNN, and Siamese Neural Network are presented separately in Sections 3.1.1, 3.1.2, and 3.1.3, respectively. Our results are presented as a series of graph, each containing both subject-wise results (one for each subject) and population-based results (identified by the label *All Subjects*).

3.1.1. EEGNet

The performance when using EEGNet to distinguish between ErrP and Non-ErrP classes is reported in Figure 2 in terms of the *F1-score* and balanced accuracy computed on the test set. The last group of bar plots, shown by the the black line on the right-hand side of each graph, is used to indicate the results obtained in the population-wise training.

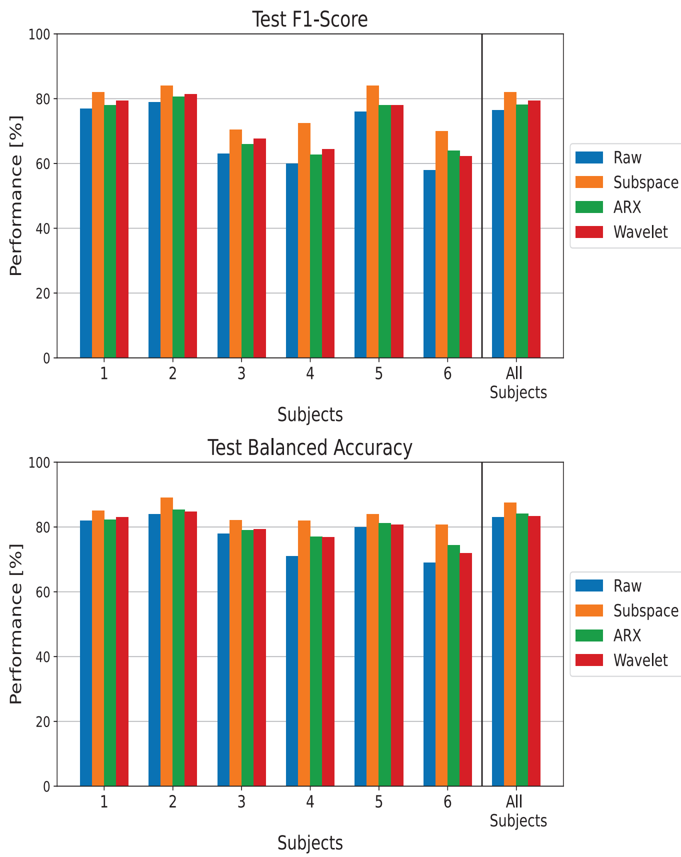

Figure 2. Performance metrics on the test set when using EEGNet as a classifier. The metrics are reported for each processing technique and in both subject-wise and population-wise analysis. The balanced accuracy and *F1-score* are reported for completeness.

In both the subject-wise and population-wise analysis, all the ST estimators led to an increase of performance compared to using raw data as input to the CNN classifier (the blue bar). This behaviour is observable for both the *F1-score* and balanced accuracy metrics. The largest increase in the metrics can be observed for subjects 4 and 6. For these two subjects, there are respective increases of 11% and 11.8% in terms of balanced accuracy and of 12.5% and 12% in terms of the F1-score. Notably, these two patients were had the two worst performances when feeding raw EEG data to the CNN. It is worth noting that the Subspace Regularization method resulted in the highest performance for all subjects (the orange lines in the figure).

The performance in terms of utility gain is reported in Figure 3, showing the improvement introduced by a correction system based on ErrP detection for a BCI with initial performance p in the range of 70–100%. In each graph, the curve above the others identifies the best-performing model. For all subjects and for the population-wise analysis (the bottom-right plot in Figure 3), most of the curves are above the blue line, demonstrating the utility of adding an ST-ErrP estimator stage. Among the ST methods, there was a slightly larger improvement when using the subspace regularization method (the orange curves). In particular, this method introduces a "productive" gain (i.e., $g(p) > 1$) until a baseline performance of 90% is reached. It can be seen that this result is more prominent for subjects 4 and 6.

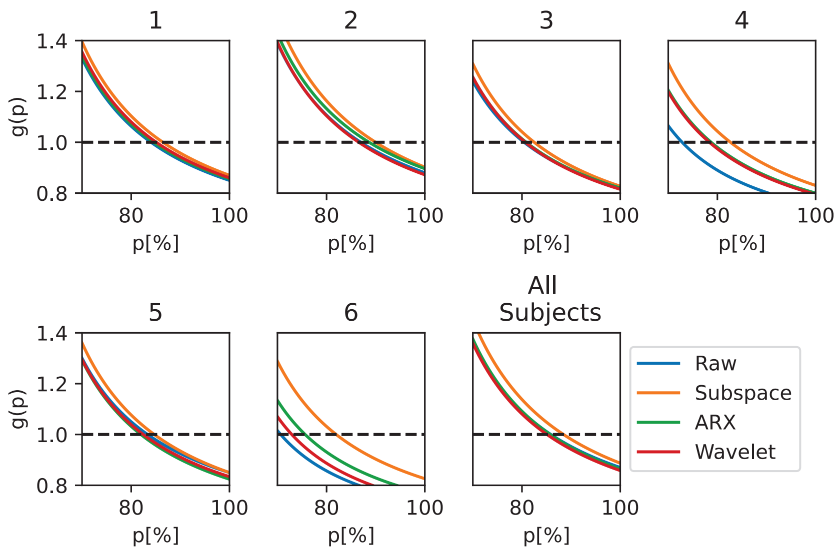

Figure 3. Utility Gain when using EEGNet as a classifier and applying different techniques for ST estimation. The metric is reported for the subject-wise and population-wise analysis for only p values over 70%, as no major differences were observed outside of this range.

3.1.2. L-CNN

Similar to the EEGNet results, we now report the results for the L-CNN classifier in Figure 4. An improvement in all metrics can be observed when the ST-ErrP extraction stage is performed. Similar to EEGNet, subspace regularization introduces the highest improvements for all metrics in most of the subjects as well as in the population-wise analysis. In particular, subjects 4 and 6 experience the highest gain in terms of performance, at 13.5% and 13% in terms of balanced accuracy and 12.8% and 12% in terms of *F1-score*, respectively. The main difference between these results and those obtained when using EEGNet is observed for subjects 1 and 5, where the CWT method method leads to the greatest improvements in performance.

The utility gain curves for the L-CNN classifier are shown in Figure 5; again, they show that the introduction of a correction system with subspace regularization for ST estimate improves the BCI performance in most cases, resulting in higher accuracy compared to the other techniques. This is particularly apparent for subjects 4 and 6, where a $g(p) > 1$ is measured until $p = 84.7\%$ and $p = 83.9\%$, respectively. For the other performance metrics, in terms of the utility gain, subjects 1 and 5 show more improvement when using the CWT to estimate the ST.

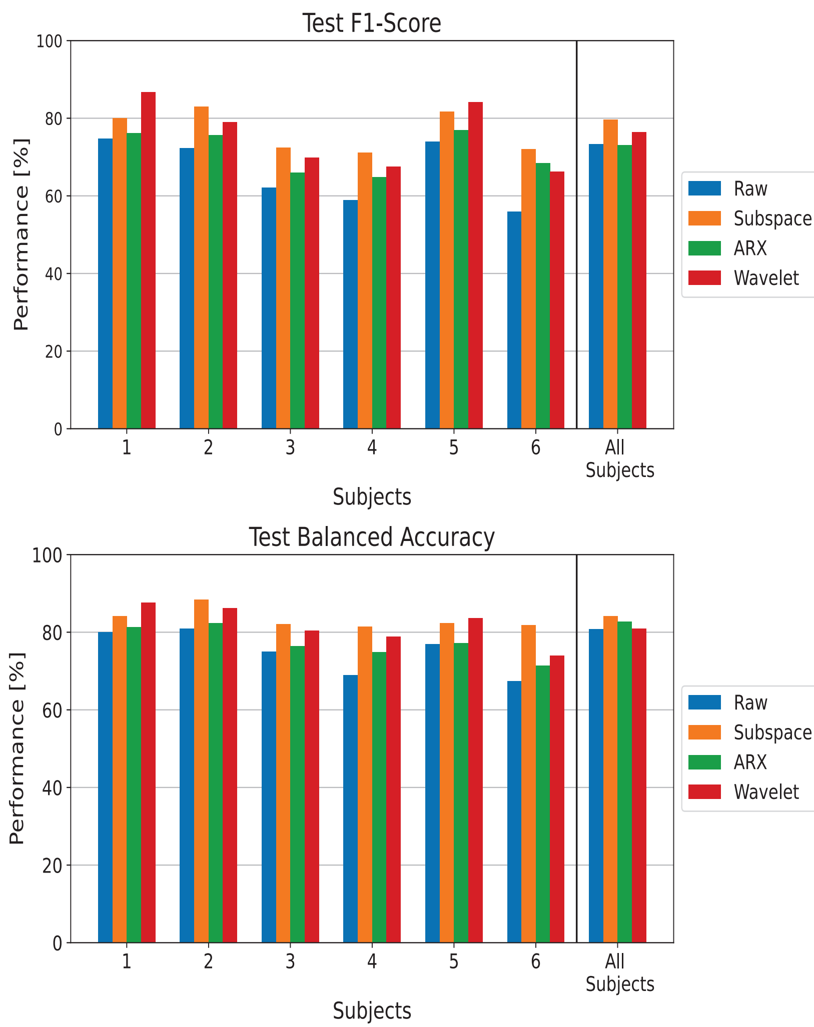

Figure 4. Performance metrics on the test set when using L-CNN as a classifier. The metrics are reported for each processing technique and in both the subject-wise and population-wise analysis. Balanced accuracy and F1-score are reported for completeness.

3.1.3. Siamese Neural Network

Figure 6 reports the results for the Siamese Neural Network. In agreement with our previous results, domain-specific preprocessing improves the performances of ErrP detection for each subject as well as in the population-wise analysis. Greater improvements in both balanced accuracy and *F1-score* result when the subspace regularization method is used. For the other two architectures, subjects 4 and 6 experience the largest improvements in terms of performance, with 12.2% and 14% in terms of balanced accuracy and 12.6% and 13.4% in terms of F1-score, respectively.

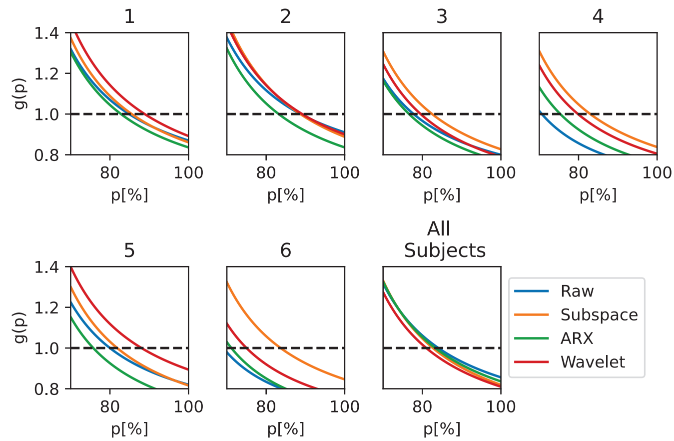

Figure 5. Utility gain obtained using L-CNN as a classifier and applying different ST estimation techniques. The metric is reported for subject-wise and population-wise analysis and for p values over 70%, as no major differences were observed below this level.

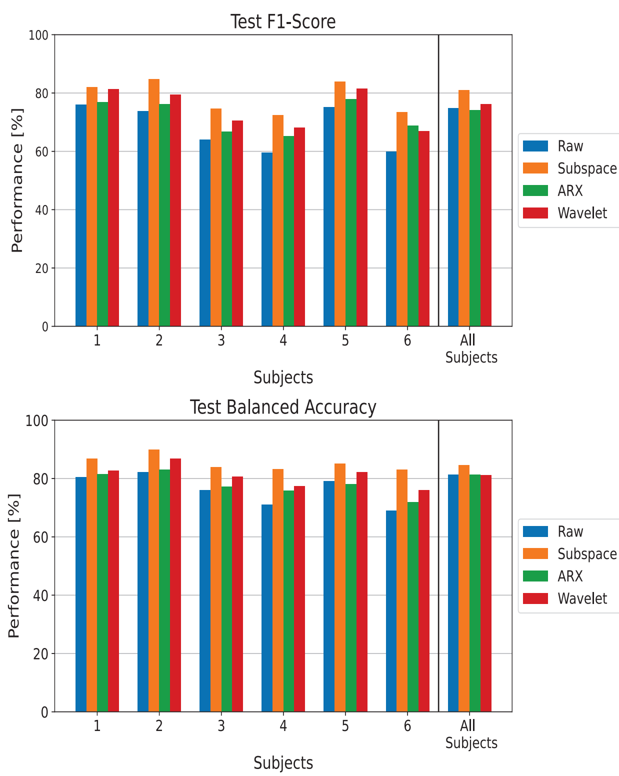

Figure 6. Performance metrics on the test set when using a Siamese Neural Network as the classifier. The metrics are reported for each processing technique and for subject-wise and population-wise analysis. Balanced accuracy and *F1-score* are reported for completeness.

The utility gain curves for the Siamese Neural Network classifier are shown in Figure 7. Again, it can be observed that the introduction of a correction system with subspace regularization for ST estimation leads to improved performance of the BCI and higher accuracy compared to the other techniques. This is particularly observable for subjects 4 and 6, where we measured a $g(p) > 1$ until $p = 85.1\%$ and $p = 84.7\%$, respectively.

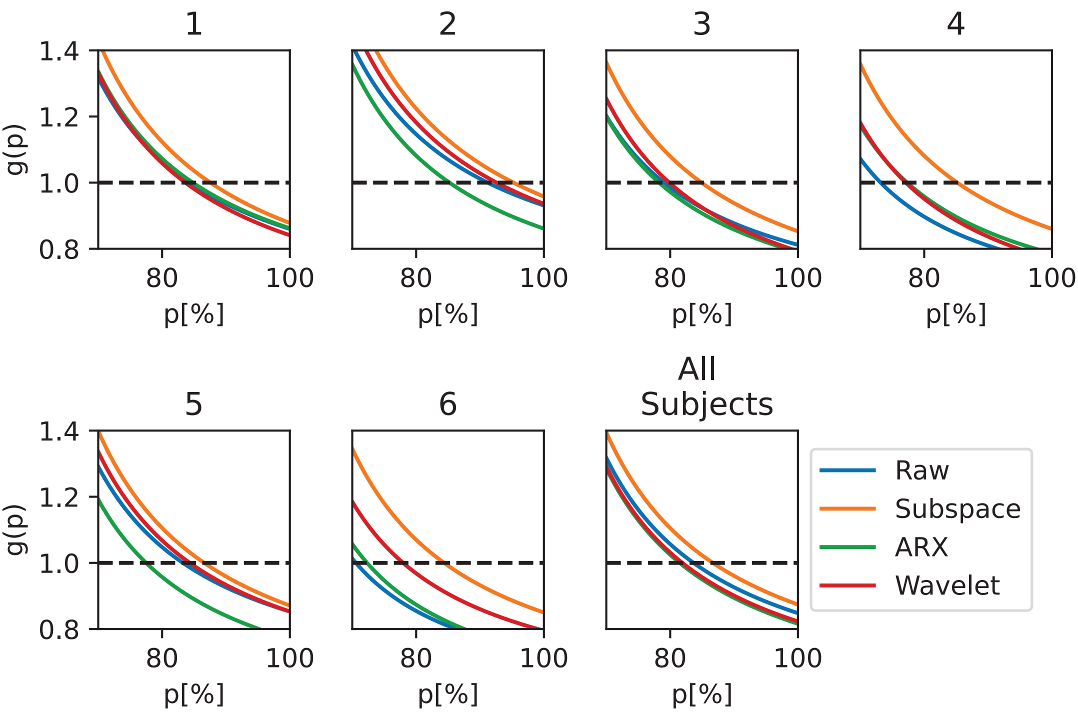

Figure 7. Utility gain obtained using a Siamese Neural Network as the classifier and applying different ST estimation techniques. The metric is reported for the subject-wise and population-wise analysis and for only those p values over 70%, as no major differences were observed below this level.

4. Discussion

Our main findings in this research can be summarized as follows: first, the introduction of a stage dedicated to ST-ErrP estimation results in improved performance on the part of the CNN classifier on detecting the occurrence of ErrP; second, the method which provides the largest improvement is the one based on subspace regularization.

The first finding indicates that domain-specific processing may significantly reduce the complexity of the classification process, leading to improved performance of CNN classifiers when detecting epochs containing ErrP. The observation that this improvement is consistent for all three CNN models leads us to conclude that this is not a bias induced by the model itself, and may have general validity. While in principle the flexibility of CNNs might be supposed to easily incorporate the estimation of ErrP within the multi-layer perception network, our findings show that it is advantageous to relieve the CNN of this task by moving it from a minimal preprocessing task to a domain-specific one. It is not surprising that, when focusing on ErrP classification, the domain-specific preprocessing task can be performed effectively by an ST-ErrP estimator.

Among the investigated single-trial estimators, the subspace regularization method slightly outperforms the others in terms of improving the performance of CNN classifiers on the ErrP detection task. This method's ability to highlight those EEG components related to error processing suggests its effectiveness in enhancing the quality of the recorded signal. In particular, it is worth noticing that this method is able to cut out the high-frequency components that are usually related to the background activity [30,31]. This filtering procedure results in epochs that closely resemble the expected ErrP waveform, which is a critical step in improving the detection of erroneous events [32].

Our evaluation of the utility gain indicates that the subspace regularization method not only permits allows effective classification of ErrP and non-ErrP events, it can enhance the overall utility of a BCI system as well. This finding suggests that the proposed architecture can provide significantly benefit in real-time BCI applications by enhancing error detection. It is noteworthy that subjects 4 and 6 showed the most improvement when using the subspace regularization method for extracting the ST. Indeed, these subjects initially had poor results when using raw signals as input for classification. This highlights the potential of the method described above to address inter-subject variability and provide improved performance for individuals for whom the model may initially struggle with ErrP detection.

In this study, we observed that when using the L-CNN classifier, the CWT resulted in better performance for subjects 1 and 5 than using the subspace regularization method. These subjects already showed good results when using the raw signals, and the improvement brought about by the two ST estimate methods were comparable. However, the differences in the results for these two subjects when using different CNNs suggest that the choice of classifier has an impact on the final signal processing performance. Further investigation into classifier-specific sensitivities could be beneficial, and might be addressed using Explainable Artificial Intelligence (XAI). From this same perspective, the adoption of an ErrP enhancer stage could facilitate the work of explainability approaches aiming to identify which parts of the signal contribute the most to classification. We hypothesize that the salient features highlighted by the ErrP enhancer are instrumental in simplifying the CNN classification task. Additionally, by reducing background EEG interference, this enhancement can contribute to the interpretability of XAI results and facilitate analysis of the relationship between relevant ErrP patterns used for classification and established evoked potential patterns. In future work, we intend to further investigate these aspects.

5. Conclusions

In conclusion, the present study provides compelling evidence that the proposed ErrP-enhanced architecture in which a CNN classifier is supported by a domain-specific preprocessing stage is highly effective in improving the accuracy of ST ErrP estimation and detection in EEG signals. The additional preprocessing stage offers several advantages, including the ability to filter out components that are not error-related and to enhance the fidelity of the ErrP waveform. These findings contribute to the ongoing advancement of EEG-based error detection systems, and have practical implications for BCI applications in domains such as assistive technology and neurofeedback.

Author Contributions: Conceptualization, A.F. and L.M.; methodology, A.F.; software, A.F.; validation, A.F. and L.M.; formal analysis, A.F. and L.M.; investigation, A.F.; resources, A.F. and L.M.; data curation, A.F.; writing—original draft preparation, A.F.; writing—review and editing, A.F. and L.M.; visualization, A.F.; supervision, L.M.; All authors have read and agreed to the published version of the manuscript.

Funding: This research received no external funding.

Institutional Review Board Statement: Not applicable.

Informed Consent Statement: Not applicable.

Data Availability Statement: Publicly available datasets were analyzed in this study. This data can be found here: https://bnci-horizon-2020.eu/database/data-sets (013-2015).

Conflicts of Interest: The authors declare no conflicts of interest.

Abbreviations

The following abbreviations are used in this manuscript:

ErrP	Error Potential
CNN	Convolutional Neural Network
DNN	Deep Convolutional Neural Network
BCI	Brain–Computer Interface
EEG	Electroencephalography
EP	Evoked Potential
ST	Single Trial
SNR	Signal-to-Noise Ratio
CAR	Common Average Reference
CWT	Continuous Wavelet Transform
DWT	Dyadic Wavelet Transform

References

1. Wolpaw, J.R.; Birbaumer, N.; McFarland, D.J.; Pfurtscheller, G.; Vaughan, T.M. Brain–computer interfaces for communication and control. *Clin. Neurophysiol. Off. J. Int. Fed. Clin. Neurophysiol.* **2002**, *113*, 767–791. [CrossRef] [PubMed]
2. Abiri, R.; Borhani, S.; Sellers, E.W.; Jiang, Y.; Zhao, X. A comprehensive review of EEG-based brain–computer interface paradigms. *J. Neural Eng.* **2019**, *16*, 011001. [CrossRef] [PubMed]
3. Seno, B.D.; Matteucci, M.; Mainardi, L. Online detection of P300 and error potentials in a BCI speller. *Comput. Intell. Neurosci.* **2010**, *2010*, 307254. [CrossRef]
4. Gemba, H.; Sasaki, K.; Brooks, V. 'Error' potentials in limbic cortex (anterior cingulate area 24) of monkeys during motor learning. *Neurosci. Lett.* **1986**, *70*, 223–227. [CrossRef] [PubMed]
5. Falkenstein, M.; Hoormann, J.; Christ, S.; Hohnsbein, J. ERP components on reaction errors and their functional significance: A tutorial. *Biol. Psychol.* **2000**, *51*, 87–107. [CrossRef]
6. Cruz, A.; Pires, G.; Nunes, U.J. Double ErrP Detection for Automatic Error Correction in an ERP-Based BCI Speller. *IEEE Trans. Neural Syst. Rehabil. Eng.* **2018**, *26*, 26–36. [CrossRef]
7. Marathe, A.R.; Ries, A.J.; McDowell, K. Sliding HDCA: Single-Trial EEG Classification to Overcome and Quantify Temporal Variability. *IEEE Trans. Neural Syst. Rehabil. Eng.* **2014**, *22*, 201–211. [CrossRef]
8. Ouyang, G.; Hildebrandt, A.; Sommer, W.; Zhou, C. Exploiting the intra-subject latency variability from single-trial event-related potentials in the P3 time range: A review and comparative evaluation of methods. *Neurosci. Biobehav. Rev.* **2017**, *75*, 1–21. [CrossRef]
9. Bellary, S.A.S.; Conrad, J.M. Classification of Error Related Potentials using Convolutional Neural Networks. In Proceedings of the 2019 9th International Conference on Cloud Computing, Data Science & Engineering (Confluence), Noida, India, 10–11 January 2019; pp. 245–249. [CrossRef]
10. Lawhern, V.J.; Solon, A.J.; Waytowich, N.R.; Gordon, S.M.; Hung, C.P.; Lance, B.J. EEGNet: A compact convolutional neural network for EEG-based brain–computer interfaces. *J. Neural Eng.* **2018**, *15*, 056013. [CrossRef]
11. Torres, J.M.M.; Clarkson, T.; Stepanov, E.A.; Luhmann, C.C.; Lerner, M.D.; Riccardi, G. Enhanced Error Decoding from Error-Related Potentials using Convolutional Neural Networks. In Proceedings of the 2018 40th Annual International Conference of the IEEE Engineering in Medicine and Biology Society (EMBC), Honolulu, HI, USA, 18–21 July 2018; pp. 360–363. [CrossRef]
12. Luo, T.; Fan, Y.; Lv, J.; Zhou, C. Deep reinforcement learning from error-related potentials via an EEG-based brain-computer interface. In Proceedings of the 2018 IEEE International Conference on Bioinformatics and Biomedicine (BIBM), Madrid, Spain, 3–6 December 2018; pp. 697–701.
13. Shahtalebi, S.; Asif, A.; Mohammadi, A. Siamese Neural Networks for EEG-based Brain-computer Interfaces. In Proceedings of the 2020 42nd Annual International Conference of the IEEE Engineering in Medicine & Biology Society (EMBC), Montreal, QC, Canada, 20–24 July 2020; pp. 442–446. [CrossRef]
14. Delorme, A.; Miyakoshi, M.; Jung, T.-P.; Makeig, S. Grand average ERP-image plotting and statistics: A method for comparing variability in event-related single-trial EEG activities across subjects and conditions. *J. Neurosci. Methods* **2015**, *250*, 3–6. [CrossRef]
15. Gaspar, C.M.; Rousselet, G.A.; Pernet, C.R. Reliability of ERP and single-trial analyses. *NeuroImage* **2011**, *58*, 620–629. [CrossRef] [PubMed]
16. Mainardi, L.T.; Kupila, J.; Nieminen, K.; Korhonen, I.; Bianchi, A.M.; Pattini, L.; Takala, J.; Karhu, J.; Cerutti, S. Single sweep analysis of event related auditory potentials for the monitoring of sedation in cardiac surgery patients. *Comput. Methods Programs Biomed.* **2000**, *63*, 219–227. [CrossRef] [PubMed]
17. Donoho, D. De-noising by soft-thresholding. *IEEE Trans. Inf. Theory* **1995**, *41*, 613–627. [CrossRef]
18. Mallat, S.G. A theory for multiresolution signal decomposition: The wavelet representation. *IEEE Trans. Pattern Anal. Mach. Intell.* **1989**, *11*, 674–693. [CrossRef]
19. Karjalainen, P.A.; Kaipio, J.P.; Koistinen, A.S.; Vauhkonen, M. Subspace regularization method for the single-trial estimation of evoked potentials. *IEEE Trans. Biomed. Eng.* **1999**, *46*, 849–860. [CrossRef] [PubMed]

20. Cerutti, S.; Baselli, G.; Liberati, D.; Pavesi, G. Single sweep analysis of visual evoked potentials through a model of parametric identification. *Biol. Cybern.* **1987**, *56*, 111–120. [CrossRef] [PubMed]
21. BNCI Horizon 2020. Available online: http://bnci-horizon-2020.eu/database/dataset (accessed on 1 October 2023).
22. Chavarriaga, R.; Millan, J.d.R. Learning From EEG Error-Related Potentials in Noninvasive Brain-Computer Interfaces. *IEEE Trans. Neural Syst. Rehabil. Eng.* **2010**, *18*, 381–388. [CrossRef]
23. Ferrez, P.W.; Millan, J.d.R. Error-Related EEG Potentials Generated During Simulated Brain–Computer Interaction. *IEEE Trans. Biomed. Eng.* **2008**, *55*, 923–929. [CrossRef]
24. Ahmadi, M.; Quiroga, R.Q. Automatic denoising of single-trial evoked potentials. *NeuroImage* **2013**, *66*, 672–680. 10.1016/j.neuroimage.2012.10.062. [CrossRef]
25. Kingma, D.P.; Ba, J. Adam: A Method for Stochastic Optimization. *arXiv* **2017**, arXiv:1412.6980.
26. Orrite, C.; Rodríguez, M.; Martínez, F.; Fairhurst, M. Classifier Ensemble Generation for the Majority Vote Rule. *Prog. Pattern Recognit. Image Anal. Appl.* **2008**, *5197*, 340–347.
27. Farabbi, A.; Aloia, V.; Mainardi, L. ARX-based EEG data balancing for error potential BCI. *J. Neural Eng.* **2022**, *19*, 3. [CrossRef] [PubMed]
28. Chollet, F. Xception: Deep Learning with Depthwise Separable Convolutions. *arXiv* **2017**, arXiv:1610.02357.
29. Dal Seno, B.; Matteucci, M.; Mainardi, L.T. The Utility Metric: A Novel Method to Assess the Overall Performance of Discrete Brain–Computer Interfaces. *IEEE Trans. Neural Syst. Rehabil. Eng.* **2010**, *18*, 20–28. [CrossRef] [PubMed]
30. Minthe, A.; Janzarik, W.G.; Lachner-Piza, D.; Reinacher, P.; Schulze-Bonhage, A.; Dümpelmann, M.; Jacobs, J. Stable high frequency background EEG activity distinguishes epileptic from healthy brain regions. *Brain Commun.* **2020**, *2*, fcaa107. [CrossRef]
31. Stovall, T.; Hunt, B.; Glynn, S.; Stacey, W.C.; Gliske, S.V. Interictal high frequency background activity as a biomarker of epileptogenic tissue. *Brain Commun.* **2021**, *3*, fcab188. [CrossRef]
32. Farabbi, A.; Mainardi, L. The Subspace Regularization Method Improves ErrP Detection by EEGNET in BCI Experiments. In Proceedings of the 16th International Joint Conference on Biomedical Engineering Systems and Technologies (BIOSTEC 2023)—Volume 4: BIOSIGNALS, Lisbon, Portugal, 16–18 Febuary 2023; pp. 260–264. [CrossRef]

sensors

Article

Illuminating the Neural Landscape of Pilot Mental States: A Convolutional Neural Network Approach with Shapley Additive Explanations Interpretability

Ibrahim Alreshidi [1,2,3,*], Desmond Bisandu [1,2] and Irene Moulitsas [1,2,*]

1 Centre for Computational Engineering Sciences, Cranfield University, Cranfield MK43 0AL, UK; desmond.bisandu@cranfield.ac.uk
2 Machine Learning and Data Analytics Laboratory, Digital Aviation Research and Technology Centre (DARTeC), Cranfield University, Cranfield MK43 0AL, UK
3 College of Computer Science and Engineering, University of Ha'il, Ha'il 81451, Saudi Arabia
* Correspondence: ibrahim.alreshidi@cranfield.ac.uk (I.A.); i.moulitsas@cranfield.ac.uk (I.M.)

Abstract: Predicting pilots' mental states is a critical challenge in aviation safety and performance, with electroencephalogram data offering a promising avenue for detection. However, the interpretability of machine learning and deep learning models, which are often used for such tasks, remains a significant issue. This study aims to address these challenges by developing an interpretable model to detect four mental states—channelised attention, diverted attention, startle/surprise, and normal state—in pilots using EEG data. The methodology involves training a convolutional neural network on power spectral density features of EEG data from 17 pilots. The model's interpretability is enhanced via the use of SHapley Additive exPlanations values, which identify the top 10 most influential features for each mental state. The results demonstrate high performance in all metrics, with an average accuracy of 96%, a precision of 96%, a recall of 94%, and an F1 score of 95%. An examination of the effects of mental states on EEG frequency bands further elucidates the neural mechanisms underlying these states. The innovative nature of this study lies in its combination of high-performance model development, improved interpretability, and in-depth analysis of the neural correlates of mental states. This approach not only addresses the critical need for effective and interpretable mental state detection in aviation but also contributes to our understanding of the neural underpinnings of these states. This study thus represents a significant advancement in the field of EEG-based mental state detection.

Keywords: aviation safety; convolutional neural network; deep learning; EEG; electroencephalogram; interpretability/explainability; machine learning; mental states classification; pilot deficiencies; SHapley Additive exPlanations

Citation: Alreshidi, I.; Bisandu, D.; Moulitsas, I. Illuminating the Neural Landscape of Pilot Mental States: A Convolutional Neural Network Approach with Shapley Additive Explanations Interpretability. *Sensors* **2023**, *23*, 9052. https://doi.org/10.3390/s23229052

Academic Editor: Yvonne Tran

Received: 26 September 2023
Revised: 31 October 2023
Accepted: 7 November 2023
Published: 8 November 2023

1. Introduction

The human brain, an intricate network of billions of neurons, is a dynamic system that constantly generates electrical activity. This electrical activity, which reflects the complex interplay of neural processes, can be measured and analysed using electroencephalography (EEG). Since the advent of EEG in the early 20th century, these signals have been extensively studied for their potential to provide insights into various cognitive states, mental conditions, and neurological disorders [1–3]. In recent years, the use of EEG in cognitive neuroscience has surged, driven by advancements in signal processing techniques and the development of portable and wearable EEG devices [4]. The non-invasive nature of EEG, its relatively low cost, high temporal resolution, and the possibility of real-time monitoring make it a particularly attractive tool for studying brain dynamics in various contexts [5,6]. One such context is the field of aviation, where understanding and monitoring the mental states of pilots is of paramount importance. The mental state of a pilot can significantly influence his decision-making ability, reaction times, and overall performance, particularly in high-stakes or stressful situations [7]. Therefore, the ability to accurately detect and classify different mental states based on EEG data could provide a valuable tool for enhancing safety and performance in aviation.

Different mental states are associated with different patterns of brain activity, which can be captured in the frequency domain of EEG signals as characteristics of power spectral density (PSD) [8]. These features represent the distribution of signal power over various frequency bands, such as delta (δ), theta (θ), alpha (α), beta (β), and gamma (γ), each of which is associated with different cognitive processes and mental states [9]. For instance, δ waves are typically associated with deep sleep or relaxation, θ waves with creativity and insight, α waves with relaxed alertness, β waves with active thinking and focus, and γ waves with higher mental activity and perception [9,10]. The analysis of these frequency bands can provide a window into the cognitive processes underlying different mental states, making them a valuable tool for mental state classification [8].

In recent years, the field of machine learning (ML), particularly convolutional neural networks (CNN), has made significant strides in the analysis of EEG data for mental state classification [11]. CNN models have demonstrated their efficacy in handling high-dimensional data, such as EEG signals, by automatically learning hierarchical representations from raw data. This ability to learn and extract salient features from raw data without the need for manual feature extraction is a significant advantage in EEG analysis, where the selection of appropriate features is often challenging [11–13].

However, while CNN models have shown promise in terms of performance, understanding the decision-making process of these models remains a challenge. To address this, we employ SHapley Additive exPlanations (SHAP) values, a powerful tool for interpreting machine learning models. SHAP values provide a measure of the contribution of each feature to the model's prediction, thereby offering insights into the model's decision-making process [14,15].

The novelty of this study lies in the comprehensive approach to mental state detection in pilots, extending the boundaries of EEG-based cognitive state detection in several significant ways:

1. It employs a one-dimensional CNN (1D-CNN) architecture optimised for EEG data, comprising five convolutional layers, thereby enhancing the model's capability to capture both spatial and temporal features.
2. The model is trained on PSD features extracted from EEG signals, offering a robust and computationally efficient approach to mental state classification.
3. We introduce the use of SHAP values for result interpretability, enabling a nuanced understanding of feature importance for each mental state class.
4. The model is validated on the Attention-related Human Performance Limiting States (AHPLS) dataset, notable for its real-world applicability to high-stakes environments like aviation.

The EEG data was sourced from the AHPLS dataset, a rich and diverse dataset that has been used in several recent studies to understand and model human cognitive states [16–21]. The AHPLS dataset is unique in its inclusion of data from pilots under various mental states, namely channelised attention (CA), diverted attention (DA), startle/surprise (SS), and normal/no event (NE) states. This provides a robust and realistic dataset for training and testing our model. The use of such a dataset is a significant contribution to the field, as it allows for the exploration of EEG-based mental state detection in a high-stakes real-world environment, such as aviation [22].

This study aims to answer the following research questions:

1. How effectively can a 1D-CNN model trained on PSD features of EEG signals detect four mental states in pilots?
2. What are the key features of PSD that contribute to the successful detection of these mental states?

3. How does the performance of the model vary across different pilots and when trained on data from all pilots combined?

The answers to these questions will provide valuable insights into the potential of EEG-based mental state detection in aviation and other high-stakes environments and will guide future research in this area.

The paper is organised as follows: In Section 2, an overview of mental states and related research studies is presented. The proposed comprehensive approach in Section 3 describes the methods used in this study. Section 4 outlines the Experimental Setup, Section 5 presents the findings, and Section 6 presents a discussion of the results. Finally, the conclusion of the study is stated in Section 7.

2. Related Work

The application of ML techniques, particularly deep learning (DL), to the analysis of EEG data for the detection of mental states, has been a topic of significant interest in recent years. This section provides an overview of the key research in this area, highlighting the methodologies used, the results obtained, and the gaps that this study aims to address.

2.1. Previous Studies on EEG-Based Mental State Detection

Several studies have explored the use of EEG data for the detection of mental states. For instance, Başar et al. [9] found that γ, α, δ, β, and θ oscillations govern cognitive processes, suggesting that these frequency bands could be used to detect different mental states. Similarly, Klimesch [8] found that EEG α and θ oscillations reflect cognitive and memory performance, indicating their potential for mental state detection. Regarding the application of ML and DL methods, Giudice et al. [23] developed a 1D-CNN model to detect and discriminate between voluntary and involuntary blinking of the eye using EEG data, demonstrating the potential of DL techniques for such tasks. Mattioli et al. [24] proposed an approach based on a 10-layer 1D-CNN to classify four motor imagery (MI) and baseline states, which showed promising results in terms of performance. Similarly, Tabar et al. [25] model based on CNN and stacked autoencoders to classify EEG MI signals, demonstrating the effectiveness of DL models compared to ML models. Furthermore, Zorzos et al. [26] extracted time-frequency domain characteristics from the EEG signal to train on a shallow CNN model with three convolutional layers for the detection of mental fatigue, which showed promising results in terms of performance and interpretability.

In the context of aviation, Wu et al. [27,28] addressed the problem of obtaining the representation of the fatigue status feature and detecting the fatigue behaviour status of pilots via EEG signals. The authors decomposed the EEG signals of pilots into four frequency bands, namely δ, θ, α, and β, and used them to train a deep contractive autoencoder network, achieving a 91.67% performance accuracy. Furthermore, Cui et al. [29] developed a CNN model to detect driver drowsiness using EEG data, achieving an average accuracy of 78.35% in 11 participants. They also employed an interpretation tool to recognise the biological features of drowsiness states. Han et al. [30] proposed a multimodal approach to classify four mental states, namely distraction, workload, fatigue, and normal, using EEG, electrocardiogram (ECG), respiration (R), and electrodermal activity (EDA). They extracted PSD features from the EEG signals, which were used to train a CNN model, and trained a long-short temporal memory (LSTM) model on the other non-brain signals, achieving an average accuracy of 85.2%. Johnson et al. [31] used the average power of the frequency bands as features to detect task complexity levels in flight simulator experiments. In addition, Roza et al. [32,33] focused on detecting the pilot’s emotions, namely happy, sad, angry, scared, surprised, and disgust, using an artificial neural network (ANN) in simulated flights. Binias et al. [34] proposed an ML approach to discriminate between states of brain activity related to idle but focused anticipation of visual signals and reaction to them.

2.2. Gaps in the Existing Literature

While these studies have made significant contributions to the field, there are several gaps that this study aims to address. Firstly, many previous studies have focused on binary or multiclass classification problems, such as distinguishing between rest and task states or between different levels of cognitive load. However, less research has been conducted on the detection of specific mental states, such as CA, DA, SS, and NE states, particularly in the context of aviation.

Second, while DL models have shown promise in EEG analysis, understanding the decision-making process of these models remains a challenge. Many previous studies have focused on improving the performance of these models, but less attention has been paid to their interpretability. This is a significant gap, as understanding the features that these models consider important can provide valuable insights into the underlying cognitive processes associated with different mental states.

2.3. Previous Research on Detecting CA, DA, SS, and NE States

Several studies have explored the detection of specific mental states using EEG data. For instance, Harrivel et al. [17,18] recorded brain signals (i.e., EEG) and non-brain signals (i.e., ECG, R, and galvanic skin response (GSR)), capturing the attention-related pilot performance limiting states, including CA, DA, SS, and NE. The authors employed various ML techniques to perform binary and multiclass classification tasks in two different studies. Terwilliger et al. [16] attempted to discriminate between the normal state and an event state, where the CA, DA, and SS states are combined and named an event state. In previous research [20], we performed a multiclass classification task to attempt to predict the CA, DA, SS, and NE states. The main purpose of the study was to measure the impact of applying different preprocessing techniques on the performance of the ML model and to investigate the feasibility of concatenating EEG datasets recorded from different environment settings. It was found that the employment of pre-processing techniques has an impact on classification performance. Thus, an automated preprocessing approach was proposed to improve the signal-to-noise ratio and classification performance [19]. The proposed approach demonstrated the importance of preprocessing EEG data before training them in ML models. The attention-related pilot performance-limiting states are heavily class imbalanced. In a recent study [21], we evaluated the impact of employing various data resampling techniques on classification performance. It was discovered that the use of a combination of downsampling and oversampling techniques improves the performance of the ML models.

However, less research has been conducted on the detection of the specific mental states of CA, DA, SS, and NE states. These states are particularly relevant in the context of aviation, where pilots need to rapidly switch between different mental states in response to varying task demands. Understanding and detecting these states could have significant implications for safety and performance in aviation and other high-stakes environments.

2.4. Positioning of the Current Work

This study builds on the existing literature in several ways. Firstly, it focuses on the detection of specific mental states that are relevant in the context of aviation, addressing a gap in the existing literature. Second, it uses a 1D-CNN model, which has been shown to be effective in handling high-dimensional data such as EEG signals. This model is trained on PSD features of EEG data, which represent the distribution of signal power over various frequency bands and are associated with different cognitive processes and mental states.

Furthermore, this study addresses the need for model interpretability in EEG analysis by employing SHAP values. SHAP values provide a measure of the contribution of each feature to the model's prediction, offering insights into the model's decision-making process. This approach not only leverages the power of CNN models for EEG analysis but also addresses the critical need for model interpretability in this domain.

The EEG data used in this study are sourced from the AHPLS dataset, a rich and diverse dataset that has been used in several recent studies to understand and model human cognitive states. The AHPLS dataset is unique in its inclusion of data from pilots under various mental states, providing a robust and realistic dataset for training and testing our model. The use of such a dataset is a significant contribution to the field, as it allows for the exploration of EEG-based mental state detection in a real-world, high-stakes environment such as aviation.

In summary, this study extends the existing literature by focusing on the detection of specific mental states in pilots using a 1D-CNN model trained on PSD features of EEG data. It also addresses the need for model interpretability by employing SHAP values to identify the important features of each mental state. The use of the AHPLS dataset further enhances the relevance and applicability of this research in the field of aviation.

3. The Proposed Approach

In this section, we describe the methods utilised to preprocess the EEG data, extract meaningful features from the EEG data, and handle the data imbalance issue. In addition, we explain the proposed 1D-CNN model and the interpretability method (i.e., SHAP) used to identify the most important features of each mental state. Figure 1 illustrates an overview of the proposed approach.

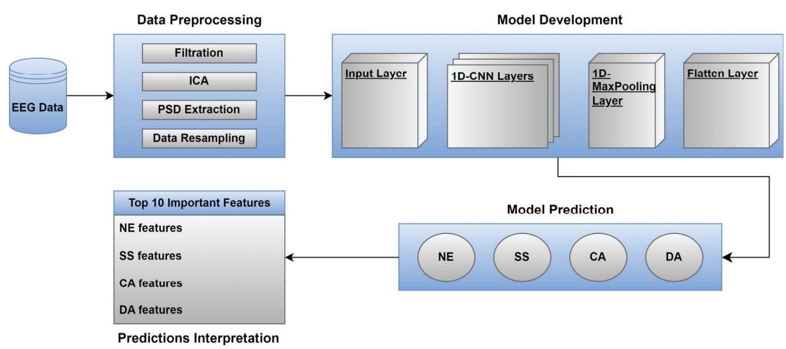

Figure 1. An overview of the proposed approach.

3.1. Data Preprocessing

EEG data was initially segmented into 1 s and filtered using a finite impulse response (FIR) filter with a frequency range of 1 to 40 Hz [35]. This step was instrumental in attenuating extraneous noise and enhancing the signal-to-noise ratio of the EEG data, thereby improving the quality of the data for subsequent analysis. Subsequent to the filtering process, the data were subjected to an artefact removal procedure to address ocular-related artefacts, a common occurrence in EEG data. This was achieved by utilising the Independent Component Analysis (ICA) algorithm, as delineated by Aapo Hyvärinen in his seminal work [36]. The ICA algorithm, renowned for its robustness in the separation of independent sources, was employed to isolate and subsequently remove components of the EEG data that were indicative of ocular movements.

Upon successful removal of artefacts, spectral analysis was performed on the sensor data. This was facilitated by the "multitaper" method, a technique that employs discrete prolate spheroidal sequences (DPSS) tapers [37]. This method was selected due to its ability to provide robust spectral estimates with minimised variance. The lower and upper-bound frequencies of interest were set to 1 and 40 Hz, respectively. This frequency range was strategically chosen to focus on the frequency bands that were pertinent to the study while concurrently excluding frequencies that could potentially introduce noise into the analysis. The rigorous preprocessing steps outlined above ensured the optimal preparation of the EEG data for the ensuing stages of the study.

Following the preprocessing of the EEG data, the dataset was partitioned into training and testing datasets, with proportions of 80% and 20%, respectively. Then, we split the partitioned training dataset into training and validation datasets, with proportions of 70% and 30%, respectively. This division was carried out to facilitate the model's learning process and to ensure a robust evaluation of its performance. To address the issue of data imbalance, the SMOTEENN method was used. This hybrid resampling technique, which combines the synthetic minority oversampling technique (SMOTE) [38] and the Edited Nearest Neighbours (ENN), is highly effective in handling imbalanced data.

The SMOTEENN method first applies SMOTE to generate synthetic samples from the minority class, thereby balancing the class distribution. Mathematically, for each minority class sample x, it chooses one of its k nearest neighbours x' and generates a new sample at a random point between x and x', i.e., $x_{new} = x + \lambda.\ (x^{'} - x)$, where λ is a random number between 0 and 1. Subsequently, the ENN method is applied to remove any instances of the majority class that are surrounded by minority class instances and any instances of the minority class that are misclassified by its three nearest neighbours. This cleaning process ensures that the oversampling does not overgeneralise the minority class by creating noisy samples. The application of SMOTEENN in this study ensured a balanced representation of classes, thereby improving the model's ability to generalise from the training data to unseen data.

3.2. The One-Dimensional Convolutional Neural Network (1D_CNN)

The 1D Convolutional Neural Network (1D-CNN) model is a variant of the traditional Convolutional Neural Network that is specifically designed for sequence data [39,40]. The model is composed of five 1D-CNN layers, followed by a MaxPooling1D layer and a flattened layer. The mathematical operation performed by a 1D-CNN layer can be described as follows.

Given an input sequence $x = [x_1, x_2, \ldots, x_n]$, a filter $w = [w_1, w_2, \ldots, w_k]$ of length k is applied to the sequence to produce a new sequence $y = [y_1, y_2, \ldots, y_{n-k+1}]$, where each element y_i is computed as

$$y_i = b + \sum_{j=1}^{k} w_j \cdot x_{i+j-1} \tag{1}$$

Here, b is a bias term. This operation is applied for each filter in the layer, and the results are typically passed through a nonlinear activation function, such as the Rectified Linear Unit (ReLU) function.

After passing through the five 1D-CNN layers, a MaxPooling1D layer is applied. This layer reduces the dimensionality of its input by applying a max operation over sliding windows of a specified size. If the window size is p, then the output $z = [z_1, z_2, \ldots, z_{n/p}]$ is computed as

$$z_i = \max_{j=(i-1)p+1} y_i \tag{2}$$

This operation helps to make the model more robust to shifts and distortions in the input data and reduces the computational complexity of subsequent layers. After passing through the five 1D-CNN and MaxPooling1D layers, the output is flattened into a one-dimensional vector. This flattened output can then be passed through one or more fully connected layers, which perform the final classification or regression task. The 1D-CNN model's strength lies in its ability to effectively capture local dependencies in the input data, making it particularly well suited for tasks involving time series or sequence data. Its architecture allows it to learn both short- and long-term patterns in the data, which can be crucial for many prediction tasks.

3.3. SHapley Additive exPlanations (SHAP)

SHAP is a unified measure of feature importance that assigns each feature an importance value for a particular prediction. The concept of SHAP is based on Shapley values, a concept from cooperative game theory that assigns payouts to players depending on their contribution to the total payout [41]. SHAP values interpret the output of the ML and DL models using a game-theoretic approach, attributing the prediction of each instance to its features [15].

The SHAP value for a feature is the average marginal contribution of that feature across all possible combinations of features. Mathematically, the SHAP value φi for a feature i is given by

$$\varphi i = \sum_{S \subseteq M \setminus \{i\}} \frac{(|S|\,!(|M| - |S| - 1))!}{|M|!} \left[f\ (S \cup \{i\}) - f(S)\right] \tag{3}$$

where M is the set of all features, S is a subset of M without feature $\{i\}$, $|S|$ is the number of features in S, $|M|$ is the total number of features, and f is the prediction function. The term $(|S|!(|M|-|S|-1)!\,/\,|M|!)$ is the weight representing the number of times a subset S of size $|S|$ appears in all possible subsets of M.

In this study, SHAP values are used to interpret the predictions of the CNN model trained on PSD features of EEG data. For each mental state prediction, SHAP values are computed for all features, providing a measure of the contribution of each feature to the prediction. This allows the identification of the top 10 most influential features for each mental state, offering insight into the neural correlates of these states. The use of SHAP values thus enhances the interpretability of the model, contributing to a deeper understanding of the neural mechanisms underlying the mental states of interest in aviation.

4. Experimental Setup

This section elaborates on the experimental setup employed in this study, encompassing the dataset, Python libraries, PC specifications, hyperparameter tuning, and evaluation metrics. Each component plays a crucial role in the overall research design and contributes to the validity and reliability of the results.

4.1. Dataset

In the present study, we employed a publicly released EEG dataset extracted from the AHPLS dataset. This dataset encompasses psychophysiological data derived from 20 EEG channels collected from 17 pilots operating within a flight simulation environment. The data were annotated with labels corresponding to different mental states, namely the CA, DA, SS, and NE states.

The EEG channels are denoted as follows: FP1, F7, F8, T4, T6, T5, T3, FP2, O1, P3, Pz, F3, Fz, F4, C4, P4, POz, C3, Cz, and O2. Each channel was sampled at a frequency of 256 Hz, ensuring a high-resolution temporal dataset.

A noteworthy characteristic of this dataset is its class imbalance. The NE class constitutes the majority of the dataset, accounting for 83% of the total instances. This is followed by the CA class, which comprises 14% of the dataset. The DA and SS classes are significantly underrepresented, making up 2% and 1% of the dataset, respectively. This class imbalance poses a challenge for conventional ML models, necessitating the use of specialised techniques to ensure robust and generalisable performance.

4.2. Python Libraries and PC Specifications

The computational experiments were conducted on a PC equipped with an Intel (R) Core (TM) i7-10700 CPU @ 2.90 GHz. The PC boasts a RAM capacity of 32.0 GB, ensuring efficient handling of large datasets and complex computations.

Python (version 3.10), renowned for its simplicity and powerful libraries, was used for all computational tasks. We utilised several Python libraries, each serving a distinct purpose. NumPy (version 1.21) and Pandas (version 1.3) were used for efficient data handling and manipulation, providing robust structures for dataset operations. MNE-Python, version 1.2, a library dedicated to processing electrophysiological signals, was used to handle the specific data types present in the AHPLS dataset. Scikit-Learn (version 1.0.2) was used for various ML tasks, including data preprocessing and model evaluation. TensorFlow, version 2.4, a powerful library for creating and training DL models, was used to construct and train our neural network models. Lastly, the SHAP library was used to interpret the predictions of the proposed framework.

4.3. Hyperparameter Tuning

In the process of model development, hyperparameter tuning was performed to optimise the performance of the 1D-CNN model. We utilised the Grid Search method to systematically explore a range of hyperparameters. The hyperparameters were fine-tuned based on the specific requirements of the task and the characteristics of the dataset. Table 1 summarises the hyperparameters that were fine-tuned for the 1D-CNN model:

Table 1. Hyperparameters of the layers of the 1D-CNN model.

Layer	Filter	Kernel Size	Activation Function	Padding	Kernel Initializer
1	64	3	Relu	Same	GlorotNormal
2	128	3	Relu	Same	GlorotNormal
3	256	3	Relu	Same	GlorotNormal
4	128	3	Relu	Same	GlorotNormal
5	64	3	Relu	Same	GlorotNormal

The output layer of the model was a dense layer with four neurons and a softmax activation function, which is suitable for multiclass classification tasks.

In addition to the layer-specific parameters, several global parameters were also set for the training process. The learning rate was set to 1×10^{-4}, which determines the step size at each iteration while moving towards a minimum of a loss function. The model was trained for 100 to 150 epochs, where an epoch is an iteration over the entire dataset. The batch size was set to 32, which is the number of samples processed before the model was updated.

The GlorotNormal initialiser was used with different seed numbers for initialising the kernel's weights. This initialiser draws samples from a truncated normal distribution centred on 0, with $stddev = sqrt(2/(fan\_in + fan\_out))$, where fan_in is the number of input units in the weight tensor and fan_out is the number of output units. This initialiser is also known as the Xavier normal initialiser.

The hyperparameters were selected to optimise the model's performance on the validation set, and the selected model was then evaluated on the test set to assess its generalisation capability.

4.4. Evaluation Metrics

The performance of the model was evaluated using a variety of metrics to provide a comprehensive assessment. Accuracy, the most intuitive performance metric, measures the proportion of correct predictions made by the model. Precision assesses the model's ability to avoid false positives, measuring the proportion of true positive predictions among all positive predictions. Recall, on the other hand, evaluates the model's ability to avoid false negatives, measuring the proportion of true positive predictions among all actual positives.

The F1 score provides a balance between precision and recall. It is particularly useful when the data have imbalanced classes, as it considers both false positives and false negatives in its calculation. A high F1 score indicates a robust model with a good balance between precision and recall.

In addition to these metrics, a confusion matrix was used to visualise the performance of the model. The confusion matrix provides a comprehensive view of how well the model performed across all classes, showing the true positives, true negatives, false positives, and false negatives. It is a powerful tool for understanding the model's performance in greater detail, allowing for the identification of any classes that the model may be struggling to predict correctly.

Accuracy: This is the proportion of the total number of predictions that were correct. It is determined using the formula

$$\text{Accuracy} = \frac{\text{TP} + \text{TN}}{\text{TP} + \text{FP} + \text{TN} + \text{FN}} \tag{4}$$

Precision: Also called the positive predictive value, this is the proportion of positive cases that were correctly identified. It is given by the formula

$$\text{Precision} = \frac{\text{TP}}{\text{TP} + \text{FP}} \tag{5}$$

Recall: Also known as sensitivity, hit rate, or true positive rate (TPR), this is the proportion of actual positive cases that are correctly identified. The formula is as follows:

$$\text{Recall} = \frac{\text{TP}}{\text{TP} + \text{FN}} \tag{6}$$

F1 score: This is the harmonic mean of precision and recall and tries to find the balance between precision and recall. It is given by the formula

$$\text{F1} - \text{score} = 2 \times \frac{\text{Precision} \times \text{Recall}}{\text{Precision} + \text{Recall}} \tag{7}$$

5. Results

The results section of this study is organised into several subsections, each addressing a distinct aspect of the analysis. The first subsection investigates the impact of different mental states on the power distribution across EEG frequency bands. This analysis further elucidates the neural mechanisms underlying the mental states of interest and their manifestation in EEG data. The second subsection presents the performance metrics of the 1D-CNN model trained on the PSD features of EEG data from 17 pilots, along with the training accuracy, loss function curves, and the confusion matrix. These metrics include accuracy, precision, recall, and F1 score, providing a comprehensive evaluation of the model's ability to detect four mental states: CA, DA, SS, and NE states. Lastly, the model interpretation subsection delves into the feature importance analysis, using SHAP values to identify the top 10 most important features for each mental state. This analysis provides insights into the EEG frequency bands and channels that are most influential in the model's decision-making process, offering a deeper understanding of the neural correlates of the mental states under study.

Together, these subsections provide a comprehensive evaluation of the model's performance, an exploration of the key features driving its predictions, and an examination of the neural underpinnings of the mental states it is designed to detect. The results presented in this section not only demonstrate the effectiveness of the proposed approach but also contribute to our understanding of the neural correlates of mental states in the context of aviation.

5.1. Examining the Effects of Mental States on EEG Frequency Bands

The PSD of the EEG signals was analysed across different mental states and frequency bands. The average power in each frequency band (delta δ, theta θ, alpha α, beta β, and gamma γ) was calculated for each mental state (NE, SS, CA, and DA) and visualised using a bar plot shown in Figure 2 and a heatmap as depicted in Figure 3.

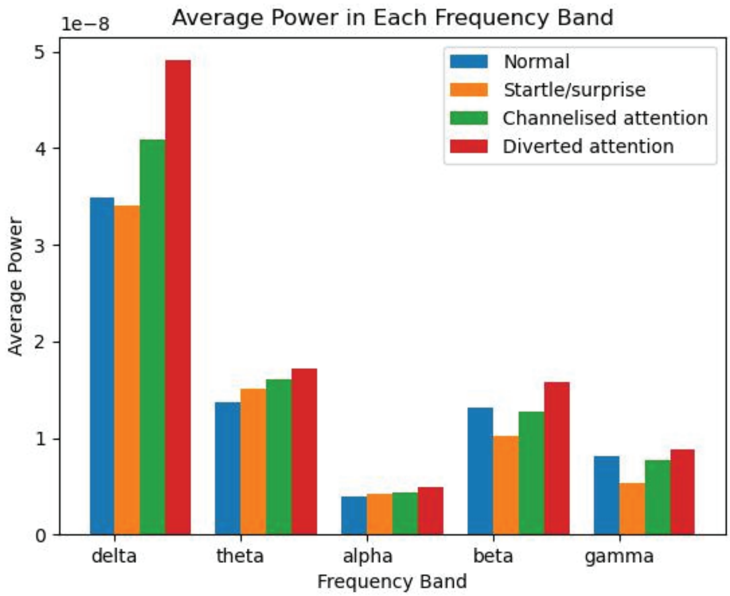

Figure 2. The average power in each frequency band across pilots.

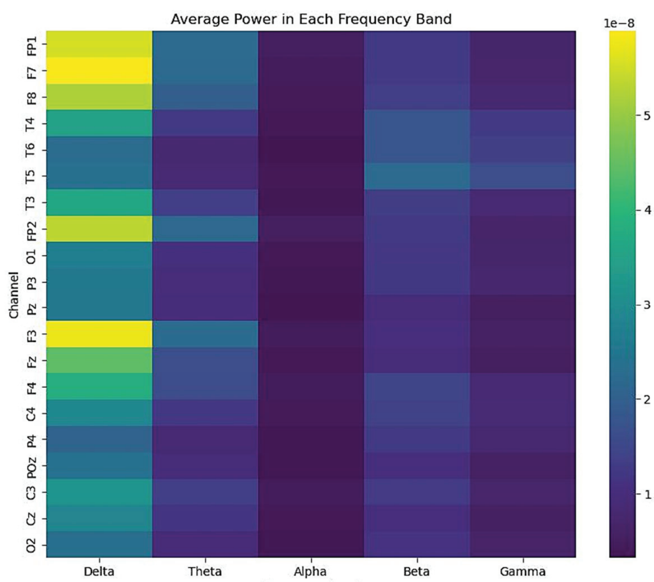

Figure 3. Heatmap for the average power in each frequency band for EEG channels.

In Figure 2, the bar plot shows the average power in each frequency band for each mental state. The height of each bar represents the average power in that band for that state. It can be observed that there are distinct differences in the power across different frequency bands for each mental state. This suggests that the power in different frequency bands may be a useful feature for distinguishing between different mental states. However, there is also considerable variability within each band and state. This suggests that there may be individual differences or other factors that are not captured by the average power alone.

In Figure 3, the heatmap shows the average power in each frequency band for each EEG channel. The colour of each cell represents the average power in that band for that channel. It can be seen that there are distinct patterns of power across different channels and frequency bands. This suggests that the spatial distribution of power in different frequency bands may also be a useful feature for distinguishing between different mental states. However, it is also apparent that there is considerable variability across different channels, suggesting that the power in different frequency bands may be influenced by the location of the electrodes and the underlying brain regions.

Together, these results suggest that the power in different frequency bands and the spatial distribution of the power across different channels may be useful features to distinguish between different mental states. However, further analysis is needed to determine the statistical significance of these differences and investigate the potential influence of other factors, such as individual differences and electrode placement. Future research could also investigate the temporal dynamics of power in different frequency bands, as the current analysis only considers the average power over the entire recording period.

5.2. Classification Results

The study utilised the proposed model to identify four distinct mental states of the pilots: CA, DA, SS, and NE states. The model was trained on PSD features derived from five frequency bands across 20 EEG channels. This approach allowed for a comprehensive representation of the EEG data, capturing the complex interplay of different frequency bands across multiple channels.

The model was trained individually on each of the 17 pilots and then on the combined data of all pilots. The performance of the model was evaluated using four key metrics: Accuracy, precision, recall, and F1 score. These metrics provide a holistic view of the model's performance, capturing its ability to make correct predictions (accuracy), its ability to correctly identify positive instances (precision), its ability to identify all positive instances (recall), and the balance between its precision and recall (F1 score).

As presented in Table 2, the results showed a high degree of consistency across all metrics for each pilot. The accuracy, precision, recall, and F1 scores all fell within a relatively narrow range of 94% to 99%. The highest accuracy and precision of 99% were achieved by Pilot 2. The lowest scores across all metrics were observed for Pilot 12, with an accuracy of 94%, precision of 91%, and an F1 score of 90%.

Table 2. Classification results of individual and combined pilots.

Pilot ID	Accuracy	Precision	Recall	F1 Score
1	97	97	95	96
2	99	99	98	98
3	97	98	95	96
4	96	94	94	94
5	97	98	96	96
6	97	96	94	95
7	97	98	96	96
8	96	95	92	93
9	97	96	97	97
10	95	96	90	92
11	95	95	89	91
12	94	91	89	90
13	96	95	93	94
14	96	97	92	93
15	97	95	96	95
16	98	98	95	96
17	98	97	96	97
All	96	96	94	95

When the model was trained on the combined PSD features of all pilots, it achieved an accuracy, precision of 96%, recall of 94%, and F1 score of 95%. This suggests that the model was able to generalise well from individual pilots to a larger population.

In addition to the proposed model performance metrics, the training process was also evaluated by examining the accuracy and loss curves for the training and validation datasets, as depicted in Figure 4. For the training dataset, the accuracy curve demonstrated a consistent upward trend, indicating a steady improvement in the model's ability to correctly predict the mental states as the training progressed. This consistent improvement suggests that the model was effectively learning the patterns in the training data and adapting its parameters accordingly. Simultaneously, the loss curve for the training dataset showed a consistent downward trend, indicating that the model was successfully reducing the error in its predictions over time. This is a positive sign of the model's learning capability as it shows that the model was able to progressively minimise the discrepancy between its predictions and the actual values.

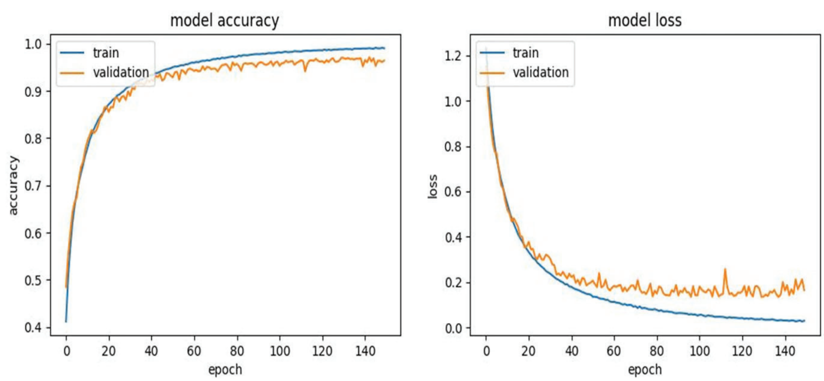

Figure 4. Training accuracy and loss curves of the proposed model.

In contrast, the accuracy and loss curves for the validation dataset showed slight irregularities. Despite these irregularities, the overall trend of the validation accuracy curve was positive, and the validation loss curve generally showed a decreasing trend. This indicates that, despite the fluctuations, the model was able to apply what it learnt from the training data to unseen data, demonstrating a good level of generalisation.

The performance of the proposed model was evaluated in a more detailed manner using a confusion matrix. This matrix provides a comprehensive view of the model's ability to correctly classify each of the four mental states: NE, SS, CA, and DA. The matrix is structured such that each row represents the instances in an actual class while each column represents the instances in a predicted class. The confusion matrix is depicted below in Figure 5.

The diagonal elements of the confusion matrix, which represent the percentage of correct predictions for each mental state, show that the model achieved high accuracy rates for each of the four mental states, with the lowest being 81.94% for the NE and the highest being 99.91% for the DA state.

In a rigorous comparative analysis, the performance of the proposed framework was benchmarked against various established neural network models outlined in existing literature. The models chosen for this comparative study encompassed Deep Contractive Autoencoder Networks (DCAEN), ANN, CNN, and LSTM. The empirical evaluation revealed that our model exhibited superior classification accuracy. Specifically, the proposed model surpassed the DCAEN model by 21%, the CNN model by 12%, the LSTM model by a substantial margin of 16%, and the ANN model by 16%. This quantitative advantage underscores the efficacy of the proposed framework in learning and generalising from the data, thereby outclassing the comparative models in terms of performance. The comparative performance metrics are succinctly tabulated below in Table 3.

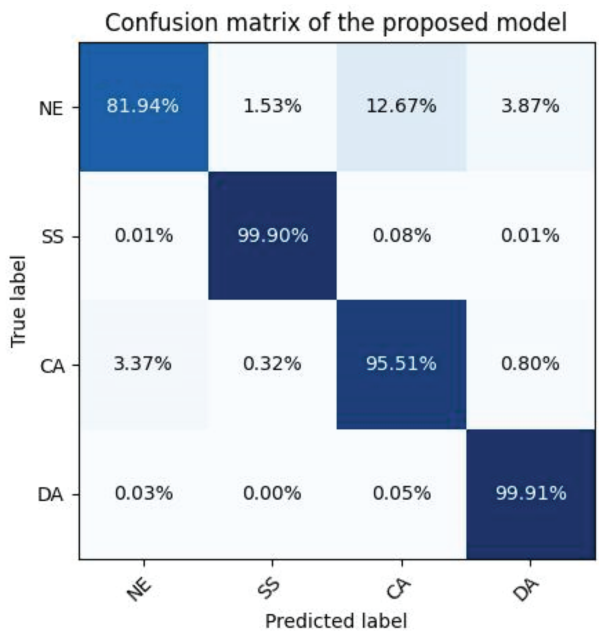

Figure 5. Confusion matrix of the proposed approach.

Table 3. Comparative performance analysis of the proposed framework with established neural network models.

Model	Authors	Performance Accuracy	Relative Performance Improvement
DCAEN	[27]	75%	21%
CNN	[30]	84%	12%
LSTM	[21]	80%	16%
ANN	[20]	80%	16%
Proposed Model	-	96%	-

5.3. Model Interpretation Using SHAP

The study employed SHAP values to identify the top 10 most important features for each mental state class: NE, SS, CA, and DA. The SHAP values provide a measure of the contribution of each feature to the model's prediction for each class, allowing for an understanding of which features are most influential in determining the mental state.

For the NE class, the top 10 features were primarily delta and beta frequency bands from various EEG channels. The mean absolute SHAP values for these characteristics, as shown in Figure 6, ranged between 0.15 and less than 0.25. The SS class showed a similar pattern, with the top 10 features being predominantly delta and beta frequency bands. As shown in Figure 7, the mean absolute SHAP values for these characteristics ranged between a little less than 0.08 and a little bit less than 0.11. The CA class also showed a predominance of delta and beta frequency bands in the top 10 features. Figure 8 illustrates that the mean absolute SHAP values for these features ranged between 0.127 and approximately 0.225. Lastly, for the DA class, the top 10 features were primarily delta and beta frequency bands. Figure 9 shows that the mean absolute SHAP values for these features ranged between a little bit less than 0.08 and a little bit more than 0.12.

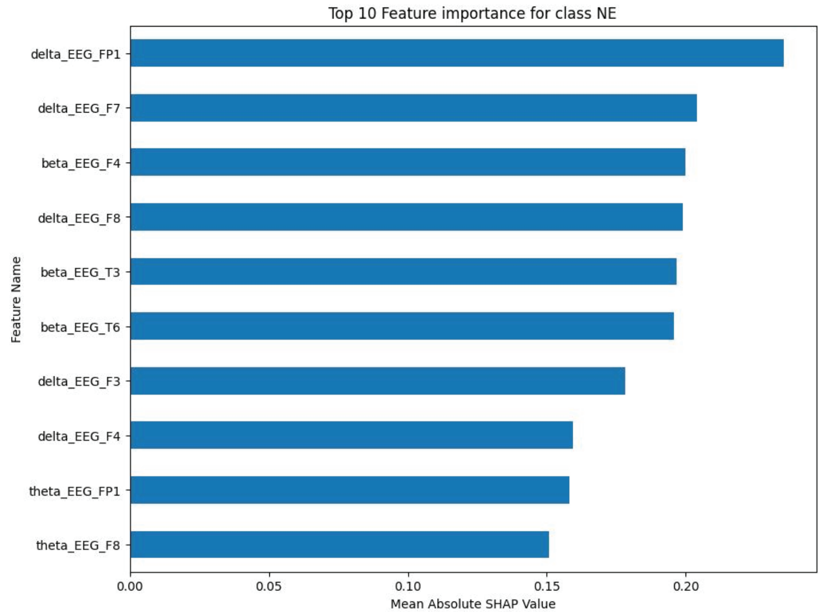

Figure 6. Top 10 important features for NE class.

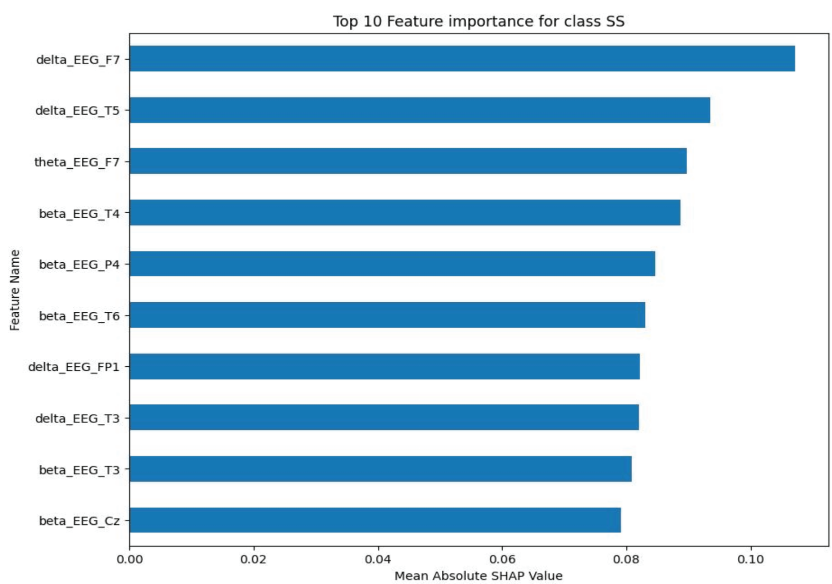

Figure 7. Top 10 important features for SS class.

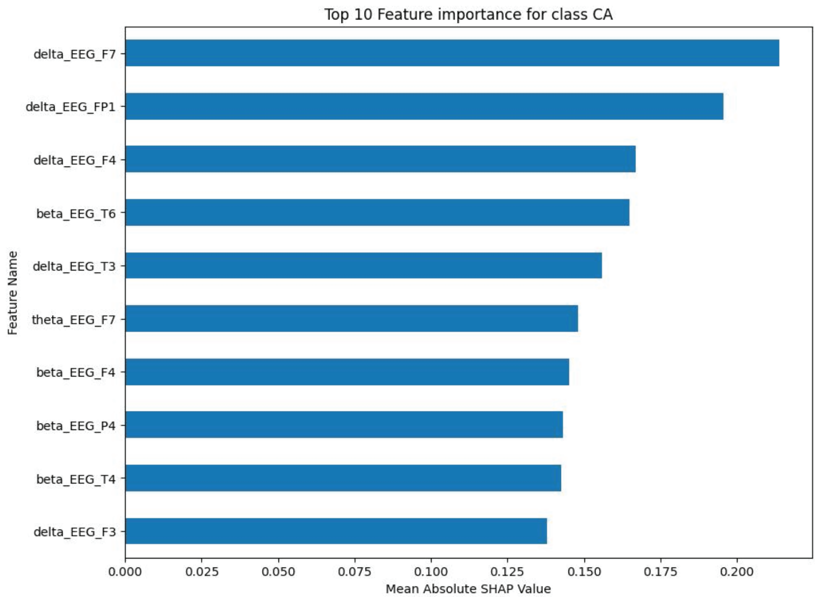

Figure 8. Top 10 important features for CA class.

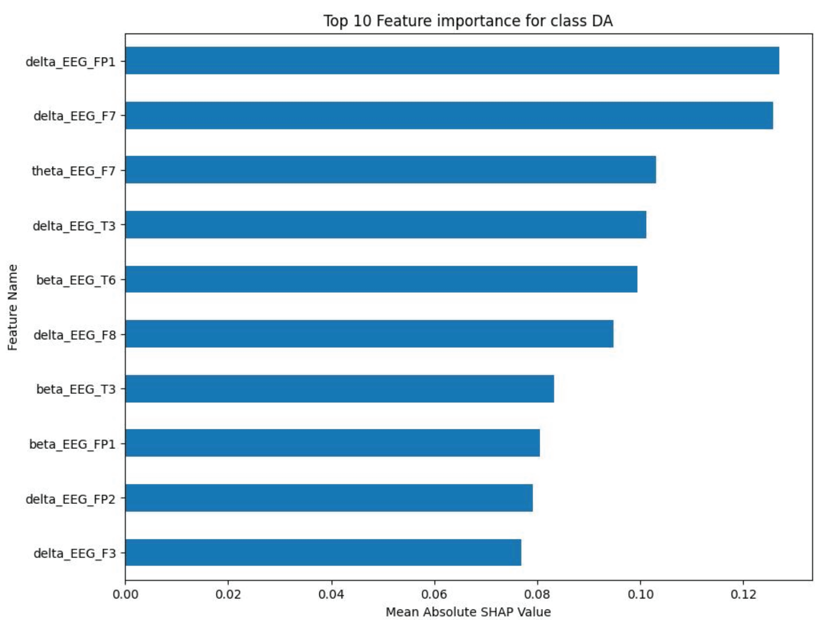

Figure 9. Top 10 important features for DA class.

6. Discussion

The results of this study demonstrate the potential of using the proposed approach to detect mental states based on PSD features of the EEG data. The high-performance metrics across all pilots suggest that the model is effective in distinguishing between the four mental states: CA, DA, SS, and NE.

The use of PSD features from five frequency bands (i.e., delta, theta, alpha, beta, and gamma) across 20 EEG channels likely contributed to the model's high performance. These features provide a rich representation of the EEG signals, capturing important frequency-specific information that is relevant for distinguishing between different mental states. PSD features encapsulate the power distribution over various frequency bands, which is a crucial aspect of EEG signals that are often linked to different mental states. However, the variation in the model's performance across different pilots indicates that individual differences may have influenced the results. Each pilot may have unique EEG patterns and responses to different mental states, which could affect the model's performance. For example, the model achieved the highest performance metrics with Pilot 2, suggesting that the features of this pilot's EEG data were particularly well-suited to the model. On the other hand, the model's performance was lowest with Pilot 12, indicating that there may be unique aspects of this pilot's EEG data that were not as effectively captured by the model.

The fact that the model performed well on the combined data of all pilots is promising. It suggests that the model is capable of generalising across different individuals, which is crucial for its potential application in real-world settings. However, the slightly lower recall score in comparison to the other metrics indicates that there is still room for improvement in the model's ability to correctly identify all instances of the different mental states. Future work could explore ways to further improve the model's performance. This could include refining the model's architecture, experimenting with different methods of preprocessing the EEG data or incorporating additional features that capture more information about the pilots' mental states. For instance, exploring different types of feature extraction methods or incorporating temporal information could potentially enhance the model's performance. Additionally, additional validation with larger datasets and in real-world settings would be beneficial to confirm these findings and further refine the model.

This study provides valuable insights into the potential of using the proposed framework for detecting mental states based on PSD features of EEG data. The high-performance metrics achieved by the model suggest that it could be a valuable tool in fields such as aviation, where monitoring pilots' mental states could contribute to safety and performance. However, it is important to note that while the model's performance is promising, the interpretation and application of these results should be carried out with caution. The model's performance is based on the specific dataset used in this study, and its performance may vary with different datasets. Therefore, further research and validation are necessary to fully understand the model's capabilities and limitations.

Analysis of the accuracy and loss curves provides valuable insights into the learning process and its ability to generalise from the training data to unseen data. The steady increase in the training accuracy and the consistent decrease in the training loss demonstrate that the model was effectively learning from the PSD features extracted from the EEG data. This suggests that the model's architecture and the preprocessing steps taken, including the use of PSD features, were well suited for the task of detecting the four mental states.

The slight irregularities observed in the validation accuracy and loss curves suggest that the model's performance varied when applied to different subsets of data. These fluctuations could be due to a variety of factors, including inherent variability in the EEG data, individual differences between pilots, or the specific division of the data into training and validation sets. Despite these irregularities, the overall positive trend in the accuracy of the validation and the general decrease in the validation loss indicates that the model was able to generalise its learning to new data, which is a crucial aspect of its performance. However, the presence of these irregularities also suggests potential areas for improvement in the model. Future work could explore different strategies for managing these irregularities, such as adjusting the model's architecture, experimenting with different methods of data preprocessing, or using different strategies for dividing the data into training and validation sets. In conclusion, the accuracy and loss curves provide additional evidence of the potential of the proposed model to detect mental states based on PSD features extracted from the EEG data. Despite some irregularities in the validation curves, the overall trends suggest that the model is capable of learning effectively from the data and generalising its learning to new data. This holds promise for the model's application in real-world settings, such as aviation, where accurate detection of pilots' mental states could contribute to safety and performance.

The confusion matrix provides a deeper understanding of the model's performance across the four mental states. It is evident that the model performs exceptionally well in classifying the SS and DA states, with almost perfect accuracy rates of 99.90% and 99.91%, respectively. This high level of accuracy suggests that the model is highly effective in distinguishing these states, likely due to the distinct PSD features associated with these mental states in the EEG data. The CA state also saw a high accuracy rate of 95.51%, indicating that the model is also capable of effectively identifying this state. However, the NE state had a noticeably lower accuracy rate of 81.94%. This could be due to the inherent complexity in distinguishing the NE state from the other mental states, as the NE state might not exhibit as distinct PSD features as the other states. The off-diagonal elements of the confusion matrix, which represent the instances where the model made incorrect predictions, provide further insights into the model's performance. For instance, the model misclassified the NE state as the CA state in 12.67% of instances. This could suggest that the EEG features of these two states might share some similarities, causing the model to confuse between them.

Despite these challenges, the overall performance of the model, as demonstrated by the confusion matrix, is highly promising. The model's ability to achieve high accuracy rates across the four mental states suggests that it is capable of effectively using PSD features extracted from EEG data to detect different mental states. Future work could focus on improving the model's ability to distinguish the normal state, potentially by incorporating additional features or refining the model's architecture. Furthermore, additional validation with larger datasets and in real-world settings would be beneficial to confirm these findings and to further refine the model.

The results stated in Table 3 reveal a compelling narrative regarding the superior performance of the proposed framework in comparison to other well-established neural network architectures. The comparative analysis unveiled a marked improvement in classification accuracy by the framework model, thereby underlining its robustness and efficacy in deciphering intricate patterns within the data. Specifically, the substantial lead of 21% over the DCAEN model, 12% over the CNN model, and 16% over the LSTM and ANN models underscores the adeptness of the proposed framework in handling the inherent complexities of the classification task. The pronounced superiority in performance could be attributed to the careful design of the proposed framework, which possibly enabled a better understanding and representation of the underlying data distributions. Furthermore, the results accentuate the potential of the proposed framework for broader applicability in related domains demanding high-accuracy classification tasks. It is salient to acknowledge that while the proposed framework outperformed the other models, the comparative analysis also sheds light on the areas where other models could be refined and optimised for better performance.

Upon the analytical examination of the model performance, a salient feature of our model's architecture merits discussion. Unlike frameworks employing recurrent layers such as LSTM layers, our model, anchored by 1D-CNN, availed a clear pathway to discern the contribution of individual features towards specific predictions. This clarity was further enhanced via the employment of the SHAP method, which enabled a detailed exploration into feature importance. The comparison of our model against those incorporating LSTM layers underscores a pervasive challenge: the inherent intricacy of recurrent mechanisms often veils the precise attribution of features, making the elucidation of individual feature contributions towards predictions a challenging endeavour. However, the integration of 1D-CNN and SHAP in our model mitigated this challenge, fostering not only superior classification accuracy but also augmented interpretability. This aspect of interpretability is crucial, especially in domains where deciphering the rationale behind model predictions is imperative for garnering trust and facilitating actionable insights.

The results of the SHAP analysis, as visualised in Figures 6–9, provide valuable insight into the most important features to predict each mental state. The predominance of delta and beta frequency bands in the top 10 features for each class suggests that these frequency bands may be particularly important for distinguishing between different mental states. Delta waves are typically associated with sleep or deep relaxation, while beta waves are associated with active thinking or focus. This aligns with the nature of the mental states being predicted, as channelised and diverted attention would likely involve more active thinking (beta waves), while a normal state might be more relaxed (delta waves).

However, it is interesting to note that the specific EEG channels that were most important varied between the classes. This suggests that different mental states may be associated with activity in different regions of the brain, which is captured by the different EEG channels. For example, the F7 channel (frontal lobe) was important for the NE, SS, and CA classes, while the T3 channel (temporal lobe) was important for the SS and DA classes. This could potentially provide insights into the neural mechanisms underlying these mental states.

The range of the mean absolute SHAP values for the top 10 features in each class also provides information about the relative importance of these features. The NE and CA classes had higher SHAP values compared to the SS and DA classes, suggesting that the top features for NE and CA may have a stronger influence on the model's predictions.

These findings highlight the complexity of predicting mental states based on EEG data and the importance of considering both the frequency and spatial information contained in the data. However, further research is needed to fully understand the implications of these results and to explore how this information can be used to improve the model's performance. For instance, it might be beneficial to incorporate these findings into the feature selection or preprocessing stages of the model development process.

7. Conclusions

The present study has made significant strides in demonstrating the potential of the proposed approach for the classification of distinct mental states, specifically CA, DA, SS and NE states, based on PSD features derived from EEG data. The model's performance, as assessed by accuracy, precision, recall, and F1 score metrics, was consistently high across all pilots, indicating its robustness and generalisability. This is a promising finding, suggesting that the model can effectively learn from individual pilots and apply this learning to a broader population.

The use of SHAP values in this study has provided a deeper understanding of the model's decision-making process. By identifying the most influential features for each mental state, we have gained insights into the importance of both frequency-specific and spatial information in EEG data for mental state classification. The predominance of delta and beta frequency bands in the top features for each class suggests that these frequency bands play a crucial role in differentiating between various mental states.

However, the study also revealed the complexity of the task at hand. The variation in the model's performance across different pilots and the range of SHAP values across classes underscore the influence of individual differences and the complexity of the mental states being predicted. These findings suggest that while the model is effective, there is still room for improvement and refinement. Future work could focus on enhancing the model's architecture, exploring different preprocessing methods, or incorporating additional features that capture more nuanced aspects of the pilots' mental states.

Furthermore, the findings need to be validated with larger datasets and in real-world settings to confirm their applicability and further refine the model. The high-performance metrics achieved by the model suggest its potential utility in fields such as aviation, where monitoring pilots' mental states could contribute to safety and performance. However, the interpretation and application of these results should be carried out with caution, considering the specific dataset used in this study and the potential variability in the model's performance with different datasets.

In conclusion, this study contributes valuable insights into the potential of CNN models for mental state detection based on PSD features of EEG data. It underscores the importance of comprehensive feature representation, the influence of individual differences, and the need for further research and validation to fully realise the potential of this approach. The findings of this study pave the way for future research in this area, with the ultimate goal of enhancing sty and performance in high-stakes fields such as aviation.

Author Contributions: Conceptualization, I.A. and I.M.; methodology, I.A. and I.M.; software, I.A.; validation, I.A. and I.M.; formal analysis, I.A.; investigation, I.A.; data curation, I.A.; writing—original draft preparation, I.A.; writing—review and editing, I.M. and D.B.; visualization, I.A.; supervision, I.M. All authors have read and agreed to the published version of the manuscript.

Funding: This research received no external funding. The APC was funded by Cranfield University.

Institutional Review Board Statement: Not applicable.

Informed Consent Statement: Not applicable.

Data Availability Statement: The input data, source code, and output data can be found via the DOI link: https://doi.org/10.17862/cranfield.rd.24155832 (accessed on 6 November 2023).

Conflicts of Interest: The authors declare no conflict of interest.

References

1. Schomer, D.L. *Niedermeyer's Electroencephalography*; Schomer, D.L., Lopes da Silva, F.H., Eds.; Oxford University Press: Oxford, UK, 2017; Volume 1, ISBN 9780190228484.
2. Buzsáki, G.; Anastassiou, C.A.; Koch, C. The Origin of Extracellular Fields and Currents-EEG, ECoG, LFP and Spikes. *Nat. Rev. Neurosci.* **2012**, *13*, 407–420. [CrossRef] [PubMed]
3. Cohen, M.X. Where Does EEG Come from and What Does It Mean? *Trends Neurosci.* **2017**, *40*, 208–218. [CrossRef] [PubMed]
4. Mihajlovic, V.; Grundlehner, B.; Vullers, R.; Penders, J. Wearable, Wireless EEG Solutions in Daily Life Applications: What Are We Missing? *IEEE J. Biomed. Health Inf.* **2015**, *19*, 6–21. [CrossRef] [PubMed]
5. Teplan, M. Fundamentals of EEG Measurement. Measurement Science Review. *Meas. Sci. Rev.* **2002**, *2*, 59–64.
6. Makeig, S.; Kothe, C.; Mullen, T.; Bigdely-Shamlo, N.; Zhilin, Z.; Kreutz-Delgado, K. Evolving Signal Processing for Brain–Computer Interfaces. *Proc. IEEE* **2012**, *100*, 1567–1584. [CrossRef]
7. Borghini, G.; Astolfi, L.; Vecchiato, G.; Mattia, D.; Babiloni, F. Measuring Neurophysiological Signals in Aircraft Pilots and Car Drivers for the Assessment of Mental Workload, Fatigue and Drowsiness. *Neurosci. Biobehav. Rev.* **2014**, *44*, 58–75. [CrossRef] [PubMed]
8. Klimesch, W. EEG Alpha and Theta Oscillations Reflect Cognitive and Memory Performance: A Review and Analysis. *Brain Res. Rev.* **1999**, *29*, 169–195. [CrossRef] [PubMed]
9. Başar, E.; Başar-Eroglu, C.; Karakaş, S.; Schürmann, M. Gamma, Alpha, Delta, and Theta Oscillations Govern Cognitive Processes. *Int. J. Psychophysiol.* **2001**, *39*, 241–248. [CrossRef] [PubMed]
10. Harmony, T. The Functional Significance of Delta Oscillations in Cognitive Processing. *Front. Integr. Neurosci.* **2013**, *7*, 83. [CrossRef]
11. Schirrmeister, R.T.; Springenberg, J.T.; Fiederer, L.D.J.; Glasstetter, M.; Eggensperger, K.; Tangermann, M.; Hutter, F.; Burgard, W.; Ball, T. Deep Learning with Convolutional Neural Networks for EEG Decoding and Visualization. *Hum. Brain Mapp.* **2017**, *38*, 5391–5420. [CrossRef]
12. Bashivan, P.; Rish, I.; Yeasin, M.; Codella, N. Learning Representations from EEG with Deep Recurrent-Convolutional Neural Networks. In Proceedings of the 4th International Conference on Learning Representations, ICLR 2016—Conference Track Proceedings, San Juan, Puerto Rico, 2–4 May 2016.
13. Oehling, J.; Barry, D.J. Using Machine Learning Methods in Airline Flight Data Monitoring to Generate New Operational Safety Knowledge from Existing Data. *Saf. Sci.* **2019**, *114*, 89–104. [CrossRef]
14. Chen, J.; Song, L.; Wainwright, M.J.; Jordan, M.I. Learning to Explain: An Information-Theoretic Perspective on Model Interpretation. In Proceedings of the 35th International Conference on Machine Learning, ICML 2018, Stockholm, Sweden, 10–15 July 2018; Volume 2, pp. 1386–1418.
15. Lundberg, S.M.; Lee, S.I. A Unified Approach to Interpreting Model Predictions. *Adv. Neural Inf. Process. Syst.* **2017**, *30*, 4766–4775.
16. Terwilliger, P.; Sarle, J.; Walker, S. A ResNet Autoencoder Approach for Time Series Classification of Cognitive State. In Proceedings of the MODSIM World, Norfolk, VA, USA, 20 March 2020; pp. 1–11.
17. Harrivel, A.R.; Liles, C.A.; Stephens, C.L.; Ellis, K.K.; Prinzel, L.J.; Pope, A.T. Psychophysiological Sensing and State Classification for Attention Management in Commercial Aviation. In Proceedings of the AIAA Infotech @ Aerospace Conference, San Diego, CA, USA, 4–8 January 2016; pp. 1–8. [CrossRef]

18. Harrivel, A.R.; Stephens, C.L.; Milletich, R.J.; Heinich, C.M.; Last, M.C.; Napoli, N.J.; Abraham, N.A.; Prinzel, L.J.; Motter, M.A.; Pope, A.T. Prediction of Cognitive States during Flight Simulation Using Multimodal Psychophysiological Sensing. In Proceedings of the AIAA Information Systems-AIAA Infotech at Aerospace, Grapevine, TX, USA, 9–13 January 2017; pp. 1–10. [CrossRef]
19. Alreshidi, I.; Moulitsas, I.; Jenkins, K.W. Multimodal Approach for Pilot Mental State Detection Based on EEG. *Sensors* **2023**, *23*, 7350. [CrossRef]
20. Alreshidi, I.M.; Moulitsas, I.; Jenkins, K.W. Miscellaneous EEG Preprocessing and Machine Learning for Pilots' Mental States Classification: Implications. In Proceedings of the 6th International Conference on Advances in Artificial Intelligence, Birmingham, UK, 20–23 October 2022; pp. 29–39. [CrossRef]
21. Alreshidi, I.; Yadav, S.; Moulitsas, I.; Jenkins, K.; Alreshidi, I.; Yadav, S.; Moulitsas, I.; Jenkins, K. A Comprehensive Analysis of Machine Learning and Deep Learning Models for Identifying Pilots' Mental States from Imbalanced Physiological Data. In *AIAA AVIATION 2023 Forum*; AIAA AVIATION Forum; American Institute of Aeronautics and Astronautics: Washington, DC, USA, 2023.
22. Prinzel, L.J.; Freeman, F.G.; Scerbo, M.W.; Mikulka, P.J.; Pope, A.T. A Closed-Loop System for Examining Psychophysiological Measures for Adaptive Task Allocation. *Int. J. Aviat. Psychol.* **2000**, *10*, 393–410. [CrossRef]
23. Lo Giudice, M.; Varone, G.; Ieracitano, C.; Mammone, N.; Bruna, A.R.; Tomaselli, V.; Morabito, F.C. 1D Convolutional Neural Network Approach to Classify Voluntary Eye Blinks in EEG Signals for BCI Applications. In Proceedings of the International Joint Conference on Neural Networks, Glasgow, UK, 19–24 July 2020. [CrossRef]
24. Mattioli, F.; Porcaro, C.; Baldassarre, G. A 1D CNN for High Accuracy Classification and Transfer Learning in Motor Imagery EEG-Based Brain-Computer Interface. *J. Neural Eng.* **2021**, *18*, 066053. [CrossRef] [PubMed]
25. Tabar, Y.R.; Halici, U. A Novel Deep Learning Approach for Classification of EEG Motor Imagery Signals. *J. Neural Eng.* **2017**, *14*, 016003. [CrossRef]
26. Zorzos, I.; Kakkos, I.; Miloulis, S.T.; Anastasiou, A.; Ventouras, E.M.; Matsopoulos, G.K. Applying Neural Networks with Time-Frequency Features for the Detection of Mental Fatigue. *Appl. Sci.* **2023**, *13*, 1512. [CrossRef]
27. Wu, E.Q.; Peng, X.Y.; Zhang, C.Z.; Lin, J.X.; Sheng, R.S.F. Pilots' Fatigue Status Recognition Using Deep Contractive Autoencoder Network. *IEEE Trans. Instrum. Meas.* **2019**, *68*, 3907–3919. [CrossRef]
28. Wu, E.Q.; Deng, P.Y.; Qiu, X.Y.; Tang, Z.; Zhang, W.M.; Zhu, L.M.; Ren, H.; Zhou, G.R.; Sheng, R.S.F. Detecting Fatigue Status of Pilots Based on Deep Learning Network Using EEG Signals. *IEEE Trans. Cogn. Dev. Syst.* **2021**, *13*, 575–585. [CrossRef]
29. Cui, J.; Lan, Z.; Sourina, O.; Muller-Wittig, W. EEG-Based Cross-Subject Driver Drowsiness Recognition With an Interpretable Convolutional Neural Network. *IEEE Trans. Neural Netw. Learn. Syst.* **2022**, *34*, 7921–7933. [CrossRef] [PubMed]
30. Han, S.Y.; Kwak, N.S.; Oh, T.; Lee, S.W. Classification of Pilots' Mental States Using a Multimodal Deep Learning Network. *Biocybern. Biomed. Eng.* **2020**, *40*, 324–336. [CrossRef]
31. Johnson, M.K.; Blanco, J.A.; Gentili, R.J.; Jaquess, K.J.; Oh, H.; Hatfield, B.D. Probe-Independent EEG Assessment of Mental Workload in Pilots. In Proceedings of the 2015 7th International IEEE/EMBS Conference on Neural Engineering (NER), Montpellier, France, 22–24 April 2015; pp. 581–584.
32. Roza, V.C.; Postolache, O.; Groza, V.; Pereira, J.M.D. Emotions Assessment on Simulated Flights. In Proceedings of the 2019 IEEE International Symposium on Medical Measurements and Applications (MeMeA), Istanbul, Turkey, 26–28 June 2019; pp. 1–6.
33. Roza, V.C.C.; Postolache, O.A. Multimodal Approach for Emotion Recognition Based on Simulated Flight Experiments. *Sensors* **2019**, *19*, 5516. [CrossRef]
34. Binias, B.; Myszor, D.; Cyran, K.A. A Machine Learning Approach to the Detection of Pilot's Reaction to Unexpected Events Based on EEG Signals. *Comput. Intell. Neurosci.* **2018**, *2018*, 2703513. [CrossRef] [PubMed]
35. Widmann, A.; Schröger, E.; Maess, B. Digital Filter Design for Electrophysiological Data—A Practical Approach. *J. Neurosci. Methods* **2015**, *250*, 34–46. [CrossRef]
36. Hyvärinen, A. Fast and Robust Fixed-Point Algorithms for Independent Component Analysis. *IEEE Trans. Neural Netw.* **1999**, *10*, 626–634. [CrossRef] [PubMed]
37. Slepian, D. Prolate Spheroidal Wave Functions, Fourier Analysis, and Uncertainty-V: The Discrete Case. *Bell Syst. Tech. J.* **1978**, *57*, 1371–1430. [CrossRef]
38. Fernández, A.; García, S.; Herrera, F.; Chawla, N.V. SMOTE for Learning from Imbalanced Data: Progress and Challenges, Marking the 15-Year Anniversary. *J. Artif. Intell. Res.* **2018**, *61*, 863–905. [CrossRef]
39. Abdoli, S.; Cardinal, P.; Lameiras Koerich, A. End-to-End Environmental Sound Classification Using a 1D Convolutional Neural Network. *Expert. Syst. Appl.* **2019**, *136*, 252–263. [CrossRef]
40. Kiranyaz, S.; Avci, O.; Abdeljaber, O.; Ince, T.; Gabbouj, M.; Inman, D.J. 1D Convolutional Neural Networks and Applications: A Survey. *Mech. Syst. Signal Process.* **2021**, *151*, 107398. [CrossRef]
41. Shapley, L.S. A Value for n-Person Games. In *Contributions to the Theory of Games (AM-28), Volume II*; Princeton University Press: Princeton, NJ, USA, 1953; pp. 307–318.

sensors

Article

Using Explainable Artificial Intelligence to Obtain Efficient Seizure-Detection Models Based on Electroencephalography Signals

Jusciaane Chacon Vieira *, Luiz Affonso Guedes, Mailson Ribeiro Santos and Ignacio Sanchez-Gendriz

Department of Computer Engineering and Automation—DCA, Federal University of Rio Grande do Norte—UFRN, Natal 59078-900, RN, Brazil; affonso@dca.ufrn.br (L.A.G.); mailsonribeiro@ufrn.edu.br (M.R.S.); ignaciogendriz@dca.ufrn.br (I.S.-G.)
* Correspondence: jusciaanechacon@gmail.com

Abstract: Epilepsy is a condition that affects 50 million individuals globally, significantly impacting their quality of life. Epileptic seizures, a transient occurrence, are characterized by a spectrum of manifestations, including alterations in motor function and consciousness. These events impose restrictions on the daily lives of those affected, frequently resulting in social isolation and psychological distress. In response, numerous efforts have been directed towards the detection and prevention of epileptic seizures through EEG signal analysis, employing machine learning and deep learning methodologies. This study presents a methodology that reduces the number of features and channels required by simpler classifiers, leveraging Explainable Artificial Intelligence (XAI) for the detection of epileptic seizures. The proposed approach achieves performance metrics exceeding 95% in accuracy, precision, recall, and F1-score by utilizing merely six features and five channels in a temporal domain analysis, with a time window of 1 s. The model demonstrates robust generalization across the patient cohort included in the database, suggesting that feature reduction in simpler models—without resorting to deep learning—is adequate for seizure detection. The research underscores the potential for substantial reductions in the number of attributes and channels, advocating for the training of models with strategically selected electrodes, and thereby supporting the development of effective mobile applications for epileptic seizure detection.

Keywords: machine learning; Explainable AI; electroencephalography; epilepsy

Citation: Vieira, J.C.; Guedes, L.A.; Santos, M.R.; Sanchez-Gendriz, I. Using Explainable Artificial Intelligence to Obtain Efficient Seizure-Detection Models Based on Electroencephalography Signals. *Sensors* **2023**, *23*, 9871. https://doi.org/10.3390/s23249871

Academic Editors: Fei He, Hua-Liang Wei, Yuzhu Guo and Yifan Zhao

Received: 29 September 2023
Revised: 9 November 2023
Accepted: 9 November 2023
Published: 16 December 2023

1. Introduction

Epilepsy is a pathology that affects approximately 50 million individuals worldwide, with an estimated 2.4 million new cases developing annually. The prevalence of the disease varies, influenced by numerous factors, yet it is predominantly observed in developing countries. This trend underscores the importance of advancements in treatment and preventive measures as pivotal in curtailing such rates [1]. Moreover, individuals diagnosed with epilepsy often experience diminished quality of life, arising from social isolation, limitations in performing daily tasks, societal stigma, and psychological impacts on the patients and their families [2].

An epileptic seizure is a transient occurrence with diverse clinical manifestations that may affect sensory, motor, and autonomic functions; consciousness; memory; and can cause perceptual distortions [2]. Electroencephalography (EEG), a technique for measuring brain activity by recording electrical signals from the scalp, is commonly employed in the diagnosis of this condition. It can reveal the abnormally heightened synchrony of neuronal activity characteristic of epileptic seizures. However, it is not uncommon for patients with recurrent seizures to exhibit normal EEG patterns during and between seizure episodes [2], thus complicating accurate diagnosis.

Epileptic events known as absence seizures are particularly subtle, often marked by minimal motor activities [3]. Clinically identifying the onset and conclusion of such seizures poses a challenge, more so with atypical absence seizures where the indicators are less pronounced. Consequently, EEG signal monitoring becomes essential to the confirmation of these types of seizures [4].

The detection of epileptic seizures can be useful for recording and monitoring seizure frequencies in patients with the disease [5], such as those who experience absence seizures [6]. Simplified models for epileptic seizure detection—using few channels and requiring low computational costs—enable the implementation of embedded and wearable systems aimed at identifying seizures for subsequent medical analysis, as demonstrated in the study conducted by [6], where they achieved a sensitivity of 98.4% in the detection of typical absence seizures.

Given the significance and intricacy of seizure detection, considerable efforts have been directed towards machine learning (ML)-based methodologies for the automated analysis of EEG signals. Supervised ML classifiers are commonly employed in this domain [7–12], along with deep learning (DL) techniques [13,14]. These approaches are geared towards developing models adept at binary classification [7–9,11,12] as well as multiclass classification tasks [15,16].

Feature extraction is a pivotal element in enhancing the performance of ML models, particularly within the realm of EEG signal analysis. The methodologies for feature extraction in this context span across time, frequency, time–frequency, and non-linear domains [17], utilizing values from EEG signals over brief temporal windows. Time domain techniques often employ statistical metrics such as standard deviation, kurtosis, skewness, and mean [8,15,16]. Frequency domain approaches typically involve the use of Fast Fourier Transform (FFT) or Discrete Wavelet Transform (DWT) coefficients, either directly or through derived statistical measures of these coefficients [7,9–12,16,18,19]. Owing to the inherent non-linearity of EEG signals [20], certain studies also focus on extracting non-linear features, including Sample Entropy, Wavelet Entropy [21], and the Lyapunov exponent [22].

In addition to feature extraction, feature selection is crucial for the development of accurate and efficient machine learning models [23]. Several studies have proposed feature extraction techniques aimed at reducing dimensionality, such as Principal Component Analysis (PCA) [9]. Nonetheless, many of these techniques do not account for the specific channels associated with the selected features, which can necessitate the use of numerous electrodes. This requirement potentially complicates the deployment of compact and embedded devices.

Explainable Artificial Intelligence (XAI) has recently emerged as a promising approach to elucidate the intricacies of model decision-making processes, offering insights into how specific outcomes are derived. Such transparency is indispensable in healthcare applications, ensuring that model behaviors can be understood and trusted by practitioners [24]. An example of an application is the work of [25], which used XAI techniques for predicting strokes through interpretable analysis of EEG signals.

Among the XAI approaches, the SHapley Additive exPlanations (SHAP) method, as presented in [26], provides significance values for each feature in predicting the data, as discussed in [24]. According to [27], where the author conducted a study to identify epileptic seizures through the analysis of EEG signals using the SHAP technique, interpreting the model's output allows us to understand where it needs improvement. They mentioned three benefits of SHAP: global interpretability (contribution of each feature), local interpretability (each individual sample has its SHAP value), and versatility (usable with any tree-based model) [27].

In this study, we aimed to develop an efficient method for detecting epileptic seizures in EEG, focusing on reducing the number of channels used for signal acquisition and data processing. To achieve this, we applied an interpretable method—SHAP—to optimize machine learning models that perform binary classifications of EEG segments from interictal (period between epileptic seizures) and ictal (seizure period) states. Additionally, we also investigated the spatial proximity of relevant channels to the focal areas of epileptic seizures in the patients' database.

The remainder of this work is organized as follows: Section 2 presents the concepts and operation of XAI and SHAP; Section 3 discusses related works; Section 4 describes the proposed approach; Section 5 presents the materials and methods, including the utilized dataset and experimental setup; Section 6 showcases the obtained results; Section 7 provides a discussion; and Section 8 highlights the main conclusions and suggests future work.

2. Explainable Artificial Intelligence

Advanced ML-based predictive models, including DL neural networks, can achieve excellent performance in mapping resources as the input to classes as the output of these models. Nonetheless, these models are often opaque, resembling 'black-box' systems, which may inadvertently contribute to misinterpretations by neglecting data errors or human biases embedded within the training data, thereby affecting the decision-making process. Conversely, a transparent ML paradigm fosters the development of open and accountable models that are designed to address and mitigate such issues [28].

The explainability of an ML model is the elaboration of an interface between the human and the machine that is understandable to the human. Thus, the decision-making actions by the ML model need to be explainable [28].

Explainability transforms a non-interpretable model into one that can be interpreted, essentially delineating cause and effect relationships. Thus, Explainable Artificial Intelligence is designed to generate results that are readily understandable to users [29]. Consequently, such models bolster interpretability while preserving the precision of their predictions [30].

SHAP (SHapley Additive exPlanations) is a tool within the Python ecosystem that quantitatively attributes importance to individual features regarding their contribution to a model's predictions, grounding its methodology in coalition game theory, where the feature values of an instance are treated analogously to players in a game [26,31,32].

One of the possible representations of SHAP values is the SHAP summary plot, in which features are ranked first by their global impact and then by points representing the SHAP values. Points that represent each feature of each sample in the graph are created—in blue, they represent low values of the contribution of the feature, and points colored in red represent high values, and there may be a color graduation between the points—which accumulate vertically, indicating the density [33]. Figure 1 shows this type of graph, in which the influence of certain attributes on mortality is observed. Thus, high SHAP values indicate, for a given attribute, a greater probability of death [33,34].

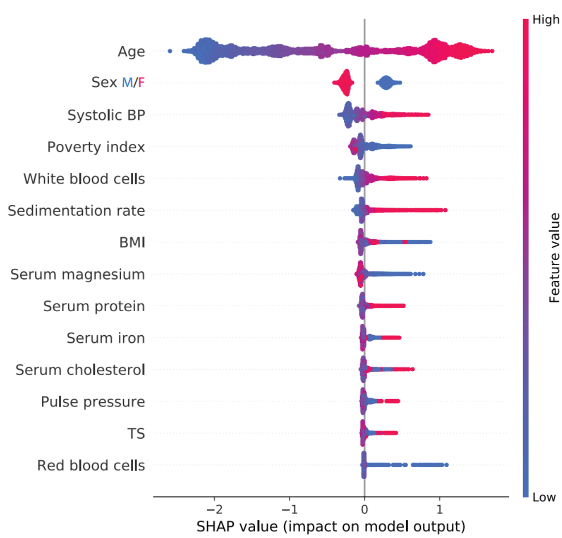

Figure 1. Shap summary plot [33].

3. Related Works

The current landscape of EEG signal analysis covers various applications. There are works focused on brain–computer interfaces for controlling orthoses/prostheses [35–37], controlling computer systems and devices [38–40], muscular rehabilitation through neurofeedback [41,42], assessing psychological states and emotions [43,44], and diagnosing and treating neurological disorders [45,46], among various applications aimed at improving the quality of life of individuals, either in a functional or health context.

In the field of epileptic seizure identification, the landscape is extensive and diverse. Some works perform seizure identification through EEG signals, as presented in Table 1, while others use medical images [47–49]. Some works aim to detect only the presence or absence of a seizure, as shown in Table 1, while others aim to differentiate between seizure types [50–52], and some seek to predict seizures [53–55].

Table 1. Comparative studies with binary classification (interictal vs. ictal) of EEG signals.

Methodology	Performance
Authors: [7] Database: TUH Domain: time and frequency Classifier: Random Forest Dimensionality reduction: None Channels: 19 Features: 19 Attributes: 19 × 19 = 361	Accuracy: 0.91 F1-score: 0.91 AUC: 0.95
Authors: [8] Database: TUH Domain: time and frequency Classifier: SVM Dimensionality reduction: None Channels: 21 Features: 13 Attributes: 21 × 13 = 273	Accuracy: 0.93 Precision: 0.94 Recall: 0.94 Specificity: 0.91 F1-score: 0.94
Authors: [9] Database: TUH Domain: frequency Classifier: Logistic Regression Dimensionality reduction: PCA Channels: 21 Features: 5 Attributes: 7	Precision: 0.73 Recall: 0.79 F1-score: 0.78
Authors: [10] Database: TUH Domain: frequency Classifier: LightGBM Dimensionality reduction: None Channels: 21 Features: 96 Attributes: 2016	F1-score: 0.84
Authors: [11] Database: TUH Domain: frequency Classifier: CatBoost Dimensionality reduction: None Channels: 21 Features: 96 Attributes: 21 × 96 = 2016	Accuracy: 0.88 Recall: 0.83 Specificity: 0.91

Table 1. *Cont.*

Methodology	Performance
Authors: [12] Database: CHB-MIT Domain: time and frequency Classifier: SVM Dimensionality reduction: None Channels: 22 Features: 18 Attributes: $22 \times 18 = 396$	(Interictal; Ictal) Accuracy: 0.99; 0.99 Precision: 1; 0.98 Recall: 1; 1 F1-score: 0.99; 0.99
Authors: [18] Database: CHB-MIT Domain: time and frequency Classifier: Random Forest Dimensionality reduction: None Channels: 20 Features: 8 Attributes: 1328	Accuracy: 0.99 Recall: 0.99 Specificity: 0.83
Authors: [19] Database: CHB-MIT Domain: frequency Classifier: KNN Dimensionality reduction: t-SNE Channels: 21 Features: 1 Attributes: 2	Precision: 0.47 Recall: 0.81 F1-score: 0.56

Literature reviews present a more comprehensive and comparative scenario. For instance, Ref. [17] discusses various feature extraction techniques in the time, frequency, time–frequency, and non-linear domains. Others highlight existing gaps in the field. Ref. [56] conducted a review on seizure prediction and reported that selecting the most significant channels is interesting for seizure prediction areas. Meanwhile, Ref. [57] conducted a bibliographic survey covering both seizure detection and prediction and concluded that channel selection is favorable for reducing computational costs, especially when the goal is to implement an online application. In their review work, Ref. [58] encourage the use of "non-black-box" classifiers as they can be more efficient when the objective is to find information about seizure localization. Ref. [59] reported some gaps in the research area, including the need to invest in a type of epilepsy known as absence seizures, due to the difficulty of visual identification [59].

In this study, a bibliographic search was conducted for publications that employed ML techniques (excluding DL) for the classification of binary data (interictal and ictal) in humans with epilepsy. It was chosen to use ML techniques because they are more feasible for performing model explainability analysis and observing the importance of features [60]. DL models, being "black-box", make it difficult to understand predictions and are therefore less interpretable [61]. In addition, DL models are more prone to overfitting [62], have longer training times, and require a large amount of data [63].

Table 1 offers a comparative analysis of related works, succinctly summarizing the methodologies employed and the performance outcomes as measured by the metrics applied in each respective study. The datasets referenced in Table 1 originate from Temple University Hospital (TUH) [64] and the Children's Hospital Boston–Massachusetts Institute of Technology (CHB-MIT) [65].

It is noticeable that works achieving around 99% accuracy require a high number of attributes, as is the case with 396 [12] and 1328 [18]. In the latter case, specificity was low compared with recall and accuracy, indicating that despite the large number of attributes, there was a challenge in achieving relative precision in identifying non-seizure data as non-seizure by the classifier.

Studies that applied methods to reduce the number of input vectors, such as Principal Component Analysis (PCA) and non-linear dimension reduction using t-distributed stochastic neighbor embedding (t-SNE), achieved precisions of 0.73 [9] and 0.47 [19], respectively. This result highlights the importance of selecting attributes using explainable methods.

Next, we provide a brief description of the works presented in Table 1.

Ref. [7] assessed various machine learning classifiers to distinguish between EEG records of patients with and without epileptic seizures. They utilized signal complexity measures and spectral power in different frequency bands for this purpose. In their findings, they indicated that the combination of complexity and spectral power achieved effective classification performance using a TUH dataset. However, in the study, they pointed out the need to consider gender differences as there is variation in EEG signals, which they intend to investigate in future work.

Ref. [8] developed a method for the automatic detection of generalized seizures in the TUH dataset by preprocessing EEG signals, extracting features in the time and frequency domains, and using machine learning classifiers, including Logistic Regression, Decision Tree, and SVM. SVM achieved the highest accuracy, reaching 0.93 in the binary classification of generalized seizures.

Ref. [9] used Logistic Regression as a classifier and extracted signal features through Fourier Analysis, with an emphasis on the energy distribution in different frequency bands. They also employed PCA and observed improvements in some performance metrics. The study involved 20 epilepsy patients and 20 healthy individuals. They suggested that proper feature selection before applying PCA is crucial to achieve significant improvements.

In [10], three wavelet-based feature extraction methods were applied and compared to classify multiple types of seizures in EEG data from the TUH database. Using the LightGBM classifier and without performing dimensionality reduction, they achieved a performance of approximately 0.84 in terms of weighted F1-score for the two classes analyzed.

Ref. [11] developed an automatic classification system for brain signals in multi-channel EEG records, using Wavelet Packet Decomposition to extract statistical features from frequency subbands such as mean absolute values, mean power, standard deviation, mean absolute value ratio, skewness, and kurtosis. Three Gradient Boosting Decision Tree-based classifiers were employed, with CatBoost achieving a classification accuracy of 0.88.

Ref. [12] developed an Automated Seizure Detection System using SVM and kNN classifiers and features extracted in the time, frequency, and time–frequency domains. The authors proposed generating metadata for the CHB-MIT database. Furthermore, they emphasized the importance of incorporating medical knowledge with machine learning methods.

Ref. [18] developed a hybrid seizure detection algorithm that combines continuous electroencephalography and integrated amplitude electroencephalography signals to diagnose epilepsy. They extracted features from multiple domains and performed classification using Random Forest. The study demonstrated high accuracy; however, they claim that the method is more suitable for longer seizures. They also developed a portable seizure detection system.

Ref. [19] employed a Random Forest classifier to select the most informative channels and a KNN classifier for the final discrimination between seizures and non-seizures. Feature extraction was based on the frequency domain of EEG signals, with 23 patients participating in the study. The combination of channel selection and non-linear dimensionality reduction enabled the method to achieve a recall performance of 0.81.

4. Proposed Approach

The proposal presented here for the efficient detection the epileptic seizures using EEG signals is composed of two phases. In the first one, the main contribution is the XAI-based approach to feature selection. Then, the second phase uses a similar procedure to obtain more efficient results. In both phases, the SHAP XAI Python library was used for feature selection.

Figure 2 shows the activity sequence of the first phase, which is described as follows:

- Raw data: In this first part, the raw data are downloaded from the site and the training and test data indicated in the dataset are used.
- Pre-processing: The initial step in pre-processing involves segregating the data into two distinct classes: interictal (non-seizure) and ictal (encompassing various seizure types). For the purpose of binary classification, all seizure types are amalgamated into a single 'ictal' class. Subsequently, data normalization is carried out followed by signal segmentation within a specified time window.
- Feature extraction: The features are extracted in the time domain for each of the channels of the segmented signal.
- Model selection: Training and testing with different ML models are performed. The ML model with the best performance in accuracy is chosen to be used in the next steps.
- Obtaining the reduced model: Based on the model selected in the previous phase, attribute selection is performed, considering the attributes that contributed the most to the prediction according to the SHAP value. New models with a reduced number of attributes are then trained.

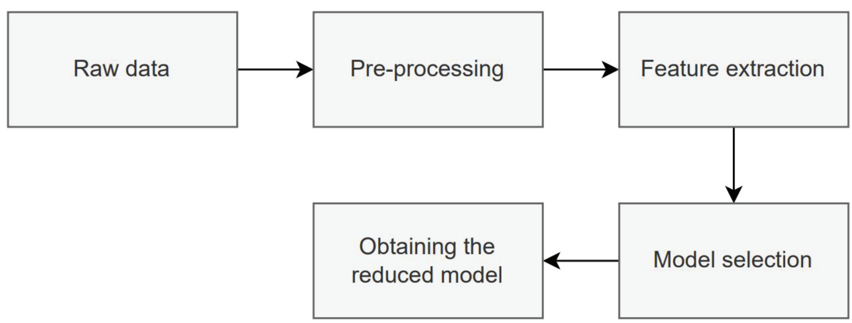

Figure 2. The first phase activity sequence of the proposed approach.

The second phase of the proposed methodology was dedicated to diminishing the quantity of input vectors by amalgamating the most recurrently significant channels and features. This phase encompassed two procedures: feature selection followed by obtaining the reduced model.

- Feature selection: a combination is made with the most recurrent channels and features (product of the number of most recurrent channels and the number of most recurrent features) among the attributes that contributed most to the prediction according to the SHAP value.
- Obtaining the reduced model: A model is trained with the attributes from the combination in the previous step. The SHAP value is used again to rank the attributes that contributed most to the prediction, and then new models with a reduced number of attributes are trained, following the order of relevance.

5. Materials and Methods

In this section, the materials and methods used are presented, including a description of the chosen dataset and experimental setup.

5.1. Dataset

The database selection for the method implementation followed several criteria: it had to be a public database; contain data from humans with epilepsy; use surface EEG channels; include interictal and ictal segments; have at least the channels arranged in the international

10-20 system; be acquired at a sampling rate between 200 and 512 Hz, as it is the ideal range for observing epileptic data information [3]; include data from at least two patients; and provide information about the type of seizures and the brain location of each patient.

The database employed in this research is the publicly accessible dataset from the University of Beirut Medical Center (UBMC) [66]. This dataset comprises recordings from six epilepsy patients. The data were captured at a sampling rate of 500 Hz, encompassing in excess of 7 h of ictal recordings—including Complex Partial Seizure, Electrographic Seizures, and Video-detected Seizures without observable EEG changes—and over 7 h of interictal recordings [66]. Recordings were conducted using twenty-one surface electrodes aligned with the international 10-20 system for electrode placement [67].

Data were selected so that analyses were performed in two classes (interictal and ictal). In addition, of the 21 available channels, only 19 were used because there were missing records of two channels (Cz and Pz) in some recordings [66].

The documentation also contains information about the type of seizure for each patient, which are electrographic or Complex Partial Seizure. The focal points were also recorded, including Fp2, F4, F8, T6, Cz, C3, C4, T3, T3-P3, T3-C3, right temporal, left hemisphere, posterior temporal, fronto-temporal, diffuse onset, and no change over surface EEG [66].

The provided dataset is pre-labeled for training and testing across four classes and is available in the .mat file format. It encompasses 3,505,500 data points designated for training and 389,500 for testing, resulting from signal acquisition with a sampling rate of 500 Hz [66].

Feature extraction was performed using a window of 1 s (500 samples per second); thus, the number of entries was reduced to 7011 samples of training data (3479 samples of interictal data and 3532 samples of all classes of ictal data) and 779 test data samples (416 interictal data samples and 363 samples from all types of ictal data).

Figure 3 illustrates the international 10-20 electrode positioning system [67], with annotations to facilitate comparison with the patient data from the UBMC database. In the figure, the electrodes corresponding to regions affected by epilepsy in the patients documented in [66] are highlighted in blue. The channels that were not recorded, Cz and Pz, are indicated in red.

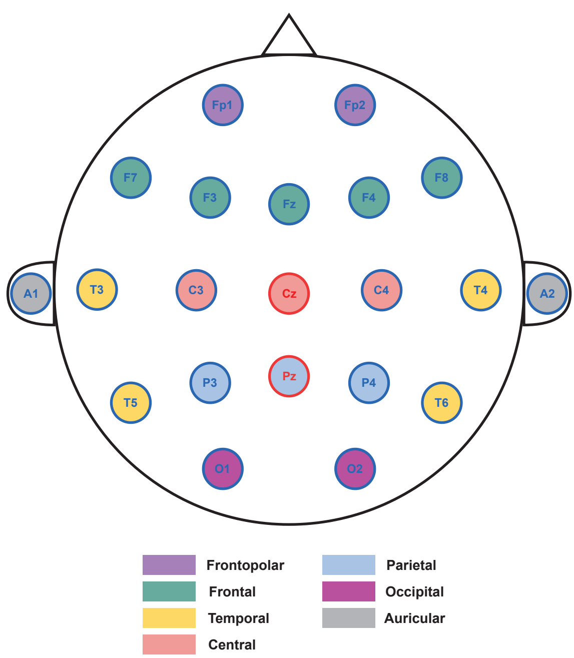

Figure 3. The international 10-20 system of electrode placement.

5.2. Experimental Setup

In this subsection, the experimental configuration of the presented proposal is detailed, in two phases.

5.2.1. First Phase

Initially, after acquiring the database, it was decided to use the training and test files indicated in the database in `.mat` format. Data were segmented into 2 classes—ictal data (Complex Partial, Electrographic, and Video-detected with no visual change) and interictal data (no seizure). Subsequently, the EEG signals were pre-processed through z-score normalization for each channel. It is important to note that, after obtaining the data from the website, no additional data cleaning or artifact removal techniques were applied.

Subsequently, the EEG signals were segmented into 1 s time windows (each time window containing 500 samples). In the next phase, 13 features were extracted in the time domain for each of the 19 channels (Fp2, Fp1, F8, F4, Fz, F3, F7, A2, T4, C4, C3, T3, A1, T6, P4, P3, T5, O2, O1): amplitude, skewness, Activity, Complexity, Zero crossing, kurtosis, Energy, Maximum, mean, Median, Minimum, Mobility, and RMS. Thus, we generated 247 attributes (19 channels $\times$ 13 features). The mentioned features, Activity, Complexity, and Mobility, known as Hjorth parameters [68], were used specifically to represent EEG signals. The mathematical formulation of these features is described as follows:

Activity

$$std^2 = \frac{\sum_{i=1}^{N}(x_i - \overline{x})^2}{N-1} \tag{1}$$

Amplitude

$$amp = x_{max} - x_{min} \tag{2}$$

Complexity

$$comp = \sqrt{\frac{mob(x(t)(\frac{dx}{dt}))}{mob(x(t))}} \tag{3}$$

Energy

$$energy = \frac{1}{N}\sum_{i=1}^{N} x_i^2 \tag{4}$$

Kurtosis

$$k = \frac{Q_3 - Q_1}{2(P_{90} - P_{10})} \tag{5}$$

Maximum value

$$max = \max_{i=1}^{N} x_i \tag{6}$$

Mean

$$\overline{x} = \frac{1}{N}\sum_{i=1}^{N} x_i \tag{7}$$

Median

$$median = \begin{cases} x_{\frac{N-1}{2}+1}, & \text{for odd N;} \quad (8) \\ \frac{1}{2}(x_{\frac{N}{2}} + x_{\frac{N}{2}+1}), & \text{for even N} \quad (9) \end{cases}$$

Minimum value

$$min = \min_{i=1}^{N} x_i \tag{10}$$

Mobility

$$mob = \sqrt{\frac{std^2(\frac{dx}{dt})}{std^2}} \tag{11}$$

Root mean square

$$rms = \sqrt{\frac{1}{N}\sum_{i=1}^{N} x_i^2} \tag{12}$$

Skewness

$$s = \frac{\overline{x} - mode}{std} \tag{13}$$

Zero crossing

$$zc = (K-1) - \frac{1}{2}\sum_{i=1}^{K}\left|\frac{x_i}{|x_i|} - \frac{x_{i+1}}{|x_{i+1}|}\right| \tag{14}$$

where x_i is the value of each sample at position i. N is the vector dimension. *mode* is the mode of the vector. *std* is the standard deviation. Q_1 is quartile 1 of the vector. Q_3 is quartile 3 of the vector. P_{90} is percentile 90 of the vector. P_{10} is percentile 10 of the vector. For the calculation of the Median, it is necessary that the data array be sorted. For the calculation of Zero crossing, observe the sign changes between x_i and x_{i+1} in a series of K samples, excluding cases where $x_i = 0$ or $x_{i+1} = 0$.

Amplitude is a visual feature observed in EEG by experts. Epileptiform brain discharges exhibit high-amplitude deflections, typically in the order of hundreds of microvolts, whereas normal amplitudes range between 10 and 100 microvolts. Furthermore, high-amplitude rhythmic oscillations are used to define the onset and progression of epileptic seizures [3].

The features Energy and RMS contain important information about the measurement of amplitude. As seen from the formulas presented, Energy is the average of the sum of a signal squared, and RMS is the square root of Energy [69].

Second, Ref. [70] argues that through skewness, it is possible to identify distinct and clinically relevant patterns in sharp waves or spikes. Furthermore, they identified differences in the distribution of asymmetries between patients with unilateral abnormalities and patients with bilateral abnormalities, making it a useful tool for characterizing these types of epilepsy.

The study by [69] indicates that the Zero crossing feature is useful for EEG signal analysis, as the number of times the signal crosses zero is an indirect measure of the signal's frequency. Therefore, high values of this feature indicate a higher frequency.

The study conducted by [69] highlights the utility of statistical parameters in distinguishing ictal and non-ictal patterns. Among these parameters, mean, Median, skewness, and kurtosis are mentioned. Additionally, the researchers note that the baseline of the EEG signal can be established based on the maximum and minimum values, which are also explored in this work.

The Hjorth parameters [68] are widely used as features in epilepsy detection studies [69]. Activity reflects signal power, indicating the spectral distribution of energy in the frequency domain. Mobility provides information about the average frequency change and variability in spectral distribution, while Complexity assesses the similarity of the signal to a sine wave, aiding in the identification of brain activity patterns [71].

The 247 attribute vectors were employed to train seven supervised learning classifiers: Decision Tree, k-Nearest Neighbor (kNN), Logistic Regression, Naive Bayes, Random Forest, eXtreme Gradient Boosting (XGBoost), and Support Vector Machine (SVM). The hyperparameters for these classifiers were optimized using GridSearchCV, with a specific focus on varying the number of estimators {5, 100, 300, 500} and the maximum depth {1, 3, 5, 10, 50}. Following the training and testing phase, the classifier demonstrating the highest accuracy on the test set was selected for use in subsequent phases.

The model achieving the highest accuracy was subsequently analyzed using SHAP, which facilitated the identification of attributes contributing most significantly to the classification. This tool enables the interpretation of the model's decision-making process in predicting the data.

Upon application of SHAP, the top 20 features with the highest contribution to the model's predictive performance were identified and visualized. Subsequently, a series of 20 models were trained and tested incrementally, each incorporating an additional SHAP-ranked feature. Specifically, model 1 was trained with only the most influential feature, model 2 with the first and second features, and so on, up to model 20, which included the first through twentieth features as ranked by SHAP.

This first phase aimed to reduce the number of attributes using models with relevant attributes incrementally.

5.2.2. Second Phase

The 4 features and the 5 most recurrent channels presented in the first 20 attributes listed by SHAP in the previous phase were selected. This refined subset, encompassing 20 new attributes (5 channels $\times$ 4 features), was employed to train a new model. Subsequently, the SHAP analysis was reapplied to this model to rank the attributes according to their contribution to the predictive accuracy.

The classifier used in this phase was the one that obtained the best accuracy performance in the previous phase; however, once again GridSearchCV was used to define the hyperparameters (with the same variation mentioned earlier) using these new attributes.

Analogously to the first stage, a series of 20 models were trained, each incorporating a progressively increasing number of SHAP-ranked attributes. This was performed with the dual purpose of minimizing the attribute count and assessing the performance efficacy of the newly selected attribute set.

The metrics used to evaluate the performance of the classifiers were as follows: accuracy, precision, recall, and F1-score.

6. Results

In this section, the results obtained following the proposal presented in the methodology—in two phases—are presented, which constitutes the method that enables the reduction of input vectors in a humanly interpretable way.

6.1. First Phase

Table 2 presents the accuracy values obtained in training and testing using the five supervised classifiers (Decision Tree, kNN, Logistic Regression, Naive Bayes, Random Forest, XGBoost, and SVM) with the specified Hyperparameter. The result displayed in the table indicates that XGBoost, with a 97.43% accuracy in the test phase, is the most suitable to be used as a learning machine for the trained data, namely 247 attribute vectors (13 features and 19 channels).

Table 2. Classification result using 247 features.

Classifier	Hyperparameter	Training Accuracy Mean	Test Accuracy
Decision Tree	Max depth: 15 Min samples split: 2	92.34%	93.07%
kNN	Num neighbors: 1	93.68%	93.58%
Logistic Regression	Default	84.69%	84.21%
Naive Bayes	Gaussian	79.46%	81.00%
Random Forest	Max depth: 50 Num estimators: 150	96.62%	96.28%
XGBoost	Max depth: 5 Num estimators: 300	97.83%	97.43%
SVM	RBF	84.74%	87.29%

Figure 4 shows the graph of SHAP values for the first 20 attributes listed by SHAP (out of the 247 used in training with the XGBoost learning machine). The technique allows attributes to be listed in order of importance.

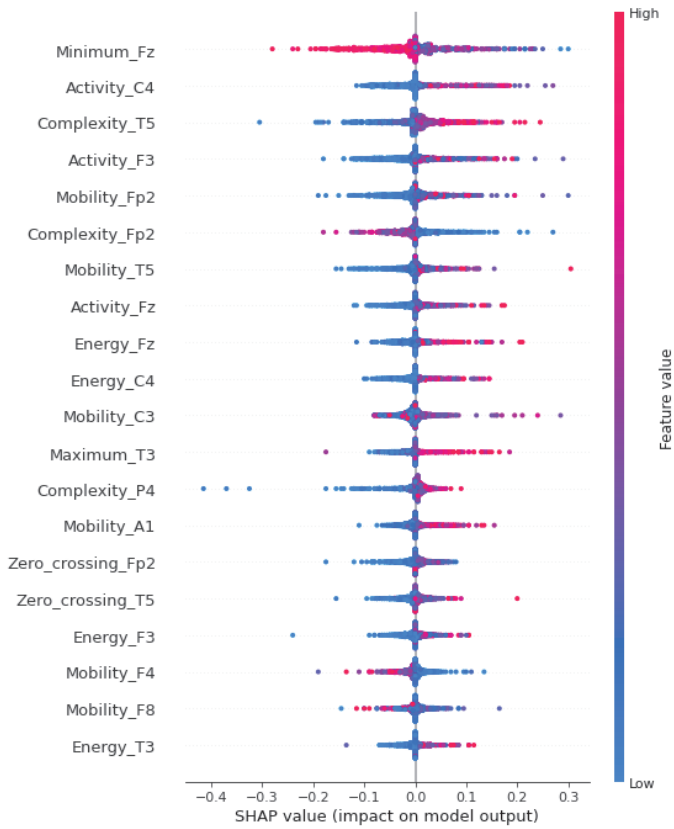

Figure 4. SHAP value—phase 1.

Observations reveal that specific attribute vectors contribute distinctly; for instance, elevated values in the Minimum_Fz vector (the Minimum feature calculated on the Fz channel) yield a negative impact on the prediction. Similarly, in the case of the second most influential attribute, Activity_C4, lower values are associated with a negative contribution.

The attributes were systematically organized for analysis: the first matrix incorporated solely the initial SHAP-ranked attribute (Minimum_Fz); the second matrix included both the first and second most influential attributes (Minimum_Fz and Activity_C4); and this sequential inclusion continued up to the twentieth matrix, which comprised the top 20 contributing attributes (Minimum_Fz, Activity_C4, Complexity_T5, Activity_F3, Mobility_Fp2, Complexity_Fp2, Mobility_T5, Activity_Fz, Energy_Fz, Energy_C4, Mobility_C3, Maximum_T3, Complexity_P4, Mobility_A1, Zero_crossing_Fp2, Zero_crossing_T5, Energy_F3, Mobility_F4, Mobility_F8, and Energy_T3). Each of these 20 matrices corresponded to one of the 20 trained models to which they were applied.

Figure 5 presents the performance metrics—accuracy, precision, recall, and F1-score—of 21 models trained using XGBoost, comparing the results obtained with the top 20 SHAP-ranked attributes against those using the full set of 247 attributes.

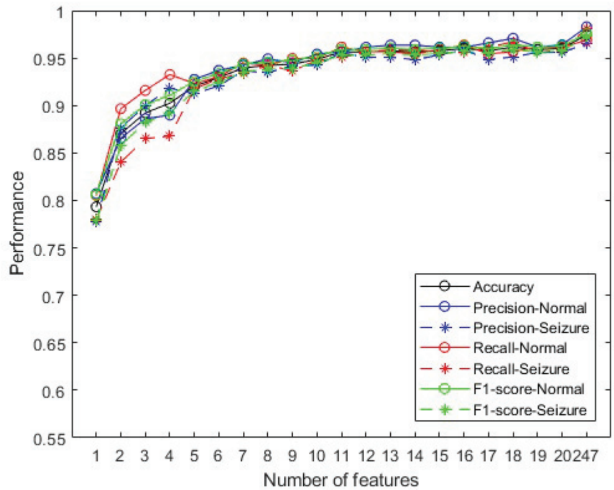

Figure 5. Phase 1—obtained performance.

6.2. Second Phase

In this second phase, the results obtained according to the steps presented in the second phase of the methodology are presented.

According to Figure 4, the four most common features were Activity, Complexity, Mobility, and Energy and the five most frequent channels were Fz, C4, T5, F3, and Fp2. In this way, the 20 new attributes are Activity_Fz, Activity_C4, Activity_T5, Activity_F3, Activity_Fp2, Complexity_Fz, Complexity_C4, Complexity_T5, Complexity_F3, Complexity_Fp2, Mobility_Fz, Mobility_C4, Mobility_T5, Mobility_F3, Mobility_Fp2, Energy_Fz, Energy_C4, Energy_T5, Energy_F3, and Energy_Fp2.

Table 3 showcases the performance metrics of the XGBoost classifier, which was configured with hyperparameters set to a maximum depth of 50 and 500 estimators, utilizing the previously identified 20 new attributes.

Table 3. Performance of XGBoost with the 20 new features.

Train Acc Mean	Test Acc	Real Class	Confusion Matrix		Precision	Recall	F1-Score
96.20	96.40	Interictal	399	17	97.32	95.91	96.61
		Ictal	11	352	95.39	96.97	96.17

Figure 6 presents a graph with the contribution of the SHAP values of the 20 most recurrent attributes selected.

It is possible to observe the contributions of each attribute vector. For example, low SHAP values in the first five attributes have a negative contribution to the prediction; similarly, the positive contribution is more present for high SHAP values.

Drawing from Figure 6, the attributes for constructing the 20 matrices were methodically organized in a manner akin to the approach taken in the preceding phase. Consequently, the initial matrix exclusively encompasses the attribute with the foremost predictive contribution, which is Activity_Fz. This sequence continues incrementally until the composition of the twentieth matrix, which incorporates all 20 attributes as ranked by SHAP (Activity_Fz, Activity_C4, Activity_T5, Activity_F3, Activity_Fp2, Complexity_Fz, Complexity_C4, Complexity_T5, Complexity_F3, Complexity_Fp2, Mobility_Fz, Mobility_C4, Mobility_T5, Mobility_F3, Mobility_Fp2, Energy_Fz, Energy_C4, Energy_T5, Energy_F3, and Energy_Fp2). Each of these matrices was subsequently applied to its corresponding model within the cohort of 20 trained models.

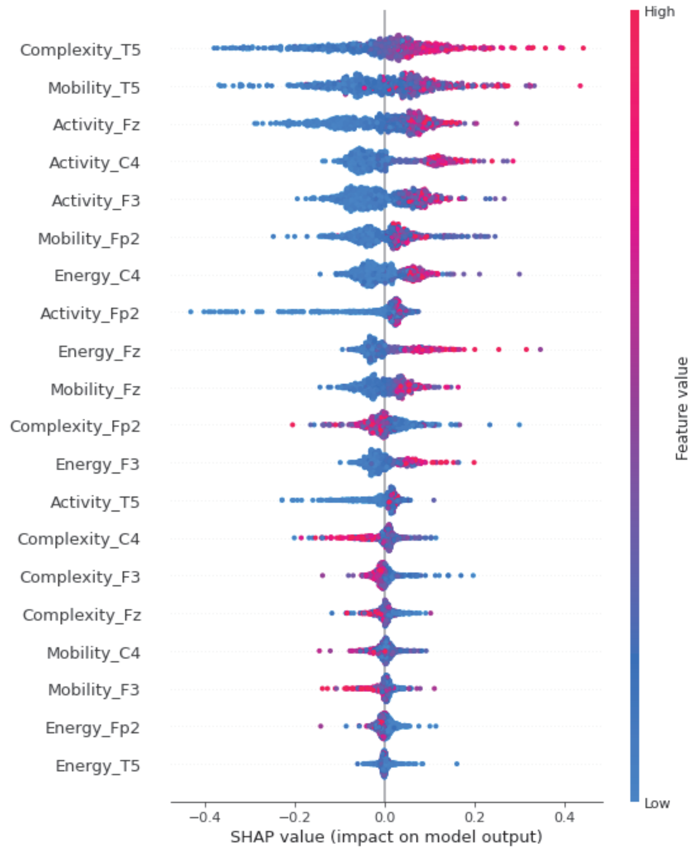

Figure 6. SHAP value—phase 2.

Figure 7 contains the performance of 20 models trained for accuracy, precision, recall, and F1-score using XGBoost with the 20 attributes listed by SHAP.

The highest accuracy achieved in this phase occurred with 19 attributes (96.53%), and with 6 it was already possible to obtain an accuracy greater than 95% (95.93%).

Figure 8 presents the accuracy obtained in the two distinct phases of model training. In the first phase, employing a single attribute from the full set of 247, the model attained an accuracy of 79.33%. Conversely, in the second phase, when using only the top SHAP-ranked attributes from a reduced set of 20, the accuracy diminished to 60.33%. This reduction is attributable to the fact that the initial selection was made from a larger pool of attributes, whereas the second was constrained to a more limited subset.

Table 4 shows the comparison of the obtained results. It represents a brief description of the methodology and the performance according to the metrics used in each experiment.

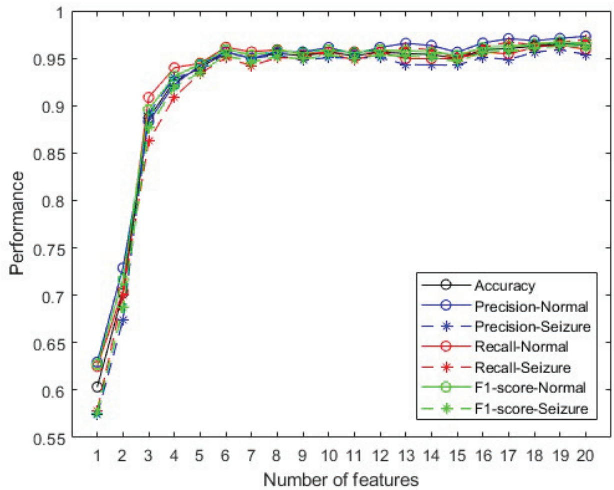

Figure 7. Phase 2—performance.

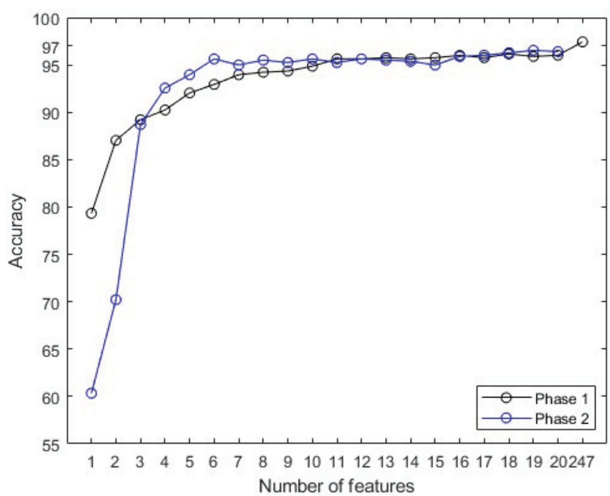

Figure 8. Phase 1 and 2 accuracies (%).

Table 4. Comparison of the results obtained in the two phases.

Methodology	Performance
Phase: 1 Dimensionality reduction: No Channels: 19 Features: 13 Attributes: 19 × 13 = 247	Accuracy: 97.43 (Interictal; Ictal) Precision: 98.29; 96.48 Recall: 96.88; 98.07 F1-score: 97.58; 97.27

Table 4. *Cont.*

Methodology	Performance
Phase: 1 Dimensionality reduction: SHAP Channels: 11 (Fz, C4, T5, F3, Fp2, C3, T3, P4, A1, F4, F8) Features: 7 (Minimum, Activity, Complexity, Mobility, Energy, Maximum, Zero crossing) Attributes: 20	Accuracy: 96.02 (Interictal; Ictal) Precision: 96.39; 95.60 Recall: 96.15; 95.87 F1-score: 96.27; 95.74
Phase: 1 Dimensionality reduction: SHAP Channels: 6 (Fz, C4, T5, F3, Fp2, C3) Features: 5 (Minimum, Activity, Complexity, Mobility, Energy) Attributes: 11	Accuracy: 95.64 (Interictal; Ictal) Precision: 95.69; 95.57 Recall: 96.15; 95.04 F1-score: 95.92; 95.30
Phase: 2 Dimensionality reduction: SHAP Channels: 5 (Fz, C4, T5, F3, Fp2) Features: 4 (Activity, Complexity, Mobility, Energy) Attributes: 20	Accuracy: 96.41 (Interictal; Ictal) Precision: 97.32; 95.39 Recall: 95.91; 96.97 F1-score: 96.61; 96.17
Phase: 2 Dimensionality reduction: SHAP Channels: 5 (Fz, C4, T5, F3, Fp2) Features: 2 (Activity, Complexity) Attributes: 6	Accuracy: 95.64 (Interictal; Ictal) Precision: 95.69; 95.57 Recall: 96.15; 95.04 F1-score: 95.92; 95.30

7. Discussion

A method for reducing channels and features using an XAI technique was introduced in the creation of an optimized model for epileptic seizure detection. The ensuing section delineates the outcomes of this approach.

Initially, the XGBoost algorithm emerged as the classifier of choice, demonstrating a high accuracy rate exceeding 97%, albeit dependent on a full set of 247 features. Subsequent application of the SHAP methodology to the trained model and corresponding test data facilitated the generation of streamlined models, which were then organized according to the predictive significance of their features.

The data depicted in Figure 5 reveal that the model encompassing 18 attributes attains the highest test accuracy at 96.15%; notwithstanding, a marginal disparity persists between the precision, recall, and F1-score metrics across both classes. These metrics attain stability upon expanding to a model with 20 attributes, evidenced by a 96.02% accuracy rate. This outcome is in close concordance with the results delineated in Table 2, where the XGBoost classifier realizes a 97.43% accuracy. Such findings corroborate the feasibility of achieving comparable model efficacy with a substantial reduction in input vectors, exceeding 91%, in this initial phase.

It is noteworthy that the model, with a configuration of merely 11 attributes, attained an accuracy of 95.63%, a figure that stands numerically on par with the accuracies reported in studies employing deep learning models [12,15].

In the subsequent phase of the study, a pattern of recurrence was noted among specific channels and features within the top 20 SHAP-identified attributes. This recurrence guided the synthesis of a new set of models, derived from the amalgamation of these frequently appearing channels and features.

Looking at Table 4, it can be noted that in the first phase, with 11 attributes (Minimum_Fz, Activity_C4, Complexity_T5, Activity_F3, Mobility_Fp2, Complexity_Fp2, Mobility_T5, Activity_Fz, Energy_Fz, Energy_C4, Mobility_C3) and using of six channels (Fz, C4, T5, F3, Fp2, and C3), it was possible to achieve satisfactory performance for binary classification. The second phase proved to be relevant by reducing the number of input vectors to six (Activity_Fz, Activity_C4, Activity_T5, Activity_F3, Activity_Fp2, Complexity_Fz) and the number of channels to five (Fz, C4, T5, F3, and Fp2), still achieving similar performance as the previous phase (above 95% accuracy).

It is relevant to relate the five channels selected in phase 2 (Fz, C4, T5, F3, and Fp2) to the regions where patients' focal points are located in the dataset. The selected channels, C4 and Fp2, correspond to focal points in some of the patients. Channel T5 is present in the following focal regions: posterior temporal and left hemisphere. Channel F3 is present in the frontotemporal focal region and left hemisphere, and channel Fz is present in the frontotemporal focal region. Therefore, the selected channels are spatially aligned with the focal points of patients' clinical events observed in EEG. This indicates that the method selects channels that are consistent with the location of clinical events in epileptic seizures.

Numerically comparing the two phases in terms of performance, as depicted in Figure 8, it becomes apparent that the second phase of the methodology excels. Specifically, within the range of three to nine attributes (x-axis), the accuracy attains higher values, which is advantageous for employing the model with a minimal number of input vectors while still achieving enhanced performance.

Observing the aspects of feature selections, in the first phase, Figure 4 highlights the most significant feature, representing the minimum value (located in channel Fz), as a key element in discriminating the data. This observation aligns with the concept mentioned in [69], emphasizing the role of the minimum value in defining a reference point for distinguishing non-ictal data from ictal signals. The chart in Figure 5 corroborates this importance, showing that this attribute alone can achieve a remarkable performance of approximately 80% in various binary classification metrics.

In the second phase, the most common attributes—Activity, Complexity, Mobility, and Energy—are often used together in related works, as cited in the study in [69]. Although 13 attributes were initially selected in the first phase, with detailed justifications, it is noteworthy that these 4 selected attributes are capable of effectively discriminating classes for specific channels. This fact demonstrates that it is feasible to reduce the number of features and channels, even in generalist models.

Some potential biases need to be considered in the interpretation of the results: the UBMC database is limited as it only includes six patients and lacks data for all types of epilepsy. Therefore, the selected channels may be specific to the patients in the database, and consequently, the computed features may not be universally applicable, even in more generalized models. Additionally, the selection based on SHAP may be influenced by the specific dataset. Hence, generalizing the results requires caution and validation on additional datasets that utilize the same data segments, such as TUH and CHB-MIT.

It is also worth noting that the SHAP value method assumes that the model features are independent of each other [26]. This suggests that SHAP may not fully capture the interactions between the features. This limitation is not favorable for this application since the sensors are spatially distributed on the scalp, where epileptic discharges are measured through the channels.

In this way, it was possible to observe that simpler classification models can be efficient in the identification of epileptic seizures. Additionally, the explainable method of feature and channel selection allowed for reducing computational effort while maintaining high performance. This method, by not transforming the dataset, allowed us to verify that the chosen channels are located in focal areas of epileptic seizures. This encourages further study with customized models, which may further reduce the number of channels and confirm if the focal point will always be the best location for extracting data for epileptic seizure detection.

8. Conclusions

In light of these observations, the proposed approach has the potential to significantly streamline computational processes by reducing both the quantity of input vectors and the complexity of the classification models. Moreover, it may contribute to the simplification of signal acquisition hardware through a minimized electrode array, all the while sustaining a high standard of accuracy in distinguishing between interictal and ictal EEG data.

Considering that the methods used in the literature have a large number of input vectors [10,11,18] (which also requires a greater number of samples for training) and make use of more robust machines such as DL [13,14], the proposed approach simplifies the solution by delivering a numerically equivalent performance, employing temporal feature extraction, using simpler classifiers (XGBoost), and reducing the dimensionality through an explainable technique (SHAP), enabling model interpretability.

Utilizing a database with detailed focal point locations enabled confirmation that the model's most significant channels are spatially proximate to the patients' focal zones. This outcome fosters the impetus for subsequent research to investigate personalized models, which could validate the hypothesis that optimal channels for seizure detection predominantly reside within these focal areas. Such advancements could further curtail the requisite number of channels and features, thereby facilitating the development of mobile applications.

Although a satisfactory performance was achieved, it is necessary to replicate the method for a database with a larger number of patients that contains information about the location of the seizures. Creating a universal generalist model is a challenge, as it depends on a representative database. However, this study encourages the application of the method in personalized models, where it is expected to further reduce the number of channels and features.

Author Contributions: Conceptualization, J.C.V. and L.A.G.; Data curation, J.C.V.; Formal analysis, J.C.V. and M.R.S.; Funding acquisition, J.C.V.; Investigation, J.C.V.; Methodology, J.C.V. and L.A.G.; Project administration, J.C.V. and L.A.G.; Resources, J.C.V.; Software, M.R.S.; Supervision, L.A.G.; Validation, J.C.V.; Visualization, J.C.V., L.A.G. and I.S.-G.; Writing—original draft, J.C.V., L.A.G. and M.R.S.; Writing—review and editing, I.S.-G. All authors have read and agreed to the published version of the manuscript.

Funding: This research was funded by the Coordenação de Aperfeiçoamento de Pessoal de Nível Superior—Brasil (CAPES), grant number 0001; APC payment and doctoral scholarships for the first author.

Data Availability Statement: The data presented in this study are openly available in Mendeley Data, titled "Epileptic EEG Dataset" by Nasreddine, Wassim (2021), V1, available at doi: https://doi.org/10.17632/5pc2j46cbc.1.

Conflicts of Interest: The authors declare no conflict of interest. The funders had no role in the design of the study; in the collection, analyses, or interpretation of data; in the writing of the manuscript; or in the decision to publish the results.

Abbreviations

The following abbreviations are used in this manuscript:

CHB-MIT	Children's Hospital Boston at the Massachusetts Institute of Technology.
DL	Deep Learning.
DWT	Discrete Wavelet Transform.
EEG	Electroencephalography.
XAI	Explainable Artificial Intelligence.
XGBoost	eXtreme Gradient Boosting.
FFT	Fast Fourier Transform.
kNN	k-Nearest Neighbor.
ML	Machine Learning.
PCA	Principal Component Analysis.

SHAP	SHapley Additive exPlanations.
SVM	Support Vector Machine.
t-SNE	t-Distributed Stochastic Neighbor Embedding.
TUH	Temple University Hospital.
UBMC	University of Beirut Medical Center.

References

1. World Health Organization. Epilepsy. 2022. Available online: https://www.who.int/en/news-room/fact-sheets/detail/epilepsy (accessed on 3 June 2023).
2. Fisher, R.; van Emde Boas, W.; Blume, W.; Elger, C.; Genton, P.; Lee, P.; Engel, J., Jr. Epileptic Seizures and Epilepsy: Definitions Proposed by the International League Against Epilepsy (ILAE) and the International Bureau for Epilepsy (IBE). *Epilepsia* **2005**, *46*, 470–472. [CrossRef] [PubMed]
3. Ebersole, J.S.; Husain, A.M.; Nordli, D.R., Jr. *Current Practice of Clinical Electroencephalography*, 4th ed.; Wolters Kluwer: Philadelphia, PA, USA, 2014.
4. Schomer, D.L.; Da Silva, F.L. *Niedermeyer's Electroencephalography: Basic Principles, Clinical Applications, and Related Fields*; Lippincott Williams & Wilkins: Philadelphia, PA, USA, 2012.
5. Biondi, A.; Santoro, V.; Viana, P.F.; Laiou, P.; Pal, D.K.; Bruno, E.; Richardson, M.P. Noninvasive mobile EEG as a tool for seizure monitoring and management: A systematic review. *Epilepsia* **2022**, *63*, 1041–1063. [CrossRef]
6. Kjaer, T.W.; Sorensen, H.B.; Groenborg, S.; Pedersen, C.R.; Duun-Henriksen, J. Detection of paroxysms in long-term, single-channel EEG-monitoring of patients with typical absence seizures. *IEEE J. Transl. Eng. Health Med.* **2017**, *5*, 2000108. [CrossRef] [PubMed]
7. Abou-Abbas, L.; Jemal, I.; Henni, K.; Ouakrim, Y.; Mitiche, A.; Mezghani, N. EEG Oscillatory Power and Complexity for Epileptic Seizure Detection. *Appl. Sci.* **2022**, *12*, 4181. [CrossRef]
8. Khan, I.; Khan, M.; Farooq, O. Epileptic Seizure Detection using EEG Signals. In Proceedings of the 2022 5th International Conference on Computing and Informatics (ICCI), New Cairo, Egypt, 9–10 March 2022. [CrossRef]
9. Guerrero, M.; Parada, J.; Espitia, H. Principal Components Analysis of EEG Signals for Epileptic Patient Identification. *Computation* **2021**, *9*, 133. [CrossRef]
10. Albaqami, H.; Hassan, G.; Datta, A. Comparison of WPD, DWT and DTCWT for Multi-Class Seizure Type Classification. In Proceedings of the 2021 IEEE Signal Processing in Medicine and Biology Symposium (SPMB), Philadelphia, PA, USA, 4 December 2021. [CrossRef]
11. Albaqami, H., Hassan, G., Subasi, A.; Datta, A. Automatic detection of abnormal EEG signals using wavelet feature extraction and gradient boosting decision tree. *Biomed. Signal Process. Control.* **2021**, *70*, 102957. [CrossRef]
12. Handa, P.; Goel, N. Peri-ictal and non-seizure EEG event detection using generated metadata. *Expert Syst.* **2021**, 39, e12929. [CrossRef]
13. Tawhid, M.; Siuly, S.; Li, T. A Convolutional Long Short-Term Memory-Based Neural Network for Epilepsy Detection From EEG. *IEEE Trans. Instrum. Meas.* **2022**, 71, 4010211. [CrossRef]
14. Lateef, H.; Ralston, G.; Bright, T.; Soundarajan, A.; Carpenter, J. SeizureSeeker: A Novel Approach to Epileptic Seizure Detection Using Machine Learning. *J. Neurol. Exp. Neurosci.* **2022**, *8*, 1–8. [CrossRef]
15. Shah, S.; Larijani, H.; Gibson, R.; Liarokapis, D. Random Neural Network Based Epileptic Seizure Episode Detection Exploiting Electroencephalogram Signals. *Sensors* **2022**, *22*, 2466. [CrossRef]
16. Shankar, A.; Dandapat, S.; Barma, S. Classification of Seizure Types Based on Statistical Variants and Machine Learning. In Proceedings of the 2021 IEEE 18th India Council International Conference (INDICON), Guwahati, India, 19–21 December 2021. [CrossRef]
17. Prasanna, J.; Subathra, M.S.P.; Mohammed, M.A.; Damaševičius, R.; Sairamya, N.J.; George, S.T. Automated epileptic seizure detection in pediatric subjects of CHB-MIT EEG database—A survey. *J. Pers. Med.* **2021**, *11*, 1028. [CrossRef] [PubMed]
18. Wu, D.; Wang, Z.; Jiang, L.; Dong, F.; Wu, X.; Wang, S.; Ding, Y. Automatic Epileptic Seizures Joint Detection Algorithm Based on Improved Multi-Domain Feature of cEEG and Spike Feature of aEEG. *IEEE Access* **2019**, *7*, 41551–41564. [CrossRef]
19. Birjandtalab, J.; Pouyan, M.B.; Cogan, D.; Nourani, M.; Harvey, J. Automated seizure detection using limited-channel EEG and non-linear dimension reduction. *Comput. Biol. Med.* **2017**, *82*, 49–58. [CrossRef] [PubMed]
20. Pritchard, W.S.; Duke, D.W. Measuring chaos in the brain: A tutorial review of nonlinear dynamical EEG analysis. *Int. J. Neurosci.* **1992**, *67*, 31–80. [CrossRef] [PubMed]
21. Hussain, L.; Saeed, S.; Awan, I.A.; Idris, A. Multiscaled complexity analysis of EEG epileptic seizure using entropy-based techniques. *Arch. Neurosci.* **2018**, *5*, e61161. [CrossRef]
22. Khoa, T.Q.D.; Huong, N.T.M.; Toi, V.V. Detecting epileptic seizure from scalp EEG using Lyapunov spectrum. *Comput. Math. Methods Med.* **2012**, *2012*, 847686. [CrossRef]
23. Khalid, S.; Khalil, T.; Nasreen, S. A survey of feature selection and feature extraction techniques in machine learning. In Proceedings of the 2014 Science and Information Conference, London, UK, 27–29 August 2014; pp. 372–378.
24. Saranya, A.; Subhashini, R. A systematic review of Explainable Artificial Intelligence models and applications: Recent developments and future trends. *Decis. Anal. J.* **2023**, *2023*, 100230.
25. Islam, M.S.; Hussain, I.; Rahman, M.M.; Park, S.J.; Hossain, M.A. Explainable artificial intelligence model for stroke prediction using EEG signal. *Sensors* **2022**, *22*, 9859. [CrossRef]
26. Lundberg, S.; Lee, S. A Unified Approach to Interpreting Model Predictions. *arXiv* **2017**, arXiv:1705.07874.

27. Ludwig, S.A. Explainability Using SHAP for Epileptic Seizure Recognition. In Proceedings of the 2022 IEEE International Conference on Big Data, Osaka, Japan, 17–20 December 2022; pp. 5305–5311.
28. Guidotti, R.; Monreale, A.; Ruggieri, S.; Turini, F.; Giannotti, F.; Pedreschi, D. A Survey of Methods for Explaining Black Box Models. *ACM Comput. Surv.* **2019**, *51*, 1–42. [CrossRef]
29. Arrieta, A.; Dıéaz-Rodrıéguez, N.; Ser, J.; Bennetot, A.; Tabik, S.; Barbado, A.; Garcia, S.; Gil-Lopez, S.; Molina, D.; Benjamins, R.; et al. Explainable Artificial Intelligence (XAI): Concepts, taxonomies, opportunities and challenges toward responsible AI. *Inf. Fusion* **2020**, *58*, 82–115. [CrossRef]
30. Futagami, K.; Fukazawa, Y.; Kapoor, N.; Kito, T. Pairwise acquisition prediction with SHAP value interpretation. *J. Financ. Data Sci.* **2021**, *7*, 22–44. [CrossRef]
31. Štrumbelj, E.; Kononenko, I. Explaining prediction models and individual predictions with feature contributions. *Knowl. Inf. Syst.* **2013**, *41*, 647–665. [CrossRef]
32. Shapley, L. A value for n-person games. *Contrib. Theory Games* **1953**, *2*, 307.
33. Lundberg, S.; Erion, G.; Lee, S. Consistent Individualized Feature Attribution for Tree Ensembles. *arXiv* **2018**, arXiv:1802.03888.
34. Miller, H. *Plan and Operation of the Health and Nutrition Examination Survey, United States, 1971–1973*; DHEW Publication No. (PHS); Department of Health, Education, and Welfare: Washington, DC, USA, 1973.
35. Shi, T.W.; Chen, K.J.; Ren, L.; Cui, W.H. Brain Computer Interface Based on Motor Imagery for Mechanical Arm Grasp Control. *Inf. Technol. Control.* **2023**, *52*, 358–366. [CrossRef]
36. Delijorge, J.; Mendoza-Montoya, O.; Gordillo, J.L.; Caraza, R.; Martinez, H.R.; Antelis, J.M. Evaluation of a p300-based brain-machine interface for a robotic hand-orthosis control. *Front. Neurosci.* **2020**, *14*, 589659. [CrossRef]
37. Piozin, C.; Altamira, G.H.; Simon, C.; Lavrard, B.; Audran, J.Y.; Waszak, F.; Eskiizmirliler, S. Motion prediction for the sensorimotor control of hand prostheses with a brain-machine interface using EEG. In Proceedings of the 2022 10th International Winter Conference on Brain-Computer Interface (BCI), Gangwon-do, Republic of Korea, 21–23 February 2022; pp. 1–8.
38. Vieira, J.C. Interface Cérebro-Máquina Utilizando o EEG Humano: Movendo o Avatar Num Ambiente Virtual Utilizando Atividade Elétrica do Cérebro. Master's Thesis, Universidade Federal de Pernambuco, Recife, Brazil, 2018.
39. Alhammadi, M.; Rasheed, S.R.B.; Bonny, T.; Al Nassan, W.; Obaideen, K. Cursor Control Using electroencephalogram (EEG) Technology. In Proceedings of the 2022 International Conference on Electrical and Computing Technologies and Applications (ICECTA), Ras Al Khaimah, United Arab Emirates, 23–25 November 2022; pp. 415–419.
40. Jiang, L.; Luo, C.; Liao, Z.; Li, X.; Chen, Q.; Jin, Y.; Lu, K.; Zhang, D. SmartRolling: A human–machine interface for wheelchair control using EEG and smart sensing techniques. *Inf. Process. Manag.* **2023**, *60*, 103262. [CrossRef]
41. Choi, I.; Kwon, G.H.; Lee, S.; Nam, C.S. Functional electrical stimulation controlled by motor imagery brain-computer interface for rehabilitation. *Brain Sci.* **2020**, *10*, 512. [CrossRef]
42. Jacob, S.; Menon, V.G.; Al-Turjman, F.; Vinoj, P.G.; Mostarda, L. Artificial muscle intelligence system with deep learning for post-stroke assistance and rehabilitation. *IEEE Access* **2019**, *7*, 133463–133473. [CrossRef]
43. Krishna, N.M.; Sekaran, K.; Vamsi, A.V.N.; Ghantasala, G.P.; Chana, P.; Kadry, S.; Blažauskas, T.; Damaševičius, R. An efficient mixture model approach in brain-machine interface systems for extracting the psychological status of mentally impaired persons using EEG signals. *IEEE Access* **2019**, *7*, 77905–77914. [CrossRef]
44. Alhalaseh, R.; Alasasfeh, S. Machine-Learning-Based Emotion Recognition System Using EEG Signals. *Computers* **2020**, *9*, 95. [CrossRef]
45. Micoulaud-Franchi, J.A.; Geoffroy, P.A.; Fond, G.; Lopez, R.; Bioulac, S.; Philip, P. EEG neurofeedback treatments in children with ADHD: An updated meta-analysis of randomized controlled trials. *Front. Hum. Neurosci.* **2014**, *8*, 906. [CrossRef] [PubMed]
46. Šverko, Z.; Vlahinić, S.; Vrankić, M.; Markovinović, I. EEG data processing in ADHD diagnosis and neurofeedback. *Eng. Rev.* **2020**, *40*, 116–123. [CrossRef]
47. Dev, K.B.; Jogi, P.S.; Niyas, S.; Vinayagamani, S.; Kesavadas, C.; Rajan, J. Automatic detection and localization of focal cortical dysplasia lesions in MRI using fully convolutional neural network. *Biomed. Signal Process. Control.* **2019**, *52*, 218–225.
48. Luckett, P.H.; Maccotta, L.; Lee, J.J.; Park, K.Y.; UFDosenbach, N.; Ances, B.M.; Hogan, R.E.; Shimony, J.S.; Leuthardt, E.C. Deep learning resting state functional magnetic resonance imaging lateralization of temporal lobe epilepsy. *Epilepsia* **2022**, *63*, 1542–1552. [CrossRef]
49. Gleichgerrcht, E.; Munsell, B.; Bhatia, S.; Vandergrift, W.A., III; Rorden, C.; McDonald, C.; Edwards, J.; Kuzniecky, R.; Bonilha, L. Deep learning applied to whole-brain connectome to determine seizure control after epilepsy surgery. *Epilepsia* **2018**, *59*, 1643–1654. [CrossRef]
50. Raghu, S.; Sriraam, N.; Temel, Y.; Rao, S.V.; Kubben, P.L. EEG based multi-class seizure type classification using convolutional neural network and transfer learning. *Neural Netw.* **2020**, *124*, 202–212. [CrossRef]
51. Tuncer, E.; Bolat, E.D. Channel based epilepsy seizure type detection from electroencephalography (EEG) signals with machine learning techniques. *Biocybern. Biomed. Eng.* **2022**, *42*, 575–595. [CrossRef]
52. Roy, S.; Asif, U.; Tang, J.; Harrer, S. Seizure Type Classification using EEG signals and Machine Learning: Setting a benchmark. *arXiv* **2019**, arXiv:1902.01012. [CrossRef]
53. Wei, X.; Zhou, L.; Zhang, Z.; Chen, Z.; Zhou, Y. Early prediction of epileptic seizures using a long-term recurrent convolutional network. *J. Neurosci. Methods* **2019**, *327*, 108395.

54. Xu, Y.; Yang, J.; Sawan, M. Multichannel synthetic preictal EEG signals to enhance the prediction of epileptic seizures. *IEEE Trans. Biomed. Eng.* **2022**, *69*, 3516–3525. [CrossRef] [PubMed]
55. Asharindavida, F.; Hossain, M.S.; Thacham, A.; Khammari, H.; Ahmed, I.; Alraddady, F.; Masud, M. A forecasting tool for prediction of epileptic seizures using a machine learning approach. *Concurr. Comput. Pract. Exp.* **2020**, *32*, e5111. [CrossRef]
56. Rasheed, K.; Qayyum, A.; Qadir, J.; Sivathamboo, S.; Kwan, P.; Kuhlmann, L.; O'Brien, T.; Razi, A. Machine learning for predicting epileptic seizures using EEG signals: A review. *IEEE Rev. Biomed. Eng.* **2020**, *14*, 139–155. [CrossRef]
57. Yang, S. Machine learning applications for electroencephalograph signals in epilepsy: A quick review. *Acta Epileptol.* **2020**, *2*, 5. [CrossRef]
58. Siddiqui, M.K.; Morales-Menendez, R.; Huang, X.; Hussain, N. A review of epileptic seizure detection using machine learning classifiers. *Brain Inform.* **2020**, *7*, 5.
59. Farooq, M.S.; Zulfiqar, A.; Riaz, S. Epileptic Seizure Detection Using Machine Learning: Taxonomy, Opportunities, and Challenges. *Diagnostics* **2023**, *13*, 1058. [CrossRef]
60. Gholizadeh, S.; Zhou, N. Model explainability in deep learning based natural language processing. *arXiv* **2021**, arXiv:2106.07410. [CrossRef]
61. Zhang, Q.; Zhu, S. Visual interpretability for deep learning: A survey. *Front. Inf. Technol. Electron. Eng.* **2018**, *19*, 27–39.
62. Li, H.; Li, J.; Guan, X.; Liang, B.; Lai, Y.; Luo, X. Research on overfitting of deep learning. In Proceedings of the 2019 15th International Conference on Computational Intelligence and Security (CIS), Macao, China, 13–16 December 2019; pp. 78–81. [CrossRef]
63. Shrestha, A.; Mahmood, A. Review of deep learning algorithms and architectures. *IEEE Access* **2019**, *7*, 53040–53065.
64. Obeid, I.; Picone, J. The Temple University Hospital EEG Data Corpus. *Front. Neurosci.* **2016**, *10*, 196. [CrossRef]
65. Shoeb, A.H. Application of Machine Learning to Epileptic Seizure Onset Detection and Treatment. Ph.D. Thesis, Massachusetts Institute of Technology, Cambridge, MA, USA, 2009. [CrossRef] [PubMed]
66. Nasreddine, W. Epileptic EEG Dataset. Mendeley. 2021. Available online: https://data.mendeley.com/datasets/5pc2j46cbc/1 (accessed on 03 March 2022).
67. Jasper, H. The ten-twenty electrode system of the International Federation. *Electroencephalogr. Clin. Neurophysiol.* **1958**, *10*, 370–375.
68. Oh, S.; Lee, Y.; Kim, H. A Novel EEG Feature Extraction Method Using Hjorth Parameter. *Int. J. Electron. Electr. Eng.* **2014**, *2*, 106–110. [CrossRef]
69. Boonyakitanont, P.; Lek-Uthai, A.; Chomtho, K.; Songsiri, J. A review of feature extraction and performance evaluation in epileptic seizure detection using EEG. *Biomed. Signal Process. Control.* **2020**, *57*, 101702. [CrossRef]
70. Gotman, J. Quantitative measurements of epileptic spike morphology in the human EEG. *Electroencephalogr. Clin. Neurophysiol.* **1980**, *48*, 551–557. [CrossRef]
71. Prasad, A. Feature Extraction and Classification for Motor Imagery in EEG Signals. Ph.D. Thesis, Kauno Technologijos Universitetas, Kaunas, Lithuania, 2016. [CrossRef]

sensors

MDPI

Article

Identifying the Effect of Cognitive Motivation with the Method Based on Temporal Association Rule Mining Concept

Tustanah Phukhachee [1], Suthathip Maneewongvatana [1], Chayapol Chaiyanan [1], Keiji Iramina [2] and Boonserm Kaewkamnerdpong [3,*]

[1] Computer Engineering Department, Faculty of Engineering, King Mongkut's University of Technology Thonburi, Bangkok 10140, Thailand; tustanah.p@mail.kmutt.ac.th (T.P.); suthathip.man@kmutt.ac.th (S.M.); chayapol.chekl82@mail.kmutt.ac.th (C.C.)
[2] Graduate School of Systems Life Sciences, Kyushu University, Fukuoka 819-0395, Japan; iramina@inf.kyushu-u.ac.jp
[3] Biological Engineering Program, Faculty of Engineering, King Mongkut's University of Technology Thonburi, Bangkok 10140, Thailand
* Correspondence: boonserm.kae@kmutt.ac.th; Tel.: +66-(0)2-470-9392

Abstract: Being motivated has positive influences on task performance. However, motivation could result from various motives that affect different parts of the brain. Analyzing the motivation effect from all affected areas requires a high number of EEG electrodes, resulting in high cost, inflexibility, and burden to users. In various real-world applications, only the motivation effect is required for performance evaluation regardless of the motive. Analyzing the relationships between the motivation-affected brain areas associated with the task's performance could limit the required electrodes. This study introduced a method to identify the cognitive motivation effect with a reduced number of EEG electrodes. The temporal association rule mining (TARM) concept was used to analyze the relationships between attention and memorization brain areas under the effect of motivation from the cognitive motivation task. For accuracy improvement, the artificial bee colony (ABC) algorithm was applied with the central limit theorem (CLT) concept to optimize the TARM parameters. From the results, our method can identify the motivation effect with only FCz and P3 electrodes, with 74.5% classification accuracy on average with individual tests.

Keywords: cognitive motivation task; electroencephalography (EEG); motivation; temporal association rule mining (TARM)

Citation: Phukhachee, T.; Maneewongvatana, S.; Chaiyanan, C.; Iramina, K.; Kaewkamnerdpong, B. Identifying the Effect of Cognitive Motivation with the Method Based on Temporal Association Rule Mining Concept. *Sensors* **2024**, *24*, 2857. https://doi.org/10.3390/s24092857

Academic Editors: Steve Ling, Yifan Zhao, Hua-Liang Wei, Yuzhu Guo and Fei He

Received: 14 February 2024
Revised: 18 April 2024
Accepted: 25 April 2024
Published: 30 April 2024

1. Introduction

Motivation is an essential state of mind that can enhance the attention and performance of learners during their learning process. With the advantages of being motivated to perform the task, many researchers have taken an interest in studying motivation. In educational psychology, motivated individuals were found to have preferable traits that enhance their learning performance [1–5]. Renninger and Wozniak [1] studied the motivation of children to the item of interest. They found that the high level of motivation the children felt for the item contributed to increased attention, recognition, and recall performance. Various studies [2–4] found that the motivation of the participants to demonstrate their competence positively correlates with the actual achievement of the participants. This type of motivation often occurs when they compare their performance to that of others. In 2022, Mussel [5] researched the curiosity of students, which is a factor leading to motivation. Their study's results suggested that curiosity is significantly related to the student's academic performance.

In studies [1–5], motivation could occur from various motives, such as interest [1], reward (grade, emotional self-rewarding) [2–4], or even curiosity [5]. Each of these motives is a factor that can motivate us to perform the task. These motives affect different areas within our brain related to their activities. Various fMRI studies [6–8] have reported the relationship of the brain areas and their activities related to these motives. Lee et al. [6] studied the effects of intrinsic and extrinsic motivation. They found that reward (extrinsic motivation) affects the right posterior cingulate cortex, which was hypothesized to be a reward-based area. On the other hand, self-satisfying feelings (intrinsic motivation) were found to affect the right insular cortex, which was hypothesized to be an emotion-based area. Ulrich et al. [7] studied the motivation resulting from the challenge of the task. Their research suggested various areas related to the process of motivation, including the putamen, related to the coding of increased outcome probability (probability to choose higher reward outcome); the inferior frontal gyrus (IFG), related to a deeper sense of cognitive control; the medial prefrontal cortex (MPFC), related to the decreased self-referential processing; and the amygdala (AMY), related to the process of decrease in negative arousal. The study of curiosity and interest by Lee and Reeve [8] found that the anterior insular cortex (AIC) and striatum work together in an intrinsic motivation system. While AIC is related to the subjective feelings resulting from the body, the striatum plays a crucial role in reward processing. The striatum is also a central part of extrinsically generated motivation. They also found a relationship between intrinsic motivation and the frontal areas of the brain (e.g., dorsolateral prefrontal cortex, medial frontal gyrus), which is believed to be related to higher-order cognitive processes.

The fMRI studies [6–8] help us understand various brain areas and their activities related to different motives. However, for use in real-world situations, fMRI is inflexible as the measurement due to the limitations of the equipment. EEG, which has advantages in the combination of low cost and flexibility for use in the real-world environment, has become one of the conventional equipments in motivation studies. These EEG studies [9–12] also found similar results to fMRI studies that motivation could affect various areas depending on the motives. The study of van der Ven et al. [9] investigated the N400 ERP component of EEG on a reading task with the reward depending on the result. They found that C3, Cz, C4, CP1, CP2, P3, Pz, and P4 from the central and parietal areas are electrodes influenced by motivation. The motivation resulting from the challenging task was studied with the mean amplitude of stimulus-preceding negativity (SPN, an ERP component) by Ma et al. [10] in 2017. They found that the challenging level of the task influenced F4, F6, F8, FC4, FC6, and FT8 of the frontal area electrodes. Jin et al. [11] researched interesting/boring tasks with P300 and feedback-related negativity (FRN) ERP components. They found a difference between the interesting and boring cases in F1, Fz, F2, FC1, FCz, FC2, C1, Cz, and C2 electrodes with the FRN and C1, Cz, C2, CP1, CPz, CP2, P1, Pz, and P2 electrodes with the P300 component. In 2018, Brydevall et al. [12] studied an information-seeking task, a curiosity-based task, with a feedback-related negativity (FRN) ERP component. In their study, Fpz, AFz, Fz, FCz, and Cz electrodes were found to be influenced by motivation.

Although EEG can also be used to detect various motivations relating to the learning process [9–12], different motives leading to motivation affect electrodes in various brain areas. In a real-world situation, such as in the classroom, we could not know the type of motive that each learner has at a different part of the lesson. If we measure the effect of motivation from all known motives, a high number of electrodes would be required. However, for educational purposes, the type of motives may not be significant enough to know; only the motivation effect on brain activities that lead to learning performance is required. Since motivation could affect task performance, we have an idea to investigate the motivation effect through the relationship among the brain areas associated with the task performance affected by motivation (e.g., attention and recognition in the cognitive motivation task). Even though the motive cannot be identified by this approach, the number of electrodes required for measuring the effect of motivation could be reduced.

The cognitive motivation task was used as an example and was focused on in this study. Therefore, the effect of motivation on the relationship between attention and memorization brain areas was analyzed. Attention and memory tasks related to motivation were studied by Robinson et al. [13]. In their study, attention was measured by response time with the

Attentional Network Test (ANT), while the Newcastle Spatial Memory Test (NSMT) was used to measure memory. The extrinsic motivation was known when the reward was given, while the Intrinsic Motivation Inventory (IMI) questionnaire was used to measure intrinsic motivation. With these measurements, they found that extrinsic and intrinsic motivation improves the participant's memory and attentional performance. Their results confirmed that motivation is related to both the attention and memory performance of participants. Additionally, the relationship between attention and memory was found in a top-down process in the case of the successful formation of episodic memories [14,15]. Episodic memory is related to the process of remembering the spatial and contextual features of the visual scene stimulus. In this top-down process, the activation of the area within the prefrontal cortex (attention-related area) leads to the activation of the area within the parietal cortex (memory-related area).

The results of our previous study [16] on the cognitive motivation task with EEG also confirmed the relationship of motivation with attention and memory in the study of Robinson et al. [13]. In our previous study, the participants could freely decide whether they wanted to remember the presented scenic stimulus. The participants were considered as being motivated when they selected that they wanted to remember the stimulus and not being motivated if otherwise. The recognition test was conducted afterward to confirm the results of their motivation for each stimulus. It was found that when the participants were motivated to remember the stimuli, there was a significant difference in attention and memorization-related areas between the cases where they could and could not remember the stimulus afterward. We found a longer continuous alpha desynchronization pattern in the "*being motivated and remembered*" case than in the "*being motivated but forgot*" case. The areas of interest are mainly around the frontal (attention-related area [17]) and left parietal (memory encoding-related area [18]) part of the head, which will be represented by FCz and P3 electrodes in this study. No difference was found among "*not being motivated*" cases where the participants were not motivated to remember the stimulus. The results suggest that motivation can affect both attention and memorization [13,16] and that the occurrence of attention brain activity leads to memorization brain activity [14].

In this study, we further our investigation. We hypothesized that the temporal relationship of brain activities between attention and memorization-related areas could identify the effect of motivation on remembering the stimulus. With this hypothesis, the number of electrodes is reduced to two, which includes the FCz and P3 electrodes. To find the temporal relationship between two brain areas, the concept of Temporal Association Rule Mining (TARM) [19], which is the idea of finding association rules or patterns between two sequences while considering time constraints, could be useful. The TARM concept has been successfully applied to various similar applications [20,21]. For example, in 2009, Hojung et al. [20] tested a TARM-based method with the Saccharomyces cerevisiae cell cycle time-series microarray gene expression dataset and found effective rules for the KEGG cell-cycle pathway. In the field of intelligent transportation systems, Feng et al. [21] proposed a hybrid temporal association rule mining method to predict traffic congestion in a road network. Their experimental results showed high accuracy in the prediction of traffic congestion levels.

We proposed a method based on the TARM concept to identify the motivation effect from the temporal relationship of brain activities between attention and memorization areas while the participants are being motivated. To determine the complex brain activity relationship, the metaheuristic algorithms could be used to optimize the parameters of the method. In this study, we employed an Artificial Bee Colony (ABC) [22] algorithm as an example of the metaheuristic algorithm. The ABC algorithm is known for its performance and simplicity; ABC requires relatively fewer algorithm parameters to adjust than other metaheuristic algorithms while performing well on a variety of benchmark functions. The concept of the Central Limit Theorem (CLT) [23] was applied to identify a suitable representative of the method parameter set. The knowledge contributed by our work not only validates the previous knowledge [13–15,17,18] but also provides a method to measure the effect of motivation with a reduced number of EEG electrodes. This contribution could improve future related studies and applications to be more suitable learning services on the individual level (personalized learning services). The knowledge from this study can be applied to help reduce the cost of equipment and improve the flexibility of measurement methods in the real-world environment while also lessening the burden on the users during their learning process in future related studies as well as educational applications.

This article comprises four sections. Section 2 describes the raw data, experiment setting, and cognitive motivation identification method based on the TARM concept. Section 3 provides the results, including the suggested optimized parameter set, accuracy of the constructed model, feature analysis, and model validation. Finally, Section 4 discusses the study's findings, limitations, and conclusion.

2. Materials and Methods

2.1. Raw Data

To identify the effect of motivation that could lead to remembering the stimulus, the EEG data from the motivation task are required for the analysis. The data used in this study are identical to those used in our previous cognitive-motivation study [16]. More information on our publicly available dataset can be found in the "Data Availability Statement" section. The participants comprised fourteen male and two female Asian volunteers between 21 and 37 years of age. None of the participants have prior visual perception or memory disorders. The data in this study were obtained from the cognitive-motivational task that was separated into two parts: the cognitive experiment and the recognition test. During the cognitive experiment, the Nihon Kohden Neurofax EEG-1100 equipment (NIHON KOHDEN CORPORATION, Tokyo, Japan) with 32 electrodes was used to measure EEG data with a sampling frequency of 500 Hz. The experiments were conducted in a room with no distractions. All experimental procedures and purposes were disclosed to the participants before the experiments.

In the cognitive experiment, participants were presented with 250 random, unique visual scenic stimuli, one by one. Each stimulus was presented for 3 s. Then, the participant had to decide whether they wanted to remember the stimulus within 9 later seconds. With this setup, the cognitive experiment was completed in around 50 min for each participant. This estimation excludes the setup time and the short break requested by participants. The participants could freely make their decision on whether they wanted to remember the scene. The decision was used as an indication of their motivation; the trial is considered a "*being motivated*" case when the participant chooses to remember the stimulus and a "*not being motivated*" case if otherwise. Because motivation is the topic of the study, it depends on the participants' motivation towards the stimulus; hence, the number of trials between two cases could be unequal for each participant.

In the recognition test, 500 random scenes, comprising 250 from the cognitive experiment and 250 new scenes, were presented. The participants were asked to answer whether they recognized the presented scene in the cognitive experiment. The answer from this test indicated the motivation effect corresponding to their motivation for the stimulus in their prior cognitive experiment. There are no time constraints in this recognition test. The brain signals were not measured during the recognition test.

By relating the motivation of the participant to the corresponding results from the recognition test, the data were categorized into four groups: "*being motivated and remembered*", "*being motivated but forgot*", "*not being motivated but remembered*", and lastly, "*not being motivated and forgot*". Since the purpose of this study is to analyze the effect of motivation, "*not being motivated*" data were excluded. The total number of data epochs used in this study is 1873 epochs from the "*being motivated*" case that resulted in 1429 remembered (RR) and 444 forgot (RF) cases.

2.2. Cognitive Motivation Effect Identification

To identify the effect of motivation on brain activities related to cognitive performance, we designed the TARM-based method for EEG. Figure 1 shows the overview of the method's process. The processes are divided into two parts: the model construction part, shown in Figure 1A, and the identification part, shown in Figure 1B. For the model construction part, the EEG data are preprocessed to remove physiological noise, power line noise, and eye-blinking artifacts. Only the epochs without saccade characteristics are used for analysis. Because alpha desynchronization is known from the previous study [16] to involve cognitive motivation, the preprocessed EEG epochs are transformed into ERSP data to prepare for determining desynchronization trends. The ERSP data are moving averaged to smoothen the spectral perturbation and to reveal the trend. Then, the trend data are represented by discretized sequences. The details of the preprocessing steps are described in Section 2.2.1. The discretized sequences are then analyzed to determine the temporal relationship between two signals; the details are explained in Section 2.2.2. The TARM concept is applied in this method to find the temporal relationship patterns. The temporal relationship patterns are used to build classification models for classifying the cognitive performance (whether the scene is remembered or forgotten); the details are given in Section 2.2.3. However, EEG signals are highly complex; the method requires some parameters along the processing pipeline to be optimized to obtain an effective classification model for identification. Section 2.2.4 describes the process for parameter and model optimization. The output parameter set and classification model are then used in the identification part. Figure 1B illustrates the procedure for the cognitive motivation effect identification part.

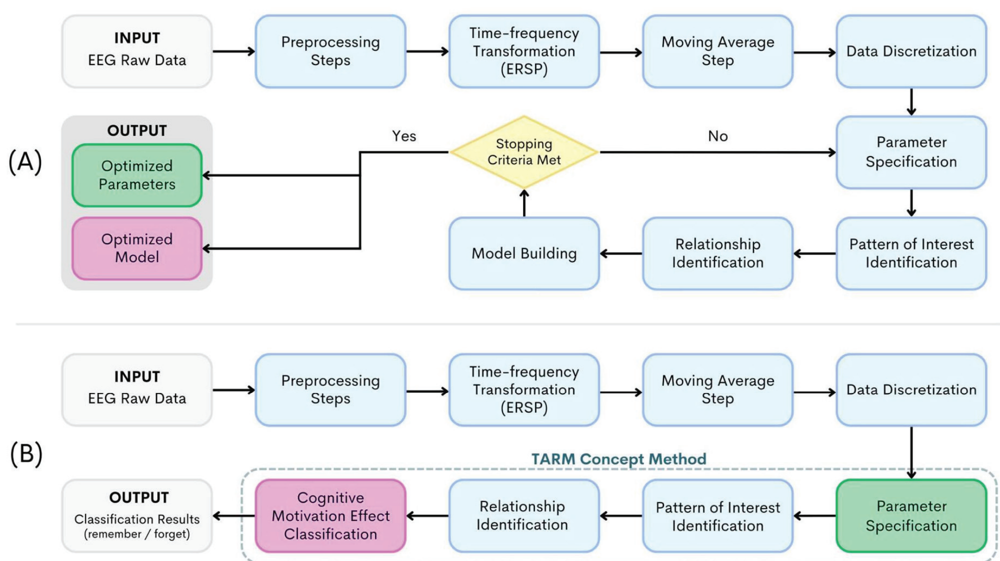

Figure 1. The processes of the cognitive motivation effect identification method proposed in this study: (**A**) the model construction part and (**B**) the identification part.

2.2.1. Preprocessing Steps

In this study, the EEG signals were analyzed by MATLAB R2014b (MathWorks, Natick, MA, USA) with the open-source toolbox EEGLAB v13.4.4b [24]. MATLAB is a commercial software that allows complex matrix manipulation and computation, which is suitable for EEG signal processing. EEGLAB, which is the open-source toolbox working on the MATLAB environment, provides comprehensive tools from visualization, processing, and analysis to in-depth self-coding for specific studies. The preprocessing steps start with mapping the EEG signals to their corresponding electrode locations on the head model. Then, the average referencing was conducted by subtracting the average potential of all electrodes from each electrode at each time point. After that, both 0.5–50 Hz bandpass and 60 Hz notch filters were applied to remove physiological and power line noise, respectively. The signals were then marked into epochs and labeled by the participants' motivation choices and recognition results regarding the scene stimuli. An epoch that has a signal voltage higher than 500 microvolts (μV) or lower than −500 microvolts was considered an abnormal value epoch and, thus, excluded from this study. The components related to eye-blinking artifacts were analyzed using the Independent Component Analysis (ICA) method and then selected and removed manually using the GUI tool of the EEGLAB toolbox. After that, the epoch with the saccade characteristic was manually selected and discarded. The epoch without response in the recognition test was also excluded. Finally, there are 1094 RR and 332 RF case epochs in this study.

All remaining epochs were transformed into the time-frequency domain using the Event-Related Spectral Perturbation (ERSP) method [25]. The average ERSP data across the alpha band (8–12Hz) were used in this study. Note that the preprocessing steps up to this point are the same as in our previous study [16]. Previously, we found that at the FCz and P3 electrodes the continuous alpha desynchronization patterns of the RR cases are significantly longer than those of the RF cases. Hence, the processed ERSP data from the FCz and P3 electrodes were used as representatives for attention and memorization areas, respectively, in this study.

To reduce the complexity of the preprocessed ERSP data, the Simple Moving Average (SMA) method was applied. The trends were revealed. Nevertheless, a suitable SMA parameter should be selected. This is one of the parameters to be optimized later. The data were then discretized into sequences representing downward and upward trends. The downward trend indicates the continuous desynchronization period, while the upward trend relates to the synchronization period of the ERSP data. Each trend was represented by the starting and ending time points. The data sequence is considered to have a downward trend when all time points have continuously lower values than the preceding points. Similarly, the data sequence with continuously higher values than the preceding points is considered an upward trend. In this study, the downward trends of the FCz and P3 electrodes were analyzed as the potential attention and memorization sequences of interest. The processes of preprocessing EEG data into discretized sequences for the cognitive motivation effect identification method are shown in Figure 2. The bottom part of Figure 2 illustrates the examples of data output from each of the processes.

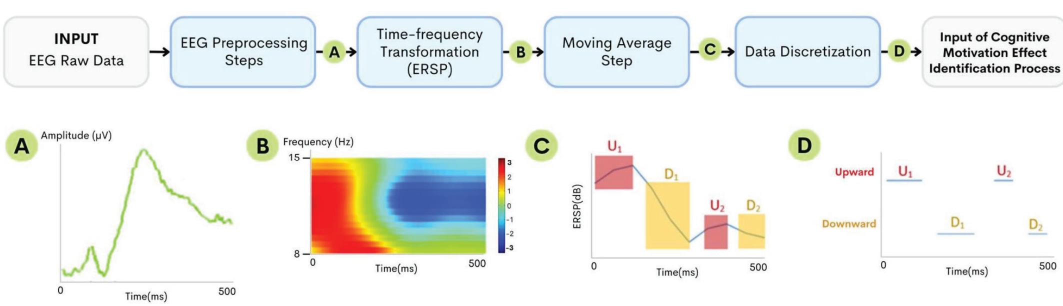

Figure 2. [**Top**] The preprocessing steps from EEG to discretized sequences with [**Bottom**] the examples of data output from each step: (A) EEG segment, (B) ERSP, (C) smoothened alpha band (8−12 Hz) ERSP, and (D) discretized trend sequences.

2.2.2. Relationship Identification

The alpha desynchronization is known to relate to the attention state [26,27]. Based on the findings in our previous study [16], the continuous alpha desynchronization patterns of the RR cases are significantly longer than those of the RF cases. In this study, we hypothesized that motivation could lead the participant to continue paying attention to the stimulus, which, in turn, resulted in stimulus memorization. It is anticipated that, for the remembered cases, the attention downward sequences should occur before the memorization downward sequences. According to Allen's 13 temporal logics [28], there are 3 possible temporal relationships between attention and memorization sequences based on this hypothesis: *before*, *contain*, and *overlap*. We explored the potential of these 3 temporal relationships for the association rules between brain areas.

For each relationship, we measured the relationship level, which indicates the likelihood that the relationship is related to the motivation that leads to the stimulus memorization. For the before relationship, the first (attention) sequence must start and end before the second (memorization) sequence starts. The longer the interval between the two sequences, the less likelihood that the second sequence is the result of the first sequence. We set a threshold window indicating that the two sequences are related. If the interval between the two sequences is within the threshold window, the two sequences are considered related. Hence, its relationship level is the ending time of the first sequence plus the length of the threshold window and then minus the starting time of the second sequence. An example of the before relationship in our study between the attention sequence (FCz downward trend) and the memorization sequence (P3 downward trend) can be presented in Figure 3. It should be noted that the suitable threshold window length is unknown; it is another parameter to be optimized later.

Figure 3. An example of before relationships.

For the contain relationship, the first sequence starts before the second sequence but ends later than the ending of the second sequence. The relationship level of the contain relationship is the length of the second sequence. Figure 4 shows an example of a contain relationship. Lastly, in the overlap relationship, the first sequence must also start before the second sequence. The first sequence ends after the second sequence starts but before the second sequence ends. The relationship level of this overlap relationship is the ending time of the first sequence minus the starting time of the second sequence. An example of the overlap relationship is shown in Figure 5.

The discretized sequences of epoch data from the FCz and P3 electrodes are determined for these temporal relationships. An epoch can comprise multiple temporal relationships. Therefore, the influence of each of these relationships must be considered together. In this study, the method based on the concept of TARM was used to analyze the cognitive motivation effect through these relationships.

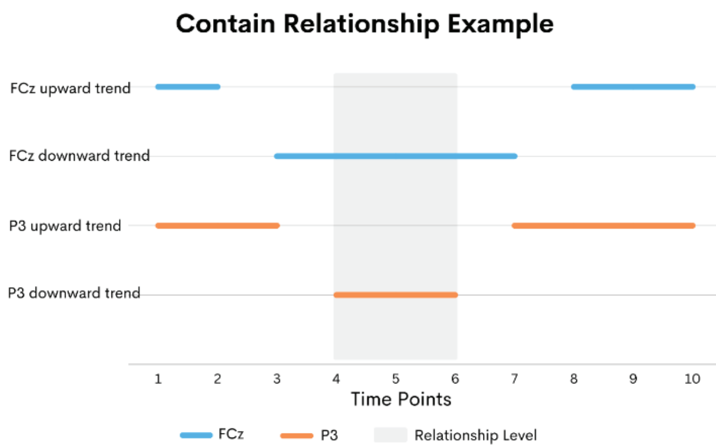

Figure 4. An example of contain relationships.

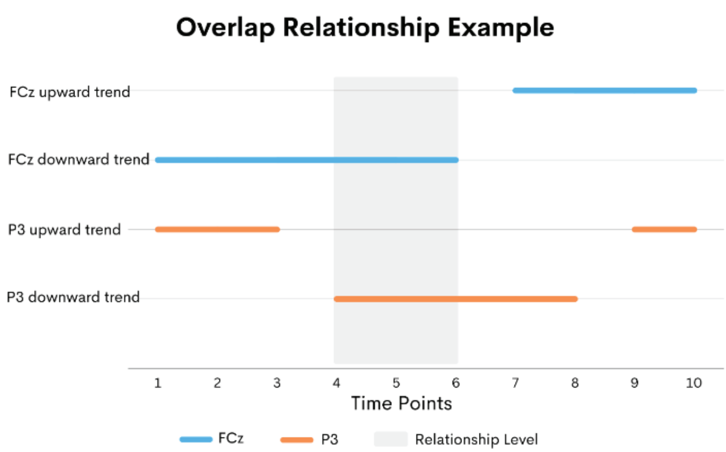

Figure 5. An example of overlap relationships.

2.2.3. The Application of Temporal Association Rule Mining Concept

Temporal Association Rule Mining (TARM) [19] is used to identify the pattern of relationship among items that occurred within the data while considering the temporal constraint. Several parameters are required to consider the confidence of the identified rule. The support threshold is used to consider whether the item has occurred frequently enough to be considered an item of interest. The temporal support threshold is used to consider whether the relationship between two items occurred for sufficiently long enough to be considered as having a relationship of interest. Lastly, the confidence of the relationship is indicated by the confidence value.

In this study, we applied the TARM concept to identify the temporal relationships between attention and memorization as the effect of motivation resulting in stimulus memorization. The attention downward sequences and memorization downward sequences are the items to which we direct interest. The alpha desynchronization trend should continue for a sufficient duration to be considered a pattern. The support threshold is the minimum length of the downward sequence that is considered a pattern; the sequence shorter than the support threshold is discarded. To our knowledge, the suitable sequence length is unknown. Because the suitable sequence length for attention could differ from that for memorization, we used 2 support thresholds to determine the FCz and P3 downward sequences separately; they are called the attention and memorization pattern length thresholds, respectively.

The temporal support threshold is the sufficient period of time that the attention downward sequences relating to memorization downward sequences are considered to have a relationship; a higher relationship level than the temporal support threshold is counted as a relationship. There are 3 temporal support thresholds, one for each of the temporal relationships described in Section 2.2.2. They are called the before-relationship length threshold, contain-relationship length threshold, and overlap-relationship length threshold.

Based on the TARM concept, this method has 5 threshold values to be designed. When including the moving average parameter and the before-relationship window size, mentioned in Section 2.2.1, there are 7 parameters to design in order to identify the association relationships between attention and memorization. Table 1 includes all 7 method parameters and their descriptions. Figure 6 shows the processes at which the required parameters of this method are located.

Table 1. The method parameters of cognitive motivation effect identification based on the TARM concept.

Method Parameter Name	Related Process	Description
Moving average window	Moving average process	To smoothen the spectral perturbation and reveal the potential hidden trend
Attention pattern length thresholds	Pattern of interest identification	To identify the attention sequence that has a sufficient alpha desynchronization trend
Memorization pattern length thresholds	Pattern of interest identification	To identify the memorization sequence that has a sufficient alpha desynchronization trend
Before-relationship window size	Relationship identification	To identify the before relationship and calculate the before-relationship level
Before-relationship length thresholds	Relationship identification	To identify the before relationship resulting from the effect of motivation and leading to stimulus memorization
Contain-relationship length thresholds	Relationship identification	To identify the contain relationship resulting from the effect of motivation and leading to stimulus memorization
Overlap-relationship length thresholds	Relationship identification	To identify the overlap relationship resulting from the effect of motivation and leading to stimulus memorization

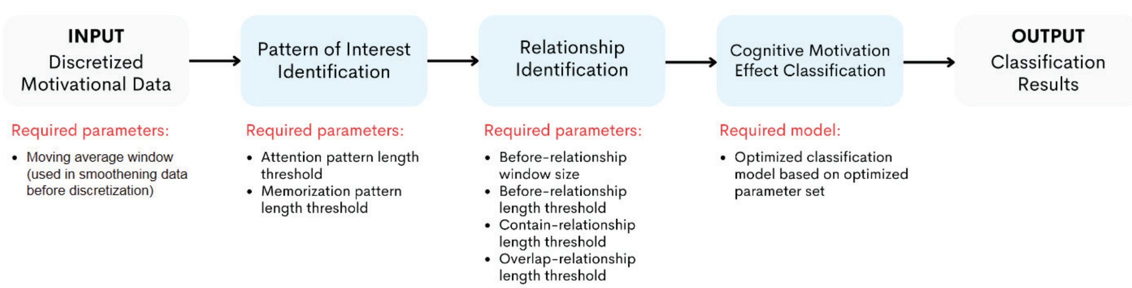

Figure 6. The processes to identify the cognitive motivation effect. The parameters and model required to be optimized for each step were listed under each corresponding red label.

The method filters the discretized downward sequences from the FCz and P3 electrodes to remove the sequences shorter than the attention and memorization pattern length thresholds. The FCz downward sequence that is longer than the attention pattern length threshold is considered an attention sequence. Likewise, the P3 downward sequence longer than the memorization pattern length threshold is considered the memorization sequence. Then, the temporal relationships of all attention and memorization sequences are analyzed.

The relationship with a lower relationship level than the corresponding threshold is discarded. Finally, the remaining relationships are considered temporal relationships between attention and memorization resulting from being motivated.

Due to the complexity of the brain, it is anticipated that the combination of temporal relationships will be involved in cognitive motivation. We introduced the use of a classification model built from the "*being motivated*" epochs to evaluate how well the combination of temporal relationships could accurately identify whether the motivation could lead to stimulus memorization. We used 6 features as input for the classification model, including the occurrence number and relationship level of before relationships, the occurrence number and relationship level of contain relationships, and the occurrence number and relationship level of overlap relationships. The relationship occurrence numbers are related to how often that attention resulting in memorization occurred while being motivated. The relationship level, as described in Section 2.2.2, indicates the likelihood that the relationship is related to the motivation that leads to the stimulus memorization.

The classification model construction can be chosen from a variety of methods. In this study, we demonstrated our method with Support Vector Machine (SVM) as an example; the "templateSVM" MATLAB function with auto kernel scale Radial Basis Function (RBF) kernel was used. The output classification model from the method can be used to predict whether the EEG input data acquired while being motivated can lead to stimulus memorization afterward.

2.2.4. Method Parameter and Model Optimization

The 7 method parameters could affect the accuracy of the identification method. To find the suitable values of these parameters and the acceptable classification model, the Artificial Bee Colony (ABC) algorithm was used. The ABC algorithm is a population-based metaheuristic optimization algorithm introduced by Karaboga [22]. The method is known for its simplicity and flexibility in implementation and combination with other algorithms. With these advantages, ABC was used as an example of a metaheuristic algorithm for the model construction part of our method. The ABC method was inspired by the intelligent foraging behavior of honeybees. The employed bees search for the positions of food sources while remembering the position for future foraging. Information on the food source is shared with the onlooker bees waiting at the hive. The onlooker bee selects its target according to the quality of the food source and searches for food sources in the target direction. When the employed bees and onlooker bees cannot find a better food source, they abandon the food source and become a scout exploring in a random direction for a new food source. In the ABC algorithm, onlooker and employed bees perform the search in the specific search space (exploitation), while scouts perform the wide exploration.

Figure 7 illustrates the processes to optimize the parameter set and obtain the optimized classification model; the processes in Figure 7 are related to Figure 1A but show more details of how ABC was incorporated. The search space for the bees is 7 dimensions for 7 parameters. The employed bee positions are randomly initialized. Then, the method proceeds to perform a set of ABC iterations and terminates when the number of iterations exceeds the specified maximum iteration. For each iteration, the employed-bee, onlooker-bee, and scout-bee phases were performed to find a good parameter set. The TARM-based processes used the best parameter set to identify temporal relationships and build an SVM classification model. The accuracy of the classification model was used as the food source quality.

Anuar et al.'s study [29] performed the ABC colony size tests ranging from 4 to 200 and suggested that the colony size should be at least 24. This study used a colony size of 28, which is 4 times the parameter numbers. The 28 bees comprised 14 employed and 14 onlooker bees. The maximum iteration number was set to 200. The range of each parameter was set based on the knowledge of our previous study [16] as 0 to 9 for the moving average window; 30 to 100 ms for attention and memorization pattern thresholds;

150 to 200 ms for before window size; and 30 to 100 ms for before-, contain-, and overlap-relationship length thresholds.

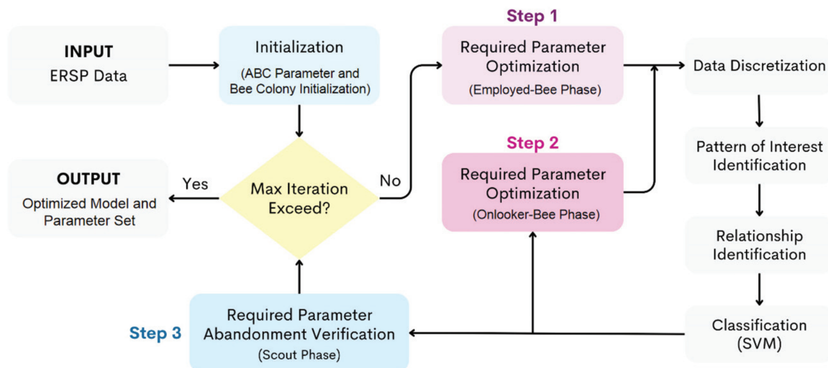

Figure 7. The detailed optimization part of the cognitive motivation effect identification method implemented with the ABC algorithm.

In the employed-bee phase, each employed bee performs a search near its employed food source. In the onlooker-bee phase, each onlooker bee selects an employed-bee food source position (parameter set) as the reference position to explore nearby areas. The selection is based on the probability function weighed on the quality (classification accuracy) of each food source [22]. A better-quality food source probably attracts more bees to exploit it. The employed and onlooker bees search for a nearby food source with the same calculation as mentioned in [22] but with different ranges. This study used 1/5 and 1/3 of the nearest neighboring food sources as the search range for employed and onlooker bees, respectively. Cosine similarity was used to identify these nearest neighboring food sources. If the quality of the new food source is better than the previous position, the bee position is updated. After both the employed-bee and onlooker-bee phases are finished, the scout phase is started. In the scout phase, the number of times each food source has been visited was counted. If any food source is visited exceeding a specified threshold, the employed bee will abandon its position and become a scout, randomly selecting a new position.

By applying the ABC algorithm, the optimized parameter set required for the identification method was obtained. However, there could be a bias problem resulting from the difference in the data of each stimulus category during the classification model-building process. In this study, the numbers of epochs in two motivated cases (RR and RF) are different. This situation is especially common when the experimental categories are based on the participants' preferences, which can be varied and cannot be controlled. Using the unequal numbers of data from each category for training and testing of the SVM method could lead to obtaining a biased classification model. To avoid this problem, an equal number of data from each cognitive motivation case were randomly selected as the training and testing set. A total of 200 training data were used in the model-building process: a hundred from the RR epochs and another hundred from the RF epochs. Another 50 random epochs were selected from the leftover data, 25 from each category, to be used as the test set.

Because there is no known knowledge about the temporal relationship between attention and memorization, the objective value that determines the quality of an ABC food source is the classification accuracy of the model from the test set. Nevertheless, the different sampled training and test sets can result in different classification accuracy and food-source quality. In turn, the resulting parameter set can be different from one repetition to another, or the same parameter set can give different classification accuracy from one sample set to another. This problem could lead to an inaccurate selection of the optimized parameter set.

To ensure that the optimized parameter set obtained from the method can be used effectively in real applications in the future, we applied the Central Limit Theorem (CLT) [23] to mitigate the problem of variant outputs due to sampling variation. The problem resulted from the different sample sets when the sampling process was used in the optimization search process. With CLT, the method can identify the mean of population accuracy as the representative. CLT is a probability theory that states that "as the sampling number increases, the mean sampling distribution will increasingly become closer to a Gaussian distribution". These Gaussian or normal distribution data are concentrated around the mean. In other words, with sufficiently large unbiased sample numbers from the whole population (with a finite level of variance), the mean of all samples from the same population will be (approximately) equal to the mean of the whole population. In this situation, the mean or median is suitable to be used as the representative of the overall sampling data and can also be used in exchange. In CLT, it is not feasible to state the exact sample size sufficient for a general approximation. However, at least 30 sample sizes are often suggested to produce an approximately normal sampling distribution from a non-normal parent distribution [30]. Additionally, in case the population is normally distributed, it is believed that if sampling at least 10 times, the sampling mean is able to assume a normal distribution [31,32]. In this study, the normal distribution cannot be assumed due to the possibility of varying relationship numbers and their temporal periods in each epoch. For our data, the number of relationships and their temporal period of a relationship could be affected by the other relationships within a limited attention period of 3 s. The longer a relationship, the lesser the temporal period available for the others. From the results in [30] and the suggestion in [31,32], the sample sizes of 10 and 50 are used as the comparison cases.

In this study, we applied the concept of CLT to identify the population median of the classification accuracies as the representative of the food source in the ABC algorithm. The CLT concept was applied through the implementation of the repeated sampling training and test set within the model-building process. Each sampling has its own model and accuracy. The median from all the repeated resulting accuracies was used as the representative quality of the food source in the ABC search process. Any food source with a Median Absolute Deviation (MAD) higher than 0.03 is regarded as an unstable food source and excluded from the quality update of the search process.

3. Results

This section presents the performance of the TARM-based method to identify the cognitive effect of motivation with only two electrodes, FCz and P3. The results of ABC with SVM, ABC with 10 times repeated sampling SVM (ABC-10RSVM), and ABC with 50 times repeated sampling SVM (ABC-50RSVM) were compared to find the best parameter set and cognitive motivation identification model. These parameters can be used as guidelines to configure parameters in the preprocessing steps, preparing the data before the model classification process. Then, the temporal relationship features were analyzed. Finally, the generalization performance of the best model was demonstrated using the data of individual participants. The accuracy of our result model is validated to be 74.5% on average with individual tests.

3.1. Cognitive Motivation Effect Classification Model Results and Parameter Set Suggestion

A set of seven parameters is required to be optimized. These parameters could affect the performance of the motivation effect identification model. These parameters include the moving average (MA) window, attention, and memorization pattern thresholds, the before-relationship window threshold, the before-relationship length threshold, the contain-relationship length threshold, and the overlap-relationship length threshold. We tested each of the three ABC-applied methods for 10 rounds to identify their average classification accuracies. These average classification accuracies will then be used as their performance representative. For the representative classification accuracy of the parameter set (from each round of the optimization), the median accuracy from 1000 random train and test sets was used. Since a large number of random samples (1000) were tested for each parameter set, the distribution of the results for each parameter set can be assumed to be a normal distribution according to CLT. The median accuracy from the accuracy results of all sampling is then suitable to be used as the representative accuracy for each of these parameter sets. These median accuracies for 10 times ABC optimization are presented in Table 2. Additionally, detailed information on the best model and parameter set of each method is presented in Table 3.

Table 2. The median accuracy results of 1000 sampling test sets for each parameter set for motivation effect identification method.

Methods	Classification Accuracy										
	1st	2nd	3rd	4th	5th	6th	7th	8th	9th	10th	Average
ABC-SVM	**73%**	71%	66%	72%	70%	72%	71%	72%	72%	72%	70.8%
ABC-10RSVM	74%	76%	**80%**	78%	71%	75%	75%	73%	75%	78%	75.5%
ABC-50RSVM	74%	73%	76%	**80%**	75%	76%	74%	77%	77%	76%	75.8%

The bold number is the highest accuracy of the method.

Table 3. The detailed information on the best results from each parameter and optimization model.

Methods	Window		Threshold (ms)					Accuracy (%)					
	MA (pts)	Before (ms)	Pattern A	Pattern B	Relationship			Min	Max	SD	Mean	Med	[Q1, Q3]
					Before	Contain	Overlap						
ABC-SVM (Round 1)	2	200	30	90	50	100	40	58	86	4.35	72.93	73	[70, 76]
ABC-10RSVM (Round 3)	4	190	50	30	50	30	30	66	91	3.99	79.8	80	[77, 82.5]
ABC-50RSVM (Round 4)	4	190	50	30	50	60	30	69	91	3.96	80.39	80	[78, 83]

With the results in Table 2, the results of the ANOVA test, comparing the 10-round median accuracies from 16-participant sampling data of ABC-SVM, ABC-10RSVM, and ABC-50RSVM methods, suggested that the classification accuracy of the ABC-SVM method is significantly different from both ABC-10RSVM and ABC-50RSVM, with a P-value lower than 0.01. Additionally, the results between ABC-10RSM and ABC-50RSVM are not significantly different (p-value = 0.7771). The standard deviation results are 5.38%, 5.30%, and 5.18% for ABC-SVM, ABC-10RSVM, and ABC-50RSVM, respectively. The ABC-50RSVM method has the lowest variance among tested methods. All of the best model results for each method have an accuracy variance lower than 5%, as presented in Table 3. Additionally, the ANOVA test of the SD variance comparison among the methods resulted in no significant difference. The suggested parameters from ABC-10RSVM and ABC-50RSVM are almost the same except for the contain-relationship threshold parameter, as presented in Table 3.

Our results suggest that applying CLT to the ABC-SVM method can help us mitigate the problem of variant outputs due to sampling variation. This improvement can leverage the accuracy of the motivation effect identification model from our ABC-SVM with the TARM-based method. Additionally, with the lowest variance and highest classification accuracy, we suggested ABC-50RSVM for the cognitive motivation effect identification method. The best model has a confidence of 80% classification accuracy. Please also be aware that the 50 sampling number is not the magic number, and the number could vary depending on the data distribution. However, even with the lower mean classification accuracy (75.5% vs. 75.8%) and higher variance (5.30% vs. 5.18%) of the ABC-10RSVM to the ABC-50RSVM method, the difference in both cases is not statistically significant. With these results, it can be suggested that ABC-10RSVM can be used in the case of limited time constraints in which lowering model-building execution time is required and a slight variance classification accuracy is acceptable. Lastly, our parameter set suggestion is based on the results from 10 rounds of ABC for each method for the scenic stimulus, which may not represent the general use in real-world applications. With this problem, we suggested applying the ABC-RSVM process to build the model and identify the suitable parameter set before the application is used for the first time. A case of validation for the general use of the best model will also be presented later in this study.

From Table 3, the suggested parameters from ABC-50RSVM are a moving average window equal to 4, 50 ms for attention pattern length threshold (FCz downward), 30 ms for memorization pattern length threshold (P3 downward), 190 ms for before window size threshold, 50 ms for before-relationship length threshold, 60 ms for contain-relationship length threshold, and 30 ms for overlap-relationship length threshold. From this parameter set, we attempted to identify the potential relationship feature that is highly distinguished by the effect of motivation. These relationships could lead to the improvement of preprocessing steps and model building in the later study.

The results of our study also give evidence that motivation influences the activities within the brain differently in "being-motivated-and-remembered" and "being-motivated-but-forgot" cases. This influence is affecting the brain activities related to FCz and P3 electrodes, which are related to attention and memorization areas within the brain. From the knowledge of previous studies [13–16], we assumed the relationships from the attention sequence occurred before the memorization sequence. With this assumption, the results in this study give evidence that the brain activities in the attention area lead to the activities in the memorization area by a top-down process while being influenced by the effect of cognitive motivation. Unfortunately, the specific difference between brain activities of RR and RF cases cannot be known from the results of our method. The problem is due to our classification model using a combination of features from the attention and memorization sequences to identify the effect of motivation. Unlike linear SVM, which can summarize data with a set of parameters with fixed size (the weight coefficient), the transformation of SVM with RBF kernels is based on the pairwise distances between the training points resulting in the number of parameters growing with the size of the support vector, which makes it a non-parametric method. Therefore, the importance of each relationship characteristic (i.e., the weight coefficient in SVM) cannot be directly identified. However, the study tries to explore how motivation affects brain activities differently by identifying the importance of a specific feature in differentiating RR and RF cases in the next section.

3.2. Potential Feature Suggestion

To identify the difference between brain activities of RR and RF cases, we performed a statistical test comparing RR and RF cases of each suggested classification model input feature from the previous section. Because the temporal period of one relationship could be affected by the temporal period of other relationships within a limited 3 s temporal attention period, for example, the longer period of an overlap relationship leads to the shorter remaining temporal period available for other relationships. Therefore, the relationship features were not in the normal distribution. The Wilcoxon signed-rank test was used. The results of this test are presented in Table 4. Note that the average relationship-level feature of each relationship is not the input feature of our classification model. The average relationship levels represent the mean relationship level of the relationship for each epoch. They were only used to statistically analyze the difference between RR and RF in this section.

From the observation of our SVM input data, the before relationship is the pattern that is always found in motivated cases; from 200 epochs of each case, all 200 RR epochs and 198 RF epochs have a before relationship. There are 143 RR epochs and 135 RF epochs with the contain relationship. Lastly, there are 187 RR epochs and 174 RF epochs with an overlap relationship. This study hypothesized that the effect of motivation is affected by the combination of multiple relationships in each epoch. However, the fact that before-relationship patterns are found in most epochs could suggest that the occurrence of the before relationship could be highly influenced by the state of being more motivated than other relationships. In concordance with this observation result, the results of Table 4 also suggest that only the "average before-relationship level" is significantly different between

RR and RF cases; the average before-relationship levels of RR cases are higher than those of RF cases. These results suggest that the brain activities of the RR cases had a memorization pattern that occurred following the ending of the attention pattern sooner than in the RF cases. However, the difference is at a 0.1 significant level, with a p-value equal to 0.07, so we suggested exploring the conditions that could affect this occurrence in more detail before using this knowledge in future studies.

Table 4. Wilcoxon signed-rank test result between RR and RF cases of each feature.

Features	Z	Asymp. Sig. (2-Tailed)
Before-relationship occurrence number	-0.906^{p}	0.365
Before-relationship level	-0.219^{p}	0.827
Average before-relationship level	-1.809^{n}	0.070
Contain-relationship occurrence number	-0.668^{n}	0.504
Contain-relationship level	-1.71^{p}	0.864
Average contain-relationship level	-1.206^{p}	0.228
Overlap relationship occurrence number	-0.845^{n}	0.398
Overlap-relationship level	-1.103^{n}	0.270
Average overlap-relationship level	-0.311^{p}	0.756

^{p}: Based on positive ranks, ^{n}: based on negative ranks.

As additional information, this study presents examples of before relationships in RR and RF cases in Figure 8. The examples are in the form of alpha frequency trend data (upward and downward) mapped onto all electrodes of the sequential temporal period head models. In Figure 8, the square symbol (■) represents the focused electrodes used in this study, which are FCz and P3. The pentagram symbol (★) represents the FCz electrode while having an attention pattern of interest, which is an attention pattern that leads to memorization. The triangle symbol (▲) represents the P3 electrode while having a memorization pattern of interest, which is the memorization pattern resulting from being motivated and having attention. The dotted red box during 190–310 ms for RR or 240–380 ms for RF represents the period between the ending of the attention pattern and the start of the memorization pattern mentioned in the previous paragraph. Since the before-threshold window has a fixed constant value, the distance between these two patterns is the counterpart of the before-relationship level. The higher before-relationship level is equal to the lower distance between the patterns. Figure 8 also shows that the RR case has a longer alpha desynchronization pattern than the RF case, as mentioned in the results of our previous work [16].

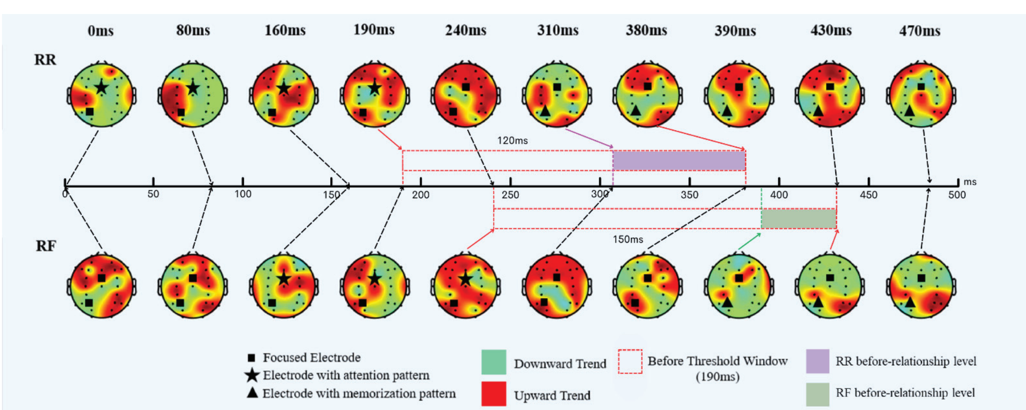

Figure 8. An example of temporal ERSP trend data of an RR epoch with a before relationship. The arrow marked the occurrence time of the corresponding head model.

3.3. Model Validation

Lastly, we verified the generalization of the suggested model with the individual participant data. Since the RF case usually has a low number of epochs, only participants with RF epochs higher than 25 were tested. The model was tested with data from six participants, each with 1000 test sets. A test set comprised 20 randomly selected epochs from the RR and RF cases each. The results of this test are summarized and presented in Table 5.

Table 5. The results of individual test sets with the best model from the ABC-50RSVM method.

Participant	Accuracy (%)		
	Median	Mean	SD
1	85	85.44	5.51
2	80	81.35	6.11
3	70	70.78	7.52
4	70	70.60	6.96
5	65	64.27	7.32
6	50	51.47	7.79

The results suggest that our model can use only FCz and P3 electrodes to identify the effect of motivation with 70.65% classification accuracy on average. The model can classify the effect of being motivated acceptably for most participants, except for participant number 6, whose classification accuracy result is lower than the others. This may be due to age; brain alpha frequency becomes higher with age [33]. Participant number 6 is 33 years old, while the others are in their 20s. We tested the model with the data of another participant who is 37 years old but who has a number of RF epochs lower than 25; this participant was excluded from the validation participants. Because the number of RF epochs for this participant is very low, we used five RR epochs and five RF epochs for the test set. A classification accuracy of 53.11 percent was returned. The results indicate that the identification model can be used for users in their 20s; separate models should be constructed for different age ranges. Considering only participants in the 20s age range, the model resulting from the proposed method can be used to identify the effect of motivation on the individual participants with 74.5% mean classification accuracy.

4. Discussion and Conclusions

With the random scene selection in the experiment, the motivation leading to memorization could be the result of various motives. Some scenes may have objects that interest the participant as the motive [1]. Some participants may have a motive to demonstrate their competence to gain a higher score than others [2–4]. Other motives could be that the scenes have a unique artistic value that piques the curiosity of the participant or looks complex and makes the participant feel challenged to remember them [5]. Even for the same individual, the motive could be different given the change in time and situations. These differences in motives can affect the various brain areas [6–12], which, in turn, results in high numbers of EEG electrodes being required to identify the effect of motivation. Table 6 concludes the motives related to cognitive motivation and the affected electrodes resulting from existing EEG studies in the literature. In total, 28 electrodes would be required to measure all listed motives.

Instead of focusing on the motives, we proposed to shift the focus to the effect of motivation; the idea could allow us to use a smaller number of electrodes to measure in real education applications. The low number of electrodes can help lessen the burden on users and improve flexibility when used in a real-world environment. We previously found that motivation can affect both attention and memorization [13,16] and that attention leads to memorization [14]. In this study, we investigated the effect of motivation through the temporal relationship between the associated brain areas with two EEG electrodes representing attention and memorization.

Table 6. The affected EEG electrodes of motivation effect resulting from motives.

Motives	Author/Year	Affected Electrodes	Affected Electrode Number
Reward	Ven et al., 2016 [9]	C3, Cz, C4, CP1, CP2, P3, Pz, and P4	8
Challenge	Ma et al., 2017 [10]	F4, F6, F8, FC4, FC6, and FT8	6
Interest	Jin et al., 2015 [11]	F1, Fz, F2, FC1, FCz, FC2, C1, Cz, C2, CP1, CPz, CP2, P1, Pz, and P2	15
Curiosity	Brydevall et al., 2018 [12]	Fpz, AFz, Fz, FCz, and Cz	5
All listed motives	-	F1, F2, F4, F6, F8, FC4, FC6, FT8, Fz, FC1, FCz, FC2, Fpz, AFz, C1, C2, C3, C4, Cz, CP1, CP2, CPz, Cz, P1, P2, P3, P4, and Pz	28

Using the proposed method, the cognitive motivation identification model can identify the effect of motivation related to the cognitive performance of participants with 74.5% accuracy when validated with individual participant test sets. The model can be used for users in the 20s age range. Due to the complexity of human brains, the sampling process for data can lead to the problem of variant output values. This study used CLT to address this problem. The CLT-applied ABC-RSVM model from this method returned the acceptable parameter set in Table 3 for analyzing the temporal relationship patterns among the associated brain areas. Based on the acceptable parameter set, the results indicate that when the participant is motivated, attention precedes memorization, with a higher average before-relationship level in the RR cases than in the RF cases.

The findings of this study can be applied to help complement studies on the characteristics of visual stimuli that lead to motivation [34–39] for later use in educational applications. In educational applications, teaching materials are usually intended not only to motivate the student but also to make sure that their key points can later be remembered. By applying our model for the stimulus that was found to motivate the participants, the predicted results of whether the stimulus will likely be remembered afterward can be used to evaluate and help improve the teaching material in the future. Additionally, the conventional cognitive tests (e.g., Newcastle Spatial Memory Test [13]) used in education studies are usually performed without brain activity measurement. There could be various effects that influence the cognitive results of the participant (e.g., information missing due to the passage of time). However, using our method to identify the cognitive results based on brain signals at the learning event can help in evaluating the stimulus and teaching materials more efficiently by reducing the other influences between the event and the testing time. By applying the knowledge from this study, the learning application can adjust the stimulus (e.g., teaching materials) at the time of learning to be more suitable for personalized learning services.

There are some limitations to this study. The participants are sampled from Asian populations, which may not represent the general populations of other races. The age of the users could also influence the performance of the application due to the difference in alpha frequency with age [33]. The effect of age range and population race (e.g., Asian, African, and European) are also topics of interest for future in-depth studies to address this limitation. When more data are collected to cover different races and age ranges, we suggest applying our method to identify the suitable parameter set and to construct the identification model. Note that as the method in this study intended to identify the effect of motivation with reduced EEG electrode requirements, the method cannot identify the motive of their motivation during their learning process. The method requires data from motivated participants as inputs to identify their cognitive performance. Therefore, the motivation of the user has to be identified before the process of this study. The method is suggested to be used with the stimulus that is known to motivate the participant.

Author Contributions: Conceptualization, K.I. and B.K.; methodology, T.P. and S.M.; software, C.C.; validation, T.P., S.M. and C.C.; formal analysis, T.P.; investigation, T.P.; resources, S.M., K.I. and B.K.; data curation, T.P.; writing—original draft preparation, T.P.; writing—review and editing, S.M. and B.K.; visualization, C.C. and B.K.; supervision, K.I.; project administration, B.K. All authors have read and agreed to the published version of the manuscript.

Funding: This research received no external funding.

Institutional Review Board Statement: The experiment in this study was approved by Experimental Ethics Committee of Faculty of Information Science and Electrical Engineering, Kyushu University (ISEE H26-3, 23 June 2014).

Informed Consent Statement: Informed consent was obtained from all participants involved in the study.

Data Availability Statement: The data used in this study are the same as our previous study [16]; the dataset is described and available in our data article [40]. The code of our methods can be found at https://drive.google.com/drive/folders/1S-_L8-zReu_AIUE6a_YoRHyQh_f67Y3Y (accessed on 5 April 2024).

Acknowledgments: The first author expressed gratitude to King Mongkut's University of Technology Thonburi for the support of The Petchra Pra Jom Klao Ph.D. Research Scholarship. This scholarship funded various activities in the process of acquiring the knowledge required to complete this study.

Conflicts of Interest: The authors declare no conflicts of interest.

Abbreviations

The following abbreviations are used in this study:

ABC	artificial bee colony
ABC-SVM	ABC with SVM
ABC-10RSVM	ABC with 10 times repeated sampling SVM
ABC-50RSVM	ABC with 50 times repeated sampling SVM
CLT	central limit theorem
ERSP	event-related spectral perturbation
ICA	independent component analysis
MA	moving average
MAD	median absolute deviation
RBF	radial basis function
RF	being motivated but forgot
RR	being motivated and remembered
SVM	support vector machine
TARM	temporal association rule mining

References

1. Renninger, K.A.; Wozniak, R.H. Effect of interest on attentional shift, recognition, and recall in young children. *Dev. Psychol.* **1985**, *21*, 624–632. [CrossRef]
2. Harackiewicz, J.M.; Sansone, C.; Manderlink, G. Competence, achievement orientation, and intrinsic motivation: A process analysis. *J. Personal. Soc. Psychol.* **1985**, *48*, 493–508. [CrossRef]
3. Durik, A.M.; Renninger, K.A. Achievement strivings: Motives and goals that promote competence. In *Handbook of Personality Development*; McAdams, D.P., Shiner, R.L., Tackett, J.L., Eds.; The Guilford Press: New York, NY, USA, 2019; pp. 295–312.
4. Wang, C.; Cho, H.J.; Wiles, B.; Moss, J.D.; Bonem, E.M.; Li, Q.; Lu, Y.; Levesque-Bristol, C. Competence and autonomous motivation as motivational predictors of college students' mathematics achievement: From the perspective of self-determination theory. *IJ STEM* **2022**, *9*, 41. [CrossRef]
5. Mussel, P. Processes underlying the relation between cognitive ability and curiosity with academic performance: A mediation analysis for epistemic behavior in a five-year longitudinal study. *J. Intell.* **2022**, *10*, 23. [CrossRef]

6. Lee, W.; Reeve, J.; Xue, Y.; Xiong, J. Neural differences between intrinsic reasons for doing versus extrinsic reasons for doing: An fMRI study. *Neurosci. Res.* **2012**, *73*, 68–72. [CrossRef]
7. Ulrich, M.; Keller, J.; Hoenig, K.; Waller, C.; Grön, G. Neural correlates of experimentally induced flow experiences. *Neuroimage* **2014**, *86*, 194–202. [CrossRef] [PubMed]
8. Lee, W.; Reeve, J. Identifying the neural substrates of intrinsic motivation during task performance. *Cogn. Affect. Behav. Neurosci.* **2017**, *17*, 939–953. [CrossRef]
9. van der Ven, S.H.G.; van Touw, S.A.C.; van Hoogmoed, A.H.; Janssen, E.M.; Leseman, P.P.M. The effect of a prospected reward on semantic processing: An N400 EEG study. *Z. Für Psychol.* **2016**, *224*, 257–265. [CrossRef]
10. Ma, Q.; Pei, G.; Meng, L. Inverted U-Shaped Curvilinear Relationship between Challenge and One's Intrinsic Motivation: Evidence from Event-Related Potentials. *Front. Neurosci.* **2017**, *11*, 131. [CrossRef]
11. Jin, J.; Yu, L.; Ma, Q. Neural Basis of Intrinsic Motivation: Evidence from Event-Related Potentials. *Comput. Intell. Neurosci.* **2015**, *2015*, 698725. [CrossRef]
12. Brydevall, M.; Bennett, D.; Murawski, C.; Bode, S. The neural encoding of information prediction errors during non-instrumental information seeking. *Sci. Rep.* **2018**, *8*, 6134. [CrossRef] [PubMed]
13. Robinson, L.J.; Stevens, L.H.; Threapleton, C.J.D.; Vainiute, J.; McAllister-Williams, R.H.; Gallagher, P. Effects of intrinsic and extrinsic motivation on attention and memory. *Acta Psychol.* **2012**, *141*, 243–249. [CrossRef] [PubMed]
14. Summerfield, C.; Greene, M.; Wager, T.; Egner, T.; Hirsch, J.; Mangels, J. Neocortical Connectivity during Episodic Memory Formation. *PLOS Biol.* **2006**, *4*, e128. [CrossRef] [PubMed]
15. Danieli, K.; Guyon, A.; Bethus, I. Episodic Memory formation: A review of complex Hippocampus input pathways. *Prog. Neuro-Psychopharmacol. Biol. Psychiatry* **2023**, *126*, 110757. [CrossRef] [PubMed]
16. Phukhachee, T.; Maneewongvatana, S.; Angsuwatanakul, T.; Iramina, K.; Kaewkamnerdpong, B. Investigating the Effect of Intrinsic Motivation on Alpha Desynchronization Using Sample Entropy. *Entropy* **2019**, *21*, 237. [CrossRef]
17. Martinez-Trujillo, J. Visual Attention in the Prefrontal Cortex. *Annu. Rev. Vis. Sci.* **2022**, *8*, 407–425. [CrossRef]
18. Emad-ul-Haq, Q.; Hussain, M.; Aboalsamh, H.; Bamatraf, S.; Malik, A.S.; Amin, H.U. A Review on understanding Brain, and Memory Retention and Recall Processes using EEG and fMRI techniques. *arXiv* **2019**, arXiv:Neurons and Cognition. Available online: https://api.semanticscholar.org/CorpusID:146121330 (accessed on 5 April 2024).
19. Schlüter, T.; Conrad, S. About the analysis of time series with temporal association rule mining. In Proceedings of the IEEE Symposium on Computational Intelligence and Data Mining (CIDM), Paris, France, 11–15 April 2011; pp. 325–332. [CrossRef]
20. Nam, H.; Lee, K.; Lee, D. Identification of temporal association rules from time-series microarray data sets. *BMC Bioinform.* **2009**, *10* (Suppl. S3), S6. [CrossRef]
21. Wen, F.; Zhang, G.; Sun, L.; Wang, X.; Xu, X. A hybrid temporal association rules mining method for traffic congestion prediction. *Comput. Ind. Eng.* **2019**, *130*, 779–787. [CrossRef]
22. Karaboga, D. *An Idea Based on Honey Bee Swarm for Numerical Optimization*; Tech. Rep. TR06; Department of Computer Engineering, Engineering Faculty, Erciyes University: Kayseri, Turkey, 2005; pp. 1–10.
23. Stark, B.A. Studying "moments" of the Central Limit theorem. *Math. Enthus.* **2017**, *14*, 53–76. [CrossRef]
24. Delorme, A.; Makeig, S. EEGLAB: An Open Source Toolbox for Analysis of Single-Trial EEG Dynamics Including Independent Component Analysis. *J. Neurosci. Methods* **2004**, *134*, 9–21. [CrossRef] [PubMed]
25. Makeig, S. Auditory Event-Related Dynamics of the EEG Spectrum and Effects of Exposure to Tones. *Electroencephalogr. Clin. Neurophysiol.* **1993**, *86*, 283–293. [CrossRef]
26. Dockree, P.M.; Kelly, S.P.; Roche, R.A.; Hogan, M.J.; Reilly, R.B.; Robertson, I.H. Behavioural and physiological impairments of sustained attention after traumatic brain injury. *Brain Res. Cogn. Brain Res.* **2004**, *3*, 403–414. [CrossRef]
27. Xie, W.; Mallin, B.M.; Richards, J.E. Development of infant sustained attention and its relation to EEG oscillations: An EEG and cortical source analysis study. *Dev. Sci.* **2018**, *3*, e12562. [CrossRef]
28. James, F.A. Maintaining knowledge about temporal intervals. *Commun. ACM* **1983**, *26*, 832–843. [CrossRef]
29. Anuar, S.; Selamat, A.; Sallehuddin, R. A modified scout bee for artificial bee colony algorithm and its performance on optimization problems. *J. King Saud. Univ. Comput. Inf. Sci.* **2016**, *28*, 395–406. [CrossRef]
30. Islam, M.R. Sample Size and Its Role in Central Limit Theorem (CLT). *Int. J. Phys. Math.* **2018**, *1*, 37–47. [CrossRef]
31. Barri, M.A. A Simulation Showing the Role of Central Limit Theorem in Handling Non-Normal Distributions. *Am. J. Educ. Res.* **2019**, *7*, 591–598. Available online: http://pubs.sciepub.com/education/7/8/8 (accessed on 5 April 2024). [CrossRef]
32. Boston University. The Central Limit Theorem. Available online: https://sphweb.bumc.bu.edu/otlt/mph-modules/bs/bs704_probability/BS704_Probability12.html (accessed on 5 April 2024).
33. Samson-Dollfus, D.; Delapierre, G.; Do Marcolino, C.; Blondeau, C. Normal and pathological changes in alpha rhythms. *Int. J. Psychophysiol.* **1997**, *26*, 395–409. [CrossRef]
34. Stephen, P.E.; Karen, S.B. An ecological valence theory of human color preference. *PNAS* **2010**, *107*, 8877–8882. [CrossRef]
35. Wilms, L.; Oberfeld, D. Color and emotion: Effects of hue, saturation, and brightness. *Psychol. Res.* **2018**, *82*, 896–914. [CrossRef] [PubMed]
36. Silvera, D.H.; Josephs, R.A.; Giesler, R.B. Bigger is better: The influence of physical size on aesthetic preference judgments. *J. Behav. Decis. Mak.* **2002**, *15*, 189–202. [CrossRef]

37. Linsen, S.; Leyssen, M.H.R.; Sammartino, J.; Palmer, S.E. Aesthetic preferences in the size of images of real-world objects. *Perception* **2011**, *40*, 291–298. [CrossRef] [PubMed]
38. Ehinger, K.A.; Aude, O. Canonical views of scenes depend on the shape of the space. In Proceedings of the 33rd Annual Cognitive Science Conference (COGSCI 2011), Boston, MA, USA, 20–23 July 2011; pp. 1–7.
39. Nag, S.; Berman, D.; Golomb, J.D. Category-selective areas in human visual cortex exhibit preferences for stimulus depth. *NeuroImage* **2019**, *196*, 289–301. [CrossRef]
40. Phukhachee, T.; Angsuwatanakul, T.; Iramina, K.; Kaewkamnerdpong, B. A simultaneous EEG-fNIRS dataset of the visual cognitive motivation study in healthy adults. *Data Brief* **2024**, *53*, 110260. [CrossRef]

sensors

Article

Optimal Channel Selection of Multiclass Motor Imagery Classification Based on Fusion Convolutional Neural Network with Attention Blocks

Joharah Khabti *, Saad AlAhmadi and Adel Soudani

Department of Computer Science, College of Computer and Information Sciences (CCIS), King Saud University, Riyadh 11543, Saudi Arabia; salahmadi@ksu.edu.sa (S.A.); asoudani@ksu.edu.sa (A.S.)
* Correspondence: jkhabti@ksu.edu.sa

Abstract: The widely adopted paradigm in brain–computer interfaces (BCIs) involves motor imagery (MI), enabling improved communication between humans and machines. EEG signals derived from MI present several challenges due to their inherent characteristics, which lead to a complex process of classifying and finding the potential tasks of a specific participant. Another issue is that BCI systems can result in noisy data and redundant channels, which in turn can lead to increased equipment and computational costs. To address these problems, the optimal channel selection of a multiclass MI classification based on a Fusion convolutional neural network with Attention blocks (FCNNA) is proposed. In this study, we developed a CNN model consisting of layers of convolutional blocks with multiple spatial and temporal filters. These filters are designed specifically to capture the distribution and relationships of signal features across different electrode locations, as well as to analyze the evolution of these features over time. Following these layers, a Convolutional Block Attention Module (CBAM) is used to, further, enhance EEG signal feature extraction. In the process of channel selection, the genetic algorithm is used to select the optimal set of channels using a new technique to deliver fixed as well as variable channels for all participants. The proposed methodology is validated showing 6.41% improvement in multiclass classification compared to most baseline models. Notably, we achieved the highest results of 93.09% for binary classes involving left-hand and right-hand movements. In addition, the cross-subject strategy for multiclass classification yielded an impressive accuracy of 68.87%. Following channel selection, multiclass classification accuracy was enhanced, reaching 84.53%. Overall, our experiments illustrated the efficiency of the proposed EEG MI model in both channel selection and classification, showing superior results with either a full channel set or a reduced number of channels.

Keywords: brain–computer interface (BCI); motor imagery (MI); electroencephalogram (EEG); deep learning (DL); convolutional neural network (CNN); attention module; channel selection; genetic algorithm (GA)

Citation: Khabti, J.; AlAhmadi, S.; Soudani, A. Optimal Channel Selection of Multiclass Motor Imagery Classification Based on Fusion Convolutional Neural Network with Attention Blocks. *Sensors* **2024**, *24*, 3168. https://doi.org/10.3390/s24103168

Academic Editors: Yifan Zhao, Hua-Liang Wei, Yvonne Tran, Yuzhu Guo and Fei He

Received: 3 April 2024
Revised: 8 May 2024
Accepted: 14 May 2024
Published: 16 May 2024

1. Introduction

A motor imagery-based brain–computer interface (BCI) is the most commonly used paradigm. The use of this system facilitates the communication between humans and machines [1,2]. In most cases, research involves recording neural activity on the scalp using non-invasive electroencephalography (EEG), as it is a practical and inexpensive method [3]. An EEG signal derived from motor imagery (MI) is generated when a subject visualizes a movement without actually performing it. During motor imagery, specific brain regions are activated similar to those engaged during physical movement, primarily within the sensorimotor cortex. EEG records this neural activity by detecting fluctuations in electrical patterns across the scalp. These fluctuations manifest as distinct patterns in the EEG signals, particularly in the alpha (8–13 Hz) and beta (13–30 Hz) sub-bands. Specifically, decreases in signal amplitude, known as Event-Related Desynchronization (ERD), occur in regions opposite the imagined movement, while increases, termed Event-Related Synchronization (ERS), appear in areas adjacent to the movement side. Such capabilities allow EEG to effectively monitor brain activity in real-time, which is vital for applications like brain–computer interfaces (BCIs) [4]. MI-EEG-based BCIs aid in rehabilitation activities for individuals with disabilities and enable them to perform everyday tasks more autonomously by controlling external devices, such as robotic prosthetics or computer interfaces.

Even with extensive research focusing on MI-EEG-based BCIs, there are still many challenges to overcome. EEG signals have a low signal-to-noise ratio (SNR) where the data could be corrupted by any artifact such as eye movements. Moreover, EEG signals are subject to non-stationarity issues, which means that they may vary considerably between trials or even within the same trial for the same subject [4]. Consequently, the variability and complexity of individual brain signals during motor imagery tasks make it difficult to develop a model that can be applied universally. Moreover, EEG signals contain redundant channels that may impact accuracy and efficiency in MI task classification. These channels carry information about background neural activity. However, some channels contain redundant information and require more calculation to be, efficiently, detected and sorted out [5]. Thus, we believe that an appropriate channel selection would contribute to improving the accuracy and reducing the computational time and complexity. However, achieving such an objective of channel selection has to be carefully performed due to the drastic impact that this action has on the accuracy of MI task detection [3]. This paper addresses this issue. It proposes a new method based on a combination of channel selection and classification techniques for efficient MI task detection.

In terms of classification methods, traditional machine learning (ML) and deep learning (DL) are the two main approaches used. The majority of ML approaches have been based upon common spatial patterns (CSPs) including the filter bank CSP (FBCSP) or regularized CSP (RCSP) to extract signal features. These achieve a good performance after being followed by a Support Vector Machine (SVM) and Linear Discriminant Analysis (LDA) classifiers [5–10]. However, the ability of DL methods to extract features from raw data has made DL methods increasingly popular in recent years in BCI studies. There has been considerable attention paid to DL for its excellent performance in a variety of fields, such as image classification, speech recognition, and text analysis [11]. As DL techniques have been successful in other fields and can be utilized for automatic feature extraction, there is a strong motivation to apply them to EEG data analysis and classification. Convolutional neural networks (CNNs) are the most common model used for extracting temporal and spatial features from MI EEG data [12,13]. Several CNN architectures have been proposed as a baseline of EEG signal classification with the ability of channel and spatial classification relying on the nature of fast training and few parameters used; such models are ShallowNet [14], DeepConvNet [14], and EEGNet [15]. Many papers provided a lot of attention in order to improve the performance of these lightweight CNN models by applying them to diverse frameworks with many types of extra blocks. The structure still needs more enhancement to have the ability to classify any type of EEG data. Despite the advancements brought about MI-EEG data by DL techniques, it should be noted that these methods often struggle with high variability in signal quality across different subjects, which can severely impact classification accuracy. This highlights that current techniques remain insufficient and require further development. The attention mechanism is another aspect of architectural design used to draw attention to the most important features gained from the neural network model. Utilizing attention-based feature optimization is useful to enhance the representation power of the CNN model with minimal overhead [16,17].

Based on the channel selection process, when selecting the optimal channels, it is possible to improve the classification results while ensuring that no significant channels are removed [3]. Due to this, the majority of researchers [18–22] selected different channels for each subject individually. Selecting a fixed channel for all subjects is a problem that has not previously been addressed. Therefore, in order to select a fixed optimal channel for all subjects while maintaining all significant channels, a novel technique must be developed.

For the purpose of responding to these concerns mentioned above and to increase the performance of lightweight neural networks, this paper proposes a multiclass MI classification based on a Fusion convolutional neural network with Attention blocks (FCNNA) and channel selection. The main contributions of this work are summarized as follows:

- Propose a CNN structure that contains two layers of convolutional blocks followed by CBAM attention methods concatenated to better classify two classes and four classes of preprocessed EEG raw data.
- Evaluate the classification performance on a publicly available dataset utilizing two strategies: within-subject strategy and cross-subject strategy. According to our experiments in multiclass and two-class classification, our model exhibits significant improvements over existing state-of-the-art approaches.
- Propose a channel selection mechanism that maintains the performance of the proposed model with less computation cost. In this study, a novel technique is employed to introduce a fixed set of channels for all subjects alongside a variable set of channels.
- Illustrate the enhancement in performance that results from adding channel selection to our model. Moreover, a comparative analysis with state-of-the-art methods is applied which demonstrates an improvement.

The rest of the paper is organized as follows: Section 2 reviews the current DL classification techniques employed in EEG signals and briefly describes various channel selection algorithms. A detailed explanation of the methods and architectures proposed in this study is provided in Section 3. In Section 4, the experimental results are presented and discussed. The paper is concluded in Section 5.

2. Related Works

2.1. EEG Signal Deep Learning Classification

The authors in manuscript [14] proposed a ConvNet structure to design two CNN models: ShallowNet and DeepConvNet models. Figure 1 demonstrates the structure of ConvNet which combines two main layers in one block which is the first CNN block. These two layers intend to handle the channels of EEG data in two ways, first by gathering the data of one channel in a specific range of time (temporal convolutional layer), and the second layer is merging all the data of all channels in this specific time (spatial convolutional layer). In light of this description, the purpose of developing ConvNet is to become a general tool for decoding brain signals. Later, Lawhern et al. [15] introduced EEGNet, a more compact and efficient CNN architecture with few parameters and fast training nature. EEGNet enhances the idea of the ConvNet structure provided by [14] to improve accuracy and efficiency. EEGNet showed encouraging results on several types of EEG datasets with significantly fewer parameters than ShallowNet and DeepConvNet. In addition, the simple architecture of EEGNet has made it a notable candidate for EEG analysis in different scenarios.

ShallowNet, DeepConvNet, and EEGNet have yielded many other techniques that may be used as benchmarks for comparison and improvement [4] such as EEG-TCNet [23], MSFBCNN [24], and TCNet Fusion [25]. In their publication [23], the authors introduced the EEG-TCNet model, which integrates the feature extraction layers of EEGNet with the temporal convolutional network (TCN). The TCN effectively utilizes temporal information through the implementation of two layers of residual blocks. Consequently, the authors presented two models; the first with a consistent set of hyperparameters for all subjects achieved an accuracy of 77.35%, while the second, incorporating subject-specific hyperparameters, attained a higher accuracy of 83.84%. The authors in [24] introduced a parallel multiscale filter bank convolutional neural network, employing four temporal convolutions with distinct kernel sizes. These convolutions are concatenated and applied to spatial convolution, resulting in an accuracy of 75.12%. Ultimately, the researchers in [25] executed a CNN model incorporating a TCN block with two stacked residual blocks. This configuration extracted additional temporal features following EEGNet, resulting in an accuracy of 83.73%.

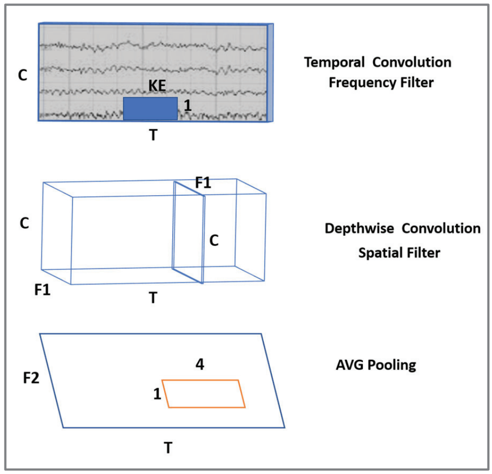

Figure 1. ConvNet structure. C = number of channels; T = number of time points; KE = kernel width; F1, and F2 = number of filters.

In addition, models of multiclass MI classification published between 2022 and 2023 will be examined to compare our results with the most recent advances in the field. In [4], a MTFB-CNN model is proposed to extract diverse information from EEG data through the use of three parallel time–frequency blocks, each containing multiple one-dimensional convolutions with different kernels and scales. Subsequently, a residual network is applied, followed by the integration of a channel attention module which yields an accuracy of 84.48%. The authors in [26] developed the CMO-CNN model, which incorporates a multi-branch one-dimensional convolutional design with a Squeeze-and-Excitation network featuring two shortcut connections to create the residual block. The model was validated using two strategies, within-subject and cross-subject, achieving accuracy rates of 83.92% and 63.34%, respectively. Following the same validation strategies, the authors in [27] introduced the EEG-ITNet model, which consists of four blocks: three layers of EEGNet, temporal convolution, dimension reduction, and classification. As a result of the validation process, the model achieved an accuracy of 76.74% with a within-subject strategy and 69.44% with a cross-subject strategy. Both models exhibit high accuracy in one strategy but not in the other, indicating that neither model is universally effective across different validation scenarios. In a similar manner to [27], the authors in [28,29] modified EEGNet to improve its performance and adapted it for general use. In [28], the MBSTCNN-ECA-LightGBM model combines EEGNet layers with a channel attention module and a LightGBM classifier to achieve up to 74% accuracy for four MI tasks of different classes. By combining EEGNet and ConvNet with transfer learning, the Siamese Deep Domain Adaptation (SDDA) framework in [29] achieved 82.01% accuracy over ConvNet. According to [30], researchers developed a Subject-to-Subject Semantic Style Transfer Network (SSSTN) that utilizes Continuous Wavelet Transform (CWT) to convert EEG data into images. In [31], the authors employed Wavelet Packet Decomposition (WPD) followed by a multiple CSP method to extract time and spatial features. These features were then used as inputs for an artificial neural network (ANN) model, resulting in an accuracy of 59.13%. The authors in [6] proposed a CNN and Riemannian Geometry Network (CRGNet) that was validated at an accuracy of 82.10% using k-fold cross-validation.

As shown in previous related papers, EEGNet has yielded promising results in EEG data classification. However, there is room for improvement in accuracy and further development. The structure should be enhanced to ensure an effective model for both binary and multiclass classification, as well as for various approaches, including within-subject and cross-subject strategies. Therefore, our goal is to provide a model that enhances accuracy across these conditions. We leverage the advantages of EEGNet by integrating it with a fusion technique and an attention block, enabling us to implement MI classification methods for both two and four MI tasks and for both within-subject and cross-subject strategies.

2.2. Channel Selection

An absence of a channel selection algorithm in BCI systems can result in noisy data and redundant channels, which in turn can lead to increased equipment and computational costs. For that reason, finding optimal channels has the potential to enhance or stabilize classification outcomes [3]. In order to find the optimal channels automatically, several approaches were used in the literature, including feature selection algorithms. In the feature selection process, the optimal subset of features is chosen after preprocessing and feature extraction to enhance classification performance. Similarly, channel selection involves identifying the most effective channels before feature extraction and classification to reduce computational demands while still ensuring robust outcomes in terms of classification accuracy [32]. Clearly, similar methodologies can be employed in both cases, where the objective is to find the best combination of elements that will improve the results.

Different methods for selecting channels have been used with the BCI IV 2a dataset, specifically when dealing with four-class classification. Researchers in [18–22] employ three main classification techniques: one-vs-one, one-vs-rest, and multiclass classification. In both one-vs-one and one-vs-rest, the means are derived from multiple binary classifications. One-vs-one considers every possible pair of two classes, whereas one-vs-rest trains classifiers for each class against the others. In contrast, multiclass classification trains a single classifier to distinguish between all classes at the same time. The authors in [19] employed the Firefly algorithm for channel selection, achieving a classification accuracy of 83.97% using the ML classifier as a regularized SVM with a one-to-one classification method. The application of the Firefly algorithm aimed at reducing the number of channels involved in calculating weighted scores for each channel near a candidate solution. Using both one-vs-one and one-vs-rest approaches, the researchers in [20] utilized various ML techniques to compute the means of several binary classifications. They demonstrated the advantages of incorporating feature extraction, feature selection, and MDA-SOGWO channel selection to enhance classification accuracy, elevating it from 67.04% to 80.82%. Additionally, the authors of [18,21] demonstrate the use of DL classification with the one-vs-rest strategy to validate channel selection methods. In their work [18], the researchers employed CSPs for optimal channel selection, followed by Fast Fourier Transform (FFT) transformation before training the DL model. They employed two specific models for their experiments: Stacked Sparse Autoencoder (SSAE) and Deep Belief Network built with stacked Restricted Boltzmann Machines (DBN-RBM). Initially, the accuracy for the SSAE model was 71.00%, and for the DBN-RBM model, it was 68.44%. As a result of channel selection, the accuracy of the SSAE model increased to 71.31%, while that of the DBN-RBM model increased to 68.63%. As detailed in [21], the authors developed a channel selection approach based on the standard deviation of wavelet coefficients across channels. They implemented CSPs using a one-vs-rest strategy and then utilized a CNN model for data classification, achieving an accuracy of 75.03%. In the multiclass classification strategy, as explored by authors in [22], channels are selected based on various metrics such as Euclidean distance, Riemannian distance, Kullback–Leibler, and Wasserstein distance divergence as criteria. Feature extraction was carried out using the one-vs-rest strategy with CSPs, coupled with an SVM for ML classification. This study's findings indicate that maintaining a uniform number of channels across the selection process yields an accuracy of 75.57%, which is lower than the 77.82% achieved when selecting varying numbers of channels.

Genetic algorithms (GAs) are one of the approaches that have been used as a feature selection to optimize the weight of the classification [33–35]. Further, genetic algorithms are applied in order to select the best subset of channels that provide the highest level of accuracy [36–39]. For further explanation, the researchers in [37] used a GA to select 10 ECoG electrodes from a set of 64. They subsequently employed multi-layer perceptions

(MLPs) for classification on the BCI Competition III dataset, increasing accuracy from 67% to 80% after selecting 10 electrodes. The authors in [36] utilized GAs with various EEG classification methods. Among these methods, the SVM performed the best, with accuracy increasing from 94.69% to 96.07% after the GA. In their study [39], the authors introduced two ML methodologies for categorizing right-hand and right-foot motor imagery into two distinct classes. They utilized the Rayleigh coefficient (RC) to extract features and employed the SVM and FDA for classification purposes. The authors used the GA, sequential forward search (SFS), and sequential backward search (SBS) to select channels, demonstrating the GA's effectiveness in enhancing accuracy and delivering superior results. The GA resulted in an average accuracy of 88.2%, while without channel selection, it achieved 76.68%.

As a general observation, utilizing GAs demonstrates promising potential to improve accuracy, which aligns with our objective. According to the channel selection strategy, most previous works focus only on selecting different channels for each subject based on the best accuracy results achieved, whereas my method uses fixed optimal channels uniformly across all subjects. Moreover, when it comes to channel selection, most researchers either use ML to perform classification or DL models based on the mean of various binary classifications. Due to these factors, our work will utilize GAs with a variety of channels and fixed channels as well as DL models to train a single classifier among all classes.

3. Materials and Methods

The purpose of this section is to introduce the main methods used to construct the general framework of our study. It starts by providing an overview of the dataset used, followed by an explanation of our framework. Further details are provided regarding the framework components, including the DL classification approach, and the channel selection technique.

To provide a better understanding of the methodology, we will briefly describe the dataset used.

3.1. Description of BCI Competition IV 2a Dataset [40]

This dataset consists of EEG data collected using 22 electrodes corresponding to the International 10–20 system from nine subjects. Four different motor imagery tasks were performed, including the imagination of the movement of the left hand (class 1), the right hand (class 2), both feet (class 3), and the tongue (class 4). There were two sessions recorded for each subject on two different days. A session consists of 288 trials divided into six runs, where one run contains 48 trials of the four possible classes. Samples were taken at 250 Hz, and bandpass filters were applied between 0.5 Hz and 100 Hz. As shown in Figure 2, the imagination period trial lasted for four seconds following cue onset and was terminated by the break at the end.

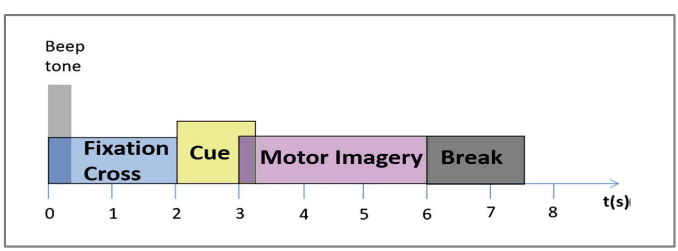

Figure 2. The timing scheme of the BCI IV 2a dataset.

To explain the general structure of our work, we will explain the framework as a baseline for the rest of this unit.

3.2. Proposed Model Framework

Figure 3 provides an overview of the proposed framework, consisting of three primary stages handling raw EEG data: preprocessing, channel selection, and classification. EEG data input involves preprocessing as the first step in order to prepare the data for the purpose of distinguishing between MI tasks. The selected optimal channels are then forwarded for classification purposes. For classifying the input data, a two-level convolutional block followed by a CBAM attention block is applied. As a result, the output should indicate the correct MI task regardless of whether two or four classes are involved.

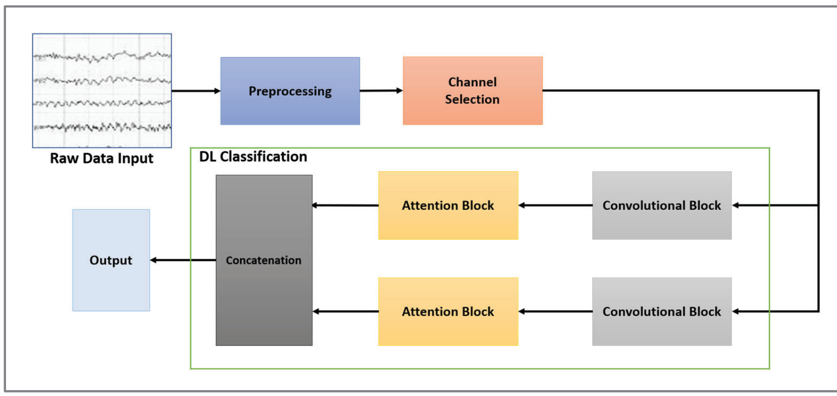

Figure 3. Overall framework.

In the following sections, each stage is described in detail, beginning with preprocessing. We will then discuss the primary processes involved in classification. Finally, the method for selecting and determining the optimal channel will be clarified.

3.3. Preprocessing

In the preprocessing stage, we extracted windows of 4.5 s from each trial to better adapt to our classification needs [23,25]. As depicted in Figure 2, this included a four-second segment during the period of imagination and an additional half-second for the pre-cue onsets. With a sampling rate of 250 samples per second over a duration of 4.5 s, a total of 1125 samples were obtained.

The raw data were later filtered in the range of [0.25–50] using a 3rd order Butterworth filter as recommended in some previous research publications [41–43]. The filtering technique was selected for its effectiveness in removing frequencies that are not relevant to our study, particularly those below 0.25 Hz, which typically include slow drifts, and those above 50 Hz, mainly consisting of muscle noise and environmental electrical noise. The use of a bandpass filter ensures that the essential frequency components relevant to motor functions are retained, thereby enhancing the signal-to-noise ratio without distorting the underlying neural signatures. In addition, as demonstrated in Section 4.3.1, this filtering technique may enhance the quality of the EEG signal by eliminating certain frequencies of noise.

Our approach focused on preserving the raw signal characteristics; for this reason, no more complex preprocessing techniques were applied.

3.4. Classification

The main components of the FCNNA model will be discussed in this section, along with a breakdown of their structure. This model contains two layers of convolutional network blocks, followed by attention blocks. In the following paragraphs, we will take a closer look to give more details for each block:

3.4.1. Convolutional Blocks

The convolutional block is an enhanced version of EEGNet models using two layers with different hypermeters. By using two layers of the convolutional block, we will be able to obtain more accurate results, as explained later in the experiment section. Figure 4 illustrates the structure of the FCNNA model with a closer look at the convolutional block. The EEG data are taken as raw input to each convolutional block in the two presented layers. The output of each layer is an input of a separate attention block.

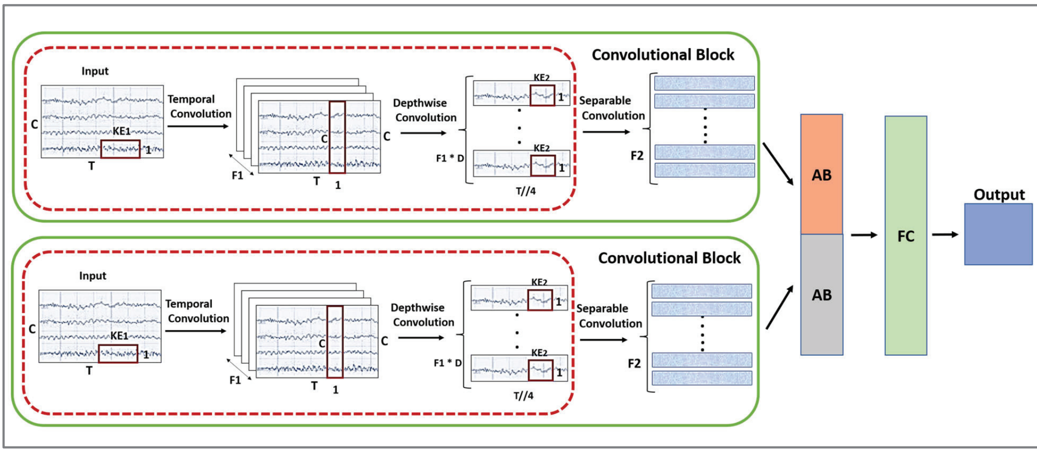

Figure 4. The structure of the FCNNA model.

Each layer consists of two blocks: the block of the ConvNet structure and a separable convolutional block. The ConvNet block is described in Figure 1, where the frequency filter and spatial filter are applied to the EEG data in the same block. The frequency filter is applied on a specific time series of the raw data of each electrode separately; this time, the range depends on the kernel size. As part of our study, we applied the model to a 250 Hz EEG dataset, using 1×64 and 1×60 kernel sizes. Here, '1' refers to the kernel height, indicating that each kernel processes one electrode channel at a time. Additionally, '64' and '60' represent the kernel width, corresponding to the number of consecutive temporal samples included in each convolution. This configuration enables us to examine and analyze EEG signals from each electrode, where the kernel widths process temporal segments approximately a quarter of a second long, based on our 250 Hz sampling rate. Later, a depthwise convolution is used to apply a spatial filter by learning from the features of all the electrodes in each frequency filter. After the depthwise convolution block, all electrodes become one as a result of frequency-specific spatial filters. The second block of each layer is a separable convolutional block, which is a combination of a depthwise convolution to apply a single frequency filter for each individual feature map, followed by a pointwise convolution. In a CNN, depthwise convolution and separable convolution provide efficient results since they reduce the number of parameters and computations [44].

Detailed information about the architecture of the convolutional block in the FCNNA model can be found in Table 1. This table shows the sequence of the model layers, the filter used, the kernel size of each convolutional block, and the shape of the output of each layer. The number of filters used is specified by three variables F1, D, and F2 where F1 is the temporal filter, D is the depth multiplier for the spatial filter, and when we multiply F1 by D, we obtain F2 which is the number of pointwise filters. It is important to note that we used different sizes of filters, kernels, and depths for each layer in the convolutional block. In the first layer, the kernel width of the first block is set to 60 temporal samples, and the number of temporal filters is 96 (denoted as F1) designed to extract different features from the input data. The layer has a depth of 2, meaning it doubles the total number of active filters to 192 (2 × F1) for depthwise convolution operations, enhancing feature extraction capabilities. On the other hand, the kernel width, depth, and filter F1 of the second layer are 64, 1, and 16, respectively. For both layers, we used the same second kernel size which is equal to 1 × 16. Furthermore, the table clarifies that batch normalization, activation, average pooling, and dropout are applied in sequence at the end of each block. Batch normalization is recommended to be used in the CNN model [45]. It standardizes the intermediate outputs of the network to zero mean and unit variance. This is meant to facilitate the optimization by keeping the inputs of layers closer to a normal distribution during training. Moreover, dropout randomly sets some inputs for a layer to zero in each training update to help prevent overfitting. The result later fits in the attention block (described in the next section) and is then merged for the classification.

Table 1. A detailed description of the convolutional block in the FCNNA model, where C = number of channels (22), T = number of time points (1125), F1 = number of temporal filters [F1First = 96, F1Second = 16], D = depth multiplier (number of spatial filters) [DFirst = 2, DSecond = 1], F2 = number of pointwise filters [F2 = F1 × D], and N = number of classes, KE = kernel width [KE1First = 60, KE1Second = 64, KE2 = 16].

Block	Layer	Layer Type	# of Filter	Kernel Size	Output	Option
			First Convolutional Block			
1	Input	Input			(C, T)	
	Reshape				(C, T, 1)	
	C1	Conv2D	F1	(1, KE1)	(C, T, F1)	padding = 'same'
	BN1	BatchNorm			(C, T, F1)	
	C2	Depthwise Conv2	F1 × D	(C, 1)	(1, T, F1 × D)	depth_multiplier = D, max norm = 1
	BN2	BatchNorm			(1, T, F1 × D)	
	A1	Activation			(1, T, F1 × D)	Function = ELU
	P1	AveragePooling2D		(1, 4)	(1, T//4, F1 × D)	
	D1	Dropout				p = 0.5
2	C3	Separable Conv2	F2	(1, KE2)	(1, T//4, F2)	
	BN3	BatchNorm			(1, T//4, F2)	
	A2	Activation			(1, T//4, F2)	Function = ELU
	P2	AveragePooling2D		(1, 8)	(1, T//32, F2)	
	D2	Dropout			(1, T//32, F2)	p = 0.5
	AB	Attention Block			(1, T//32, F2first)	
			Second Convolutional Block "the same Previous Step"			
	AB	Attention Block			(1, T//32, F2Second)	
	Con1	Concatenation			(1, T//32, F2first+ F2Second)	
	FC1	Flatten			(T//32 × (F2first+ F2Second))	
	Dense	Dense			N	Softmax

3.4.2. Attention Block

Attention mechanisms are DL techniques that allow the network to focus on different parts of its input. These mechanisms have been shown to be very effective in a variety of tasks, including image classification, natural language processing, and speech recognition [46–48]. One of these attention models is the Convolutional Block Attention Module (CBAM) [17]. The CBAM is often used together with other neural network models, such as CNNs, to improve their performance. It combines spatial and channel-specific attention mechanisms to improve the representation of features within input data. The two sub-module channels and spatial modules of the CBAM mechanism are illustrated in Figure 5. Starting with the channel attention module which receives the feature map F, $F \in \mathbb{R}^{H \times W \times C}$, where in our mode, H = 1, W = 35, C = 192 for the first layer, and C = 16 for the second layer.

This module returns Mc as defined in Equation (1), representing a 1D channel attention map that belongs to $\mathbb{R}^{1\times1\times C}$.

$$Mc(F) = \sigma(MLP(\text{AvgPool}(F)) + MLP(\text{MaxPool}(F))) \quad (1)$$

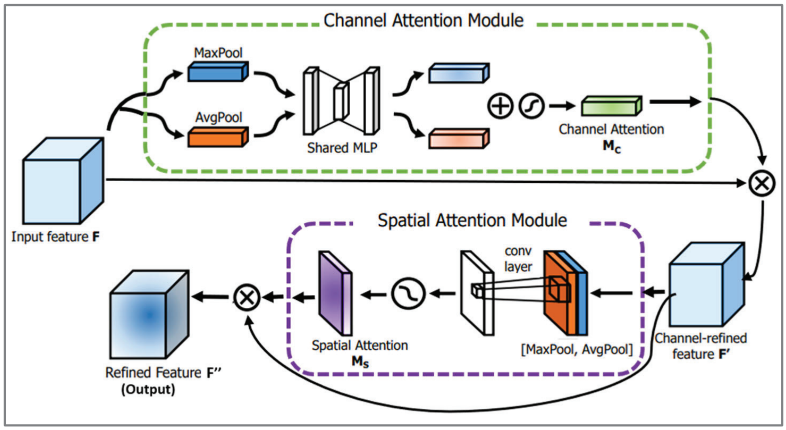

Figure 5. CBAM.

$Mc(F)$ is calculated by subjecting the input feature maps F to both average and maximum pooling separately. These pooled results are then individually processed by three-layer feedforward artificial neural networks (MLP). The outcomes obtained from these MLPs are aggregated first and then processed through a sigmoid function (σ) to derive Mc. The result of Mc is then multiplied by the feature map F to give F', where F' is the context given by (3) and used by (4). On the other hand, spatial attention utilizes the input F' through a process involving average pooling and max pooling. This is followed by a convolution operation with a kernel size of 7, as shown in Equation (2).

$$Ms(F') = \sigma\left(f^{7\times7}([\text{AvgPool}(F');\text{MaxPool}(F')])\right) \quad (2)$$

The main two formulas of the general process of this module are as below:

$$F' = Mc(F) \bigotimes F \quad (3)$$

$$F'' = Ms(F') \bigotimes F' \quad (4)$$

where $\otimes$ denotes elementwise multiplication. Equation (4) illustrates the ultimate result of the CBAM. The refined feature, represented as F'', is obtained through the multiplication of Ms and F'.

3.5. Channel Selection

This section will discuss the use of a genetic algorithm (GA) as a way of channel selection. In ML EEG classification, genetic algorithms are one of the most effective algorithms for channel selection [36,39]. The GA addresses a combinatorial optimization problem, aiming to select the optimal subset of EEG channels to maximize classification accuracy. This process involves evaluating various combinations of channels (chromosomes) and determining the most effective set based on a fitness function. This fitness function primarily measures classification accuracy, making it a crucial component in assessing the effectiveness of each channel combination. Genetic algorithms are particularly suited to this task as they can efficiently explore numerous potential combinations [36]. In our case, we applied GAs uniformly across all subjects to choose the optimal channels and determine the most appropriate combination that achieves the highest level of classification accuracy.

The GA is a concept derived from science, where genes are the smallest components of a problem that eventually combine to form a chromosome. Specifically, the chromosome represents a possible solution to the problem. In our case, the gene is an input channel, and the chromosome is a combination of channels. In general, the algorithm consists of three main steps: First: Initialize the population by providing the initial possible solutions of a random set of channels. Second: Evaluate the fitness, which assesses each possible solution and validates the results. Third: Deliver a new generation based on choosing the solutions with the highest probability of achieving the greatest accuracy (parents) to generate a new generation of solutions (children). The new solution is generated after applying crossover and mutation. Figure 6 illustrates these steps and how they will be entered into our model. Here, in the following, we will explain each of these three steps in detail.

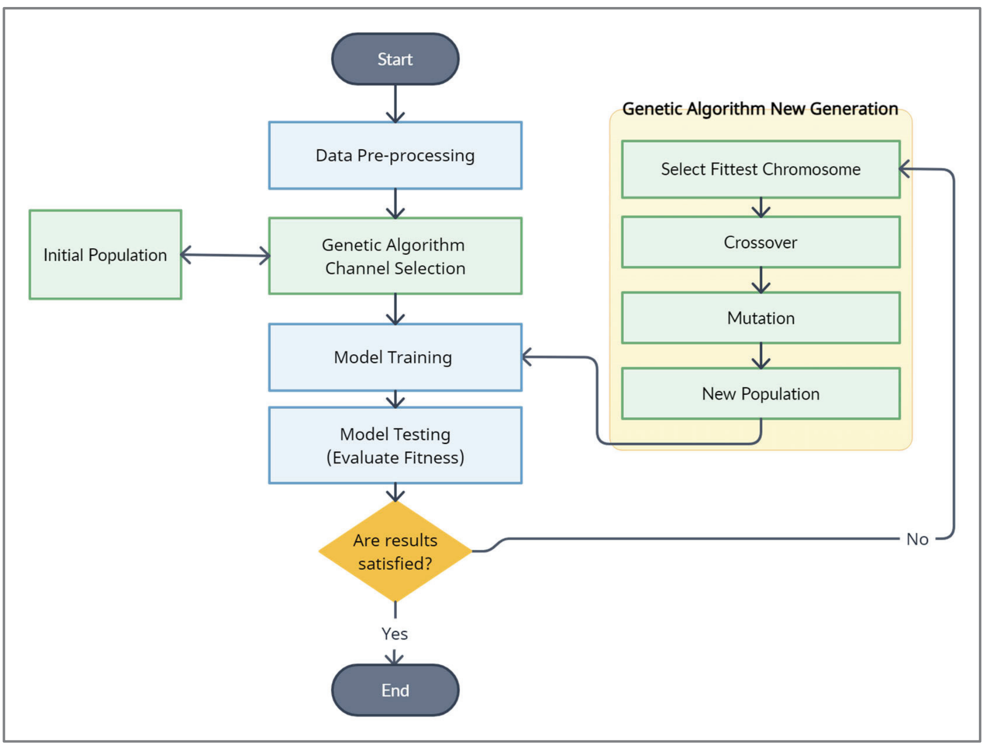

Figure 6. Genetic algorithm applied in our model.

Step1: Initialize the population:

In this step, we will introduce a population consisting of n chromosomes, each carrying a random number of genes in order to ensure that every potential solution is possible. The population is denoted as {X1, X2, . . ., Xn}, where X represents a chromosome. For our study, we specifically set n to equal 6. The chromosome comprises a random selection of channels (genes) chosen from a list ranging from 1 to 22, representing the primary electrodes from the BCI Competition IV 2a dataset: $[Fz, FC3, FC1, FCz, FC2, FC4, C5, C3, C1, Cz, C2, C4, C6, CP3, CP1, CPz, CP2, CP4, P1, Pz, P2, POz]$.

Step 2: Evaluate the Fitness:

Once the initial population has been prepared, each chromosome in the population is treated as a parent. Our classification process, as explained in Section 3.4.1, is utilized at this stage to assess each parent. Further, the dataset is divided into training and testing trials using a cross-subject strategy, details of which can be found in Sections 4.1 and 4.4. Accordingly, a model is trained using only the channels included in that parent. Through this approach, the model's performance reflects the effectiveness of the specific subset of channels. To evaluate the chosen channel subset, we examine the model using the test dataset and compute accuracy, denoted as $f(x)$.

Step 3: Deliver a new generation:

If the classification results $f(x)$ of the possible solution do not meet the threshold, a new generation will be provided. To deliver the new generation and have new children, these steps are followed:

- **Select the Fittest Chromosome:** The fitness-proportional roulette wheel approach is used to select three parents from a population. The mathematical formula for this approach can be found in Equation (5). In this approach, parents are selected based on their likelihood of having higher fitness values. From these parents, a new generation is produced.

$$p = \frac{f(x)}{\sum_{j=0}^{n-1} f(x)} \tag{5}$$

- **Apply Crossover:** In order to perform crossover, two fitness parents are divided into halves, and then the genes are switched between them in the manner shown below.

$$Child\ 1 = [[Parent1[0 \ldots p1]], [Parent2[p2 \ldots end]]]$$

$$Child\ 2 = [[Parent2[0 \ldots p3]], [Parent1[p4 \ldots end]]]$$

where $p1,\ p2,\ p3,\ p4$ are the list index randomly chosen each time.

As an example, let us consider that we have these two fitness parents $Parent1 = [1,3,7,15,19,22]$ and $Parent2 = [2,7,15,21]$. Assume that $p1 = 3,\ p2 = 2,\ p3 = 2,$ and $p4 = 4$. As a result, the produced children are as follows:

$$Child\ 1 = [1,3,7,15,21]\ and\ Child\ 2 = [2,7,15,19,22]$$

- **Apply Mutation**

The mutation process was applied to the third parent with a probability of 0.5. This process entails altering certain genes within this parent; specifically, randomly chosen genes are modified to values not previously employed on this parent.

- **Generate a new population**

To complete the formation of the new population, we include the three newly generated offspring while eliminating three of the least fit chromosomes (parents) from the prior generation.

As a next step, we will repeat the algorithm, starting with Step 2, and continue until the threshold is met or the maximum generation time is reached.

4. Results and Discussion

In this section, we will examine our model's classification performance using two different strategies. We intend to illustrate the differences in performance between our methodology and other state-of-the-art studies. Subsequently, we will demonstrate the performance after implementing channel selection.

4.1. Classification Strategy

For training and deriving the structure of our model, we used publicly available EEG data collected from the BCI Competition IV dataset. These data relate to four motor imaging tasks performed by a variety of subjects.

Training and Testing splitting:

To examine the BCI IV 2a dataset with our model, two techniques were applied for handling data from multiple subjects or individuals: within-subject and cross-subject. These strategies are used to determine how data are split, processed, and used for training and testing, with further elaboration provided in the subsequent sections.

Within-Subject strategy:

For BCI IV 2a, where each subject has two sessions, one of the sessions is used for training and the second session for testing. So, we have 288 trials in training and 288 trials in testing. Consequently, each subject will have a unique model that is used for individual classification.

Cross-subject strategy:

According to the idea of the cross-subject, one of the subjects is used for testing the model that was trained by the other subjects. In BCI IV 2a, we choose a different subject each time to test the model and combine its two sessions to obtain a total of 576 trials. Additionally, we included all 288 trials from both sessions of the remaining eight subjects, amounting to 4608 trials in total, to train this model.

Using these strategies, the dataset was classified into four motor imagery classes: the left hand, the right hand, both feet, and the tongue. Furthermore, we also classified two tasks based on left/right hands or feet/tongue.

4.2. Performance Metrics

Performance metrics are measurements used to evaluate the effectiveness of the proposed model. In our work, six different performance metrics are employed to assess specific aspects of the model which are accuracy, Kappa, precision, recall, the F1-score, and Receiver Operating Characteristic curves (ROC curves) [49]. As there are four distinct classes, the metrics are computed for each individual class. Nevertheless, in the case of accuracy, it is computed collectively across all classes to represent the overall classification accuracy for this particular model. In the following, you can see the definition and the equation of each metric [50,51].

Accuracy measures the proportion of correct predictions over the total predictions.

$$Accuracy = \frac{TP + TN}{TP + FP + TN + FN} \tag{6}$$

Precision is a ratio of correct predictions for a specific class.

$$Precision = \frac{TP}{TP + FP} \tag{7}$$

Recall measures how many of the positive classes are labeled correctly.

$$\text{Recall} = \frac{TP}{TP + FN} \tag{8}$$

The F1-score is the harmonic mean or weighted average of precision and recall.

$$\text{F1 score} = 2 \times \frac{Precision \times Recall}{Precision + Recall} \tag{9}$$

In context, TP, TN, FP, and FN are defined as follows:

TP (True Positives) are the number of correct positive predictions.
TN (True Negatives) are the number of correct negative predictions.
FP (False Positives) are the number of incorrect positive predictions.
FN (False Negatives) are the number of incorrect negative predictions.

In the meantime, positive prediction refers to the class that the model identifies or predicts as the class of interest; on the other hand, negative prediction refers to the opposite class/classes.

The Cohen Kappa statistic (Kappa) is a metric that compares observed accuracy with expected accuracy (random chance). The model estimates how well it can classify instances correctly.

$$Kappa = \frac{P_o - P_e}{1 - P_e} \tag{10}$$

P_o denotes the observed agreement which represents the proportion of times the classifiers agree on the classification of items. Moreover, P_e refers to the expected agreement by chance which is derived based on the marginal probabilities of each classifier agreeing, considering only random chance.

Finally, ROC curves are visual representations of the binary classifier diagnostic ability as its discrimination threshold changes. These curves plot the true positive rate (sensitivity) on the y-axis versus the false positive rate (1—specificity) on the x-axis. The Area Under the ROC curve (AUC) ranges from 0.5 to 1.0, with values nearer 1.0 signifying higher authenticity and better classification performance. The AUC acts as a single numerical metric that encapsulates the ROC curve's overall effectiveness, balancing sensitivity and specificity.

4.3. Classification Results

In our study, we built the FCNNA model using Python TensorFlow (version 2.15.0) and deployed it to the Google Colab platform equipped with a T4 GPU and 15.0 GB of GPU RAM. To ensure the robustness and reproducibility of our results, each model was trained ten times, with each session consisting of 1000 epochs. The models were trained using a batch size of 64 and a learning rate of 0.0009. A cross-entropy error function and an Adam optimizer were used to enhance learning efficiency. During the training phase, a callback function was used to save the model weights when the best accuracy was achieved, highlighting an efficient use of computational resources. The best model was then evaluated on the test set using comprehensive metrics, including accuracy, precision, recall, and F1-score. Additionally, we utilized ROC curves to assess the trade-offs between sensitivity and specificity and confusion matrices to provide a detailed breakdown of the model's performance across different classes.

The following sections demonstrate the results of applying our model according to within-subject and cross-subject strategies.

4.3.1. Within-Subject Classification

By applying the suggested classification methodology to categorize the four tasks within the BCI IV 2a dataset for each subject separately (within-subject), the results obtained are presented in Table 2. Among the results obtained, a total of three subjects exceeded the 90% threshold, with Subject 3 particularly excelling with a 95.97% result. Furthermore, Subject 3 also demonstrated strong performance across all metric measurements. Figure 7 displays visual representations of the confusion matrix for each subject, which illustrates the difference in performance across classes on different subjects. According to the confusion matrix, the diagonal entries indicate how many predictions are accurate for each class. It can be concluded that higher values along this diagonal, from the top left to the bottom right, indicate more precise predictions for those particular classes.

Table 2. The results of our model using the within-subject strategy of 4 classes in the BCI IV 2a dataset.

	Accuracy	Kappa	Precision	Recall	F1-Score
Subject 1	90.04%	86.71%	90%	90%	90%
Subject 2	75.62%	67.51%	75%	76%	75%
Subject 3	95.97%	94.63%	96%	96%	96%
Subject 4	76.32%	68.38%	77%	76%	76%
Subject 5	78.26%	70.98%	79%	78%	78%
Subject 6	69.30%	59.05%	70%	69%	69%
Subject 7	91.70%	88.93%	92%	92%	92%
Subject 8	88.93%	85.24%	89%	89%	89%
Subject 9	87.88%	83.83%	88%	88%	88%
AVG	83.78%	78.36%			

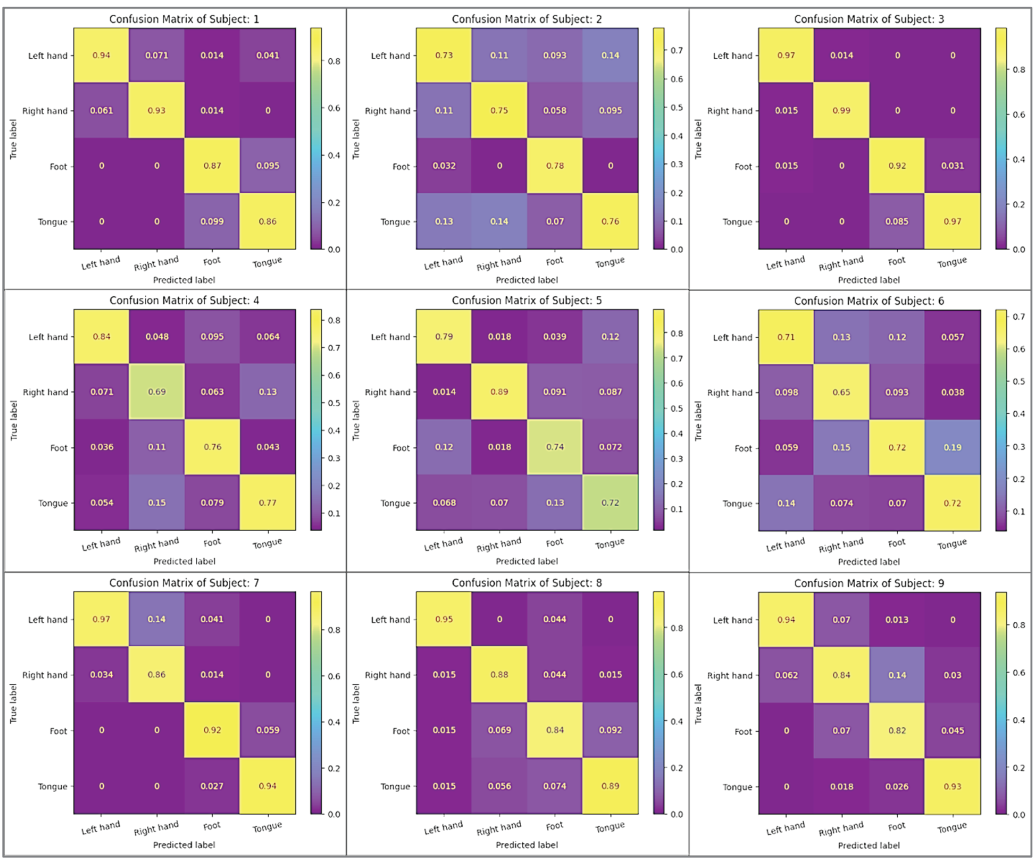

Figure 7. Confusion matrix of proposed model applied on 4 classes in BCI IV 2a using within-subject strategy.

In light of the use of a Butterworth filter in the preprocessing step of the classification process, Table 3 shows the results obtained with and without preprocessing. Despite the fact that Subjects 3 and 4 performed better without preprocessing, the general result is more accurate when preprocessing is performed. In Table 4, we illustrate the variations in accuracy when utilizing one, two, or three layers of the convolutional block in the classification process. It reveals that the two-layer configuration generally delivers the best performance, although it should be noted that Subjects 1 and 9 performed better with the three-layer configuration. Employing two layers offers an optimal balance by providing better accuracy while maintaining manageable complexity and processing time. This two-layer approach outperforms the single-layer configuration and avoids the increased computational demands associated with a three-layer configuration. Due to this, in our model, we chose to apply the preprocessing and a two-layer configuration of the convolutional block.

Table 3. A comparison of the classification accuracy between the preprocessed and unprocessed BCI IV 2a dataset using within-subject four-class analysis. The best scores are shown in bold.

	Sub 1	Sub 2	Sub 3	Sub 4	Sub 5	Sub 6	Sub 7	Sub 8	Sub 9	AVG
No Preprocessing Accuracy	87.54%	72.08%	**97.07%**	**80.26%**	77.54%	68.84%	90.97%	88.19%	87.50%	83.33%
With Preprocessing Accuracy	**90.04%**	**75.62%**	95.97%	76.32%	**78.26%**	**69.30%**	**91.70%**	**88.93%**	**87.88%**	**83.78%**

Table 4. A comparison of the classification accuracy between one-layer, two-layer, and three-layer convolutional blocks in the BCI IV 2a dataset using four within-subject classes. The best scores are shown in bold.

	Sub 1	Sub 2	Sub 3	Sub 4	Sub 5	Sub 6	Sub 7	Sub 8	Sub 9	AVG
One-Layer	89.32%	74.20%	95.24%	69.74%	75.72%	60.47%	90.97%	85.98%	87.50%	81.02%
Two-Layer	90.04%	**75.62%**	**95.97%**	**76.32%**	**78.26%**	**69.30%**	**91.70%**	**88.93%**	87.88%	**83.78%**
Three-Layer	**90.75%**	74.56%	95.60%	74.56%	77.54%	68.37%	90.61%	88.56%	**88.64%**	83.24%

We employed two validations of two classes to assess our model, as detailed in Table 5, demonstrating the outcomes for each combination. Specifically, we differentiated between the right hand and left hand, as well as between both feet and the tongue. The findings indicated that the average accuracy in classifying left and right hands yielded superior results of 93.09%. Notably, we achieved a 100% validation rate when classifying Subject 8 in class 1 and class 2, as well as Subject 3 in class 3 and class 4. Moreover, a confusion matrix of the model is shown in Figures A1 and A2 of Appendix A to aid in the evaluation of the model's performance when categorized into two classes, as well as identifying areas in which we may need to improve. Essentially, the confusion matrix visually presents how well the classifier performs by showcasing both correct and incorrect predictions for each class. The purpose of this visual aid is to enable you to evaluate the model's precision, recall, accuracy, and overall performance.

Table 5. The within-subject classification accuracy of two classes in the BCI IV 2a dataset, classified between class 1 (left hand) and class 2 (right hand) and also between class 3 (both feet) and class 4 (tongue).

	Sub 1	Sub 2	Sub 3	Sub 4	Sub 5	Sub 6	Sub 7	Sub 8	Sub 9	AVG
Class 1 and Class 2	88.65%	88.03%	98.54%	90.52%	97.78%	89.81%	91.43%	100.00%	93.08%	93.09%
Class 3 and Class 4	92.14%	90.07%	100.00%	86.61%	91.49%	82.24%	94.16%	90.51%	95.52%	91.42%

As part of the comparison, we assess how well our model classifies four MI tasks compared with the baseline models [4] which are EEGNet [15], EEG-TCNet [23], MSF-BCNN [24], and TCNet Fusion [25], ShallowNet [14], and DeepConvNet [14] as well as advanced models that are illustrated in Tables 6 and 7. According to the results presented in Table 6, our study shows a significant improvement in the measured accuracy of 6.41% over most baseline models. In this regard, our results are comparable to those of study [25], in which the training phase was the same as in our study by using the callback function. Comparing the classification results of our model with advanced models in terms of accuracy, as shown in Table 7, reveals that the average performance of our study exceeded those of most other studies. As illustrated in Table 7, the highest accuracy values are noted in [4,26], and our model showcases remarkable consistency with variances of less than 1%. It is worth noting that studies [4,26] used 5-fold cross-validation to train their models. The authors in [4] merged all sessions and divided them into five groups. Each group was used as a validation set once, and the remaining four were utilized for training. Model accuracy is determined by averaging the maximum accuracy of the five folds. Meanwhile, the authors in [26] performed a random split, allocating 80% of each subject's data for training and 20% for testing. Furthermore, our model significantly outperforms the models in [27–29] that incorporate EEGNet or ConvNet for performance enhancement. Additionally, Subject 2 and Subject 3 achieve the highest level of superiority in comparison with existing methods. Subject 2 experienced a 5% increase, while Subject 3 saw a 2% increase across previous advanced works.

Table 6. A comparison of our model accuracy with the baseline model on the BCI IV 2a dataset using a within-subject approach. The best scores are shown in bold.

	ShallowNet [4]	**DeepConvNet [4]**	**EEGNet [4]**	**MSFBCNN [4]**	**EEG-TCNet [23]**	**TCNet Fusion [25]**	**Our Model**
Accuracy	74.31%	75.64%	73.39%	75.12%	77.35%	83.73%	**83.78%**
Kappa	0.66	0.67	0.65	0.67	0.70	0.78	0.78

Table 7. A comparison of our model accuracy with the state-of-the-art model on the BCI IV 2a dataset using a within-subject approach. The best scores are shown in bold.

	CMO-CNN [26]	**SSSTN [30]**	**SDDA [29]**	**MTFB-CNN [4]**	**CRGNet [6]**	**EEG-ITNet [27]**	**Echtioui et al. [31]**	**MBSTCNN-ECA-LightGBM [28]**	**Our Model**
Subject 1	86.95%	86.46%	**90.62%**	90.52%	83.80%	84.38%	70.1 7%	82%	90.04%
Subject 2	67.47%	58.33%	62.84%	68.10%	70.60%	62.85%	57.75%	61%	**75.62%**
Subject 3	92.69%	92.57%	93.40%	93.97%	90.80%	89.93%	83.62%	89%	**95.97%**
Subject 4	77.21%	75.35%	**84.02%**	74.14%	75.60%	69.10%	38.79%	63%	76.32%
Subject 5	**82.78%**	80.90%	68.05%	80.17%	80.60%	74.31%	47.41%	71%	78.26%
Subject 6	**73.73%**	67.01%	61.80%	72.41%	73.00%	57.64%	38.96%	64%	69.30%
Subject 7	92.52%	93.06%	**97.20%**	96.55%	95.80%	88.54%	74.82%	72%	91.70%
Subject 8	90.43%	85.76%	90.97%	**91.38%**	89.20%	83.68%	69.65%	79%	88.93%
Subject 9	91.47%	86.46%	89.23%	**93.10%**	79.30%	80.21%	51.03%	84%	87.88%
AVG	83.92%	80.66%	82.01%	**84.48%**	82.10%	76.74%	59.13%	74%	83.78%

Table 8 compares the accuracy of our model with the state-of-the-art model using two classes of right-hand and left-hand classification. According to papers [8,52,53], ML techniques were employed to distinguish between two classes using Multi-task Transfer Learning (MTL), SVM, and LDA classifiers. In contrast, models based on DL were implemented in [28,54,55]. In particular, [28,54] utilized CNN architecture, while [55] utilized DBN and LSTM architecture. Based on the results, our model performed overwhelmingly well across most subjects and on average, as well.

Table 8. A comparison of the accuracy of two classes (left hand and right) between our model and the current state-of-the-art models on the BCI IV 2a dataset using a within-subject approach. The best scores are shown in bold.

	HS-CNN [54]	SW-LCR [8]	CSP+ DBN [55]	CSP+ LSTM [55]	KMDA [53]	VFB-RCSP [52]	MBSTCNN-ECA-LightGBM [28]	Our Model
Subject 1	**90.07%**	86.81%	48.15%	48.15%	79.01%	86.11%	88%	88.65%
Subject 2	80.28%	64.58%	51.85%	51.85%	72.52%	70.83%	78%	**88.03%**
Subject 3	97.08%	95.83%	48.15%	51.85%	90.25%	94.44%	87%	**98.54%**
Subject 4	89.66%	67.36%	50.00%	50.00%	70.25%	73.61%	76%	**90.52%**
Subject 5	97.04%	68.06%	50.00%	50.00%	68.55%	61.11%	93%	**97.78%**
Subject 6	87.04%	67.36%	52.38%	47.62%	71.02%	70.83%	77%	**89.81%**
Subject 7	**92.14%**	80.56%	50.00%	50.00%	88.29%	63.89%	87%	91.43%
Subject 8	98.51%	97.22%	50.00%	50.00%	90.71%	93.06%	94%	**100.00%**
Subject 9	92.31%	92.36%	52.63%	47.37%	90.66%	88.19%	78%	**93.08%**
AVG	91.57%	80.02%	50.35%	49.65%	80.14%	78.01%	84%	**93.09%**

4.3.2. Cross-Subject Classification

As previously noted, the cross-subject strategy serves as a method to evaluate the model's performance by assessing the data of each subject, which remain unutilized during the training phase. Table 9 shows the accuracy results of our model, where individual subject data are allocated for testing purposes. The results indicate that cross-subject strategies perform less well than within-subject strategies, which is reasonable considering that the data of the subjects in testing were not included in the training process. Despite this, the table also illustrates how we provide competitive results when compared with state-of-the-art works, with four subjects showing superior results. As indicated in the table, the EEGNet model [15], as well as EEG-TCNet [23], which includes a TCN block following EEGNet, and EEG Inception [56], which consists of two inception modules, demonstrates that our model performs better than those of others. According to [26,27], the authors assess their methodology based on two approaches: within-subject and cross-subject. Examining the data presented in Tables 7 and 9 highlights the differences in performance between our model and the mentioned papers. In spite of the fact that [26] yields slightly better average results in a within-subject analysis, our model outperforms it when it comes to Subjects 1, 2, and 3. In contrast, our model produces better average results in cross-subject analysis and across all subjects, with the exception of Subject 9, where [26] performs slightly better. Moreover, our model outperforms all results presented in [27] in terms of within-subject accuracy. Although this study demonstrates notable outcomes in cross-subject analysis, Subject 3 in our model consistently maintains their superior performance, in both within-subject and cross-subject evaluations, along with Subjects 1, 6, and 8 in cross-subject analysis. It should be noted that the authors in [27] used the same splitting strategy as we did; however, they employed 10-fold cross-validation to divide the data into training and validation sets. For more detailed results of our model using cross-subject classification, refer to Table A1 of Appendix A, which includes metrics such as accuracy, Kappa, precision, recall, and the F1-score.

Table 9. A comparison of our model accuracy with the state-of-the-art model on the BCI IV 2a dataset using a cross-subject approach. The best scores are shown in bold.

	CMO-CNN [26]	EEG-ITNet [27]	EEG Inception [27]	EEGNet 8,2 [27]	EEG-TCNet [27]	Our Model
Subject 1	68.75%	71.88%	66.32%	68.75%	69.10%	**72.56%**
Subject 2	44.44%	**62.85%**	48.26%	50.00%	52.08%	53.71%
Subject 3	78.47%	81.94%	73.61%	80.21%	81.94%	**86.37%**
Subject 4	55.90%	**65.62%**	56.60%	59.38%	61.81%	60.82%
Subject 5	53.12%	63.19%	**65.62%**	64.24%	60.42%	59.11%
Subject 6	51.56%	56.25%	56.25%	48.26%	51.39%	**59.91%**
Subject 7	67.70%	**80.21%**	73.61%	72.57%	76.39%	72.63%
Subject 8	76.38%	78.12%	70.49%	77.43%	74.31%	**81.68%**
Subject 9	**73.78%**	64.93%	61.11%	55.56%	58.68%	73.05%
AVG	63.34%	**69.44%**	63.54%	64.04%	65.12%	68.87%

4.4. Channel Selection Results

In our study, we utilized a GA to select identical optimal channels for all subjects. The channels selected must maintain or increase the subjects' performance. Consequently, employing a cross-subject strategy to evaluate the fitness ensured that the chosen channels were based on the most effective features identified by training and testing all subjects' data simultaneously. Choosing channels can be a complex task since we need to apply the classification process several times to obtain the most accurate results. According to the GA, we applied three generations, where each generation has six populations to be evaluated. Therefore, 300 epochs were used to train and evaluate the results in a reasonable amount of time. Following this, we carried out three separate runs of the whole GA. After each run, the algorithm identified the top three sets of channels based on accuracy. We then selected the best-performing set of channels across all runs for use in our classification tasks.

Table 10 presents the selected channels which are chosen based on the best accuracy obtained after applying cross-subject classification through the GA to test each subject individually. Further clarification can be found in Figure 8, which illustrates the distribution of these optimal channels, which were selected from 22 main electrodes following the International 10–20 system.

Table 10. Chosen channels based on best accuracy results using genetic algorithm and cross-subject classification.

	Selected Channels	# of Channels	Accuracy
Subject 1 in Testing	[2, 3, 8, 9, 12, 15, 16, 19, 21, 22]	10	76.90%
Subject 2 in Testing	[2, 5, 7, 10, 14, 16, 17, 18, 21, 22]	10	52.98%
Subject 3 in Testing	[2, 5, 6, 7, 8, 9, 10, 11, 13, 14, 15, 18, 22]	13	85.82%
Subject 4 in Testing	[2, 6, 7, 10, 12, 15, 17, 18, 19, 20, 21, 22]	12	61.22%
Subject 5 in Testing	[1, 2, 3, 5, 8, 9, 13, 14, 15, 16, 17, 20, 21]	13	57.81%
Subject 6 in Testing	[3, 4, 5, 7, 8, 10, 12, 15, 17, 19]	10	58.06%
Subject 7 in Testing	[4, 5, 6, 8, 9, 10, 11, 12, 13, 14, 17, 19]	12	68.25%
Subject 8 in Testing	[3, 7, 9, 10, 13, 15, 17, 18, 21, 22]	10	80.56%
Subject 9 in Testing	[5, 9, 13, 17, 18]	5	70.66%

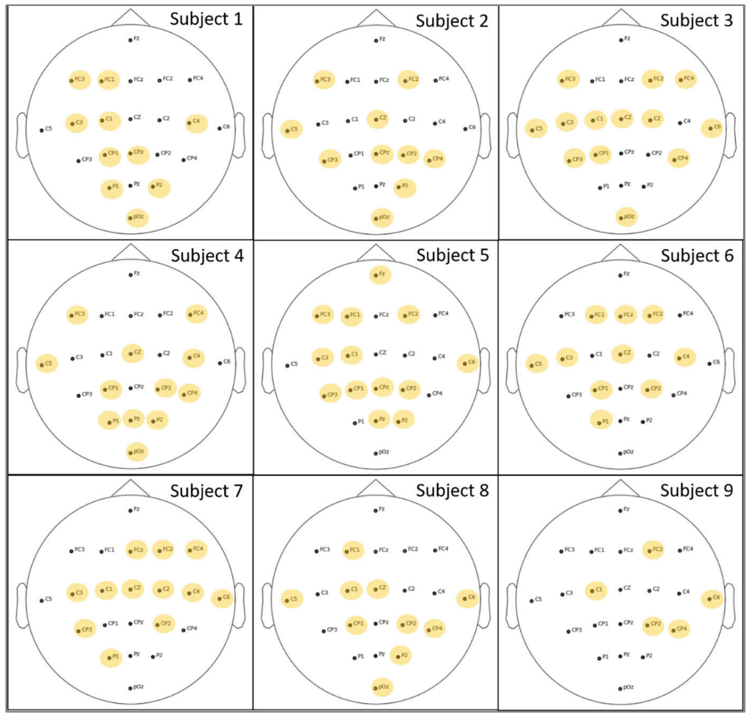

Figure 8. Optimal channels were selected based on GA and cross-subject classification after testing each subject individually. The highlighted electrodes indicate the positions of the selected channels for each subject.

While no identical electrodes were selected, the results indicate that some electrodes were used more frequently than others. Figure 9 shows the average number of electrodes chosen for all subjects according to the different classification processes applied in Table 10. The most popular choice, channel 17, was chosen by seven out of nine participants. Following closely are channels 5, 9, and 10, which were all used by six subjects. In contrast, channel 1 was the least favored, chosen by only one subject, specifically Subject 5.

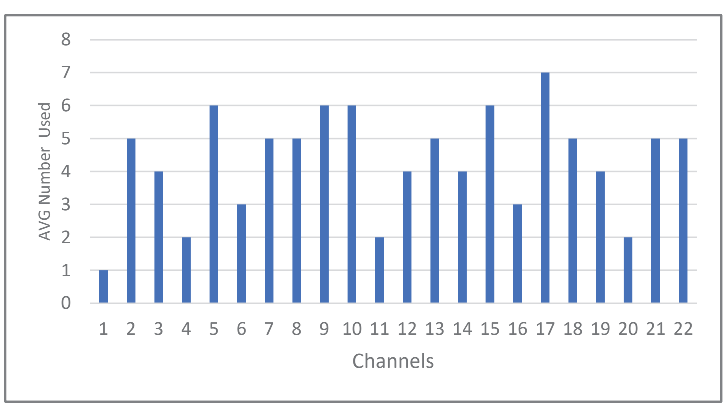

Figure 9. The average number of channels (electrodes) selected for all subjects after applying the genetic algorithm through cross-subject classification.

Cross-subject classification is used to validate the performance of the selected subset channels. Therefore, all subjects' data were involved in the training or testing process. This will assist in the establishment of fixed optimal channels for all subjects. However, our goal is to choose one set of identical channels for all subjects. According to Table 10, testing Subject 3 provides the highest level of accuracy. Furthermore, by comparing the results in Table 10 (with channel selection) with Table 9 (using the entire electrodes), it is evident that testing Subject 1 shows a significant improvement of more than 4% when certain channels are reduced. As a result, it may appear that either the set of channels of Subject 1 or Subject 3 is the best for fixed channels. To verify this result, we evaluated the performance of each set of channels in Table 10 in order to choose the best combinations. The performance of the selected channels was measured based on within-subject classification using these selected channels. As expected, the highest average accuracy values are observed in channel sets associated with testing Subjects 1 and 3. For additional details, see Table A2 of Appendix A. Table 11 presents a detailed breakdown of the accuracy, Kappa values, and time duration for the within-subject classification results after applying the selected channels obtained from testing Subject 1 and Subject 3. Additionally, the results of a full channel classification are presented so that a clear comparison can be made. The results indicate that channel selections improve the performance reflected by the used metrics for many subjects, including Subject 1, Subject 2, Subject 4, Subject 6, and Subject 8. Specifically, Subject 6 exhibits increased accuracy with both combinations of channel selection. In addition, the classification duration is reduced from one and a half hours to two hours, resulting in more efficient results. Therefore, we will consider the set of channels "[2, 3, 8, 9, 12, 15, 16, 19, 21, 22]" that are produced by testing Subject 1 as the fixed optimal in our proposed work since they provide the best accuracy with the shortest computation time.

Table 11. Within-subject classification based on the fixed channel selections. The best scores are shown in bold.

	Optimal Channels of Subject 1 in Testing [2, 3, 8, 9, 12, 15, 16, 19, 21, 22]		**Optimal Channels of Subject 3 in Testing [2, 5, 6, 7, 8, 9, 10, 11, 13, 14, 15, 18, 22]**		**All Channels Classification [1,2, 3, 4, 5, 6, 7, 8, 9, 10, 11, 12, 13, 14, 15, 16, 17, 18, 19, 20, 21, 22]**	
	Accuracy	**Kappa**	**Accuracy**	**Kappa**	**Accuracy**	**Kappa**
Subject 1	87.90%	83.86%	**90.75%**	87.67%	90.04%	86.71%
Subject 2	**77.39%**	69.86%	67.84%	57.16%	75.62%	67.51%
Subject 3	95.60%	94.14%	94.51%	92.67%	**95.97%**	94.63%
Subject 4	75.88%	67.77%	**77.19%**	69.50%	76.32%	68.38%
Subject 5	73.19%	64.30%	77.90%	70.51%	**78.26%**	70.98%
Subject 6	**73.02%**	64.03%	**70.23%**	60.29%	69.30%	59.05%
Subject 7	88.81%	85.09%	89.53%	86.05%	**91.70%**	88.93%
Subject 8	87.82%	83.76%	**89.67%**	86.22%	88.93%	85.24%
Subject 9	87.12%	82.81%	84.85%	79.77%	**87.88%**	83.83%
AVG	82.97%		82.50%		83.78%	78.36%
Time Duration	2 h: 36 min		3 h: 04 min		4 h: 38 min	

Selecting the optimal channels for each subject contributes to reducing noises and increasing the accuracy. In depth, after using within-subject classification across the channel sets listed in Table 10, we identified channel sets that improved accuracy for certain subjects. Table 12 demonstrates variable optimal channels for each subject, presenting their corresponding accuracy results. The table represents the cross-subject experiments conducted to determine these optimal channels. Furthermore, it shows a significant increase in overall accuracy as well as substantial improvements in individual accuracy.

Table 12. Variable optimal channels for each subject.

	Accuracy	Kappa	Variable Optimal Channels	Belong to Which Cross-Subject	Time Duration
Subject 1	90.75%	87.67%	[2, 5, 6, 7, 8, 9, 10, 11, 13, 14, 15, 18, 22]	Testing Subject 3	3:04 h
Subject 2	77.39%	69.86%	[2, 3, 8, 9, 12, 15, 16, 19, 21, 22]	Testing Subject 1	2:36 h
Subject 3	96.34%	95.12%	[2, 5, 7, 10, 14, 16, 17, 18, 21, 22]	Testing Subject 2	2:34 h
Subject 4	77.19%	69.50%	[2, 5, 6, 7, 8, 9, 10, 11, 13, 14, 15, 18, 22]	Testing Subject 3	3:04 h
Subject 5	77.90%	70.51%	[2, 5, 6, 7, 8, 9, 10, 11, 13, 14, 15, 18, 22]	Testing Subject 3	3:04 h
Subject 6	73.02%	64.03%	[2, 3, 8, 9, 12, 15, 16, 19, 21, 22]	Testing Subject 1	2:36 h
Subject 7	89.53%	86.05%	[2, 5, 6, 7, 8, 9, 10, 11, 13, 14, 15, 18, 22]	Testing Subject 3	3:04 h
Subject 8	89.67%	86.22%	[2, 6, 7, 10, 12, 15, 17, 18, 19, 20, 21, 22]	Testing Subject 4	2:51 h
Subject 9	89.02%	89.02%	[2, 6, 7, 10, 12, 15, 17, 18, 19, 20, 21, 22]	Testing Subject 4	2:51 h
AVG	84.53%	79.78%			2:51 h

Below is a comparison of our proposed work with the existing state-of-the-art related research contributions according to the channel selection process. As shown in Table 13, our study provides an advantage over the previous work in terms of the identicality of the channels and used strategy. In particular, the proposed variable channel approach differs from previous studies in the fact that it combines two strategies, resulting in the highest accuracy. As well as using a new strategy, our fixed channel approach also uses the same channels for all subjects, resulting in a significant increase in accuracy. Figure 10 demonstrates how our work performs compared to the previous one by presenting the number of channels used and the average accuracy obtained through the channel selection process. As shown by the figure, the proposed variable channel methodology demonstrates the highest degree of accuracy, followed by the work presented in [19], and then our fixed channel methodology. While the study in [19] achieves notable accuracy with fewer channels, it employs the one-vs-one strategy, which involves the use of multiple binary classifications and averages their results. In contrast, our approach uses a single classifier to accurately differentiate between four classes, achieving not only higher accuracy but also a more efficient reduction in the number of channels used.

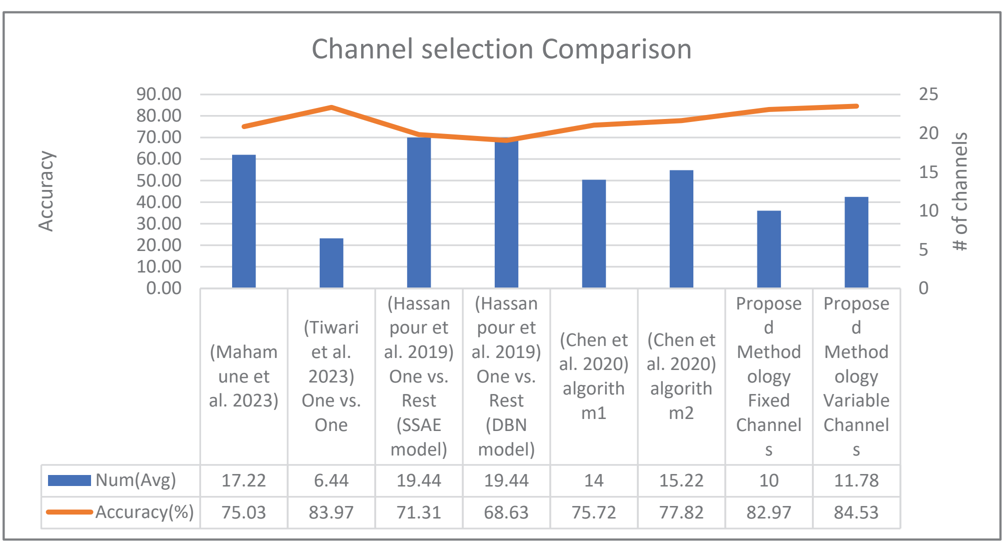

Figure 10. A comparison of our work with the state-of-the-art research in terms of accuracy and the number of channels used, as discussed in Hassanpour et al. (2019) [18], Tiwari et al. (2023) [19], Mahamune et al. (2023) [21], and Chen et al. (2020) [22].

Table 13. A comparison between our work and the state-of-the-art research on channel selection in the BCI IV 2a dataset.

	Accuracy	#of Channels	Use the Same Number of Channels	Use the Same Channels?	Strategy
(Mahamune et al. 2023) [21]	75.03%	17.22	No	No	Within-subject
(Tiwari et al. 2023) [19]	83.97%	6.44	No	No	One vs. One
(Hassanpour et al. 2019) [18] (SSAE model)	71.31%	19.44	No	No	One vs. Rest
(Hassanpour et al. 2019) [18] (DBN model)	68.63%	19.44	No	No	One vs. Rest
(Chen et al. 2020) [22] algorithm1	75.72%	14	Yes	No	Within-subject in classification One vs. Rest in feature extraction
(Chen et al. 2020) [22] algorithm2	77.82%	15.22	No	No	Within-subject in classification One vs. Rest in feature extraction
Proposed Methodology Fixed Channels	82.97%	10	Yes	Yes	Cross-subject in channel selection Within-subject in classification
Proposed Methodology Variable Channels	84.53%	11.78	No	No	Cross-subject in channel selection Within-subject in classification

Finally, in our experiment, we validated classification performance based on four distinct methods: within-subject with all channels, cross-subject, within-subject with fixed channels, and within-subject with variable channels. We found that the within-subject method utilizing variable channels achieved the most significant results within a reasonable duration. Conversely, the within-subject strategy with a fixed set of channels produced the highest accuracy and Kappa values, particularly when considering the shortest computation time. Standardizing the number of channels across all participants has proven to be a particularly effective technique. This technique produces impressive results that demonstrate the method's effectiveness and importance in terms of accuracy, Kappa scores, and processing time. This novel approach represents a significant advancement in the field, potentially introducing an innovative direction in how channels could be selected. It allows for the use of a consistent set of channels across all subjects, a method not previously applied. This approach not only challenges traditional approaches but also addresses existing channel selection limitations, opening up new opportunities for research and application.

Based on our results, we can say that all four methods demonstrated high accuracy in classification, overcoming the average accuracy value shown in most similar studies. The within-subject with all channels method was assessed with two-class and four-class classifications. The two-class classification achieved the highest accuracy among all studies, while the four-class classification recorded the highest accuracy in most studies and exceeded all others for Subjects 2 and 3. Subjects 1, 3, 6, and 8 achieved the highest accuracy scores using cross-subject classification, delivering competitive results on average. The within-subject with variable channel method outperformed previous studies in accuracy by using an average of 11.78 channels. On the other hand, the within-subject with fixed channels method was more accurate than most other studies, except for one. By employing a single classifier, our method distinguishes itself from this previous study, which used a one-to-one approach.

For further evaluation, Figure 11 illustrates the ROC curve and AUC for each subject across these four methods. The results of the AUC are generally good, with most scores remaining above 90. There is no doubt that the AUC for Subject 3 is impressive, scoring 100 for the within-subject method, 98 for the cross-subject method, and 100 for both the fixed and variable channel methods. Contrary to this, the cross-subject method yields the lowest AUC, particularly for Subject 2, where it reaches 79. Additionally, all the within-subject methods, either with all channels or with selected channels, demonstrate similar results, showing the various channel selection strategies consistently outperforming the others.

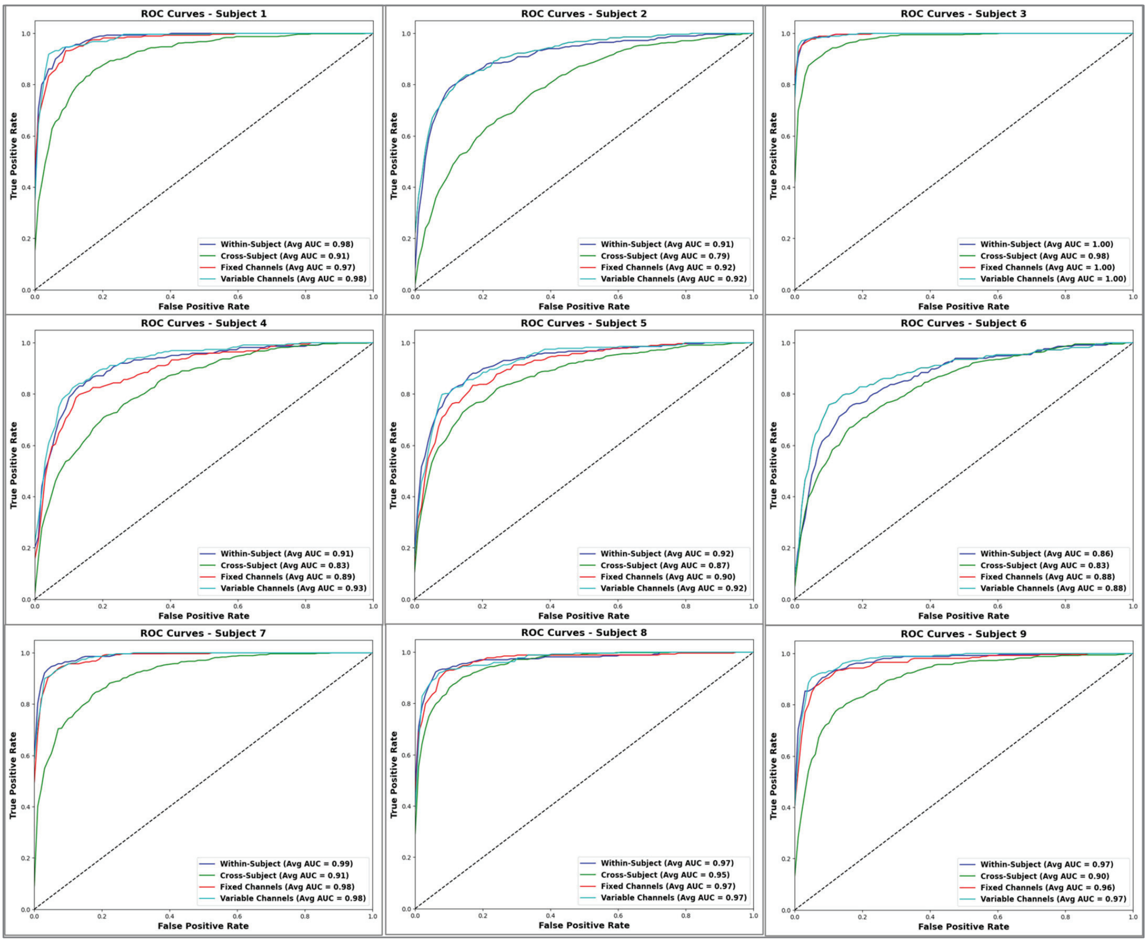

Figure 11. ROC curves and AUC for each subject across different methods: within-subject with all channels ("Within-subject"), cross-subject, within-subject with fixed channel selection ("Fixed Channels"), and within-subject with variable channel selection ("Variable Channels"). The dotted black lines reflect the performance of a random predictor, serving as a reference for comparing the classification performance of the four methods.

5. Conclusions

In the research area addressing MI-EEG-based BCIs, several challenges limit the growth of classification accuracy involving the complexity and the redundancy of EEG signal data. In this paper, we presented a Fusion convolutional neural network with Attention blocks (FCNNA) model to perform multiclass classification with a channel selection mechanism. Our approach began with preprocessing to eliminate noise and prepare the EEG raw data. Afterward, the FCNNA model was used for classification, which consists of layers of convolutional blocks followed by a CBAM attention block. Based on a comparison between one, two, and three layers of convolutional blocks, it was determined that two layers provide the best performance in terms of accuracy, complexity, and processing time. Lastly, a genetic algorithm was used for channel selection. The novelty of this stage is the use of a new technique that combines cross-subject and within-subject methods. Many cross-subject classifications were applied through the channel selection process to provide various sets of optimal channels. Following this, within-subject classifications were performed so that fixed and variable channels can be selected for each subject.

The experimental results on BCI IV 2a showed that our method effectively addressed the issues of existing CNN-based EEG motor imagery classification and improved the performance. Our proposed work is evaluated through four different scenarios: within-subject classification, cross-subject classification, a fixed set of channel selection, and a variable set of channel selection. As a result of our within-subject strategy, multiclass classification showed an impressive improvement of 83.78%. The accuracy of the model was considered to be higher than the EEGNet, MSFBCNN, EEG-TCNet, ShallowNet, and DeepConvNet models by 6.41%. Moreover, in comparison to advanced works, Subject 2 had a 5% increase in accuracy, and Subject 3 had a 2% increase. In addition, a within-subject strategy with two classes resulted in the best performance at 93.09%. The second multiclass classification applied using a cross-subject strategy resulted in an impressive accuracy score of 68.87%. In both scenarios, the fixed set of channels and the variable set of channels, only one classifier was used to distinguish between the four classes with a superior accuracy of 82.97% and 84.53%, with an average number of channels between 10 and 11.78. As a result of analyzing the four scenarios, the within-subject method employing variable channels achieved the highest accuracy and Kappa results. Meanwhile, the strategy with a fixed set of channels achieved the highest accuracy in the shortest computation time.

In future work, we intend to improve performance and efficiency through the incorporation of transfer learning. Using the concepts introduced in this paper, we aim to further develop classification methods and channel selection techniques to improve performance. This will significantly contribute to the advancement of BCI systems. Additionally, the insights gained from our study collectively suggest promising directions for future research and practical applications in EEG MI classification and EEG channel selection.

Author Contributions: Conceptualization, J.K., S.A. and A.S.; methodology, J.K.; software, J.K.; validation, J.K.; formal analysis, J.K; investigation, J.K.; resources, J.K., S.A. and A.S.; data curation, J.K.; writing—original draft preparation, J.K.; writing—review and editing, J.K., S.A. and A.S.; visualization, J.K.; supervision, S.A. and A.S.; project administration, S.A. and A.S.; funding acquisition, S.A. and A.S. All authors have read and agreed to the published version of the manuscript.

Funding: This research received no external funding.

Institutional Review Board Statement: Not applicable.

Informed Consent Statement: Not applicable.

Data Availability Statement: The BCI-IV-2a dataset can be downloaded from the following link: https://www.bbci.de/competition/iv/#datasets, accessed on 10 March 2023.

Acknowledgments: The authors extend their appreciation to the Deputyship for Research & Innovation, "Ministry of Education" in Saudi Arabia for funding this research work through the project no.(IFKSUOR3-506-1).

Conflicts of Interest: The authors declare no conflicts of interest.

Appendix A

Table A1. Cross-subject classification results of 4 classes in the BCI IV 2a dataset.

	Accuracy	Kappa	Precision	Recall	F1-Score
Subject 1	72.56%	63.42%	74%	73%	73%
Subject 2	53.71%	38.29%	55%	54%	54%
Subject 3	86.37%	81.83%	87%	86%	86%
Subject 4	60.82%	47.63%	65%	61%	61%
Subject 5	59.11%	45.62%	62%	59%	58%
Subject 6	59.91%	46.52%	61%	60%	59%
Subject 7	72.63%	63.52%	74%	73%	73%
Subject 8	81.68%	75.57%	82%	82%	82%
Subject 9	73.05%	64.06%	73%	73%	73%
AVG	68.87%	58.50%			

Table A2. Within-subject classification based on the set of channels in Table 10.

	Table 10 Selected Channels According to								
	Testing Subject 1	Testing Subject 2	Testing Subject 3	Testing Subject 4	Testing Subject 5	Testing Subject 6	Testing Subject 7	Testing Subject 8	Testing Subject 9
Accuracy (Avg)	82.97%	81.69%	82.5%	81.54%	79.87%	80.49%	80.05%	79.94%	69.46%

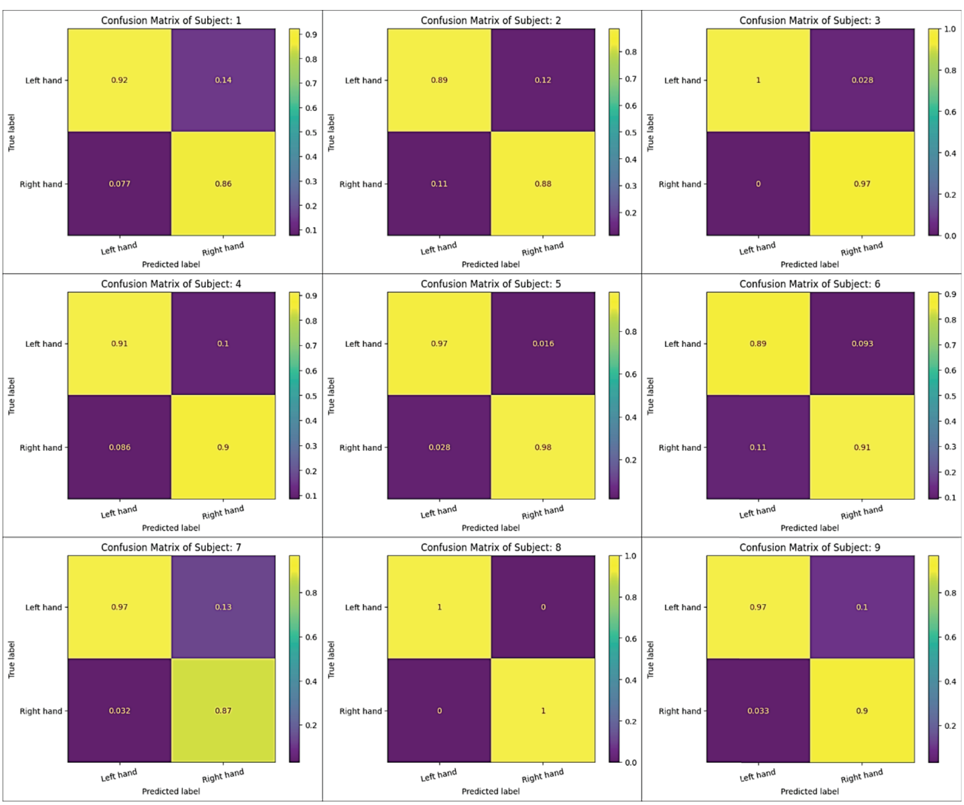

Figure A1. Confusion matrix of proposed model applied on 2 classes of left and right hand in BCI IV 2a using within-subject strategy.

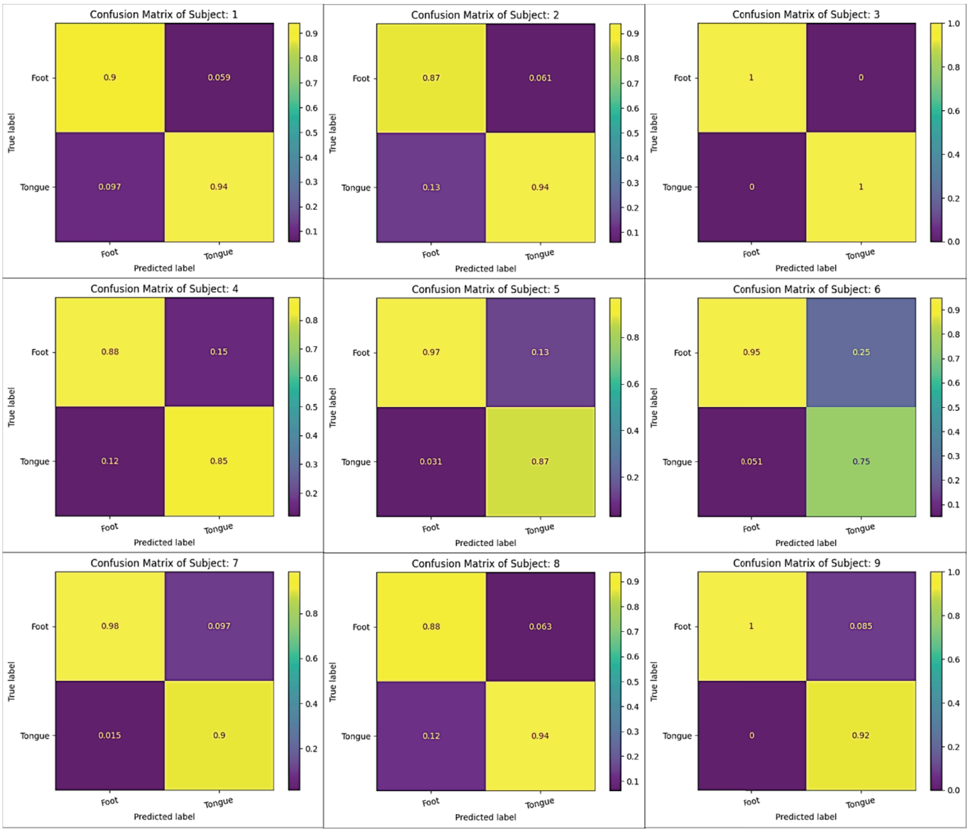

Figure A2. Confusion matrix of proposed model applied on 2 classes of both feet and tongue in BCI IV 2a using within-subject strategy.

References

1. Ramadan, R.A.; Refat, S.; Elshahed, M.A.; Rasha, A.A. Basics of Brain Computer Interface. In *Brain-Computer Interfaces. Intelligent Systems Reference Library*; Hassanien, A.E., Azar, A.T., Eds.; Springer: Cham, Switzerland, 2015; Volume 74, pp. 51–95, ISBN 9783319109770.
2. Pfurtscheller, G.; Neuper, C. Motor Imagery and Direct Brain-Computer Communication. *Proc. IEEE* **2001**, *89*, 1123–1134. [CrossRef]
3. Baig, M.Z.; Aslam, N.; Shum, H.P.H. Filtering Techniques for Channel Selection in Motor Imagery EEG Applications: A Survey. *Artif. Intell. Rev.* **2020**, *53*, 1207–1232. [CrossRef]
4. Li, H.; Chen, H.; Jia, Z.; Zhang, R.; Yin, F. A Parallel Multi-Scale Time-Frequency Block Convolutional Neural Network Based on Channel Attention Module for Motor Imagery Classification. *Biomed. Signal Process. Control* **2023**, *79*, 104066. [CrossRef]
5. Varsehi, H.; Firoozabadi, S.M.P. An EEG Channel Selection Method for Motor Imagery Based Brain–Computer Interface and Neurofeedback Using Granger Causality. *Neural Netw.* **2021**, *133*, 193–206. [CrossRef] [PubMed]
6. Gao, C.; Liu, W.; Yang, X. Convolutional Neural Network and Riemannian Geometry Hybrid Approach for Motor Imagery Classification. *Neurocomputing* **2022**, *507*, 180–190. [CrossRef]
7. Zancanaro, A.; Cisotto, G.; Paulo, J.R.; Pires, G.; Nunes, U.J. CNN-Based Approaches For Cross-Subject Classification in Motor Imagery: From the State-of-the-Art to DynamicNet. In Proceedings of the 2021 IEEE Conference on Computational Intelligence in Bioinformatics and Computational Biology (CIBCB), Melbourne, Australia, 13–15 October 2021; IEEE: Piscataway, NJ, USA, 2021; pp. 1–7.
8. Gaur, P.; Gupta, H.; Chowdhury, A.; McCreadie, K.; Pachori, R.B.; Wang, H. A Sliding Window Common Spatial Pattern for Enhancing Motor Imagery Classification in EEG-BCI. *IEEE Trans. Instrum. Meas.* **2021**, *70*, 1–9. [CrossRef]
9. Jin, J.; Miao, Y.; Daly, I.; Zuo, C.; Hu, D.; Cichocki, A. Correlation-Based Channel Selection and Regularized Feature Optimization for MI-Based BCI. *Neural Netw.* **2019**, *118*, 262–270. [CrossRef] [PubMed]

10. Park, Y.; Chung, W. Optimal Channel Selection Using Correlation Coefficient for CSP Based EEG Classification. *IEEE Access* **2020**, *8*, 111514–111521. [CrossRef]
11. Chen, J.; Yi, W.; Wang, D.; Du, J.; Fu, L.; Li, T. FB-CGANet: Filter Bank Channel Group Attention Network for Multi-Class Motor Imagery Classification. *J. Neural Eng.* **2022**, *19*, 016011. [CrossRef]
12. Varone, G.; Boulila, W.; Driss, M.; Kumari, S.; Khan, M.K.; Gadekallu, T.R.; Hussain, A. Finger Pinching and Imagination Classification: A Fusion of CNN Architectures for IoMT-Enabled BCI Applications. *Inf. Fusion* **2024**, *101*, 102006. [CrossRef]
13. Altaheri, H.; Muhammad, G.; Alsulaiman, M.; Amin, S.U.; Altuwaijri, G.A.; Abdul, W.; Bencherif, M.A.; Faisal, M. *Deep Learning Techniques for Classification of Electroencephalogram (EEG) Motor Imagery (MI) Signals: A Review*; Springer: London, UK, 2021; Volume 5, ISBN 0052102106.
14. Schirrmeister, R.T.; Springenberg, J.T.; Fiederer, L.D.J.; Glasstetter, M.; Eggensperger, K.; Tangermann, M.; Hutter, F.; Burgard, W.; Ball, T. Deep Learning with Convolutional Neural Networks for EEG Decoding and Visualization. *Hum. Brain Mapp.* **2017**, *38*, 5391–5420. [CrossRef] [PubMed]
15. Lawhern, V.J.; Solon, A.J.; Waytowich, N.R.; Gordon, S.M.; Hung, C.P.; Lance, B.J. EEGNet: A Compact Convolutional Network for EEG-Based Brain-Computer Interfaces. *J. Neural Eng.* **2018**, *15*, 056013. [CrossRef] [PubMed]
16. Hu, J.; Shen, L.; Sun, G. Squeeze-and-Excitation Networks. In Proceedings of the IEEE Conference on Computer Vision and Pattern Recognition (CVPR), Salt Lake City, UT, USA, 18–23 June 2018.
17. Woo, S.; Park, J.; Lee, J.-Y.; Kweon, I.S. CBAM: Convolutional Block Attention Module. In Proceedings of the Proceedings of the European Conference on Computer Vision (ECCV), Munich, Germany, 8–14 September 2018.
18. Hassanpour, A.; Moradikia, M.; Adeli, H.; Khayami, S.R.; Shamsinejadbabaki, P. A Novel End-to-End Deep Learning Scheme for Classifying Multi-Class Motor Imagery Electroencephalography Signals. *Expert. Syst.* **2019**, *36*, e12494. [CrossRef]
19. Tiwari, A.; Chaturvedi, A. Automatic EEG Channel Selection for Multiclass Brain-Computer Interface Classification Using Multiobjective Improved Firefly Algorithm. *Multimed. Tools Appl.* **2023**, *82*, 5405–5433. [CrossRef]
20. Jindal, K.; Upadhyay, R.; Singh, H.S. A novel EEG channel selection and classification methodology for multi-class motor imagery-based BCI system design. *Int. J. Imaging Syst. Technol.* **2022**, *32*, 1318–1337. [CrossRef]
21. Mahamune, R.; Laskar, S.H. An Automatic Channel Selection Method Based on the Standard Deviation of Wavelet Coefficients for Motor Imagery Based Brain–Computer Interfacing. *Int. J. Imaging Syst. Technol.* **2023**, *33*, 714–728. [CrossRef]
22. Chen, S.; Sun, Y.; Wang, H.; Pang, Z. Channel Selection Based Similarity Measurement for Motor Imagery Classification. In Proceedings of the 2020 IEEE International Conference on Bioinformatics and Biomedicine (BIBM), Seoul, Republic of Korea, 16–19 December 2020; IEEE: Piscataway, NJ, USA, 2020; pp. 542–548.
23. Ingolfsson, T.M.; Hersche, M.; Wang, X.; Kobayashi, N.; Cavigelli, L.; Benini, L. EEG-TCNet: An Accurate Temporal Convolutional Network for Embedded Motor-Imagery Brain–Machine Interfaces. In Proceedings of the 2020 IEEE International Conference on Systems, Man, and Cybernetics (SMC), Toronto, ON, Canada, 11–14 October 2020; IEEE: Piscataway, NJ, USA, 2020; pp. 2958–2965.
24. Wu, H.; Niu, Y.; Li, F.; Li, Y.; Fu, B.; Shi, G.; Dong, M. A Parallel Multiscale Filter Bank Convolutional Neural Networks for Motor Imagery EEG Classification. *Front. Neurosci.* **2019**, *13*, 1275. [CrossRef] [PubMed]
25. Musallam, Y.K.; AlFassam, N.I.; Muhammad, G.; Amin, S.U.; Alsulaiman, M.; Abdul, W.; Altaheri, H.; Bencherif, M.A.; Algabri, M. Electroencephalography-Based Motor Imagery Classification Using Temporal Convolutional Network Fusion. *Biomed. Signal Process. Control* **2021**, *69*, 102826. [CrossRef]
26. Liu, X.; Xiong, S.; Wang, X.; Liang, T.; Wang, H.; Liu, X. A Compact Multi-Branch 1D Convolutional Neural Network for EEG-Based Motor Imagery Classification. *Biomed. Signal Process. Control* **2023**, *81*, 104456. [CrossRef]
27. Salami, A.; Andreu-Perez, J.; Gillmeister, H. EEG-ITNet: An Explainable Inception Temporal Convolutional Network for Motor Imagery Classification. *IEEE Access* **2022**, *10*, 36672–36685. [CrossRef]
28. Jia, H.; Yu, S.; Yin, S.; Liu, L.; Yi, C.; Xue, K.; Li, F.; Yao, D.; Xu, P.; Zhang, T. A Model Combining Multi Branch Spectral-Temporal CNN, Efficient Channel Attention, and LightGBM for MI-BCI Classification. *IEEE Trans. Neural Syst. Rehabil. Eng.* **2023**, *31*, 1311–1320. [CrossRef]
29. Zhang, X.; Miao, Z.; Menon, C.; Zheng, Y.; Zhao, M.; Ming, D. Priming Cross-Session Motor Imagery Classification with a Universal Deep Domain Adaptation Framework. *Neurocomputing* **2023**, *556*, 126659. [CrossRef]
30. Kim, D.-H.; Shin, D.-H.; Kam, T.-E. Bridging the BCI Illiteracy Gap: A Subject-to-Subject Semantic Style Transfer for EEG-Based Motor Imagery Classification. *Front. Hum. Neurosci.* **2023**, *17*. [CrossRef]
31. Echtioui, A.; Zouch, W.; Ghorbel, M.; Mhiri, C.; Hamam, H. Classification of BCI Multiclass Motor Imagery Task Based on Artificial Neural Network. *Clin. EEG Neurosci.* **2023**, 155005942211482. [CrossRef]
32. Abdullah; Faye, I.; Islam, M.R. EEG Channel Selection Techniques in Motor Imagery Applications: A Review and New Perspectives. *Bioengineering* **2022**, *9*, 726. [CrossRef]
33. Khan, M.A.; Lali, M.I.U.; Sharif, M.; Javed, K.; Aurangzeb, K.; Haider, S.I.; Altamrah, A.S.; Akram, T. An Optimized Method for Segmentation and Classification of Apple Diseases Based on Strong Correlation and Genetic Algorithm Based Feature Selection. *IEEE Access* **2019**, *7*, 46261–46277. [CrossRef]
34. Liu, Z.; Chang, B.; Cheng, F. An Interactive Filter-Wrapper Multi-Objective Evolutionary Algorithm for Feature Selection. *Swarm Evol. Comput.* **2021**, *65*, 100925. [CrossRef]
35. Maleki, N.; Zeinali, Y.; Niaki, S.T.A. A K-NN Method for Lung Cancer Prognosis with the Use of a Genetic Algorithm for Feature Selection. *Expert. Syst. Appl.* **2021**, *164*, 113981. [CrossRef]

36. Padfield, N.; Ren, J.; Murray, P.; Zhao, H. Sparse Learning of Band Power Features with Genetic Channel Selection for Effective Classification of EEG Signals. *Neurocomputing* **2021**, *463*, 566–579. [CrossRef]
37. Yang, J.; Singh, H.; Hines, E.L.; Schlaghecken, F.; Iliescu, D.D.; Leeson, M.S.; Stocks, N.G. Channel Selection and Classification of Electroencephalogram Signals: An Artificial Neural Network and Genetic Algorithm-Based Approach. *Artif. Intell. Med.* **2012**, *55*, 117–126. [CrossRef]
38. Albasri, A.; Abdali-Mohammadi, F.; Fathi, A. EEG Electrode Selection for Person Identification Thru a Genetic-Algorithm Method. *J. Med. Syst.* **2019**, *43*, 297. [CrossRef]
39. He, L.; Hu, Y.; Li, Y.; Li, D. Channel Selection by Rayleigh Coefficient Maximization Based Genetic Algorithm for Classifying Single-Trial Motor Imagery EEG. *Neurocomputing* **2013**, *121*, 423–433. [CrossRef]
40. Brunner, C.; Leeb, R.; Müller-Putz, G.R.; Schlögl, A.; Pfurtscheller, G. BCI Competition 2008--Graz Data Set A. *Inst. Knowl. Discov. (Lab. Brain-Comput. Interfaces) Graz Univ. Technol.* **2008**, *16*, 1–6.
41. Tragoudaras, A.; Antoniadis, C.; Massoud, Y. Enhancing DNN Models for EEG/ECoG BCI With a Novel Data-Driven Offline Optimization Method. *IEEE Access* **2023**, *11*, 35888–35900. [CrossRef]
42. Tragoudaras, A.; Fanaras, K.; Antoniadis, C.; Massoud, Y. Data-Driven Offline Optimization of Deep CNN Models for EEG and ECoG Decoding. In Proceedings of the 2023 IEEE International Symposium on Circuits and Systems (ISCAS), Monterey, CA, USA, 21–25 May 2023; IEEE: Piscataway, NJ, USA, 2023; pp. 1–5.
43. Li, Y.; Guo, L.; Liu, Y.; Liu, J.; Meng, F. A Temporal-Spectral-Based Squeeze-and- Excitation Feature Fusion Network for Motor Imagery EEG Decoding. *IEEE Trans. Neural Syst. Rehabil. Eng.* **2021**, *29*, 1534–1545. [CrossRef]
44. Howard, A.G.; Zhu, M.; Chen, B.; Kalenichenko, D.; Wang, W.; Weyand, T. Mobilenets: Efficient Convolutional Neural Networks for Mobile Vision Applications. *arXiv* **2017**, arXiv:1704.04861.
45. Ioffe, S.; Szegedy, C. Batch Normalization: Accelerating Deep Network Training by Reducing Internal Covariate Shift. In Proceedings of the 32nd International Conference on Machine Learning, Lille, France, 7–9 July 2015.
46. Chaudhari, S.; Mithal, V.; Polatkan, G.; Ramanath, R. An Attentive Survey of Attention Models. *ACM Trans. Intell. Syst. Technol.* **2021**, *12*, 1–32. [CrossRef]
47. Madhu, G.; Gajapaka, S.M.; Bharadwaj, L. A Simple Attention Block Embedded in Standard CNN for Image Classification. In Proceedings of the 2022 International Conference on Applied Artificial Intelligence and Computing (ICAAIC), Salem, India, 9–11 May 2022; IEEE: Piscataway, NJ, USA, 2022; pp. 279–284.
48. Karmakar, P.; Teng, S.W.; Lu, G. Thank You for Attention: A Survey on Attention-Based Artificial Neural Networks for Automatic Speech Recognition. *arXiv* **2021**, arXiv:2102.07259.
49. Lun, X.; Yu, Z.; Wang, F.; Chen, T.; Hou, Y. A Novel Approach of CNN for Human Motor Imagery Recognition Using the Virtual Electrode Pairs. *J. Intell. Fuzzy Syst.* **2021**, *40*, 5275–5288. [CrossRef]
50. Roots, K.; Muhammad, Y.; Muhammad, N. Fusion Convolutional Neural Network for Cross-Subject Eeg Motor Imagery Classification. *Computers* **2020**, *9*, 72. [CrossRef]
51. Magboo, V.P.C.; Magboo, M.S.A. Machine Learning Classifiers on Breast Cancer Recurrences. *Procedia Comput. Sci.* **2021**, *192*, 2742–2752. [CrossRef]
52. Long, T.; Wan, M.; Jian, W.; Dai, H.; Nie, W.; Xu, J. Application of Multi-Task Transfer Learning: The Combination of EA and Optimized Subband Regularized CSP to Classification of 8-Channel EEG Signals with Small Dataset. *Front. Hum. Neurosci.* **2023**, *17*, 1143027. [CrossRef]
53. Jiang, Q.; Zhang, Y.; Zheng, K. Motor Imagery Classification via Kernel-Based Domain Adaptation on an SPD Manifold. *Brain Sci.* **2022**, *12*, 659. [CrossRef]
54. Dai, G.; Zhou, J.; Huang, J.; Wang, N. HS-CNN: A CNN with Hybrid Convolution Scale for EEG Motor Imagery Classification. *J. Neural Eng.* **2020**, *17*, 016025. [CrossRef]
55. Saputra, M.F.; Setiawan, N.A.; Ardiyanto, I. Deep Learning Methods for EEG Signals Classification of Motor Imagery in BCI. *IJITEE (Int. J. Inf. Technol. Electr. Eng.)* **2019**, *3*, 80. [CrossRef]
56. Santamaria-Vazquez, E.; Martinez-Cagigal, V.; Vaquerizo-Villar, F.; Hornero, R. EEG-Inception: A Novel Deep Convolutional Neural Network for Assistive ERP-Based Brain-Computer Interfaces. *IEEE Trans. Neural Syst. Rehabil. Eng.* **2020**, *28*, 2773–2782. [CrossRef]

sensors

Article

Detection Method of Epileptic Seizures Using a Neural Network Model Based on Multimodal Dual-Stream Networks

Baiyang Wang [1,†], Yidong Xu [1,†], Siyu Peng [2], Hongjun Wang [1,*] and Fang Li [2,*]

[1] School of Information Science and Engineering, Shandong University, Qingdao 266237, China; 202320482@mail.sdu.edu.cn (B.W.)
[2] School of Information Engineering, Changji University, Changji Hui Autonomous Prefecture, Changji 831100, China
* Correspondence: hjw@sdu.edu.cn (H.W.); cjxy_lf@cjc.edu.cn (F.L.)
† These authors contributed equally to this work.

Abstract: Epilepsy is a common neurological disorder, and its diagnosis mainly relies on the analysis of electroencephalogram (EEG) signals. However, the raw EEG signals contain limited recognizable features, and in order to increase the recognizable features in the input of the network, the differential features of the signals, the amplitude spectrum and the phase spectrum in the frequency domain are extracted to form a two-dimensional feature vector. In order to solve the problem of recognizing multimodal features, a neural network model based on a multimodal dual-stream network is proposed, which uses a mixture of one-dimensional convolution, two-dimensional convolution and LSTM neural networks to extract the spatial features of the EEG two-dimensional vectors and the temporal features of the signals, respectively, and combines the advantages of the two networks, using the hybrid neural network to extract both the temporal and spatial features of the signals at the same time. In addition, a channel attention module was used to focus the model on features related to seizures. Finally, multiple sets of experiments were conducted on the Bonn and New Delhi data sets, and the highest accuracy rates of 99.69% and 97.5% were obtained on the test set, respectively, verifying the superiority of the proposed model in the task of epileptic seizure detection.

Keywords: EEG signal; convolutional neural network; epilepsy diagnosis; feature extraction; classification and diagnosis

Citation: Wang, B.; Xu, Y.; Peng, S.; Wang, H.; Li, F. Detection Method of Epileptic Seizures Using a Neural Network Model Based on Multimodal Dual-Stream Networks. *Sensors* **2024**, *24*, 3360. https://doi.org/10.3390/s24113360

Academic Editor: Yvonne Tran

Received: 30 April 2024
Revised: 17 May 2024
Accepted: 18 May 2024
Published: 24 May 2024

1. Introduction

Epilepsy is a common neurological disorder characterized by abnormal electrical activity in the brain. These abnormal electrical activities can trigger various forms of seizures, which vary from person to person. Seizures may cause generalized convulsions, which are violent, involuntary contractions and spasms of muscles throughout the body. This type of seizure is often called a generalized seizure. However, epileptic seizures do not always manifest as generalized convulsions. Some types of seizures, such as focal seizures, may be limited to one part of the body and manifest as localized muscle twitching or abnormal sensations. In addition, some seizures may include brief loss of consciousness, abnormal behavior, or confusion without obvious convulsions. Epilepsy can manifest in many different ways, depending on where in the brain the abnormal electrical activity occurs and how it spreads [1]. The diagnosis and monitoring of epilepsy relies heavily on electroencephalography (EEG), a non-invasive brain testing technique that measures electrical signals in the brain through electrodes attached to the scalp. EEG can capture changes in brain activity during seizures. However, EEG signals are complex, noisy, and high-dimensional, which poses a challenge for accurate and efficient classification of EEG signals [2].

EEG signals for the detection and diagnosis of epilepsy can be divided into the following steps: signal preprocessing, feature extraction, feature selection and classification [3].

Signal preprocessing is carried out to remove noise and interference from the EEG signal and improve the signal quality. Then, useful features are extracted from the EEG signal that reflect the time domain, frequency domain, or time–frequency domain characteristics of the signal. However, not all of the extracted features are favorable for epilepsy diagnosis, so feature selection is also needed to select the optimal subset from the extracted features to reduce the feature dimensionality and computational complexity. Finally, the EEG signals are categorized as either normal or abnormal based on the features, which also help to further differentiate the type and degree of epilepsy. In recent years, many researchers have proposed many intelligent epilepsy diagnostic methods, some of which are based on traditional signal processing methods, and some of which are based on machine learning and deep learning methods.

Conventional methods usually require an artificially designed approach to feature extraction and selection [4–11]. Guangpeng et al. [12] extracted the time–frequency feature maps of interval EEG signals. Then a single-channel method was used to reduce the network parameters, and finally a convolutional neural network was used to predict epilepsy, with a prediction accuracy of 87.9%. Cansel et al. [13] used discrete wavelet transform to process EEG signals and thus diagnose temporal lobe epilepsy (TLE) patients and psychogenic nonepileptic seizure (PNES) in an automated discriminative method to quickly and accurately determine different epilepsy types. Sirin et al. [14] investigated the interaction between sleep architecture and seizure probability, using dual-channel subcutaneous EEG signals to account for changes in brain dynamics in each patient. Seyed Morteza et al. [15] also used discrete wavelet transform to decompose the EEG signal; however, it was based on the Modified Binary Salp Swarm Algorithm (MBSSA) to extract the time domain features, thus avoiding manual and time-consuming computations. Ying et al. [16] used a wearable EEG monitoring device to capture EEG and automated epilepsy detection using support vector machines, providing a new approach to real-time monitoring. Traditional methods have certain limitations and need to set up appropriate recognition methods according to specific scenarios, which is not conducive to the rapid diagnosis of epilepsy diseases for complex and variable epilepsy types [17–19].

Deep learning methods can automatically learn feature representations from raw signals. Deep learning methods can also process multi-channel EEG signals, utilizing the spatial relationships between the signals [20–24]. Zixu et al. [25] developed a unified framework early-seizure detection and epilepsy diagnosis using mainly autoregressive moving average-model and support-vector machine classifiers for epilepsy diagnosis, which achieved classification accuracies of 93% and 94%, respectively. Weidon et al. [26] used multichannel EEG signals to construct a multilayer deep convolutional neural network model, thus effectively utilizing the relevant information such as time, frequency, and channel of EEG to extract relevant features about epilepsy, which greatly improved the diagnostic accuracy of epilepsy. Abdelhamid et al. [27] proposed a framework combining deep learning and EEG signal processing without any manual feature extraction for the detection of seizures and non-seizures, with a combination of one-dimensional convolutional neural networks, recurrent neural networks, and attentional mechanisms, which achieved high recognition accuracy in several publicly available datasets. Mingyang et al. [28] proposed a neural network based on wavelet envelope analysis, which combines discrete wavelet transform with the envelope analysis method to extract important features from EEG signals. Aayesh et al. [23] performed time domain, frequency domain and nonlinear analysis on the signal to extract pattern features; they performed feature selection on the extracted features, obtained more discriminative features, and constructed a fuzzy machine learning classifier for epileptic seizure detection.

Combining these methods, for the feature extraction of EEG signals, in this study we used the differential features of the EEG signal, the amplitude spectrum and the phase spectrum to jointly extract the features of the EEG signal. Differential feature extraction is a commonly used signal processing method that captures changes in a signal by calculating the difference between consecutive time points. In EEG signal processing, the change trend of the signal can be obtained by calculating the difference between adjacent time points, thereby extracting the differential features and capturing the instantaneous or periodic changes in the signal. Frequency domain analysis is the process of converting signals from the time domain to the frequency domain. The amplitude spectrum represents the amplitude of the signal at different frequencies, while the phase spectrum represents the phase information of the signal at different frequencies. In EEG signal processing, frequency domain analysis can help reveal the different frequency components present in the signal, such as alpha waves, beta waves, etc., as well as the phase relationship between them, and help identify activity patterns at specific frequencies in the signal, thereby better understanding and analyzing the characteristics of EEG signals. Differential feature extraction helps capture the instantaneous changes in the signal, while the amplitude spectrum and phase spectrum in the frequency domain provide information about the amplitude and phase of the signal at different frequencies. The combined use of these methods can more comprehensively describe the characteristics of EEG signals. This provides richer feature information for subsequent signal analysis and processing.

The preprocessed data uses a neural network model based on a multi-modal dual-stream network to process temporal features and spatial features, respectively. Specifically, it is divided into two streams, one for processing temporal features and the other for processing spatial features. The two streams can each adopt network structures and algorithms suitable for processing their respective characteristics, with improved processing and representation capabilities of complex signals.

The remainder of this article is organized as follows. Section 2 introduces the EEG dataset and methods. Section 3 describes the experimental procedure and results. Section 4 concludes the paper and suggests some future directions.

2. EEG Data Sets and Methods

2.1. Dataset

2.1.1. The University of Bonn Dataset

Bonn EEG Dataset is one of the public data sets widely used in the field of brain–computer interface (BCI) and neuroscience research [29]. The dataset was created by the Center for Medical Epilepsy at the University of Bonn in Germany. This data set contains EEG data from 5 healthy people and 5 epilepsy patients. It was collected using the international 10–20 system EEG acquisition system. It contains a total of 5 data subsets, namely F, S, N, Z, and O. The data are described in Table 1 and visualized in Figure 1. The Bonn data set is a single-channel data set, in which each sub-data set contains 100 data segments: the time length of each data segment is 23.6 s, the data points are 4097, and the sampling frequency is 173.61 Hz.

Table 1. Bonn EEG Dataset EEG Type.

	Healthy Control		Patients with Epilepsy		
Identifier	**Z**	**O**	**N**	**F**	**S**
State	Opened eyes	Closed eyes	Interictal period	Interictal period	Ictal period
Electrode position	Scalp	Scalp	Intracranial hippocampus	Intracranial lesion area	Intracranial lesion area

Subsets Z and O were collected from a control group of 5 healthy individuals. The clip in Z is the EEG when the subject's eyes are open, and the clip in O is the EEG when the subject's eyes are closed. Subsets N, F, and S are intracranial EEG, collected from 5 patients who were diagnosed before surgery. Subset N comes from the intracranial hippocampal formation area of the patient's interictal period. Subset N comes from the intracranial hippocampal formation area of the patient's interictal period. Subset F comes from the intracranial lesion area of the patient during the interictal period. Subset S comes from the intracranial lesion area during the patient's ictal period. In the experiment, Z, O, N, and F are regarded as one category and marked as Interictal period. E is marked Ictal period. Slice the data into a 2 s time window to obtain a single training sample.

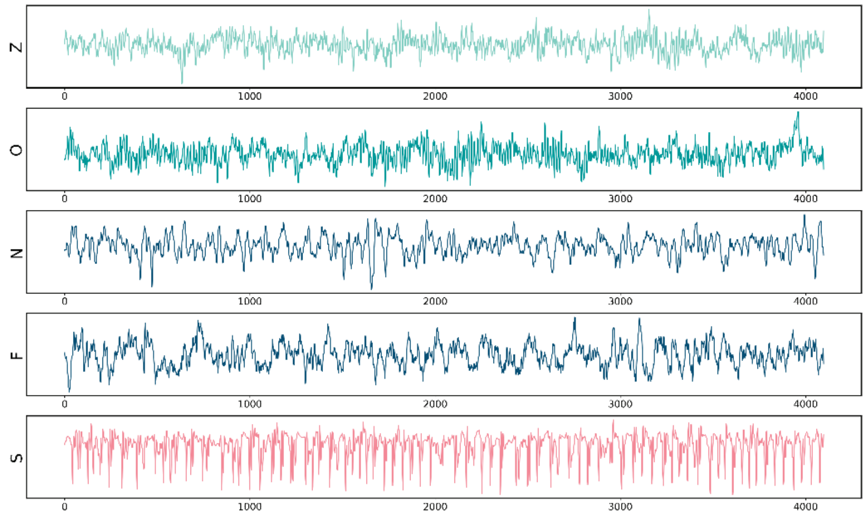

Figure 1. Bonn EEG Dataset EEG visualization.

2.1.2. New Delhi Dataset

The New Delhi dataset is a publicly available dataset created from the Center for Neurology and Sleep, Hauz Khas, New Delhi. The dataset contains EEG recordings of ten epilepsy patients [30]. Data were collected using a Grass Telefactor Comet AS40 amplification system at a sampling rate of 200 Hz. During the acquisition process, gold-coated scalp EEG electrodes were placed according to the 10–20 electrode placement system. The signal is filtered between 0.5 and 70 Hz and then divided into pre-ictal, interictal and ictal. Each category contains MAT files of 50 EEG time-series signals. The sampling frequency is 200 Hz, and each MAT file contains 1024 samples. Each sample represents a set of EEG time-series data with a duration of 5.12 s. The EEG signal is shown in Figure 2.

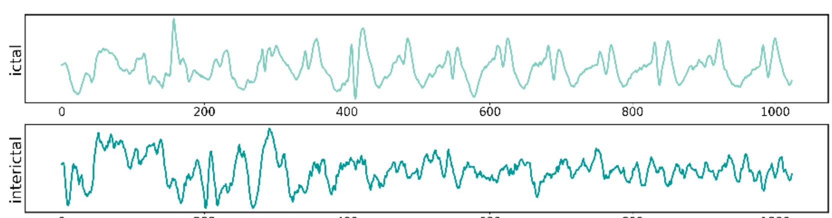

Figure 2. New Delhi EEG Dataset EEG Visualization.

2.2. Data Set Preprocessing

The EEG signal reflects the activity process of the brain. The amplitude of the EEG signal changes within the entire range of 2~100 μV, and the frequency range is 1~100 Hz. In the study, the EEG was divided into five frequency sub bands. In general, delta waves often appear in the cerebral cortex during deep sleep. Specifically, this electrical activity brain waveform with a frequency between 0.5 and 4 Hz is consistent with the deepest stage of non-rapid eye movement sleep, and is associated with an extremely relaxed and restorative state of the brain and body. In contrast, theta waves, with frequencies between 4 and 8 Hz, usually appear in the shallow stages of sleep and during meditation, reflecting a transitional state between wakefulness and sleep, involving memory and learning process. Alpha waves, with a frequency between 8 and 12 Hz, are clearly present in the cerebral cortex when a person is not stressed and calm, especially in the occipital area. This waveform is most significant when resting with eyes closed or lightly relaxed, marking a state of being awake but relaxed. The frequency of beta waves is between 12 and 30 Hz. It generally appears when the frontal lobe is excited and thinking. It is related to active cognitive activities and high concentration. It is commonly seen in problem solving, decision-making and reasoning processes. Finally, gamma waves, with frequencies above 30 Hz, typically occur when the brain feels anxious or in a state of emotional stress. Although this waveform is associated with high levels of cognitive function and information processing, in states of stress or anxiety, gamma wave activity also increases significantly [31–33].

In this study, in order to better observe the different EEG signal characteristics of patients, a signal is first converted from the time domain to the frequency domain. Its Fourier-transformed x_1 is the representation of the signal in the frequency domain, which contains the signal amplitude and phase information of x. The amplitude of the signal in the frequency domain is then calculated. By taking the absolute value of the Fourier transform result x_1, we obtain the amplitude spectrum x_2 of the signal. By taking the angle of the Fourier transform result x_1, the phase spectrum x_3 of the signal is obtained.

Finally, calculate the first-order difference x_4 and the second-order difference x_5 of the signal x. Finally, a feature matrix $[x,\ x_2,\ x_3,\ x_4,\ x_5]$ is formed with the original signal. On the other hand, the short-time Fourier transform is performed on the original signal to obtain spectrum data x_6, which contain the signal at different frequencies. The EEG processing flow is shown in Figure 3.

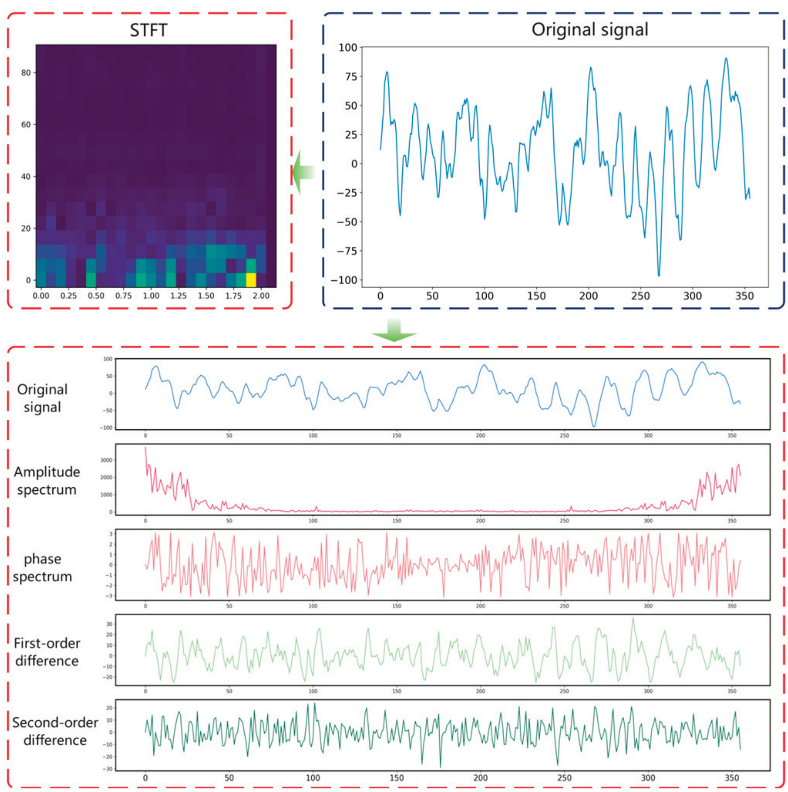

Figure 3. EEG signal processing process.

2.2.1. FFT (Fast Fourier Transform) and (Short-Time Fourier Transform) STFT

FFT functions to calculate the Discrete Fourier Transform (DFT) of the input signal x_0 [34–36]. It converts a signal from the time domain to the frequency domain and represents the signal as a collection of frequency components. The discrete form of DFT can be expressed as Formula (1), where $x[n]$ is the discrete sample of the input signal, $X[k]$ is the transformed signal, N is the number of samples of the signal, and i is the imaginary unit.

$$X[k] = \sum_{n=0}^{N-1} x[n] \times e^{-2\pi i \cdot \frac{kn}{N}} \tag{1}$$

STFT decomposes the signal into two dimensions: time and frequency. It segments the signal in time and applies Fourier transform to each time segment to obtain the representation of the signal in frequency [37]. The specific principle formula is as follows: Formula (2), where $X(t,\omega)$ is the STFT result of the time domain signal $x(t)$ at frequency ω, $w(\tau - t)$ is the window function, usually using the Hanning window and other window functions, and ω is the angular frequency.

$$X(t,\omega) = \int_{-\infty}^{\infty} x(\tau) \cdot w(\tau - t) \cdot e^{-j\omega\tau} d\tau \tag{2}$$

STFT is usually implemented through discretization, replacing continuous time and frequency with discrete time and frequency. For discrete signals, STFT can be expressed as Formula (3), where $X[m,\omega]$ is the STFT result of the discrete time-domain signal $x[n]$ at frequency ω, $w[n-m]$ is the discrete window function, and m is the time index.

$$X[m,\omega] = \sum_{n=-\infty}^{\infty} x[n] \cdot w[n-m] \cdot e^{-j\omega n} \tag{3}$$

2.2.2. First-Order Difference and Second-Order Difference

The difference operation refers to calculating the difference between each element in the array and the adjacent element to obtain a new array. When the calculation result is the difference between the current data point and the next data point, it is called the forward difference. The calculation result is a positive value, which means that the function is rising at that point; if it is a negative value, it means that the function is falling at that point. The formula for directional difference is shown as Formula (4).

$$\Delta^2 f(x) = f(x+1) - f(x) \tag{4}$$

When the calculation result is the difference between the current data point and the previous data point, it is called backward difference. When the calculated result is positive, it means that the function is rising at that point. If it is negative, it means that the function decreases at that point. The principle is shown in Formula (5).

$$\nabla^2 f(x) = f(x) - f(x-1) \tag{5}$$

First difference refers to the operation of calculating the difference between each element in a sequence and its previous element. Second-order difference refers to a new sequence obtained by performing two difference operations on a sequence. The formula of the forward second-order difference is shown in Formula (6).

$$\Delta^2 f(x) = f(x+2) - 2f(x+1) + f(x) \tag{6}$$

The formula for the backward second-order difference is shown in Formula (7).

$$\nabla^2 f(x) = f(x) - 2f(x-1) + f(x-2) \tag{7}$$

For a sequence $[a_1, a_2, a_3, \ldots, a_n]$, its first difference can be expressed as $[b_1, b_2, b_3, \ldots, b_{n-1}]$, where $b_i = a_{i+1} - a_i$; then perform a difference operation on the first-order difference sequence, and the result is the second-order difference sequence $[c_1, c_2, c_3, \ldots, c_{n-2}]$, where $c_i = b_{i+1} - b_i$.

2.3. Neural Network Module

2.3.1. One-Dimensional Convolutional Neural Network

One-dimensional convolution is often used to process time series data, using a one-dimensional convolution kernel of a specified size to perform a one-dimensional convolution operation on the input multi-channel one-dimensional input signal [38]. Assume that the size of the input is (N, C_{in}, L_{in}), where N represents the batch size, C_{in} represents the number of channels, and L_{in} represents the length of the signal sequence. The size of the output is (N, C_{out}, L_{out}), where C_{out} represents the number of output channels and L_{out} represents the length of the output signal. The operation formula is as shown in Formula (8), and $*$ represents a valid cross-correlation operator. The principle is shown in Figure 4.

$$\text{out}(N_i, C_{out_j}) = \text{bias}(C_{out_j}) + \sum_{k=0}^{C_{in}-1} \text{weight}\left(C_{out_j}, k\right) * \text{input}(N_i, k) \tag{8}$$

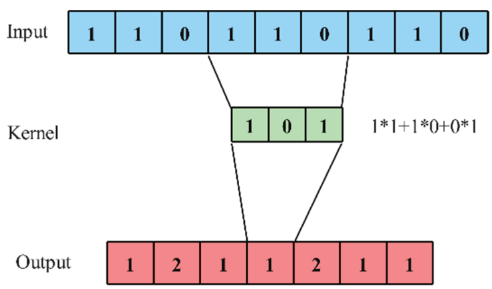

Figure 4. One-dimensional convolution principle.

2.3.2. Two-Dimensional Convolutional Neural Network

Two-dimensional convolutional layers are used to process two-dimensional input signals [39]. Assume that the size of the input is $(N, C_{in}, H_{in}, W_{in})$, where N represents the batch size, C_{in} represents the number of input channels, and H_{in} and W_{in} represent the height and width of the input image, respectively. The size of the output is $(N, C_{out}, H_{out}, W_{out})$, where C_{out} represents the number of output channels, and H_{out} and W_{out} represent the height and width of the output image, respectively. Here, $*$ represents a valid two-dimensional cross-correlation operator. The formula of two-dimensional convolutional is as shown in Formula (9). The principle is shown in Figure 5.

$$\text{out}(N_i, C_{out_j}) = \text{bias}(C_{out_j}) + \sum_{k=0}^{C_{in}-1} \text{weight}(C_{out_j}, k) * \text{input}(N_i, k) \tag{9}$$

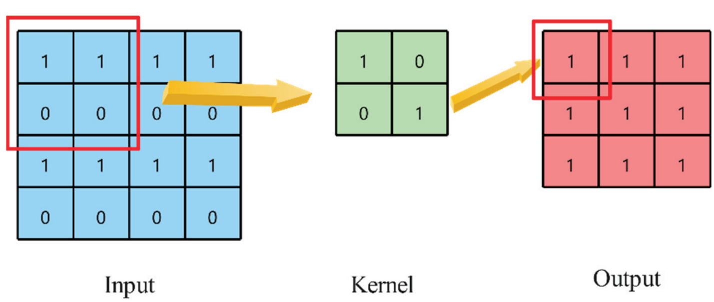

Figure 5. Two-dimensional convolution principle.

2.3.3. Long Short-Term Memory (LSTM)

LSTM is a special type of RNN. In order to solve the problems of gradient disappearance and gradient explosion that exist in traditional RNN, memory cells and gating mechanisms are introduced, which can retain old feature information in feature extraction of sequence data, thereby extracting relevant features. This achieves a better performance in data feature extraction [40]. Figure 6 below shows the network structure of LSTM.

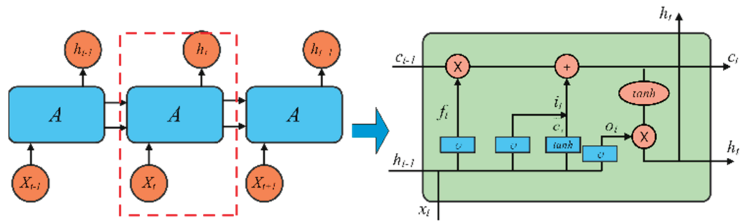

Figure 6. LSTM structure.

There are three types of gates in the LSTM gate: input gate i, forget gate f and output gate o. The input gate is used to control the update information of the storage unit. The forget gate is used to control the amount of storage unit information used at the previous moment. The output gate is used to control the amount of information output to the next hidden state. At time t, given the input vector t_x and the hidden state h_{t-1} at the previous moment, the LSTM unit calculates the hidden state h_t at the current moment through internal loops and updates, and the formula is shown in (10)–(15).

$$f_t = \sigma\left(w_{fx}x_t + w_{fh}h_{t-1} + b_f\right) \quad (10)$$

$$i_t = \sigma(w_{ix}x_t + w_{ih}h_{t-1} + b_i) \quad (11)$$

$$\widetilde{c}_t = \varphi(w_{cx}x_t + w_{ch}h_{t-1} + b_c) \quad (12)$$

$$c_t = \sigma\left(\widetilde{c}_t i_t + f_t c_{t-1}\right) \quad (13)$$

$$o_t = \sigma(w_{ox}x_t + w_{oh}h_{t-1} + b_0) \quad (14)$$

$$h_t = \varphi(c_t o_t) \quad (15)$$

Among them, w_{fx}, w_{ix}, w_{cx}, and w_{ox} represent the weight matrix between the input layer and the corresponding gate at time t. w_{fh}, w_{ih}, w_{ch}, and w_{oh} are the hidden-layer weight matrices between time values t and $t-1$, and b_f, b_i, b_c, and b_o represent the corresponding deviations. h_{t-1} and c_{t-1} are the hidden state and cell state of time value $t-1$, and i_t, f_t, and o_t are the output values of the input gate, forgetting gate and output gate respectively. c_t and h_t correspond to the cell state and hidden state at the current time t, respectively, c_t represents the temporary cell state, and φ and σ represent the tanh and sigmoid activation functions, respectively.

3. Methods

3.1. Overall Process of Detection Method of Epileptic Seizures Using a Neural Network Model Based on Multimodal Dual-Stream Networks

In order to utilize EEG signals to identify patients with epilepsy, a neural network model based on a multimodal two-stream network was adopted, with a mixed use of one-dimensional convolution, two-dimensional convolution and the LSTM neural network to extract the spatial characteristics of EEG and the temporal characteristics of the signal, respectively. Combining the advantages of the two networks can more comprehensively extract EEG features. This method includes the following steps.

A. Data preparation: obtain and prepare Bonn and New Delhi datasets for experiments; these contain EEG signal data on epileptic seizures.
B. Feature extraction: Preprocess the original EEG signal, including filtering and noise removal. Extract the differential characteristics of the signal, the amplitude spectrum and the phase spectrum in the frequency domain to form a two-dimensional feature vector.
C. Establish a multi-modal dual-stream network model: Design and build a multi-modal dual-stream network model, combining one-dimensional convolution, two-dimensional convolution and the LSTM neural network. The first-class network is used to extract the spatial features of the EEG two-dimensional vector, while the other-stream network focuses on extracting the temporal features of the signal. Utilizing a hybrid neural network structure, temporal and spatial features are simultaneously extracted from signals to enhance recognition performance. A channel attention module is introduced to improve the model's attention to features related to epileptic seizures.
D. Experiment: The Bonn and New Delhi data sets are divided into training sets, validation sets and test sets. Train, validate, and test the model to evaluate its performance. The performance of the model on the epileptic seizure detection task was evaluated using accuracy, recall, precision, and F1 score.
E. Result analysis: analyze the experimental results and compare the performance differences between the proposed model and the baseline model.

3.2. Neural Network Model Based on Multimodal Dual-Stream Networks

Based on one-dimensional convolution, two-dimensional convolution and LSTM modules, we designed a neural network model of a multi-modal two-stream network to solve the epileptic seizure detection task. The architecture of the model is as follows.

Time-series signal processing flow:

A. Input: 5×356 time-series signal, including original signal, first-order difference, second-order difference, amplitude spectrum and phase spectrum in frequency domain.
B. Processed through three one-dimensional convolution modules, a 256×356 feature vector y_1 is output.
C. Perform batch normalization and ReLU activation function on y_1, and then add it to the feature vector y_2 processed by a one-dimensional convolution module to obtain y_3.
D. Input y1 into the LSTM network to obtain a 356×4 output feature vector y_4.

STFT matrix processing flow:

A. Input: STFT matrix of the original signal.
B. Processed through three two-dimensional convolution modules, batch normalization and ReLU activation function, a $256 \times 11 \times 18$ feature matrix y_5 is obtained.

Feature fusion and classification:

A. Flatten y_3, y_4, and y_5 and concatenate them into one eigenvector.
B. Output the feature vector to the fully connected layer and output the classification probability through softmax.

Based on EEG signals, the model fuses features from time series signals and STFT matrices, uses one-dimensional convolution, two-dimensional convolution, and LSTM modules to extract temporal and spatial features, respectively, and performs classification through fully connected layers to achieve automatic epileptic seizure detection. The network structure is shown in Figure 7.

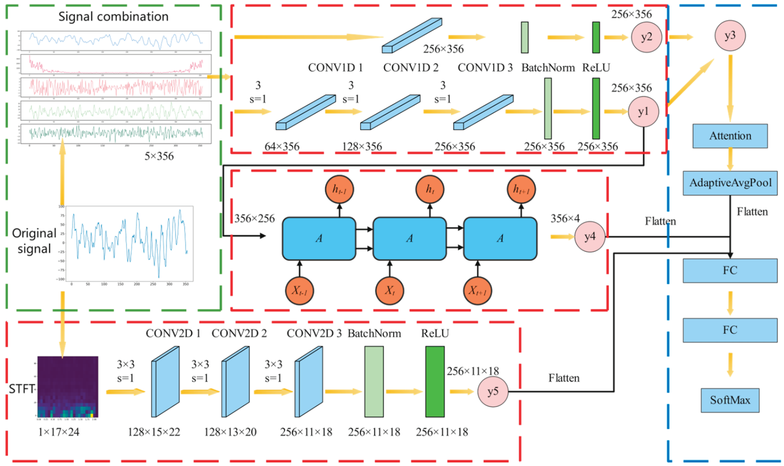

Figure 7. The overall process involved in the detection method for epileptic seizures.

4. Experimental Results and Analysis

The hardware devices used in this article are Inter i7 13700k and Nvidia RTX4080, Intel i7-13700K, is sourced from Intel Corporation, which is headquartered in Santa Clara, CA, USA. Nvidia RTX 4080 is sourced from Nvidia Corporation, which is headquartered in Santa Clara, CA, USA. These two devices have high-performance processing capabilities and can meet complex computing needs. The ratio of training set, validation set and test set is set to 8:1:1. The software environment used is Python 3.8. Using accuracy, recall rate, and *F*1-*score* as the evaluation criteria of the model, these three indicators reflect the prediction ability, coverage ability, and comprehensive ability of the model, respectively.

Precision refers to the proportion of samples that are actually positive samples among all the samples that are predicted to be positive. The calculation formula is as shown in Formula (16), where TP represents true examples, TN represents true counterexamples, FP represents a false positive example, and FN represents a false negative example.

$$precision = \frac{TP}{TP + FP} \tag{16}$$

Recall refers to the proportion of samples that are successfully predicted as positive samples among all positive samples. The calculation formula is shown as Formula (17).

$$recall = \frac{TP}{TP + FN} \tag{17}$$

*F*1-*score* represents the balance between *precision* and *recall*, and the calculation formula is shown as Formula (18).

$$f1{-}score = \frac{2 \times precision \times recall}{precision + recall} \tag{18}$$

Use a confusion matrix to place the predicted results and true results of all categories into the same table by category. In this table, there are the number of correct identifications and the number of incorrect identifications for each category. Cluster analysis of data can better observe experimental results, find out the relationship between various categories, and make the data concise. t-SNE technology can reduce the dimensionality of high-dimensional data in the CNN fully connected layer to two dimensions, so that we can intuitively judge the performance of the current model [41].

4.1. Bonn Dataset

In the EEG data from the University of Bonn, we treat Z, O, N and F as one category, labeled as the interictal period. The E mark indicates the ictal period. Then, we use the proposed neural network model for training. The experiment is divided into two phases: the training phase and testing phase.

In the training phase, we trained for 30 epochs. Finally, on the validation set, we achieved an accuracy of 99.2% with a loss function of 0.03082. Cross-validation is a method used to observe the stability of the model. We divide the data into n parts, use one part as the test set, one part as the validation set, and the other n − 2 parts as the training set, and calculate multiple times. The accuracy of the model is used to evaluate the average accuracy of the model, as shown in Equation (19).

$$p = \frac{1}{10}\sum\nolimits_{i=1}^{10} p_i \tag{19}$$

where p refers to the accuracy obtained by each verification. After cross-validation, the average accuracy decreased slightly, and an accuracy of 98.55% was obtained.

In addition, we also conducted ablation experiments, removing the LSTM module and two-dimensional convolution module of the network, and removing both the LSTM and two-dimensional convolution modules to verify the effectiveness of the network. The results are shown in Figures 8 and 9.

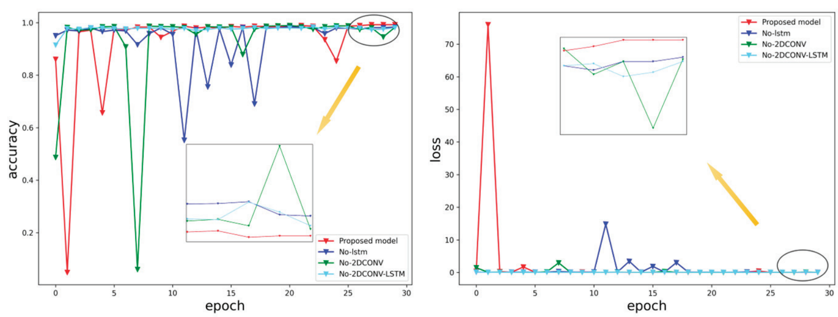

Figure 8. The training accuracy and loss function of the proposed network, as well as the removal of the LSTM module, the removal of the two-dimensional convolution module, and the accuracy and loss functions of the ablation experiment in the Bonn data set by removing the LSTM and two-dimensional convolution module at the same time.

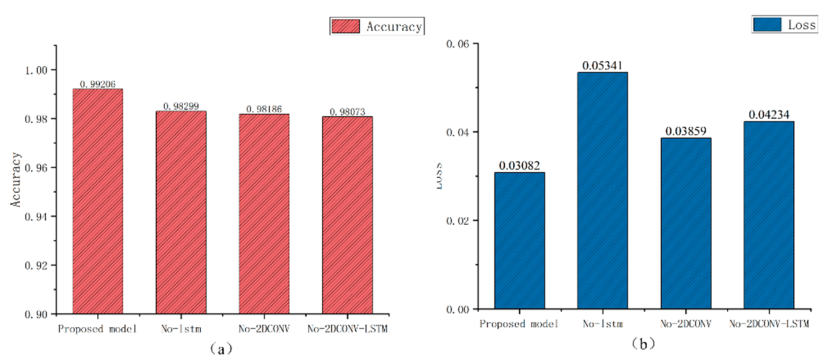

Figure 9. The proposed network removes the LSTM module, removes the two-dimensional convolution module, and simultaneously removes the LSTM and two-dimensional convolution module. Ablation experimental performance on the Bonn dataset: (**a**) highest training accuracy (**b**) loss function.

The results of the training phase:

A. Remove the LSTM module: the accuracy is 98.2%, and the loss function is 0.05341.
B. Remove the two-dimensional convolution module: the accuracy is 98.1%, and the loss function is 0.03859.
C. Remove the LSTM and two-dimensional convolution modules at the same time: the accuracy is 98%, and the loss function is 0.04234.

The combination of multiple modules has the advantage of better extracting the characteristics of EEG signals.

In the testing phase, the performance of the saved network model was tested using the test set and evaluated using precision, recall, and F1 scores. Finally, on the test set, the accuracy of our proposed network model was 0.9969, precision was 0.9944, recall was 1, and *F*1-*score* was 0.9972. In the ablation experiment, the LSTM module and two-dimensional convolution module of the network were removed respectively, and the accuracy, recall rate, and *F*1-*score* results of removing the LSTM and two-dimensional convolution module at the same time are shown in Figure 10.

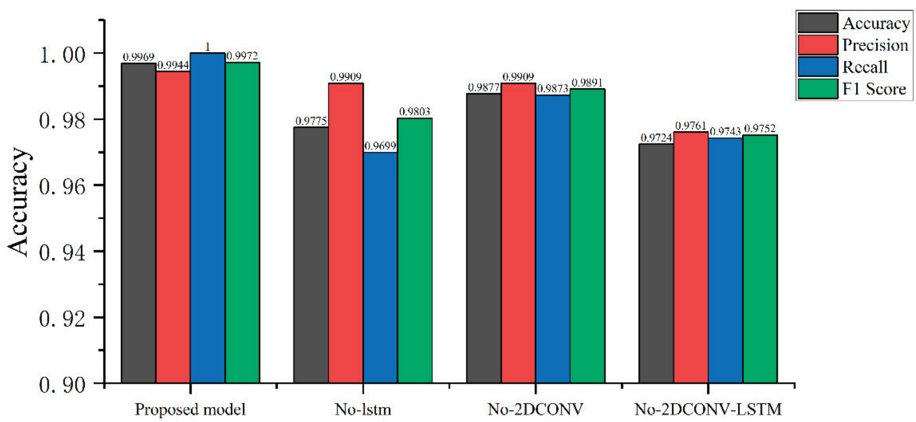

Figure 10. The proposed network removes the LSTM module, removes the two-dimensional convolution module, and simultaneously removes the LSTM and two-dimensional convolution modules in the Bonn test set ablation experiment. *Accuracy*, *precision*, *recall*, and *F*1-*score* are shown.

A. Remove the LSTM module: accuracy 0.9775, *precision* 0.9909, *recall* 0.9699, *F*1-*score* 0.9803.
B. Remove the two-dimensional convolution module: *accuracy* 0.9877, *precision* 0.9909, *recall* 0.9873, *F*1-*score* 0.9891.
C. Remove the LSTM and two-dimensional convolution modules at the same time: *accuracy* 0.9724, *precision* 0.9761, *recall* 0.9743, *F*1-*score* 0.9752.

In the test set, the neural network combined with one-dimensional convolution, two-dimensional convolution and the LSTM multi-module achieved greater performance advantages in the face of test data that did not appear during the training process, which shows that multi-modal feature extraction is more conducive to improving the generalization ability of the model.

Finally, the confusion matrix and t-SNE are used to visualize the predicted distribution of the test data. Figure 11 contains the confusion matrices of four different models, namely, the proposed model, No-lstm, No-2DCONV and No-2DCONV-LSTM. Each confusion matrix shows the classification results between two categories (interictal and ictal), including true examples, false-positive examples, true-negative examples, and false-negative examples. Each confusion matrix represents different classification situations with different colors, and darker colors represent higher numbers. The model proposed in this article has obtained the best classification effect.

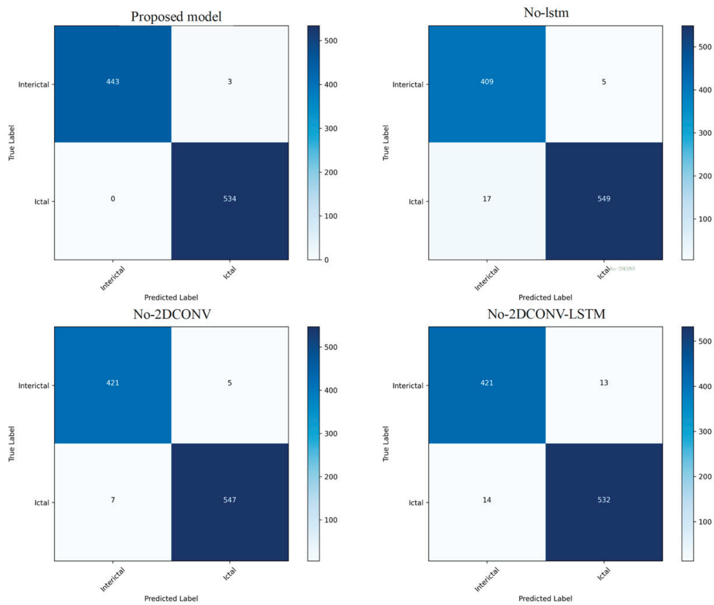

Figure 11. The proposed network, the LSTM module is removed, the two-dimensional convolution module is removed, and the LSTM and two-dimensional convolution modules are removed at the same time, and the confusion matrix of the Bonn test set ablation experiment is shown.

Figure 12 of t-SNE shows the clustering of data for four different models. Each subgraph has two colors of points, representing two different types of data. The proposed model has the least confounded classification results between the two categories (interictal and ictal).

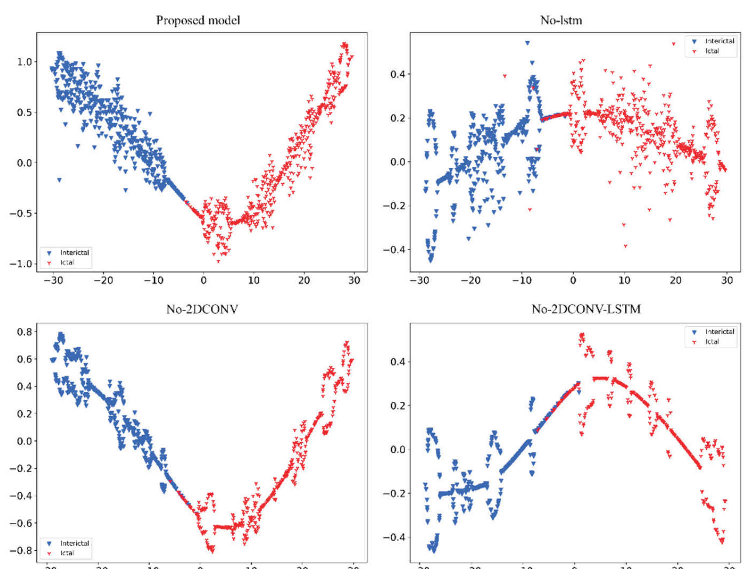

Figure 12. The proposed network removes the LSTM module, removes the two-dimensional convolution module, removes both the LSTM and the two-dimensional convolution module, and performs cluster analysis on the Bonn test set ablation experiment.

4.2. New Delhi Dataset

In order to verify the effectiveness and generalization ability of the proposed network, the public New Delhi dataset was used to verify the model performance. In the EEG data of New Delhi, we used two categories of EEG data: interictal and ictal. The experiment is divided into two phases: the training phase and testing phase. In the training phase, 30 epochs were trained. The accuracy and loss functions in the training phase are shown in the figure. The final accuracy is 1 and the loss function is 6.71×10^{-8}. The results are shown in Figure 13.

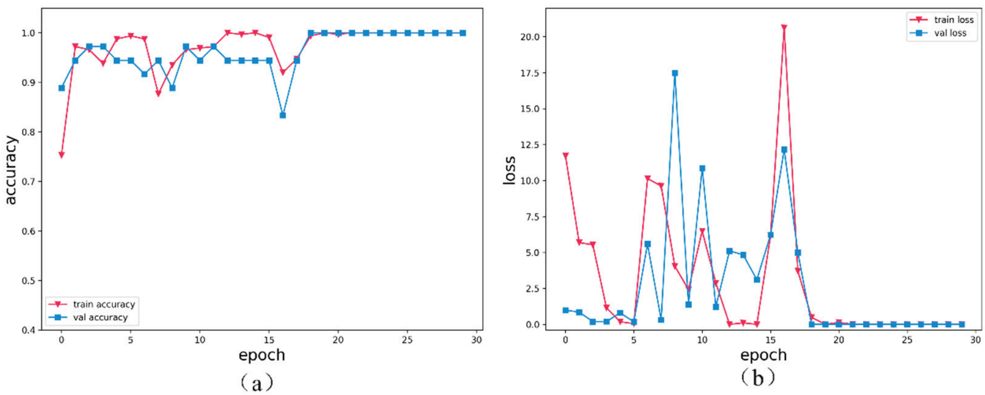

Figure 13. Performance of the proposed network on the New Delhi dataset: (**a**) accuracy (**b**) loss function.

On the test set, the obtained *accuracy* is 0.975, *precision* is 0.9444, *recall* is 1, and *F*1-*score* is 0.9714. The confusion matrix and cluster analysis are shown in Figure 14. It can be seen that the proposed model still has good accuracy when training and predicting using a new EEG data set without changing the network structure, verifying the improvement in the effectiveness and generalization ability of the model.

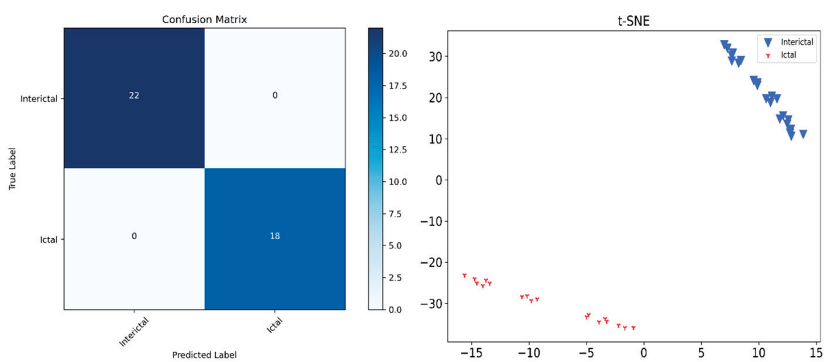

Figure 14. Confusion matrix and cluster analysis of the proposed network on New Delhi dataset.

4.3. Comparison and Discussion with Related Studies

A seizure detection method based on multimodal two-stream networks is proposed and validated using the widely recognized University of Bonn dataset, as shown in Table 2. Compared with the existing methods, the proposed method outperforms the existing methods in all main performance metrics [42]. Richhariya and Tanveer [15] used PCA, ICA and DWT to achieve an accuracy of 99.0%. Li et al.'s [28] method based on wavelet envelope analysis achieved an accuracy of 98.8%. Shen et al. [43] adopted the methods of discrete wavelet transform and support vector machine and achieved an accuracy of 97%

and a sensitivity of 96.67%, while Xu et al. [44] used the 1D CNN-LSTM method to improve *accuracy*, *precision*, *recall* and *F*1-*score*, respectively, reaching 99.39%, 98.39%, 98.79% and 98.59%. In contrast, the multi-modal dual-stream network method we proposed achieved an *accuracy* of 99.69%, a *precision* of 99.44%, a *recall* of 99.00%, and an *F*1-*score* of 99.72%. These results show that our method not only achieves the highest value in accuracy, but also significantly outperforms existing methods in key performance indicators such as *precision*, *recall*, and *F*1-*score*. This further verifies the effectiveness of the multi-modal dual-stream network in processing complex data features and identifying samples of different categories. Future research can further optimize the model structure and try to verify its generality and robustness on more diverse data sets.

Table 2. Comparison and discussion with related studies.

Authors	Modeling Method	Dataset	Performance Metrics
Richhariya and Tanveer [15]	PCA, ICA and DWT	University of Bonn	*Accuracy* 99.0%
Li et al. [28]	Wavelet-based envelope analysis	University of Bonn	*Accuracy* 98.8%
Shen et al. [43]	Discrete wavelet transform and support vector machine	University of Bonn	*Accuracy* 97%, *sensitivity* 96.67%
Xu et al. [44]	1D CNN-LSTM	University of Bonn	*Accuracy* 99.39%, *Precision* 98.39%, *Recall* 98.79%, *F*1-*score* 98.59%
Proposed method	Multimodal dual-stream networks	University of Bonn	*Accuracy* 99.69%, *Precision* 99.44%, *Recall* 1%, *F*1-*score* 99.72%

5. Conclusions

This paper studies the application of hybrid neural network models in epilepsy diagnosis using EEG signals. First, the complexity features of the EEG signal are extracted using various feature methods such as signal differential features, frequency domain amplitude spectrum and phase spectrum, etc., to form a two-dimensional time-series signal and two-dimensional spectrum features. In terms of network models, in order to extract the characteristics of EEG signals in multiple dimensions, three network structures are used, namely, one-dimensional convolution, two-dimensional convolution and lstm. Through the combination of multiple network structures, the multi-dimensional characteristics of EEG signals are trained. Finally, experiments were conducted on the public Bonn and New Delhi datasets to evaluate the effectiveness of the proposed model using indicators such as precision, recall, F1 score, etc. Finally, the test set results were analyzed using the confusion matrix and t-SNE. Our research results prove that the proposed network model achieved the best diagnostic effect in the experiment, with an *accuracy* of 0.9969, *precision* of 0.9944, *recall* of 1, and *F*1 *score* of 0.9972. Even after changing the data set, the hybrid mesh wheel still has the most stable classification performance and can achieve high accuracy in the diagnosis of epilepsy. This article provides a hybrid neural network model based on EEG for EEG signal epilepsy diagnosis, and uses a variety of feature extraction methods to provide a useful reference for the early detection and treatment of epilepsy.

Author Contributions: Conceptualization and revision: H.W. and F.L.; methodology: B.W. and Y.X.; formal analysis: S.P.; writing—original draft preparation: B.W. and Y.X.; Writing—review and editing: B.W. and Y.X. All authors have read and agreed to the published version of the manuscript.

Funding: This research received no external funding.

Institutional Review Board Statement: Not applicable.

Informed Consent Statement: Not applicable.

Data Availability Statement: The publicly available datasets used in this paper are from the Bonn Epilepsy Dataset (https://repositori.upf.edu/handle/10230/42894), accessed on 1 November 2023. The Center for Neurology and Sleep at Hauz Khas, New Delhi (https://www.researchgate.net/publication/308719109_EEG_Epilepsy_Datasets), accessed on 1 November 2023.

Conflicts of Interest: The authors declare no conflicts of interest.

References

1. Deivasigamani, S.; Senthilpari, C.; Wong, H.Y. Computer Aided Automatic Detection and Classification of EEG Signals for Screening Epilepsy Disorder. *J. Inf. Sci. Eng.* **2018**, *34*, 687–700.
2. Lasefr, Z.; Elleithy, K.; Reddy, R.R.; Abdelfattah, E.; Faezipour, M. An Epileptic Seizure Detection Technique Using EEG Signals with Mobile Application Development. *Appl. Sci.* **2023**, *13*, 9571. [CrossRef]
3. Fatma, N.; Singh, P.; Siddiqui, M.K. Survey on Epileptic Seizure Detection on Varied Machine Learning Algorithms. *Int. J. Image Graph.* **2023**, 2550013. [CrossRef]
4. Harikumar, R.; Babu, C.G.; Shankar, M.G. Extreme Learning Machine (ELM) based Performance Analysis and Epilepsy Identification from EEG Signals. *Iete J. Res.* **2021**, *69*, 6304–6314. [CrossRef]
5. Ibrahim, S.; Djemal, R.; Alsuwailem, A. Electroencephalography (EEG) signal processing for epilepsy and autism spectrum disorder diagnosis. *Biocybern. Biomed. Eng.* **2018**, *38*, 16–26. [CrossRef]
6. Iranmanesh, S.; Raikos, G.; Imtiaz, S.A.; Rodriguez-Villegas, E. A Seizure-Based Power Reduction SoC for Wearable EEG in Epilepsy. *IEEE Access* **2019**, *7*, 151682–151691. [CrossRef]
7. Khan, K.A.; Shanir, P.P.; Khan, Y.U.; Farooq, O. A hybrid Local Binary Pattern and wavelets based approach for EEG classification for diagnosing epilepsy. *Expert Syst. Appl.* **2020**, *140*, 112895. [CrossRef]
8. Kumar, G.; Chander, S.; Almadhor, A. An intelligent epilepsy seizure detection system using adaptive mode decomposition of EEG signals. *Phys. Eng. Sci. Med.* **2022**, *45*, 261–272. [CrossRef] [PubMed]
9. Murariu, M.G.; Dorobantu, F.R.; Tarniceriu, D. A Novel Automated Empirical Mode Decomposition (EMD) Based Method and Spectral Feature Extraction for Epilepsy EEG Signals Classification. *Electronics* **2023**, *12*, 1958. [CrossRef]
10. Sikdar, D.; Roy, R.; Mahadevappa, M. Epilepsy and seizure characterisation by multifractal analysis of EEG subbands. *Biomed. Signal Process. Control* **2018**, *41*, 264–270. [CrossRef]
11. Sunaryono, D.; Sarno, R.; Siswantoro, J. Gradient boosting machines fusion for automatic epilepsy detection from EEG signals based on wavelet features. *J. King Saud Univ.-Comput. Inf. Sci.* **2022**, *34*, 9591–9607. [CrossRef]
12. Ai, G.P.; Zhang, Y.J.; Wen, Y.Z.; Gu, M.H.; Zhang, H.H.; Wang, P.J. Convolutional neural network-based lightweight hardware IP core design for EEG epilepsy prediction. *Microelectron. J.* **2023**, *137*, 105810. [CrossRef]
13. Ficici, C.; Telatar, Z.; Erogul, O. Automated temporal lobe epilepsy and psychogenic nonepileptic seizure patient discrimination from multichannel EEG recordings using DWT based analysis. *Biomed. Signal Process. Control* **2022**, *77*, 103755. [CrossRef]
14. Gangstad, S.W.; Mikkelsen, K.B.; Kidmose, P.; Tabar, Y.R.; Weisdorf, S.; Lauritzen, M.H.; Hemmsen, M.C.; Hansen, L.K.; Kjaer, T.W.; Duun-Henriksen, J. Automatic sleep stage classification based on subcutaneous EEG in patients with epilepsy. *Biomed. Eng. Online* **2019**, *18*, 106.
15. Ghazali, S.M.; Alizadeh, M.; Mazloum, J.; Baleghi, Y. Modified binary salp swarm algorithm in EEG signal classification for epilepsy seizure detection. *Biomed. Signal Process. Control* **2022**, *78*, 103858.
16. Gu, Y.; Cleeren, E.; Dan, J.; Claes, K.; Van Paesschen, W.; Van Huffel, S.; Hunyadi, B. Comparison between Scalp EEG and Behind-the-Ear EEG for Development of a Wearable Seizure Detection System for Patients with Focal Epilepsy. *Sensors* **2018**, *18*, 29. [CrossRef]
17. Gaurav, G.; Shukla, R.; Singh, G.; Sahani, A.K. A Machine Learning Approach to the Smartwatch-based Epileptic Seizure Detection System. *IETE J. Res.* **2022**, 1–13. [CrossRef]
18. Gini, A.T.P.; Queen, M.P.F. Epileptic seizure detection in EEG using improved entropy. *Int. J. Biomed. Eng. Technol.* **2020**, *33*, 325–345. [CrossRef]
19. Hussein, R.; Elgendi, M.; Wang, Z.J.; Ward, R.K. Robust detection of epileptic seizures based on L1-penalized robust regression of EEG signals. *Expert Syst. Appl.* **2018**, *104*, 153–167. [CrossRef]
20. Majzoub, S.; Fahmy, A.; Sibai, F.; Diab, M.; Mahmoud, S. Epilepsy Detection with Multi-channel EEG Signals Utilizing AlexNet. *Circuits Syst. Signal Process.* **2023**, *42*, 6780–6797. [CrossRef]
21. Sidaoui, B.; Sadouni, K. Epilepsy Seizure Prediction from EEG Signal Using Machine Learning Techniques. *Adv. Electr. Comput. Eng.* **2023**, *23*, 47–54. [CrossRef]
22. Vani, S.; Suresh, G.R.; Balakumaran, T.; Ashawise, C.T. EEG Signal Analysis for Automated Epilepsy Seizure Detection Using Wavelet Transform and Artificial Neural Network. *J. Med. Imaging Health Inform.* **2019**, *9*, 1301–1306. [CrossRef]
23. Aayesh; Qureshi, M.B.; Afzaal, M.; Qureshi, M.S.; Gwak, J. Fuzzy-Based Automatic Epileptic Seizure Detection Framework. *CMC-Comput. Mater. Contin.* **2022**, *70*, 5601–5630. [CrossRef]
24. Glory, H.A.; Vigneswaran, C.; Jagtap, S.S.; Shruthi, R.; Hariharan, G.; Sriram, V.S.S. AHW-BGOA-DNN: A novel deep learning model for epileptic seizure detection. *Neural Comput. Appl.* **2021**, *33*, 6065–6093. [CrossRef]

25. Chen, Z.X.; Lu, G.L.; Xie, Z.H.; Shang, W. A Unified Framework and Method for EEG-Based Early Epileptic Seizure Detection and Epilepsy Diagnosis. *IEEE Access* **2020**, *8*, 20080–20092. [CrossRef]
26. Dang, W.D.; Lv, D.M.; Rui, L.G.; Liu, Z.A.; Chen, G.R.; Gao, Z.K. Studying Multi-Frequency Multilayer Brain Network via Deep Learning for EEG-Based Epilepsy Detection. *IEEE Sens. J.* **2021**, *21*, 27651–27658. [CrossRef]
27. Lebal, A.; Moussaoui, A.; Rezgui, A. Epilepsy-Net: Attention-based 1D-inception network model for epilepsy detection using one-channel and multi-channel EEG signals. *Multimed. Tools Appl.* **2023**, *82*, 17391–17413. [CrossRef]
28. Li, M.Y.; Chen, W.Z.; Zhang, T. Classification of epilepsy EEG signals using DWT-based envelope analysis and neural network ensemble. *Biomed. Signal Process. Control* **2017**, *31*, 357–365. [CrossRef]
29. Andrzejak, R.G.; Lehnertz, K.; Mormann, F.; Rieke, C.; David, P.; Elger, C.E. Indications of nonlinear deterministic and finite-dimensional structures in time series of brain electrical activity: Dependence on recording region and brain state. *Phys. Rev. E* **2001**, *64*, 061907. [CrossRef]
30. Swami, P.; Panigrahi, B.; Nara, S.; Bhatia, M.; Gandhi, T. EEG Epilepsy Datasets. 2016. Available online: https://www.researchgate.net/publication/308719109_EEG_Epilepsy_Datasets (accessed on 28 February 2024).
31. Tsipouras, M. Spectral information of EEG signals with respect to epilepsy classification. *Eurasip J. Adv. Signal Process.* **2019**, *2019*, 10. [CrossRef]
32. Lenkov, D.N.; Volnova, A.B.; Pope, A.R.D.; Tsytsarev, V. Advantages and limitations of brain imaging methods in the research of absence epilepsy in humans and animal models. *J. Neurosci. Methods* **2013**, *212*, 195–202. [CrossRef] [PubMed]
33. Hussain, I.; Hossain, M.A.; Jany, R.; Bari, M.A.; Uddin, M.; Kamal, A.R.M.; Ku, Y.; Kim, J.S. Quantitative evaluation of EEG-biomarkers for prediction of sleep stages. *Sensors* **2022**, *22*, 3079. [CrossRef]
34. Samiee, K.; Kovács, P.; Gabbouj, M. Epileptic Seizure Classification of EEG Time-Series Using Rational Discrete Short-Time Fourier Transform. *IEEE Trans. Biomed. Eng.* **2015**, *62*, 541–552. [CrossRef] [PubMed]
35. San-Segundo, R.; Gil-Martín, M.; D'Haro-Enríquez, L.F.; Pardo, J.M. Classification of epileptic EEG recordings using signal transforms and convolutional neural networks. *Comput. Biol. Med.* **2019**, *109*, 148–158. [CrossRef] [PubMed]
36. Sonmezocak, T.; Guler, G.; Yildiz, M. Classification of Resampled Pediatric Epilepsy EEG Data Using Artificial Neural Networks with Discrete Fourier Transforms. *Elektron. Ir Elektrotechnika* **2023**, *29*, 19–25. [CrossRef]
37. Shayeste, H.; Asl, B.M. Automatic seizure detection based on Gray Level Co-occurrence Matrix of STFT imaged-EEG. *Biomed. Signal Process. Control* **2023**, *79*, 104109. [CrossRef]
38. Tahir, M.; Halim, Z.; Waqas, M.; Sukhia, K.N.; Tu, S.S. Emotion detection using convolutional neural network and long short-term memory: A deep multimodal framework. *Multimed. Tools Appl.* **2023**, *83*, 53497–53530. [CrossRef]
39. Do, N.T.; Kim, S.H.; Yang, H.J.; Lee, G.S.; Yeom, S. Context-Aware Emotion Recognition in the Wild Using Spatio-Temporal and Temporal-Pyramid Models. *Sensors* **2021**, *21*, 2344. [CrossRef]
40. Graves, A.; Graves, A. Long short-term memory. In *Supervised Sequence Labelling with Recurrent Neural Networks*; Springer: Berlin/Heidelberg, Germany, 2012; pp. 37–45.
41. Han, X.; Ghaemi, M.S.; Ando, K.; Einhaus, J.; Wong, R.J.; Stevenson, D.K.; Gaudilliere, B. Differential dynamics of the maternal immune system in healthy pregnancy and preeclampsia. *Front. Immunol.* **2019**, *10*, 450842. [CrossRef]
42. Riccio, C.; Martone, A.; Zazzaro, G.; Pavone, L. Training Datasets for Epilepsy Analysis: Preprocessing and Feature Extraction from Electroencephalography Time Series. *Data* **2024**, *9*, 61. [CrossRef]
43. Shen, M.; Wen, P.; Song, B.; Li, Y. An EEG based real-time epilepsy seizure detection approach using discrete wavelet transform and machine learning methods. *Biomed. Signal Process. Control* **2022**, *77*, 103820. [CrossRef]
44. Xu, G.; Ren, T.; Chen, Y.; Che, W. A One-Dimensional CNN-LSTM Model for Epileptic Seizure Recognition Using EEG Signal Analysis. *Front. Neurosci.* **2020**, *14*, 578126. [CrossRef]

sensors

MDPI

Article

An Innovative EEG-Based Pain Identification and Quantification: A Pilot Study

Colince Meli Segning [1,2], Rubens A. da Silva [2,3] and Suzy Ngomo [2,*]

1 Department of Applied Sciences, UQAC (Université du Québec à Chicoutimi), Chicoutimi, QC G7H 2B1, Canada; colince.meli-segning1@uqac.ca
2 Biomechanical and Neurophysiological Research Laboratory in Neuro-Musculoskeletal Rehabilitation (Lab BioNR), Department of Health Sciences, UQAC (Université du Québec à Chicoutimi), Chicoutimi, QC G7H 2B1, Canada; rdsilva@uqac.ca
3 Centre Intégré de Santé et Services Sociaux du Saguenay-Lac-Saint-Jean (CIUSSS SLSJ), Specialized Geriatrics Rehabilitation Services at the La Baie Hospital, CIUSSS-SLSJ, Saguenay, QC G7H 7K9, Canada
* Correspondence: suzy_ngomo@uqac.ca; Tel.: +1-418-545-5011 (ext. 5404)

Abstract: Objective: The present pilot study aimed to propose an innovative scale-independent measure based on electroencephalographic (EEG) signals for the identification and quantification of the magnitude of chronic pain. Methods: EEG data were collected from three groups of participants at rest: seven healthy participants with pain, 15 healthy participants submitted to thermal pain, and 66 participants living with chronic pain. Every 30 s, the pain intensity score felt by the participant was also recorded. Electrodes positioned in the contralateral motor region were of interest. After EEG preprocessing, a complex analytical signal was obtained using Hilbert transform, and the upper envelope of the EEG signal was extracted. The average coefficient of variation of the upper envelope of the signal was then calculated for the beta (13–30 Hz) band and proposed as a new EEG-based indicator, namely Piq_β, to identify and quantify pain. Main results: The main results are as follows: (1) A Piq_β threshold at 10%, that is, $Piq_\beta \geq 10\%$, indicates the presence of pain, and (2) the higher the Piq_β (%), the higher the extent of pain. Conclusions: This finding indicates that Piq_β can objectively identify and quantify pain in a population living with chronic pain. This new EEG-based indicator can be used for objective pain assessment based on the neurophysiological body response to pain. Significance: Objective pain assessment is a valuable decision-making aid and an important contribution to pain management and monitoring.

Keywords: quantification of pain; EEG signal; pain identification and quantification indicator (Piq); beta EEG frequency band; electrodes on contralateral motor regions

Citation: Segning, C.M.; da Silva, R.A.; Ngomo, S. An Innovative EEG-Based Pain Identification and Quantification: A Pilot Study. *Sensors* **2024**, *24*, 3873. https://doi.org/10.3390/s24123873

Academic Editors: Yifan Zhao, Hua-Liang Wei, Yuzhu Guo and Fei He

Received: 22 May 2024
Revised: 10 June 2024
Accepted: 11 June 2024
Published: 14 June 2024

1. Introduction

Background: Chronic pain continues to be a global public health issue, with an estimated prevalence of approximately 30% in adults worldwide [1–3]. Among other issues related to this important global health problem, assessing chronic pain remains a challenge. Traditionally, pain assessment relies on hetero- or self-reported pain [4–6]. Although verbal description is only one of several behaviors to express pain, these possibilities for assessing chronic pain unfortunately lose all their robustness when it comes to people who have difficulty expressing themselves, such as the older, those with cognitive disorders, or those suffering from a psychological disorder [7,8]. This is why our research over the last few years has aimed towards a proposal for pain assessment, which is not based on the verbal or behavioral expression of pain. It is consensual that the experience of pain is related to alterations in brain excitability [9,10]. Specifically, motor regions seem to be largely involved, even though the underlying neurological mechanisms still need to be clarified [11,12]. Therefore, our proposal echoes the community's understanding of the mechanisms involved in the production and maintenance of pain. The relationship between beta band activity and pain perception is supported by previous research indicating that beta oscillations are involved in sensory and motor processing, which are crucial in the experience of pain [13–15]. Beta band activity is often found to be altered in conditions of pain, reflecting changes in cortical excitability. For example, Teixeira et al. [16] recently evaluated beta (β) oscillations as a potential objective marker for pain assessment. Twelve adult right-handed males with chronic neuropathic pain and 10 matched controls participated in this pilot study. Participants underwent pain assessment using a visual analog scale. The authors then calculated the global power spectrum within the low beta frequency sub-band (13–20 Hz) and the high beta frequency sub-band (20–30 Hz). Their results showed that the global power spectrum was significantly lower in patients compared to controls. Additionally, the visual analog scale for pain was negatively correlated with the global power spectrum in both the low beta ($R = -0.931$, $p = 0.007$) and high beta bands ($R = -0.805$; $p = 0.053$). We recently (2022) published a proof-of-concept paper for pain identification, based on brain signal activity, collected via electroencephalography (EEG) [17], with a small homogeneous sample of participants living with moderate chronic pain ($n = 4$). EEG signal collection was conducted in two parts: (1) at rest and (2) in the active state, that is, participants executing a visuo-motor task, and three frequency bands (alpha (8–13 Hz), beta (13–30 Hz), and gamma (30–43 Hz)) were analyzed. The results showed that beta band measurements at rest offered better results in the pain condition tested, that is, in moderate pain status. Currently, our research team is interested in better generalizing these data to different pain contexts: tonic pain induced by capsaicin cream and induced by thermal pain and in a real chronic pain condition. This demonstration contributes to testing our algorithm's sensitivity to deliver meaningful results in real-life chronic pain conditions in real patients. The literature, along with our own observations, indicates that the beta band is the most appropriate for studying pain identification and quantification. Consequently, the present work has been conducted with data collected in this frequency band.

Objective: The goal of this pilot study was to propose an innovative scale-independent measure for pain identification and quantification based on an analysis of the envelope of the EEG signal [18–20]. Specifically, the objectives achieved were: (1) developing a methodological approach for identifying and quantifying pain in real-world settings; (2) quantifying a threshold to detect the presence of pain; (3) analyzing the relationship between the new EEG-based indicator and self-reported pain, assessed using a verbal numerical rating scale (VNRS); and (4) examining the effect size of medication on brain activity within this new framework for chronic pain assessment. Based on a previous study [17], we hypothesized that the pain message on the EEG signal would amplify the envelope variability of the EEG signal and that dynamic changes in envelope variation in the presence of pain could be proportional to the magnitude of pain experienced.

2. Materials and Methods

2.1. Participants

Pain was quantified in three groups of volunteers by convenience (see Table 1): Group 1 related to seven healthy participants (six men, one woman: 24–45 years of age) who submitted in two main experimental conditions: "No pain" and "With tonic pain" induced by a capsaicin cream. Group 2 included 15 healthy participants (14 men, one woman: 22–45 years of age) who experienced experimentally induced thermal pain, and Group 3 included 66 individuals (21 men, 45 women: 15–78 years of age) living with chronic pain, such as shoulder pain, fibromyalgia, and low back pain. For this group, in addition to sociodemographic data, daily medication use was also ascertained. Among the 66 participants with real chronic pain, 36 took medications known to be centrally acting [21]. Therefore, a sub-objective was to verify the effect size of medication on brain activity using the new approach. The local Research Ethics Committee (CER #2023-1200 and CER # 2023-1307) approved the study, and the participants provided written consent for their participation.

Table 1. Participants' characteristics.

	Group 1 (n = 7)		Group 2 (n = 15)	Group 3 (n = 66)	
	Condition—Capsaicin		Condition—Thermal Stimulus	Condition—Chronic Pain	
	No Pain	With Pain	Thermal Pain	Centrally Acting Medication (n = 36)	Other Treatment (n = 30)
Average age (years)	32.40		31.70	41.17	52.10
Average of pain duration (months)	–		–	55.34	105.03
Average pain scores (Numerical scale/10)	0.00	4.00	Decrease in pain from 6.1 to 0.7	2.63	4.10

2.2. Experimental Procedures

Given that pain mechanisms evolve through brain activity, the main physiological material used in our study was EEG signals. For EEG collection, the participants were seated at rest, with eyes opened focused on a black dot located 1.5 m away on the wall in front of them at eye level. An EMOTIV wireless electroencephalographic headset was placed on the participant's head to collect brain activity; electrodes were positioned according to the 10–20 international system. Pain intensity was assessed using a 0–10 verbal numerical rating scale (VNRS), where 0 corresponded to no pain and 10 to the worst imaginable pain [22].

2.2.1. Procedure for Group 1: Healthy Participants— "No Pain" and "with Pain"

In the condition "With pain", pain was induced with a topical application of a ~1 cm wide band of capsaicin cream (1%) (~1 mm thick) on the right upper trapezius in the same previous group. The capsaicin cream contained 1% capsaicin, the hot ingredient in chili peppers. This cream induced localized moderate tonic pain at the site of application. The aim of this study was to create experimental pain similar to musculoskeletal pain. This cream was used in accordance with previous studies [23,24]. The plateau of pain was attained approximately 30 min after application and corresponded to the moment when the participant consecutively showed the same pain intensity three times (pain intensity was assessed every 2 min).

Data from this group were collected in two conditions: (1) "No pain and (2) "With pain". EEG signals were collected first in the "No pain" condition and second in the "With pain" condition. Analyses were performed on the EEG signals collected during the last 60 s for each condition. Given that the pain plateau was not reached until 30 min after the application of the capsaicin cream, we chose the last 60 s of the recordings from each of the two conditions to obtain two comparable moments.

2.2.2. Procedure for Group 2: Healthy Participants Subjected to Thermal Experimental Pain

A thermal stimulus was applied to the non-dominant forearm using a thermode (Figure 1) initially heated to 44 °C. Knowing that, on contact with the skin, the temperature of the thermode would begin to decrease, we held the thermode on the skin for 5 min to allow it to reach the baseline temperature at around 32 °C [25–27]. An initial temperature of 44 °C was chosen based on previous work, where it is commonly accepted that at this temperature most subjects report a transformation of heat sensation into pain [28,29]. Three variables (pain stimulus (°C), pain score/10, and EEG signals) were collected simultaneously for 5 min (Figure 2).

Experimental pain induced by a thermal stimulus:

1. Fill the thermos with hot water
2. Immerse the thermode equipped with a needle thermometer in the thermos
3. At a temperature of 44 °C, take the thermode out of the thermos
4. Place the end of the hot thermode on the forearm for 5 min
5. Note the level of the temperature (hot stimulus) of the thermode every 30 s (temperature decreases)
6. Note the intensity of the pain every 30 s

Figure 1. The thermal stimulus kit.

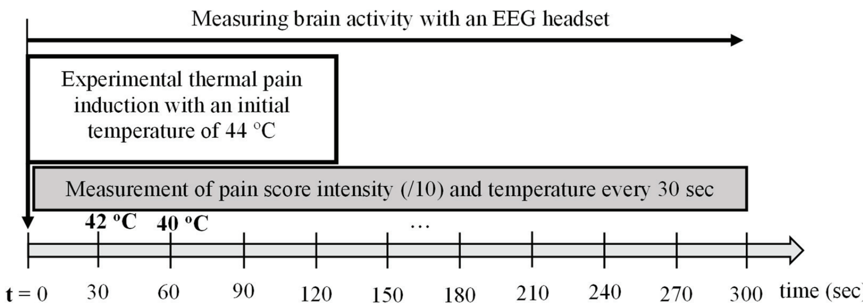

Figure 2. Experimental design—Thermal stimulus, pain score, and EEG recording during 300 s or 5 min.

2.2.3. Procedure for Group 3: Participants Living with Chronic Pain

Data were collected in a clinical setting. EEG recordings lasted 5 min (300 s) and every 30 s (metronome Bip), and the score of pain intensity felt by the participant was recorded, as well as in group 2.

2.3. EEG Data Acquisition

A wireless EEG device, an Emotiv EPOC X 16-channel headset (Emotiv Systems Inc., San Francisco, CA, USA), including 14 active and two ground electrodes, was used. Impedance was maintained in a 10–20 KΩ range by properly wetting the sponge electrodes with a saline solution and controlling the electrode contact quality map, which should be green during EEG data collection to ensure the good quality of the EEG signal. EEG data were acquired with an internal sampling frequency of 2048 Hz. Data were then digitalized using an embedded 16-bit analog-to-digital converter and down-sampled to 128 samples per second before being transmitted to the acquisition computer. The digitalized EEG signals were online-filtered by the EPOC X hardware with a 5th-order digital sinc filter using a bandpass of 0.2–45 Hz and a notch digital filter at 60 Hz (for North America) to eliminate power line frequency noise.

2.3.1. EEG Data Preprocessing

The preprocessing of the EEG signals was performed in three steps, as illustrated in Figures 3 and 4, and is described in the following subsections: Step 1—EEG signal filtering in two substeps: (a) Direct Current (DC) offset removal, also known as baseline correction, and (b) EEG artifact removal; Step 2—EEG frequency band selection; and Step 3—Normalization of filtering EEG signals in two substeps (min–max and baseline normalization). Signals from electrodes positioned over the bilateral motor regions (FC6/T8 on the right side and FC5/T7 on the left side) were of interest. These electrodes cover the recommended positioning on the motor regions according to the EPOC X headset [30]. These electrodes are located over the frontal and temporal regions of the scalp, corresponding to areas involved in motor function. Moreover, previous studies have reported the involvement of motor cortex areas in the pain process [31–33]. The preprocessing was conducted using the MATLAB software, version: 9.10.0.1602886 (R2021a) (MathWorks Inc., Natick, MA, USA).

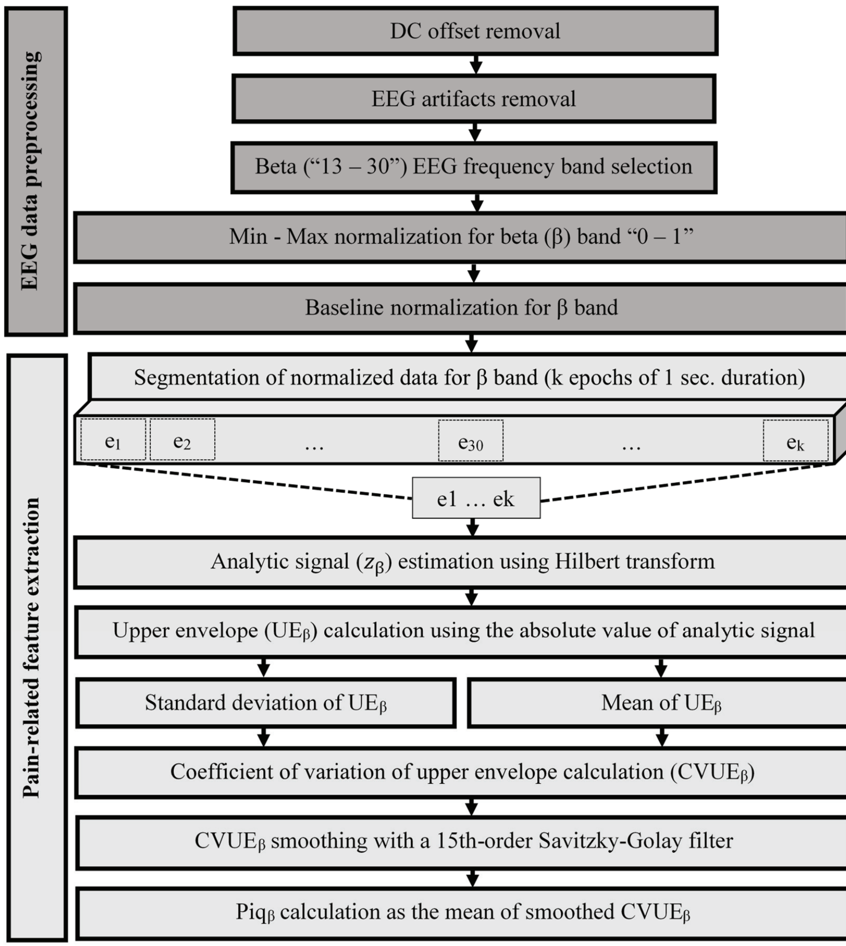

Figure 3. Methodological approach from the filtering of the EEG signal, through the estimation of the coefficient of variation of the upper envelope in beta ($CVUE_\beta$), to the calculation of pain identification and quantification (Piq_β).

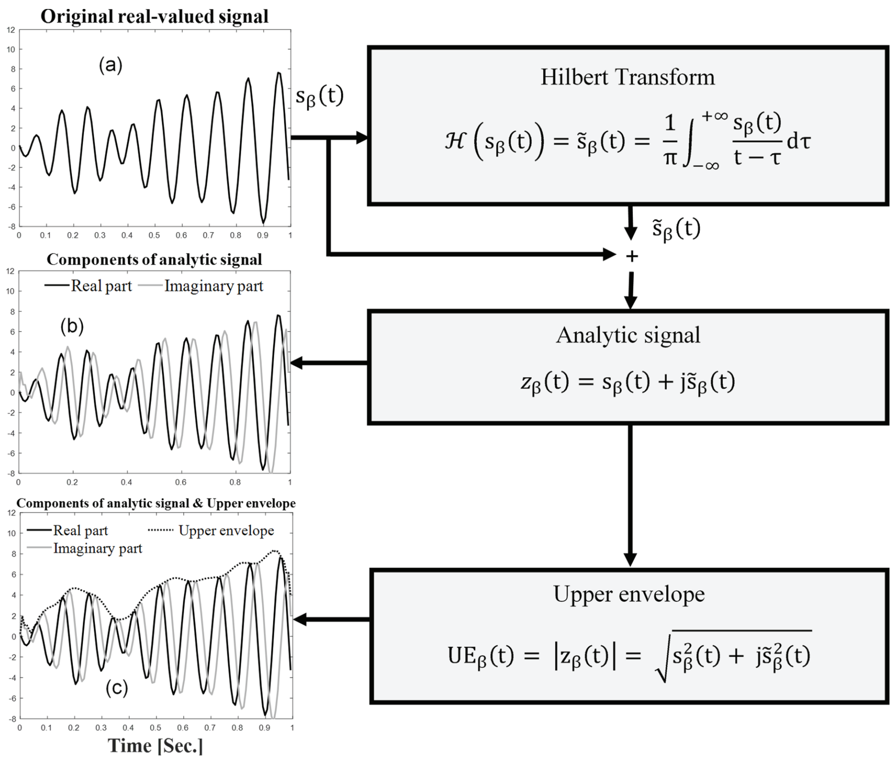

Figure 4. Methodological steps showing the detail of the application of the Hilbert transform until the extraction of the upper envelope. (**a**)—original real-valued signal, (**b**)—real and imaginary parts of analytic signal, (**c**)—superposition of real and imaginary parts of analytic signal and upper envelope of original signal.

EEG Signals Filtering

The first step of pre-processing was to remove noise from the EEG signals. The direct current (DC) voltage offset, that is, the offset of a signal from 0, was first removed using the simplest method consisting of subtracting the average value (approximately 4200 μV) from the entire selected data channel. The second substep of filtering was to remove the remaining artifacts due to eye blinks or eye movements, and the electromyography (EMG) signal and all well-known noise, such as poor electrode contact quality, were identified during the experiments. To this end, an outlier detection and replacement filter was used by applying Matlab's "filloutliers" function [34,35]. First, the outlier values defined as EEG values that were over 1.5 interquartile ranges above the upper quartile (75%) or below the lower quartile (25%) were detected using the quartiles find method. Second, the linear interpolation of neighboring non-outlier values method was used to replace the detected outlier values.

EEG Frequency Band Selection

The second step of preprocessing was the selection of the beta (13–30 Hz) EEG frequency sub-band over the electrode positioned contralateral to the pain site for further analyses [36–40]. Indeed, previous studies and our previous work have reported the relevance of beta for pain identification [17]. Finally, a 5th-order IIR Butterworth bandpass filter was used for the selected frequency band [41].

EEG Signal Normalization

The third preprocessing step was EEG signal normalization in two substeps. The first substep was to adjust for the inter-variability of EEG data within the selected frequency band by scaling the EEG data using min–max normalization. This substep involves placing artifact-free EEG signals in the interval between 0 and 1 [42,43]. Min–max normalization performs a linear transformation of the original data values while preserving the relationships between them. The equation to achieve this processing is as follows [44]:

$$\mathrm{EEG}^{\beta}_{\mathrm{min-max}} = \frac{\mathrm{EEG}^{\beta}_{\mathrm{AF}} - \min\left(\mathrm{EEG}^{\beta}_{\mathrm{AF}}\right)}{\max\left(\mathrm{EEG}^{\beta}_{\mathrm{AF}}\right) - \min\left(\mathrm{EEG}^{\beta}_{\mathrm{AF}}\right)} \tag{1}$$

where $\mathrm{EEG}^{\beta}_{\mathrm{AF}}$ and $\mathrm{EEG}^{\beta}_{\mathrm{min-max}}$ correspond to the artifact-free EEG signal and min–max normalized signal, respectively, and $\min\left(\mathrm{EEG}^{\beta}_{\mathrm{AF}}\right)$ and $\max\left(\mathrm{EEG}^{\beta}_{\mathrm{AF}}\right)$ denote the minimum and maximum of all artifact-free EEG signals within the beta frequency band. Finally, the second substep was baseline normalization, which re-scales the previous min–max normalization values by the weight of each single min–max normalized EEG value. It divides each min–max normalized EEG value using a selected reference. The resulting equation is as follows:

$$\mathrm{EEG}^{\beta}_{\mathrm{N}} = \frac{\mathrm{EEG}^{\beta}_{\mathrm{min-max}}}{\mathrm{Ref}^{\beta}} \tag{2}$$

where $\mathrm{EEG}^{\beta}_{\mathrm{N}}$ represents the normalized EEG signals for the beta frequency band and Ref^{β} is the reference, which is defined as the mean of the min–max EEG signals in the reference interval for the beta frequency band. In this study, Ref^{β} was considered as the first 60 s of EEG collection for each participant.

2.3.2. Extracting Pain-Related Feature from EEG Signals to Pain Identification and Quantification Indicator (Piq)

As shown in Figures 3 and 4, after the EEG signals were filtered and normalized, the complex analytical signal $z_{\beta}(\mathrm{t})$, which considers non-stationarity and nonlinearity as these are the characteristics of the EEG signal, was obtained using the Hilbert transform (Figure 4) [19,45]. This type of analytic signal is a two-dimensional signal whose value at some instant in time is specified by two parts: a real part (Figure 4a) and an imaginary one (Figure 4b) [46]. The upper envelope of the EEG signal was then extracted as the absolute of the analytical digital signal (Figure 4c) [19]. Finally, the coefficient of variation of the upper envelope (CVUE) was calculated for the beta frequency band (13–30 Hz). The coefficient of variation represents the ratio of the standard deviation to the mean and is a useful statistic for comparing the degree of variation from one data series to another. The Piq indicator was computed in beta (Piq_{β}) in five steps.

(1) The first step was the estimation of the analytic EEG signals for the beta frequency band ($z_{\beta}(\mathrm{t})$) using Hilbert transform, as follows:

$$z_{\beta}(\mathrm{t}) = \mathrm{s}_{\beta}(\mathrm{t}) + \mathrm{j}\tilde{\mathrm{s}}_{\beta}(\mathrm{t}) \tag{3}$$

where $\tilde{\mathrm{s}}_{\beta}(\mathrm{t}) = \mathcal{H}(\mathrm{s}_{\beta}(\mathrm{t}))$ represents Hilbert transform, the steps of which are illustrated in Figure 4.

(2) The second step was the extraction of the upper envelope (UE) of the EEG signals for the beta frequency band (UE_{β}), defined as the absolute value of the analytic signal, as follows:

$$\mathrm{UE}_{\beta}(\mathrm{t}) = \left|z_{\beta}(t)\right| = \sqrt{\mathrm{s}^{2}_{\beta}(\mathrm{t}) + \mathrm{j}\tilde{\mathrm{s}}^{2}_{\beta}(\mathrm{t})} \tag{4}$$

The upper envelope (UE) of a given cortical oscillation reflects the energy range over time [45]. The UE was high when energy was high. Because of the time-variant behavior and nonlinear neuronal system responsible for generating the EEG signals, preprocessed EEG signals were segmented in sliding windows (epochs) of 1 s duration, and UE_{β} was then calculated within each epoch.

(3) The third step was the estimation of the coefficient of variation of the upper envelope in the beta EEG frequency band ($CVUE_{\beta}$). To this end, the mean and standard deviation (std) of UE_{β} were computed in each epoch to obtain $CVUE_{\beta}$ as follows:

$$\mathrm{CVUE}_{\beta}(\%) = \frac{\mathrm{std}(\mathrm{UE}_{\beta}(\mathrm{t}))}{\mathrm{mean}(\mathrm{UE}_{\beta}(\mathrm{t}))} \times 100 \quad (5)$$

Low CVUE values reflect more stable sinusoidal oscillations, that is, more neuronal synchronization or inhibition [47]. In contrast, a high CVUE corresponds to neuronal desynchronization [18,47], that is, less inhibition (more facilitation).

(4) The fourth step consisted of smoothing $CVUE_{\beta}$ using a 15th-order Savitzky–Golay filter.

In each sliding window, the so-called edge effects can be preserved and affect the CVUE values [48,49]. Smoothing filters, such as a Savitzky–Golay filter, make it possible to correct inter alia spikes present in the data [50,51]. The Savitzky–Golay filter is a least-squares smoothing filter (digital polynomial filter). Its working principle involves replacing each value with a new value, previously obtained from polynomial fitting, which is performed with basic linear least-squares fitting to the $2k + 1$ neighboring points, where the value k could be equal to or greater than the order of the applied polynomial. The more neighbors that are applied, the smoother the final signal [50]. It smooths the fluctuations in data and increases the signal-to-noise ratio (SNR) without significantly distorting the analyzed data [51,52]. In this study, a 15th-order Savitzky–Golay filter was used.

(5) The fifth step was the calculation of the pain identification and quantification (Piq) indicator in the beta frequency band (Piq_{β}).

The mean smoothing $CVUE_{\beta}$ was calculated and proposed as a pain identification and quantification (Piq) indicator. The higher the Piq (%), the higher the magnitude of pain.

2.4. Statistical Analysis

Objective 1 was already completed in Section 2.3.2 (Figures 3 and 4), showing each step of the methodological approach proposed to extract the relevant indicator for the identification and quantification of pain. The mean and standard deviation values were used for descriptive statistics in relation to the second objective (2), that is, to determine the threshold quantified for the identification of the presence of pain. The correlation coefficient was used to determine the relationship between the main variables, that is, $Piq_{\beta} \times$ pain scores, across groups to address objective (3), that is, the relationship between the proposed approach and self-reported pain on a verbal numerical rating scale. Finally, to achieve the secondary objective, we utilized effect size (ES) and clinical difference (Δ) to measure the impact of medication on brain activity, thus fulfilling this sub-objective, that is, the magnitude of the effect of medication acting on brain activity in the new approach. ES was calculated based on the Cohen criteria, i.e., d = 0.2 to 0.49 is small, d = 0.5 to 0.79 is medium, and $d \geq 0.8$ is large [53]. A decrease in pain of less than 15% was judged as a non-important change, of 15% or more as a minimally important change, of 30% or more as a moderately important change, and of 50% or more as a substantially important change [54]. The significance level of the tests was set at $p < 0.05$, and all statistical analyses were conducted using SPSS version 24 (IBM Corp., Armonk, NY, USA).

3. Results

3.1. New Approach to Identify and Quantify Pain

In this study, as illustrated in Figures 3 and 4, a method for extracting pain-related features from EEG signals, that is, a pain identification and quantification indicator (Piq), was proposed. This innovative methodological approach inspired by the variation in the morphology of EEG signals in animals [47] and humans [20], which utilizes beta (β) brain rhythm, is proposed for pain identification and quantification. Piq_β is proposed as a pain indicator for pain identification and quantification in the beta band frequency. As a reminder, the higher the Piq_β (%), the higher the magnitude of pain.

3.2. Descriptive Statistics of Groups to Meet Objective (2) i.e., Determine the Threshold Quantified for the Identification of the Presence of Pain

A visual inspection of the results showed that $Piq_\beta \geq 10\%$ was indicative of the presence of pain (Tables 2 and 3). Therefore, $Piq \leq 10\%$ corresponded to little or no pain.

Table 2. Descriptive statistics of group 1 ($n = 7$).

ID	Sex: 1 = Male 2 = Female	Age (Years)	Pain Duration (Month)	Pain Scores (/10)		Piq_β (%)	
				No Pain Condition	With Pain Condition	No Pain Condition	With Pain Condition
1	1	35	–	0	5	7.13	12.35
2	2	45	–	0	5	8.28	11.23
3	1	33	–	0	4	7.16	13.00
4	1	30	–	0	2	8.15	12.54
5	1	28	–	0	5	8.24	13.56
6	1	24	–	0	5	7.13	14.12
7	1	26	–	0	2	9.00	10.15
Mean (SD)		**31.6 (7.0)**		**0 (0)**	**4 (1.4)**	**7.83 (0.74)**	**12.42 (1.4)**

Table 3. Descriptive statistics of group 3 ($n = 66$).

ID	Sex: 1 = Male 2 = Female	Age (Years)	Pain Duration (Month)	Pain Score (/10)	Piq_β (%)	Medication with Central Effect: 1 = Yes 0 = Other Medications
1	1	21	30	0.00	8.81	0
2	2	40	37	4.36	15.75	1
3	1	32	18	2.36	14.05	1
4	2	59	29	1.05	10.18	0
5	2	64	120	1.09	10.76	1
6	2	63	396	6.00	19.17	1
7	2	58	5	2.73	14.29	1
8	2	63	36	0.64	8.25	1
9	1	30	4	5.27	24.99	0
10	1	68	120	4.55	15.05	1
11	1	69	24	0.09	9.33	0
12	1	78	6	1.00	12.66	0
13	1	30	5	0.36	7.84	0
14	2	17	6	4.64	13.74	0
15	2	28	84	3.00	13.65	0
16	2	21	12	1.00	11.92	0
17	2	22	6	0.55	7.92	0
18	2	26	84	4.45	18.68	0
19	2	54	4	5.77	12.34	0
20	1	42	22	3.82	11.34	0
21	1	66	72	2.00	10.19	0
22	2	59	84	0.09	6.93	1
23	1	21	4	2.27	11.12	0
24	2	19	7	2.00	12.30	0
25	1	23	1	1.27	12.98	0

Table 3. *Cont.*

ID	Sex: 1 = Male 2 = Female	Age (Years)	Pain Duration (Month)	Pain Score (/10)	Piq$_\beta$ (%)	Medication with Central Effect: 1 = Yes 0 = Other Medications
26	1	22	204	2.91	12.59	0
27	2	60	2	1.77	10.74	0
28	2	57	1	2.91	11.78	1
29	2	31	8	4.23	22.41	1
30	2	52	0.75	2.27	12.48	0
31	2	33	7	6.91	15.57	0
32	2	37	12	0.86	7.59	1
33	2	22	120	2.00	11.89	0
34	2	36	2	0.00	9.39	0
35	2	59	84	2.00	13.02	1
36	2	63	6	4.00	14.82	0
37	2	64	3	0.00	5.66	1
38	2	15	6	4.00	16.59	0
39	1	32	16	10.00	18.9	1
40	1	45	96	8.00	17.7	1
41	2	44	24	2.10	14.9	1
42	2	45	240	7.50	19.1	1
43	2	46	240	4.00	15.5	0
44	2	47	48	4.00	11.4	0
45	2	32	216	0.50	12.9	0
46	2	45	24	5.70	17.5	1
47	2	71	120	10.0	29.2	1
48	1	56	4	3.50	11.15	0
49	2	27	60	1.60	16.1	1
50	1	68	120	6.80	15.1	1
51	2	73	24	3.40	13.8	0
52	2	55	240	2.10	15.1	1
53	1	45	48	5.70	20.3	0
54	2	62	60	2.10	16.2	1
55	1	66	144	3.00	17.7	0
56	1	65	3	2.20	13.3	1
57	2	49	192	1.20	10.8	0
58	2	61	360	7.20	13.9	1
59	1	60	84	5.80	12.44	1
60	1	53	5	0.00	12.68	0
61	2	44	48	7.00	16.78	1
62	2	59	120	1.10	13.94	1
63	2	59	300	2.00	17.78	0
64	2	24	96	7.00	23.67	1
65	2	61	516	5.00	32.10	1
66	2	27	24	5.00	18.23	0
Mean (SD)		**46.1 (17.3)**	**77.9 (105.9)**	**3.30 (2.50)**	**14.3 (4.8)**	

3.2.1. Group 1: Healthy Participants—"No Pain" and "with Pain"

Table 2 shows the descriptive statistics of Group 1 subjected to capsaicin application.

In the pain condition, participants had moderate pain on average (pain score $\geq$ 4 on the VNRS). All participants in the "no pain" condition had a Piq$_\beta$ of less than 10% and, conversely, in the experimental pain condition.

3.2.2. Group 2: Healthy Participants Submitted to Thermal Pain

The protocol for Group 2 was specifically designed to evaluate the effectiveness of the proposed algorithm in tracking pain changes in very short timeframes, achieving Objective 1 (the identification and quantification of pain). A visual inspection of the graph (Figure 5) showed that Piq_{β} can track the magnitude of pain. In addition, this study provides evidence that 5 min of EEG signal collection is sufficient to address the variation in pain magnitude.

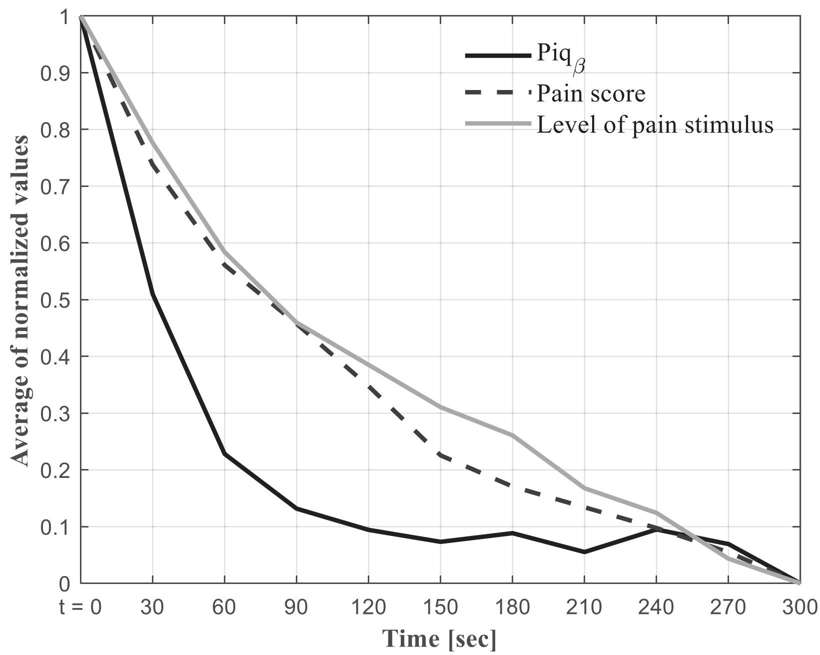

Figure 5. Normalized mean [0–1] for all participants (n = 15) of the three variables: (1) Normalized pain score intensity (black dotted line curve), (2) normalized level of pain stimulus (grid curve), and (3) normalized pain identification and quantification in beta frequency band (Piq_{β}) (black curve).

For Group 2, we performed normalization by bringing all the values of each pain indicator between 0 and 1 while maintaining the distances between the values and allowing for the comparison of the three variables on the same scale (Figure 5). This min–max normalization was performed using Equation (6), as follows:

$$Normalized\ value = \frac{Z - minimum(Z)}{maximum(Z) - minimum(Z)} \tag{6}$$

where z represents the value of each pain indicator (score intensity, level of pain stimulus, and Piq_{β}).

This study showed a simultaneous decrease in the level of pain stimulus, pain score intensity, and Piq_{β} indicator.

3.2.3. Group 3: Participants Living with Chronic Pain

This third study also confirmed that the pain threshold of the EEG-based indicator Piq_{β} is 10% to identify individuals with chronic pain as well as sensitive to quantify the extent of pain (Piq_{β} higher than 10%, Table 3 and Figure 6).

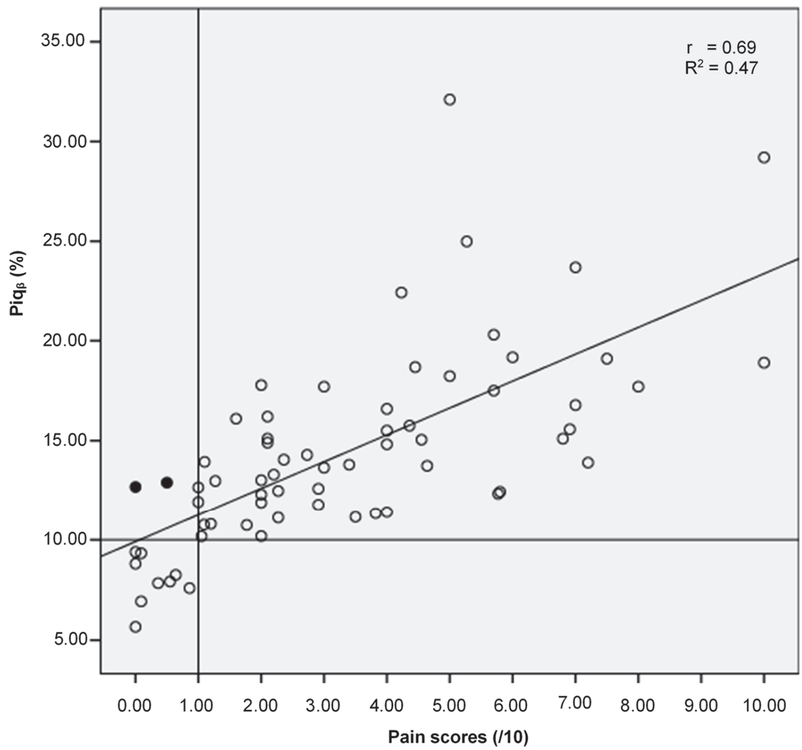

Figure 6. Scatter plot—Piq$_{\beta}$ indicator and pain score. 100% of participants living with chronic pain show a Piq$_{\beta}$ $\geq$ 10%. The two solid points represent participants who reported a pain score lower than 1/10 but had a Piq$_{\beta}$ indicator $\geq$10%. The hollow points represent participants whose pain scores are consistent with their Piq$_{\beta}$ indicator values.

3.3. Results for Objective (3) i.e., the Relationship between the Proposed Approach for the Identification and Quantification of Pain (Piq$_{\beta}$) and Self-Reported Pain (Score/10)

For healthy participants with capsaicin pain (group 1), no correlation test was performed because of the small sample size. In Group 3, for the participants living with chronic pain, a significant and strong positive correlation (r = 0.69, p < 0.0001) was found between Piq$_{\beta}$ and pain scores from the VNRS, while a moderate relationship between variances (R^2 = 0.47) was observed.

Considering all three studies, our findings indicate that Piq$_{\beta}$ (%) appears to be affected by pain variability. This implies that varying levels of pain could potentially affect Piq$_{\beta}$ measurements or that Piq$_{\beta}$ might serve as a sensitive gauge for changes in pain across the individuals under study. Nevertheless, it is crucial to emphasize that this observation warrants further investigation to ascertain a causal relationship.

3.4. Results for the Secondary Objective, i.e., the Effect Size of Medication Acting on Brain Activity on the New Approach

The participants in group 3 were divided into two subgroups according to their medication: (1) with (n = 36) and (2) without centrally acting (n = 30). The effect sizes and clinical differences were then calculated (Table 4).

According to Cohen’s classification, the effect size of medication on the pain score was moderate (d = 0.61). The subgroup of participants taking centrally acting medication achieved a significant reduction in pain scores (p = 0.016), and this reduction (55.8%) was considered to be a substantially important change [55]. In addition, in the same group, the effect size of the medication on Piq_{β} was moderate ($d = 0.51$). The Piq_{β} indicator displayed significantly lower values ($p = 0.041$), with an average decrease of 18.5%, suggesting a minimally important change. Overall, these results showed that medication had a significant negative and moderate effect on the magnitude of pain. Consistently, we noted that Piq_{β} (%) and the pain score (/10) were higher in the absence of medication acting on brain activity.

Table 4. Comparative results. * Indicates statistical differences ($p < 0.05$).

Variables	Sub-Groups		*p* Value	Effect Size	Clinical Difference Δ (%)
	Medication with Centrally Acting (*n* = 36)	Medication without Centrally Acting (*n* = 30)			
Pain scores (/10)	2.63 (1.87) IC: 1.9–3.2	4.10 (2.91) IC: 3.0–5.1	0.016 *	0.61	55.8%
Piq_{β} (%)	13.23 (3.66) IC: 11.9–14.6	15.68 (5.80) IC: 13.5–17.8	0.041 *	0.51	18.5%

4. Discussion

This pilot study aimed to propose (1) developing a methodological approach for identifying and quantifying pain in real-world settings; (2) quantifying a threshold to detect the presence of pain; (3) analyzing the relationship between the new EEG-based indicator and self-reported pain, assessed using a verbal numerical rating scale (VNRS); and (4) examining the effect size of medication on brain activity within this new framework for chronic pain assessment.

4.1. New Methodological Approach for Pain Identification and Quantification

Our methodological approach demonstrates the promising potential for objective pain identification and quantification based on the analysis of the envelope of EEG signals, which is related to relevant aspects of EEG signal morphology and remains more stable over time and conditions [17,20,47]. The main advantage of this methodology is that it keeps the EEG signal complex, thus preserving almost all of its intrinsic properties, such as non-stationarity and nonlinearity, offering the maximum amount of relevant information. This new approach, which is based on the morphological stability parameters of the EEG signal, provides great methodological robustness. In addition, EEG systems are typically multichannel in nature, resulting in numerous features being extracted from multichannel signals [56]. It is widely recognized that employing a large number of channels or features in pain identification or quantification poses practical limitations in real-life scenarios [57–59]. Such limitations include prolonged experimental setup times, subject discomfort, and increased computational complexity associated with handling multichannel EEG recordings [60]. Given these constraints, there is considerable value in developing a portable pain identification and quantification method that focuses on the optimal feature from the representative channel. Thus, the complexity and dynamic nature of pain identification and quantification can be circumvented by optimizing the hardware setup. This approach not only streamlines the experimental process but also reduces the burden on the subjects and computational resources. Therefore, feature selection is vital for EEG-based pain identification and quantification. For this purpose, we applied a simple and easy-to-implement algorithm to an EEG signal collected for five minutes over the motor cortex region, without altering patient comfort in the clinical setting. Although the proposed indicator seems optimal for pain identification and quantification, it is important to validate it using different machine learning classifiers to propose an automatic system that produces satisfactory accuracy.

4.2. Identification of Pain

We propose a quantitative indicator that we called "Piq" for Pain identification and quantification. Although there is no gold standard for quantitative measures of pain, the self-reported intensity score of pain remains one of the relevant comparative variables in the context of our study. Our results (group 1 et 3) suggest that a Piq greater than or equal to 10% (Piq $\geq$ 10%) is indicative of the presence of pain. Therefore, for Piq < 10%, there was little to no pain. In our recent study that utilized the current method, we observed that among healthy participants not experiencing pain, the Piq value was consistently below 10% [17].

4.3. Quantification of Pain

We propose Piq as an indicator to reflect the magnitude of pain experienced by an individual. Our results showed a strong positive correlation between Piq_β and self-reported pain in both experimental and real chronic pain conditions. These results suggest the ability of Piq_β to track the presence and extent of acute, subacute, and chronic pain. In other words, the higher the self-reported pain score, the higher the Piq_β (%), and vice versa. Of course, this study comprised experimental acute pain, given the practical improbability of collecting acute pain data in a real-world setting. Our results are similar to those of Nir et al. [38], who evaluated the perception of tonic pain using a thermal contact-heat simulator, showing that increased peak alpha frequency values derived from EEG recordings of the resting state and noxious conditions were correlated with higher pain intensity. However, to the best of our knowledge, no study has proposed the use of all EEG signals to detect pain. Given that pain is a complex biopsychosocial experience, it became evident that the appropriate method for conducting the analyses was to use EEG signals with complex values for the selected sub-band rather than EEG signals with real values. Complex-valued signals seemed appropriate, as they captured the complex information of the pain process, integrating the multidimensional aspects of this phenomenon. In the chronic pain group (n = 66), our results showed a moderate relationship between the variances of self-reported pain scores and Piq_β (%) ($R^2 = 0.47$; $p < 0.001$). Note that R^2, the coefficient of determination, measures the percentage of variation in the dependent variable that is explained by a variation in the independent variable [61]. However, there is no rule for interpreting the strength of R^2 in terms of clinical relevance; a low R^2 can still provide a useful clinical model [62,63].

Our hypothesis about the moderate variance found in participants with chronic pain is that Piq_β (%) reflects a combination of cerebral mechanisms implemented in the context of a painful condition, whereas the self-reported pain score is an expression of the overall biopsychosocial experience of pain. Several studies have shown alterations in cerebral excitability or even a cerebral reorganization in the context of prolonged pain [64,65]. Our results showed a positive relationship between Piq_β and the duration of pain ($p < 0.05$, $r = 0.36$), as well as between the duration of pain and pain score ($p < 0.05$, $r = 0.25$) in the chronic pain group (n = 66). However, these relationships are weak, reinforcing the idea of alteration in cortical excitability rather than cerebral reorganization. In general, studies have shown that pain is accompanied by a decrease in cortical inhibition [18,47,66–69]; therefore, we hypothesized that an increase in Piq_β is indicative of less cortical inhibition. One possible approach to validate this hypothesis is to integrate EEG with TMS to enable the measurement of cortical inhibition.

4.4. Effect Size of Brain-Acting Medication on Pain Measurement (Piq_β (%))

As we identified the presence and quantification of pain magnitude from brain activity, centrally acting medication may influence the outcome. We found that the effect size of medication was moderate on the pain score (d = 0.61) as well as on Piq_β, suggesting that Piq_β (d = 0.51) reflects the effectiveness of pain treatments in this sample, ranging from moderate to low [55]. Persistent pain in a sample of 66 participants was typically treated with medications such as antidepressants, anticonvulsants, and opioids [70]. The clinical difference in the Piq_{β} indicator between both subgroups was 18.5% i.e., a minimally important change in favor of the centrally acting medication in the subgroup.

Taken together, our results show that the Piq_{β} indicator can track pain variation via brain activity, even in the presence of a centrally acting treatment, which can be advantageous for monitoring pain treatment in various contexts, from outpatient to postoperative orthopedic care.

4.5. Perspective

Several questions require additional research to fill these gaps. For example, what is the minimum Piq_{β} value (%) that indicates a clinically relevant change in pain magnitude? Alternatively, does the measurement time frame with the proposed approach change depending on the type of treatment, or, for example, what is the optimal time for the identification and quantification of pain after a physical, pharmacological, or surgical intervention? For minimum clinical change, it is recommended that two or more different methods be used to evaluate the clinical importance of improvement or worsening for chronic pain clinical trial outcome measures [54,71]. Pain assessment is generally classified into 11 levels on the NRS [72]: 0–1: Weak or no pain. 1–6: Mild to moderate pain, invisible. 7–10: For intense to severe pain, several physiological signs make it possible to identify that a person is experiencing pain. This study showed that the presence of pain was set at 10% for Piq_{β}. Thus, work needs to be carried out to establish Piq_{β} values that can be considered as the minimally relevant clinical change in Piq_{β} between the two interventions. In the forthcoming phases of this project, we intend to expand the participant sample to include more individuals experiencing pain, and we will assess their pain as part of a protocol aiming to test the reliability of the Piq_{β} indicator. This endeavor holds significance, as enhancing clinical relevance will offer a more profound insight into its practical applicability. Furthermore, we aimed to confirm the observed Piq_{β} threshold value of 10% across the three studies through a static analysis conducted in a study with a broader sample size.

4.6. Limits

The main limitation of the present pilot study is the absence of real pain data showing large variations in the levels of pain, as for experimental thermal pain. This would have enabled a more robust corroboration that Piq_{β} tracks acute pain. Nonetheless, it is important to bear in mind that this study serves as a pilot study aimed at testing our algorithm designed to identify and quantify chronic pain under real-life conditions. The algorithm outlined in our 2022 paper, incorporating a sample comprising four individuals experiencing fibromyalgia pain [17], is being implemented and evaluated in this context. Our primary focus was the objective assessment of chronic pain, ranging from mild to moderate intensity, which may be accompanied by episodes of intense pain. It is an invisible disease that is difficult to objectively assess. In line with the 11th International Classification of Diseases, our work aims to advance the recognition of chronic pain as a health problem on its own [73].

5. Conclusions

In conclusion, we have successfully met the objectives of this pilot study, which included: (a) developing a new method for identifying and quantifying pain, (b) establishing a threshold to detect the presence of pain, (c) exploring the correlation between the new EEG-based indicator and self-reported pain using a verbal numerical rating scale (VNRS), and (d) assessing the impact of medication on brain activity as a secondary objective within the new chronic pain assessment. Specifically, from a methodological perspective, here are the key parameters from the pilot study that are essential for the algorithm's functionality: (1) Five (5) min for EEG collection at rest posture provides sufficient material for the purpose of analysis, without necessarily affecting the sufferer's comfort; (2) one (1) electrode positioned above the motor regions contralateral to the site of pain is sufficient and allows us to respect the physiological decussation of the ascending and descending pathways of information; (3) the frequency band of interest of EEG signal is beta (13–30 Hz), and this frequency is the one that allows us to optimally capture useful and interesting information in the painful state; (4) Piq_{β} threshold at 10%, i.e., $Piq_{\beta} \geq 10\%$ is indicative of the presence of pain; and (5) the higher the Piq_{β} (%), the higher the extent of the pain.

This finding could have strong implications for the population living with pain, specifically persistent pain, and we are thinking here of all the workers on prolonged sick leave for musculoskeletal pain, as well as of healthcare professionals, insurance companies, the pharmaceutical industry, etc. An objective assessment is a valuable decision-making aid and an important contribution to pain management and monitoring.

Author Contributions: C.M.S. performed the experiments, wrote MATLAB codes, treated and analyzed the data, and wrote the manuscript. R.A.d.S. interpreted the results and provided a critical review of the manuscript. S.N. developed the idea, designed the project and experiments, led the writing of this manuscript, and ensured the scientific content of this project. All authors have read and agreed to the published version of the manuscript.

Funding: This study was supported by the Fonds de Recherche du Québec-Nature et Technologies (FRQNT)—Programme de subvention destiné à soutenir les étudiantes inventrices et les étudiants inventeurs de technologies prometteuses [grant number 339336].

Institutional Review Board Statement: The study was approved by the Ethics Committee of Université du Québec à Chicoutimi (CER #2023-1200 and CER # 2023-1307).

Informed Consent Statement: Informed consent was obtained from all subjects involved in the study.

Data Availability Statement: The raw data supporting the reported results cannot be publicly shared due to confidentiality and their inclusion in an ongoing patent application, submitted in March 2024.

Acknowledgments: We would like to thank the Axelys team for supporting us in promoting intellectual property linked to this new process. Thank you to the BioNR-UQAC Laboratory for Logistics. Thank you to the Université du Québec à Chicoutimi (UQAC) for its constant support. Gratitude is extended to Clinique Remix Santé and Centre Physio + Sport, Chicoutimi, for granting access to their valued clientele i.e., the participants of this pilot study.

Conflicts of Interest: The authors declare that they have no known competing financial interests or personal relationships that could have influenced the work reported in this study. None of the authors have any potential conflicts of interest to disclose.

References

1. Yong, R.J.; Mullins, P.M.; Bhattacharyya, N. Prevalence of chronic pain among adults in the United States. *Pain* **2022**, *163*, e328–e332. [CrossRef]
2. Zimmer, Z.; Fraser, K.; Grol-Prokopczyk, H.; Zajacova, A. A global study of pain prevalence across 52 countries: Examining the role of country-level contextual factors. *Pain* **2022**, *163*, 1740–1750. [CrossRef]
3. Sá, K.N.; Moreira, L.; Baptista, A.F.; Yeng, L.T.; Teixeira, M.J.; Galhardoni, R.; de Andrade, D.C. Prevalence of chronic pain in developing countries: Systematic review and meta-analysis. *Pain Rep.* **2019**, *4*, e779. [CrossRef]
4. Shieh, J.-S.; Dai, C.-Y.; Wen, Y.-R.; Sun, W.-Z. A novel fuzzy pain demand index derived from patient-controlled analgesia for postoperative pain. *IEEE Trans. Biomed. Eng.* **2007**, *54*, 2123–2132. [CrossRef]
5. Kamdar, M.M. *Principles of Analgesic Use in the Treatment of Acute Pain and Cancer Pain*; Mary Ann Liebert, Inc.: Larchmont, NY, USA, 2010.
6. Walsh, T. Practical problems in pain measurements. *Pain* **1984**, *19*, 96–98. [CrossRef]
7. Schnakers, C.; Zasler, N.D. Pain assessment and management in disorders of consciousness. *Curr. Opin. Neurol.* **2007**, *20*, 620–626. [CrossRef]
8. Herr, K.; Coyne, P.J.; McCaffery, M.; Manworren, R.; Merkel, S. Pain assessment in the patient unable to self-report: Position statement with clinical practice recommendations. *Pain Manag. Nurs.* **2011**, *12*, 230–250. [CrossRef]
9. Tiwari, V.K.; Nanda, S.; Arya, S.; Kumar, U.; Sharma, R.; Kumaran, S.S.; Bhatia, R. Correlating cognition and cortical excitability with pain in fibromyalgia: A case control study. *Adv. Rheumatol.* **2021**, *61*, 10. [CrossRef]
10. Jenkins, L.C.; Chang, W.-J.; Buscemi, V.; Liston, M.; Skippen, P.; Cashin, A.G.; McAuley, J.H.; Schabrun, S.M. Low somatosensory cortex excitability in the acute stage of low back pain causes chronic pain. *J. Pain* **2022**, *23*, 289–304. [CrossRef] [PubMed]
11. Desmeules, J.A.; Cedraschi, C.; Rapiti, E.; Baumgartner, E.; Finckh, A.; Cohen, P.; Dayer, P.; Vischer, T. Neurophysiologic evidence for a central sensitization in patients with fibromyalgia. *Arthritis Rheum.* **2003**, *48*, 1420–1429. [CrossRef] [PubMed]

12. Williams, D.A.; Gracely, R.H. Biology and therapy of fibromyalgia. Functional magnetic resonance imaging findings in fibromyalgia. *Arthritis Res. Ther.* **2007**, *8*, 224. [CrossRef]
13. Misra, G.; Ofori, E.; Chung, J.W.; Coombes, S.A. Pain-related suppression of beta oscillations facilitates voluntary movement. *Cereb. Cortex* **2017**, *27*, 2592–2606. [CrossRef]
14. Nickel, M.M.; May, E.S.; Tiemann, L.; Schmidt, P.; Postorino, M.; Dinh, S.T.; Gross, J.; Ploner, M. Brain oscillations differentially encode noxious stimulus intensity and pain intensity. *Neuroimage* **2017**, *148*, 141–147. [CrossRef]
15. Diers, M.; de Vos, C.C.; Gandhi, W.; Hoeppli, M.E.; Becker, S.; Bock, E.; Baillet, S.; Schweinhardt, P. Induced oscillatory signaling in the beta frequency of top-down pain modulation. *Pain Rep.* **2020**, *5*, e806. [CrossRef]
16. Teixeira, M.; Mancini, C.; Wicht, C.A.; Maestretti, G.; Kuntzer, T.; Cazzoli, D.; Mouthon, M.; Annoni, J.-M.; Chabwine, J.N. Beta electroencephalographic oscillation is a potential GABAergic biomarker of chronic peripheral neuropathic pain. *Front. Neurosci.* **2021**, *15*, 594536. [CrossRef]
17. Segning, C.M.; Harvey, J.; Ezzaidi, H.; Fernandes, K.B.P.; da Silva, R.A.; Ngomo, S. Towards the objective identification of the presence of pain based on electroencephalography signals' analysis: A proof-of-concept. *Sensors* **2022**, *22*, 6272. [CrossRef]
18. Díaz, J.; Razeto-Barry, P.; Letelier, J.-C.; Caprio, J.; Bacigalupo, J. Amplitude modulation patterns of local field potentials reveal asynchronous neuronal populations. *J. Neurosci.* **2007**, *27*, 9238–9245. [CrossRef]
19. Díaz, J.A.; Arancibia, J.M.; Bassi, A.; Vivaldi, E.A. Envelope analysis of the airflow signal to improve polysomnographic assessment of sleep disordered breathing. *Sleep* **2014**, *37*, 199–208. [CrossRef]
20. Hidalgo, V.M.; Díaz, J.; Mpodozis, J.; Letelier, J.-C. Envelope analysis of the human alpha rhythm reveals EEG gaussianity. *IEEE Trans. Biomed. Eng.* **2022**, *70*, 1242–1251. [CrossRef] [PubMed]
21. Salinsky, M.C.; Oken, B.S.; Storzbach, D.; Dodrill, C.B. Assessment of CNS effects of antiepileptic drugs by using quantitative EEG measures. *Epilepsia* **2003**, *44*, 1042–1050. [CrossRef] [PubMed]
22. Karcioglu, O.; Topacoglu, H.; Dikme, O.; Dikme, O. A systematic review of the pain scales in adults: Which to use? *Am. J. Emerg. Med.* **2018**, *36*, 707–714. [CrossRef]
23. Bouffard, J.; Bouyer, L.J.; Roy, J.-S.; Mercier, C. Pain induced during both the acquisition and retention phases of locomotor adaptation does not interfere with improvements in motor performance. *Neural Plast.* **2016**, *2016*, 8539096. [CrossRef]
24. Lomond, K.V.; Côté, J.N. Movement timing and reach to reach variability during a repetitive reaching task in persons with chronic neck/shoulder pain and healthy subjects. *Exp. Brain Res.* **2010**, *206*, 271–282. [CrossRef] [PubMed]
25. Strulov, L.; Zimmer, E.Z.; Granot, M.; Tamir, A.; Jakobi, P.; Lowenstein, L. Pain catastrophizing, response to experimental heat stimuli, and post–cesarean section pain. *J. Pain* **2007**, *8*, 273–279. [CrossRef]
26. Granot, M.; Lowenstein, L.; Yarnitsky, D.; Tamir, A.; Zimmer, E.Z. Postcesarean section pain prediction by preoperative experimental pain assessment. *J. Am. Soc. Anesthesiol.* **2003**, *98*, 1422–1426. [CrossRef] [PubMed]
27. Pan, P.H.; Coghill, R.; Houle, T.T.; Seid, M.H.; Lindel, W.M.; Parker, R.L.; Washburn, S.A.; Harris, L.; Eisenach, J.C. Multifactorial preoperative predictors for postcesarean section pain and analgesic requirement. *J. Am. Soc. Anesthesiol.* **2006**, *104*, 417–425. [CrossRef]
28. Willis Jr, W. The pain system: The neural basis of nociceptive transmission in the mammalian nervous system. *Pain Headache* **1985**, *8*, 1–346. [PubMed]
29. LaMotte, R.H.; Thalhammer, J.G.; Robinson, C.J. Peripheral neural correlates of magnitude of cutaneous pain and hyperalgesia: A comparison of neural events in monkey with sensory judgments in human. *J. Neurophysiol.* **1983**, *50*, 1–26. [CrossRef]
30. Athif, M.; Ren, H. WaveCSP: A robust motor imagery classifier for consumer EEG devices. *Australas. Phys. Eng. Sci. Med.* **2019**, *42*, 159–168. [CrossRef]
31. Ngomo, S.; Mercier, C.; Bouyer, L.J.; Savoie, A.; Roy, J.-S. Alterations in central motor representation increase over time in individuals with rotator cuff tendinopathy. *Clin. Neurophysiol.* **2015**, *126*, 365–371. [CrossRef]
32. Farzan, F.; Bortoletto, M. Identification and verification of a 'true' TMS evoked potential in TMS-EEG. *J. Neurosci. Methods* **2022**, *378*, 109651. [CrossRef] [PubMed]
33. Lefaucheur, J.-P.; Nguyen, J.-P. A practical algorithm for using rTMS to treat patients with chronic pain. *Neurophysiol. Clin.* **2019**, *49*, 301–307. [CrossRef] [PubMed]
34. Segning, C.M.; Ezzaidi, H.; da Silva, R.A.; Ngomo, S. A Neurophysiological Pattern as a Precursor of Work-Related Musculoskeletal Disorders Using EEG Combined with EMG. *Int. J. Environ. Res. Public Health* **2021**, *18*, 2001. [CrossRef] [PubMed]
35. Power, J.D.; Lynch, C.J.; Dubin, M.J.; Silver, B.M.; Martin, A.; Jones, R.M. Characteristics of respiratory measures in young adults scanned at rest, including systematic changes and "missed" deep breaths. *Neuroimage* **2020**, *204*, 116234. [CrossRef] [PubMed]
36. Liberati, G.; Klöcker, A.; Algoet, M.; Mulders, D.; Maia Safronova, M.; Ferrao Santos, S.; Ribeiro Vaz, J.-G.; Raftopoulos, C.; Mouraux, A. Gamma-band oscillations preferential for nociception can be recorded in the human insula. *Cereb. Cortex* **2018**, *28*, 3650–3664. [CrossRef] [PubMed]
37. Nir, R.-R.; Sinai, A.; Moont, R.; Harari, E.; Yarnitsky, D. Tonic pain and continuous EEG: Prediction of subjective pain perception by alpha-1 power during stimulation and at rest. *Clin. Neurophysiol.* **2012**, *123*, 605–612. [CrossRef] [PubMed]
38. Nir, R.-R.; Sinai, A.; Raz, E.; Sprecher, E.; Yarnitsky, D. Pain assessment by continuous EEG: Association between subjective perception of tonic pain and peak frequency of alpha oscillations during stimulation and at rest. *Brain Res.* **2010**, *1344*, 77–86. [CrossRef] [PubMed]

39. Ploner, M.; May, E.S. Electroencephalography and magnetoencephalography in pain research—Current state and future perspectives. *Pain* **2018**, *159*, 206–211. [CrossRef]
40. Shao, S.; Shen, K.; Yu, K.; Wilder-Smith, E.P.; Li, X. Frequency-domain EEG source analysis for acute tonic cold pain perception. *Clin. Neurophysiol.* **2012**, *123*, 2042–2049. [CrossRef]
41. Aboalayon, K.A.; Almuhammadi, W.S.; Faezipour, M. A comparison of different machine learning algorithms using single channel EEG signal for classifying human sleep stages. In Proceedings of the 2015 Long Island Systems, Applications and Technology, Farmingdale, NY, USA, 1 May 2015; pp. 1–6.
42. Zhang, X.; Yao, L.; Zhang, D.; Wang, X.; Sheng, Q.Z.; Gu, T. Multi-person brain activity recognition via comprehensive EEG signal analysis. In Proceedings of the 14th EAI International Conference on Mobile and Ubiquitous Systems: Computing, Networking and Services, Melbourne, Australia, 7–10 November 2017; pp. 28–37.
43. Zhao, Y.; Cen, Y. *Data Mining Applications with R*; Academic Press: Cambridge, MA, USA, 2013.
44. Cohen, M.X. *MATLAB for Brain and Cognitive Scientists*; MIT Press: Cambridge, MA, USA, 2017.
45. Zamm, A.; Debener, S.; Bauer, A.K.R.; Bleichner, M.G.; Demos, A.P.; Palmer, C. Amplitude envelope correlations measure synchronous cortical oscillations in performing musicians. *Ann. N. Y. Acad. Sci.* **2018**, *1423*, 251–263. [CrossRef]
46. Schreier, P.J.; Scharf, L.L. *Statistical Signal Processing of Complex-Valued Data: The Theory of Improper and Noncircular Signals*; Cambridge University Press: Cambridge, UK, 2010.
47. Díaz, J.; Bassi, A.; Coolen, A.; Vivaldi, E.A.; Letelier, J.-C. Envelope analysis links oscillatory and arrhythmic EEG activities to two types of neuronal synchronization. *Neuroimage* **2018**, *172*, 575–585. [CrossRef] [PubMed]
48. Baranowski, J.; Bauer, W.; Zagórowska, M.; Piątek, P. On digital realizations of non-integer order filters. *Circuits Syst. Signal Process.* **2016**, *35*, 2083–2107. [CrossRef]
49. Liu, J. Smoothing filter-based intensity modulation: A spectral preserve image fusion technique for improving spatial details. *Int. J. Remote Sens.* **2000**, *21*, 3461–3472. [CrossRef]
50. Jahani, S.; Setarehdan, S.K.; Boas, D.A.; Yücel, M.A. Motion artifact detection and correction in functional near-infrared spectroscopy: A new hybrid method based on spline interpolation method and Savitzky–Golay filtering. *Neurophotonics* **2018**, *5*, 015003. [CrossRef]
51. Pander, T. EEG signal improvement with cascaded filter based on OWA operator. *Signal Image Video Process.* **2019**, *13*, 1165–1171. [CrossRef]
52. Puzdrowska, P. Signal filtering method of the fast-varying diesel exhaust gas temperature. *Combust. Engines* **2018**, *57*, 48–52. [CrossRef]
53. Cohen, J. *Statistical Power Analysis for the Behavioral Sciences*; Academic Press: Cambridge, MA, USA, 2013.
54. Marston, L.; Spencer, S.; De Souza, L.; Wand, B. Non-invasive brain stimulation techniques for chronic pain. *Cochrane Database Syst. Rev.* **2018**, *3*, CD008208.
55. Wiffen, P.J.; Derry, S.; Bell, R.F.; Rice, A.S.; Tölle, T.R.; Phillips, T.; Moore, R.A. Gabapentin for chronic neuropathic pain in adults. *Cochrane Database Syst. Rev.* **2017**, *6*, CD007938. [CrossRef]
56. Taran, S.; Bajaj, V. Emotion recognition from single-channel EEG signals using a two-stage correlation and instantaneous frequency-based filtering method. *Comput. Methods Programs Biomed.* **2019**, *173*, 157–165. [CrossRef]
57. Alazrai, R.; Al-Rawi, S.; Alwanni, H.; Daoud, M.I. Tonic cold pain detection using Choi–Williams time-frequency distribution analysis of EEG signals: A feasibility study. *Appl. Sci.* **2019**, *9*, 3433. [CrossRef]
58. Elsayed, M.; Swee, S.K.; Chiang, T.S. The Pain Signals: A Systematic Review on the Electroencephalogram of the Nociceptive Pain. *Eng. Lett.* **2023**, *31*, 1747–1758.
59. Mussigmann, T.; Bardel, B.; Lefaucheur, J.-P. Resting-state electroencephalography (EEG) biomarkers of chronic neuropathic pain. A systematic review. *NeuroImage* **2022**, *258*, 119351. [CrossRef] [PubMed]
60. Athavipach, C.; Pan-Ngum, S.; Israsena, P. A wearable in-ear EEG device for emotion monitoring. *Sensors* **2019**, *19*, 4014. [CrossRef] [PubMed]
61. Schroeder, L.D.; Sjoquist, D.L.; Stephan, P.E. *Understanding Regression Analysis: An Introductory Guide*; Sage Publications: New York, NY, USA, 2016; Volume 57.
62. Maempel, J.; Clement, N.; Brenkel, I.; Walmsley, P. Validation of a prediction model that allows direct comparison of the Oxford Knee Score and American Knee Society clinical rating system. *Bone Jt. J.* **2015**, *97*, 503–509. [CrossRef] [PubMed]
63. Hamilton, D.; Ghert, M.; Simpson, A. Interpreting regression models in clinical outcome studies. *Bone Jt. Res.* **2015**, *4*, 152–153. [CrossRef] [PubMed]
64. Bazzari, A.H.; Bazzari, F.H. Advances in targeting central sensitization and brain plasticity in chronic pain. *Egypt. J. Neurol. Psychiatry Neurosurg.* **2022**, *58*, 38. [CrossRef]
65. Jutzeler, C.; Curt, A.; Kramer, J. Relationship between chronic pain and brain reorganization after deafferentation: A systematic review of functional MRI findings. *NeuroImage Clin.* **2015**, *9*, 599–606. [CrossRef] [PubMed]
66. Volz, M.S.; Medeiros, L.F.; da Graça Tarragô, M.; Vidor, L.P.; DallAgnol, L.; Deitos, A.; Brietzke, A.; Rozisky, J.R.; Rispolli, B.; Torres, I.L. The relationship between cortical excitability and pain catastrophizing in myofascial pain. *J. Pain* **2013**, *14*, 1140–1147. [CrossRef]

67. Vidor, L.P.; Torres, I.L.; Medeiros, L.F.; Dussán-Sarria, J.A.; Dall'Agnol, L.; Deitos, A.; Brietzke, A.; Laste, G.; Rozisky, J.R.; Fregni, F. Association of anxiety with intracortical inhibition and descending pain modulation in chronic myofascial pain syndrome. *BMC Neurosci.* **2014**, *15*, 42. [CrossRef]
68. Caumo, W.; Deitos, A.; Carvalho, S.; Leite, J.; Carvalho, F.; Dussán-Sarria, J.A.; Lopes Tarrago, M.d.G.; Souza, A.; Torres, I.L.d.S.; Fregni, F. Motor cortex excitability and BDNF levels in chronic musculoskeletal pain according to structural pathology. *Front. Hum. Neurosci.* **2016**, *10*, 357. [CrossRef]
69. Botelho, L.M.; Morales-Quezada, L.; Rozisky, J.R.; Brietzke, A.P.; Torres, I.L.; Deitos, A.; Fregni, F.; Caumo, W. A framework for understanding the relationship between descending pain modulation, motor corticospinal, and neuroplasticity regulation systems in chronic myofascial pain. *Front. Hum. Neurosci.* **2016**, *10*, 308. [CrossRef] [PubMed]
70. Dickenson, A.; Ghandehari, J. Anti-convulsants and anti-depressants. In *Analgesia*; Springer: Berlin/Heidelberg, Germany, 2007; pp. 145–177.
71. Dworkin, R.H.; Turk, D.C.; Wyrwich, K.W.; Beaton, D.; Cleeland, C.S.; Farrar, J.T.; Haythornthwaite, J.A.; Jensen, M.P.; Kerns, R.D.; Ader, D.N. Interpreting the clinical importance of treatment outcomes in chronic pain clinical trials: IMMPACT recommendations. *J. Pain* **2008**, *9*, 105–121. [CrossRef] [PubMed]
72. Giusti, G.D.; Reitano, B.; Gili, A. Pain assessment in the Emergency Department. Correlation between pain rated by the patient and by the nurse. An observational study. *Acta Biomed.* **2018**, *89*, 64.
73. Stoopler, M.; Choinière, M.; Nam, A.; Guigui, A.; Walfish, L.; Mohamed, N.; Vigouroux, M.; González-Cárdenas, V.-H.; Ingelmo, P. Chronic pain-related consultations to the emergency department of children with complex pain conditions: A retrospective analysis of healthcare utilization and costs. *Can. J. Pain* **2022**, *6*, 86–94. [CrossRef] [PubMed]

sensors

Article

Latent Prototype-Based Clustering: A Novel Exploratory Electroencephalography Analysis Approach

Sun Zhou [1,*], Pengyi Zhang [1] and Huazhen Chen [2]

1 Department of Automation, Xiamen University, Xiamen 361102, China; zhangpengyi@stu.xmu.edu.cn
2 School of Sociology and Anthropology, Xiamen University, Xiamen 361005, China; chenhuazhen@stu.xmu.edu.cn
* Correspondence: zhousun@xmu.edu.cn

Abstract: Electroencephalography (EEG)-based applications in brain–computer interfaces (BCIs), neurological disease diagnosis, rehabilitation, etc., rely on supervised approaches such as classification that requires given labels. However, with the ever-increasing amount of EEG data, incomplete or incorrectly labeled or unlabeled EEG data are increasing. It likely degrades the performance of supervised approaches. In this work, we put forward a novel unsupervised exploratory EEG analysis solution by clustering based on low-dimensional prototypes in latent space that are associated with the respective clusters. Having the prototype as a baseline of each cluster, a compositive similarity is defined to act as the critic function in clustering, which incorporates similarities on three levels. The approach is implemented with a Generative Adversarial Network (GAN), termed W-SLOGAN, by extending the Stein Latent Optimization for GANs (SLOGAN). The Gaussian Mixture Model (GMM) is utilized as the latent distribution to adapt to the diversity of EEG signal patterns. The W-SLOGAN ensures that images generated from each Gaussian component belong to the associated cluster. The adaptively learned Gaussian mixing coefficients make the model remain effective in dealing with an imbalanced dataset. By applying the proposed approach to two public EEG or intracranial EEG (iEEG) epilepsy datasets, our experiments demonstrate that the clustering results are close to the classification of the data. Moreover, we present several findings that were discovered by intra-class clustering and cross-analysis of clustering and classification. They show that the approach is attractive in practice in the diagnosis of the epileptic subtype, multiple labelling of EEG data, etc.

Keywords: EEG; GAN; clustering; GMM

Citation: Zhou, S.; Zhang, P.; Chen, H. Latent Prototype-Based Clustering: A Novel Exploratory Electroencephalography Analysis Approach. *Sensors* **2024**, *24*, 4920. https://doi.org/10.3390/s24154920

Academic Editors: Yifan Zhao, Hua-Liang Wei, Yuzhu Guo and Fei He

Received: 12 July 2024
Revised: 26 July 2024
Accepted: 28 July 2024
Published: 29 July 2024

1. Introduction

Electroencephalography (EEG) is a well-established non-invasive tool to record brain electrophysiological activity. Compared to other neuroimaging techniques that provide information about the anatomical structure (e.g., MRI, CT, and fMRI), EEG offers ultra-high time resolution, which is critical in understanding brain function. As the mainstream means for examining brain electrical activities, EEG techniques have wide applications in cognitive neuroscience, emotion recognition [1], motor imagery [2], and the diagnosis of diseases such as autism, schizophrenia, and epilepsy [3]. However, these applications are mostly focused on supervised tasks that require a priori knowledge such as EEG labels that define the class they belong to. However, not all EEG labels associated with specific patterns of brain activity can be completely or correctly obtained from subjects across different recording sessions. This is especially so for patients with complex situations, such as those suffering from stroke [4], Alzheimer's disease (AD) [5], amyotrophic lateral sclerosis (ALS) [6], or epileptic seizures [7], etc. Therefore, the increasing amount of incomplete or incorrectly labeled or unlabeled EEG data likely degrades the efficacy of supervised techniques, e.g., classification that is crucial to brain–computer interface (BCI)-based applications and disease diagnosis. Moreover, in fact, the EEG signals often have multiple attributes, consequently needing to be annotated with multiple labels. Some EEG data may have subclasses that deserve more attentions in clinical applications, like epileptic subtype diagnosis. In practice, either multiple labelling or subclass labelling is almost infeasible due to the multiple labor and time costs of the labelling.

Dai et al. suggested a semi-supervised EEG clustering method that makes good use of limited a priori knowledge [8]. In our work, we focus on unsupervised clustering. Clustering aims to organize the data elements of a dataset into distinct clusters according to the resemblance of the intrinsic patterns of the data. Data elements of the same cluster are characterized by a similarity higher than those of other clusters [9]. Clustering is probably the most important and fundamental means of exploratory data analysis for finding intrinsic hidden information and patterns (if any) without requirement for a priori knowledge, such as to detect unknown kinds of abnormal states from brain imaging data.

The most widely applied clustering techniques, such as K-means, rely on distance to assign a cluster, which determine the cluster members to centers based on their minimum distances and find the most appropriate cluster centers by the optimization of an objective function based on distance [10]. Distance-based algorithms are the most commonly used benefiting from this simple principle.

To adapt to the diversity of data, distribution-based approaches such as the Gaussian Mixture Model (GMM) have drawn more attentions. They employ predefined probability distribution functions to reproduce data elements [11]. If the predefined distribution cannot be adaptively adjusted, the clustering efficacy relies on the capability of the trial probability in representing the data. Based on the Density Peaks Clustering (DPC) algorithm [12], Gao et al. formed an adaptive density peaks clustering (ADPC) solution towards exploratory EEG analysis [13].

Generative Adversarial Networks (GANs) have obtained remarkable success in many unsupervised learning tasks [14]. In recent times, in order to provide a better fit to the target data distribution when the image dataset includes many different classes, some variants of the basic GAN model, including Gaussian Mixture GAN (GM-GAN), dynamic GM-GAN [15], and Deli-GAN [16], have been proposed where the probability distribution over the latent space is a mixture of Gaussians. These models tend to map latent vectors sampled from different Gaussians in the latent space to samples of different classes in the image data space. This phenomenon implies that it may be exploited for the task of unsupervised clustering. However, these GANs do not provide inverse mapping from the data space $\boldsymbol{X}$ to the latent space $\boldsymbol{Z}$. Therefore, given a query data point, we cannot know which latent variable it is generated from, or to say, we cannot obtain its latent space representation.

Some GAN techniques make use of an encoder that has the potential to provide another form of back-projection, such as InfoGAN [17], Variational Auto-Encoder GAN (VAE-GAN) [18], and Stein Latent Optimization for GANs (SLOGAN) [19]. Usually, they are not specifically designed for clustering.

The main contributions of this work are as follows.

A novel unsupervised approach is put forward for exploratory EEG analysis. The basic idea is to form a kind of GAN to learn the Gaussian mixture distribution in latent space wherefrom the prototype or center associated with each cluster can be abstracted. Then, based on the latent prototypes, according to a well-defined similarity metric, the query EEG data will be assigned to a cluster.

By applying the proposed approach to two public EEG or intracranial EEG (iEEG) epilepsy datasets, our experiments demonstrate that the clustering results are close to the classification of the data. Moreover, several findings show that the approach is attractive in practice in the diagnosis of epileptic subtypes and multiple labelling of EEG data, etc.

2. Materials

In this work, two publicly available EEG epilepsy datasets were used in the experiments, the benchmark Bonn dataset and the HUP iEEG dataset.

2.1. Bonn Dataset

The Bonn dataset [20], collected by the University of Bonn, contains EEG and iEEG signals from healthy volunteers and epileptics. The muscle activity and eye movement artifacts were already removed from the collected data on the basis of visual inspection [21]. The complete database consists of by five sets denoted as A–E. Sets A and B contain scalp EEG signals collected from healthy volunteers with their eyes open (A) and closed (B). Set C contains iEEG recordings that were recorded from the hippocampal formation of opposite hemispheric regions during inter-ictal periods [22]. Set D comprises the iEEG signals collected from within the epileptic zone of the brain of patients during seizure-free intervals. Set E contains data collected from within the epileptogenic zone of patients during the ictal period. Detailed descriptions of the dataset are shown in Table 1. Each set contains 100 single-channel EEG or iEEG segments with a sampling rate of 173.61 Hz and a duration of 23.6 s.

Table 1. Description of the Bonn dataset.

Subjects	**Set A**	**Set B**	**Set C**	**Set D**	**Set E**
	Healthy Volunteers		**Epileptic Patients**		
Patient state	Eyes open	Eyes closed	Inter-ictal	Inter-ictal	Ictal
Electrode types	Surface	Surface	Intracranial	Intracranial	Intracranial
Electrode placement	International 10/20 systems	International 10/20 systems	Opposite epileptogenic zone	Within epileptogenic zone	Within epileptogenic zone
No. of samples	100	100	100	100	100
Sampling points	4096	4096	4096	4096	4096

2.2. HUP IEEG Epilepsy Dataset

The HUP dataset [23], collected by the Hospital of the University of Pennsylvania, contains intracranial EEG (iEEG) signals from 58 patients diagnosed as drug-resistant epilepsy. Each of the 58 subjects underwent iEEG with subdural grid, strip, and depth electrodes (electrocorticography (ECoG)) or purely stereotactically placed depth electrodes (sEEGs). Since each patient's epilepsy type may not be the same, a patient-specific study is necessary [24]. We chose the ECoG signals of three de-identified patients, HUP65, HUP88, and HUP89, to be used in the experiments. Details of the dataset are provided in Table 2. The data for each patients include three ictal and two inter-ictal segments, stored in EDF format. Each ictal segment includes recordings from two minutes before the seizure onsets, which were viewed as the pre-ictal period in this study. Therefore, data of each patient can be categorized into three periods: pre-ictal, ictal, and inter-ictal. Figure 1 illustrates the different periods in EEG data collected from epileptics.

Table 2. Description of electrocorticography (ECoG) data of three patients in the HUP dataset.

Patients	Gender	Age	Target	Therapy	Electrode
HUP65	M	36	Temporal	Resection	RG 11-Ref
HUP88	F	35	Temporal	Resection	LMST 02-Ref
HUP89	M	29	Temporal	Resection	AD 04-Ref

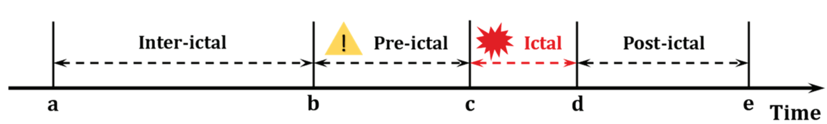

Figure 1. Different periods of electroencephalography (EEG) signals of an epileptic. a–e denote different time points.

3. Methods

Given a test data, the probability for each cluster can be calculated using a given critic function, which enables us to assign a cluster for the data. We propose a critic function based on the test data's low-dimensional prototype in the latent space, termed latent prototype. Each prototype is responsible for a certain attribute of the data, namely a cluster. Having the prototype as a baseline of each cluster, we are able to define a compositive critic metric that incorporates the similarities between the test data and the prototype of a given cluster on three levels, which are the latent representation level, image level, and deep feature map level.

3.1. Schematic of Latent Prototype-Based Clustering

According to the above consideration, we put forward an unsupervised EEG clustering approach based on latent prototypes. Its schematic is briefly illustrated in Figure 2. First, train a W-SLOGAN from the EEG dataset to learn a generator, a discriminator, an encoder as well as the latent prototype $\boldsymbol{\mu}_k$ that are responsible for each cluster. Given a query signal, transform it with continuous wavelet transform to a scalogram x_{query}. Wavelet transform is an effective technique to analyze the local characteristics of non-stationary signals, offering both time domain resolution and frequency domain resolution. Then, utilizing the trained W-SLOGAN, calculate three levels of similarities separately between (i) the latent space representation of the query signal and the latent prototype of each cluster, (ii) scalogram of the query signal and the baseline scalogram of each cluster, and (iii) the deep feature map (DFM) of the query signal and the baseline deep feature map of each cluster. Obtain the compositive similarity between the query signal and the prototype of each cluster by incorporating the above three levels of similarities. Finally, convert the compositive similarity to a probability with the SoftMax function, which enables us to assign a cluster for the query signal.

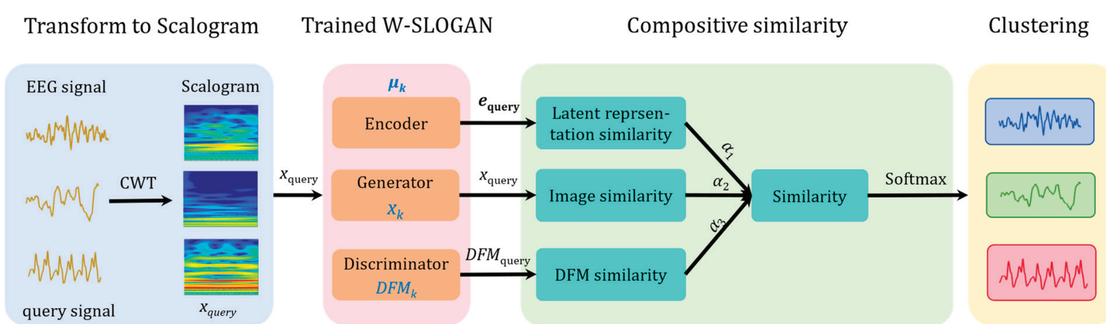

Figure 2. Schematic of EEG clustering solution based on latent prototypes. CWT, continuous wavelet transform. DFM, deep feature map. $\boldsymbol{e}_{\text{query}}$, latent space representation of the query signal. $\boldsymbol{\mu}_k$, latent prototype of the kth cluster. x_{query}, scalogram of the query signal. x_k, baseline scalogram of the kth cluster. DFM_{query}, deep feature map of the query signal. DFM_k, baseline deep feature map of the kth cluster. α_1, α_2, and α_3 are weights.

3.2. Gaussian Mixture Distribution in Latent Space

GANs usually uses a unimodal distribution as the prior distribution for Z, such as the multivariate uniform distribution (i.e., $U[-1,1]^{d_z}$) and the multivariate normal distribution (i.e., $\mathcal{N}(0, I_{d_z \times d_z})$) [15]. To better adapt to diversity of the real data, the W-SLOGAN adopts the multimodal Gaussian mixture distribution as the prior to sample from latent space, as shown in Figure 3.

The Gaussian mixture distribution is defined as follows:

$$q(\boldsymbol{z}) = \sum_{k=1}^{N} p(k) q(\boldsymbol{z}|k) \tag{1}$$

where N is the number of Gaussian components and can be predefined by the number of data clusters, $p(k)$ is mixing coefficient, and $q(z|k)$ denotes the probability distribution of the kth Gaussian component, formulated as $q(z|k) = \mathcal{N}(\boldsymbol{z}; \boldsymbol{\mu}_k, \boldsymbol{\Sigma}_k)$, where $\boldsymbol{\mu}_k$ and $\boldsymbol{\Sigma}_k$ denote the mean vector and covariance matrix of the kth Gaussian component, respectively.

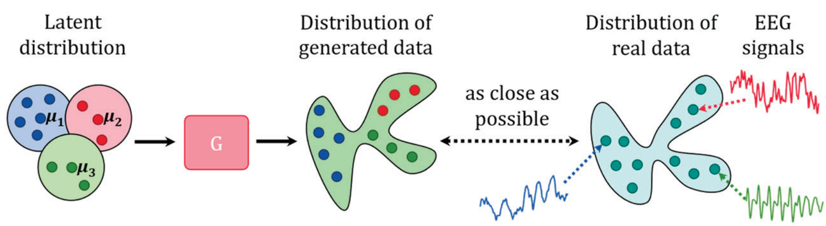

Figure 3. Latent distribution defined as Gaussian mixture distribution and distribution of generated data and that of real data. Suppose there are three clusters in the dataset. μ_1, μ_2, and μ_3 can be regarded as the latent prototypes of the three clusters.

3.3. W-SLOGAN

We decided to form a kind of GAN to obtain the latent prototype of each cluster that is needed in the calculation of compositive similarity. GAN is a generative model that learns a generator (G) capable of generating samples from the data distribution (p_{data}), by converting latent vectors from a lower-dimension data space (Z) to samples in a higher-dimension data space (X). Specifically, we need a kind of GAN such that: (i) The latent space distribution of the GAN should be defined as a Gaussian mixture distribution to model the diversity of the data. (ii) It should be able to learn the latent prototype that is responsible for each cluster from the data distribution. (iii) It is able to back-project the query image to the latent space; therefore, an encoder (E) is needed. (iv) Well-defined objective functions are needed for training G, D, and E and the latent distribution. Based on the above consideration, we put forward a GAN, termed W-SLOGAN, which takes advantage of both the Wasserstein GAN with Gradient Penalty (WGAN-GP) and the Stein Latent Optimization for GANs (SLOGAN), especially the latter. The W-SLOGAN adopts a discriminator objective function and adversarial loss function proposed in WGAN-GP, with which the training can be more stable, and the generated images can be of better quality. Also, it utilizes an encoder as well as an Unsupervised Conditional Contrastive loss (U2C loss), ensuring that the encoded vector of the generated image is similar to its assigned low-dimensional prototype in the latent space.

In the following, the network architecture, objective functions, and optimization algorithm of the W-SLOGAN will be described.

3.3.1. Network Architecture

Figure 4 shows the network architecture of W-SLOGAN, which consists of a generator (G), a discriminator (D), and an encoder (E). G is responsible for mapping the latent space (Z) defined by Gaussian mixture distribution to the real image domain (X) ($G(z) : Z \to X$). In this mapping, the mean vector $\boldsymbol{\mu}_k$ of each Gaussian component in the latent space can be viewed as a prototype of samples with certain salient attribute, and the average representation of that attribute in the latent space. D receives the generated images ($\boldsymbol{x}_g$) and real images ($\boldsymbol{x}_r$) to train its capability to discriminate between real and fake, providing the driving force for the training of the generator. E maps the image onto a space of the same dimension as the latent space. In order to stabilize the process of adversarial learning and improve the learning of images, W-SLOGAN adopts the convolutional layer structure that was introduced in Deep Convolutional GAN (DCGAN) [25]. Table 3 provides the implementation details of the W-SLOGAN model.

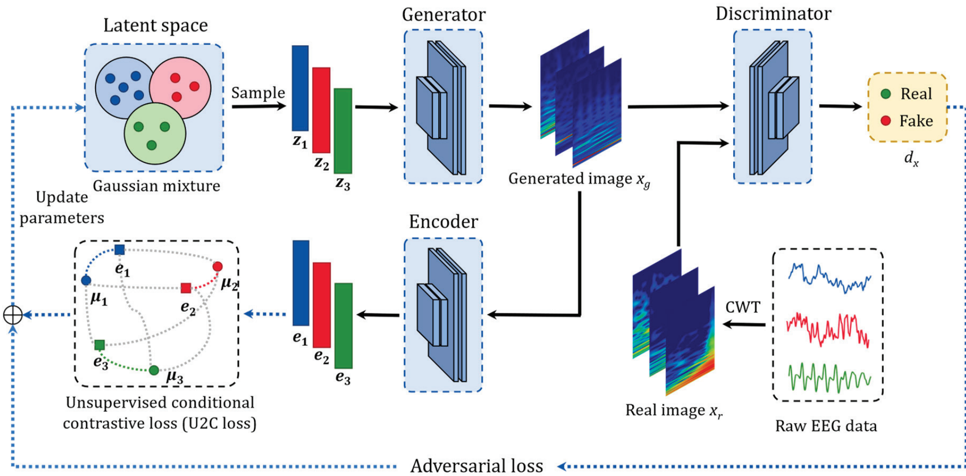

Figure 4. Network architecture of W-SLOGAN. The latent distribution is defined as Gaussian mixture distribution. Assume the number of Gaussian components is 3. z_1, z_2, and z_3 denote the latent vectors sampled from latent space. e_1, e_2, and e_3 denote the encoded vectors of the scalograms calculated by the encoder. μ_1, μ_2, and μ_3 denote the mean vectors of the three Gaussian components, corresponding to the latent prototypes of the three clusters. d_x denotes the output of the discriminator.

Table 3. Implementation details of the W-SLOGAN model.

Network	Layer (Type)	Maps	Size	Kernel Size	Activation	BN [a] Layer
Generator	Input_1	None	100	None	None	None
	Dense	None	8192	None	None	None
	Reshape	512	4 × 4	None	ReLU	yes
	ConvTranspose2D	256	8 × 8	5 × 5	ReLU	yes
	ConvTranspose2D	128	16 × 16	5 × 5	ReLU	yes
	ConvTranspose2D	64	32 × 32	5 × 5	ReLU	yes
	ConvTranspose2D	3	64 × 64	5 × 5	ReLU	yes
Discriminator	Input_2	3	64 × 64	None	None	None
	Conv2D	64	32 × 32	5 × 5	LeakyReLU	None
	Conv2D	128	16 × 16	5 × 5	LeakyReLU	None
	Conv2D	256	8 × 8	5 × 5	LeakyReLU	None
	Conv2D	512	4 × 4	5 × 5	LeakyReLU	None
	Flatten	None	8192	None	None	None
	Dense	None	1	None	None	None
Encoder	Input_3	3	64 × 64	None	None	None
	Conv2D	64	32 × 32	5 × 5	ReLU	yes
	Conv2D	128	16 × 16	5 × 5	ReLU	yes
	Conv2D	256	8 × 8	5 × 5	ReLU	yes
	Conv2D	512	4 × 4	5 × 5	ReLU	yes
	GAP [b]	None	512	None	None	None
	Dense	None	100	None	None	None

[a] Batch Normalization. [b] Global Average Pooling.

3.3.2. Objective Functions

W-SLOGAN is trained to learn the parameters of the generator G, discriminator D, and encoder E from the data, as well as the parameters (μ_k, Σ_k, and $p(k)$) of the Gaussian mixture distribution of the latent space. It is necessary to define well the objective functions for the training. We chose a discriminator objective function and an adversarial loss function that were the same as those of WGAN-GP. The unsupervised conditional contrastive loss (U2C loss) proposed by Hwang et al. [19] for SLOGAN was also employed in the training. In the training of W-SLOGAN, D and (G, E, $\boldsymbol{\mu}_k$, $\boldsymbol{\Sigma}_k$, and $p(k)$) were updated alternately. D was trained with the discriminator objective function, and G, E, $\boldsymbol{\mu}_k$, $\boldsymbol{\Sigma}_k$, and $p(k)$ were trained with a total objective function that comprises the adversarial loss and the U2C loss.

Discriminator objective function. The discriminator objective function is defined as that of WGAN-GP, which helps to stabilize the training process and provide the driving force for the training of generator [26–28]. It is defined as

$$L_D = -E_{x \in P_{data}}[D(x)] + E_{z \in q(z)}[D(G(z))] + \lambda_1 E_{\widetilde{x} \in P_{penalty}}\left[\left(\left\|\nabla_{\widetilde{x}} D\left(\widetilde{x}\right)\right\|_2 - 1\right)^2\right] \quad (2)$$

where λ_1 denotes the gradient penalty coefficient, and $\widetilde{x}$ is sampled from the line between the real training data distribution and the generated data distribution. Such a design can make the model converge faster.

Adversarial loss function. The purpose of minimizing adversarial loss is to make the samples generated by the generator as realistic as possible, so that the discriminator cannot accurately distinguish between the generated samples and the fake ones. The adversarial loss function is defined as that of WGAN-GP, as formulated in (3).

$$l_{adv}\left(\boldsymbol{z^i}\right) = -D\left(G\left(\boldsymbol{z^i}\right)\right) \quad (3)$$

Total objective function. W-SLOGAN learns the parameters of the generator (G), encoder (E), and the Gaussian mixture distribution of the latent space by minimizing the total objective function, including unsupervised conditional contrastive loss (U2C loss) and adversarial loss. The total objective function is defined as follows:

$$L_{total} = \frac{1}{B}\sum\nolimits_{i=1}^{B}\left(l_{adv}\left(\boldsymbol{z}^i\right) + \lambda_2 l_{U2C}\left(\boldsymbol{z}^i\right)\right) \quad (4)$$

where λ_2 denotes the weight coefficient of the U2C loss.

U2C loss. With U2C loss, the training allows each salient attribute to cluster in the latent space, and each component of the learned latent distribution is responsible for a certain attribute of the data. Given a batch of latent vectors $\{\boldsymbol{z^i}\}_{i=1}^{B} \sim q(z)$ (where B is the batch size), we can find the corresponding Gaussian component K^i (the mean vector is $\boldsymbol{\mu_K^i}$) to which $\boldsymbol{z^i}$ is most likely belong by the use of (5).

$$K^i = argmax_k q\left(k\middle|\boldsymbol{z}^i\right) = argmax_k \frac{q\left(k, \boldsymbol{z}^i\right)}{q\left(\boldsymbol{z}^i\right)} = argmax_k \frac{q\left(\boldsymbol{z}^i|k\right)p(k)}{q\left(\boldsymbol{z}^i\right)} \quad (5)$$

The generator receives the latent vector $\boldsymbol{z^i}$ and generates the corresponding sample $x_g^i = G(\boldsymbol{z^i})$. Then, the generated sample x_g^i is mapped by the encoder to an encoded vector $x_g^i = G(\boldsymbol{z^i})$. The cosine similarity between $\boldsymbol{e}^i$ and $\boldsymbol{\mu}_K^j$ can be calculated using $cos\theta_{ij} = \boldsymbol{e}^i \cdot \boldsymbol{\mu}_K^j / \left\|\boldsymbol{e}^i\right\| \left\|\boldsymbol{\mu}_K^j\right\|$. The U2C loss is defined as

$$l_{U2C}\left(\boldsymbol{z}^i\right) = -log\frac{\exp(cos\theta_{ii})}{\frac{1}{B}\sum_{j=1}^{B}\exp\left(cos\theta_{ij}\right)} \quad (6)$$

In this way, by minimizing the U2C loss, the training encourages the encoded vectors of samples with the same prototype to be as similar as possible to the prototype. This allows each component of the learned latent distribution to be responsible for a certain cluster of the data.

3.3.3. Optimization Algorithm of Latent Distribution Parameters

In order to train the parameters of Gaussian mixture distribution of latent space, it is crucial to obtain the gradient of the parameters during the training. Gurumurthy et al. [16] and Ben-Yosef et al. [15] adopted the "reparameterization trick" proposed by Kingma et al. [29] in their related work to update the mean vectors $\boldsymbol{\mu}_k$ and covariance matrices $\boldsymbol{\Sigma}_k$ of each Gaussian component. However, the above method assumes uniform mixing coefficients $p(k)$ that are fixed. As a consequence, it fails to generate data in the case of imbalanced datasets. Based on the generalized Stein lemma, Hwang et al. [19] derived gradient identities of the parameters of Gaussian mixture distribution, which not only enables $\boldsymbol{\mu}_k$ and $\boldsymbol{\Sigma}_k$ to be updated, but also ensures that the mixing coefficients $p(k)$ can be updated. It is called the Stein latent optimization algorithm. The W-SLOGAN employs the Stein latent optimization algorithm to enable the imbalanced attributes to be naturally clustered in a continuous latent space. Table 4 presents a comparison of these two reparameterization techniques.

Table 4. Comparison of two reparameterization methods.

Models	Reparameterization Form	Trainable Parameters	Characteristics of Gradient Estimation
AEVB [29] DeLiGAN [16] GM-GAN [15]	Explicit	$\boldsymbol{\mu}_k$ and $\boldsymbol{\Sigma}_k$	Unbiased; high variance
SLOGAN [19]	Implicit	$\boldsymbol{\mu}_k$, $\boldsymbol{\Sigma}_k$ and $p(k)$	Unbiased; low variance

3.3.4. Training Process

Step 1. Parameter initialization. Initialize parameters of the Gaussian mixture distribution, including $\boldsymbol{\mu}_k$, $\boldsymbol{\Sigma}_k$, and $p(k)$, as well as the parameters of three networks G, D, and E.

Step 2. Train D for b_D times. Train D with the discriminator objective function as presented in Equation (2).

Step 3. Train G, E, $\boldsymbol{\mu}_k$, $\boldsymbol{\Sigma}_k$, and $p(k)$ for one time. Train them with the total objective function as presented in Equation (4). Go to Step 2.

The loop of step 2 and step 3 stops after it is carried out for a predefined number of times.

3.4. Compositive Similarity Metric

In our clustering approach, the similarity metric plays the role of critic function, which will enable us to assign a cluster for the query data. Having the prototype as a baseline of each cluster, we put forward a compositive similarity metric that combines similarities between the test data and the prototype of a given cluster on three levels, namely latent representation, image, and deep feature map. Figure 5 illustrates three levels of similarity for clustering.

Latent representation similarity. The scalogram $\boldsymbol{x}_{\text{query}}$ of the query signal is mapped to the latent space by the encoder (E) to become an encoded vector, which can be viewed as the latent representation of the query signal, denoted by $\boldsymbol{e}_{\text{query}} = E(\boldsymbol{x}_{\text{query}})$. Latent representation similarity measures similarity between $\boldsymbol{e}_{\text{query}}$ and the latent prototype that is responsible for a given cluster. It is defined in (7), using cosine similarity to measure the similarity between two vectors.

$$S_{latent}^{k} = \frac{\boldsymbol{e}_{\text{query}} \cdot \boldsymbol{\mu}_k}{\left\|\boldsymbol{e}_{\text{query}}\right\| \left\|\boldsymbol{\mu}_k\right\|} \tag{7}$$

where S_{latent}^{k} denotes the similarity between the query signal and the k-th cluster in latent space.

Image similarity. It measures similarity between the scalogram of the query signal $\boldsymbol{x}_{\text{query}}$ and the baseline scalogram $\boldsymbol{x}_k$ of a given cluster that is generated by the generator G from the prototype $\boldsymbol{\mu}_k$ of the given cluster, and is formulated by $\boldsymbol{x}_k = G(\boldsymbol{\mu}_k)$. Image similarity is defined as follows:

$$S_{image}^k = \frac{1}{\left\|\boldsymbol{x}_{\text{query}} - G(\boldsymbol{\mu}_k)\right\|_1} \tag{8}$$

DFM. similarity. It measures the similarity between the DFM of the query signal, DFM_{query}, and the DFM of the baseline DFM of a given cluster, $DFM_k = DFM(\boldsymbol{x}_k)$. DFM refers to the output of the last convolution layer of the discriminator that can be viewed as deep feature map of a given image. This kind of deep feature is inspired by the work of NHAN et al. [30], where the discriminator is employed as an unsupervised feature extractor. DFM similarity is defined as

$$S_{DFM}^k = \frac{1}{\left\|DFM(\boldsymbol{x}_{\text{query}}) - DFM(\boldsymbol{x}_k)\right\|_1} \tag{9}$$

Compositive similarity. We define a compositive similarity between the query signal and the centroid of the kth cluster that incorporates all the three levels of similarities as

$$S_{\text{com}}^k = \alpha_1 * S_{latent}^k + \alpha_2 * S_{image}^k + \alpha_3 * S_{DFM}^k \tag{10}$$

$$\alpha_1 + \alpha_2 + \alpha_3 = 1 \tag{11}$$

where α_1, α_2, and α_3 are weight coefficients of the three similarities. As the dimensions are different, it is necessary to normalize S_{latent}^k, S_{image}^k, and S_{DFM}^k separately before calculating the compositive similarity.

Through some sensitivity tests, we found that the proposed clustering approach is somehow sensitive to α_1 and α_2 values. Therefore, to seek good settings for them, we carried out multiple experiments where α_1 and α_2 were set to different values. Then, based on the resulting clustering performance evaluated with external clustering indexes, we determined the optimal values. In real applications where the data are unlabeled, optimal values can also be determined by use of internal clustering indexes.

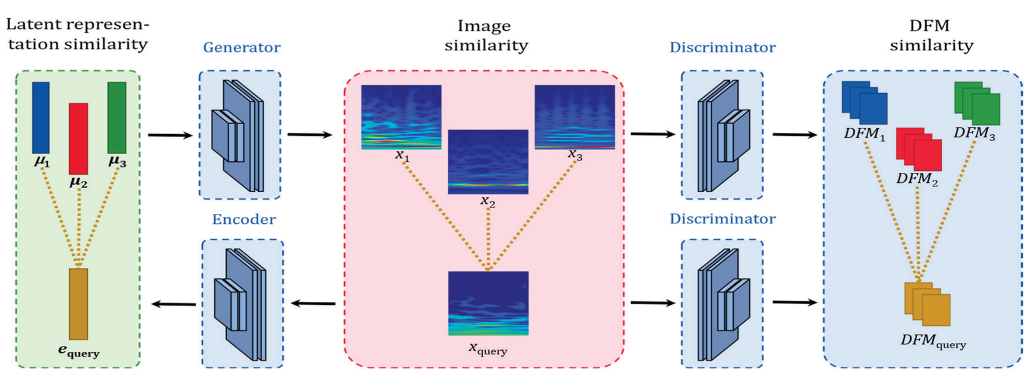

Figure 5. Three levels of similarity for clustering. Assume the number of Gaussian components is 3. DFM: deep feature map. μ_1, μ_2, and μ_3 denote the mean vectors of the three Gaussian components, corresponding to the latent prototypes of the three clusters. $\boldsymbol{e}_{\text{query}}$ denotes the latent representation of the query signal. x_1, x_2, and x_3 denote the baseline scalograms of the three clusters. x_{query} denotes the scalogram of the query signal. DFM_1, DFM_2, and DFM_3 denote the baseline deep feature maps of the three clusters. DFM_{query} denotes the deep feature map of the query signal.

The query data can then be assigned to the cluster with the highest compositive similarity (i.e., $\underset{k}{\mathrm{argmax}} S_{\mathrm{com}}^{k}$).

With respect to computational complexity, when applied to a dataset with size n, the complexity of both the training and clustering of the W-SLOGAN algorithm are O(n), which is linear.

3.5. External Clustering Indexes

To evaluate the closeness between the clustering results from the proposed approach and classification of the data, three widely used external clustering indexes were adopted, namely Purity, Adjusted Rand Index (ARI), and Normalized Mutual Information (NMI).

Purity. Purity is an intuitive evaluation index that indicates the degree of agreement between the clustering results and the real data distribution. It is defined as

$$Purity = \frac{1}{n}\sum_{i=1}^{k} max_j\left(n_{ij}\right) \tag{12}$$

where n denotes the total number of samples. k denotes the total number of clusters. n_{ij} denotes the number of samples in both class u_j and cluster v_i. The range of the Purity value is [0, 1], where a higher value indicates a purer clustering result.

ARI. ARI measures the degree of similarity between two data distributions [31]. It takes into consideration the consistency between the resulted cluster labels and class labels. The definition of ARI is

$$ARI = \frac{\sum_i\sum_j \binom{n_{ij}}{2} - \left[\sum_i \binom{a_i}{2}\sum_j \binom{b_j}{2}\right]/\binom{n}{2}}{\frac{1}{2}\left[\sum_i \binom{a_i}{2} + \sum_j \binom{b_j}{2}\right] - \left[\sum_i \binom{a_i}{2}\sum_j \binom{b_j}{2}\right]/\binom{n}{2}} \tag{13}$$

where n_{ij} denotes the number of samples in both class u_j and cluster v_i. a_i denotes the number of samples in class u_i and b_j denotes the number of samples in cluster v_j. n is the total number of samples. $\binom{n_{ij}}{2}$ represents a combination and is equal to $C_{n_{ij}}^2$.

NMI. NMI evaluates the consistency between two distributions by measuring their mutual information [32]. The definition of NMI is presented as follows:

$$NMI(C,K) = \frac{MI(C,K)}{\sqrt{H(C)\cdot H(K)}} \tag{14}$$

where $MI(C,K)$ denotes the mutual information between class labels and the resulted cluster labels, $H(C)$ is the entropy of classification labels, and $H(K)$ is the entropy of clustering results. The range of the NMI value is [0, 1], where 1 indicates perfect consistency, which means the clustering is exactly consistent with the classification.

3.6. Experimental Setup and Running Environment

The Bonn dataset consists of five subsets (A, B, C, D, and E), which were organized into four groups in the experiments. Such grouping considers the complexity of signals of each subset and the relevance of the subsets in clinical. We segmented the scalp EEG and iEEG signals from the Bonn dataset using a sliding time window of 2.88 s with 50% overlap. For each subset, all the 100 signals each with 23.6 s duration were segmented to 1500 samples each with 2.88 s duration. In the experiments, the cluster number was set according to the class number in each group. Detailed descriptions of the four groups are shown in Table 5.

The HUP dataset comprises three classes of signals: pre-ictal, ictal, and inter-ictal. The pre-ictal one is defined as two minutes before the seizure onset. The ECoG signals were segmented with a sliding time window of 5 s with 50% overlap. The number of clusters was set to 3. The description of the ECoG data of three de-identified epileptics in the HUP dataset is outlined in Table 6.

Table 5. Description of four experimental groups of the Bonn dataset.

Group	Set	Description	# Class	# Cluster	Class Ratio
CD_E	Sets C and D versus Set E	Inter-ictal and ictal	2	2	3000:1500
AB_CD	Sets A and B versus Sets C and D	Healthy and inter-ictal	2	2	3000:3000
ABCD_E	Sets A, B, C, and D versus Set E	Non-seizure and seizure	2	2	6000:1500
AB_CD_E	Sets A and B versus Sets C and D versus Set E	Healthy, inter-ictal, and ictal	3	3	3000:3000:1500

Table 6. Description of the ECoG data of three de-identified epileptics in the HUP dataset.

Case	Description	# Class	# Cluster	# Pre-Ictal	# Ictal	# Inter-Ictal
HUP65	pre-ictal, inter-ictal, and ictal	3	3	348	592	251
HUP88	pre-ictal, inter-ictal, and ictal	3	3	348	592	724
HUP89	pre-ictal, inter-ictal, and ictal	3	3	348	592	252

In each experimental group, all the data were used for the unsupervised training of W-SLOGAN; then, with the trained model, all the EEG segments were clustered; at last, the clustering results were evaluated with three external clustering indexes.

Preprocessing. Each signal was filtered by an FIR bandpass filter, preserving information within the frequency range from 0.5 to 40 Hz. The scalp EEGs and iEEGs from the Bonn dataset were segmented into 2.88-s segments, while the ECoG signals from the HUP dataset were segmented into 5-s segments. The 1-d time series segments were transformed to 2-d scalograms. The Morlet wavelet was selected as the mother wavelet in the continuous wavelet transform. The scalogram dimension is $64 \times 64 \times 3$ (3 is the number of RGB channels). Before feeding these scalograms into the W-SLOGAN model for training, each pixel value of the scalograms was scaled to ensure their range fell within $(-1, 1)$.

Parameter settings. For simplicity, we denote the learning rate of generator as η, the learning rate of the covariance $\boldsymbol{\Sigma}_k$ as γ, the gradient penalty coefficient as λ_1, the weight coefficient of the U2C loss as λ_2, and the weights for the latent representation, image, and DFM similarities as α_1, α_2, and α_3, respectively. In the experiments, the learning rate of discriminator was set to 4η, and the learning rate of encoder to η. The learning rate of latent prototype $\boldsymbol{\mu}_k$ was set to 10γ, and the learning rate of mixing coefficient $p(k)$ to γ. Specifically, the parameter values were $\eta = 0.0001$, $\gamma = 0.004$, and $\lambda = 10$. In addition, we initialized the $p(k) = 1/N$, $\boldsymbol{\Sigma}_k = I_{d_z \times d_z}$, and $\boldsymbol{\mu}_k$ sampling from $\mathcal{N}(0, I_{d_z \times d_z})$. The three weights α_1, α_2, and α_3 were empirically set to 1/3.

During the training, the Adam optimizer was employed to train G, D, and E, and the stochastic gradient descent (SGD) optimizer was adopted to train $\boldsymbol{\Sigma}_k$, $\boldsymbol{\mu}_k$, and $p(k)$. The batch size (B) was 64 and the number of training iterations was set to 18,000 to ensure sufficient training. In the clustering experiments, we repeated each experiment several times and reported the means and standard deviations of model performances. Table 7 shows the details of the experimental parameter settings.

Table 7. Details of the experimental parameter settings.

Parameters	Initialization	Optimizer	Learning Rate
Generator	Random	Adam	0.0001
Discriminator	Random	Adam	0.0004
Encoder	Random	Adam	0.0001
$\boldsymbol{\mu}_k$	$\mathcal{N}(0, I_{d_z \times d_z})$	SGD	0.04
$\boldsymbol{\Sigma}_k$	$I_{d_z \times d_z}$	SGD	0.004
$p(k)$	$1/N$	SGD	0.004

Table 7. *Cont.*

Parameters	Initialization	Optimizer	Learning Rate
λ_1	10	None	None
λ_2	1	None	None
Batch size		64	
Iterations		18,000	

Running environment. The experimental conditions include a desktop computer equipped with an Inter(R) Core (TM) i9-10900K CPU (Inter, Santa Clara, CA, USA) and an NVIDIA GeForce RTX 3080 GPU (Nvidia, Santa Clara, CA, USA). Segmentation and continuous wavelet transform of the signals were implemented with MATLAB (R2019a), while the training and evaluation of W-SLOGAN were carried out with Python 3.7 and TensorFlow 2.6.0.

4. Results

4.1. Clustering Results

From applying the proposed approach to the benchmark Bonn EEG datasets, the clustering results and the classification of the data are highly consistent. Taking the group AB_CD_E of the Bonn dataset as an example, the three subplots of Figure 6A depict the probability density functions for signals to belong to Cluster 1, Cluster 2, and Cluster 3. Red, green, and purple indicate samples from Class AB (healthy), Class CD (inter-ictal, epileptic) and Class E (ictal, epileptic), respectively. Taking Cluster 1 as an example, as shown in Figure 6A1, the probability that Class AB samples belong to this cluster is the highest, while the probability that Class CD and Class E samples belong to that cluster is relatively low. It indicates that Cluster 1 gathers the general samples of Class AB. In other words, Cluster 1 corresponds to class AB. Likewise, from Figure 6A2,A3, it is obvious that Cluster 2 and Cluster 3 correspond to Class E and Class CD, respectively. On the other hand, there are also some samples whose resulted clustering labels are inconsistent with their class labels. For example, a few samples of Class CD and E are clustered into Cluster 1, although the probability that they belong to that cluster is not high. It does not necessarily indicate clustering error, but rather reveals the intra-class diversity.

The samples whose resulted cluster label is consistent with its class label represent the generic attributes of that class. The following analysis will focus on this part of samples. Figure 6B shows the probability density function of Class AB samples that are clustered into Cluster 1. These samples can be divided into two parts; one comprises 95% of samples with higher probabilities, and the other comprises the other 5% with lower probabilities. The red color indicates high-probability samples. Several high-probability samples with their respective scalograms are shown in the upper row, representing the typical attributes of Class AB. The yellow color indicate low-probability samples that are shown in the lower row. Similarly, Figure 6C shows the probability density functions of Class CD samples clustered into Cluster 3, several high-probability samples, and low-probability samples. As for Class E samples, see Section 4.4 for a more detailed analysis.

It is obvious that (i) the high-probability samples of each cluster are quite similar, reflecting the typical characteristic of that cluster or class. For example, the high-probability samples of Cluster 1 reflect the characteristics of the EEG signals of healthy volunteers with eyes opened or closed, i.e., the amplitude fluctuates between -180 and 100, fluctuations with a relatively high frequency that suggest rapid changes in the brain activity. The high-probability samples of Cluster 3 reflect the characteristics of iEEG signals during inter-ictal periods of epileptics, i.e., the amplitude fluctuates between -70 and 70 with a relatively low frequency. (ii) Low-probability samples exhibit significant differences in terms of waveforms and scalograms compared to high-probability samples. They show diverse patterns. It could reflect intra-class diversity or may be caused by noise.

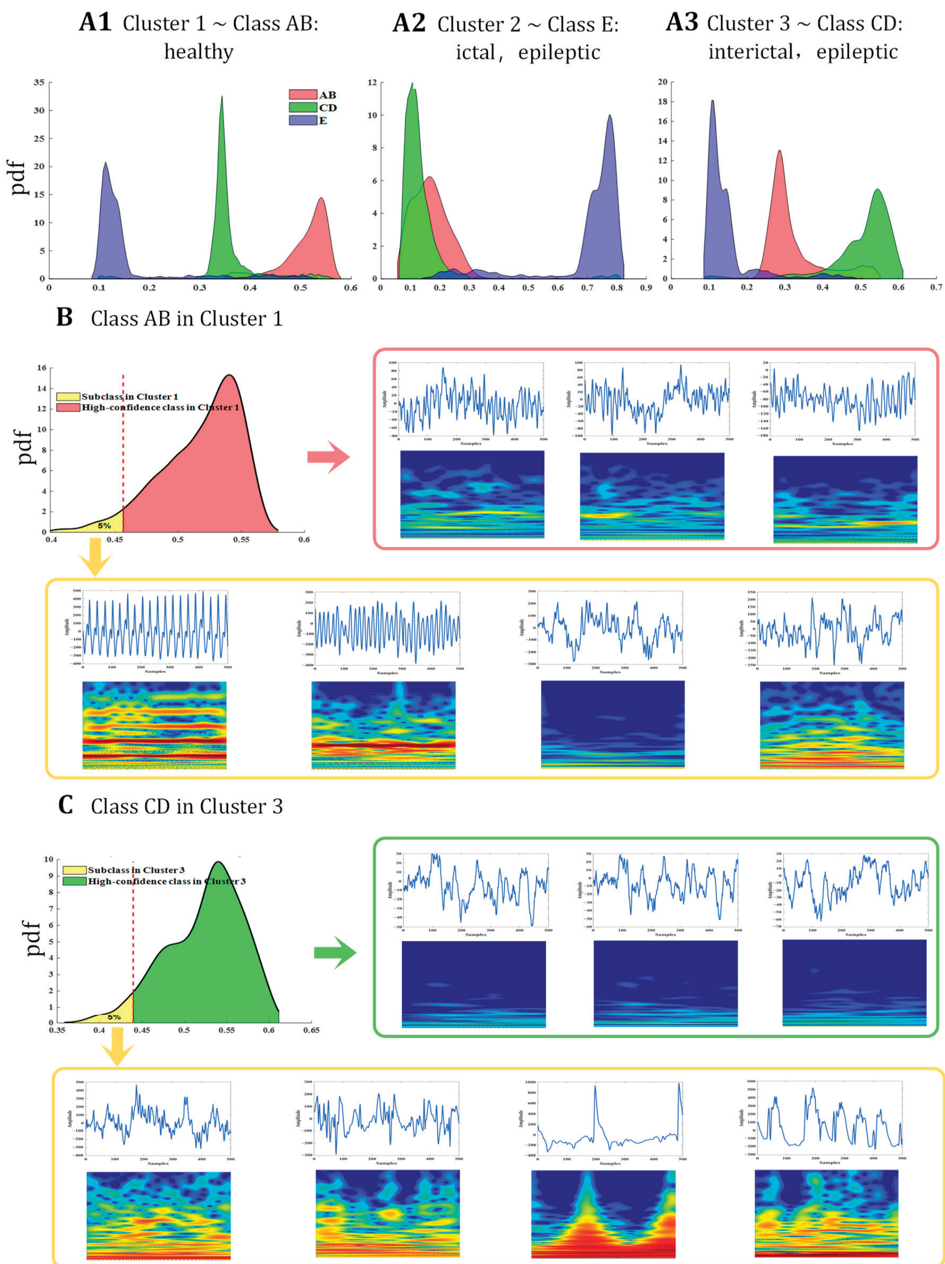

Figure 6. Clustering results and intra-class diversity. (**A1**–**A3**) show the probability density functions for samples belonging to Cluster 1, Cluster 2, and Cluster 3, respectively. (**B**) shows the probability density function of Class AB samples clustered into Cluster 1, several high-probability samples with their scalograms (in the upper row), and several low-probability samples with their respective scalograms (in the lower row). (**C**) shows the probability density functions of Class CD samples clustered into Cluster 3, several high-probability samples with their scalograms, and several low-probability samples with their scalograms (in the lower row).

4.2. Clustering Results from Different Similarity Metrics

According to the class labels provided in the dataset, the closeness of the resulted clustering to the data classification can be measured by three external clustering evaluation indexes, namely Purity, ARI, and NMI. In order to observe the role that different similarity plays in clustering in the four groups of EEG data of the Bonn dataset and the three epileptic patient's ECoG data of the HUP dataset, we applied clustering separately with three kinds of similarity metrics (namely single latent representation similarity, latent representation similarity + image similarity, and the compositive similarity that incorporates all the three levels of similarities). The results are shown in Tables 8 and 9.

Table 8. The clustering results of the Bonn dataset by the use of different kinds of similarity metrics.

Group	Criteria	Latent Representation Similarity	Latent Representation + Image Similarity	Latent Representation + Image + DFM Similarity
CD_E # Cluster:2 # Class:2	Purity	0.9033 ± 0.0200	0.9620 ± 0.0030	0.9633 ± 0.0015
	ARI	0.6410 ± 0.0680	0.8518 ± 0.0115	0.8568 ± 0.0056
	NMI	0.5704 ± 0.0472	0.7510 ± 0.0137	0.7592 ± 0.0089
AB_CD # Cluster:2 # Class:2	Purity	0.7798 ± 0.0147	0.7778 ± 0.0161	0.7768 ± 0.0172
	ARI	0.3139 ± 0.0335	0.3096 ± 0.0365	0.3076 ± 0.0389
	NMI	0.2503 ± 0.0265	0.2475 ± 0.0277	0.2466 ± 0.0288
ABCD_E # Cluster:2 # Class:2	Purity	0.9494 ± 0.0043	0.9644 ± 0.0081	0.9638 ± 0.0089
	ARI	0.7694 ± 0.0199	0.8382 ± 0.0377	0.8354 ± 0.0412
	NMI	0.6396 ± 0.0199	0.7199 ± 0.0408	0.7162 ± 0.0442
AB_CD_E # Cluster:3 # Class:3	Purity	0.8925 ± 0.0048	0.8977 ± 0.0032	0.9015 ± 0.0020
	ARI	0.6882 ± 0.0124	0.7003 ± 0.0088	0.7102 ± 0.0055
	NMI	0.6341 ± 0.0125	0.6491 ± 0.0090	0.6613 ± 0.0031
Avg Purity		0.8813	0.9005	0.9014
Avg Purity Rank		2.5	1.75	1.75
# Best Purity		1	1	2
Avg ARI		0.6031	0.6750	0.6775
Avg ARI Rank		2.5	1.75	1.75
# Best ARI		1	1	2
Avg NMI		0.5236	0.5919	0.5958
Avg NMI Rank		2.5	1.75	1.75
# Best NMI		1	1	2

Best Purity, # Best ARI, and # NMI, respectively, indicate the largest number of the best Purity, ARI, and NMI across four groups of the Bonn dataset.

Table 9. The clustering results of the HUP dataset by the use of different kinds of similarity metrics.

Case	Criteria	Latent Representation Similarity	Latent Representation + Image Similarity	Latent Representation + Image + DFM Similarity
HUP65 # Cluster:3 # Class:3	Purity	0.7834 ± 0.0086	0.8013 ± 0.0152	0.8044 ± 0.0195
	ARI	0.4774 ± 0.0067	0.5368 ± 0.0222	0.5421 ± 0.0336
	NMI	0.4893 ± 0.0096	0.5356 ± 0.0064	0.5375 ± 0.0148
HUP88 # Cluster:3 # Class:3	Purity	0.9804 ± 0.0042	0.9982 ± 0.0017	0.9982 ± 0.0015
	ARI	0.9471 ± 0.0144	0.9956 ± 0.0041	0.9956 ± 0.0036
	NMI	0.9180 ± 0.0175	0.9904 ± 0.0078	0.9905 ± 0.0074
HUP89 # Cluster:3 # Class:3	Purity	0.8249 ± 0.0039	0.8333 ± 0.0024	0.8686 ± 0.0020
	ARI	0.5483 ± 0.0076	0.5627 ± 0.0046	0.6344 ± 0.0054
	NMI	0.5408 ± 0.0069	0.5460 ± 0.0036	0.6253 ± 0.0052

Table 9. *Cont.*

Case	Criteria	Latent Representation Similarity	Latent Representation + Image Similarity	Latent Representation + Image + DFM Similarity
	Avg Purity	0.8629	0.8776	0.8904
	Avg Purity Rank	3.0	1.6667	1.0
	# Best Purity	0	1	3
	Avg ARI	0.6576	0.6984	0.7240
	Avg ARI Rank	3.0	1.6667	1.0
	# Best ARI	0	1	3
	Avg NMI	0.6494	0.6907	0.7178
	Avg NMI Rank	3.0	2.0	1.0
	# Best NMI	0	0	3

Best Purity, # Best ARI, and # NMI, respectively, indicate the largest number of the best Purity, ARI, and NMI across three epileptic subjects of the HUP dataset.

Tables 7 and 8 show that, in either the Bonn dataset or the HUP dataset, clustering by the use of the compositive similarity outperforms that of the other two kinds of similarities. Specifically, clustering using the compositive similarity achieves the best average rank (1.43) when evaluated with Purity, ARI, and NMI. Also, the compositive similarity achieved the largest number of the best Purity, ARI, and NMI out of the seven groups of experiments (five out of seven).

Figures 7 and 8 show the bar charts of the three external clustering indexes for clustering using different kinds of similarities on the Bonn dataset and the HUP dataset, respectively. Compared to using a single latent representation similarity, the inclusion of image similarity significantly improved the clustering performance in most experimental groups. In the Bonn dataset, the average Purity, ARI, and NMI increased by 2.18%, 11.92%, and 13.04%, respectively. In the HUP dataset, those three indexes averagely increased by 1.70%, 6.20%, and 6.36%, respectively. The improvement in the performance implies that the scalogram has the potential to capture the time-frequency characteristics of different EEG signals. However, compared to the combination of latent representation similarity and image similarity, the inclusion of DFM similarity has little effect on the improvement in clustering performance. In the Bonn dataset, the three indexes increased by 0.1%, 0.37%, and 0.66%, respectively.

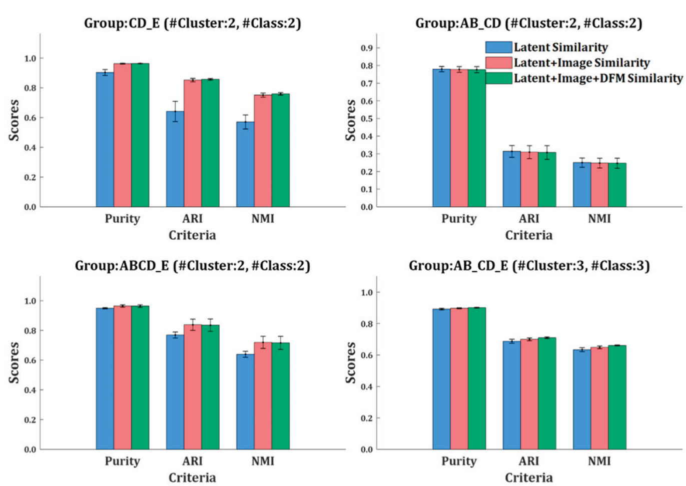

Figure 7. Purity, ARI, and NMI of the results of clustering on four groups of EEG/intracranial EEG (iEEG) data of the Bonn dataset separately using different kinds of similarities.

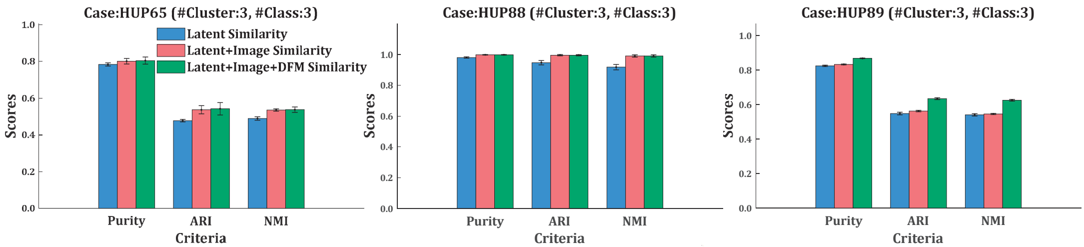

Figure 8. Purity, ARI, and NMI of the results of clustering on three epileptic subjects of ECoG data of the HUP dataset separately using different kinds of similarities.

4.3. W-SLOGAN's Training

4.3.1. Impact of the Number of Iterations in Training W-SLOGAN

We investigated the impact of the number of iterations during the training on the clustering performance of the W-SLOGAN model. We evaluated the clustering performance of the proposed approach on the two datasets separately when the model was iterated 0, 3000, 6000, 9000, 12000, 15,000, and 18,000 times, respectively. The results are shown in Figures 9 and 10. It is shown that, in most groups, a fairly good clustering performance was achieved by 9000 iterations. Before that, the performance increases rapidly with the increase in the iteration number, whereas after that, it changes smoothly. Nevertheless, for part of groups such as AB_CD_E, the clustering performance continues to increase with the increase in the iteration number.

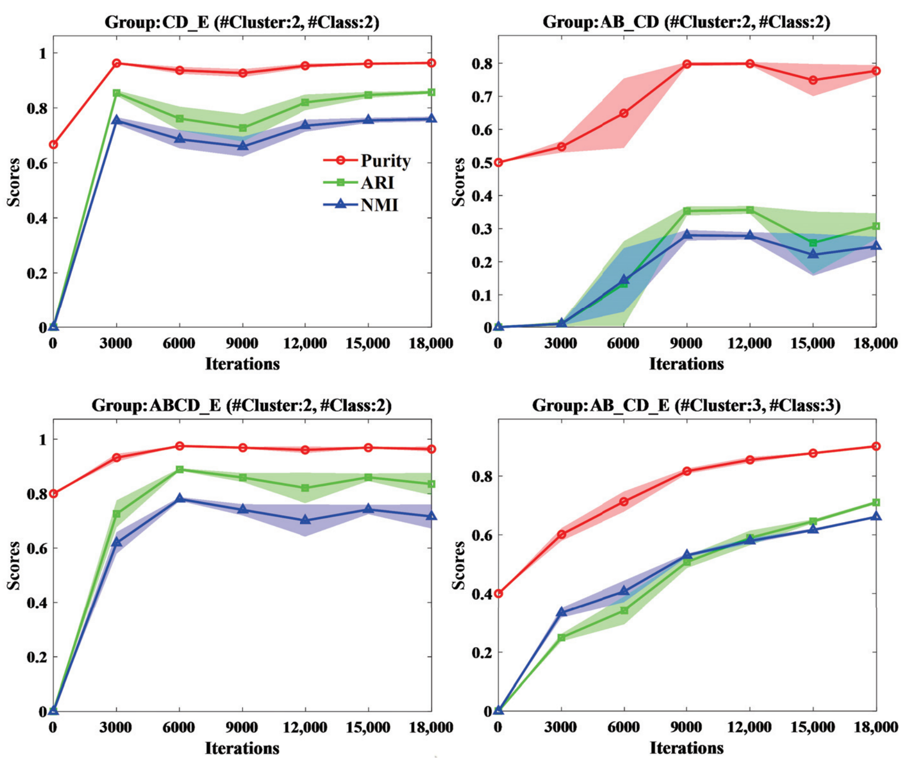

Figure 9. Impact of the iteration number during training W-SLOGAN on the clustering performance on four groups of EEG data of the Bonn dataset separately evaluated with Purity, ARI, and NMI.

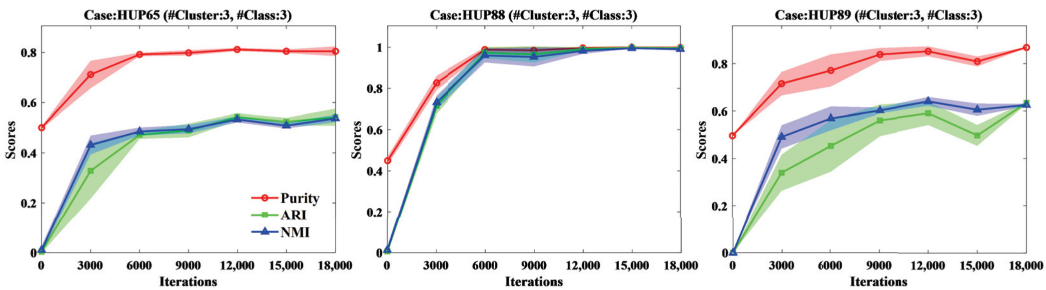

Figure 10. Impact of the iteration number duringtraining W-SLOGAN on the clustering performance on three epileptic subjects of ECoG data of the HUP dataset separately evaluated with Purity, ARI and NMI.

4.3.2. Reproducibility of the Results

The results are to some extent reproducible. It is based on our experiments to test the reproducibility on each experimental group. Taking the group of AB_CD_E of Bonn dataset as example, we trained three W-SLOGAN models with the same experimental setup and parameters. The mixing coefficients $p(k)$ of the latent mixture components obtained from different trained models are displayed in Table 10. It can be seen that they are close. Also, the ratios of the Gaussian mixture components are all close to 2:2:1. They fit the true class ratio (3000:3000:1500) of that group.

Table 10. Mixing coefficients $p(k)$ of the latent mixture components obtained from different trained W-SLOGAN models.

Model	Model_1	Model_2	Model_3
$p(k=1)$	0.3869	0.3969	0.373
$p(k=2)$	0.448	0.439	0.4627
$p(k=3)$	0.1651	0.1641	0.1643

4.4. Exploratory EEG Analysis

4.4.1. Discovery of Different Types of Epileptiform Waves

In order to explore the diversity of ictal iEEG signals, we carried out clustering on the ictal data of the Bonn dataset. The number of clusters was set to five. It is noteworthy that the three resulting clusters were highly consistent with three typical kinds of epileptiform waves in the characteristic patterns. Epileptic seizures are accompanied by some typical discharge waveforms, which serve as significant characteristics and diagnostic criteria for epileptic seizures. Common epileptiform waves include sharp wave, spike wave, spike and slow wave complex, sharp and slow wave complex, highly rhythmic disorganization, and so on. We found several clusters that correspond to rhythmic sharp wave, spike and slow wave complex, and highly rhythmic disorganization from the iEEG recordings.

Figure 11 shows the three types of epileptiform waveforms and the corresponding clusters that resulted from our approach. On each row are displayed the characteristic waveform of a type of epileptiform discharge, three epileptiform waves of that type that were clustered into a same cluster found from the iEEG recordings by our approach, as well as the baseline scalogram of that cluster.

For reference, the definitions and characteristics of sharp wave, spike and slow wave complex, and highly rhythmic disorganization are listed below [33].

Sharp wave. Sharp waves are the most basic form of burst EEG activity, lasting from 70 to 200 ms (5–14 Hz). The amplitudes range from 100 to 200 µV. They are usually with the form of negative phase waves.

Spike and slow wave complex. A pattern of epileptiform waveform composed of spike waves and slow waves. The slow wave is the predominant component of this complex, lasting approximately from 200 to 500 ms. The spike and slow wave complex typically has higher amplitudes, ranging from 105 to 300 µV, and can reach even more than 500 µV.

Highly rhythmic disorganization. Usually composed of sharp waves, spikes, etc., the frequency and amplitude are highly irregular, often seen in complex partial seizures.

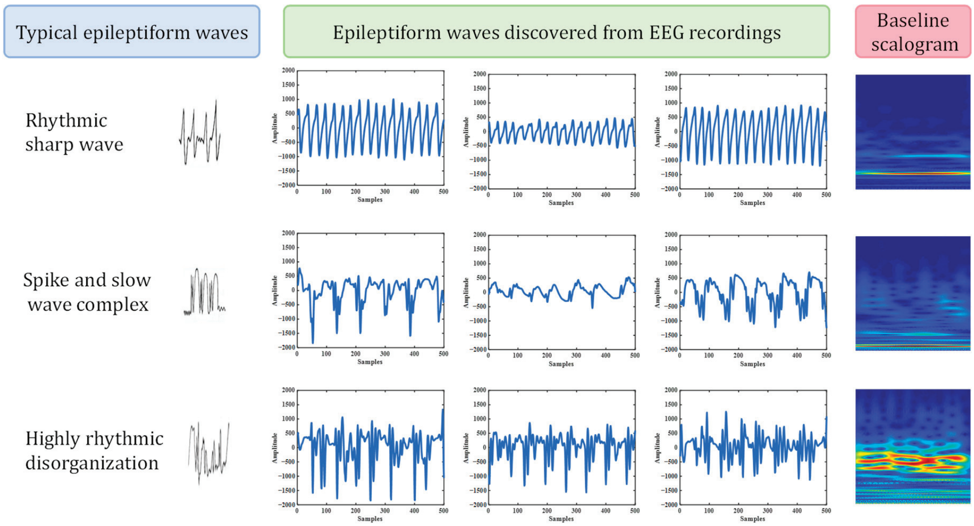

Figure 11. Typical kinds of epileptiform waveforms were found by clustering the ictal iEEG data of the Bonn dataset. In each row are displayed the characteristic waveform of a type of epileptiform discharge, three epileptiform waves of that type that were clustered into a same cluster found from the iEEG recordings by our approach, as well as the baseline scalogram of that cluster.

4.4.2. Multiple Labels of EEG Data

The cross-analysis of clustering and classification has the potential to discover interesting knowledge, including multiple labels of data. Taking the group AB_CD_E of the Bonn dataset as an example, Figure 12 shows the class labels and clustering results of several samples. Samples in each row belong to a same class and those in each column are clustered into a same cluster. Each grid displays four samples. Row 1 and column 1 both correspond to Class AB, i.e., healthy; Row 2 and column 2 both correspond to Class CD, i.e., inter-ictal; and Row 3 and column 3 both correspond to Class E, i.e., inter-ictal.

The class labels of waveforms on the diagonal in the Figure 12 are consistent with their respective cluster labels. These waveforms best reflect the salient attributes of that type of EEG signal. For example, the samples in row 1, column 1 (AB) represent scalp EEG in healthy volunteers, showing high frequency components compared to the inter-ictal iEEG (CD) in row 2, column 2. The four ictal iEEG signals in row 3, column 3 (E) exhibit various morphology, including some typical epileptiform discharge waveforms such as rhythmic sharp waves and spike and slow wave complexes.

Perhaps, it is signals whose class label and cluster label do not refer to the same attribute that deserve more attention. Taking the waveforms in row 2 and column 3 as an example, they belong to the inter-ictal, epileptic class; however, they are clustered as an ictal, epileptic cluster. They exhibit characteristics of typical epileptiform waveforms, such as spike waves and spike and slow wave complex. These findings are consistent with the clinical experience about the existence of epileptiform discharges in inter-ictal periods. In fact, these signals with multiple attributes should be annotated with multiple labels so that the information within the recordings can be reflected more comprehensively and objectively.

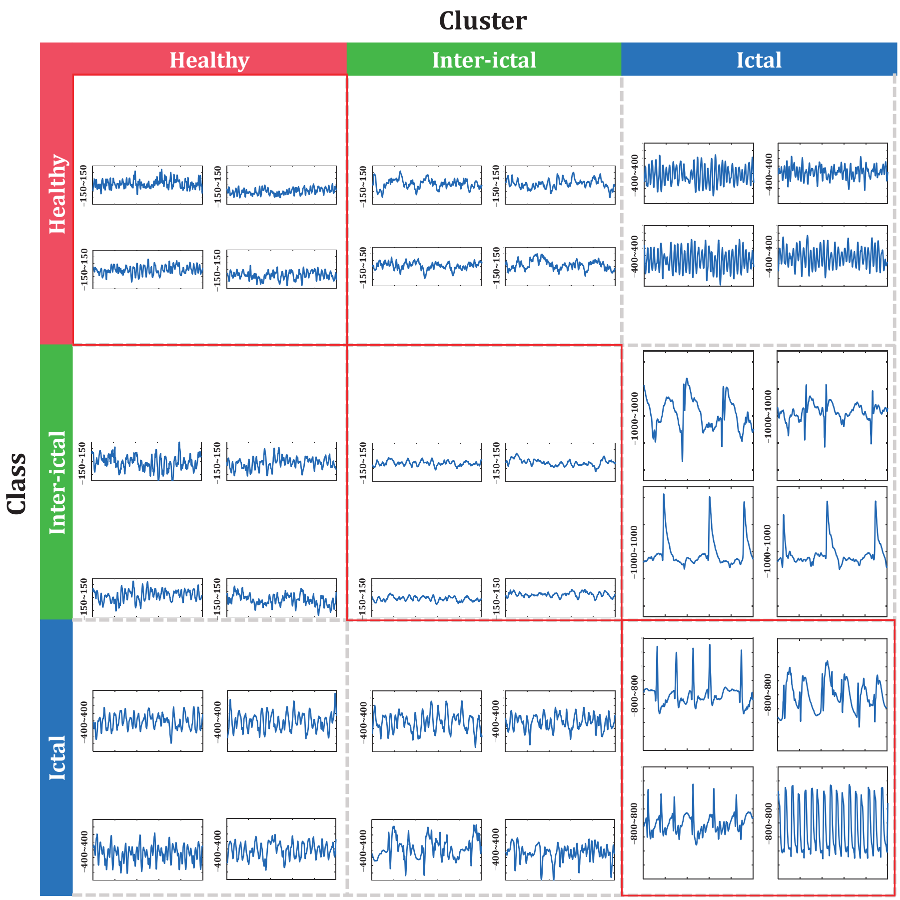

Figure 12. Class labels and clustering results of several samples in group AB_CD_E of the Bonn dataset. Samples on each row belong to a same class and those on each column are clustered into a same cluster. Each grid displays four samples. Row 1 and column 1 both correspond to Class AB, i.e., healthy; Row 2 and column 2 both correspond to Class CD, i.e., inter-ictal, epileptic; Row 3 and column 3 both correspond to Class E, i.e., ictal, epileptic.

5. Discussion

Clustering plays a unique role in exploratory EEG analysis. It is unsupervised, and consequently, has low labor and time costs. With our approach, the adaptively learned Gaussian mixing coefficients make the model remain effective in dealing with imbalanced datasets. By means of intra-class clustering or cross-analysis of clustering and classification, it is possible to reveal intra-class diversity or other interesting information. As demonstrated in this work, the proposed approach is attractive for practice in epileptic subtype diagnosis, multiple labelling of EEG data, etc.

With the latent prototype-based clustering approach, the clustering results are close to the classification of the data (with reference to the results in Sections 4.1 and 4.2). It is in part due to the sound definition of the critic function, which is based on latent prototypes and measures the similarity on three levels. In this way, the approach is able to detect underlying unknown patterns in the data. Nevertheless, we would like to point out that, even if the clustering result is inconsistent with the classification, it does not mean that the performance of the clustering method is not good. This is because the objectives of clustering and classification are different. Classification is task-oriented, while clustering organizes data elements according to the resemblance of the intrinsic patterns (if any) of the data.

Different types of epileptiform waves were discovered from EEG recordings, as shown in Figure 11, in an unsupervised way without any given type label. It has been found that some types of epileptic waveforms are related to specific epilepsy subtypes. For example, rhythmic sharp waves are often associated with focal seizures, while the spike and slow wave complex is more common in absence seizures. Therefore, our approach can not only reveal the diversity of EEG signals during seizures and provide with a representative scalogram of each subtype, but also can point out when and what type of epileptic discharge occurs in the brain so as to assist the doctor in epilepsy subtype diagnosis.

Multiple labels of EEG or iEEG data can be discovered by means of the cross-analysis of clustering and classification, as shown in Figure 12. Such cross-analysis between unknown kinds and known classes has the potential to reveal novel knowledge. Sometimes, it is the signal whose class label and cluster label do not refer to the same attribute that deserve more attention. They reflect intra-class diversity. On the other hand, such analysis helps to better understand multiple attributes of the data. As revealed in Figure 12, in ictal-period iEEG signals of an epileptic, there exist waveforms similar to that of a healthy subject, while in the interictal period, some epileptiform discharges are found. In fact, these signals with multiple attributes should be annotated with multiple labels so that the information within the recordings can be reflected more comprehensively and objectively.

Discussion on DFM similarity. As shown in Figures 7 and 8, the inclusion of DFM similarity has little effect on the improvement in clustering performance. This may be due to the fact that the discriminator's task is to distinguish between real and fake samples. The features extracted by its convolutional layer are those that focus on that task. Hence, in most cases, the DFM level similarity plays a less important role in clustering than the other two levels of similarity. But, in a few cases, e.g., ECoG of HUP89, the use of DFM similarity is more effective than that of image similarity. This detail problem is pending for further study.

With respect to the W-SLOGAN model, the number of Gaussian components of the latent distribution need to be set in advance according to a predetermined number of clusters. The optimization of the cluster number may be a future research direction.

Author Contributions: Conceptualization, S.Z.; Methodology, S.Z. and P.Z.; Software, P.Z. and H.C.; Supervision, S.Z.; Writing—original draft, S.Z. and P.Z.; Writing—review and editing, S.Z. and H.C. All authors have read and agreed to the published version of the manuscript.

Funding: This research received no external funding.

Institutional Review Board Statement: Not applicable.

Informed Consent Statement: Not applicable.

Data Availability Statement: The original data presented in the study are openly available in the Bonn Dataset at https://www.ukbonn.de/epileptologie/arbeitsgruppen/ag-lehnertz-neurophysik/downloads/ (accessed on 12 April 2024) and in the HUP iEEG Epilepsy Dataset at https://openneuro.org/datasets/ds004100/versions/1.1.3 (accessed on 2 May 2024).

Acknowledgments: Jing Li and Zikang Wu are acknowledged for their help in the early stage of this study. Shaorong Fang and Tianfu Wu from Information and Network Center of Xiamen University are acknowledged for the help with the GPU computing.

Conflicts of Interest: The authors declare no conflicts of interest.

References

1. Chakravarthi, B.; Ng, S.-C.; Ezilarasan, M.R.; Leung, M.-F. EEG-based emotion recognition using hybrid CNN and LSTM classification. *Front. Comput. Neurosci.* **2022**, *16*, 1019776. [CrossRef] [PubMed]
2. Luo, T.-J. Dual regularized spatial-temporal features adaptation for multi-source selected cross-subject motor imagery EEG classification. *Expert Syst. Appl.* **2024**, *255*, 124673. [CrossRef]

3. Hassan, A.R.; Subasi, A.; Zhang, Y.C. Epilepsy seizure detection using complete ensemble empirical mode decomposition with adaptive noise. *Knowl.-Based Syst.* **2020**, *191*, 105333. [CrossRef]
4. Foong, R.; Ang, K.K.; Quek, C.; Guan, C.T.; Phua, K.S.; Kuah, C.W.K.; Deshmukh, V.A.; Yam, L.H.L.; Rajeswaran, D.K.; Tang, N.; et al. Assessment of the Efficacy of EEG-Based MI-BCI With Visual Feedback and EEG Correlates of Mental Fatigue for Upper-Limb Stroke Rehabilitation. *IEEE Trans. Biomed. Eng.* **2020**, *67*, 786–2795. [CrossRef]
5. Yu, H.T.; Lei, X.Y.; Song, Z.X.; Liu, C.; Wang, J. Supervised Network-Based Fuzzy Learning of EEG Signals for Alzheimer's Disease Identification. *IEEE Trans. Fuzzy Syst.* **2020**, *28*, 60–71. [CrossRef]
6. Jayaram, V.; Widmann, N.; Förster, C.; Fomina, T.; Hohmann, M.; Hagen, J.M.V.; Synofzik, M.; Schölkopf, B.; Schöls, L.; Grosse-Wentrup, M. Brain-Computer Interfacing in Amyotrophic Lateral Sclerosis: Implications of a Resting-State EEG Analysis. In Proceedings of the 37th Annual International Conference of the IEEE-Engineering-in-Medicine-and-Biology-Society (EMBC), Milan, Italy, 25–29 August 2015; IEEE: Milan, Italy, 2015; pp. 6979–6982.
7. Xia, K.J.; Ni, T.G.; Yin, H.S.; Chen, B. Cross-Domain Classification Model with Knowledge Utilization Maximization for Recognition of Epileptic EEG Signals. *IEEE-Acm Trans. Comput. Biol. Bioinform.* **2021**, *18*, 53–61. [CrossRef]
8. Dai, C.L.; Wu, J.; Monaghan, J.J.M.; Li, G.H.; Peng, H.; Becker, S.I.; McAlpine, D. Semi-Supervised EEG Clustering with Multiple Constraints. *IEEE Trans. Knowl. Data Eng.* **2023**, *35*, 8529–8544. [CrossRef]
9. Pimentel, B.A.; de Carvalho, A. A Meta-learning approach for recommending the number of clusters for clustering algorithms. *Knowl.-Based Syst.* **2020**, *195*, 105682. [CrossRef]
10. Deng, J.Z.; Guo, J.P.; Wang, Y. A Novel K-medoids clustering recommendation algorithm based on probability distribution for collaborative filtering. *Knowl.-Based Syst.* **2019**, *175*, 96–106. [CrossRef]
11. Bouveyron, C.; Girard, S.; Schmid, C. High-dimensional data clustering. *Comput. Stat. Data Anal.* **2007**, *52*, 502–519. [CrossRef]
12. Rodriguez, A.; Laio, A. Clustering by fast search and find of density peaks. *Science* **2014**, *344*, 1492–1496. [CrossRef] [PubMed]
13. Gao, T.F.; Chen, D.; Tang, Y.B.; Du, B.; Ranjan, R.; Zomaya, A.Y.; Dustdar, S. Adaptive density peaks clustering: Towards exploratory EEG analysis. *Knowl.-Based Syst.* **2022**, *240*, 108123. [CrossRef]
14. Goodfellow, I.; Pouget-Abadie, J.; Mirza, M.; Xu, B.; Warde-Farley, D.; Ozair, S.; Courville, A.; Bengio, Y. Generative adversarial nets. In *Advances in Neural Information Processing Systems*; Ghahramani, Z., Welling, M., Cortes, C., Lawrence, N., Weinberger, K.Q., Eds.; Curran Associates, Inc.: Red Hook, NY, USA, 2014; pp. 2672–2680.
15. Ben-Yosef, M.; Weinshall, D.J. Gaussian Mixture Generative Adversarial Networks for Diverse Datasets, and the Unsupervised Clustering of Images. *arXiv* **2018**, arXiv:1808.10356.
16. Gurumurthy, S.; Sarvadevabhatla, R.K.; Babu, R.V. DeLiGAN: Generative Adversarial Networks for Diverse and Limited Data. In Proceedings of the 30th IEEE/CVF Conference on Computer Vision and Pattern Recognition (CVPR), Honolulu, HI, USA, 21–26 July 2017; IEEE: Piscataway, NJ, USA; pp. 4941–4949.
17. Chen, X.; Duan, Y.; Houthooft, R.; Schulman, J.; Sutskever, I.; Abbeel, P. InfoGAN: Interpretable Representation Learning by Information Maximizing Generative Adversarial Nets. In Proceedings of the 30th Conference on Neural Information Processing Systems (NIPS), Barcelona, Spain, 5–10 December 2016.
18. Larsen, A.B.L.; Sonderby, S.K.; Larochelle, H.; Winther, O. Autoencoding beyond pixels using a learned similarity metric. In Proceedings of the 33rd International Conference on Machine Learning, New York, NY, USA, 20–22 June 2016.
19. Hwang, U.; Kim, H.; Jung, D.; Jang, H.; Lee, H.; Yoon, S. Stein Latent Optimization for Generative Adversarial Networks. *arXiv* **2021**, arXiv:2106.05319.
20. Andrzejak, R.G.; Lehnertz, K.; Mormann, F.; Rieke, C.; David, P.; Elger, C.E. Indications of nonlinear deterministic and finitedimensional structures in time series of brain electrical activity: Dependence on recording region and brain state. *Phys. Rev. E* **2001**, *64*, 061907. [CrossRef]
21. Rashed-Al-Mahfuz, M.; Moni, M.A.; Uddin, S.; Alyami, S.A.; Summers, M.A.; Eapen, V. A Deep Convolutional Neural Network Method to Detect Seizures and Characteristic Frequencies Using Epileptic Electroencephalogram (EEG) Data. *IEEE J. Transl. Eng. Health Med.* **2021**, *9*, 2000112. [CrossRef]
22. Li, M.Y.; Chen, W.Z.; Zhang, T. Automatic epilepsy detection using wavelet-based nonlinear analysis and optimized SVM. *Biocybern. Biomed. Eng.* **2016**, *36*, 708–718. [CrossRef]
23. Bernabei, B.M.; Li, A.; Revell, A.Y.; Smith, R.J.; Gunnarsdottir, K.M.; Ong, I.Z.; Davis, K.A.; Sinha, N.; Sarma, S.; Litt, B. HUP iEEG Epilepsy Dataset. 2023. Available online: https://openneuro.org/datasets/ds004100/versions/1.1.3 (accessed on 2 May 2024).
24. Albaqami, H.; Hassan, G.M.; Datta, A. MP-SeizNet: A multi-path CNN Bi-LSTM Network for seizure-type classification using EEG. *Biomed. Signal Process. Control.* **2023**, *84*, 104780. [CrossRef]
25. Radford, A.; Metz, L.; Chintala, S. Unsupervised representation learning with deep convolutional generative adversarial networks. *arXiv* **2015**, arXiv:1511.06434.
26. Gulrajani, I.; Ahmed, F.; Arjovsky, M.; Dumoulin, V.; Courville, A. Improved Training of Wasserstein GANs. In Proceedings of the 31st Annual Conference on Neural Information Processing Systems (NIPS), Long Beach, CA, USA, 4–9 December 2017; Volume 30.
27. Yang, X.L.; Liu, L.P.; Li, Z.W.; Xia, Y.X.; Fan, Z.P.; Zhou, J.Y. Semi-Supervised Seizure Prediction Model Combining Generative Adversarial Networks and Long Short-Term Memory Networks. *Appl. Sci.* **2023**, *13*, 11631. [CrossRef]
28. Wei, Z.C.; Zou, J.Z.; Zhang, J.; Xu, J.Q. Automatic epileptic EEG detection using convolutional neural network with improvements in time-domain. *Biomed. Signal Process. Control.* **2019**, *53*, 101551. [CrossRef]

29. Kingma, D.P.; Welling, M. Auto-encoding variational bayes. *arXiv* **2013**, arXiv:1312.6114.
30. Truong, N.D.; Kuhlmann, L.; Bonyadi, M.R.; Querlioz, D.; Zhou, L.P.; Kavehei, O.M. Epileptic Seizure Forecasting with Generative Adversarial Networks. *IEEE Access* **2019**, *7*, 143999–144009. [CrossRef]
31. Hubert, L.; Arabie, P. Comparing partitions. *J. Classif.* **1985**, *2*, 193–218. [CrossRef]
32. Zhang, H.; Ho, T.B.; Zhang, Y.; Lin, M.-S. Unsupervised feature extraction for time series clustering using orthogonal wavelet transform. *Informatica* **2006**, *30*, 305–319.
33. McCallan, N.; Davidson, S.; Ng, K.Y.; Biglarbeigi, P.; Finlay, D.; Lan, B.L.; McLaughlin, J. Epileptic multi-seizure type clas-sification using electroencephalogram signals from the Temple University Hospital Seizure Corpus: A review. *Expert Syst. Appl.* **2023**, *234*, 121040. [CrossRef]

sensors

Article

Detection of Pilots' Psychological Workload during Turning Phases Using EEG Characteristics

Li Ji [1,2,*], Leiye Yi [1,2,*], Haiwei Li [3], Wenjie Han [3] and Ningning Zhang [4]

1 School of Mechatronics Engineering, Shenyang Aerospace University, Shenyang 110136, China
2 Key Laboratory of Rapid Development & Manufacturing Technology for Aircraft, Shenyang Aerospace University, Ministry of Education, Shenyang 110136, China
3 Shenyang Aircraft Corporation, Shenyang 110136, China; lihaiwei007@126.com (H.L.); hwj623@126.com (W.H.)
4 School of Design & Art, Shenyang Aerospace University, Shenyang 110136, China; znninging@aliyun.com
* Correspondence: 20083041@sau.edu.cn (L.J.); yileiye@stu.sau.edu.cn (L.Y.)

Abstract: Pilot behavior is crucial for aviation safety. This study aims to investigate the EEG characteristics of pilots, refine training assessment methodologies, and bolster flight safety measures. The collected EEG signals underwent initial preprocessing. The EEG characteristic analysis was performed during left and right turns, involving the calculation of the energy ratio of beta waves and Shannon entropy. The psychological workload of pilots during different flight phases was quantified as well. Based on the EEG characteristics, the pilots' psychological workload was classified through the use of a support vector machine (SVM). The study results showed significant changes in the energy ratio of beta waves and Shannon entropy during left and right turns compared to the cruising phase. Additionally, the pilots' psychological workload was found to have increased during these turning phases. Using support vector machines to detect the pilots' psychological workload, the classification accuracy for the training set was 98.92%, while for the test set, it was 93.67%. This research holds significant importance in understanding pilots' psychological workload.

Keywords: beta wave; EEG map; sample entropy; Shannon entropy; psychological workload; SVM

Citation: Ji, L.; Yi, L.; Li, H.; Han, W.; Zhang, N. Detection of Pilots' Psychological Workload during Turning Phases Using EEG Characteristics. *Sensors* **2024**, *24*, 5176. https://doi.org/10.3390/s24165176

Academic Editors: Yifan Zhao, Hua-Liang Wei, Yuzhu Guo and Fei He

Received: 26 June 2024
Revised: 2 August 2024
Accepted: 5 August 2024
Published: 10 August 2024

1. Introduction

The "Statistical Bulletin on the Development of the Civil Aviation Industry in 2021" highlights the rapid growth in aircraft utilization across multiple sectors. In 2021, the civil aviation industry achieved notable metrics, including a total transport turnover of 59.928 billion tonne-kilometers, a passenger turnover of 391.387 billion person-kilometers, and 6.28 million completed flight hours for transport airlines. As the number of flights increases, ensuring safety remains a paramount concern in the contemporary airline industry [1].

Safety is of paramount importance in the contemporary airline industry, especially with the increasing number of flights. According to statistics from the Aviation Safety Network, Figure 1 illustrates the likelihood of accidents at different stages of an airplane's navigation process. Although the cruise phase has a comparatively lower accident probability—around 30 percent compared to other phases—aviation safety hazards during this phase can jeopardize the lives and property of passengers, leading to unpredictable consequences [2].

Among the numerous factors affecting aviation safety, pilot behavior stands out as one of the most significant. As shown in Figure 2, pilots must maintain prolonged concentration during flight missions [3]. Therefore, studying pilots' behavior and identifying underlying patterns has become an urgent priority to enhance aviation safety and reduce the occurrence of accidents.

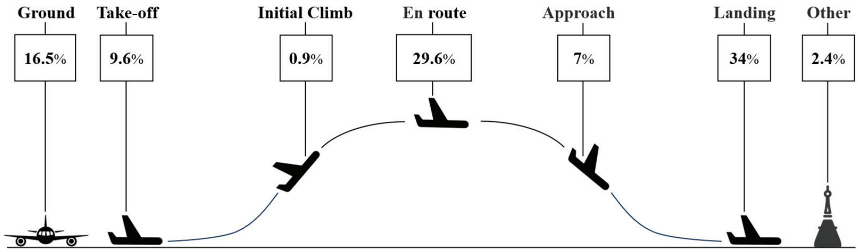

Figure 1. Percentage of fatal accidents.

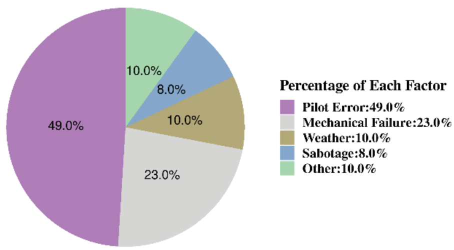

Figure 2. The proportion of factors causing accidents.

Enhancing pilots' flight skills stands out as the pivotal measure to reduce the probability of flight accidents and consequently improve flight safety [4]. Continuous monitoring of pilots' operational processes during flight training is imperative to ensure the timely correction of any irregular operations. Standardizing pilots' operations is essential to mitigate the safety risks associated with pilot error [5].

Traditionally, flight performance assessment has relied solely on the instructor's subjective experience. This method's drawback lies in its susceptibility to the instructor's subjective influence at any given moment, potentially leading to inconsistent assessment standards. To address this, scholars have proposed various assessment methods based on traditional flight training systems that utilize monitoring data to refine pilot training techniques [6,7].

Recently, researchers began assessing pilots' conditions during flight training using physiological signal data. Li Jie et al. examined the impact of hypoxic training during high-altitude flights on pilots' electrocardiographic (ECG) activity and concluded that ECG could effectively monitor the pilots' training status [8]. Additionally, M. Dilli Babu independently gauged the cognitive load of pilots based on ocular parameters in a military aviation context, finding a significant correlation between pilots' cognitive load and eye parameters [9].

Electroencephalography (EEG) is a technique for recording electrical activity generated by neurons in the brain, detected on the surface of the scalp. Compared to ECG and EOG, EEG signals offer more direct insights into the brain's activity changes [10]. EEG has been extensively utilized in various studies to explore different aspects of cognitive and psychological states. G. F. Wilson's research revealed that while both ECG and EEG data can indicate the pilots' psychological workload, EEG is more reliable as it directly records the brain's evoked potentials, providing a clearer reflection of brain activity [11]. Bartosz Binias et al. investigated the correlation between brainwave activity and reaction time in short-haul pilots using EEG data [12,13]. Additionally, Peng Zhang et al. examined brain attributes related to pilots' error awareness during flight missions, employing EEG in their study [14]. Zhendong Lan et al. analyzed EEG characteristics during fatigue driving and classified fatigue states using support vector machines (SVM) [15]. These studies collectively underscore the importance of EEG in understanding cognitive and psychological states, offering valuable contributions to the field of pilot performance and safety.

This study aims to process and analyze EEG data collected from pilots during left and right turns in simulated flight scenarios. The analysis includes examining the changes in EEG signals, variations in EEG power, and the correlations between EEG power and turning maneuvers. Additionally, NASA-TLX is used to assess the pilots' psychological workload during cruising and turning phases, and support vector machine (SVM) algorithms are employed to classify their psychological workload. The expected outcome is that applying neuroscience research to flight performance will provide a theoretical foundation for flight training methods, ultimately enhancing flight safety.

2. Materials and Methods

2.1. Participants

The study involved ten professionally trained male pilots, each with at least 50 h of flight simulation training. These participants met the following specific criteria to ensure the consistency and reliability of the experiment:

1. No prior EEG experiment participation: participants had no history of participating in EEG experiments, ensuring that their brain activity recordings were not influenced by prior experience.
2. Good physical health: all pilots were in good physical health, crucial for accurate EEG readings and experimental reliability.
3. Age: participants were aged between 20 and 24 years old, with an average age of 22 years (± 2).
4. Right-handedness: right-handedness was a requirement, possibly to maintain consistency in motor responses or due to established correlations between handedness and brain activity.
5. Socio-economic status: participants were from a middle-class socio-economic background.

In order to optimize conditions and minimize external factors [16], the following conditions were observed:

1. Timing: the experiment was scheduled for 9:00 a.m. to minimize the impact of drowsiness, ensuring participants were alert and well-rested.
2. Weather and environmental conditions: the weather was clear, with no wind or other natural factors that could affect the flight simulation or participants' performance.
3. Health precautions: pilots were instructed to maintain proper eating habits, get adequate sleep, and avoid alcohol or medication for three days before the experiment.

Before the experiment began, participants received a comprehensive briefing on the flight process and experimental equipment, including the EEG cap and other devices. Ethical considerations were also addressed: all participants voluntarily agreed to take part in the experiment and signed a "Consent to Participate in the Experiment" form. At the conclusion of the study, participants were compensated according to the terms outlined in the consent form, ensuring transparency and fairness in their involvement.

These measures collectively aimed to create the optimal conditions for studying EEG data during flight simulation, ensuring that the results would be reliable and applicable to enhancing aviation safety through a better understanding of pilot behavior and psychological workload.

2.2. Experimental Equipment

Flight Simulator: The study utilized a KDKJ-FX-172-6D four-seat Cessna professional flight simul ator. The flight simulator features a six-degree-of-freedom kinetic platform, an accurate aerodynamic model, real-time flight sound effects, a full-scale aircraft joystick, and a variety of virtual terrains to ensure that the flight simulation process is as similar as possible to the actual flight process (as depicted in Figure 3).

Figure 3. Professional flight simulator.

EEG cap: In this study, the Emotiv EPOC+ EEG cap was used to record EEG data during pilot driving scenarios. The device comprises fourteen data acquisition channels (AF3, F3, F7, FC5, T7, P7, O1, AF4, F4, FC6, F8, T8, P8, O2), as shown in Table 1.

Table 1. The corresponding brain regions for EEG electrodes.

Electrodes	Lobe
AF3, AF4, F3, F4 F7, F8, FC5, FC6	Frontal
T7, T8	Temporal
P7, P8	Parietal
O1, O2	Occipital

This EEG cap supports wireless transmission, commonly used for recording action EEG and mitigating the impact of EEG caps on pilots (as depicted in Figure 4) [17]. The cap's ability to transmit data wirelessly reduces movement restrictions on pilots, making it ideal for dynamic and realistic simulation environments.

Figure 4. Emotiv EPOC+ EEG cap.

Psychological Workload Questionnaire: The NASA-TLX (Task Load Index) is a cognitive load assessment scale developed by NASA. It is a widely recognized subjective psychological workload assessment tool. The scale encompasses six dimensions: mental demand, physical demand, temporal demand, performance, effort, and frustration.

2.3. Experimental Steps

The KDKJ-FX-172-6D flight simulator is set in natural plains scenery, where participants conduct their flight experiments using the simulated flight platform. Each participant performs five segments: take-off, level flight, left turn, right turn, and landing (as depicted in Figure 5). The average aircraft flight altitude is 1000 feet, and the average flight speed is 70 knots [18].

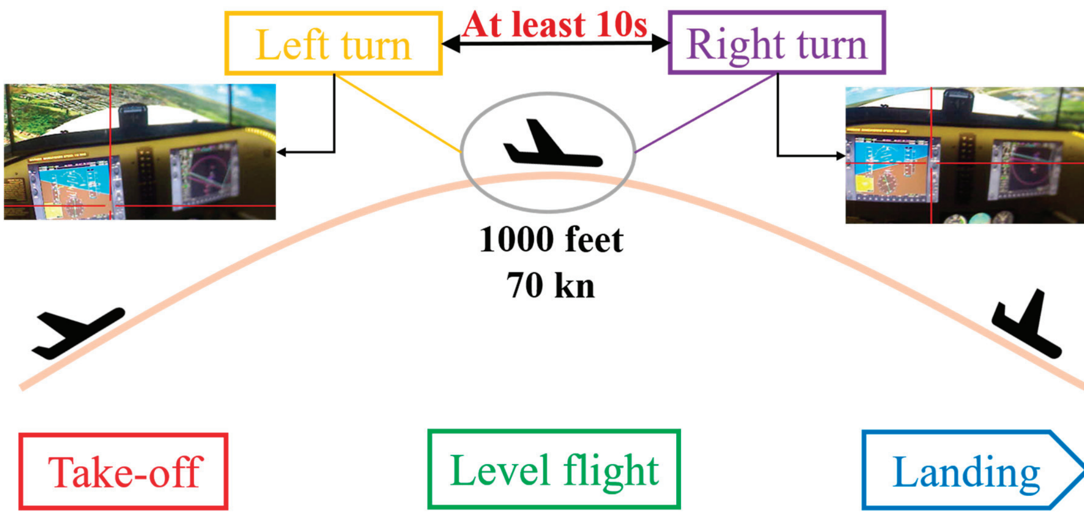

Figure 5. Flight simulation experiment.

For the left and right turns, pilots follow visual flight rules (VFR) without specific speed or altitude requirements, ensuring they maintain at least a 10 s interval between maneuvers to avoid interference. The detailed flight parameters are as follows:

Take-off phase: The aircraft ascends to 400 feet at a speed of 60 knots.

Climb phase: The aircraft continues to ascend to an altitude of 1000 feet.

Cruise phase: The pilot performs left and right turns.

Descent phase: The aircraft descends back to 400 feet.

Landing phase: The aircraft gradually decreases speed and altitude for a smooth landing.

Throughout the flight, the pilots' EEG data were continuously recorded using an EEG cap, while changes in cockpit instrumentation and flight attitude were recorded using video equipment.

After completing the experiment, the pilots filled out the NASA-TLX subjective questionnaire based on their flight experiences during the cruising and turning phases. The subjective questionnaire assesses six dimensions of psychological workload. For each dimension, the pilots rated their experiences on a scale from 0 to 10. By calculating the weighted average across different dimensions, the level of psychological workload experienced by the pilots during different flight phases was determined.

2.4. Data Processing

The collected pilot EEG data were first preprocessed to ensure accurate analysis. The various functions and operating states of the brain can be determined based on human behavior and cognition, allowing corresponding EEG signals to be identified for analysis. EEG signals are commonly categorized into four main frequency bands: δ wave, θ wave, α wave, and β wave, as shown in Table 2 [19].

Table 2. The corresponding frequency and physiological meaning of EEG rhythms.

EEG Rhythm	Frequency (Hz)	Amplitude (μV)	Function	Main Location
δ	0.5~3	20~200	Sleep, hypoxia, etc.	Occipital and parietal areas.
θ	4~7	20~100	Burnout, sleep, etc.	Frontal and temporal areas.
α	8~13	10~100	Closed eyes, relaxation, etc.	Occipital lobe area.
β	14~30	5~20	Emotional tension, thinking activity, etc.	Temporal lobe and frontal lobe area.

To filter the EEG signals and eliminate the impact of high and low-frequency noise, FIR (finite impulse response) filters were employed within the 0.1–40 Hz range. This preprocessing step is crucial for isolating the relevant EEG signals and improving the accuracy of subsequent analyses [20,21].

ICA is a powerful statistical technique used to decompose multichannel EEG signals into independent components. Each component represents a distinct source of neural activity contributing to the overall EEG signal [22]. During the ICA process, components associated with artifacts such as EMG (muscle activity) and EOG (eye movements) can be identified based on their characteristic patterns and frequencies. These components can then be effectively removed or filtered out from the EEG data. By isolating and removing artifacts through ICA, the quality and reliability of the EEG signals are significantly improved [23]. This allows more accurate analysis of brain activity patterns related to cognitive processes or specific tasks performed during the flight simulation. Figure 6 likely depicts the results of ICA, showing how independent components are extracted from the EEG data and how artifacts are separated from genuine brain signals. This visualization aids in validating the effectiveness of artifact removal and ensuring the integrity of the EEG data for subsequent analysis.

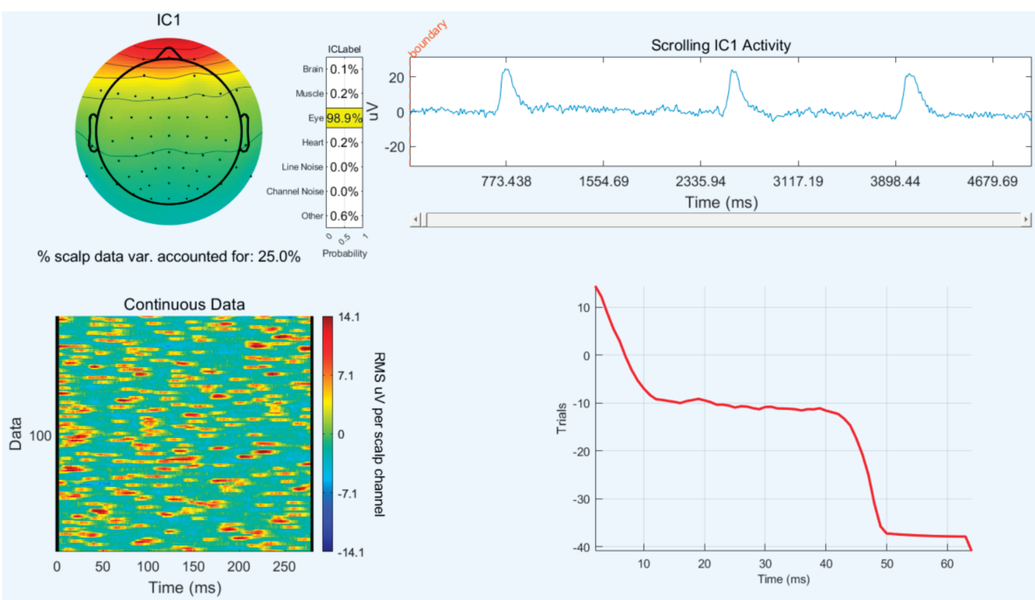

Figure 6. Artifact rejection—VEOG.

3. Results

3.1. Analysis of EEG Maps in the Left Turn Phase and Right Turn Phase

The EEG (electroencephalogram) data of the pilot were collected throughout the simulated aircraft operation process. During this simulation, the EEG signals specifically associated with beta waves were of particular interest during the pilot's performance of left and right turns. These beta wave data underwent a series of preprocessing steps and characteristic extractions to isolate the relevant signals from the raw EEG data.

To enhance the quality of the EEG signals, particularly by reducing noise, a method called superimposed averaging was employed. This technique improves the signal-to-noise ratio, making the desired beta wave signals more distinguishable from background noise. After this enhancement, an EEG map was generated. This map provides a visual representation of the energy fluctuations in the beta wave signals across each electrode channel, allowing for a clear and comprehensive view of the pilot's brain activity during the turning maneuvers [24].

During the cruise phase, the electrodes on the pilot's EEG typically display light colors, indicating low signal energy levels. However, during a left turn, a notable surge in energy occurs at the T7 electrode, resulting in a darkening of its color, indicating increased neural activity levels. This surge is prominently displayed on the left side of the EEG map, showing heightened energy levels observed in the electrode channels. After the pilot completes the left turn maneuver, the energy levels at electrode T7 gradually diminish, resulting in a return to lighter coloration as the aircraft resumes level flight. Similarly, during right turns, there is an increase in energy at electrode T8, resulting in darker coloration at this electrode site. The right half of the EEG map shows elevated energy levels corresponding to this rise. Once the right turn is completed, the energy levels in each electrode gradually decrease again, indicating a return to level flight. These dynamic changes, including the shifts in energy levels and corresponding color changes, are illustrated in Figure 7, providing a clear visual representation of the pilot's neural activity during different phases of the flight. However, the map does not facilitate quantitative analysis.

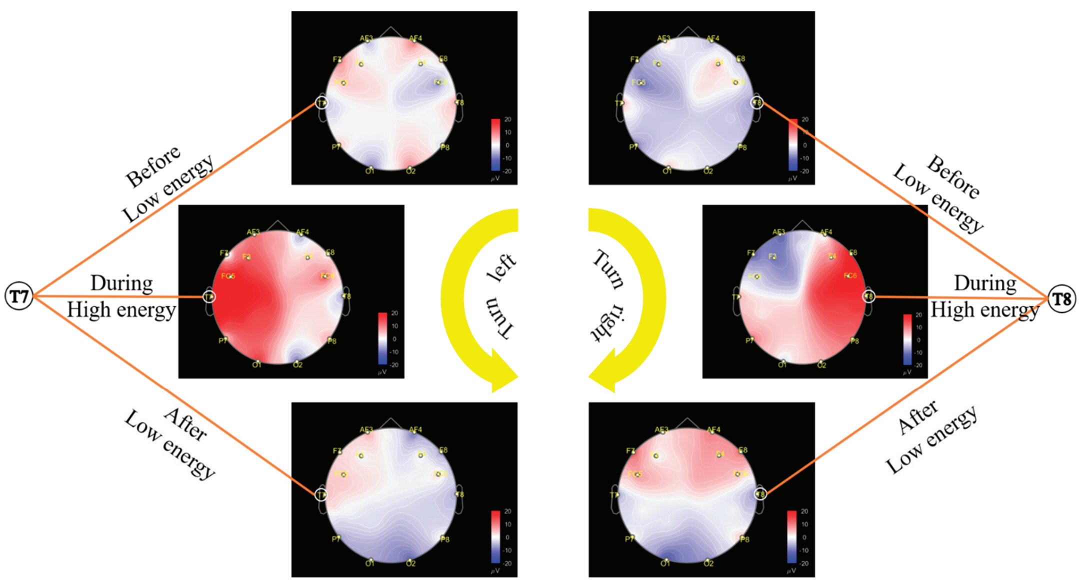

Figure 7. EEG map before, during and after turns.

3.2. EEG Signal Correlation

During flight tasks, EEG signals exhibit variations across different electrodes. For correlation analysis, the study selected the beta waves of EEG signals recorded during the left and right turning phases. This study utilized Pearson correlation analysis to examine the EEG signals collected from the various electrodes [25,26]. The Pearson correlation coefficient formula used in this study is as follows:

$$r = \frac{\sum_{i=1}^{n}(X_i - \overline{X})(Y_i - \overline{Y})}{\sqrt{\sum_{i=1}^{n}(X_i - \overline{X})^2}\sqrt{\sum_{i=1}^{n}(Y_i - \overline{Y})^2}} \quad (1)$$

where X_i and Y_i represent the EEG signal values from two different electrodes at corresponding time points, while $\overline{X}$ and $\overline{Y}$ are the mean values of these signals over the selected time period. The resulting correlation coefficient r quantifies the linear relationship between the EEG signals from the two electrodes during the turning maneuvers. An r value close to 1 indicates a strong positive correlation, while an r value near -1 signifies a strong negative correlation. A value around 0 indicates no linear relationship between the signals of the electrodes.

In left-turn maneuvers, the highest degree of correlation was observed at electrode T7, indicating a strong correlation between the brain regions associated with T7 during left-turn maneuvers, as depicted in Figure 8.

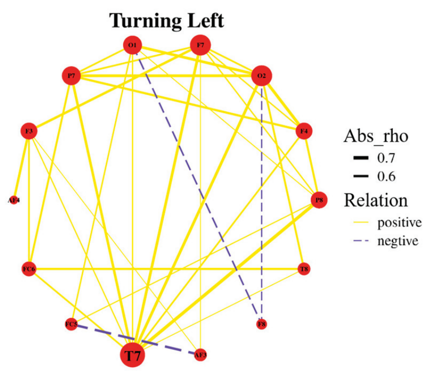

Figure 8. Spherical correlation graph for left turns.

In contrast, during right-turn maneuvers, the highest degree of correlation was observed at electrode T8, indicating strong correlations between the brain regions associated with T8 during these maneuvers. This finding highlights the necessity for further investigation into the relationship between turning directions and EEG signals, as depicted in Figure 9.

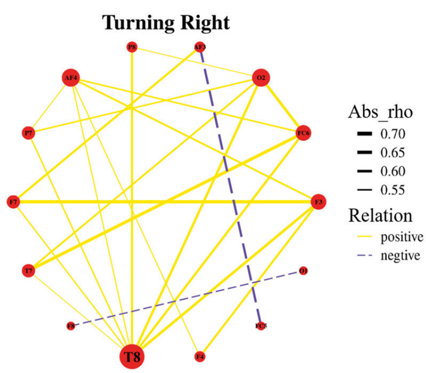

Figure 9. Spherical correlation graph for right turns.

3.3. Extraction of EEG Energy Ratio

The study employed wavelet packet decomposition to extract four distinct rhythmic waves from the EEG signal. Within the frequency range of 0–30 Hz, the EEG signals were decomposed into delta waves (0–4 Hz), theta waves (4–8 Hz), alpha waves (8–12 Hz), and beta waves (12–30 Hz). This method decomposed the EEG signals, enabling the separation and analysis of these rhythmic waves. It yielded insights into varying states of consciousness during flight operations [27,28].

The mother wavelet selected for decomposition was db4, with each sub-band having a bandwidth of 2 Hz [29]. The formula is

$$W_{j,k} = \left\langle x, \psi_{j,k} \right\rangle = \sum_n x[n]\psi_{j,k}[n] \tag{2}$$

where x represents the EEG signal. $\psi_{j,k}$ represents the wavelet basis function. $W_{j,k}$ represents the wavelet packet coefficients of the EEG signal at scale j and position k. $\left\langle x, \psi_{j,k} \right\rangle$ represents the inner product of the EEG signal and the wavelet basis function. Subsequently, the energy of the EEG signal within various frequency bands is computed utilizing the wavelet packet decomposition coefficients. The EEG energy is computed using the following equation:

$$E_{j,k} = \sum_{j,k} \left| W_{j,k} \right|^2 \tag{3}$$

where $E_{j,k}$ represents the energy at the j scale and k position. Subsequently, the total energy for each rhythm is calculated by aggregating the energies of individual wavelets within specific frequency bands.

For each type of rhythmic wave, the ratio of EEG energy to $\beta/(\theta + \alpha)$ wave energy is computed to assess the proportion of EEG energy relative to the total energy. This method enables further analysis of how the distribution of EEG signal energy changes before and after task performance, providing deeper insights into variations across different task states. Figure 10 visually represents changes in EEG signal energy distribution across task phases.

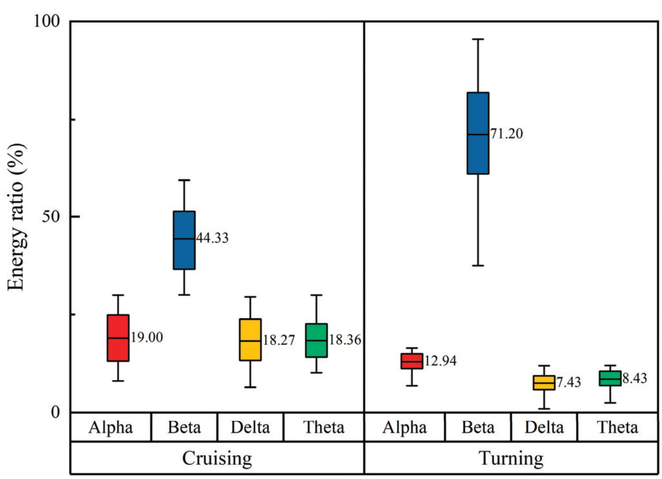

Figure 10. Energy ratios across different task phases.

In contrast to the cruising phase, during the turning phase, there is a significant increase in energy in the beta wave rhythm, with relatively lower energy levels observed in the delta, theta, and alpha wave rhythms, respectively.

Figure 11 illustrates the beta wave energy ratio and the $\beta/(\theta + \alpha)$ wave energy of pilots' EEG data during different flight phases. These metrics are higher during the turning phases and lower during the cruising phase. This indicates that pilots experience a greater cognitive load and increased brain activity during turns compared to cruising.

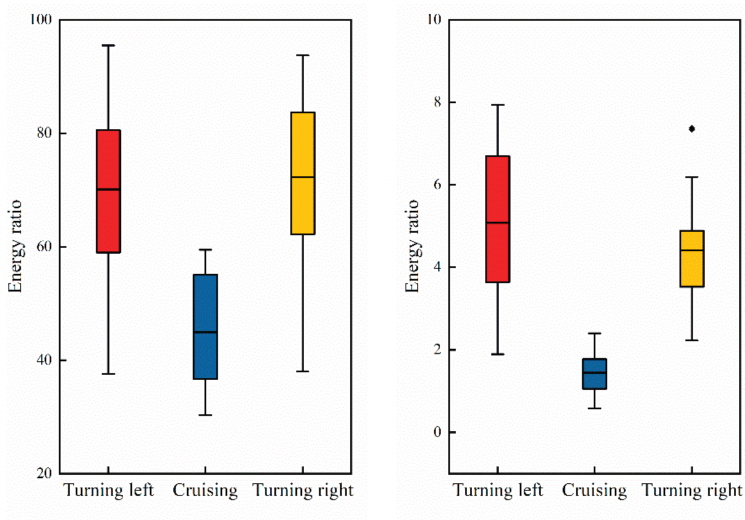

(**a**) (**b**)

Figure 11. EEG energy characteristics. (**a**) Beta wave energy ratio; (**b**) $\beta/(\theta + \alpha)$ wave energy.

This finding is consistent with the understanding that turning maneuvers necessitate more intensive focus and decision-making, thereby increasing the psychological workload on pilots. During turns, pilots must constantly monitor and adjust the aircraft's orientation, speed, and trajectory, which demands heightened attention and cognitive resources. Conversely, cruising typically involves more stable flight conditions, requiring less active control and allowing for reduced cognitive engagement.

Increased beta wave activity during turns reflects the brain's response to heightened cognitive demands and stress, as beta waves are often associated with active thinking, focus, and problem-solving. Conversely, relatively lower beta activity during cruising suggests a more relaxed state, where the brain is engaged in routine monitoring rather than intensive problem-solving.

3.4. Extraction of EEG Entropy

EEG entropy serves as a metric for quantifying the complexity and randomness of EEG signals. It is commonly utilized in EEG signal analysis to assess the complexity of brain activity. In this study, we computed both Shannon entropy and sample entropy of the EEG signals to elucidate the variations in brain activity across different tasks [30–32].

Shannon entropy measures the average uncertainty or information content in the EEG signals, providing an indication of the overall complexity and unpredictability of brain activity. Higher Shannon entropy values suggest more complex and varied brain activity, while lower values indicate more predictable and less complex activity. The calculation formula is as follows:

$$H(X) = -\sum_{i} p(x_i) \log_{10}(p(x_i)) \tag{4}$$

where $H(X)$ represents the Shannon entropy of signal X, and $p(x_i)$ represents the probability of the signal taking on value x_i. We computed the Shannon entropy associated with the pilot's EEG signals in both cruising and turning phases, as depicted in Figure 12.

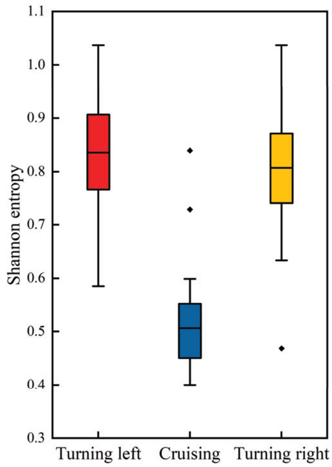

Figure 12. EEG Shannon entropy during different task phases.

Sample entropy is a nonlinear analysis method used to evaluate the complexity and regularity of time-series data. In EEG signal analysis, sample entropy is used to measure the repeatability or regularity of the signal at different time scales. Specifically, sample entropy can help identify patterns or events in EEG signals and assess the signal's predictability and the system's stability. The calculation of sample entropy typically involves defining a window size and a matching tolerance threshold to compare signal segments across different time scales. The calculation formula is

$$SampEn(m, r, N) = -\ln \frac{A^m(r)}{B^m(r)} \tag{5}$$

where m is the embedding dimension, which defines the length of the sequences that are compared. r denotes the tolerance parameter. N is the length of the time series. $A^m(r)$ and $B^m(r)$ are counts of similar sequences in the time series: $A^m(r)$ is the count of sequences of length $m + 1$ that are similar within tolerance r, and $B^m(r)$ is the count of sequences of length m that are similar within tolerance r, as depicted in Figure 13.

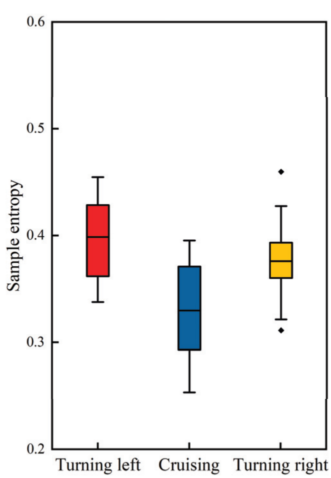

Figure 13. EEG sample entropy during different task phases.

By separately computing these two types of entropy, the study aimed to obtain a comprehensive understanding of how brain activity complexity varies across different task phases. Compared to the cruising phase, pilots exhibit higher EEG entropy during turning phases. This increased entropy signifies a higher level of cognitive activity and complexity in brain function during turning maneuvers.

3.5. NASA-TLX Psychological Workload Assessment

Pilots' psychological workload is subjectively assessed using the NASA Task Load Index (NASA-TLX). This tool collects pilots' ratings of their psychological workload during different flight phases, specifically cruising and left and right turning phases. Pilots assess their workload across multiple dimensions, rating each dimension on a scale from "0" to "10". A score of "0" indicates minimal workload, whereas a score of "10" indicates a high workload. This subjective assessment helps in understanding the perceived effort and stress experienced by pilots during different flight maneuvers and complements the objective EEG data analysis, providing a comprehensive view of pilots' cognitive and psychological states [33].

Additionally, pilots must make pairwise comparisons across six dimensions, selecting the dimension they believe is more closely related to psychological workload, as shown in Figure 14. The formula for calculating the overall psychological workload is

$$F = \sum_{i=1}^{6} M_i \times \frac{P_i}{15}, \tag{6}$$

where F is the total score of the cognitive workload assessment. M_i is the score of the subject in different dimensions. P_i is the number of times different dimensions were selected in the weight testing table shown in Figure 14.

Mental Demand☐ Physical Demand☐	Physical Demand☐ Temporal Demand☐	Temporal Demand☐ Effort☐
Mental Demand☐ Temporal Demand☐	Physical Demand☐ Performance☐	Temporal Demand☐ Frustration Level☐
Mental Demand☐ Performance☐	Physical Demand☐ Effort☐	Performance☐ Effort☐
Mental Demand☐ Effort☐	Physical Demand☐ Frustration Level☐	Performance☐ Frustration Level☐
Mental Demand☐ Frustration Level☐	Temporal Demand☐ Performance☐	Effort☐ Frustration Level☐

Figure 14. NASA-TLX weight test table.

Subsequently, reliability and validity analyses were conducted on the weight proportions of different dimensions. The reliability ($\alpha = 0.715$) and validity ($K = 0.734$) were found to be acceptable, ensuring the robustness of the weightings used in the workload assessment. The final psychological workload scores were 5.02 for the cruising phase and 6.13 for the turning phase. These results indicate that pilots experience a higher psychological workload during the turning phases than during the cruising phase, emphasizing the increased cognitive demands associated with maneuvering the aircraft during turns.

4. Psychological Workload Detection Model

4.1. Characteristic Parameter

A total of 2700 data sets, randomly selected from a pool of 3000 samples (comprising 1500 turn samples and 1500 cruising samples), were used for training. The remaining 300 data sets were reserved for testing. This approach ensures a balanced representation of both turning and cruising phases in the training data while reserving a separate set of data for evaluating the model's performance.

Considering the variability in EEG data among different pilots, it was necessary to normalize the EEG energy ratio, Shannon entropy, and sample entropy to ensure consistency and comparability across individuals [34]. Normalization was performed using the following formula:

$$X_n = \frac{X - X_{min}}{X_{max} - X_{min}}, \tag{7}$$

where X indicates the original characteristic parameter. X_n is the normalized value of X. X_{min} is the minimum value of X in the dataset. X_{max} is the maximum value of X in the dataset.

Firstly, a normality test was conducted on the normalized characteristic parameters. The energy ratio of the EEG wave, $\beta/(\theta + \alpha)$ wave energy, Shannon entropy, and sample entropy all satisfied the assumption of normal distribution ($p > 0.05$) [35].

Subsequently, Pearson correlation analysis was used to calculate the correlation coefficients between Shannon entropy, sample entropy, and the energy ratio at various flight stages. This statistical method quantifies the degree of linear relationship between these variables, providing insights into how changes in entropy metrics correlate with variations in the energy ratio across different flight phases.

Figures 15 and 16 illustrate the correlation between Shannon entropy and sample entropy with the energy ratio of EEG. The beta band energy ratio and Shannon entropy exhibit the highest correlation among EEG characteristic quantities. The correlation coefficients are presented in Table 3.

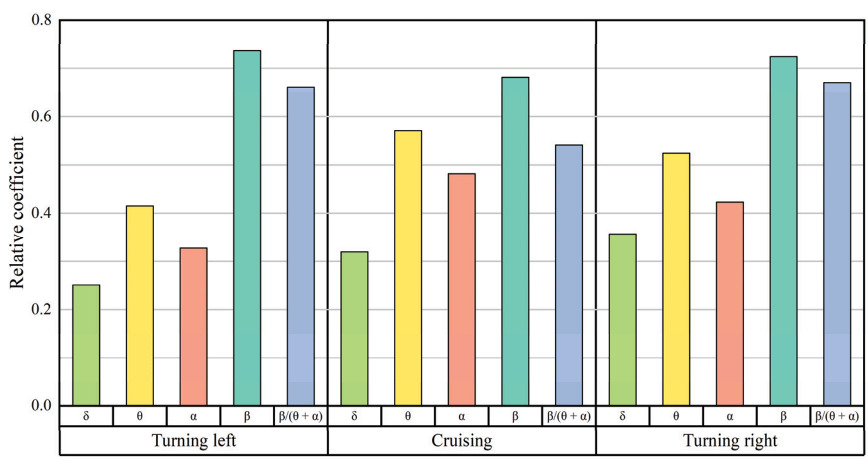

Figure 15. Pearson correlation coefficients between Shannon entropy and energy ratio at various flight stages.

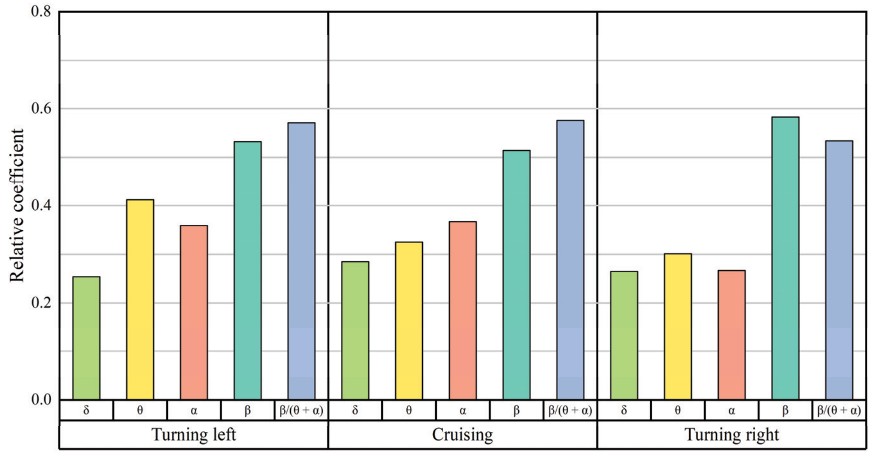

Figure 16. Pearson correlation coefficients between sample entropy and energy ratio at various flight stages.

Table 3. Pearson correlation coefficients.

EEG Entropy	Phases	δ Wave	θ Wave	α Wave	β Wave	β/(θ + α)
Shannon entropy	Turning left	0.251	0.415	0.327	0.736	0.662
	Cruising	0.319	0.571	0.482	0.682	0.541
	Turning right	0.357	0.524	0.423	0.724	0.671
Sample entropy	Turning left	0.254	0.412	0.359	0.532	0.571
	Cruising	0.285	0.325	0.367	0.514	0.576
	Turning right	0.265	0.301	0.267	0.583	0.534

Figure 17 shows that, during the turning phases, the correlation between the beta wave energy ratio and the Shannon entropy of EEG signals is stronger than the correlation between the $\beta/(\theta + \alpha)$ wave energy and the Shannon entropy of EEG signals. The Pearson correlation coefficient for left turns is 0.736, and for right turns, it is 0.724. During the cruising phase, the correlation coefficient between these two parameters is 0.682.

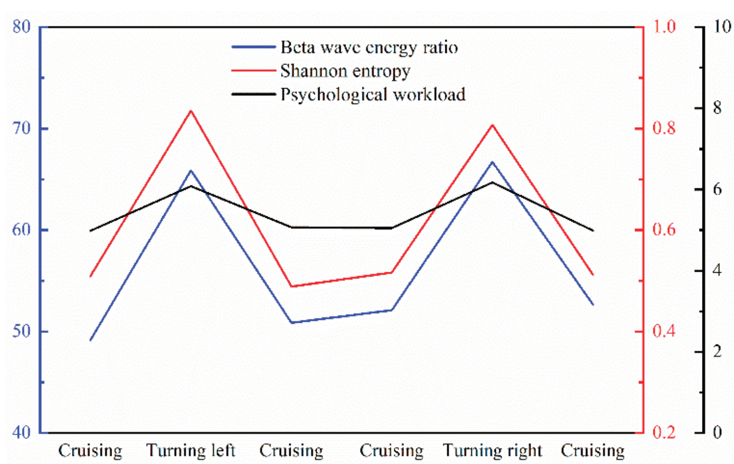

Figure 17. EEG characteristics and psychological workload during different flight maneuvers.

Figure 17 clearly demonstrates that both left and right turns are associated with a higher beta wave energy ratio, increased Shannon entropy, and greater psychological workload compared to the cruising phase. Furthermore, the trends of these parameters are consistent.

4.2. Detection Model

Our EEG characteristic detection model utilizes support vector machine (SVM). This method employs a radial basis kernel function to determine the flight phase in which the current EEG characteristics are located. This functionality guarantees high classification accuracy [36]. The radial basis kernel function $k(x_i, y_i)$ is represented by the following function relationship:

$$k(x_i, y_i) = x_i^T y_i, \tag{8}$$

where (x_i, y_i) denotes the training samples. The following system of equations elaborates on the SVM process. The concept of a support vector machine involves finding the separating hyperplane that correctly divides the training dataset and has the maximum geometric margin. The separating hyperplane is

$$\lambda x + c = 0, \tag{9}$$

where λ and c represent two parameters in separated hyperplanes. Subsequently, secondary optimization was conducted to determine the optimal boundary between the two variables. The calculation formula is as follows:

$$\min_{\lambda,c}\left[\frac{1}{2}\|\lambda\|^2\right], \tag{10}$$

Subsequently, the objective function is transformed into an unconstrained Lagrangian function.

$$L(\lambda, c, \omega) = \frac{1}{2}\|\lambda\|^2 - \sum_{i=1}^{l} \omega_i[y_i((\lambda \cdot x_i) + c) - 1], \tag{11}$$

where ω_i represents the Lagrange multiplier. Based on the Karush–Kuhn–Tucker (KKT) conditions, we can derive the solution for the Lagrangian function.

$$\begin{cases} \frac{\partial L(\lambda,c,\omega)}{\partial \lambda} = 0 \\ \frac{\partial L(\lambda,c,\omega)}{\partial c} = 0 \end{cases}, \tag{12}$$

The primal problem can be transformed into its dual form using Lagrange multipliers, resulting in

$$\max L(\omega) = \sum_{i=1}^{l} \omega_i - \frac{1}{2}\sum_{i=1}^{l}\sum_{j=1}^{l} \omega_i \omega_j y_i y_j (x_i \cdot x_j), \tag{13}$$

where ω_i and ω_j represent the Lagrange multiplier. x_i and x_j are samples, and y_i and y_j are the corresponding labels.

The final discriminant function is as follows:

$$f(x) = \operatorname{sgn}\left(\sum_{i=1}^{k} \omega_i y_i (x_i \cdot x) + c\right) \tag{14}$$

The NASA-TLX assessment indicates that pilots' psychological workload is significantly higher during the turning phase compared to the cruising phase. The turning phase is characterized by high workload, whereas the cruising phase is characterized by low workload. The input EEG characteristics comprise the beta wave energy ratio and EEG Shannon entropy, which form the combination with the strongest correlation. The classification results of the pilots' psychological workload in the test set are depicted in Figure 18.

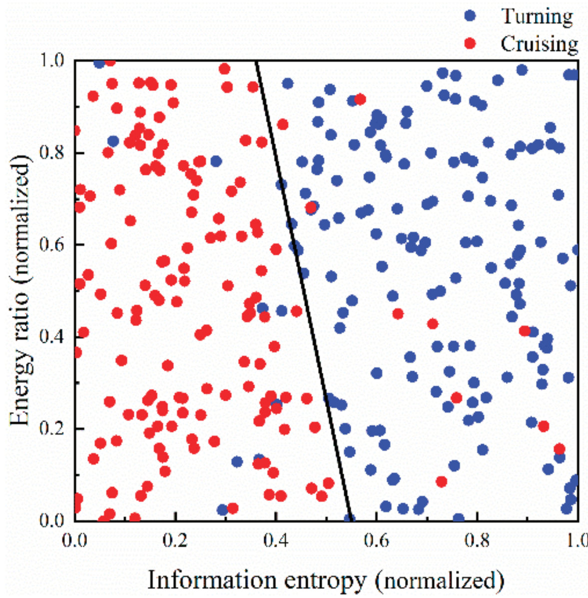

Figure 18. Classification results of psychological workload.

The classification model results are depicted in Figure 18. The final classification accuracy on the training set is 98.92%. The classification accuracy on the test set is 93.67%.

5. Discussion

The study titled "Detection of Pilot's Psychological Workload During Turning Phases Using EEG Characteristics" has clarified critical aspects of the cognitive workload experienced by pilots across various flight phases. The incorporation of electroencephalography (EEG) data for this purpose has created new opportunities to improve aviation safety and training methodologies. Several key points and implications stem from this research, warranting further discussion.

Interpretation of Results:

The observed increase in the ratio of beta wave energy and Shannon entropy during left and right turns indicates heightened cognitive activity. This aligns with existing literature that suggests beta waves are linked to active concentration and mental effort. The consistency of these findings across all pilots reinforces the robustness of EEG as a tool for assessing cognitive workload. The correlation analysis further supports these observations, demonstrating strong relationships between changes in EEG signals and specific flight maneuvers. This provides a quantitative basis for understanding the mental demands placed on pilots during various flight phases.

The subjective workload assessments using the NASA-TLX questionnaire aligned well with the EEG-based findings, thereby validating the objective measures. This dual approach strengthens the argument for using EEG in combination with traditional assessment tools to achieve a comprehensive understanding of pilot workload. The higher workload scores reported by the pilots during turns are consistent with the EEG data, thereby reinforcing the reliability of these measures in reflecting actual cognitive states.

The high classification accuracy of the SVM model in distinguishing between different workload states demonstrates the potential of machine learning in cognitive monitoring. The slight drop in accuracy from the training set to the test set is expected and underscores the need for further refinement and validation of the model with larger data sets. The SVM's ability to classify workload states based on EEG data underscores the feasibility of developing real-time monitoring systems. Such systems could provide immediate feedback to pilots and support personnel, thereby enhancing decision-making processes during flights.

This in-depth analysis will not only enhance our understanding of the role of EEG in monitoring cognitive states but also offer a clearer perspective on the practical applications of these insights. Exploring how these systems can provide immediate feedback and support decision-making processes during flights may pave the way for significant advancements in aviation safety and training methodologies. Highlighting these practical applications may bridge the gap between theoretical research and its implementation, ultimately contributing to more effective and responsive aviation practices.

6. Conclusions

The study employed the EPOC + EEG headset to monitor signal variations in different brain regions of pilots during left and right turns. It analyzed EEG characteristics and the pilots' psychological workload states using support vector machines for classification [37]. The study's conclusions are summarized as follows:

EEG Maps and Beta Wave Energy: the EEG maps show a significant increase in beta wave energy at the T7 electrode during the left turn phase and at the T8 electrode during the right turn phase. During the cruising phase, the energy levels at various electrode points remain stable and relatively low.

Entropy and EEG Complexity: the results show that during aircraft turns, the entropy of EEG signals is higher compared to the cruising phase, indicating that EEG activity during the turning phase is characterized by increased complexity and irregularity.

NASA-TLX and Psychological Workload: statistical analysis using the NASA-TLX scale shows that pilots experience a higher psychological workload during turning phases compared to the cruising phase. This increased psychological workload may contribute to the complexity and irregularity of EEG signals during turning maneuvers.

Support Vector Machine Classification: By classifying EEG characteristics using a support vector machine, the psychological workload detection accuracy for the test set was 93.67%. These results indicate that this method has high accuracy in distinguishing the EEG characteristics associated with different levels of psychological workload, providing a reliable foundation for further application in the real-time monitoring of pilots' psychological workload during flight operations.

Future Work

The gender and age of pilots might influence the ratio of EEG energy and Shannon entropy. Additionally, pilots with varying levels of flying experience might experience different levels of psychological workload during cruising and turning phases. Therefore, further collection of EEG data from a diverse group of pilots is necessary to enhance the SVM dataset and improve classification accuracy. This will help gain a deeper understanding of pilots' flying states and provide a theoretical basis for pilot training, thereby enhancing flight safety. Considering these additional factors will ensure a more comprehensive and accurate assessment of pilots' cognitive and psychological states, leading to better training protocols and safer flight operations.

Author Contributions: Conceptualization, L.J., L.Y. and H.L.; data curation, L.Y.; formal analysis, H.L., W.H. and N.Z.; funding acquisition, L.J.; methodology, L.J. and L.Y.; project administration, L.J., H.L., W.H. and N.Z.; supervision, N.Z.; validation, L.J. and L.Y.; writing—original draft, L.Y.; writing—review and editing, L.J. All authors have read and agreed to the published version of the manuscript.

Funding: This research was funded by 2020 Ministry of Education Humanities and Social Science Research Project (20YJCZH227), Liaoning Province Education Department Youth Fund Project (L2021029), Innovative training program for College Students (D202104012053547909) and Liaoning Province Education Department Project (JYT2020059).

Institutional Review Board Statement: Not applicable.

Informed Consent Statement: Informed consent was obtained from all subjects involved in the study.

Data Availability Statement: Given the ongoing research value of the data, scholars may reach out to the author to obtain access to it.

Conflicts of Interest: Authors Haiwei Li and Wenjie Han were employed by the company Shenyang Aircraft Corporation. The remaining authors declare that the research was conducted in the absence of any commercial or financial relationships that could be construed as a potential conflict of interest.

References

1. CAAC. *Report of Civil Aviation Airspace Development in China 2021*; China Civil Aviation Annual Report; CAAC: Beijing, China, 2022.
2. Aviation Safety Network. Available online: https://aviation-safety.net/database/2022-analysis (accessed on 26 November 2023).
3. Donmez, K.; Uslu, S. The effect of management practices on aircraft incidents. *J. Air Transp. Manag.* **2020**, *84*, 101784. [CrossRef]
4. Li, M.J.; Zhou, X.; Si, Q.M.; Fu, S.; Guan, H.Y. Investigation method of civil helicopter flight accident basedon fishbone diagram. *Sci. Technol. Innov.* **2020**, *17*, 34–35.
5. Boyd, D.D.; Scharf, M.; Cross, D. A Comparison of General Aviation Accidents Involving Airline Pilots and Instrument-Rated Private Pilots. *J. Safety Res.* **2021**, *76*, 127–134. [CrossRef] [PubMed]
6. Xu, J. The influence of pilot emotional stability on flight safety and countermeasures analysis. *J. Shandong Ind. Technol.* **2015**, *8*, 241.
7. Zhang, G.; Yu, Z. Flight Training Safety Monitoring and Evaluation Equipment Design. *Radio Eng.* **2021**, *51*, 1012–1016.
8. Li, J.; Li, S.; Jing, C.; Wang, Y.; Xue, X.; Wang, D.J.; Liu, Q.M.; Xiao, Q. Analysis of ECG changes in high-altitude hypoxia training for high-performance fighter pilots. *S. China J. Natl. Def. Med.* **2019**, *33*, 39–41+57.
9. Babu, M.D.; Shree, D.V.J.; Prabhakar, G.; Saluja, K.P.; Pashilkar, A.; Biswas, P. Estimating pilots' cognitive load from ocular parameters through simulation and in-flight studies. *J. Eye Move. Res.* **2019**, *12*, 3. [CrossRef] [PubMed]
10. Aggarwal, S.; Chugh, N. Review of Machine Learning Techniques for EEG Based Brain Computer Interface. *Arch. Comput. Methods Eng.* **2022**, *29*, 3001–3020. [CrossRef]
11. Wilson, G.F.; Fullenkamp, P.; Davis, I. Evoked potential, cardiac, blink, and respiration measures of pilot workload in air-to-ground missions. *Aviat. Space Environ. Med.* **1994**, *65*, 100–105.
12. Bartosz, B.; Dariusz, M.; Cyran, K.A. A Machine Learning Approach to the Detection of Pilot's Reaction to Unexpected Events Based on EEG Signals. *Comput. Intell. Neurosci.* **2018**, *2018*, 2703513.
13. Binias, B.; Myszor, D.; Binias, S.; Cyran, K.A. Analysis of Relation between Brainwave Activity and Reaction Time of Short-Haul Pilots Based on EEG Data. *Sensors* **2023**, *23*, 6470. [CrossRef] [PubMed]
14. Zhang, P.; Yan, J.; Liu, Z.; Zhou, Q. Brain signatures of error awareness during cognitive tasks for humans in the flight environment. *Front. Neurosci.* **2022**, *16*, 1007258. [CrossRef] [PubMed]
15. Lan, Z.; Zhao, J.; Liu, P.; Zhang, C.; Lyu, N.; Guo, L. Driving fatigue detection based on fusion of EEG and vehicle motion information. *Biomed. Signal Process. Control.* **2024**, *92*, 106031. [CrossRef]
16. Zhang, S.; Zhang, Y.; Sun, Y.; Thakor, N.; Bezerianos, A. Graph theoretical analysis of EEG functional network during multiworkload flight simulation experiment in virtual reality environment. In Proceedings of the 2017 39th Annual International Conference of the IEEE Engineering in Medicine and Biology Society (EMBC), Jeju, Republic of Korea, 11–15 July 2017; pp. 3957–3960.
17. Chen, K.; Zhang, S.L.; Ding, F. Brain-computer interface research based on Emotiv. *Inf. Technol. Netw. Secur.* **2018**, *37*, 116–118.
18. Zhang, N.N.; Fan, S.; Wang, D.D.; Zou, Y.Y.; Ren, H. Research on the cockpit display interface of navigable aircraft based on mental load. *Eng. Des. J.* **2019**, *26*, 409–415.
19. Gurudath, N.; Riley, H.B. Drowsy Driving Detection by EEG Analysis Using Wavelet Transform and K-means Clustering. *Procedia Comput. Sci.* **2014**, *34*, 400–409. [CrossRef]
20. Jerzy, B.; Paweł, P. Fractional Band-Pass Filters: Design, Implementation and Application to EEG Signal Processing. *J. Circuits Syst. Comput.* **2017**, *26*, 1750170:1–1750170:21.
21. Irene, W.; Stefan, D.; Klaus-Robert, M.; Michael, T. On the influence of high-pass filtering on ICA-based artifact reduction in EEG-ERP. *Annu. Int. Conf. IEEE Eng. Med. Biol. Soc.* **2015**, *2015*, 4101–4105.
22. Yang, C.J.; Nomena; Li, Y.Y.; Zhang, R. Denoising Method of Epilepsy Brain Telecom Number Based on ICA and Wavelet Thresholds. *J. Northwest Univ. (Nat. Sci. Ed.).* **2016**, *46*, 795–800.
23. Wang, C.F.; Sun, Y. Study on Eye Electro artifact Removal by Improving Independent Component Algorithm. *Comput. Eng. Appl.* **2018**, *54*, 167–173.
24. Yang, Y.; Feng, Y.; Easa, S.M.; Zheng, X. Evaluation of Mental Load of Drivers in Long Highway Tunnel Based on Electroencephalograph. *Front. Psychol.* **2021**, *12*, 646406. [CrossRef] [PubMed]
25. Silva, P.; Duarte, R.; Esteves, P.; Travassos, B.; Vilar, L. Application of entropy measures to analysis of performance in team sports. *Int. J. Perform. Anal. Sport.* **2016**, *16*, 753–768. [CrossRef]
26. Fu, R.; Du, Y.; Wang, S.; Wen, G.; Chen, J.; Li, Y. Dynamical Differential Covariance Based Brain Network for Motor Intent Recognition. *IEEE Sens. J.* **2024**, *24*, 6515–6522. [CrossRef]
27. Wu, B. *Analysis of Exercise Intention Based on EEG Rhythm Feature Optimization and Synchronicity*; Zhejiang University: Zhejiang, China, 2011.

28. Yang, Y.; Du, Z.; Jiao, F.; Pan, F. Analysis of EEG characteristics of drivers and driving safety in undersea tunnel. *Int. J. Environ. Res. Public Health* **2021**, *18*, 9810. [CrossRef] [PubMed]
29. Kar, S.; Bhagat, M.; Routray, A. EEG signal analysis for the assessment and quantification of driver's fatigue. *Transp. Res. F Traffic Psychol. Behav.* **2010**, *13*, 297–306. [CrossRef]
30. Ibrahim, S.; Djemal, R.; Alsuwailem, A. Electroencephalography (EEG) signal processing for epilepsy and autism spectrum disorder diagnosis. *Biocybern. Biomed. Eng.* **2018**, *38*, 16–26. [CrossRef]
31. Namazi, H. Information-Based Classification of Electroencephalography (EEG) Signals for Healthy Adolescents and Adolescents with Symptoms of Schizophrenia. *Fluct. Noise Lett.* **2020**, *19*, 4. [CrossRef]
32. Devos, H.; Gustafson, K.; Ahmadnezhad, P.; Liao, K.; Mahnken, J.D.; Brooks, W.M.; Burns, J.M. Psychometric Properties of NASA-TLX and Index of Cognitive Activity as Measures of Cognitive Workload in Older Adults. *Brain Sci.* **2020**, *10*, 994. [CrossRef] [PubMed]
33. Noyes, J.M.; Bruneau, D.P. A self-analysis of the NASA-TLX workload measure. *Ergonomics* **2007**, *50*, 514–519. [CrossRef]
34. Wang, X.; Huang, F.; Cheng, Y. Computational performance optimization of support vector machine based on support vectors. *Neurocomputing* **2016**, *211*, 66–71. [CrossRef]
35. Simić, M. Testing for normality with neural networks. *Neural Comput. Appl.* **2021**, *33*, 16279–16313. [CrossRef]
36. Hao, Z.; Shaohong, L.; Jinping, S. Unit Model of Binary SVM with DS Output and its Application in Multi-class SVM. In Proceedings of the 2011 Fourth International Symposium on Computational Intelligence and Design, Hangzhou, China, 28–30 October 2011; Volume 1, pp. 101–104.
37. Feng, Z.; Yang, M.; Zhang, W.; Du, Y.; Bai, H. Effect of longitudinal slope of urban underpass tunnels on drivers' heart rate and speed: A study based on a real vehicle experiment. *Tunn. Undergr. Space Technol.* **2018**, *81*, 525–533. [CrossRef]

sensors

Article

User Evaluation of a Shared Robot Control System Combining BCI and Eye Tracking in a Portable Augmented Reality User Interface

Arnau Dillen [1,2,3,*], Mohsen Omidi [3,4], Fakhreddine Ghaffari [2], Olivier Romain [2], Bram Vanderborght [3,4], Bart Roelands [1,3], Ann Nowé [5] and Kevin De Pauw [1,3,*]

1 Human Physiology and Sports Physiotherapy Research Group, Vrije Universiteit Brussel, 1050 Brussels, Belgium
2 Equipes Traitement de l'Information et Systèmes, UMR 8051, CY Cergy Paris Université, École Nationale Supérieure de l'Electronique et de ses Applications (ENSEA), Centre National de la Recherche Scientifique (CNRS), 95000 Cergy, France; fakhreddine.ghaffari@cyu.fr (F.G.); olivier.romain@cyu.fr (O.R.)
3 Brussels Human Robotics Research Center (BruBotics), Vrije Universiteit Brussel, 1050 Brussels, Belgium; mohsen.omidi@vub.be (M.O.); bram.vanderborght@vub.be (B.V.)
4 IMEC, 1050 Brussels, Belgium
5 Artificial Intelligence Lab, Vrije Universiteit Brussel, 1050 Brussels, Belgium
* Correspondence: arnau.dillen@vub.be (A.D.); kevin.de.pauw@vub.be (K.D.P.)

Abstract: This study evaluates an innovative control approach to assistive robotics by integrating brain–computer interface (BCI) technology and eye tracking into a shared control system for a mobile augmented reality user interface. Aimed at enhancing the autonomy of individuals with physical disabilities, particularly those with impaired motor function due to conditions such as stroke, the system utilizes BCI to interpret user intentions from electroencephalography signals and eye tracking to identify the object of focus, thus refining control commands. This integration seeks to create a more intuitive and responsive assistive robot control strategy. The real-world usability was evaluated, demonstrating significant potential to improve autonomy for individuals with severe motor impairments. The control system was compared with an eye-tracking-based alternative to identify areas needing improvement. Although BCI achieved an acceptable success rate of 0.83 in the final phase, eye tracking was more effective with a perfect success rate and consistently lower completion times ($p < 0.001$). The user experience responses favored eye tracking in 11 out of 26 questions, with no significant differences in the remaining questions, and subjective fatigue was higher with BCI use ($p = 0.04$). While BCI performance lagged behind eye tracking, the user evaluation supports the validity of our control strategy, showing that it could be deployed in real-world conditions and suggesting a pathway for further advancements.

Keywords: brain-computer interface; human-robot interaction; user evaluation; usability; assistive robotics; augmented reality; shared control; user experience

Citation: Dillen, A.; Omidi, M.; Ghaffari, F.; Romain, O.; Vanderborght, B.; Roelands, B.; Nowé, A.; De Pauw, K. User Evaluation of a Shared Robot Control System Combining BCI and Eye Tracking in a Portable Augmented Reality User Interface. *Sensors* **2024**, *24*, 5253. https://doi.org/10.3390/s24165253

Academic Editors: Fei He, Hua-Liang Wei, Yuzhu Guo and Yifan Zhao

Received: 13 June 2024
Revised: 2 August 2024
Accepted: 9 August 2024
Published: 14 August 2024

1. Introduction

Physically assistive robots aim to enhance the autonomy of individuals with physical disabilities by enabling interaction with their environment through the robot [1]. In the European Union, there are 9.53 million stroke survivors, often resulting in impaired motor function, and an additional 2.58 million stroke cases are predicted by 2047 [2]. Thus, there is an urgent need for assistive technologies that enable motor-impaired individuals to interact with their surroundings. An ideal assistive robot should anticipate the user's intentions while avoiding unintended actions. This requires an interaction modality that monitors the user's attention and infers their intentions from physiological behavior.

One promising interaction modality for addressing motor function impairments is the brain–computer interface (BCI). Formally defined by [3], "A BCI is a system that measures central nervous system (CNS) activity and converts it into artificial output that replaces restores, enhances, supplements, or improves natural CNS output and thereby changes the ongoing interactions between the CNS and its external or internal environment". In the context of human–computer interaction, a BCI is defined as a system that allows users to operate devices with their thoughts by measuring and decoding neural activity.

BCI control systems interpret neural activity from brain-related physiological signals, such as the electroencephalogram (EEG), by applying machine learning (ML) techniques trained on labeled data from individuals engaged in mental tasks [4]. In BCI control systems, classification is used alongside high-level control software to convert decoded mental tasks into device actions. Various modalities of the EEG signal are utilized for BCI control [5], with one commonly used paradigm being motor imagery (MI). MI refers to the mental process of imagining a movement without physically executing it [6], defined as "the mental simulation of an action without the corresponding motor output" [7]. A BCI system employing MI decodes the imagined movement from the EEG signal and executes a command corresponding to the decoded class.

Currently, BCI technologies are primarily confined to lab settings where environmental conditions are controlled, and distractions are minimized. Before BCI can be used in real-world applications, several key issues need resolving [8]. Developing a BCI control system with a good user experience requires a user-centered design approach for the control strategy and user interface (UI) [9]. This approach has gained traction within the BCI community [10–12], although most BCI research focuses only on technical validation [13].

A key component of a user-centered approach is evaluating the control system with users in realistic scenarios to ensure its performance under real-world conditions. Assessing the real-world readiness of a BCI control system requires appropriate performance measures to quantify its usability [14]. A comprehensive usability assessment should encompass effectiveness, efficiency, and user experience through both objective and subjective measures [15].

Objective measures should include decoding-related metrics such as accuracy, as well as performance metrics for task completions, including completion time and success rate [10]. Subjective measures can be collected through qualitative interviews and quantitative metrics that facilitate comparisons between different control systems or versions of the same system. Tools like visual analog scales and questionnaires can provide quantitative user experience metrics [16]. To ensure thorough user studies, it is crucial to establish standard guidelines and an evaluation framework that supports the user assessment of novel BCI control systems. The recent efforts to standardize BCI usability research are ongoing [17,18], but more work is still required to facilitate the usability evaluation of BCI prototypes.

The user study described in this article aims to evaluate the real-world usability of a BCI control system developed in the previous research. The central research question is to evaluate whether our MI-based BCI control system prototype could be deployed in real-world applications. The study involved able-bodied participants using the BCI control system to operate a robotic arm in tasks representative of daily activities. Additionally, the BCI control system was compared with an alternative eye-tracking-based control system to assess the added value of BCI in everyday scenarios for a physically assistive robot. The results are intended to provide insights into areas needing improvement and quantify the usability of the BCI control system, also providing a framework for other BCI researchers to evaluate their control system prototypes.

2. Related Work

Most BCI user studies primarily address the effectiveness and efficiency aspects of usability [18–20]. An exemplary study that thoroughly evaluates all aspects of usability was conducted by Kuhner et al. [21], who present an extensive experiment with their prototype. Usability studies can vary in focus depending on the application and method being investigated.

Some studies explicitly compare different control paradigms [22,23], while others aim to validate the technical feasibility of a new prototype before proceeding to more comprehensive user studies or clinical trials [24–26]. User studies may involve clinical trials with specific patient populations [27–30] or studies with able-bodied individuals that focus on the user experience of a new approach [31,32]. Usability is also crucial when developing new hardware [25]. The review by Ortega and Mezura-Godoy [33] offers a recent systematic overview of BCI user evaluation literature.

3. Materials and Methods

3.1. The BCI Control System

3.1.1. Control Strategy

The BCI control system that is evaluated in this user study uses a shared control approach, which is depicted in Figure 1.

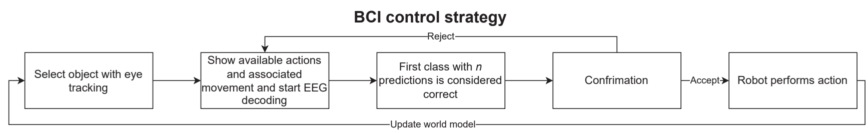

Figure 1. The control strategy of the MI BCI control system. The user selects an object with their gaze and uses MI to select one of the possible actions. After accepting or rejecting the decoded MI class, the robot executes the associated action or returns to the action selection stage.

The control strategy involves several stages, beginning with object selection. To interact with an object in the environment, the user gazes at the chosen object for 2 s, prompting the system to advance to the action selection stage. Here, possible actions appear as a menu above the object, indicating the specific movement the user should imagine in order to select an action. The shared control system utilizes an internal world model, updated by sensors such as cameras, to identify the object's type, location, and state. This allows the system to determine which actions are available to the user.

Next, real-time EEG decoding initiates, putting the system in the decoding stage. In this stage, the user imagines one of the movements associated with a robot action, continuing to do so until the EEG decoding software makes n predictions for the same MI class. The prediction threshold was set to 5 for this study. Once the decoding threshold is met, the system transitions to the confirmation stage, where the user is presented with a holographic modal window showing the action that was determined and asked to accept or reject it.

If the user accepts the decoding result, the robot executes the corresponding action. If the user rejects the result, decoding resumes, and the user imagines the intended movement again. This method prevents the robot from performing unintended actions, avoiding the need for the user to cancel an action during its execution. After the robot completes the selected action, the system returns to object selection mode. The movement inferred by the control system is referred to as a decision, as opposed to a prediction from the decoding pipeline for a single window of EEG. We use the term decision hereafter to refer to the expected action resulting from several MI predictions.

An eye-tracking-based variant was implemented to compare the usability of the BCI control system with an alternative control modality. The object selection strategy mirrors that of the BCI control system. However, in the eye-tracking variant, the menu displaying possible actions consists of buttons that are selectable via eye tracking. The associated robot action is executed when the user gazes at an action button for 2 s. Thus, the decoding and confirmation stages are eliminated from the control strategy, made possible by the near-perfect accuracy of eye tracking.

The UI software that handles the logic of the decoding strategy and the contextual display of graphical components, such as menus and virtual evaluation environments, was implemented using the Unity 3D [34] game engine and the mixed reality toolkit version

2.8 [35]. Communication with the real-time EEG decoding process, which is detailed in Section 3.1.3, is achieved with a publish/subscribe strategy. The UI process sends messages to start and stop decoding to the EEG decoding process and the EEG decoding process sends decoding results back to the UI.

3.1.2. Hardware

Two EEG devices were used in this user study. Initially, the OpenBCI EEG device with a 16-electrode cap was employed for the first three participants in Phase 1. This device uses passive gel-based Ag/AgCl electrodes, samples at 125 Hz, and transmits data wirelessly via Bluetooth. Subsequently, the Smarting ProX (mBrainTrain, Belgrade, Serbia) was used, featuring a 64-electrode cap with active gel-based electrodes. The sampling rate was set to 250 Hz in this study to reduce computational costs for real-time processing. The Smarting ProX was used from Phase 2 onward to allow for more detailed analysis of the EEG data in future research, such as investigating cognitive processes related to MI. The OpenBCI device was initially used to demonstrate the feasibility of using consumer-grade EEG with our control system. Both electrode layouts follow the international 10–20 system [36].

Microsoft™ HoloLens 2.0 was chosen for the head-mounted AR display. It uses waveguide-based AR and provides off-the-shelf eye-tracking and spatial awareness functionality through its built-in sensors. This device enabled the AR display of the UI overlaid on the real world while also providing the necessary sensor information for the shared control strategy. The Franka Research robot (Franka Robotics GmbH, Munich, Germany) was employed as the robot arm in this experiment. This robotic arm offers 7 degrees of freedom and is equipped with a gripper to pick up objects [37].

Real-time EEG decoding was performed by a laptop equipped with a 6-core Intel(R) Core(TM) i7-10850H CPU running at 2.70 GHz. The laptop has 16 GB of RAM and an NVIDIA GeForce RTX 2070 Max-Q GPU. It connects to the robot via Ethernet and communicates with the HoloLens through a USB-C cable.

3.1.3. Real-Time EEG Decoding

The real-time EEG decoding component of the control system was implemented with the Python 3.10 programming language. The MNE library [38] was used for operations relating to EEG data processing such as reading data files, filtering, and epoching, among others. MNE was also used to implement the feature extraction step of our decoding pipeline. The lab streaming layer [39] software was used with its Python client PyLSL to integrate the real-time EEG data stream with our software. The Scikit Learn (SKLearn) library [40] was used for the implementation of ML models and decoding pipeline management.

When the decoding stage begins, the process starts by sampling chunks of EEG data from the EEG data stream. For this study, each chunk is 4 s long, meaning that the most recent 4 s of EEG data are sampled. Multiple windows of EEG data are then extracted from each chunk using a sliding window approach with a stride of 0.25 s. Each input window is 2 s long, resulting in 9 overlapping windows per chunk. These windows are subsequently sent to the decoding pipeline for classification.

The first step in the decoding pipeline involves filtering the EEG data using a finite impulse response band-pass filter. The filter design is a windowed time-domain (firwin) design, as recommended by Widmann et al. [41]. This filter is a one-pass, zero-phase, non-causal band-pass filter using a Hamming window with 0.0194 passband ripple and 53 dB stopband attenuation. The lower passband edge is set at 8 Hz with a 2 Hz transition bandwidth for a -6 dB cutoff frequency at 7 Hz. The upper passband edge is at 30 Hz with a 7.5 Hz transition bandwidth for a -6 dB cutoff frequency at 33.75 Hz. The filter length is automatically set to 413 samples (1.652 seconds) based on the default settings of the MNE filter functions.

After filtering, features are extracted from the input windows using common spatial patterns [42], with 6 components utilized in this step. These features are then used to predict the MI class using a linear discriminant analysis model [43]. The decoding pipeline was trained on calibration data that were previously acquired according to the procedure detailed in Section 3.2.3. The decoding pipeline was always trained with all the calibration data that were acquired during the current session and never used data from other sessions.

3.2. User Study

The real-world usability of the prototype control system was assessed through a user study where participants operated a virtual robotic arm using our control system. The study was divided into three distinct phases to allow iterative improvements of the software, ensuring a stable experience for the final phase. Participants completed various scenarios representing everyday chores in a virtual AR environment. The evaluation tasks utilize holograms to simulate the robot arm and objects within a real-world environment. In the final session of Phase 3, a real robot is incorporated to replicate the actions performed by the virtual robot. The procedure was consistent across phases, differing only in the number of sessions and the tasks to be completed.

New participants were recruited for each phase to assess the experience of users unfamiliar with BCI and to improve the control system between phases. The number of participants was increased with each phase to ensure rapid iteration while maintaining the validity of the results. The sample sizes were determined based on best practices in the literature [10,13,44].

In Phase 1, a validation study was conducted using the OpenBCI EEG headset, involving 3 participants (all male, aged 23–24), each attending 2 sessions. Phase 2 involved 5 participants (1 female, 4 male, aged 23–29), each attending 3 sessions. This phase allowed for validation of the procedure and further technical validation of the system. Since the statistical comparison of outcomes was not required at this stage, 5 participants provided a good balance between thorough assessment and time efficiency. The performance assessment used the same sorting task as in Phase 1, with the main difference being that participants had to complete 10 repetitions of the sorting task to consider a run successful.

In the final phase, the procedure was expanded by introducing a pick-and-place task and using a real robot in each participant's final session. This phase involved 12 participants (3 female, 9 male, aged 22–30), each attending 3 sessions. The sample size was determined using established usability engineering guidelines [14,15]. The procedure for each session is detailed in Section 3.2.3.

The participants received an explanation of the procedure upon registration and provided written informed consent at the start of the first session. The instructions were orally given before each run of a usage scenario. This study was approved by the Medical Ethics Committee of UZ Brussel and VUB (BUN1432023000232) and adhered to the principles of the Declaration of Helsinki for medical research involving human participants [45].

The questionnaire results were collected using the Redcap software version 14.1.0 [46]. The result data were processed with the Python programming language using the Pandas library for organizing the data [47] and the Seaborn library for generating figures [48]. The statistical tests presented in this study were performed using the stats package of the SciPy library [49].

3.2.1. Evaluation Scenarios

The first evaluation scenario involves sorting a cube using the robotic arm, simulating everyday tasks such as sorting garbage or laundry. In this scenario, the participant is seated and equipped with EEG and AR devices. A virtual robot arm is placed on a virtual table in front of them, with two differently colored baskets on either side. A colored cube appears before the participant, indicating which basket to select based on the cube's color. The user must choose the correct side by following instructions from the action menu that appears after looking at the cube for 2 s. Each run includes multiple repetitions of the task until the specified end conditions, detailed in Section 3.2.3, are met.

The second task is a pick-and-place scenario where the participant, still seated and equipped with EEG and AR devices, interacts with the virtual robot arm and four virtual objects on the table: an orange, a Rubik's cube, a TV remote, and a smartphone. The objects are placed at fixed positions and the possible actions always consist of instructing the robot to pick up the object and either give it to the user (simulated by placing the object at a fixed position in front of the user) or put it away at an object-dependent fixed position. When the real robot is connected, the virtual objects are represented by cubes placed in a fixed location on the table the robot is placed on. The participant completes a fixed sequence of actions that was determined beforehand to complete the run. The order of objects and actions is randomized for each run.

3.2.2. Usability Measures

To assess the control system's objective performance, several metrics were used. The main performance metric of this study is the success rate for task completion, calculated as

$$success - rate = \frac{n_c}{n_r}, \tag{1}$$

where n_c is the number of completed runs and n_r is the total number of runs performed. This metric represents the system's effectiveness in enabling users to complete their assigned tasks using the control system.

The efficiency of the control system is measured by the task completion time. The completion time is calculated as the time between the start signal and placing the final object in its intended location.

To assess the online decoding performance of our decoding pipeline, we compute the decision accuracy based on rejected and accepted actions during the final evaluation runs of participants. We chose balanced accuracy as our prediction performance measure, which is computed as

$$balanced - accuracy = \frac{1}{2}(\frac{TP}{TP + FN} + \frac{TN}{TN + FP}) \tag{2}$$

where TP is the number of true positives, FN is the number of false negatives, TN is the number of true negatives, and FP is the number of false positives. When referring to accuracy in the remainder of this manuscript, balanced accuracy is implied.

The often-used user experience questionnaire (UEQ; [50]) and a semi-structured interview were used to assess the user experience of the system quantitatively and qualitatively, respectively. The UEQ questionnaire asks participants to give their opinion regarding several concepts on a scale from 1 to 7. The questions for the user interview can be found in Appendix A.

To assess the amount of subjective fatigue that is induced by the control system, a visual analog scale was used where users had to indicate their perceived mental (mVAS) and physical (pVAS) fatigue levels [51]. The indicated VAS levels were subsequently discretized to scores ranging from 0 to 100. The VAS approach was chosen for its short application time and easy explainability to participants. Subjective fatigue was chosen as opposed to more objective measures, such as features from the EEG signal, as we are mostly interested in user perception. The participant's mood state was also assessed using the profile of mood states (POMS) questionnaire [52]. The participant's aptitude for MI is evaluated with the motor imagery questionnaire 3 (MIQ3; [53]).

We compared the performance outcomes of the control system variants using statistical testing. The significance level was set to 0.05 for all tests. The data were first checked for normality using D'Agostino and Pearson's test [54]. For paired samples, such as UEQ responses between BCI and eye tracking and fatigue levels before or after using the control system, paired tests were used. If normality was ensured, a paired t-test [55] was used to investigate if there was a statistical difference between the mean scores for BCI and eye tracking. The Wilcoxon signed-rank test [56] was used if the normality of the data was rejected.

When the data were independent, such as when comparing eye tracking and BCI mVAS outcomes from the final evaluation session (since the order of the control system variant was alternated for participants), independent sample tests were used. When the data were normally distributed, an independent samples t-test was used [55] and the Mann–Whitney U test [57] was chosen if this was not the case.

3.2.3. Procedure

Each phase consisted of multiple sessions where the first sessions were intended to support participant's familiarization with the concept of MI BCI and the interaction design of the control system. During these sessions, participants were encouraged to ask questions if something was unclear while completing a task and were frequently questioned about their experience. The first session always started with signing the informed consent after a briefing and giving the participant time to read the document in detail. This was then followed by the MIQ3 questionnaire, after which participants were requested to complete the POMS, mVAS, and pVAS questionnaires. Participants were instructed to complete the latter three questionnaires at the start of each subsequent session and to fill out the pVAS and mVAS again at the end of every session.

Ensuing sessions focused on training the participant in using the control system with the last session culminating in a performance assessment employing one of the evaluation tasks. After completing the questionnaires, the acquisition of calibration data that were used to train an MI decoding pipeline ensued. The subsequent tasks were dependent on the study phase and session number. Figure 2 shows an overview of the procedure for Phase 1, highlighting the differences between the sessions.

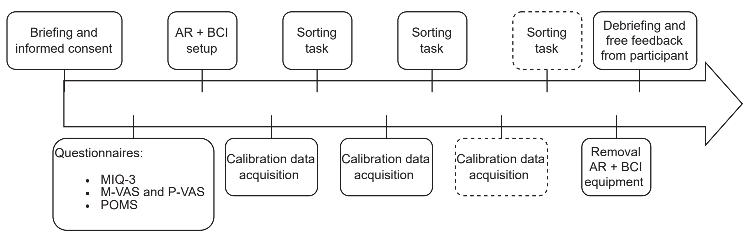

(**a**)

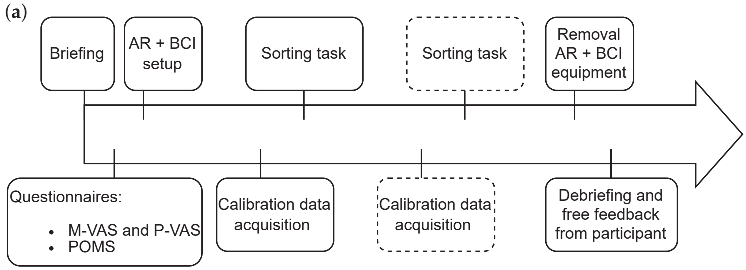

(**b**)

Figure 2. The experimental procedure that was followed for Phase1 in (**a**) session 1 and (**b**) session 2.

In Phase 1, participants performed the sorting task with the robot. After filling in the questionnaire and setting up the EEG and AR devices, calibration and sorting runs were alternated. There was no fixed amount of trials or runs as this phase was merely intended to validate the technical feasibility of using our control system with OpenBCI. The session ended when the planned 3-h time limit was reached or the participant decided that they were satisfied with their performance, having attempted at least two sorting runs. The second session followed the same procedure as the first with the difference that informed consent and MIQ3 are omitted and only 1 run is required to complete the session.

Phases 2 and 3 use the same procedure with some key differences in the evaluation tasks that are used. The order of session events is exactly the same. Figure 3 shows the procedure for each session with Figure 3c showing variants of session 3, labeled as A (eye tracking first) and B (BCI first).

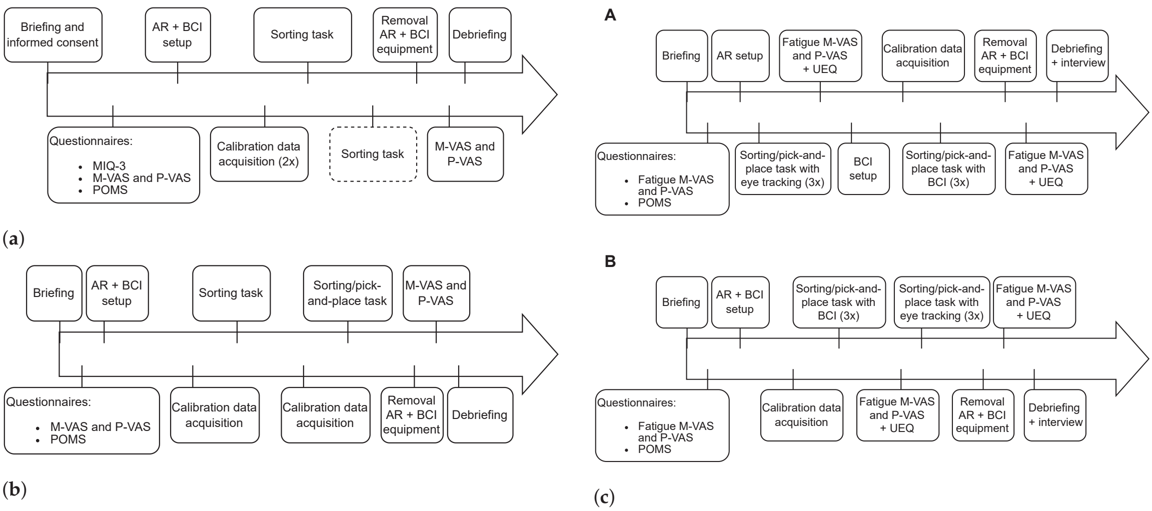

Figure 3. The experimental procedure that was followed for Phase 3 in (**a**) session 1, (**b**) session 2, and (**c**) session 3 with options **A** and **B**.

For the first session of Phase 2, shown in Figure 3a, participants completed two consecutive calibration runs with a 5-min break in between. Subsequently, they were requested to perform one sorting run with the possibility of an optional second run if there was time and they were willing. The second session, depicted in Figure 3b, consisted of an alternation of calibration and sorting runs with a maximum of 2 calibration runs. Participants were encouraged to perform a third sorting run if possible. There was no time limit for the first two sessions.

In session 3, illustrated in Figure 3c, the participant had to perform three consecutive sorting runs that were timed using either the BCI or eye tracking control system variant. A calibration run was performed beforehand if the BCI variant was used first (B). If participants used eye tracking first (A), we performed the EEG setup and calibration run after they completed the evaluation runs with eye tracking. The time limit was set to 15 min and a run was considered failed if the participant was unable to complete the tasks within this limit. After completing the required runs, the participant was requested to complete the mVAS and pVAS to assess their intermediate fatigue levels.

This was followed by the UEQ questionnaire in relation to their experience with the used control system. Afterward, following the necessary setup and eventual BCI calibration, the participant performed 3 runs with the other control system variant. This was again followed by the mVAS, pVAS, and UEQ questionnaires in relation to the current variant. The order of variants used was alternated between participants to avoid possible bias resulting from the participant's experience with the other variant and to investigate the change in fatigue levels compared to the baseline at the beginning of the session. Finally, the interview was performed as a debriefing to assess if participants had suggestions.

The first session of Phase 3 was identical to Phase 2, and the second session also started with a calibration run followed by a sorting run. After the second calibration run, the pick-and-place task was introduced. Participants were asked to choose the order of objects and the actions themselves. They had to announce their choice before initiating the object selection stage of the control system. Afterward, they were encouraged to perform an optional run where the experimenter provided the sequence of object–action pairs to prepare them for the final session.

Finally, the last session introduced the real robot and took place at the AI Experience Center at VUB, located in Brussels, Belgium, where the robot arm is located. This resulted in more noisy, although more realistic, conditions. The pick-and-place task was used for all evaluation runs of this session.

4. Results

The success rate in completing the evaluation tasks with BCI in the final session for each participant is shown in Figure 4a, together with the mean value over each phase. The performance metrics were only recorded in Phases 2 and 3 and data are missing for participants 9 and 17 due to a technical issue resulting in the loss of timings for one or more runs of the last session. Figure 4b displays boxplots comparing the eye tracking and BCI control system variants for both tasks.

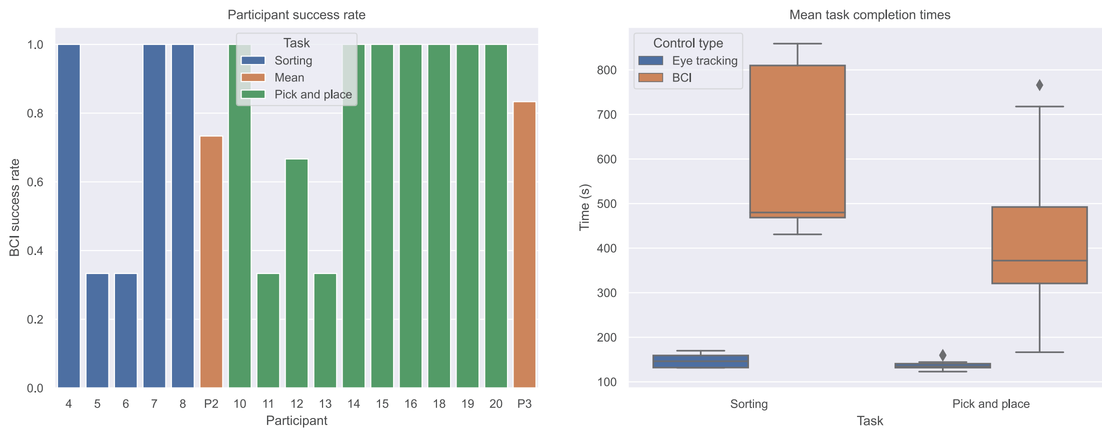

(**a**) (**b**)

Figure 4. (**a**) Success rate for individual participants together with the mean for each phase and (**b**) boxplots comparing the mean completion times between the eye tracking and BCI control system variants for each task.

We can observe that during both phases, most users achieved a perfect success rate. However, participants who did not reach a perfect success rate experienced runs where the system repeatedly made incorrect predictions, which significantly impacted their motivation and caused frustration. Notably, participants 11 and 13 exhibited high baseline fatigue levels at the start of the session, with mVAS scores of 72 and 55, respectively. Additionally, participant 12's final session was disrupted by a fire drill, likely affecting their ability to regain focus and maintain an appropriate mental state. The mean success rates for phases 2 and 3 were 0.73 and 0.83, respectively. In contrast, the success rate for eye tracking was consistently 1 for all participants.

Figure 4b illustrates that completion time is longer when using the BCI control system compared to the eye tracking variant. The variance is also significantly higher for BCI, indicating less consistent efficiency. Despite the mean completion time for BCI being significantly higher ($p < 0.001$), some participants were able to nearly match the eye tracking performance in the pick-and-place task during Phase 3. The lower efficiency of BCI can be attributed to the added confirmation step and its lower accuracy. While eye tracking achieved a perfect recognition rate, BCI's online decoding accuracy was only 0.52. However, this was offset by our decision strategy, resulting in the observed success rates.

The mean results for each question in the UEQ questionnaire are presented in Table 1. The left term in the Question column represents the left side of the scale and corresponds to a value of 1 while the right term corresponds with a value of 7.

Table 1. Mean and standard deviation of UEQ scores for BCI and Eye tracking control types with *p*-values for statistical tests.

Question	BCI	Eye Tracking	*p*-Value
annoying—enjoyable	5.00(±1.78)	6.08(±0.86)	0.052
not understandable—understandable	4.92(±1.75)	6.38(±0.77)	**0.019**
creative—dull	2.31(±1.25)	2.54(±1.66)	0.570
easy to learn—difficult to learn	4.00(±1.96)	1.85(±1.57)	**0.008**
valuable—inferior	2.85(±1.28)	1.77(±0.73)	**0.005**
boring—exciting	4.54(±1.66)	4.85(±1.52)	0.677
not interesting—interesting	5.85(±1.28)	6.31(±0.75)	0.139
unpredictable—predictable	4.00(±1.68)	5.38(±1.94)	0.050
fast—slow	3.69(±1.55)	2.85(±1.77)	**0.027**
inventive—conventional	2.08(±1.12)	2.00(±0.91)	1.000
obstructive—supportive	4.23(±2.01)	5.62(±0.96)	**0.015**
good—bad	2.92(±1.75)	1.69(±0.75)	**0.014**
complicated—simple	4.15(±1.77)	5.69(±1.65)	**0.048**
unlikable—pleasing	5.38(±1.04)	5.46(±0.97)	0.837
usual—leading edge	4.69(±1.84)	5.00(±1.73)	0.751
unpleasant—pleasant	4.31(±1.60)	5.23(±1.24)	0.165
secure—not secure	3.54(±1.66)	2.69(±1.44)	**0.020**
motivating—demotivating	3.62(±1.76)	2.46(±1.13)	0.050
meets expectations—does not meet expectations	3.62(±2.02)	2.00(±1.35)	0.060
inefficient—efficient	4.31(±1.60)	5.77(±1.17)	**0.014**
clear—confusing	3.15(±1.68)	2.00(±1.15)	**0.046**
impractical—practical	4.77(±1.48)	5.54(±1.13)	0.165
organized—cluttered	2.38(±1.26)	2.23(±1.01)	0.549
attractive—unattractive	2.77(±1.09)	2.46(±1.45)	0.596
friendly—unfriendly	2.85(±1.34)	2.15(±1.07)	0.069
conservative—innovative	6.00(±0.82)	5.77(±0.93)	0.337

For most questions in the UEQ, there is no statistically significant difference in the user's experience. This indicates that the user experience was mostly similar regarding these aspects of the control system. The aspects where significant differences were found are shown in Figure 5 for a closer investigation.

We observe that all differences favor the eye tracking variant and that the questions pertain to efficiency and perceived complexity. In most cases, except *fast—slow*, *secure—not secure*, and *motivating—demotivating*, the variance is larger for BCI than for eye tracking. This indicates that the experience of participants was more variable when using BCI, which can be related to the variance in success rate and completion time that was observed in the objective performance metrics. We also note that there was a large agreement that eye tracking was efficient, as the majority of participants scored 6, with only 4 participants giving another score.

Finally, we investigate the changes in mental fatigue entrained by the control systems. Figure 6 shows the difference in mVAS scores between the start of the session and the end for the first two sessions and between the beginning, the intermediate, and final fatigue assessments, split by control system type, used for session 3.

We can observe a significant increase in fatigue between the beginning and the end of a session ($p < 0.001$) when analyzing the session 1 and 2 plots. This shows that the calibration procedure followed by using the BCI control system induces significant mental fatigue. From the session 3 results, we notice that the intermediate result for BCI is significantly higher ($p = 0.04$), while the difference is lower, and not significant anymore ($p = 0.78$) at the end of the session.

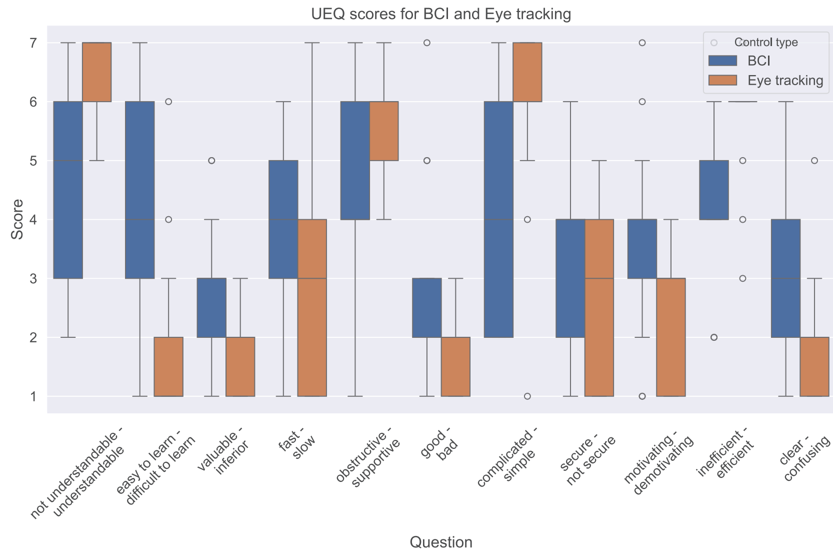

Figure 5. UEQ questions where a significant difference was found between the participant's answers for the eye tracking and BCI variants. A score of 1 indicates that users felt more that the top term of the label was applicable, while 7 means that the bottom term was more applicable.

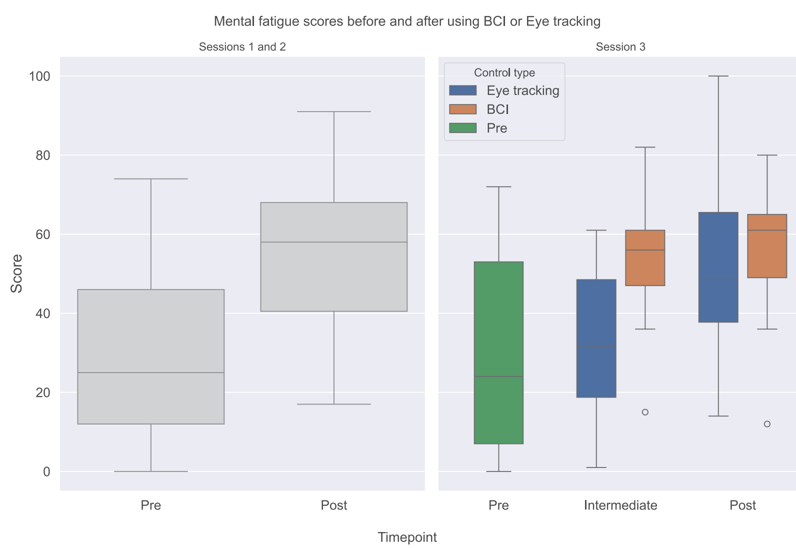

Figure 6. mVAS scores at the beginning of each session and the end for the first two sessions and for sessions 3 before, between the first and second evaluation rounds, and at the end of the session, split by the control system that was used.

5. Discussion

This study aimed to evaluate the real-world usability of a BCI control system designed to operate an assistive robotic arm for physically incapacitated users. The system employs a shared control approach, combining BCI with eye tracking in a mobile AR UI. To balance the need for rapid software development [58] with system stability during user studies [59], the evaluation was divided into three phases. To assess the additional value provided by

BCI and establish a performance benchmark, the study compared the BCI control system with a version using only eye tracking to navigate the system UI.

The first phase of the user study demonstrated the feasibility of using consumer-grade EEG devices for BCI control with our control strategy. This finding, along with the previous research [60], suggests the potential for using low-cost EEG devices in real-world BCI applications. Such advancements could make BCI technology more accessible to consumers, paving the way for commercial applications.

In Phases 2 and 3, we found that eye tracking outperformed BCI in all aspects of usability. All participants successfully completed the evaluation tasks in the final session using eye tracking, whereas the success rates were only 73% and 83% for Phases 2 and 3, respectively, when using BCI. The performance gap between the two methods was even more evident when comparing task completion times. Although these issues were previously recognized [6], our study quantifies these discrepancies and sets a performance benchmark for BCI to be considered a viable alternative to eye tracking for navigating an AR UI.

While most participants successfully completed all evaluation runs, some exhibited poorer task completion performance. This underperformance is likely due to participants arriving fatigued for the experiment, as fatigue is known to diminish the reliability of MI performance [61]. Additionally, effective MI requires sustained focus, which can be compromised by frustration from repeated failures or external distractions [62]. The poor performers all exhibited high baseline fatigue levels or were distracted by external events, such as one participant who experienced a fire drill during the experiment.

In terms of user experience, the differences were fewer and smaller, but participants showed a significant preference for eye tracking for some aspects. Despite this, several participants expressed during interviews at the end of the final session that they would prefer BCI if it could be made more reliable. The aspects where eye tracking performed significantly better were related to complexity and efficiency, which are primarily engineering issues that can be addressed with existing technologies [63,64] and a user-centered UI design [12].

Despite the challenge of comparing our usability outcomes with the existing literature due to the diversity of evaluation methods and control strategies, we can make high-level comparisons with similar studies. Our decision accuracy aligns with the expected decoding accuracy for the models used [65,66]. Additionally, our task completion performance is consistent with previous studies employing a shared control strategy [21,65]. Regarding user experience, the participant responses were comparable to those reported in the previous research on similar concepts [23,31].

BCI was found to be more fatiguing according to the mVAS results. However, it is important to note that the evaluation runs for BCI were preceded by a calibration run, which could also induce fatigue. Participants indicated that the calibration procedure was the most cognitively demanding task of the study, which is in line with the fact that vigilance tasks with low information load are more fatiguing than higher-demand tasks [67]. Therefore, it is unclear whether the high fatigue levels were due to the BCI control system itself or the calibration process. Moreover, people often confuse mental fatigue with boredom and sleepiness, which are common responses to the repetitive nature of the calibration task [51].

The strengths of this study include its flexible procedure, which accommodates the iterative nature of software development and can be applied to any type of BCI control system. The comprehensive assessment of usability measures using realistic evaluation tasks ensures the relevance of the results for real-world applications. Furthermore, the control system's portability is a notable strength, as all devices used are portable, making in-field evaluation studies trivial.

A notable weakness of the user study is the small sample size. Additionally, the limited number of sessions does not guarantee the participants' optimal performance, and the effect of training was not directly assessed. Another limitation is that the study was not conducted with the target population of stroke patients. However, the current research suggests that BCI decoding models can be transferred from able-bodied individuals to stroke patients [68], and our previous research on the effects of neuroplasticity on BCI decoding performance in individuals with lower limb amputation [69] showed that there is no significant change in decoding performance between decoding models trained on data from able-bodied individuals and individuals with a lower limb amputation.

There are several enhancements available for the BCI control system. Increased efficiency without compromising effectiveness could be achieved through software optimizations aimed at improving the decision accuracy of the system. The potential optimizations include examining the chunk size when sampling EEG data and increasing the required number of predictions to make a decision. The former would enhance filtering by using a longer segment of EEG data, while the latter could prevent erroneous decisions caused by a few consecutive incorrect predictions. Studies investigating these specific aspects would, therefore, be worthwhile future work.

Better pre-processing beyond the currently limited filtering could improve decoding accuracy [70]. However, such modifications could lengthen decoding times, potentially reducing system efficiency. Using advanced decoding methods, such as deep learning, could also enhance decoding accuracy [13]. However, these methods often require large amounts of data and take longer to train before reaching optimal performance. Promising methods that improve decoding while addressing the need for more training data include transfer learning [71], continual learning [72], and novel data augmentation techniques such as diffusion models [73]. Benchmarks on the effect of including such methods are necessary to determine if it would be worth including these methods in a real-time EEG decoding pipeline.

Another potential improvement is to enhance the calibration and user training procedures through gamification. Observations during the user study suggested that users perform best when they intuitively think of the required movement as part of a familiar action, without over-concentrating on the movement itself. Previous research has shown that gamification boosts motivation and focus, which are essential for effective BCI use [66,74]. Making the calibration process more engaging could also reduce perceived fatigue and ensure that the data are collected at peak focus levels of the user. Therefore, training users through a game could help them familiarize themselves with MI and the control system in an immersive and motivating environment. Additionally, analyzing the recorded EEG data to identify markers of mental fatigue [75] could offer further insights into the extent to which the calibration procedure induces fatigue.

In the long term, one of our goals would be to integrate all hardware and software components of the BCI control system into a single, all-in-one device. This device could resemble an AR headset like the HoloLens 2, with built-in EEG sensors and potentially other useful sensors. Concepts already exist for such a device [76]. It would also need embedded computing hardware to ensure it is self-contained, comfortable, and privacy-guaranteed. Embedded EEG decoding is an active area of research [77,78].

To further validate the real-world usability of BCI control systems, the user study procedure could be expanded to include in-field studies where participants use the control system in their own homes. Such a study could investigate the long-term effects of the control system and periodically assess if usability evolves over time. This would also provide a suitable evaluation of proposed long-term machine learning methods such as continual learning.

6. Conclusions

Our findings indicate that the shared BCI control system is effective for task completion, demonstrating the feasibility of our shared control strategy in real-world settings. However, the current efficiency of BCI is inadequate for practical real-world applications, and the calibration process induces significant user fatigue.

While the system could be deployed in real-world conditions, our study shows that eye tracking offers superior usability for operating an assistive robotic arm. Currently, BCI is practical only for niche applications that require the user to maintain their gaze on a fixed point, such as in assembly tasks. Further advancements are needed to justify the increased hardware and software complexity.

We see substantial potential for improving the system's reliability and efficiency through advanced AI methods like deep learning, which can enhance decoding accuracy and reduce user training time. We are confident that this would result in our approach surpassing the current state of the art in terms of usability. Additionally, gamifying the calibration process could reduce fatigue and enhance user experience. With improvements in decoding robustness and strategies to boost focus and mitigate calibration-induced fatigue, BCI could become a practical choice for real-world applications.

Author Contributions: Conceptualization, A.D., M.O., F.G., O.R. and K.D.P.; methodology, A.D., M.O. and K.D.P.; software, A.D. and M.O.; validation, F.G., O.R., B.V., B.R., A.N. and K.D.P.; formal analysis, A.D.; investigation, A.D. and M.O.; resources, F.G., O.R. and K.D.P.; data curation, A.D.; writing—original draft preparation, A.D.; writing—review and editing, A.D., M.O., B.V. and K.D.P.; visualization, A.D.; supervision, F.G., O.R., B.V., B.R., A.N. and K.D.P.; project administration, K.D.P. All authors have read and agreed to the published version of the manuscript.

Funding: This research received no external funding.

Institutional Review Board Statement: This study was approved by the Medical Ethics Committee of UZ Brussel and VUB (BUN1432023000232) and adhered to the principles of the Declaration of Helsinki for medical research involving human participants.

Informed Consent Statement: Participants received an explanation of the procedure upon registration and provided written informed consent at the start of the first session.

Data Availability Statement: The data presented in this study are available on request from the corresponding author due to the highly personal nature of the data.

Acknowledgments: This research was made possible through the support of the EUTOPIA alliance of universities, which is funding AD's PhD. We extend our gratitude to all participants of the user study for their involvement and enthusiasm, which enabled a comprehensive assessment of our control system's capabilities. We also sincerely appreciate the contributions of the undergraduate students and interns who assisted with the evaluation study.

Conflicts of Interest: Author Bram Vanderborght was employed by the company IMEC. The remaining authors declare that the research was conducted in the absence of any commercial or financial relationships that could be construed as a potential conflict of interest.

Appendix A. User Experience Interview

Did you feel like you were able to successfully complete the tasks with the BCI control system?
Did you feel like you were in control of the robotic arm?
Do you think that BCI provides an added value to the control system, assuming that you are not able to move or talk?
Which control system variant did you prefer? (Only when eye tracking and BCI were compared)
Do you think a different approach would work better? If yes, what do you suggest?
Do you have any suggestions for improving the current control system?

References

1. Selvaggio, M.; Cognetti, M.; Nikolaidis, S.; Ivaldi, S.; Siciliano, B. Autonomy in Physical Human-Robot Interaction: A Brief Survey. *IEEE Robot. Autom. Lett.* **2021**, *6*, 7989–7996. [CrossRef]
2. Wafa, H.A.; Wolfe, C.D.; Emmett, E.; Roth, G.A.; Johnson, C.O.; Wang, Y. Burden of Stroke in Europe. *Stroke* **2020**, *51*, 2418–2427. [CrossRef] [PubMed]
3. Wolpaw, J.; Wolpaw, E.W. *Brain–Computer Interfaces: Principles and Practice*; Oxford University Press: Oxford, UK, 2012. [CrossRef]

4. Gu, X.; Cao, Z.; Jolfaei, A.; Xu, P.; Wu, D.; Jung, T.P.; Lin, C.T. EEG-Based Brain-Computer Interfaces (BCIs): A Survey of Recent Studies on Signal Sensing Technologies and Computational Intelligence Approaches and Their Applications. *IEEE/ACM Trans. Comput. Biol. Bioinform.* **2021**, *18*, 1645–1666. [CrossRef] [PubMed]
5. Abiri, R.; Borhani, S.; Sellers, E.W.; Jiang, Y.; Zhao, X. A Comprehensive Review of EEG-based Brain–Computer Interface Paradigms. *J. Neural Eng.* **2019**, *16*, 011001. [CrossRef] [PubMed]
6. Singh, A.; Hussain, A.A.; Lal, S.; Guesgen, H.W. A Comprehensive Review on Critical Issues and Possible Solutions of Motor Imagery Based Electroencephalography Brain-Computer Interface. *Sensors* **2021**, *21*, 2173. [CrossRef] [PubMed]
7. Decety, J. The Neurophysiological Basis of Motor Imagery. *Behav. Brain Res.* **1996**, *77*, 45–52. [CrossRef] [PubMed]
8. Rashid, M.; Sulaiman, N.; Abdul Majeed, A.P.P.; Musa, R.M.; Ab. Nasir, A.F.; Bari, B.S.; Khatun, S. Current Status, Challenges, and Possible Solutions of EEG-Based Brain-Computer Interface: A Comprehensive Review. *Front. Neurorobotics* **2020**, *14*, 15. [CrossRef] [PubMed]
9. Norman, D. *The Design of Everyday Things: Revised and Expanded Edition*; Hachette: London, UK, 2013.
10. Kübler, A.; Holz, E.M.; Riccio, A.; Zickler, C.; Kaufmann, T.; Kleih, S.C.; Staiger-Sälzer, P.; Desideri, L.; Hoogerwerf, E.J.; Mattia, D. The User-Centered Design as Novel Perspective for Evaluating the Usability of BCI-Controlled Applications. *PLoS ONE* **2014**, *9*, e112392. [CrossRef] [PubMed]
11. Garro, F.; McKinney, Z. Toward a Standard User-Centered Design Framework for Medical Applications of Brain-Computer Interfaces. In Proceedings of the 2020 IEEE International Conference on Human-Machine Systems (ICHMS), Rome, Italy, 7–9 September 2020; pp. 1–3. [CrossRef]
12. Gena, C.; Hilviu, D.; Chiarion, G.; Roatta, S.; Bosco, F.M.; Calvo, A.; Mattutino, C.; Vincenzi, S. The BciAi4SLA Project: Towards a User-Centered BCI. *Electronics* **2023**, *12*, 1234. [CrossRef]
13. Dillen, A.; Steckelmacher, D.; Efthymiadis, K.; Langlois, K.; Beir, A.D.; Marusic, U.; Vanderborght, B.; Nowé, A.; Meeusen, R.; Ghaffari, F.; et al. Deep Learning for Biosignal Control: Insights from Basic to Real-Time Methods with Recommendations. *J. Neural Eng.* **2022**, *19*, 011003. [CrossRef]
14. Sauro, J.; Lewis, J. *Quantifying the User Experience: Practical Statistics for User Research*, 2nd ed.; Elsevier Science: Amsterdam, The Netherlands, 2016.
15. Nielsen, J. *Usability Engineering*; Morgan Kaufmann: Burlington, MA, USA, 1994.
16. Mridha, M.F.; Das, S.C.; Kabir, M.M.; Lima, A.A.; Islam, M.R.; Watanobe, Y. Brain-Computer Interface: Advancement and Challenges. *Sensors* **2021**, *21*, 5746. [CrossRef]
17. Pan, H.; Ding, P.; Wang, F.; Li, T.; Zhao, L.; Nan, W.; Fu, Y.; Gong, A. Comprehensive Evaluation Methods for Translating BCI into Practical Applications: Usability, User Satisfaction and Usage of Online BCI Systems. *Front. Hum. Neurosci.* **2024**, *18*, 1429130. [CrossRef]
18. Ortega-Gijon, Y.N.; Mezura-Godoy, C. Usability Evaluation of Brain Computer Interfaces: Analysis of Methods and Tools. In Proceedings of the 2019 IEEE International Conference on Engineering Veracruz (ICEV), Boca del Rio, Mexico, 14–17 October 2019; Volume I, pp. 1–8. [CrossRef]
19. Cobos, J.; Moreira, C.; Cárdenas-Delgado, P.; Cedillo, P. Use and Product Quality of Brain-Computer Interface (BCI) Systems: A Systematic Literature Review. In Proceedings of the Doctoral Symposium on Information and Communication Technologies, Manta, Ecuador, 12–14 October 2022; Abad, K., Berrezueta, S., Eds.; Springer: Cham, Switzerland, 2022; pp. 208–222. [CrossRef]
20. Choi, I.; Rhiu, I.; Lee, Y.; Yun, M.H.; Nam, C.S. A Systematic Review of Hybrid Brain-Computer Interfaces: Taxonomy and Usability Perspectives. *PLoS ONE* **2017**, *12*, e0176674. [CrossRef]
21. Kuhner, D.; Fiederer, L.; Aldinger, J.; Burget, F.; Völker, M.; Schirrmeister, R.; Do, C.; Boedecker, J.; Nebel, B.; Ball, T.; et al. A Service Assistant Combining Autonomous Robotics, Flexible Goal Formulation, and Deep-Learning-Based Brain–Computer Interfacing. *Robot. Auton. Syst.* **2019**, *116*, 98–113. [CrossRef]
22. Ron-Angevin, R.; Fernández-Rodríguez, Á.; Dupont, C.; Maigrot, J.; Meunier, J.; Tavard, H.; Lespinet-Najib, V.; André, J.M. Comparison of Two Paradigms Based on Stimulation with Images in a Spelling Brain–Computer Interface. *Sensors* **2023**, *23*, 1304. [CrossRef]
23. Plass-Oude Bos, D.; Poel, M.; Nijholt, A. A Study in User-Centered Design and Evaluation of Mental Tasks for BCI. In *Advances in Multimedia Modeling*; Lee, K.T., Tsai, W.H., Liao, H.Y.M., Chen, T., Hsieh, J.W., Tseng, C.C., Eds.; Springer: Berlin/Heidelberg, Germany, 2011; pp. 122–134. [CrossRef]
24. Li, Q.; Sun, M.; Song, Y.; Zhao, D.; Zhang, T.; Zhang, Z.; Wu, J. Mixed Reality-Based Brain Computer Interface System Using an Adaptive Bandpass Filter: Application to Remote Control of Mobile Manipulator. *Biomed. Signal Process. Control* **2023**, *83*, 104646. [CrossRef]
25. Craik, A.; González-España, J.J.; Alamir, A.; Edquilang, D.; Wong, S.; Sánchez Rodríguez, L.; Feng, J.; Francisco, G.E.; Contreras-Vidal, J.L. Design and Validation of a Low-Cost Mobile EEG-Based Brain–Computer Interface. *Sensors* **2023**, *23*, 5930. [CrossRef] [PubMed]
26. Casey, A.; Azhar, H.; Grzes, M.; Sakel, M. BCI Controlled Robotic Arm as Assistance to the Rehabilitation of Neurologically Disabled Patients. *Disabil. Rehabil. Assist. Technol.* **2021**, *16*, 525–537. [CrossRef]
27. Ferrero, L.; Quiles, V.; Ortiz, M.; Iáñez, E.; Gil-Agudo, Á.; Azorín, J.M. Brain-Computer Interface Enhanced by Virtual Reality Training for Controlling a Lower Limb Exoskeleton. *iScience* **2023**, *26*, 106675. [CrossRef]

28. Chen, X.; Yu, Y.; Tang, J.; Zhou, L.; Liu, K.; Liu, Z.; Chen, S.; Wang, J.; Zeng, L.L.; Liu, J.; et al. Clinical Validation of BCI-Controlled Wheelchairs in Subjects With Severe Spinal Cord Injury. *IEEE Trans. Neural Syst. Rehabil. Eng.* **2022**, *30*, 579–589. [CrossRef]
29. Holz, E.M.; Höhne, J.; Staiger-Sälzer, P.; Tangermann, M.; Kübler, A. Brain–Computer Interface Controlled Gaming: Evaluation of Usability by Severely Motor Restricted End-Users. *Artif. Intell. Med.* **2013**, *59*, 111–120. [CrossRef]
30. Athanasiou, A.; Arfaras, G.; Pandria, N.; Xygonakis, I.; Foroglou, N.; Astaras, A.; Bamidis, P.D. Wireless Brain-Robot Interface: User Perception and Performance Assessment of Spinal Cord Injury Patients. *Wirel. Commun. Mob. Comput.* **2017**, *2017*, 2986423. [CrossRef]
31. Lyu, X.; Ding, P.; Li, S.; Dong, Y.; Su, L.; Zhao, L.; Gong, A.; Fu, Y. Human Factors Engineering of BCI: An Evaluation for Satisfaction of BCI Based on Motor Imagery. *Cogn. Neurodynamics* **2023**, *17*, 105–118. [CrossRef] [PubMed]
32. Si-Mohammed, H.; Petit, J.; Jeunet, C.; Argelaguet, F.; Spindler, F.; Évain, A.; Roussel, N.; Casiez, G.; Lecuyer, A. Towards BCI-Based Interfaces for Augmented Reality: Feasibility, Design and Evaluation. *IEEE Trans. Vis. Comput. Graph.* **2020**, *26*, 1608–1621. [CrossRef] [PubMed]
33. Ortega, Y.N.; Mezura-Godoy, C. Usability Evaluation of BCI Software Applications: A Systematic Review of the Literature. *Program. Comput. Softw.* **2022**, *48*, 646–657. [CrossRef]
34. Unity Technologies. Unity, 2024. Game Development Platform. Available online: https://unity.com/ (accessed on 5 May 2023).
35. Microsoft. *MRTK2-Unity Developer Documentation—MRTK 2*; Microsoft: Houston, TX, USA, 2022.
36. Klem, G.H.; Lüders, H.O.; Jasper, H.H.; Elger, C. The Ten-Twenty Electrode System of the International Federation. The International Federation of Clinical Neurophysiology. *Electroencephalogr. Clin. Neurophysiol. Suppl.* **1999**, *52*, 3–6.
37. Haddadin, S.; Parusel, S.; Johannsmeier, L.; Golz, S.; Gabl, S.; Walch, F.; Sabaghian, M.; Jähne, C.; Hausperger, L.; Haddadin, S. The franka emika robot: A reference platform for robotics research and education. *IEEE Robot. Autom. Mag.* **2022**, *29*, 46–64. [CrossRef]
38. Gramfort, A.; Luessi, M.; Larson, E.; Engemann, D.; Strohmeier, D.; Brodbeck, C.; Goj, R.; Jas, M.; Brooks, T.; Parkkonen, L.; et al. MEG and EEG Data Analysis with MNE-Python. *Front. Neurosci.* **2013**, *7*, 267. [CrossRef]
39. LSL contributors. *Sccn/Labstreaminglayer*; Swartz Center for Computational Neuroscience: San Diego, CA, USA, 2023.
40. Pedregosa, F.; Varoquaux, G.; Gramfort, A.; Michel, V.; Thirion, B.; Grisel, O.; Blondel, M.; Prettenhofer, P.; Weiss, R.; Dubourg, V.; et al. Scikit-Learn: Machine Learning in Python. *J. Mach. Learn. Res.* **2011**, *12*, 2825–2830.
41. Widmann, A.; Schröger, E.; Maess, B. Digital Filter Design for Electrophysiological Data—A Practical Approach. *J. Neurosci. Methods* **2015**, *250*, 34–46. [CrossRef]
42. Koles, Z.J.; Lazar, M.S.; Zhou, S.Z. Spatial Patterns Underlying Population Differences in the Background EEG. *Brain Topogr.* **1990**, *2*, 275–284. [CrossRef] [PubMed]
43. McLachlan, G.J. *Discriminant Analysis and Statistical Pattern Recognition*; Wiley Series in Probability and Mathematical Statistics: Applied Probability and Statistics; John Wiley & Sons, Inc.: New York, NY, USA, 1992. [CrossRef]
44. Xu, B.; Li, W.; Liu, D.; Zhang, K.; Miao, M.; Xu, G.; Song, A. Continuous Hybrid BCI Control for Robotic Arm Using Noninvasive Electroencephalogram, Computer Vision, and Eye Tracking. *Mathematics* **2022**, *10*, 618. [CrossRef]
45. World Medical Association. World Medical Association Declaration of Helsinki: Ethical Principles for Medical Research Involving Human Subjects. *JAMA* **2013**, *310*, 2191–2194. [CrossRef] [PubMed]
46. Harris, P.A.; Taylor, R.; Minor, B.L.; Elliott, V.; Fernandez, M.; O'Neal, L.; McLeod, L.; Delacqua, G.; Delacqua, F.; Kirby, J.; et al. The REDCap Consortium: Building an International Community of Software Platform Partners. *J. Biomed. Informatics* **2019**, *95*, 103208. [CrossRef] [PubMed]
47. Reback, J.; McKinney, W.; Jbrockmendel; den Bossche, J.V.; Augspurger, T.; Cloud, P.; Gfyoung; Sinhrks; Klein, A.; Roeschke, M.; et al. *Pandas-Dev/Pandas: Pandas 1.0.3*; Zenodo: Geneva, Switzerland 2020. [CrossRef]
48. Waskom, M.L. Seaborn: Statistical Data Visualization. *J. Open Source Softw.* **2021**, *6*, 3021. [CrossRef]
49. Virtanen, P.; Gommers, R.; Oliphant, T.E.; Haberland, M.; Reddy, T.; Cournapeau, D.; Burovski, E.; Peterson, P.; Weckesser, W.; Bright, J.; et al. SciPy 1.0: Fundamental Algorithms for Scientific Computing in Python. *Nat. Methods* **2020**, *17*, 261–272. [CrossRef] [PubMed]
50. Laugwitz, B.; Held, T.; Schrepp, M. Construction and Evaluation of a User Experience Questionnaire. In *HCI and Usability for Education and Work*; Holzinger, A., Ed.; Springer: Berlin/Heidelberg, Germany, 2008; Lecture Notes in Computer Science; pp. 63–76. [CrossRef]
51. Smith, M.R.; Chai, R.; Nguyen, H.T.; Marcora, S.M.; Coutts, A.J. Comparing the Effects of Three Cognitive Tasks on Indicators of Mental Fatigue. *J. Psychol.* **2019**, *153*, 759–783. [CrossRef]
52. McNair, D.M.; Lorr, M.; Droppleman, L.F. *Profile of Mood States*; Educational and Industrial Testing Service: San Diego, CA, USA, 1992.
53. Williams, S.E.; Cumming, J.; Ntoumanis, N.; Nordin-Bates, S.M.; Ramsey, R.; Hall, C. Further Validation and Development of the Movement Imagery Questionnaire. *J. Sport Exerc. Psychol.* **2012**, *34*, 621–646. [CrossRef] [PubMed]
54. D'Agostino, R.; Pearson, E.S. Tests for Departure from Normality. Empirical Results for the Distributions of B2 and $\sqrt{b1}$. *Biometrika* **1973**, *60*, 613–622. [CrossRef]
55. Student. The Probable Error of a Mean. *Biometrika* **1908**, *6*, 1–25. [CrossRef]
56. Wilcoxon, F. Individual Comparisons by Ranking Methods. *Biom. Bull.* **1945**, *1*, 80–83. [CrossRef]

57. Mann, H.B.; Whitney, D.R. On a Test of Whether One of Two Random Variables Is Stochastically Larger than the Other. *Ann. Math. Stat.* **1947**, *18*, 50–60. [CrossRef]
58. Kotonya, G. *Requirements Engineering: Processes and Techniques*; Chichester, [Eng.]; J. Wiley: New York, NY, USA, 1998.
59. McGraw, K.L.; Harbison, K. *User-Centered Requirements: The Scenario-based Engineering Process*; CRC Press: Boca Raton, FL, USA, 2020. [CrossRef]
60. Sawangjai, P.; Hompoonsup, S.; Leelaarporn, P.; Kongwudhikunakorn, S.; Wilaiprasitporn, T. Consumer Grade EEG Measuring Sensors as Research Tools: A Review. *IEEE Sensors J.* **2020**, *20*, 3996–4024. [CrossRef]
61. Talukdar, U.; Hazarika, S.M.; Gan, J.Q. Motor Imagery and Mental Fatigue: Inter-Relationship and EEG Based Estimation. *J. Comput. Neurosci.* **2019**, *46*, 55–76. [CrossRef]
62. Sakurada, T.; Hirai, M.; Watanabe, E. Optimization of a Motor Learning Attention-Directing Strategy Based on an Individual's Motor Imagery Ability. *Exp. Brain Res.* **2016**, *234*, 301–311. [CrossRef] [PubMed]
63. Nouri, M.; Moradi, F.; Ghaemi, H.; Motie Nasrabadi, A. Towards Real-World BCI: CCSPNet, a Compact Subject-Independent Motor Imagery Framework. *Digit. Signal Process.* **2023**, *133*, 103816. [CrossRef]
64. Zhao, H.; Zheng, Q.; Ma, K.; Li, H.; Zheng, Y. Deep Representation-Based Domain Adaptation for Nonstationary EEG Classification. *IEEE Trans. Neural Networks Learn. Syst.* **2021**, *32*, 535–545. [CrossRef]
65. Xu, Y.; Ding, C.; Shu, X.; Gui, K.; Bezsudnova, Y.; Sheng, X.; Zhang, D. Shared Control of a Robotic Arm Using Non-Invasive Brain–Computer Interface and Computer Vision Guidance. *Robot. Auton. Syst.* **2019**, *115*, 121–129. [CrossRef]
66. Vourvopoulos, A.; Blanco-Mora, D.A.; Aldridge, A.; Jorge, C.; Figueiredo, P.; i Badia, S.B. Enhancing Motor-Imagery Brain-Computer Interface Training With Embodied Virtual Reality: A Pilot Study With Older Adults. In Proceedings of the 2022 IEEE International Conference on Metrology for Extended Reality, Artificial Intelligence and Neural Engineering (MetroXRAINE), Rome, Italy, 26–28 October 2022; pp. 157–162. [CrossRef]
67. Lorist, M.M.; Faber, L.G. Consideration of the Influence of Mental Fatigue on Controlled and Automatic Cognitive Processes and Related Neuromodulatory Effects. In *Cognitive Fatigue: Multidisciplinary Perspectives on Current Research and Future Applications*; Decade of Behavior/Science Conference, American Psychological Association: Washington, DC, USA, 2011; pp. 105–126. [CrossRef]
68. Nagarajan, A.; Robinson, N.; Ang, K.K.; Chua, K.S.G.; Chew, E.; Guan, C. Transferring a Deep Learning Model from Healthy Subjects to Stroke Patients in a Motor Imagery Brain–Computer Interface. *J. Neural Eng.* **2024**, *21*, 016007. [CrossRef]
69. Dillen, A.; Lathouwers, E.; Miladinović, A.; Marusic, U.; Ghaffari, F.; Romain, O.; Meeusen, R.; De Pauw, K. A Data-Driven Machine Learning Approach for Brain-Computer Interfaces Targeting Lower Limb Neuroprosthetics. *Front. Hum. Neurosci.* **2022**, *16*, 949224. [CrossRef]
70. Abenna, S.; Nahid, M.; Bouyghf, H.; Ouacha, B. EEG-based BCI: A Novel Improvement for EEG Signals Classification Based on Real-Time Preprocessing. *Comput. Biol. Med.* **2022**, *148*, 105931. [CrossRef] [PubMed]
71. Wan, Z.; Yang, R.; Huang, M.; Zeng, N.; Liu, X. A Review on Transfer Learning in EEG Signal Analysis. *Neurocomputing* **2021**, *421*, 1–14. [CrossRef]
72. Lee, P.L.; Chen, S.H.; Chang, T.C.; Lee, W.K.; Hsu, H.T.; Chang, H.H. Continual Learning of a Transformer-Based Deep Learning Classifier Using an Initial Model from Action Observation EEG Data to Online Motor Imagery Classification. *Bioengineering* **2023**, *10*, 186. [CrossRef] [PubMed]
73. Klein, G.; Guetschel, P.; Silvestri, G.; Tangermann, M. Synthesizing EEG Signals from Event-Related Potential Paradigms with Conditional Diffusion Models. *arXiv* **2024**, arXiv:2403.18486. https://doi.org/10.48550/arXiv.2403.18486.
74. Roc, A.; Pillette, L.; Mladenovic, J.; Benaroch, C.; N'Kaoua, B.; Jeunet, C.; Lotte, F. A Review of User Training Methods in Brain Computer Interfaces Based on Mental Tasks. *J. Neural Eng.* **2021**, *18*, 011002. [CrossRef] [PubMed]
75. Kyriaki, K.; Koukopoulos, D.; Fidas, C.A. A Comprehensive Survey of EEG Preprocessing Methods for Cognitive Load Assessment. *IEEE Access* **2024**, *12*, 23466–23489. [CrossRef]
76. Joseph Artuso. Slush 2023: OpenBCI Unveils Galea Beta and Galea Unlimited Roadmap. 2023. Available online: https://galea.co/blog/slush-2023-openbci-unveils-galea-beta-and-galea-unlimited-roadmap (accessed on 17 May 2024).
77. Belwafi, K.; Gannouni, S.; Aboalsamh, H. Embedded Brain Computer Interface: State-of-the-Art in Research. *Sensors* **2021**, *21*, 4293. [CrossRef]
78. Pacini, F.; Pacini, T.; Lai, G.; Zocco, A.M.; Fanucci, L. Design and Evaluation of CPU-, GPU-, and FPGA-Based Deployment of a CNN for Motor Imagery Classification in Brain-Computer Interfaces. *Electronics* **2024**, *13*, 1646. [CrossRef]

sensors

Article

Diagnosis of Schizophrenia Using EEG Sensor Data: A Novel Approach with Automated Log Energy-Based Empirical Wavelet Reconstruction and Cepstral Features

Sumair Aziz [1,†], Muhammad Umar Khan [1,*,†], Khushbakht Iqtidar [2] and Raul Fernandez-Rojas [1]

1 Human-Centred Technology Research Centre, Faculty of Science and Technology, University of Canberra, Canberra, ACT 2617, Australia; sumair.aziz@canberra.edu.au (S.A.); raul.fernandezrojas@canberra.edu.au (R.F.-R.)
2 Department of Computer and Software Engineering, National University of Sciences and Technology, Islamabad 44000, ICT, Pakistan; khushbakht.iqtidar18@ce.ceme.edu.pk
* Correspondence: umar.khan@canberra.edu.au
† These authors contributed equally to this work.

Abstract: Schizophrenia (SZ) is a severe mental disorder characterised by disruptions in cognition, behaviour, and perception, significantly impacting an individual's life. Traditional SZ diagnosis methods are labour-intensive and prone to errors. This study presents an innovative automated approach for detecting SZ acquired through electroencephalogram (EEG) sensor signals, aiming to improve diagnostic efficiency and accuracy. We utilised Fast Independent Component Analysis to remove artefacts from raw EEG sensor data. A novel Automated Log Energy-based Empirical Wavelet Reconstruction (ALEEWR) technique was introduced to reconstruct decomposed modes based on their variability, ensuring effective extraction of meaningful EEG signatures. Cepstral-based features—cepstral activity, cepstral mobility, and cepstral complexity—were used to capture the power, rate of change, and irregularity of the cepstrum of preprocessed EEG signals. ANOVA-based feature selection was applied to refine these features before classification using the K-Nearest Neighbour (KNN) algorithm. Our approach achieved an exceptional accuracy of 99.4%, significantly surpassing previous methods. The proposed ALEEWR and cepstral analysis demonstrated high precision, sensitivity, and specificity in the automated diagnosis of schizophrenia. This study introduces a highly accurate and efficient method for SZ detection using EEG technology. The proposed techniques offer significant improvements in diagnostic accuracy, with potential implications for enhancing SZ diagnosis and patient care through automated systems.

Keywords: schizophrenia; electroencephalography (EEG); cepstral features; automated log energy-based empirical wavelet reconstruction (ALEEWR); feature extraction; machine learning

Citation: Aziz, S.; Khan, M.U.; Iqtidar, K.; Fernandez-Rojas, R. Diagnosis of Schizophrenia Using EEG Sensor Data: A Novel Approach with Automated Log Energy-Based Empirical Wavelet Reconstruction and Cepstral Features. *Sensors* **2024**, *24*, 6508. https://doi.org/10.3390/s24206508

Academic Editors: Yifan Zhao, Hua-Liang Wei, Yuzhu Guo and Fei He

Received: 27 August 2024
Revised: 30 September 2024
Accepted: 8 October 2024
Published: 10 October 2024

1. Introduction

Schizophrenia is a chronic mental disorder where the human mind becomes disconnected from the real world. The condition is specified by relapsing episodes of psychosis, where the symptoms include hallucination, delusion, and paranoia. The mental disorder influences the thinking ability and general behaviour of a person, hence, his or her personal, family, social, and professional functioning is highly affected [1,2]. Worldwide, every 1 in 300 people (0.32%) is affected by this disease. Roughly 24 million people are affected by this disorder. The World Health Organisation (WHO) declares that schizophrenia is curable with an early diagnosis. With early detection, the patient can be given appropriate health care assistance [3]. Early diagnosis can help in curing or limiting the effects of schizophrenia on a person. No specific clinical test is available for the detection of schizophrenia. Mostly, the diagnosis is made through long interviews with a clinical psychiatrist. No definitive biological sample analysis technique can assure the diagnosis of the disorder [4]. A systematic review is given by Davison et al. [5], where they have enlisted the possibility of diagnosis through metabolomics in the discovery of disease biomarkers. Researchers have been trying to devise non-invasive techniques to diagnose the problem. These techniques include imaging and signal processing methods such as Magnetic Resonance Imaging (MRI) and Computed Tomography (CT) scans. The high costs of these tests are not affordable for everyone. Therefore, signalling techniques are gaining popularity. The human brain activity and functionality can be examined through electroencephalogram (EEG) signals acquired with appropriate electrode placement. An EEG is recorded by placing the electrodes at predefined positions on the scalp. EEG has been used in the detection of multiple brain disorders such as insomnia, dementia, epilepsy, schizophrenia, etc. [6].

EEG signals have been actively studied for schizophrenia detection through the use of machine learning techniques. For instance, Weikoh et al. [7] analysed 1142 EEG signals over 25 s, converting these into images using a spectrogram and extracting local configuration pattern features. This approach achieved a high accuracy of 97.20% using a KNN classifier. Ahmad et al. [8] segmented EEG signals into five standard frequency bands to classify schizophrenia, utilising these segments as features in a support vector machine (SVM) that attained an 89.21% accuracy. Sima et al. [9] transformed sensor-level EEGs to source level, analysing phase lag via a functional connectivity network and employing logistic regression on theta band features from brain-complex network analysis to achieve 97% accuracy. Talha et al. [10] selected electrodes with high signal-to-noise ratios from raw EEG signals, computed linear and non-linear features, and obtained a 93% classification accuracy for schizophrenia. Schizophrenia detection has also been explored using graph theory-based network connectivity analysis, with a study [11] utilising EEG data from 39 healthy and 45 schizophrenic subjects, achieving an 82.3% accuracy with a Random Forest (RF) classifier. Zhang et al. applied machine learning classifiers to event-related potential (ERP) features from EEG signals [12,13]. They achieved classification accuracies up to 98.5% using RF and Artificial Neural Networks (ANNs), incorporating five temporal and two demographic features in the model.

Empirical Mode Decomposition (EMD) is a highly effective method for analysing non-linear and non-stationary signals such as EEG recordings [14,15]. EMD iteratively decomposes a signal into a set of intrinsic mode functions (IMFs) that represent simple oscillatory modes. EMD was employed to decompose the EEG signal into IMFs [14]. Their proposed model extracted entropy features and used a Support Vector Machine classifier to achieve a 0.98 AUC value for the detection of SZ. Siuly et al. [15] applied EMD to decompose EEG signals into IMFs, followed by feature extraction. In the classification step, the ensemble bagged tree offered an overall accuracy of 89.5% using IMF2. Jahmunah et al. proposed an automated diagnosis tool based on non-linear features using a 19-channel EEG for the screening of schizophrenia [16] and obtained an accuracy of 92.91%. However, while EMD is effective, it can suffer from mode mixing and relies heavily on the selection of IMFs.

Deep learning (DL) techniques have also been implemented for the study of schizophrenia. For example, Oh et al. proposed an eleven-layered Convolutional Neural Network (CNN) architecture for schizophrenia recognition using EEG signals [17]; the deep learning model yielded an overall recognition accuracy of 98% for non-subject-based analysis. Singh et al. proposed a spectral features-based CNN architecture for the accurate prediction of schizophrenia using EEG signals [18]; they reported accuracies of 94% and 98.5% classification accuracies for two EEG datasets. Chandran et al. proposed schizophrenia classification using a four-layered long short-term memory (LSTM) network, a type of artificial recurrent neural network [19]; approximate entropy, Katz fractal dimension, and variance features were computed from a 19-channel EEG and passed to LSTM for prediction of disorder. Authors in [20] developed a framework by combining a CNN and logistic regression for the diagnosis of schizophrenia using only three channels of EEG; they reported accuracies of 90% and 98% for the subject-based and non-subject-based experimentation, respectively. In another study, Lillo et al. [4] analysed EEG data from fourteen patients using a high-pass filter and microstate transformation, achieving 93% diagnostic accuracy with a CNN. Wu et al. [21] applied a recurrent auto-encoder model, achieving a classification accuracy of 81.81%. Phang et al. [22] proposed a framework using various time and frequency domain features with a CNN, reaching 91.69% accuracy. In another study, Phang et al. [23] used directed connectivity and complex network measures, achieving an overall accuracy of 95% with Deep Neural Networks.

Existing EEG-based diagnostic methods for schizophrenia face several limitations. Time- and frequency-based methods require careful consideration and may not fully capture the complex, non-linear characteristics of EEG signals. EMD-based methods, while adaptive, can suffer from issues such as mode mixing, where different scales of data are mixed within a single IMF, complicating the analysis and potentially reducing diagnostic accuracy. Deep learning approaches, despite their capability to automate feature extraction, heavily rely on large datasets and substantial computational resources, which limits their practicality in medical settings. These models typically utilise all available EEG channels, increasing computational burdens and the risk of overfitting. Therefore, our proposed computer-aided diagnosis system addresses these limitations by employing Automated Log Energy-based Empirical Wavelet Reconstruction (ALEEWR) for automated noise reduction and selective signal reconstruction. This approach enhances signal processing efficiency and accuracy by proposing cepstral domain features that demonstrate high discriminative power. Unlike traditional methods, our system utilises only ten features and identifies important EEG channels, significantly reducing computational complexity. This targeted and efficient approach not only lowers computational demands, making the system suitable for real-time applications in battery-powered devices, but also achieves superior diagnostic performance. The key contributions of our work are listed below:

1. We propose the Automated Log Energy-based Empirical Wavelet Reconstruction (ALEEWR) for noise reduction in EEG signals.
2. We introduce a novel feature set derived from three cepstral parameters that, when used in our proposed computer-aided diagnosis system, outperforms state-of-the-art methods by classifying schizophrenia and healthy patients through EEG signals using only ten features.
3. This study also identifies crucial EEG channels (e.g., possible biomarkers) that contain distinct information pertinent to schizophrenia. By pinpointing key features and channels, we reduce the computational complexity and enhance the feasibility of continuous monitoring in battery-powered embedded systems.

The structure of this article is organised as follows: Section 2 provides a detailed description of the EEG dataset and outlines the proposed framework for diagnosing schizophrenia, emphasising innovative signal processing and feature extraction techniques. In Section 3, we present the experimental results of our method. Section 4 delivers an in-depth analysis of our approach and compares it with existing studies. Finally, Section 5 summarises the key findings and concludes the article.

2. Materials and Methods

2.1. Overview

Our proposed diagnostic framework for schizophrenia utilises advanced signal processing and machine learning techniques to enhance accuracy with EEG data. Figure 1 presents the proposed framework for computer-aided diagnosis of schizophrenia. In the first step, EEG signals are cleaned using FastICA to remove artefacts and isolate independent components. These signals are then processed through Automated Log Energy-based Empirical Wavelet Reconstruction (ALEEWR) to highlight EEG signatures. Cepstral features are extracted from the reconstructed signal, and ANOVA-based feature selection refines these features to those most indicative of schizophrenia. The final step involves classification using a Fine KNN algorithm, effectively distinguishing between healthy individuals and patients with schizophrenia based on EEG data.

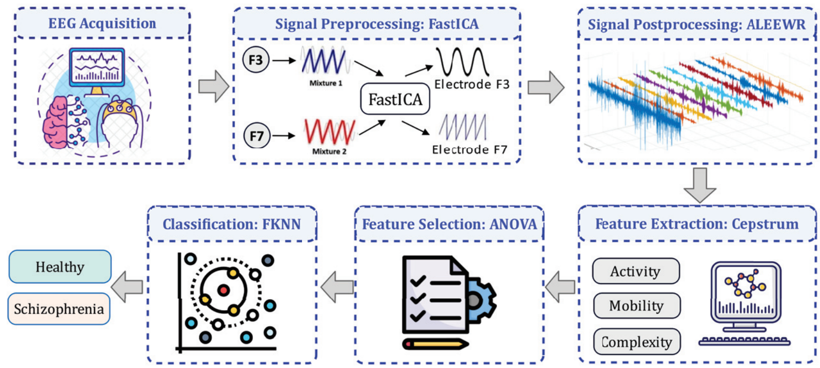

Figure 1. Framework of the proposed computer-aided diagnosis system of schizophrenia.

2.2. EEG Dataset

In this study, a publicly available dataset of EEGs was employed for the evaluation of the proposed methodology for the detection of schizophrenia (SZ) [24]. The data were acquired at the Institute of Psychiatry and Neurology in Warsaw, Poland. The EEG data contain 19 channels (Fp1, Fp2, F7, F3, Fz, F4, F8, T3, C3, Cz, C4, T4, T5, P3, Pz, P4, T6, O1, O2) obtained at a sampling rate of 250 Hz using standard 10-20 EEG system (Figure 2).

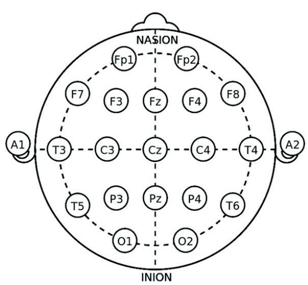

Figure 2. Standard placement of electrodes for EEG acquisition.

This EEG dataset includes recordings from 14 patients diagnosed with schizophrenia (SZ), consisting of seven females (average age: 28.3 ± 4.1 years) and seven males (average age: 27.9 ± 3.3 years). Additionally, EEG data were gathered from 14 healthy controls, split evenly by gender with seven females (mean age: 28.7 ± 3.4 years) and seven males (average age: 26.8 ± 2.9 years. Recordings were conducted over fifteen minutes while subjects rested with their eyes closed. The signals were then segmented into 20 s intervals, with each segment containing 5000×19 data points. Figure 3 displays a segment of the raw signals from both healthy individuals and those with schizophrenia.

2.3. Preprocessing: FastICA

To address the challenges of artefact removal and the separation of EEG channels that are independent of each other, we employed Independent Component Analysis (ICA) [25,26]. ICA is pivotal in enhancing the quality of EEG data by isolating components associated with noise and interference from those reflecting genuine brain activity. ICA endeavours independence by transforming feature space linearly into a new feature space such that each component in the new feature space is mutually independent. Nonetheless, the mutual information between the original and transformed feature space is kept as high as possible. Consider y is an input matrix with a dimension of $[m \times n]$ where m is the total number of samples and n is the number of variables. The ICA model is mathematically given as:

$$z \in \mathbb{R} \tag{1}$$

$$y = Az \tag{2}$$

where A is the mixing matrix and z represents the data from individual sources that indicate the independent components. It is assumed that the data are linearly combined (non-Gaussian data distribution) from individual sources. To reconstruct the independent signal, an unmixing matrix W is constructed, which is an inverse of the mixing matrix A.

Therefore,

$$z = Wy \tag{3}$$

where

$$W = A^{-1} \tag{4}$$

Among the various ICA algorithms available, we opted for FastICA [27–29] due to its computational efficiency and robust performance in dealing with biomedical signal processing. The use of FastICA allowed us to effectively clean the EEG data (Figure 4), preparing them for further analysis and ensuring that our feature extraction methods could operate on the most relevant and least contaminated signals.

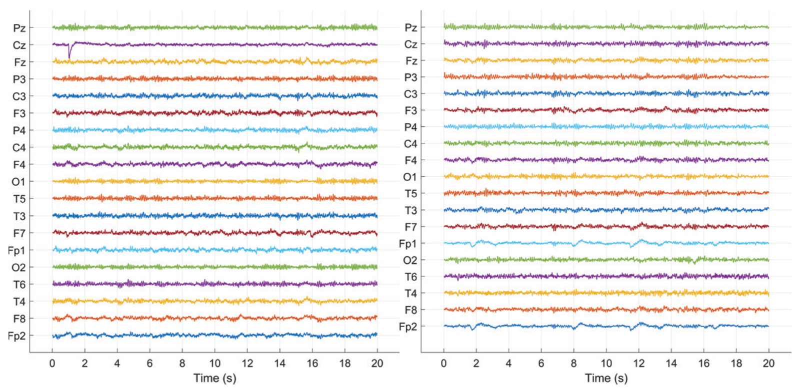

(**a**) EEG signal of healthy person. (**b**) EEG signal of person with schizophrenia.

Figure 3. Raw EEG signals of healthy and schizophrenic subjects.

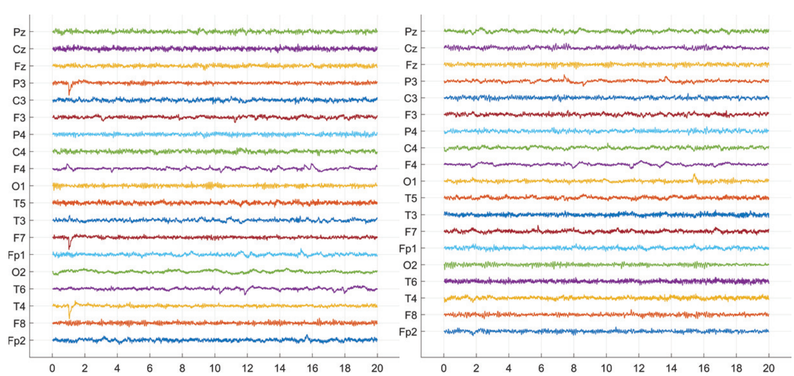

(**a**) (**b**)

Figure 4. FastICA- based preprocessing of EEG signals. (**a**) FastICA based preprocessing for healthy person. (**b**) FastICA-based preprocessing for person with schizophrenia.

2.4. EEG Postprocessing: Automated Log Energy-Based Empirical Wavelet Reconstruction (ALEEWR)

The field of EEG signal analysis has seen significant advances in preprocessing and feature extraction techniques, with popular methods including Empirical Mode Decomposition (EMD) [15,30], Variational Mode Decomposition (VMD) [31–33], and Wavelet Transform (WT) [34,35]. Each of these methods, however, has its specific limitations: EMD faces mode selection issues and mode mixing, VMD suffers from over-decomposition, and WT, despite better energy preservation compared to EMD and VMD, is hindered by the non-adaptive nature of the basis functions.

To address these shortcomings, the Empirical Wavelet Transform (EWT) [36–38] emerges as an adaptive method that effectively preserves energy during decomposition. However, EWT itself faces challenges, particularly in deciding which decomposed modes should be selected for reconstructing a preprocessed signal. This selection is crucial as it influences the quality and effectiveness of the subsequent signal analysis, particularly when handling the inherently weak signals typical of human brain EEG data.

In response to these challenges, we introduce the Automated Log Energy-based Empirical Wavelet Reconstruction (ALEEWR). This novel approach leverages the strengths of EWT while incorporating an automated mechanism to enhance the selection of relevant modes based on their energy content. The Log operator incorporated in the ALEEWR plays a critical role in enhancing the detection of weak changes within EEG signals. The EEG channels were first normalised to remove any dependencies on gain. ALEEWR utilises a family of wavelets specifically adapted for particular signal processing applications. It extracts several modes from the Fourier transform of the input signal by creating adaptive wavelet filter banks. These modes are subsequently combined based on the log energy threshold to reconstruct a preprocessed signal. The significant steps of ALEEWR are presented in Figure 5 and are described next.

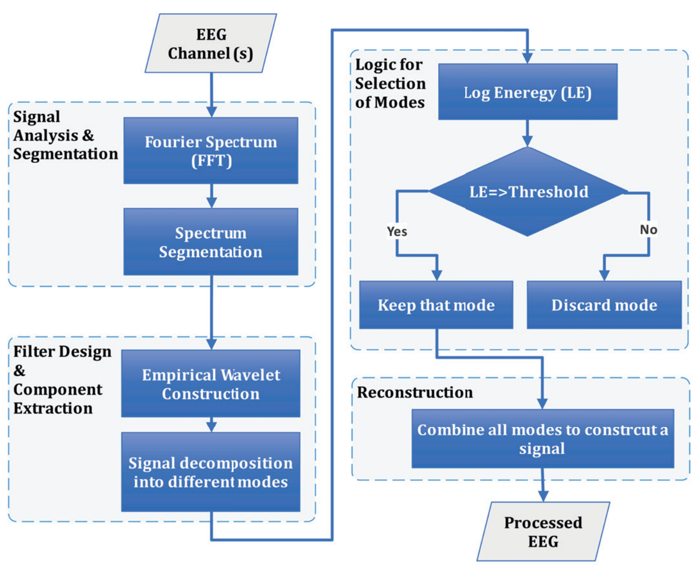

Figure 5. Steps involved in computing ALEEWR.

Step 1: Apply Fast Fourier Transform (FFT) to the input signal (s), where $f(s)$ denotes its discrete version, $s = \{s_i\}, i = 1, 2, 3, \ldots, n$. Here, n is the number of samples and the FFT spectrum denoted by $X(w)$ is computed. Compute the set of maxima $n = \{n_i\}$, $i = 1, 2, 3, \ldots, m$ of FFT spectrum and find their concerned frequencies $w = \{w_i\}$, $i = 1, 2, \ldots, m$. The number of maxima is denoted by m.

Step 2: The boundary detection algorithm is used to accurately separate the Fourier spectrum of the EEG signals. To find the border of each segment, the centre of two progressive local maxima is computed as defined by the following equation:

$$\phi_i = \frac{W_i + W_{i+1}}{2} \tag{5}$$

where ϕ_i defines the boundaries set $\phi = \{\phi_1, \phi_1, \ldots, \phi_{N-1}\}$ and W_i and W_{i+1} denotes two frequencies.

Step 3: In this stage, based on boundaries, an adaptive filter bank of m wavelet filter is designed. This adaptive filter consists of one low pass filter and $m-1$ bandpass filter. The following equation defines the relationships between boundaries and frequencies with the scaling function $\rho_1(w)$:

$$\rho_1 = \begin{cases} 1, |w| \leq (1-\sigma)\phi_i \\ cos(\frac{\pi}{2}\alpha(\sigma, \phi_1))(1-\sigma)\phi_1 \prec |w|(1+\sigma)\phi_1 \\ 0,\ else \end{cases} \tag{6}$$

Empirical wavelets are denoted by $\Psi_i(w)$ and defined as follows:

$$\Psi_i = \begin{cases} 1(1+\sigma)\phi_i \prec |w| \prec (1-\sigma)\phi_{i+1} \\ cos(\frac{\pi}{2}\alpha(\sigma, \phi_{i+1}))(1-\sigma)\phi_{i+1} \leq |w| \leq (1+\sigma)\phi_{i+1} \\ sin(\frac{\pi}{2}\alpha(\sigma, \phi_i))(1-\sigma)\phi_i \leq |w| \leq (1+\sigma)\phi_i \\ 0,\ else \end{cases} \tag{7}$$

where $\alpha(\gamma, \phi_i) = \beta\Big((\frac{1}{2\gamma\phi_i})(|w| - (1-\gamma)\phi_i)\Big)$. The γ function makes sure that there is no overlap between two successive transitions. The equation of γ is formed using the following relation:

$$\gamma \prec min_i\left(\frac{\phi_{i+1} - \phi_i}{\phi_{i+1} + \phi_i}\right) \tag{8}$$

$\beta(x)$ is a random function defined below as follows:

$$\beta(x) = \begin{cases} 0x \leq 0 \\ 1x \geq 1 \\ \beta(x) + \beta(1-x) = 1, x \in (0,1) \end{cases} \tag{9}$$

Step 4: Wavelet functions are applied to extract instantaneous frequency (IF) and instantaneous amplitude (IA) from each mode scaling. Approximate coefficients are the product of the scaling function with the input signal under consideration, defined as follows:

$$W_f(0,s) = \langle f, \theta_i \rangle = \int f(\tau)\overline{\theta_i(\tau - s)d_\tau} \tag{10}$$

Similarly, detailed coefficients were obtained by multiplying input signal f by empirical wavelet as follows:

$$W_f(i,s) = \langle f, \psi_i \rangle = \int f(\tau)\overline{\psi_i(\tau - s)d_\tau} \tag{11}$$

Here, $W_f(i,s)$ represents the detailed coefficients for the ith filter bank at the sth time instant. sub-band modes of both the healthy and schizophrenia classes are presented in Figure 6.

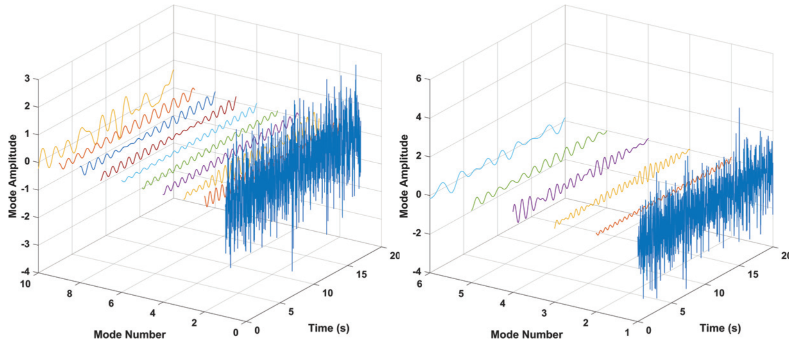

(**a**) Healthy. (**b**) Schizophrenia.

Figure 6. Multi-resolution analysis of EEG signal (1 channel) of healthy and schizophrenic subjects.

Step 5: To determine which sub-band modes contain the most information about subtle changes in the overall EEG signal, the log energy of each sub-band mode is calculated using the following equation:

$$LE_{W_f} = \log\left(\sum_n |W_f|^2\right) \tag{12}$$

In this equation, LE_{W_f} represents the log energy of the sub-band. The modes that exhibit a log energy of 10% (a threshold experimentally selected) or higher are then combined to create a newly preprocessed EEG signal, effectively capturing and emphasising the subtle changes within the EEG data. The processed EEG channels after employing ALEEWR are shown in Figure 7. ALEEWR aims to optimise EEG signal preprocessing and feature extraction, providing a robust tool for handling weak and often noisy EEG signals. By automating the mode selection process, ALEEWR not only simplifies the preprocessing workflow but also enhances the reliability and accuracy of EEG signal analysis, thereby facilitating more precise diagnostics and research outcomes in neurological studies.

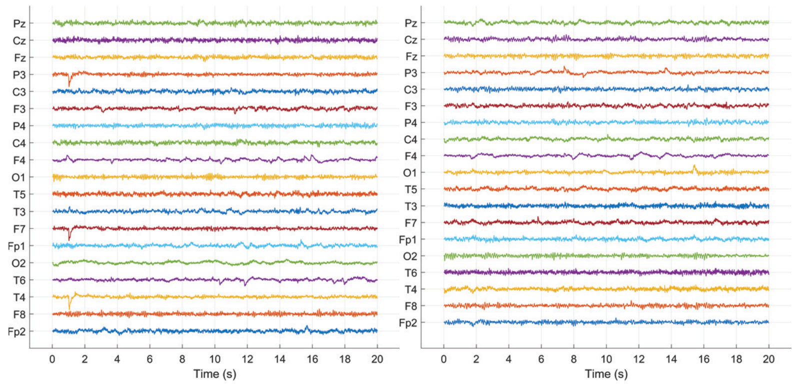

(**a**) Healthy class (**b**) Schizophrenia class

Figure 7. Preprocessed EEG signals of healthy and schizophrenic subjects using proposed ALEEWR.

2.5. Feature Extraction: Novel Cepstral Features

To create reliable and relevant predictors, feature extraction is a crucial step in the learning process. Despite having sophisticated classification algorithms, low feature quality might result in poor performance and generalisation properties. In this study, we propose three powerful features for the detection of a schizophrenic EEG, i.e., cepstral activity, cepstral mobility, and cepstral complexity. These features provide numerical variations in the cepstrum of EEG channels, hence proving the fact that the EEG cepstrum contains rich schizophrenic information as compared to simple time-domain EEGs.

Real cepstrum c of input x can be defined as the inverse FFT of the logarithm FFT of EEG channels (Equation (13)).

$$c_x = \frac{1}{2\pi} \int_{-\pi}^{\pi} log|X(e^{j\omega})|e^{j\omega n} d\omega \tag{13}$$

In EEG signal analysis, capturing fine variations in both time and frequency domains is vital for accurately assessing brain activity, especially when differentiating between healthy and pathological conditions like schizophrenia. While conventional methods typically break down EEG signals into sub-bands such as alpha, beta, and gamma rhythms [39,40], this study extracts features from the entire EEG channels to account for individual differences in brain structure and function. Given the complexity of EEG signals and the issues with aliasing and overlapping frequencies, cepstral analysis provides a more comprehensive solution by isolating intrinsic periodicities and harmonics [41]. By extending beyond traditional time-domain or frequency-domain approaches, the cepstrum effectively decomposes the EEG signal into meaningful components, making it particularly suitable for non-stationary signals like EEG. We extracted three main features, cepstral activity, cepstral mobility, and cepstral complexity from the cepstrum of each EEG channel, which provide a detailed and refined characterisation of brain dynamics that traditional filters often fail to capture.

2.5.1. Cepstral Activity

The cepstral activity (A) parameter quantifies the variance in the cepstrum of an EEG signal. It is analogous to the power of the signal in the cepstral domain and is defined as:

$$A = \frac{1}{N} \sum_{i=1}^{N} (c_x - \mu)^2 \tag{14}$$

where μ is the mean of the c_x, and N is the total number of cepstral coefficients.

2.5.2. Cepstral Mobility

The cepstral mobility (M) parameter measures the rate of change in the cepstrum, analogous to the standard mobility parameter but applied to the cepstral coefficients of the EEG signal. It indicates the smoothness of the variations in the cepstrum and is defined as:

$$M = \sqrt{\frac{\mathrm{A}(d_c)}{\mathrm{A}(c_x)}} \tag{15}$$

where d_c is the derivative of the cepstral coefficients c_x, and $\mathrm{A}(c_x)$ and $\mathrm{A}(d_c)$ are the activities of the cepstral coefficients and their derivatives, respectively.

2.5.3. Cepstral Complexity

Cepstral complexity (C) measures the irregularity or complexity of the cepstrum of the EEG. It evaluates how much the cepstral behaviour deviates from that of a simple sinusoidal form. This metric is defined as follows:

$$C = \frac{\mathrm{M}(d_c)}{\mathrm{M}(c_x)} \tag{16}$$

where $\mathrm{M}(c_x)$ and $\mathrm{M}(d_c)$ are the mobilities of the cepstral coefficients and their derivatives, respectively.

These three Cepstral features were extracted from each of the 19 EEG channels, resulting in a comprehensive feature vector that captures the essential characteristics of the EEG signals across all channels. The feature vector, therefore, consists of 57 features.

2.6. Feature Reduction: ANOVA

The dimensions of the extracted EEG features were further reduced by eliminating irrelevant information or redundancy using a one-way analysis of variance (ANOVA). The objective of performing ANOVA is to determine whether different classes (or levels) of a factor have significantly different means. ANOVA evaluates the impact of each feature on the class label or response variable, identifying the features that significantly distinguish between classes [42,43].

Variation of the class is the overall mean, i.e., $\bar{v}.j - \bar{v}..$ (variation between classes), where $v.j$ is the sample mean value of class j and $\bar{v}$ is the overall sample mean value. ANOVA examines the diversity in the class means by dividing the total variation in the feature data into two parts:

1. Variation of observations in each group from their group mean estimates;
2. Variation of instances in each class from their class means estimates $v_{ij} - \bar{v}.j$ (variation within a category).

ANOVA divides the total sum of squares (SST) into a sum of squares due to the between-classes effect (SSR) and the sum of squared error (SEE).

$$\sum_i \sum_j (v_{ij} - \bar{v}..)^2 = \sum_j n_j (\bar{v}.j - \bar{y})^2 + \sum_i \sum_j (v_{ij} - \bar{v}.j)^2 \tag{17}$$

where n_j is the sample size for the j^{th} group, $j = 1, 2, \ldots, k$.

ANOVA was used to identify the most significant features for classification as demonstrated in [44,45]. These features were then used to train and test the classification models. This process ensures that the selected features significantly contribute to distinguishing between the healthy and SZ classes.

2.7. Classification

The discrimination between the two classes of EEG signals was achieved through the application of various well-known machine learning classification algorithms. These models were decision trees (DTs), Support Vector Machines (SVMs), K-nearest neighbours (KNNs), ensemble classifiers, and Artificial Neural Networks (ANNs). The DT classifier predicts the output by following decisions in the tree structure, from the root node down to the leaf. The EEG signals of healthy controls and SZ subjects were also classified using a linear SVM classifier and its several non-linear kernel versions like Quadratic-SVM (QSVM) and Cubic-SVM (CSVM) [46]. Another classification method employed to differentiate healthy and SZ EEG signals using extracted features was KNN [47]. KNN works by finding the closest points to the new input [48]. The new input is assigned a class label based on the highest posterior probability of response of nearest neighbours. The 'K' value is the number of neighbours for voting. KNN with the value of K set to one is Fine KNN (FKNN) with Euclidean distance. KNN with the value of K set to 100 and squared inverse distance metric is Weighted KNN (WKNN). In Cubic KNN (CKNN), the cubic distance metric is used to measure the distance between current input features and dataset points.

The employment of ensemble machine learning algorithms for the classification of biomedical signals has received due attention [15,49]. In ensemble classification algorithms, the output is predicted using a set of learned classifiers in combination with some voting scheme. The resultant composite model is robust and often has better performance as compared to individual learners. Ensemble Boost Tree (EBoosTT) learns from the errors generated by a set of weak classifiers and turns them into a strong classifier using an iterative algorithm. AdaBoost with 30 decision tree learners was employed, and the number of splits was set to 20. The Ensemble Bagged Tree (EBagT) classification algorithm is constructed by bootstrapped training of several decision tree classifiers. The results of all predictors are averaged to produce the final output. The maximum number of splits was set to 1540 and the number of learners was 30. Ensemble subspace KNN (ESKNN) is assembled by combining several KNNs as base classifiers using a random subspace strategy [50]. The selected number of learners was 30 with a subspace dimension set to 40. Artificial Neural Networks (ANNs) are widely employed in biomedical signal processing for classification tasks [51,52]. An ANN contains neurons connected in input, hidden, and output layers. In this article, we analysed the classification performance using three types of ANN. An ANN structure with only one hidden layer is a Narrow Neural Network (NNN), with ten hidden layers (MNN), and with a hundred hidden layers is a Wide Neural Network (WNN). All networks used ReLu activations.

3. Results

The performance of the proposed EEG-based computer-aided diagnosis system for SZ was assessed using various well-known classification algorithms. The proposed features were extracted from all channels of EEG and were selected using ANOVA. Performance with KNN, DT, SVM, ANN, and Ensemble methods is presented. First, we present the feature importance analysis, then provide the classification performance of the best model, and finally, compare the performance of the proposed model with other classifiers. All experiments were conducted using 10-fold cross-validation to prevent overfitting, utilising MATLAB R2023b software on an Intel Core i7 system with 32 GB RAM. The dataset was divided into ten equal subsets, with each subset used for training while the remaining subsets were used for testing across ten iterations [9,53]. The experiments were repeated 20 times, and the average results were reported.

3.1. Feature Importance Determination

Table 1 provides the results of applying ANOVA on all 57 features extracted from EEG signals. The importance of features is determined by the ANOVA weight. The higher value of weight signifies that the attribute is influential and contains strong discriminatory information. Figure 8 depicts the ANOVA-based weights for extracted EEG features in descending order. In Figure 8, C_{Pz}, M_{Pz}, and A_{Pz} represent the proposed *cepstrum complexity*, *cepstrum mobility*, and *cepstrum activity* features extracted from the 19^{th} EEG channel (Pz), respectively. The classification was performed using ten features showing the highest weights (C_{Pz}, M_{Pz}, M_{T4}, M_{C4}, A_{F4}, C_{F4}, C_{C4}, C_{T3}, A_{Fp1}, A_{Pz}). It can be observed that features extracted from the 19^{th} EEG channel (C_{Pz}, M_{Pz}, A_{Pz}) have high ANOVA weights to be considered in the final feature vector. The statistical parameters in terms of mean, standard deviation (SD), and p-value of the principal features are shown in Table 2.

Figure 9 illustrates the box plot analysis of the most significant features ranked using ANOVA, showing that the most discriminating information for healthy vs. SZ was available in the 19^{th} EEG channel. These ten most significant features were used to train and test the classification models using 10-fold cross-validation.

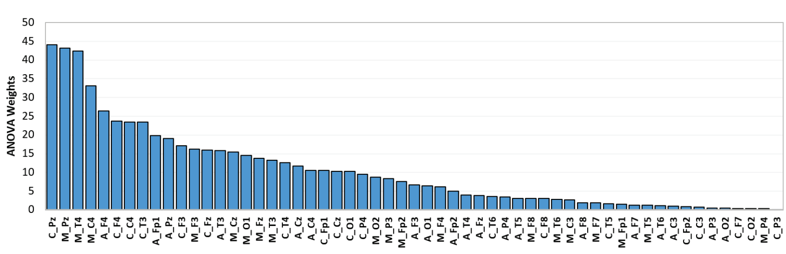

Figure 8. EEG feature ranking through ANOVA in a sorted manner.

Table 1. Feature ranking results of applying ANOVA on extracted features from EEG signals.

Features	ANOVA Weights	Features	ANOVA Weights	Features	ANOVA Weights
C_{Pz}	44.1411	A_{Cz}	11.7543	C_{F8}	3.0421
M_{Pz}	43.2403	A_{C4}	10.5856	M_{T6}	2.7608
M_{T4}	42.4737	C_{Fp1}	10.4968	M_{C3}	2.6829
M_{C4}	33.1581	C_{Cz}	10.3155	A_{F8}	1.9436
A_{F4}	26.4594	C_{O1}	10.2426	M_{F7}	1.8861
C_{F4}	23.7429	C_{P4}	9.4774	C_{T5}	1.5994
C_{C4}	23.4761	M_{O2}	8.7708	M_{Fp1}	1.5252
C_{T3}	23.4276	M_{P3}	8.3576	A_{F7}	1.3270
A_{Fp1}	19.9070	M_{Fp2}	7.5335	M_{T5}	1.2159
A_{Pz}	19.1349	A_{F3}	6.6283	A_{T6}	1.1489
C_{F3}	17.1812	A_{O1}	6.4004	A_{C3}	0.9762
M_{F3}	16.2406	M_{F4}	6.1457	C_{Fp2}	0.8294
C_{Fz}	16.0346	A_{Fp2}	4.9863	C_{C3}	0.7992
A_{T3}	15.8375	A_{T4}	3.9301	A_{P3}	0.5133
M_{Cz}	15.5225	A_{Fz}	3.8874	A_{O2}	0.5116
M_{O1}	14.6075	C_{T6}	3.5882	C_{F7}	0.3653
M_{Fz}	13.7222	A_{P4}	3.5193	C_{O2}	0.3426
M_{T3}	13.3062	A_{T5}	3.0801	M_{P4}	0.3206
C_{T4}	12.6136	M_{F8}	3.0692	C_{P3}	0.1421

Table 2. Principal features selected using ANOVA.

Selected Features	Healthy		Schizophrenia		*p*-Value
	Mean	SD	Mean	SD	
M_{Pz}	0.79137	0.05777	0.74883	0.08591	4.8×10^{-26}
M_{T4}	0.79151	0.06131	0.7446	0.09756	1×10^{-22}
M_{C4}	0.80313	0.05694	0.76543	0.08949	2×10^{-21}
C_{Pz}	1.44425	0.12681	1.56597	0.26407	4.8×10^{-20}
C_{C4}	1.41478	0.1102	1.50065	0.27018	1.6×10^{-12}
A_{F4}	0.00211	0.00052	0.00183	0.00072	2.4×10^{-11}
C_{T3}	1.45274	0.12621	1.53644	0.2552	2.1×10^{-10}
A_{Pz}	0.00218	0.00063	0.00192	0.00077	7×10^{-10}
C_{F4}	1.47059	0.11914	1.54518	0.22191	1×10^{-9}
A_{Fp1}	0.00229	0.00068	0.002	0.00086	7.5×10^{-9}

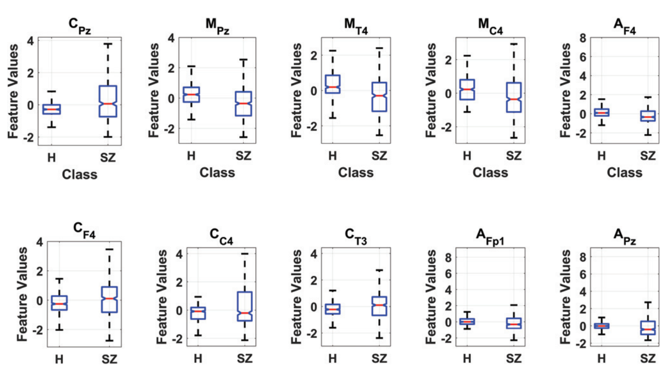

Figure 9. Box plots of the extracted features demonstrating the differences between healthy (H) and schizophrenia (SZ) classes.

3.2. Performance of the Proposed Model

Table 3 enlists the experimental results of applying different versions of KNN for the classification of SZ and healthy EEG observations. The FKNN model achieved 99.4% accuracy, 99.21% sensitivity, and 99.6% specificity for distinguishing the healthy and SZ instances using only 10 features shown in Figure 9. A slightly low performance of 98.2% was obtained through WKNN, where the value of K is set to 100. This model attained 97.6% and 99% sensitivity and specificity, respectively. Comparatively poor performance of 69% accuracy was obtained using CKNN, where the cubic distance metric was employed instead of Euclidean. The overall best performance was obtained via FKNN, where out of 504 SZ observations, only 4 were misclassified as healthy. Similarly, only 2 out of 504 observations from healthy controls were misclassified by the model.

Table 3. Performance of KNN classifiers using selected features for classification of normal and SZ EEG features.

Classifier	TN	FP	FN	TP	Acc	Sen	Sp	Prediction Speed	Training Time
FKNN	502	2	4	500	99.40%	99.21%	99.60%	19,000 obs/s	10.748 s
CKNN	499	5	301	203	69.60%	40.30%	99.00%	16,000 obs/s	1.039 s
WKNN	498	6	12	492	98.20%	97.60%	99.00%	20,000 obs/s	0.949 s

3.3. Performance Comparison with Other Classifiers

3.3.1. Decision Tree

Table 4 provides detailed results of testing different variants of the decision tree classifier for distinguishing SZ and healthy EEG features. DTF is constructed using a large number of leaves and yields 93.1% classification accuracy. DTM contains a moderate number of branches and provides 91.3% prediction accuracy. A comparatively low accuracy of 74.4% was obtained using DTC, which uses a fewer number of splits. We observe a trend in reduction in accuracy as the number of branches in the decision tree goes down.

Table 4. Performance of DT using selected features for classification of normal and SZ EEG features.

Classifier	TN	FP	FN	TP	Acc	Sen	Sp	Prediction Speed	Training Time
Fine Tree	462	42	28	476	93.10%	94.40%	91.70%	5000 obs/s	10.328 s
Medium Tree	472	32	56	448	91.30%	88.90%	93.70%	10,000 obs/s	5.411 s
Coarse Tree	393	111	147	357	74.40%	70.80%	78.00%	11,000 obs/s	3.178 s

3.3.2. Support Vector Machines

The experimental results of applying SVM with different kernel functions are shown in Table 5. LSVM was able to distinguish EEG features of healthy and SZ with 70.6% accuracy. Low performance confirms the complexity of the problem, as features of both classes were not linearly separable. QSVM provided enhanced results with accuracy reaching up to 95.1%, 92.5% sensitivity, and 97.8% specificity. The highest results of 96.5% accuracy were obtained through the CSVM. Non-linear kernel-based SVM classification models yielded better prediction performance as compared to linear SVM.

Table 5. Performance of SVM using selected features for classification of normal and SZ EEG features.

Classifier	TN	FP	FN	TP	Acc	Sen	Sp	Prediction Speed	Training Time
LSVM	437	67	229	275	70.60%	54.60%	86.70%	9500 obs/s	80.473 s
QSVM	493	11	38	466	95.10%	92.50%	97.80%	12,000 obs/s	7.1329 s
CSVM	474	30	5	499	96.50%	99.00%	94.00%	12,000 obs/s	4.833 s

3.3.3. Ensemble Classification Methods

Ensemble classifiers used a combination of various models with a voting strategy to predict the response. All ensemble classifiers used in this study have shown better performance, illustrated in Table 6. EBoosTT yielded an accuracy of 96.3% for the detection of SZ using extracted ten most significant cepstrum features. A slight increase in performance (96.9%) was shown using EbagT. Among all ensemble techniques, ESKNN achieved the highest results of 97.4% accuracy, 96.6% sensitivity, and 98% specificity.

Table 6. Performance of Ensemble classifiers using selected features for classification of normal and SZ EEG features.

Classifier	TN	FP	FN	TP	Acc	Sen	Sp	Prediction Speed	Training Time
EBoosTT	493	11	26	478	96.30%	94.80%	97.80%	5700 obs/s	9.667 s
EBagT	494	10	21	483	96.90%	95.80%	98.00%	6400 obs/s	4.677 s
ESKNN	495	9	17	487	97.40%	96.60%	98.00%	2800 obs/s	3.541 s

3.3.4. Artificial Neural Networks

Table 7 provides a performance analysis of applying different versions of ANNs for the classification of SZ and healthy EEG signals. Almost similar accuracy performances of 96.6% and 96.7% were observed using an NNN and WNN, respectively. These results demonstrated that raising the number of neurons in the hidden layer from 10 to 100 in narrow and wide networks has no substantial impact on the classification performance. A slightly better performance (97.1%) was obtained using MNN, which used 25 neurons in the hidden layers.

Table 7. Performance of ANNs using selected features for classification of normal and SZ EEG features.

Classifier	TN	FP	FN	TP	Acc	Sen	Sp	Prediction Speed	Training Time
NNN	491	13	21	483	96.60%	95.80%	97.40%	31,000 obs/s	15.206 s
MNN	490	14	15	489	97.10%	97.00%	97.20%	44,000 obs/s	1.748 s
WNN	487	17	16	488	96.70%	96.80%	97.00%	39,000 obs/s	1.522 s

4. Discussion

This research introduces a novel approach to the EEG-based diagnosis of schizophrenia, employing a combination of FastICA and ALEEWR for artefact removal, signal decomposition, and reconstruction. The proposed cepstral-based features further enhance diagnostic accuracy by capturing critical variations in the EEG signals. Through an ANOVA-based feature selection and classification via the FKNN algorithm, our system achieved an accuracy of 99.6%. Figure 10 shows the graphical comparison of performance in terms of accuracy, sensitivity, and specificity for several classifiers. The FKNN algorithm outperforms other classifiers with an accuracy of 99.4%, alongside high sensitivity (99.21%) and specificity (99.6%). The Fine Tree classifier shows a performance of 93%. The CSVM provides a high sensitivity of 99% but falls short of specificity compared to the FKNN. This indicates a slightly higher rate of false positives, which can be detrimental in clinical diagnostics. The ESKNN and MNN also demonstrate robust performance with accuracies above 97%, but they still do not reach the balanced performance of the FKNN in our specific application. The choice of the FKNN classifier is based not only on its superior accuracy but also on its ability to maintain balancing sensitivity and specificity, which is particularly advantageous in a clinical setting, where the accurate diagnosis of schizophrenia has profound implications for patient treatment and management.

Figure 11 illustrates the performance of the FKNN classifier with different numbers of features, showing a significant increase in accuracy as the number of features is incrementally increased from one to ten. Beyond ten features, the accuracy stabilises, peaking at 99.4% and maintaining a similar performance as additional features are considered up to forty. This trend indicates that a minimal set of ten features is sufficient for near-optimal diagnostic performance, as additional features do not significantly improve the classifier’s effectiveness, suggesting an optimal balance between feature complexity and diagnostic accuracy.

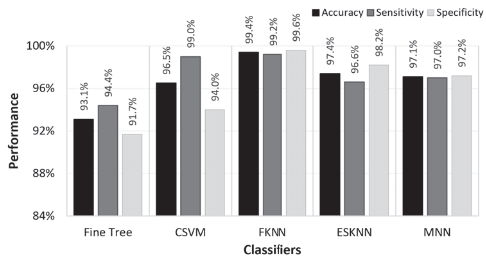

Figure 10. Comparison of the classification algorithms.

This performance significantly outperforms previous studies listed in Table 8. For instance, Zhang et al. [13] and Nikhil et al. [19] reported high accuracies of 98.5% and 99.0%, respectively, and utilised neural networks but did not focus on reducing feature space. Siuly et al. [15] used EMD for the classification of schizophrenia and healthy subjects with EEG signals, achieving an accuracy of 89.5%. However, their approach had the limitation of selecting an appropriate number of IMFs when using EMD. Jahmunah et al. [16] extracted 157 features from EEG signals and reduced them to 14 to achieve a 92.9% accuracy for the classification of schizophrenia and control groups. Kumar et al. [54] proposed a computer-aided approach for schizophrenia detection using EEG signals, employing local descriptors with a correlation-based feature selection algorithm. The reduced features are classified using AdaBoost, with temporal lobe EEG channels yielding the best performance of 99.3% accuracy. Das et al. [39] employed Multivariate Iterative Filtering with Hjorth parameters, achieving 98.9% accuracy using SVM. However, their approach required 30 features and involved extracting features from EEG bands, specifically delta, theta, alpha, beta, and gamma rhythms, which added significant computational overhead. The use of advanced EEG feature extraction techniques and KNN classification has proven effective. For instance, Akbari et al. [53] obtained an accuracy of 94.8% using 36 features from 12 channels using KNN classification. They used graphical features from the phase space dynamic of EEG signals. In another study, Aziz et al. [55] proposed brain textures for effective classification of schizophrenia using KNN classification and obtained 94.9% accuracy. The authors used EMD to decompose EEG into IMFs and after manual analysis, only the first two IMFs were added together to form a reconstructed preprocessed signal. Our method stands out by using fewer but highly discriminative features (10 features), with automated signal preprocessing through ALEEWR, eliminating the need for manual mode selection.

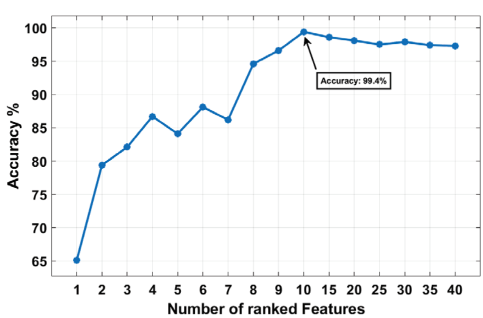

Figure 11. Accuracies of the proposed system across the ranked features.

Deep learning methods, such as those employed by Lillo et al. [4], Wu et al. [21], and Oh et al. [17], typically require large datasets to train effectively. Lillo et al. employed a CNN and achieved an accuracy of 93%. Wu et al. utilised a Recurrent Auto-encoder, resulting in an accuracy of 81.8%. Oh et al. used a CNN and obtained a high accuracy of 98.0%. Hassan et al. [20] proposed a fusion of CNN and machine learning classifiers for schizophrenia classification, achieving 98% accuracy. They introduced a CNN-based channel selection mechanism, evaluating individual channels to assess their contribution to classification accuracy. However, a limitation of this approach is the need to select different channel subsets for each identification problem. The current algorithm lacks an automated channel selection method, making it highly dependent on the specific dataset used. Singh et al. [18] proposed a spectral analysis-based CNN model for identifying schizophrenia using multichannel EEG signals. The model processes EEG signals by filtering, segmenting, and converting them into the frequency domain, dividing them into six spectral bands: delta, theta-1, theta-2, alpha, beta, and gamma. However, CNN is computationally complex, and the extraction of spectral information from frequency bands further adds to the computational overhead, making the approach resource-intensive. The need for large datasets can be a significant challenge in medical contexts. Additionally, data augmentation techniques, which are less viable in medical contexts due to the high specificity required for accurate diagnosis, cannot always compensate for the lack of extensive data. Our proposed approach not only improves classification accuracy but also reduces computational complexity, making it feasible for continuous monitoring and embedded systems and edge computing. Moreover, the cepstral features introduced in our study offer a novel dimension of analysis not explored in other studies.

EEG signals are non-stationary and non-linear, with properties that change over time, making traditional time- and frequency-domain analyses insufficient. Cepstral analysis, transforming the signal into the quefrency domain, handles these complexities by analysing the power and rate of change in quefrency content. Additionally, cepstral features are less sensitive to noise and artefacts, which is crucial for reliable EEG analysis. This novel feature set, with its high discriminatory power, allows for precise differentiation between healthy and schizophrenic EEG signals, as evidenced by the high sensitivity (97.8%) and specificity (98.8%) achieved. In conclusion, our study advances the field of EEG-based schizophrenia diagnosis by introducing a method that not only improves diagnostic accuracy but also optimises computational efficiency and application potential in real-world settings. The introduction of ALEEWR and cepstral analysis as a methodological innovation represents a significant step forward in the automated diagnosis of schizophrenia, setting a new benchmark for future studies in this area.

Table 8. Summary of EEG-based studies on schizophrenia detection.

Study	Method	Results
[12]	Event-related potential features, Random Forest	81.1%
[22]	Multi-domain connectome CNN	91.7%
[23]	Deep Belief Network	95.0%
[16]	Non-linear features, *t*-test	92.9%
[17]	Convolutional Neural Network	98.0%
[11]	Graph Theory-based Network Connectivity Analysis	82.3%
[13]	Artificial Neural Network	98.5%
[15]	Empirical Mode Decomposition, Ensemble Bagged Tree	89.5%
[19]	Long short-term memory	99.0%
[9]	Logistic Regression	97.0%
[53]	Graphical Features, KNN	94.8%
[39]	Multivariate Iterative Filtering, Hjorth parameters	94.8%
[18]	Spectral Features, CNN	98.5%
[4]	Convolutional Neural Network	93.0%
[21]	Recurrent Auto-encoder	81.8%
[55]	Brain Textures, KNN	94.9%
[20]	Convolutional Neural Network, Logistic Regression	98.0%
[7]	Spectrogram, Local Configuration Patterns	97.2%
[54]	Local descriptors, AdaBoostM1	99.3%
This work	FastICA, ALEEWR, Cepstral Features, FKNN	99.4%

5. Conclusions and Future Directions

In this study, we have presented an EEG-based framework for the early and precise diagnosis of SZ. The proposed framework employs Automated Log Energy-based Empirical Wavelet Reconstruction (ALEEWR) coupled with novel cepstral features. This multifaceted approach integrates advanced signal processing techniques with robust feature extraction and selection methods, significantly improving diagnostic accuracy and efficiency. By utilising FastICA for artefact removal and ALEEWR for signal reconstruction, we effectively enhance the EEG signal's clarity and relevance. Subsequent extraction of cepstral features, i.e., cepstral activity, mobility, and complexity, provides a nuanced understanding of EEG dynamics, which is further refined through ANOVA-based feature selection. The employment of the Fine KNN classifier enables our system to achieve remarkable diagnostic performance with an accuracy of 99.40%, sensitivity of 99.21%, and specificity of 99.60%. These metrics not only underscore the effectiveness of our approach but also demonstrate its superiority over traditional diagnostic methods, which are often labour-intensive and prone to errors. Moving forward, the scalability of this framework offers promising avenues for broader clinical applications, ensuring robust, real-time diagnostics that can significantly impact patient outcomes and treatment strategies in mental health care.

However, there are some limitations to this study. Firstly, we used only one dataset to validate the algorithm. To ensure broader applicability and robustness, future studies should incorporate multiple datasets. Secondly, the data size is relatively small, which might limit the generalisability of our findings. Increasing the dataset size would help in better training and validation of the models. Thirdly, the current implementation of ALEEWR uses a static log energy threshold of 10%, which was selected experimentally. This threshold should be made adaptive to accommodate various signal-to-noise conditions dynamically.

Looking forward, this study sets the stage for significant advancements in schizophrenia diagnosis using EEG signals. Incorporating deep learning models like CNNs and LSTMs, particularly with cepstral features, promises deeper insights into EEG dynamics and potentially higher diagnostic accuracies. Expanding our dataset will further refine and validate our models, enhancing their generalisability and effectiveness. Additionally, integrating our methods into low-power, portable embedded systems could revolutionise mental health care delivery, enabling real-time, accessible diagnostics in remote settings. This approach not only aims to improve the clinical management of schizophrenia through earlier interventions but also optimises system design for energy efficiency and minimal computational demands, crucial for practical deployments in resource-limited environments.

Author Contributions: Conceptualisation, S.A. and M.U.K.; Methodology, S.A. and M.U.K.; Writing—Original Draft, S.A. and M.U.K.; Validation, M.U.K. and S.A.; Investigation, S.A.; Software, M.U.K. and K.I.; Visualisation, K.I.; Writing—Review and Editing, K.I. and R.F.-R.; Supervision, R.F.-R. All authors have read and agreed to the published version of the manuscript.

Funding: This research received no external funding.

Institutional Review Board Statement: Not applicable.

Informed Consent Statement: Not applicable.

Data Availability Statement: For the development and validation of the proposed method, we used a public domain dataset [24].

Conflicts of Interest: The authors have no conflicts of interest.

References

1. World Health Organization. Schizophrenia. 2022. Available online: https://www.who.int/news-room/fact-sheets/detail/schizophrenia (accessed on 21 March 2023).
2. Zhu, M.H.; Liu, Z.J.; Hu, Q.Y.; Yang, J.Y.; Jin, Y.; Zhu, N.; Huang, Y.; Shi, D.H.; Liu, M.J.; Tan, H.Y.; et al. Amisulpride augmentation therapy improves cognitive performance and psychopathology in clozapine-resistant treatment-refractory schizophrenia: A 12-week randomized, double-blind, placebo-controlled trial. *Mil. Med. Res.* **2022**, *9*, 59. [CrossRef] [PubMed]

3. Jaeschke, K.; Hanna, F.; Ali, S.; Chowdhary, N.; Dua, T.; Charlson, F. Global estimates of service coverage for severe mental disorders: Findings from the WHO Mental Health Atlas 2017. *Glob. Ment. Health* **2021**, *8*, e27. [CrossRef] [PubMed]
4. Lillo, M.E.; Mora, M.; Lucero, B. Automated diagnosis of schizophrenia using EEG microstates and Deep Convolutional Neural Network. *Expert Syst. Appl.* **2022**, *209*, 118236. [CrossRef]
5. Davison, J.; O'Gorman, A.; Brennan, L.; Cotter, D.R. A systematic review of metabolite biomarkers of schizophrenia. *Schizophr. Res.* **2018**, *195*, 32–50. [CrossRef]
6. Alturki, F.A.; AlSharabi, K.; Abdurraqeeb, A.M.; Aljalal, M. EEG signal analysis for diagnosing neurological disorders using discrete wavelet transform and intelligent techniques. *Sensors* **2020**, *20*, 2505. [CrossRef]
7. WeiKoh, J.E.; Rajinikanth, V.; Vicnesh, J.; Pham, T.H.; Oh, S.L.; Yeong, C.H.; Sankaranarayanan, M.; Kamath, A.; Bairy, G.M.; Barua, P.D.; et al. Application of local configuration pattern for automated detection of schizophrenia with electroencephalogram signals. *Expert Syst.* **2024**, *41*, e12957. [CrossRef]
8. Zandbagleh, A.; Mirzakuchaki, S.; Daliri, M.R.; Premkumar, P.; Sanei, S. Classification of low and high schizotypy levels via evaluation of brain connectivity. *Int. J. Neural Syst.* **2022**, *32*, 2250013. [CrossRef]
9. Azizi, S.; Hier, D.B.; Wunsch, D.C. Schizophrenia classification using resting state EEG functional connectivity: Source level outperforms sensor level. In Proceedings of the 2021 43rd Annual International Conference of the IEEE Engineering in Medicine & Biology Society (EMBC), Virtual, 1–5 November 2021; IEEE: New York, NY, USA, 2021; pp. 1770–1773.
10. Anwar, T.; Rehmat, N.; Naveed, H. A generic approach for classification of psychological disorders diagnosis using EEG. In Proceedings of the 2021 43rd Annual International Conference of the IEEE Engineering in Medicine & Biology Society (EMBC), Virtual, 1–5 November 2021; IEEE: New York, NY, USA, 2021; pp. 2025–2029.
11. Bougou, V.; Mporas, I.; Schirmer, P.; Ganchev, T. Evaluation of EEG Connectivity Network Measures based Features in Schizophrenia Classification. In Proceedings of the 2019 International Conference on Biomedical Innovations and Applications (BIA), Varna, Bulgaria, 8–9 November 2019; IEEE: New York, NY, USA, 2019; pp. 1–4.
12. Zhang, L. EEG signals classification using machine learning for the identification and diagnosis of schizophrenia. In Proceedings of the 2019 41st Annual International Conference of the IEEE Engineering in Medicine and Biology Society (EMBC), Berlin, Germany, 23–27 July 2019; IEEE: New York, NY, USA, 2019; pp. 4521–4524.
13. Zhang, L. Eeg signals feature extraction and artificial neural networks classification for the diagnosis of schizophrenia. In Proceedings of the 2020 IEEE 19th International Conference on Cognitive Informatics & Cognitive Computing (ICCI* CC), Beijing, China, 26–28 September 2020; IEEE: New York, NY, USA, 2020; pp. 68–75.
14. Krishnan, P.T.; Raj, A.N.J.; Balasubramanian, P.; Chen, Y. Schizophrenia detection using MultivariateEmpirical Mode Decomposition and entropy measures from multichannel EEG signal. *Biocybern. Biomed. Eng.* **2020**, *40*, 1124–1139. [CrossRef]
15. Siuly, S.; Khare, S.K.; Bajaj, V.; Wang, H.; Zhang, Y. A computerized method for automatic detection of schizophrenia using EEG signals. *IEEE Trans. Neural Syst. Rehabil. Eng.* **2020**, *28*, 2390–2400. [CrossRef]
16. Jahmunah, V.; Oh, S.L.; Rajinikanth, V.; Ciaccio, E.J.; Cheong, K.H.; Arunkumar, N.; Acharya, U.R. Automated detection of schizophrenia using nonlinear signal processing methods. *Artif. Intell. Med.* **2019**, *100*, 101698. [CrossRef]
17. Oh, S.L.; Vicnesh, J.; Ciaccio, E.J.; Yuvaraj, R.; Acharya, U.R. Deep convolutional neural network model for automated diagnosis of schizophrenia using EEG signals. *Appl. Sci.* **2019**, *9*, 2870. [CrossRef]
18. Singh, K.; Singh, S.; Malhotra, J. Spectral features based convolutional neural network for accurate and prompt identification of schizophrenic patients. *Proc. Inst. Mech. Eng. Part H J. Eng. Med.* **2021**, *235*, 167–184. [CrossRef] [PubMed]
19. Nikhil Chandran, A.; Sreekumar, K.; Subha, D. EEG-based automated detection of schizophrenia using long short-term memory (LSTM) network. In Proceedings of the International Conference on Machine Learning and Computational Intelligence, Bhubaneswar, India, 6–7 April 2019; Springer: Singapore, 2021; pp. 229–236.
20. Hassan, F.; Hussain, S.F.; Qaisar, S.M. Fusion of multivariate EEG signals for schizophrenia detection using CNN and machine learning techniques. *Inf. Fusion* **2023**, *92*, 466–478. [CrossRef]
21. Wu, Y.; Xia, M.; Wang, X.; Zhang, Y. Schizophrenia detection based on EEG using recurrent auto-encoder framework. In Proceedings of the 29th International Conference on Neural Information Processing-2022, New Delhi, India, 22–26 November 2022; Springer: Cham, Switzerland, 2022; pp. 62–73.
22. Phang, C.R.; Noman, F.; Hussain, H.; Ting, C.M.; Ombao, H. A multi-domain connectome convolutional neural network for identifying schizophrenia from EEG connectivity patterns. *IEEE J. Biomed. Health Inform.* **2019**, *24*, 1333–1343. [CrossRef]
23. Phang, C.R.; Ting, C.M.; Samdin, S.B.; Ombao, H. Classification of EEG-based effective brain connectivity in schizophrenia using deep neural networks. In Proceedings of the 2019 9th International IEEE/EMBS Conference on Neural Engineering (NER), San Francisco, CA, USA, 20–23 March 2019; IEEE: New York, NY, USA, 2019; pp. 401–406.
24. Olejarczyk, E.; Jernajczyk, W. Graph-based analysis of brain connectivity in schizophrenia. *PLoS ONE* **2017**, *12*, e0188629. [CrossRef]
25. Al-Qazzaz, N.K.; Hamid Bin Mohd Ali, S.; Ahmad, S.A.; Islam, M.S.; Escudero, J. Automatic artifact removal in EEG of normal and demented individuals using ICA–WT during working memory tasks. *Sensors* **2017**, *17*, 1326. [CrossRef] [PubMed]
26. Awan, A.W.; Usman, S.M.; Khalid, S.; Anwar, A.; Alroobaea, R.; Hussain, S.; Almotiri, J.; Ullah, S.S.; Akram, M.U. An ensemble learning method for emotion charting using multimodal physiological signals. *Sensors* **2022**, *22*, 9480. [CrossRef] [PubMed]

27. Mwata-Velu, T.; Navarro Rodríguez, A.; Mfuni-Tshimanga, Y.; Mavuela-Maniansa, R.; Martínez Castro, J.A.; Ruiz-Pinales, J.; Avina-Cervantes, J.G. EEG-BCI Features Discrimination between Executed and Imagined Movements Based on FastICA, Hjorth Parameters, and SVM. *Mathematics* **2023**, *11*, 4409. [CrossRef]
28. Çınar, S. Design of an automatic hybrid system for removal of eye-blink artifacts from EEG recordings. *Biomed. Signal Process. Control* **2021**, *67*, 102543. [CrossRef]
29. Haider, U.; Hanif, M.; Rashid, A.; Qaisar, S.M.; Subasi, A. EEG-based schizophrenia classification using penalized sequential dictionary learning in the context of mobile healthcare. *Biomed. Signal Process. Control* **2024**, *90*, 105856. [CrossRef]
30. Zülfikar, A.; Mehmet, A. Empirical mode decomposition and convolutional neural network-based approach for diagnosing psychotic disorders from eeg signals. *Appl. Intell.* **2022**, *52*, 12103–12115. [CrossRef]
31. Raveendran, S.; Kenchaiah, R.; Kumar, S.; Sahoo, J.; Farsana, M.; Chowdary Mundlamuri, R.; Bansal, S.; Binu, V.; Ramakrishnan, A.; Ramakrishnan, S.; et al. Variational mode decomposition-based EEG analysis for the classification of disorders of consciousness. *Front. Neurosci.* **2024**, *18*, 1340528. [CrossRef] [PubMed]
32. Khan, M.U.; Aziz, S.; Iqtidar, K.; Fernandez-Rojas, R. Computer-aided diagnosis system for cardiac disorders using variational mode decomposition and novel cepstral quinary patterns. *Biomed. Signal Process. Control* **2023**, *81*, 104509. [CrossRef]
33. Singh, B.K.; Tikka, S.K.; Singh, L.K. Investigation of quantitative electroencephalography markers for schizophrenia diagnosis using variational mode decomposition. In Proceedings of the 2021 International Conference on Emerging Smart Computing and Informatics (ESCI), Pune, India, 5–7 March 2021; IEEE: New York, NY, USA, 2021; pp. 466–470.
34. Sairamya, N.; Subathra, M.; George, S.T. Automatic identification of schizophrenia using EEG signals based on discrete wavelet transform and RLNDiP technique with ANN. *Expert Syst. Appl.* **2022**, *192*, 116230. [CrossRef]
35. Türk, Ö.; Aldemir, E.; Acar, E.; Ertuğrul, Ö.F. Diagnosis of schizophrenia based on transformation from EEG sub-bands to the image with deep learning architecture. *Soft Comput.* **2023**, *28*, 6607–6617. [CrossRef]
36. Khare, S.K.; Bajaj, V.; Siuly, S.; Sinha, G. Classification of schizophrenia patients through empirical wavelet transformation using electroencephalogram signals. In *Modelling and Analysis of Active Biopotential Signals in Healthcare, Volume 1*; IOP Publishing: Bristol, UK, 2020; p. 1.
37. Jain, S.; Thakkar, H.; Singh, B.K.; Tikka, S.K.; Singh, L.K. Electroencephalograph (EEG) signal analysis for the Detection of Schizophrenia using Empirical Wavelet Transform. In Proceedings of the 2022 Second International Conference on Power, Control and Computing Technologies (ICPC2T), Raipur, India, 1–3 March 2022; IEEE: New York, NY, USA, 2022; pp. 1–6.
38. Gilles, J. Empirical wavelet transform. *IEEE Trans. Signal Process.* **2013**, *61*, 3999–4010. [CrossRef]
39. Das, K.; Pachori, R.B. Schizophrenia detection technique using multivariate iterative filtering and multichannel EEG signals. *Biomed. Signal Process. Control* **2021**, *67*, 102525. [CrossRef]
40. Kumar, J.S.; Bhuvaneswari, P. Analysis of electroencephalography (EEG) signals and its categorization—A study. *Procedia Eng.* **2012**, *38*, 2525–2536. [CrossRef]
41. Ren, H.; Qu, J.; Chai, Y.; Huang, L.; Tang, Q. Cepstrum coefficient analysis from low-frequency to high-frequency applied to automatic epileptic seizure detection with bio-electrical signals. *Appl. Sci.* **2018**, *8*, 1528. [CrossRef]
42. Kutafina, E.; Heiligers, A.; Popovic, R.; Brenner, A.; Hankammer, B.; Jonas, S.M.; Mathiak, K.; Zweerings, J. Tracking of mental workload with a mobile EEG sensor. *Sensors* **2021**, *21*, 5205. [CrossRef]
43. Hasan, M.M.; Watling, C.N.; Larue, G.S. Validation and interpretation of a multimodal drowsiness detection system using explainable machine learning. *Comput. Methods Programs Biomed.* **2024**, *243*, 107925. [CrossRef] [PubMed]
44. Harpale, V.; Bairagi, V. An adaptive method for feature selection and extraction for classification of epileptic EEG signal in significant states. *J. King Saud Univ.-Comput. Inf. Sci.* **2021**, *33*, 668–676. [CrossRef]
45. Kim, K.; Duc, N.T.; Choi, M.; Lee, B. EEG microstate features for schizophrenia classification. *PLoS ONE* **2021**, *16*, e0251842. [CrossRef]
46. Mai, N.D.; Lee, B.G.; Chung, W.Y. Affective computing on machine learning-based emotion recognition using a self-made EEG device. *Sensors* **2021**, *21*, 5135. [CrossRef] [PubMed]
47. Khan, M.U.; Aziz, S.; Iqtidar, K.; Zaher, G.F.; Alghamdi, S.; Gull, M. A two-stage classification model integrating feature fusion for coronary artery disease detection and classification. *Multimed. Tools Appl.* **2022**, *81*, 13661–13690. [CrossRef]
48. Gonzalez-Carabarin, L.; Castellanos-Alvarado, E.; Castro-Garcia, P.; Garcia-Ramirez, M. Machine Learning for personalised stress detection: Inter-individual variability of EEG-ECG markers for acute-stress response. *Comput. Methods Programs Biomed.* **2021**, *209*, 106314. [CrossRef] [PubMed]
49. Chatterjee, S.; Byun, Y.C. EEG-based emotion classification using stacking ensemble approach. *Sensors* **2022**, *22*, 8550. [CrossRef]
50. Rashid, M.; Bari, B.S.; Hasan, M.J.; Razman, M.A.M.; Musa, R.M.; Ab Nasir, A.F.; Majeed, A.P.A. The classification of motor imagery response: An accuracy enhancement through the ensemble of random subspace k-NN. *PeerJ Comput. Sci.* **2021**, *7*, e374. [CrossRef]
51. Subasi, A.; Ercelebi, E. Classification of EEG signals using neural network and logistic regression. *Comput. Methods Programs Biomed.* **2005**, *78*, 87–99. [CrossRef]
52. Khan, A.; Aziz, S.; Bashir, M.; Khan, M.U. IoT and wireless sensor network based autonomous farming robot. In Proceedings of the 2020 International Conference on Emerging Trends in Smart Technologies (ICETST), Karachi, Pakistan, 26–27 March 2020; IEEE: New York, NY, USA, 2020; pp. 1–5.

53. Akbari, H.; Ghofrani, S.; Zakalvand, P.; Sadiq, M.T. Schizophrenia recognition based on the phase space dynamic of EEG signals and graphical features. *Biomed. Signal Process. Control* **2021**, *69*, 102917. [CrossRef]
54. Kumar, T.S.; Rajesh, K.N.; Maheswari, S.; Kanhangad, V.; Acharya, U.R. Automated Schizophrenia detection using local descriptors with EEG signals. *Eng. Appl. Artif. Intell.* **2023**, *117*, 105602. [CrossRef]
55. Aziz, S.; Khan, M.U.; Faraz, M.; Sharma, S.; Gareeballah, A.; Montes, G.A. Intelligent System for the Diagnosis of Schizophrenia featuring Brain Textures from EEG. In Proceedings of the 2023 3rd International Conference on Artificial Intelligence (ICAI), Islamabad, Pakistan, 22–23 February 2023; IEEE: New York, NY, USA, 2023; pp. 82–87.

sensors

MDPI

Article

Dynamical Embedding of Single-Channel Electroencephalogram for Artifact Subspace Reconstruction

Doli Hazarika [1], K. N. Vishnu [1], Ramdas Ransing [2] and Cota Navin Gupta [1,*]

[1] Neural Engineering Lab, Department of Biosciences and Bioengineering, Indian Institute of Technology, Guwahati 781039, India; dhazarika@iitg.ac.in (D.H.); kvishnu@iitg.ac.in (K.N.V.)

[2] Department of Psychiatry, Clinical Neurosciences, and Addiction Medicine, All India Institute of Medical Sciences, Guwahati 781101, India; ramdasransing@aiimsguwahati.ac.in

* Correspondence: cngupta@iitg.ac.in; Tel.: +91-361-258-2232

Abstract: This study introduces a novel framework to apply the artifact subspace reconstruction (ASR) algorithm on single-channel electroencephalogram (EEG) data. ASR is known for its ability to remove artifacts like eye-blinks and movement but traditionally relies on multiple channels. Embedded ASR (E-ASR) addresses this by incorporating a dynamical embedding approach. In this method, an embedded matrix is created from single-channel EEG data using delay vectors, followed by ASR application and reconstruction of the cleaned signal. Data from four subjects with eyes open were collected using Fp1 and Fp2 electrodes via the CameraEEG android app. The E-ASR algorithm was evaluated using metrics like relative root mean square error (RRMSE), correlation coefficient (CC), and average power ratio. The number of eye-blinks with and without the E-ASR approach was also estimated. E-ASR achieved an RRMSE of 43.87% and had a CC of 0.91 on semi-simulated data and effectively reduced artifacts in real EEG data, with eye-blink counts validated against ground truth video data. This framework shows potential for smartphone-based EEG applications in natural environments with minimal electrodes.

Keywords: artifact removal; artifact subspace reconstruction; eye blink; single channel; electroencephalography; signal processing; smartphone

Citation: Hazarika, D.; Vishnu, K.N.; Ransing, R.; Gupta, C.N. Dynamical Embedding of Single-Channel Electroencephalogram for Artifact Subspace Reconstruction. *Sensors* **2024**, *24*, 6734. https://doi.org/10.3390/s24206734

Academic Editors: Yifan Zhao, Hua-Liang Wei, Yuzhu Guo and Fei He

Received: 30 August 2024
Revised: 7 October 2024
Accepted: 12 October 2024
Published: 19 October 2024

1. Introduction

Electroencephalography (EEG) is a non-invasive method employed for capturing the electrical patterns generated by cortical neurons, achieved by positioning electrodes on the scalp [1]. EEG amplifiers, known for their portability and capacity to offer precise temporal resolution in signal recording, establish EEG as the optimal brain imaging tool for assessing human brain activity during motion [2]. In recent years, there has been an increasing interest in conducting EEG experiments in natural environments using smartphones, marking a significant shift in EEG experimentation [3]. Smartphone-based EEG offers several advantages, including portability and affordability, positioning it as a promising next-generation technique for real-time brain activity investigation [4]. Furthermore, as technology continues to advance, these systems have evolved to feature low instrumentation and computational complexity [5,6]. Notably, portable EEG devices equipped with a single EEG channel have gained widespread use in non-laboratory and non-clinical applications, reflecting their practicality [7,8]. These devices have found utility in diverse domains, ranging from BCI research to driver fatigue detection and the study of various brain disorders [9–11].

However, EEG is susceptible to contamination by artifacts. Non-physiological artifacts can include high impedance, faulty electrodes, or noise from surrounding electrical equipment. Physiological and biological artifacts, including blinks, eye movements, muscular activity, and heart-related signals, pose a substantial challenge in EEG signal analysis, making their removal a primary focus when addressing EEG artifacts [12,13]. The activity of the eyes including blinks and saccades produce large amplitude changes in prefrontal (Fp1 and Fp2) electrodes. As we traverse from front to the back of the scalp, the eye-blink amplitude decreases. Typically, these artifacts exhibit an amplitude of 500 microvolts and a frequency below 20 Hz [12,13], characteristics that are also linked to upper-limb movements and drivers' cognitive states [14–16]. Electrical activity produced by muscle movements including jaw clenching, swallowing, and changes in facial expression results in large amplitude changes in EEG signal. Nonetheless, improper artifact filtering can impact the signal in terms of both its temporal and frequency characteristics, potentially leading to a loss of critical information, which could, in turn, jeopardize the effectiveness of various natural environment EEG application.

The artifact subspace reconstruction (ASR) algorithm is an adaptive spatial filtering method for removal of artifacts from EEG signals, developed and patented by C.A.E. Kothe and T.P. Jung in 2016 [17]. This method performs a Principal Component Analysis (PCA) on the EEG data using a sliding window approach. In the initial step, ASR automatically derives reference data from the raw signal based on the distribution of signal variance. Subsequently, it establishes thresholds for identifying artifact components by considering the standard deviation across the principal components of the windows, which is then multiplied by a user-defined parameter 'k'. Then, ASR identifies and eliminates artifact components within each time window if their principal component surpasses the rejection threshold. Finally, the method reconstructs the cleaned signals using the remaining data [18]. According to [19], the 'k' parameter dictates the aggressiveness of the faulty data removal process. A smaller 'k' results in a more aggressive removal procedure. An enhanced variant called Riemannian ASR employs manifold techniques for computing covariance matrices, a method proven to be effective for artifact removal [20]. In an investigation involving motor imagery EEG data [21], it was observed that an ASR technique with default settings performs better than the Independent Component Analysis (ICA) and PCA methods. In [18], researchers illustrated the efficacy of ASR as an automated approach for removing artifacts from EEG data collected during attention tasks in a driving simulator. Additionally, ref. [22] highlights the application of ASR to EEG data recorded during activities such as fast walking and maintaining a single-leg stance. Lately, ASR has been incorporated into the Smarting Pro smartphone application, enabling the automatic removal of artifacts from multiple channels [6]. However, existing ASR algorithms cannot be applied to single-channel EEG recordings and their performance can be impaired when the number of channels is small [18].

In a study [23], the feasibility of employing Singular Spectrum Analysis (SSA) to mitigate eye-blink artifacts in single-channel EEG data was explored. The technique is applied to extract low-frequency, oscillatory, and noisy components from singular time series data [24]. However, traditional SSA requires a crucial step in which the relevant signal eigenvectors must be identified. A novel set of criteria for the selection of these eigenvectors, crucial for reconstructing the desired signal, was also introduced [24]. SSA was subsequently integrated into the Adaptive Filter (AF) framework to enhance performance in [25]. Furthermore, single-channel EEG recordings have been subjected to ICA after undergoing SSA processing [26]. In a recent development, SSA was employed as a smoothing filter to mitigate the Electrooculogram (EOG) artifacts present in EEG signals [27]. A study [28] explored the integration of SSA-ICA and wavelet thresholding techniques to eliminate EOG artifacts in single-channel contaminated EEG signals. Reference [29] introduced a versatile approach for EEG artifact removal with limited supervision. They presented an innovative wavelet-based technique enabling the elimination of artifacts from single-channel EEG through a data-driven adjustment of wavelet coefficients. Their method demonstrates the ability to dynamically reduce artifacts of varying types. Nevertheless, the utilization of the aforementioned SSA algorithms into Android smartphone applications for artifact removal from EEG signals remains an area that has not been explored.

The majority of the approaches for eliminating eye-blink artifacts as mentioned earlier are primarily employed for offline artifact elimination. However, in situations like natural environment EEG experiments and epilepsy monitoring, where real-time signal processing is essential, it becomes imperative that artifact removal algorithms are capable of handling real-time processing. Consequently, to accommodate the needs of real-time artifact removal, these methods or algorithms must meet specific criteria. The foremost requirement is that the algorithm must operate automatically, without the need for any manual intervention. Secondly, it is crucial to use minimum number of electrodes for natural environment applications as this can cause discomfort and inconvenience to the subject during prolonged EEG recordings. One of the major advantages of using single-channel EEG is its simplicity and ease of use, as it requires less setup time and minimal equipment compared to multiple-channel EEG. Additionally, it offers cost-effective solutions for researchers, especially those working with limited resources, while still providing valuable data. For instance, studies have shown that single-channel EEG can be used to identify cognitive states such as driver drowsiness detection [30], as well as brain activity associated with specific mental disorders like depression and anxiety [31]. Lastly, for real-time implementation on a smartphone app, the artifact removal algorithm should have minimal computational complexity to ensure that it does not introduce unacceptable time delays [3].

The dynamical embedding concept to perform ICA using single-channel EEG was introduced in [32] for the separation of ocular artifacts. Pseudo-multichannel data called the embedding matrix was created using delayed vectors spanning a few seconds, from a single-channel EEG recording. This embedding matrix was used as the input to ICA. Embedding is also a fundamental part of SSA, allowing for the separation of underlying artifact components from single-channel EEG [24]. ASR has been successfully implemented on an android smartphone [6] for addressing real-time artifacts, leveraging multiple channel inputs. However, to the best of our knowledge, no work has studied ASR for single-channel EEG. Therefore, our primary objective was to investigate the effectiveness of embedding as a method for implementing ASR on single-channel EEG data. We achieved this by creating an *EmbeddedMatrix* from a single-channel EEG signal and then applying ASR. This framework may be a potential solution for artifact reduction on a smartphone for natural environment EEG experiments. As a first step, to assess the performance of our novel E-ASR framework, we focused on metrics (calculated before and after E-ASR framework) such as relative root mean square error, correlation coefficient, average power ratio, and reduction in number of eye-blinks. We evaluated the performance on semi-simulated and real EEG signals. Figure 1 illustrates the graphical abstract of the proposed framework.

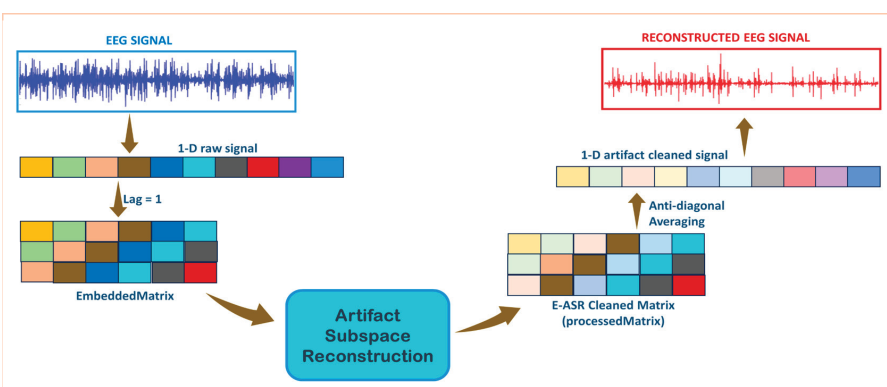

Figure 1. Graphical abstract for the proposed E-ASR framework on a single electroencephalogram channel. Each color represents a single time point.

2. Materials and Methods

2.1. Data Acquisition and Pre-Processing

The Indian Institute of Technology Guwahati Human Ethics Committee approved this research work. It was conducted in accordance with the principles embodied in the Declaration of Helsinki and in accordance with local statutory requirements. We obtained EEG data for four (two male and two female, with a mean age of 28 years and standard deviation of 4.33) subjects with the CameraEEG android application, which synchronously records video and EEG data [33]. The app is compatible with all Android smartphones running Android OS Lollipop or higher. We employed the CameraEEG app alongside an EasyCap 24-channel headcap [34] and the mBrainTrain Smarting device [5]. The subjects were asked to keep their eyes open for 5 min. The acquired video and EEG data were saved as mp4 and bdf files, respectively, on the smartphone's memory. The sampling frequency was set at 500 Hz. Figure 2 shows the photographs of the recording setup used for this work.

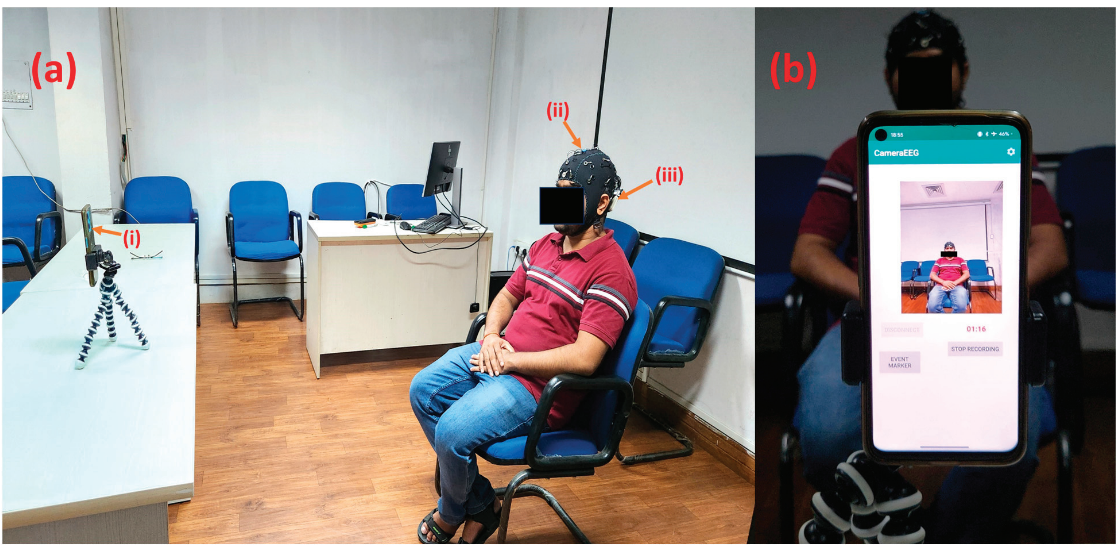

Figure 2. (**a**) The data recording setup for the resting-state eyes-open task, featuring (**i**) a OnePlus Nord CE 2 Lite 5G smartphone placed on a tripod in front of the subject, (**ii**) an EasyCap 24-channel EEG cap, and (**iii**) an mBrainTrain Smarting device mounted on the EEG cap. (**b**) The CameraEEG Android app running on the smartphone, recording synchronized EEG and video data.

The 5 min eyes-open data from the all the subjects is considered here throughout for the analysis. The Fp1 and Fp2 channels from the EEG data were selected and considered as single-channel EEG signals for further use, as they would contain the most eye-blinks and eye movement-related artifacts. We normalized the data using zero-centered normalization [18]. Following this, the single-channel signal was filtered by a band-pass filter (0.5–100 Hz) and a notch filter was used to remove 50 Hz line noise (electrical shifts) [18,35]. There was no linear trend observed in the signal through visual inspection; hence, detrending of the signal was not considered. This might be a potential limitation of the current study. The MATLAB codes used were developed using MATLAB version 2022b (MathWorks, Natick, MA, USA) on a system with an Intel® Core (TM) i7-8700 CPU @ 3.19 GHz and 16 GB memory.

2.2. Construction of Multichannel EEG Matrix Using Embedding Approach

The embedding matrix is a way of representing the temporal structure of an EEG signal [32]. It is created by making a series of delay vectors on a single channel EEG data. This matrix captures information about underlying EEG generators based on single-channel data [36,37]. Let us consider a single-channel electroencephalogram signal as $x = [x(1), x(2), \ldots\ldots\ldots, x(N)]$, where N is the total number of samples. Then, the multidimensional series can be written as Equation (1):

$$X = \begin{bmatrix} x(1) & x(2) & \cdots & x(K) \\ x(2) & x(3) & \cdots & x(K+1) \\ \vdots & \vdots & \ddots & \vdots \\ x(M) & x(M+1) & \cdots & x(N) \end{bmatrix} \tag{1}$$

where M is the embedding dimension and $K = N - M + 1$. If f_s is the sampling frequency of the signal and f_L is the lowest frequency of interest, then the embedding dimension M [32] can be determined by Equation (2):

$$M \geq \frac{f_s}{f_L} \tag{2}$$

In our approach, the time lag is set to 1, which is supported by empirical evidence from [32]. We shall henceforth refer to Equation (1) as *EmbeddedMatrix*.

The embedding dimension (M) is a crucial parameter in decomposing a time series data. It determines the number of lagged components of the time series. Selecting an appropriate embedding dimension M is essential because it influences the quality of the decomposition and the ability to extract meaningful information from the time series. If M is too small, important information may be lost, leading to incomplete decomposition. On the other hand, if M is too large, it can lead to overcomplexity and noise in the decomposition, making it harder to extract meaningful components [32]. Choosing the optimal M often involves a balance between capturing important patterns and minimizing noise [32].

2.3. Artifact Subspace Reconstruction

In the first step of ASR (i.e., calibration phase), the EEG data (X) is input for the *asr_calibrate* function along with the sampling frequency in Hertz (Hz) to construct the calibration data and determine rejection thresholds from the calibration data [18]. To do so, the covariance matrix of X is calculated. Mixing matrix (M_C) is calculated as the square root of covariance matrix as in Equation (3).

$$M_C M_C^T = Cov(X) \tag{3}$$

The eigenvalue decomposition of M_C results in eigenvectors (V_C) and eigenvalues (D_C). The principal component space is calculated as Equation (4).

$$Y_C = X * V_C \tag{4}$$

Component-wise root mean square (RMS) values with a non-overlapping sliding window of 1 s [18] are calculated and transformed into z-score. ASR selects the windows with z-score in range of $-3.5 < z < 5.5$ [18], defines them as clean (artifact-free) sections, and concatenates them to generate the calibration data. From the clean sections of each principal component, the mean (μ) and standard deviation (σ) of each component are calculated. The threshold of each component is calculated as Equation (5), where i refers to the principal component number and k is the cut-off parameter, whose value was 17 [18].

$$T_i = \mu_i + k\sigma_i \tag{5}$$

The threshold matrix T is the matrix product of diagonal matrix of threshold values T_i and the transpose of eigenvectors V_C. The threshold matrix T and the mixing matrix M_C are the outputs of this calibration phase, which are stored in a variable 'state' [18].

In the second step (i.e., process phase) of ASR, eigenvalue decomposition is performed on data within a sliding window (0.5 s) [18] to obtain the eigenvalues (D_T) and eigenvectors (V_T) of the data. Then *asr_process* function applies thresholds determined in the calibration phase to create X_T [18]. If an eigenvalue within that sliding window exceeds the threshold, its corresponding eigenvector is removed. The leftover eigenvectors (V_{trunc}) are hence truncated and the data are reconstructed within that window according to Equation (6) from [18].

$$(X_T)_{clean} = M_C \left(V_T^T M_c\right)^+_{trunc} V_T^T X_T \tag{6}$$

Due to the rank reduction from truncation, the Moore–Penrose pseudoinverse (+) ensures a reliable reconstruction by finding an optimal solution that minimizes reconstruction error. This approach allows for accurate data recovery, even when the matrix is singular or lacks full rank. The clean windows ($(X_T)_{clean}$) are concatenated to form the clean artifact-free signal X_{Clean}. More details on the ASR algorithm can be found in [17,35].

2.4. Proposed Method: Embedded Artifact Subspace Reconstruction

The embedded matrix is created by time lagging the pre-processed single-channel EEG data. We determined the embedding dimension (M) to be large enough to capture the information content in the signal. For the EEG signals described in this study, we derived M using the equation given in (2). The pre-processed 1D EEG data were transformed into *EmbeddedMatrix* as explained in Section 2.2, with time lag as 1. ASR is applied on the *EmbeddedMatrix* using the MATLAB codes available in EEGLAB [38] as an open-source plug-in function *clean_rawdata*. The output of application of ASR on *EmbeddedMatrix* is the *processedMatrix* of the same dimensions. Anti-diagonal averaging [37] is then applied to *processedMatrix* to reconstruct the E-ASR-cleaned signal.

3. Performance Metrics

We evaluated the effectiveness of our method on a semi-simulated single-channel EEG signal using two well-known metrics: the relative root mean square error (RRMSE) and the correlation coefficient (CC). The RRMSE is a commonly used measure for assessing the performance of artifact removal techniques in semi-simulated EEG data [39]. The correlation coefficient (CC), a statistically based metric, indicates the relationship between two signals and is employed to evaluate the effectiveness of the artifact removal process [39]. A higher CC value suggests a stronger linear relationship, implying better performance of the artifact removal method [39]. These metrics are calculated between the ground truth signal, which is free of eye-blink artifacts, and the artifact-cleaned signal [39,40]. Additionally, we analyzed the average power ratio across different frequency bands and the reduction in eye-blinks [40]. This analysis involves dividing the average power of each frequency band by the overall average power of the entire signal to gauge the relative contribution of each frequency band to the total signal strength [40]. In addition to these parameters, we employed blink count estimation using an amplitude threshold technique, as detailed below.

Blink Count Estimation Using Amplitude Threshold

The eye-blinks in the signal are calculated using amplitude, which ensures that any large-amplitude artifacts arising from the single channel in prefrontal region can be attributed to eye-blinks or eye movements. Any signal amplitude value exceeding a threshold would be considered as an eye-blink [41]. We experimented by varying the constant parameter from 1 to 10 for Fp1 and Fp2 electrodes of three subjects. The ground truth of eye-blink count obtained from the CameraEEG [33] video data was used for cross-examining the various counts from the amplitude threshold formula. The counted eye-blinks were also manually cross-checked with the CameraEEG video data. We observed that the constant parameter of 6 matched with the ground truth eye-blink count. A minimum distance between values exceeding this blink amplitude threshold was used to differentiate one eye-blink from another and to avoid multiple detections of a single blink event [41]. The minimum peak distance and threshold values were varied until the expected separation and occurrence of eye-blinks was reached for the EEG signals used in this study. Therefore, the blink amplitude threshold used was determined as given in Equation (7) and the minimum distance between subsequent peaks was set at 250 ms [42].

$$Blink\ Amplitude\ Threshold = 6 \times \frac{\sum_{i=1}^{n} |x_i|}{n} \tag{7}$$

where x is the amplitude of the signal at sample number i with total sample points n.

The eye-blinks are counted in this manner for the single channel EEG data before and after application of E-ASR. The large amplitude artifacts were calculated for each subject (Fp1 and Fp2). The percentage reduction in artifacts was calculated as given in Equation (8).

$$Percentage\ reduction = \frac{Before\ ASR - After\ ASR}{Before\ ASR} \times 100 \tag{8}$$

4. Results

4.1. Construction of Semi-Simulated Single Channel EEG and Eye-Blink Artifact

We created a semi-simulated dataset as given in [27] for testing the proposed method. The EEG signals were acquired using the Smarting device, sampled at 500 Hz with a resolution of 24 bits [5]. Two clean EEG segments about ten seconds long, without eye-blinks, are manually identified and extracted from Fp1 channel of subject 4. These two segments are then replicated and concatenated to a form 1-minute-long ground truth single-channel EEG signal. Further, two eye-blink artifacts are manually segmented and extracted from the same dataset, which is about 2 s long. To achieve a consistent signal length of 10 s, we extended the isolated eye-blink segments by adding zeros on both ends. Each clean segment is combined with one eye-blink segment using Equation (9):

$$z = s + \propto m \tag{9}$$

where z is the semi-simulated contaminated EEG segment, s is the clean EEG segment, m is the eye-blink segment, and $\propto$ is the mixing coefficient that controls the signal-to-noise ratio (SNR) of the constructed noisy signal [39,40]. The mixing coefficient $\propto$ can be calculated using Equation (10):

$$SNR = 10log\left(\frac{RMS(s)}{RMS(\propto m)}\right) \tag{10}$$

The SNR values were considered within the range −7 dB to 2 dB to calculate $\propto$ [40]. The root mean square (RMS) is given by Equation (11):

$$RMS(s) = \sqrt{\frac{1}{n}\sum_{i=1}^{n} s_i^2} \tag{11}$$

Four variations were created by combining these clean and eye-blink segments in different orders. Finally, these were combined to create a 1 min semi-simulated contaminated EEG signal. Figure 3 shows the schematic representation of the steps involved in creating semi-simulated signal.

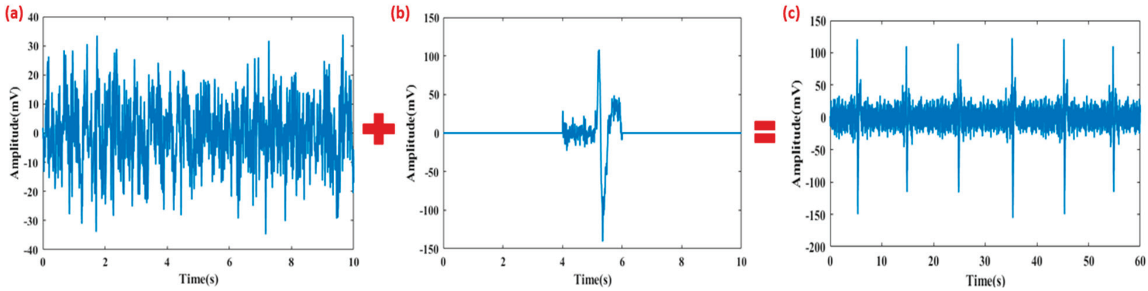

Figure 3. Framework for creating semi-simulated signal: (**a**) 10 s clean EEG segment from subject 4, (**b**) eye-blink, and (**c**) superposition of both clean EEG and eye-blink to create semi-simulated signal.

4.2. Results with Semi-Simulated Single Channel EEG Signal

The superposition plots of semi-simulated contaminated EEG, E-ASR-cleaned, and ground truth signal using the proposed method are shown in Figure 4.

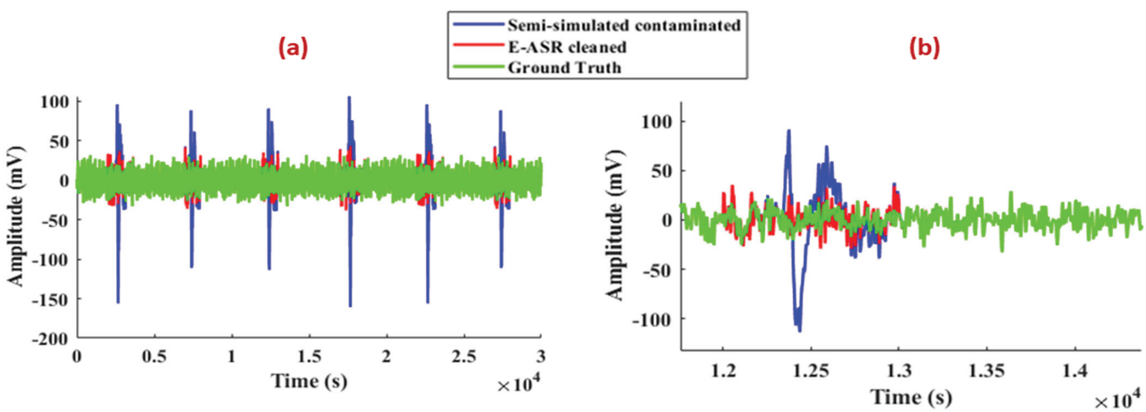

Figure 4. The superposition plots of semi-simulated contaminated EEG, E-ASR-cleaned, and ground truth signal using the proposed algorithm: (**a**) plot for 1 min time duration signal; (**b**) zoomed version of (**a**) showing one eye-blink.

It can be observed from Figure 4b that the eye-blinks are visibly reduced after applying E-ASR to the contaminated signal. An RRMSE of 43.87% and a CC of 0.91 were achieved for E-ASR when applied to the semi-simulated signal. To enable a comparison with the state-of-the-art ASR algorithm, an additional semi-simulated signal was generated, forming a two-channel dataset. ASR was then applied to this two-channel semi-simulated dataset, and its performance was assessed by calculating the RRMSE and CC for the first channel of the ASR-cleaned data, yielding an RRMSE of 56.82% and a CC of 0.85. To assess how well our method performed across different EEG frequencies, we analyzed the average power distribution within each band relative to the entire spectrum for eyeblink artifact removal (Table 1). We focused on the delta (0.5–4 Hz), theta (4–8 Hz), alpha (8–13 Hz), beta (13–30 Hz), and gamma (30–100 Hz) bands, encompassing the whole 0.5–100 Hz range. We also counted the eye-blinks using Equation (7); the semi-simulated contaminated signal contained six eye-blinks and E-ASR effectively removed all of them.

Table 1. Average power distribution of EEG frequency bands for semi-simulated contaminated signal, ground truth, and E-ASR-cleaned signal.

Frequency Bands	Contaminated EEG	E-ASR-Cleaned EEG	Ground Truth EEG
Delta (0.5–4)	0.63	**0.21**	0.23
Theta (4–8)	0.14	**0.14**	0.15
Alpha (8–13)	0.04	**0.10**	0.10
Beta (13–30)	0.15	**0.44**	0.41
Gamma (30–100)	0.04	**0.12**	0.10

4.3. Results with Real EEG Signals

Unlike simulated data where we have a perfect version of the signal, real EEG recordings lack a ground truth. Therefore, to assess our method's performance, we manually identified sections of the recordings (from 5 min eyes-open data) that did not contain artifacts and concatenated them to obtain an artifact-free signal of 1 min. To evaluate the effectiveness of our method, we calculated the RRMSE and CC between the artifact-free signal and its E-ASR-cleaned version, as shown in Table 2. It demonstrates that the method consistently achieves high correlation (CC values close to 0.9) while maintaining reasonable error levels (RRMSE) across all subjects and channels. We also show the comparison of average power ratio between these two signals for all subjects in Figure 5.

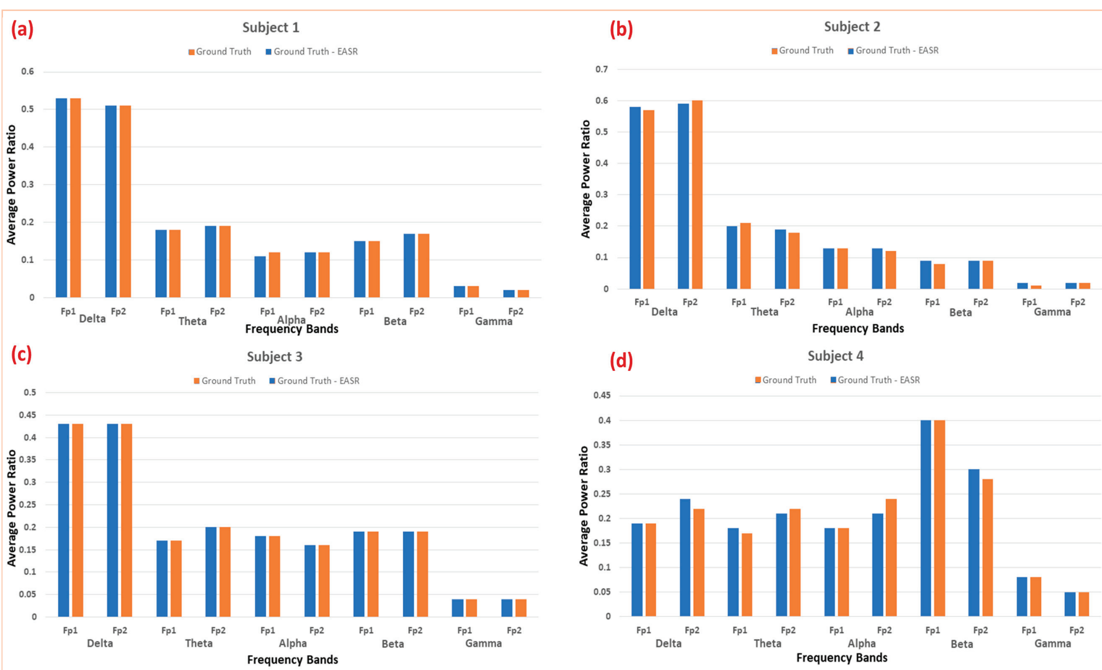

Figure 5. Comparison of average power ratio between the artifact-free signal and its E-ASR-cleaned version for all subjects. The E-ASR algorithm successfully restored the power distribution across the EEG spectrum for each subject (**a**–**d**).

We sought to evaluate the performance of the proposed EASR algorithm against the original ASR algorithm. The 24-channel data we originally collected was cleaned by the ASR algorithm. In contrast, for application of E-ASR, a single channel was used from the

24-channel montage. The ASR-cleaned Fp1 and Fp2 channels were considered for the time domain comparison with the proposed EASR algorithm in Figure 6. Eye-blinks exhibit a distinctive peak that becomes evident in time-domain EEG signals. Notably, the distinct peaks corresponding to eye-blinks in the signal are eradicated after the application of E-ASR. Table 3 presents the number of eye-blinks recorded before and after the application of E-ASR for each subject. All subjects demonstrated a complete elimination of eye-blinks post-E-ASR, indicating a 100% reduction. The computational time reflects the duration taken for processing, varying slightly among subjects. Also, the generality of the framework is shown by considering different sampling frequency and electrode locations (Appendix A: Tables A1 and A2).

Table 2. RRMSE and CC between the artifact-free signal and its E-ASR-cleaned version.

Subject	Channel	RRMSE (%)	CC
1	Fp1	41.06	0.91
	Fp2	38.72	0.92
2	Fp1	47.37	0.88
	Fp2	52.07	0.86
3	Fp1	46.26	0.89
	Fp2	45.98	0.89
4	Fp1	43.53	0.90
	Fp2	40.45	0.91

Table 3. Change in number of eye-blinks before and after E-ASR on 1 min single-channel real EEG data for all subjects. Their computational time is also reported.

Subject	Channel	No. of Eye-Blinks Before E-ASR	No. of Eye-Blinks After E-ASR	Percentage Reduction of Eye-Blinks (%)	Computational Time (Seconds)
Subject 1	Fp1	9	0	100	5.2
	Fp2	9	0	100	4.9
Subject 2	Fp1	8	0	100	5.3
	Fp2	4	0	100	5.3
Subject 3	Fp1	14	0	100	5.6
	Fp2	16	0	100	5.4
Subject 4	Fp1	7	0	100	4.7
	Fp2	7	0	100	4.5

To illustrate the impact of applying E-ASR to a single channel, topographic plots were generated at a specific time point during which the subject exhibited an eye-blink. Figure 7A illustrates that in the absence of ASR application, distinct high-amplitude peaks (dark red regions) were observed in the prefrontal region from eye-blinks [43]. Upon applying single-channel E-ASR to Fp1, the resulting ASR-cleaned channel was used in the 24-channel EEG configuration for the purpose of generating topographic plots.

The associated scalp map in Figure 7B demonstrates the successful removal of the blink artifact from Fp1. However, Fp2 continued to have blink-related activity. E-ASR was also independently applied on both Fp1 and Fp2 electrodes, and we observed effective elimination of the eye-blink activity, as depicted in Figure 7C. This suggests that the single-channel E-ASR framework is reasonably effective in removing artifact content.

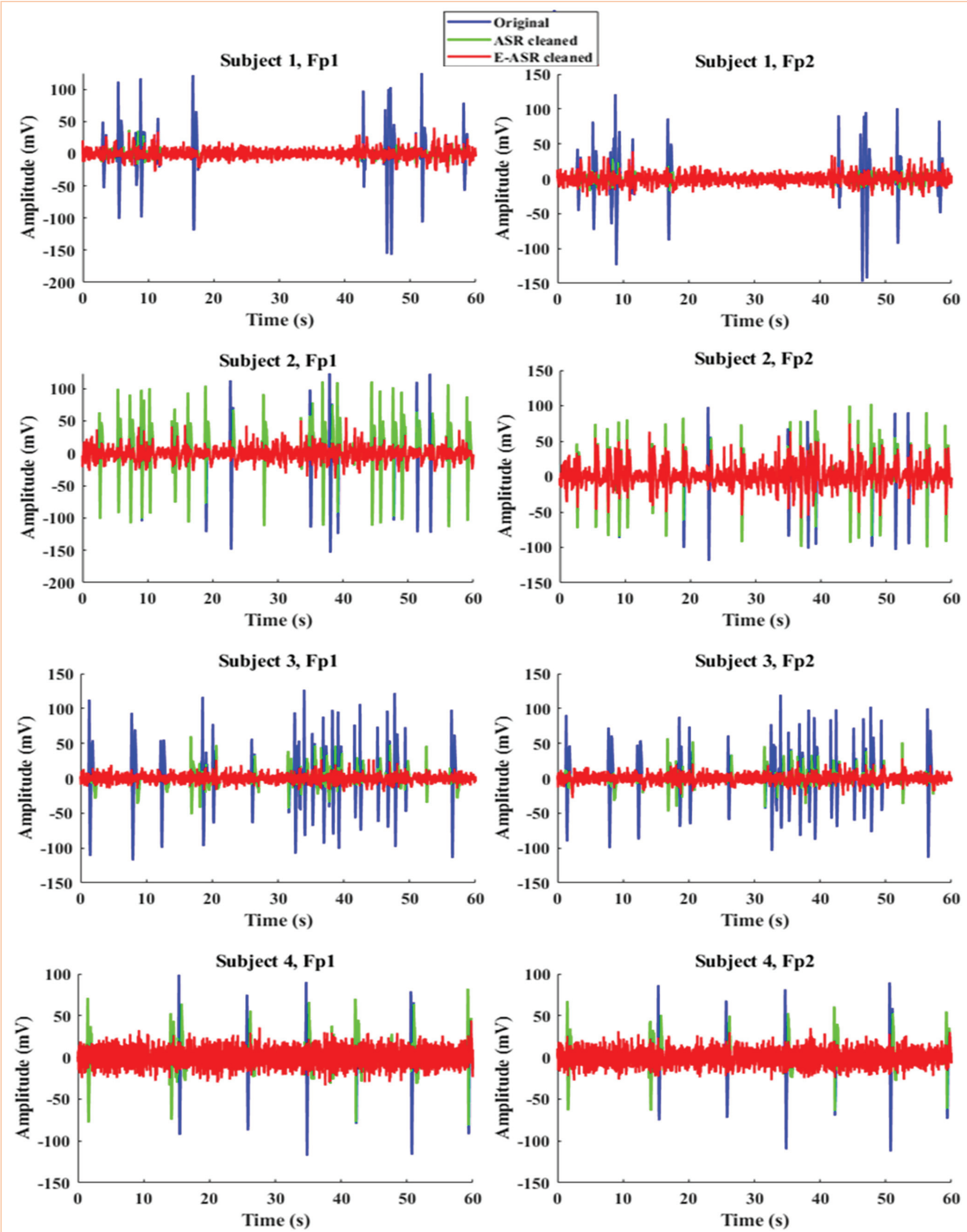

Figure 6. Time-domain comparison of original (blue), ASR-cleaned (green), and E-ASR-cleaned (red) on Fp1 and Fp2 channels across all subjects.

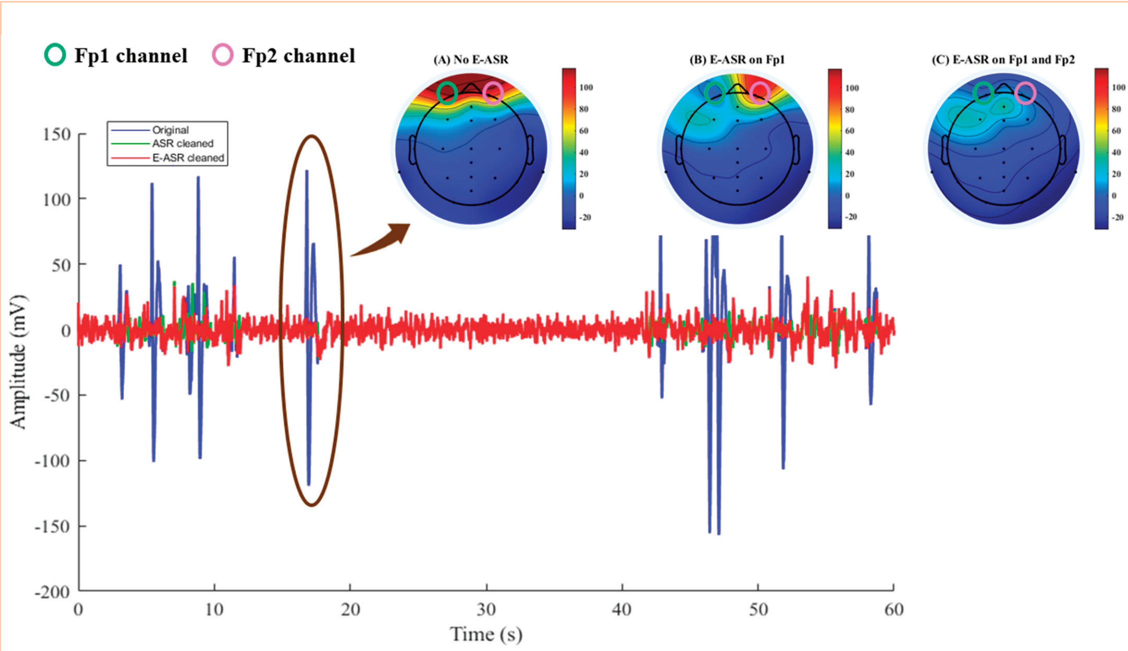

Figure 7. Spatial distribution of source activities at an eye-blink time point for (**A**) no E-ASR, (**B**) E-ASR only applied on Fp1, and (**C**) E-ASR applied on Fp1 and Fp2 channels of subject 1. Red indicates the presence of an eye-blink artifact whereas blue indicates the absence. The green circle indicates the location of Fp1 electrode and pink indicates the location of Fp2 electrode.

5. Discussion

The developed framework aims to explore the efficacy of a novel Embedded Artifact Subspace Reconstruction (E-ASR) for addressing artifact removal for single-channel EEG data. The concept draws inspiration from dynamical embedding, initially proposed for single-channel ICA in the separation of ocular artifacts [36]. This idea was extended to create an embedding matrix from single-channel EEG data for implementing an artifact subspace reconstruction algorithm. Notably, while ASR has been successfully applied in a multichannel setting on an android smartphone [6], this study investigates the implementation of ASR specifically for single-channel EEG data. The primary goal was to assess the performance of the E-ASR framework by employing metrics such as RRMSE, CC, average power ratio, and percentage reduction in eye-blinks. We used an embedding dimension of 90 and lag ($L = 1$) for the proposed work, as in [32,44].

The application of the E-ASR algorithm on semi-simulated EEG data demonstrated highly promising results (Figure 4). The algorithm successfully removed 100% of the eye-blink artifacts, as evidenced by the achieved RRMSE of 43.87% and a high correlation coefficient (CC) of 0.91. These metrics suggest that the E-ASR method not only effectively eliminates artifacts but also retains the essential features of the original EEG signal, which is crucial for maintaining data integrity. To compare its performance with the state-of-the-art ASR algorithm, a two-channel semi-simulated dataset was generated. ASR was applied to this dataset, and its performance was evaluated by calculating the RRMSE and CC for the first channel of the ASR-cleaned data. This resulted in a higher RRMSE of 56.82% and a lower CC of 0.85. These findings suggest that E-ASR outperforms ASR, offering a more optimal balance between artifact reduction and signal preservation. Eye-blink artifacts predominantly interfere with the low-frequency EEG bands (0–12 Hz) [27,42], often leading to a shift in power distribution towards the delta band and subsequently weakening other frequency bands. This effect was evident when we introduced eye-blink artifacts into the semi-simulated data. However, the E-ASR algorithm managed to restore the power balance across the EEG spectrum, as observed in Table 1. Specifically, the power distribution in the delta, theta, alpha, beta, and gamma bands of the E-ASR-cleaned signal closely matched that of the ground truth, indicating that our method effectively mitigates the distortions caused by eye-blinks without compromising the inherent frequency characteristics of the EEG signal.

Real EEG recordings inherently lack a definitive ground truth, making the evaluation of artifact removal methods particularly challenging. In this study, we addressed this issue by manually constructing a 1 min artifact-free signal from clean sections of the EEG recordings. By comparing this signal with the E-ASR-cleaned version, we calculated the relative root mean square error (RRMSE) and correlation coefficient (CC) to quantify the performance of our method. The obtained mean RRMSE of 44.43% and a CC of 0.89 (from Table 2) indicate that our E-ASR algorithm performs consistently well in preserving the underlying signal characteristics while effectively reducing artifacts.

In real EEG data, the variability and complexity of eye-blinks are more pronounced, making artifact removal more challenging. Despite this, the E-ASR algorithm demonstrated robustness when applied to real EEG signals (Figure 6), effectively eliminating the distinct peaks associated with eye-blinks. This result suggests that the E-ASR method is capable of handling the dynamic nature of eye-blink artifacts in real-world scenarios, further emphasizing its practical applicability. The complete elimination of eye-blink artifacts, as demonstrated by the 100% reduction in eye-blinks across all subjects (Table 3), underscores the efficacy of the E-ASR algorithm. Eye-blinks are particularly problematic in EEG analysis, as they can obscure the brain activity of interest. Our results not only confirm the robustness of E-ASR in mitigating such artifacts but also highlight its potential utility in improving the quality of EEG data for subsequent analyses, such as event-related potentials or brain connectivity studies.

The results from applying E-ASR to 1 min segments of real EEG data (Table 3) revealed a complete (100%) reduction in eye-blinks. Although we have not yet conducted real-time implementation, we have provided the computational time required for our algorithm to run on a desktop computer using MATLAB software, version 2022b. The average processing time was measured at 5.14 s for 1 min of EEG data. While the original ASR algorithm requires slightly less computational time for the same data with equivalent sampling frequency, it is important to note that ASR cannot be applied to single-channel data. The difference in processing time primarily arises from the embedding and reconstruction steps in the E-ASR algorithm. Overall, the balance between effectiveness and processing time underscores the practicality of the E-ASR algorithm in mitigating eye-blink artifacts without significantly compromising information.

Additionally, the comparison of the E-ASR performance with the traditional ASR algorithm provided valuable insights into the advantages of our method. While ASR demonstrated some effectiveness in cleaning the EEG data, the persistence of eye-blink activity in Figure 6 after its application highlights the limitations of conventional methods. In contrast, the E-ASR algorithm's ability to fully eliminate eye-blinks from both Fp1 and Fp2 channels illustrates its superior capacity for artifact removal. The topographic plots (in Figure 7) further illustrate the impact of E-ASR in enhancing the clarity of EEG data. The absence of distinct high-amplitude peaks in the prefrontal region after applying E-ASR not only validates our approach but also emphasizes its potential relevance in clinical and research settings. The preservation of brain activity during periods of blinks could significantly improve the interpretability of EEG results and contribute to more accurate clinical assessments and cognitive neuroscience research.

6. Conclusions

In this paper, we present a novel approach for implementing ASR on single-channel EEG data. We generated a multichannel dataset by time-lagging prefrontal single-channel EEG data, known as dynamical embedding. We evaluated the effectiveness of the E-ASR method in removing eye-blink artifacts from this *EmbeddedMatrix*. Our findings reveal that the proposed E-ASR method achieved an average reduction of 100% in detected eye-blinks for the real dataset. This significant result underscores how eye-blink artifacts can interfere with the analysis of neural activity, potentially leading to misleading interpretations. The complete removal of these artifacts enhances the quality and reliability of EEG signals, making the data more suitable for subsequent analyses, such as cognitive assessments and clinical diagnostics. Furthermore, this achievement demonstrates the E-ASR algorithm's robustness in handling the variability inherent in real-world data, suggesting its potential as a standard pre-processing tool in EEG studies. Importantly, the algorithm also maintained the integrity of the underlying neural signals, as evidenced by consistent correlation coefficients and reduced relative root mean square error. Additionally, we used an embedding dimension value of 90 for the current dataset. Utilizing the ASR algorithm with a cut-off parameter of 17 ensured the preservation of brain activity.

The embedding dimension (M) plays a crucial role in the E-ASR algorithm. It determines the lowest frequency that can be extracted from the spectral decomposition of the *EmbeddedMatrix*. Exploring the effect of M on performance metrics is a promising avenue for future research. Additionally, computational efficiency is also linked to the embedding dimension. As a result, reducing M can potentially lead to faster processing times.

The framework's minimal channel requirements facilitate straightforward implementation, providing a practical advantage. Along with its performance and minimal electrode requirement, the novel single-channel E-ASR algorithm may be well suited for integration into a smartphone android application. We speculate that forthcoming natural environment EEG applications may see advantages in using this framework. To further validate these findings, future research should encompass more extensive investigations involving larger datasets.

Author Contributions: C.N.G. proposed the E-ASR algorithm idea to D.H. Then, the entire framework was built by D.H. and the verification was done by D.H., K.N.V. and C.N.G. The manuscript was written by D.H., C.N.G. and K.N.V.; R.R. contributed to discussions and revisions of the first written draft and later versions. All authors have read and agreed to the published version of the manuscript.

Funding: DH and KNV are funded by the MoE doctoral scholarship and NEWGEN-IEDC, DST, Project no.—D4, 2023–2024 from the Government of India. CNG's time was funded by NEWGEN-IEDC, Project no.—D4, 2023–2024. R.R's time was funded by Project ID: NHRP-Suicide/DL/MH-3/2024. IIT Guwahati and AIIMS Guwahati contributed equally to the APC funding.

Institutional Review Board Statement: This study was conducted in accordance with the Declaration of Helsinki and approved by the Institutional Ethics Committee of IIT Guwahati for recording data from human participants.

Informed Consent Statement: Informed consent was obtained from all subjects involved in this study.

Data Availability Statement: The MATLAB code developed for this work is available at our GitHub link below (accessed on 28 June 2024): https://github.com/NeuralLabIITGuwahati/E-ASR. Real electroencephalogram data for one subject is also provided as a .mat file.

Conflicts of Interest: The authors declare no conflicts of interest.

Appendix A

Table A1. Eye-blinks and computational time corresponding to occipital, temporal, parietal, and midline central electrodes for all subjects.

Subject	Channel	No. of Eye-Blinks Before E-ASR	No. of Eye-Blinks After E-ASR	Computational Time
Subject 1	O2	0	0	4.88
	T8	0	0	4.82
	P7	0	0	4.98
	Cz	1	1	4.90
Subject 2	O2	2	2	4.67
	T8	0	0	4.65
	P7	1	1	4.69
	Cz	0	0	4.73
Subject 3	O2	0	0	4.80
	T8	0	0	4.65
	P7	0	0	4.67
	Cz	0	0	4.84
Subject 4	O2	0	0	4.64
	T8	0	0	4.62
	P7	0	0	4.72
	Cz	0	0	4.67

Table A2. E-ASR results of 250 Hz sampling frequency for all subjects.

Subject	Channel	No. of Eye-Blinks Before E-ASR	No. of Eye-Blinks After E-ASR	Computational Time (Seconds)
1	Fp1	6	0	1.44
	Fp2	9	0	1.45
2	Fp1	8	0	1.29
	Fp2	5	2	1.50
3	Fp1	15	0	1.42
	Fp2	16	0	1.32
4	Fp1	7	0	1.35
	Fp2	7	0	1.23

References

1. Cohen, M.X. *Analyzing Neural Time Series Data: Theory and Practice*; MIT Press: Cambridge, MA, USA, 2014. [CrossRef]
2. Gwin, J.T.; Gramann, K.; Makeig, S.; Ferris, D.P. Removal of Movement Artifact From High-Density EEG Recorded during Walking and Running. *J. Neurophysiol.* **2010**, *103*, 3526–3534. [CrossRef]
3. Hazarika, D.; Chanda, S.; Gupta, C.N. Smartphone-Based Natural Environment Electroencephalogram Experimentation-Opportunities and Challenges. In Proceedings of the 2022 IEEE-EMBS Conference on Biomedical Engineering and Sciences (IECBES), Kuala Lumpur, Malaysia, 7–9 December 2022; pp. 370–375.

4. Hölle, D.; Bleichner, M.G. Smartphone-Based Ear-Electroencephalography to Study Sound Processing in Everyday Life. *Eur. J. Neurosci.* **2023**, *58*, 3671–3685. [CrossRef]
5. Wireless EEG Headset—Smarting—Mbt | Mbraintrain. Available online: https://mbraintrain.com/smarting-wireless-eeg/ (accessed on 20 September 2023).
6. Smarting PRO Line for Neuroscience—Mbt | MBrainTrain. Available online: https://mbraintrain.com/smarting-pro-line/ (accessed on 20 September 2023).
7. Ridwan, S.D.; Thompson, R.; Jap, B.T.; Lal, S.; Fischer, P. Single Channel Wireless EEG: Proposed Application in Train Drivers. In Proceedings of the 2008 Third International Conference on Broadband Communications, Information Technology & Biomedical Applications, Pretoria, South Africa, 23–26 November 2008; pp. 58–63.
8. Koley, B.; Dey, D. An Ensemble System for Automatic Sleep Stage Classification Using Single Channel EEG Signal. *Comput. Biol. Med.* **2012**, *42*, 1186–1195. [CrossRef]
9. Salyers, J.B.; Dong, Y.; Gai, Y. Continuous Wavelet Transform for Decoding Finger Movements From Single-Channel EEG. *IEEE Trans. Biomed. Eng.* **2019**, *66*, 1588–1597. [CrossRef]
10. Ogino, M.; Kanoga, S.; Muto, M.; Mitsukura, Y. Analysis of Prefrontal Single-Channel EEG Data for Portable Auditory ERP-Based Brain–Computer Interfaces. *Front. Hum. Neurosci.* **2019**, *13*, 250. [CrossRef]
11. Wang, P.; Min, J.; Hu, J. Ensemble Classifier for Driver's Fatigue Detection Based on a Single EEG Channel. *IET Intell. Transp. Syst.* **2018**, *12*, 1322–1328. [CrossRef]
12. Kasim, Ö.; Tosun, M. Effective Removal of Eye-Blink Artifacts in EEG Signals with Semantic Segmentation. *Signal Image Video Process.* **2022**, *16*, 1289–1295. [CrossRef]
13. Chang, W.-D.; Cha, H.-S.; Kim, K.; Im, C.-H. Detection of Eye Blink Artifacts from Single Prefrontal Channel Electroencephalogram. *Comput. Methods Programs Biomed.* **2016**, *124*, 19–30. [CrossRef]
14. Ofner, P.; Schwarz, A.; Pereira, J.; Wyss, D.; Wildburger, R.; Müller-Putz, G.R. Attempted Arm and Hand Movements Can Be Decoded from Low-Frequency EEG from Persons with Spinal Cord Injury. *Sci. Rep.* **2019**, *9*, 7134. [CrossRef]
15. Lin, C.-T.; Chung, I.-F.; Ko, L.-W.; Chen, Y.-C.; Liang, S.-F.; Duann, J.-R. EEG-Based Assessment of Driver Cognitive Responses in a Dynamic Virtual-Reality Driving Environment. *IEEE Trans. Biomed. Eng.* **2007**, *54*, 1349–1352. [CrossRef]
16. Ofner, P.; Schwarz, A.; Pereira, J.; Müller-Putz, G.R. Upper Limb Movements Can Be Decoded from the Time-Domain of Low-Frequency EEG. *PLoS ONE* **2017**, *12*, e0182578. [CrossRef]
17. Kothe, C.A.E.; Jung, T.-P. Artifact Removal Techniques with Signal Reconstruction. U.S. Patent Application No. 14/895,440, 28 April 2016.
18. Chang, C.-Y.; Hsu, S.-H.; Pion-Tonachini, L.; Jung, T.-P. Evaluation of Artifact Subspace Reconstruction for Automatic Artifact Components Removal in Multi-Channel EEG Recordings. *IEEE Trans. Biomed. Eng.* **2020**, *67*, 1114–1121. [CrossRef]
19. Cataldo, A.; Criscuolo, S.; De Benedetto, E.; Masciullo, A.; Pesola, M.; Schiavoni, R.; Invitto, S. A Method for Optimizing the Artifact Subspace Reconstruction Performance in Low-Density EEG. *IEEE Sens. J.* **2022**, *22*, 21257–21265. [CrossRef]
20. Blum, S.; Jacobsen, N.S.J.; Bleichner, M.G.; Debener, S. A Riemannian Modification of Artifact Subspace Reconstruction for EEG Artifact Handling. *Front. Hum. Neurosci.* **2019**, *13*, 141. [CrossRef]
21. Plechawska-Wojcik, M.; Kaczorowska, M.; Zapala, D. The Artifact Subspace Reconstruction (ASR) for EEG Signal Correction. A Comparative Study. In *Information Systems Architecture and Technology: Proceedings of the 39th International Conference on Information Systems Architecture and Technology—ISAT 2018, Nysa, Poland, 16–18 September 2018*; Świątek, J., Borzemski, L., Wilimowska, Z., Eds.; Springer International Publishing: Cham, Switzerland, 2019; pp. 125–135.
22. Anders, P.; Müller, H.; Skjæret-Maroni, N.; Vereijken, B.; Baumeister, J. The Influence of Motor Tasks and Cut-off Parameter Selection on Artifact Subspace Reconstruction in EEG Recordings. *Med. Biol. Eng. Comput.* **2020**, *58*, 2673–2683. [CrossRef]
23. Teixeira, A.R.; Tome, A.M.; Lang, E.W.; Gruber, P.; Martins da Silva, A. On the Use of Clustering and Local Singular Spectrum Analysis to Remove Ocular Artifacts from Electroencephalograms. In Proceedings of the 2005 IEEE International Joint Conference on Neural Networks, Montreal, QC, Canada, 31 July–4 August 2005; Volume 4, pp. 2514–2519.
24. Maddirala, A.K.; Shaik, R.A. Removal of EOG Artifacts From Single Channel EEG Signals Using Combined Singular Spectrum Analysis and Adaptive Noise Canceler. *IEEE Sens. J.* **2016**, *16*, 8279–8287. [CrossRef]
25. Peng, H.; Hu, B.; Shi, Q.; Ratcliffe, M.; Zhao, Q.; Qi, Y.; Gao, G. Removal of Ocular Artifacts in EEG—An Improved Approach Combining DWT and ANC for Portable Applications. *IEEE J. Biomed. Health Inform.* **2013**, *17*, 600–607. [CrossRef]
26. Maddirala, A.K.; Shaik, R.A. Separation of Sources From Single-Channel EEG Signals Using Independent Component Analysis. *IEEE Trans. Instrum. Meas.* **2018**, *67*, 382–393. [CrossRef]
27. Maddirala, A.K.; Veluvolu, K.C. Eye-Blink Artifact Removal from Single Channel EEG with k-Means and SSA. *Sci. Rep.* **2021**, *11*, 11043. [CrossRef]
28. Noorbasha, S.K.; Sudha, G.F. Removal of EOG Artifacts and Separation of Different Cerebral Activity Components from Single Channel EEG—An Efficient Approach Combining SSA–ICA with Wavelet Thresholding for BCI Applications. *Biomed. Signal Process. Control* **2021**, *63*, 102168. [CrossRef]
29. Dora, M.; Holcman, D. Adaptive Single-Channel EEG Artifact Removal with Applications to Clinical Monitoring. *IEEE Trans. Neural Syst. Rehabil. Eng.* **2022**, *30*, 286–295. [CrossRef]
30. Ogino, M.; Mitsukura, Y. Portable Drowsiness Detection through Use of a Prefrontal Single-Channel Electroencephalogram. *Sensors* **2018**, *18*, 4477. [CrossRef]

31. Bachmann, M.; Päeske, L.; Kalev, K.; Aarma, K.; Lehtmets, A.; Ööpik, P.; Lass, J.; Hinrikus, H. Methods for Classifying Depression in Single Channel EEG Using Linear and Nonlinear Signal Analysis. *Comput. Methods Programs Biomed.* **2018**, *155*, 11–17. [CrossRef]
32. James, C.J.; Lowe, D. Extracting Multisource Brain Activity from a Single Electromagnetic Channel. *Artif. Intell. Med.* **2003**, *28*, 89–104. [CrossRef]
33. Hazarika, D.; Madhavan, S.; Gupta, C.N. CameraEEG: Synchronous Recording of Electroencephalogram and Video Data for Neuroergonomics Applications. *Eng. Proc.* **2023**, *55*, 46. [CrossRef]
34. Home—Easycap GmbH | EEG Recording Caps and Related Products. Available online: https://www.easycap.de/ (accessed on 6 October 2024).
35. Chang, C.-Y.; Hsu, S.-H.; Pion-Tonachini, L.; Jung, T.-P. Evaluation of Artifact Subspace Reconstruction for Automatic EEG Artifact Removal. In Proceedings of the 2018 40th Annual International Conference of the IEEE Engineering in Medicine and Biology Society (EMBC), Honolulu, HI, USA, 18–21 July 2018; pp. 1242–1245.
36. Davies, M.E.; James, C.J. Source Separation Using Single Channel ICA. *Signal Process.* **2007**, *87*, 1819–1832. [CrossRef]
37. Maddirala, A.K.; Shaik, R.A. Motion Artifact Removal from Single Channel Electroencephalogram Signals Using Singular Spectrum Analysis. *Biomed. Signal Process. Control* **2016**, *30*, 79–85. [CrossRef]
38. Delorme, A.; Makeig, S. EEGLAB: An Open Source Toolbox for Analysis of Single-Trial EEG Dynamics Including Independent Component Analysis. *J. Neurosci. Methods* **2004**, *134*, 9–21. [CrossRef]
39. Maddirala, A.K.; Veluvolu, K.C. SSA with CWT and K-Means for Eye-Blink Artifact Removal from Single-Channel EEG Signals. *Sensors* **2022**, *22*, 931. [CrossRef]
40. Acharjee, R.; Ahamed, S.R. Automatic Eyeblink Artifact Removal from Single Channel EEG Signals Using One-Dimensional Convolutional Denoising Autoencoder. In Proceedings of the 2024 International Conference on Computer, Electrical & Communication Engineering (ICCECE), Kolkata, India, 2–3 February 2024; pp. 1–7.
41. Aarabi, A.; Kazemi, K.; Grebe, R.; Moghaddam, H.A.; Wallois, F. Detection of EEG Transients in Neonates and Older Children Using a System Based on Dynamic Time-Warping Template Matching and Spatial Dipole Clustering. *NeuroImage* **2009**, *48*, 50–62. [CrossRef]
42. Halder, S.; Bensch, M.; Mellinger, J.; Bogdan, M.; Kübler, A.; Birbaumer, N.; Rosenstiel, W. Online Artifact Removal for Brain-Computer Interfaces Using Support Vector Machines and Blind Source Separation. *Comput. Intell. Neurosci.* **2007**, *2007*, e82069. [CrossRef]
43. Hoffmann, S.; Falkenstein, M. The Correction of Eye Blink Artefacts in the EEG: A Comparison of Two Prominent Methods. *PLoS ONE* **2008**, *3*, e3004. [CrossRef]
44. Balli, T.; Palaniappan, R. Classification of Biological Signals Using Linear and Nonlinear Features. *Physiol. Meas.* **2010**, *31*, 903. [CrossRef]

MDPI AG
Grosspeteranlage 5
4052 Basel
Switzerland
Tel.: +41 61 683 77 34

Sensors Editorial Office
E-mail: sensors@mdpi.com
www.mdpi.com/journal/sensors

MDPI

Academic Open
Access Publishing

mdpi.com

ISBN 978-3-7258-3608-6